THE FUTURE OF NUCLEAR STRUCTURE: CHALLENGES AND OPPORTUNITIES IN THE MICROSCOPIC DESCRIPTION OF NUCLEI

EDITED BY: Luigi Coraggio, Saori Pastore and Carlo Barbieri
PUBLISHED IN: Frontiers in Physics

frontiers Research Topics

frontiers

ISSN 1664-8714
ISBN 978-2-88966-585-3
DOI 10.3389/978-2-88966-585-3

About Frontiers

Frontiers is more than just an open-access publisher of scholarly articles: it is a pioneering approach to the world of academia, radically improving the way scholarly research is managed. The grand vision of Frontiers is a world where all people have an equal opportunity to seek, share and generate knowledge. Frontiers provides immediate and permanent online open access to all its publications, but this alone is not enough to realize our grand goals.

Frontiers Journal Series

The Frontiers Journal Series is a multi-tier and interdisciplinary set of open-access, online journals, promising a paradigm shift from the current review, selection and dissemination processes in academic publishing. All Frontiers journals are driven by researchers for researchers; therefore, they constitute a service to the scholarly community. At the same time, the Frontiers Journal Series operates on a revolutionary invention, the tiered publishing system, initially addressing specific communities of scholars, and gradually climbing up to broader public understanding, thus serving the interests of the lay society, too.

Dedication to Quality

Each Frontiers article is a landmark of the highest quality, thanks to genuinely collaborative interactions between authors and review editors, who include some of the world's best academicians. Research must be certified by peers before entering a stream of knowledge that may eventually reach the public - and shape society; therefore, Frontiers only applies the most rigorous and unbiased reviews.
Frontiers revolutionizes research publishing by freely delivering the most outstanding research, evaluated with no bias from both the academic and social point of view. By applying the most advanced information technologies, Frontiers is catapulting scholarly publishing into a new generation.

What are Frontiers Research Topics?

Frontiers Research Topics are very popular trademarks of the Frontiers Journals Series: they are collections of at least ten articles, all centered on a particular subject. With their unique mix of varied contributions from Original Research to Review Articles, Frontiers Research Topics unify the most influential researchers, the latest key findings and historical advances in a hot research area! Find out more on how to host your own Frontiers Research Topic or contribute to one as an author by contacting the Frontiers Editorial Office: frontiersin.org/about/contact

THE FUTURE OF NUCLEAR STRUCTURE: CHALLENGES AND OPPORTUNITIES IN THE MICROSCOPIC DESCRIPTION OF NUCLEI

Topic Editors:
Luigi Coraggio, University of Campania 'Luigi Vanvitelli', Italy
Saori Pastore, Washington University in St. Louis, United States
Carlo Barbieri, University of Surrey, United Kingdom

Citation: Coraggio, L., Pastore, S., Barbieri, C., eds. (2021). The Future of Nuclear Structure: Challenges and Opportunities in the Microscopic Description of Nuclei. Lausanne: Frontiers Media SA. doi: 10.3389/978-2-88966-585-3

Table of Contents

frontiers in Physics

EDITORIAL
published: 05 February 2021
doi: 10.3389/fphy.2020.626976

Editorial: The Future of Nuclear Structure: Challenges and Opportunities in the Microscopic Description of Nuclei

Luigi Coraggio[1]*, *Saori Pastore*[2]* and *Carlo Barbieri*[3,4,5]*

[1]Istituto Nazionale di Fisica Nucleare, Sezione di Napoli, Napoli, Italy, [2]Physics Department and McDonnell Center for the Space Sciences at Washington University in St. Louis, St. Louis, MO, United States, [3]Department of Physics, University of Surrey, Guildford, United Kingdom, [4]Dipartimento di Fisica, Universita Degli Studi di Milano, Milano, Italy, [5]INFN, Sezione di Milano, Milano, Italy

Keywords: Ab initio (calculations), nuclear theory, nuclear reactions, effective field theories, many-body physics, nuclear structure

Editorial on the Research Article

The Future of Nuclear Structure: Challenges and Opportunities in the Microscopic Description of Nuclei

OPEN ACCESS

Edited and reviewed by:
Sonia Bacca,
Johannes Gutenberg University Mainz, Germany

***Correspondence:**
Luigi Coraggio
coraggio@na.infn.it
Saori Pastore
saori.pastore@gmail.com
Carlo Barbieri
carlo.barbierio@unimi.it

Specialty section:
This article was submitted to Nuclear Physics, a section of the journal Frontiers in Physics

Received: *07 November 2020*
Accepted: *20 November 2020*
Published: *05 February 2021*

Citation:
Coraggio L, Pastore S and Barbieri C (2021) Editorial: The Future of Nuclear Structure: Challenges and Opportunities in the Microscopic Description of Nuclei. Front. Phys. 8:626976. doi: 10.3389/fphy.2020.626976

The past two decades have witnessed tremendous progress in the microscopic description of atomic nuclei. Within this approach, nuclei are described in terms of nucleons interacting via realistic two- and three-body forces, constrained to accurately reproduce a large body of data for few nucleons systems. The goal of the nuclear theory community is to gain an accurate and predictable understanding of how the properties of many-body systems, along with their dynamics and structure, emerge from internucleon correlations induced by the strong interaction.

Progress in the microscopic (or, *ab initio*) theory has been quite notable and it has been supported by two major pillars: First, thanks to the advent of Effective Field Theories (EFTs), we can now systematically develop nuclear Hamiltonians that are rooted in the fundamental properties and symmetries of the underlying theory of QCD. Second, advances in computational resources and novel powerful algorithms allow us to solve 1) the many-nucleon problem efficiently, and 2) quantify the degree of reliability of theoretical calculations and predictions. In many cases, microscopic computations achieve an accuracy that is comparable or superior to the precision delivered by current EFT interactions. This sparked a renewed interest to further broaden the focus of *ab initio* theory and address open problems in nuclear physics.

While the status of the first pillar has been recently discussed by "The Long-Lasting Quest for Nuclear Interactions: The Past, the Present and the Future" Topical Review on this Journal, here we focus on the exciting new developments in microscopic theory. At present, *ab initio* computations of nuclear structure include up to medium-mass isotopes. The heaviest systems currently reached—with different degrees of accuracy—have mass number $A \approx 140$. These computational limits are constantly being pushed forward. At the same time, the community is expanding into new directions, in particular toward the study of electroweak observables and nuclear reactions, that nowadays require predictions with an accuracy never reached before for similar mass ranges.

In collecting the contributions for this Research Topic, we sought to gather contributions from authors who could summarize the current state-of-the-art microscopic calculations in Nuclear Theory, favoring a selected but broad view over an attempt to cover every application. All presented contributions stem from well-established methods in computational nuclear structure, and indicate recent theoretical advances and prospective outlooks, challenges and opportunities for Nuclear

Theory. Most importantly, it is our hope that this collection will confer a big picture, including references to basic material, that will be valuable for young researches who intend to enter this exciting discipline.

The richness of applications in modern *ab initio* nuclear theory can be appreciated in *Hergert*'s contribution that provides us with a general overview of the most successful microscopic many-body approaches currently in use. Traditionally, the refinement and sophistication of these computational tools has given fundamental support to advance the theories of nuclear forces. Quantum Monte Carlo (QMC) techniques allow to solve the many-body Schrödinger equation with high accuracy for light nuclei up to masses A $\sim$ 16–40. *Gandolfi et al.* discuss the use of QMC methods (namely, Variational, Green's Function, and Auxiliary Diffusion Monte Carlo methods) in combination with local chiral interactions in coordinate space. QMC methods are used in lattice effective field theory, where the EFT Lagrangian is implemented in momentum space with nucleons and pions placed on a lattice. *Lee* discusses the basic features of this approach and its high potential for understanding clustering phenomena.

For heavier isotopes, *ab initio* theories can be pushed to masses A $\sim$ 140 provided that one retains only the relevant nuclear excitations, as it is done through all-orders resummations. Among these methods, the self-consistent Green's function (SCGF) theory gives direct access to the spectral information probed by a wide range of experiments as reviewed in detail by *Somà*'s contributions. Once in the region of the nuclear chart that corresponds to medium masses, open shell isotopes become the next challenge to be addressed by the theory. In fact, resolving the degeneracy in uncorrelated systems requires large scale configuration mixing. *Coraggio and Itaco* demonstrate how this can be handled by projecting the correlated many-body states into a shell model Hamiltonian, using the so-called "Q-box" formalism. A similar strategy is shared by other computational frameworks, such as coupled cluster and in-medium SRG, that are touched upon in the contribution by *Hergert*. A less conventional approach to open shells is to break SU(1) symmetry (in short, allowing for breaking particle number conservation). This is discussed by *Somà* within SCGFs and by *Tichai et al.* in the framework of many-body perturbation theory.

The remainder of this topical review focuses on selected open challenges in Nuclear Theory that require an *ab initio* approach. Two contributions show different aspect of studying infinite nucleon systems and the implications for astrophysical scenarios. *Tews* covers QMC calculations of the equation of state (EoS) of dense matter in neutron stars. With the recent observation of star mergers and the birth of multi-messenger astronomy, it has become of prime importance to understand the finite temperature properties of the EoS. *Rios* discusses this topic and how the structure of neutron matter depends on temperature, using SCGF theory.

In the quest for physics beyond the Standard Model, Nuclear Theory, and in particular accurate calculations of neutrino-nucleus interactions at all energy scaler, plays a crucial role. This is carefully analyzed by *Rocco*'s contribution that address this challenge with emphasis on impacts to neutrino oscillations experimental programs. The last contribution of this Topical Review addresses one of the hardest open challenges in the interpretation of experimental data: the lack of a truly first-principles theory that can describe *consistently* both structure and reaction processes. *Rotureau* highlights recent steps in deriving an *ab inito* optical potential using the coupled cluster method (that, together with SCGF, is one of the two possible approaches to this problem).

We are really grateful to all the scientists participating in this project and hope that the reader will enjoy this Topical Review.

AUTHOR CONTRIBUTIONS

All authors listed have made a substantial, direct, and intellectual contribution to the work and approved it for publication.

Conflict of Interest: The authors declare that the research was conducted in the absence of any commercial or financial relationships that could be construed as a potential conflict of interest.

The handling editor declared a past co-authorship with one of the authors SP.

frontiers in Physics

REVIEW
published: 07 October 2020
doi: 10.3389/fphy.2020.00379

A Guided Tour of *ab initio* Nuclear Many-Body Theory

*Heiko Hergert**

Facility for Rare Isotope Beams and Department of Physics & Astronomy, Michigan State University, East Lansing, MI, United States

Over the last decade, new developments in Similarity Renormalization Group techniques and nuclear many-body methods have dramatically increased the capabilities of *ab initio* nuclear structure and reaction theory. Ground and excited-state properties can be computed up to the tin region, and from the proton to the presumptive neutron drip lines, providing unprecedented opportunities to confront two- plus three-nucleon interactions from chiral Effective Field Theory with experimental data. In this contribution, I will give a broad survey of the current status of nuclear many-body approaches, and I will use selected results to discuss both achievements and open issues that need to be addressed in the coming decade.

Keywords: similarity renormalization group, nuclear theory, many-body theory, *ab initio* nuclear structure, *ab initio* nuclear reactions

OPEN ACCESS

Edited by:
Luigi Coraggio, National Institute of Nuclear Physics of Naples, Italy

Reviewed by:
Furong Xu, Peking University, China
Youngman Kim, Institute for Basic Science (IBS), South Korea

***Correspondence:**
Heiko Hergert
hergert@frib.msu.edu

Specialty section:
This article was submitted to Nuclear Physics, a section of the journal Frontiers in Physics

Received: *01 July 2020*
Accepted: *05 August 2020*
Published: *07 October 2020*

Citation:
Hergert H (2020) A Guided Tour of ab initio *Nuclear Many-Body Theory. Front. Phys. 8:379. doi: 10.3389/fphy.2020.00379*

1. INTRODUCTION

Over the past decade, the reach and capabilities of *ab initio* nuclear many-body theory have grown exponentially. The widespread adoption of Renormalization Group (RG) techniques, in particular the Similarity Renormalization Group (SRG) [1], and Effective Field Theory (EFT) [2–4] in the 2000s laid the foundation for these developments. Consistent two-nucleon (NN) and three-nucleon (3N) interactions from chiral EFT were quickly established as a new "standard" inputs for a variety of approaches, which made true multi-method benchmarks possible. The SRG equipped us with the ability to dial the resolution scale of nuclear interactions, accelerating model-space and many-body convergence alike. Suddenly, even (high-order) Many-Body Perturbation Theory (MBPT) became a viable tool for rapid benchmarking [5, 6], and exact diagonalization approaches were able to extend their reach into the lower *sd*-shell [7–9]. A variety of computationally efficient techniques with controlled truncations were readied, like the Self-Consistent Green's Function method (SCGF) [10], the In-Medium SRG (IMSRG) [11] and Coupled Cluster (CC) [12], the prodigal son [13, 14] who returned home after finding success in foreign lands, i.e., quantum chemistry and solid state physics.

At the start of the last decade the race was on, and **Figure 1** documents the progress that ensued. Calculations started at closed-shell nuclei [15–19] and their vicinity before extending to semi-magic isotopic chains with the development of the Multi-Reference IMSRG [20, 21] and Gor'kov SCGF [22, 23] techniques, and just a couple of years later, the use of CC [24, 25] and IMSRG [26, 27] techniques to construct valence-space interactions opened all nuclei that were amenable to Shell Model calculations for exploration. Owing to very recent developments that extend these combined approaches to multi-shell valence spaces, the open region between the nickel and tin isotopic chain is poised to be filled in rapidly [28]. Development of the no-core versions of these methods has continued as well, and made direct calculations for intrinsically deformed nuclei possible [29].

The growing reach of *ab initio* many-body methods made it possible to confront chiral NN+3N forces with a wealth of experimental data, revealing shortcomings of those interactions and sparking new efforts toward their improvement. There were other surprises along the way, some good, some bad. Due to the benchmarking capabilities and further developments in many-body theory, we are now often able to understand the reasons for the failure of certain calculations (see, e.g., reference [27])—hindsight is 2020, as they say[1].

The present collection of Frontiers in Physics contributions provides us with a timely and welcome opportunity to attempt a look back at some of the impressive results from the past decade and the developments that brought us here, as well as a look ahead at the challenges to come as we enter a new decade.

Let us conclude this section with a brief outline of the main body of this work. In section 2, I will discuss the main ingredients of modern nuclear many-body calculations: The input interactions from chiral EFT, the application of the SRG to process Hamiltonians and operators, and eventually a variety of many-body methods that are used to solve the Schrödinger equation. I will review key ideas but keep technical details to a minimum, touching only upon aspects that will become relevant again later on. Section 3 presents selected applications from the past decade, and discusses both the advances they represent as well as open issues. This will provide a starting point for section 4, which presents ideas for addressing the aforementioned issues and highlights important directions for the next decade.

Naturally, the discussion in sections 3 and 4 is highly subjective. While this work grew from a more restricted scope into a rambling, albeit not random, walk through the landscape of modern nuclear many-body theory, it still cannot encompass the field in its entirety. The upside is that this reflects the breadth of ideas that are being pursued by the *ab initio* nuclear theory community, including those with cross-disciplinary impact, as well as our community's ability to attract junior researchers. The downside is that the present work can only scratch the tip of the iceberg of impressive results from the past decade. I hope that the readers will use it as a jumping-off point for delving into the cited literature, including the contributions to this volume.

2. PLAYERS ON A STAGE: ELEMENTS OF NUCLEAR MANY-BODY THEORY

2.1. Interactions From Chiral Effective Field Theory

Quantum Chromodynamics (QCD) is the fundamental theory of the strong interaction between quarks and gluons. One of its characteristic features is that the strong coupling, which governs the strength of interaction processes, is sufficiently small to allow perturbative expansions at high energies, but large in the low-energy domain relevant for nuclear structure and dynamics [30, 31]. This makes the description of all but the lightest nuclei at the QCD level inefficient at best, and impossible at worst. However, strongly interacting matter undergoes a phase transition that leads to the confinement of quarks in composite hadronic particles, like nucleons and pions. These particles can be used as the degrees of freedom for a hierarchy of EFTs that describe the strong interaction across multiple scales.

Following Weinberg [32, 33], one can construct effective Lagrangians that consist of interactions that are consistent with the symmetries of QCD and organized by an expansion in (Q/Λ). Here, Q is a typical momentum of the interacting system, and Λ is the breakdown scale of the theory, which is associated with physics that is not explicitly resolved. In chiral EFT with explicit nucleons and pions, $\Lambda = \Lambda_\chi$ is traditionally considered to be in the range $700 - 1000$ MeV, although newer analyses of observable truncation errors using Bayesian methods favor slightly lower values [34–36]. From a chiral EFT Lagrangian, one can then construct a systematic low-momentum expansion of nuclear interactions, as shown in **Figure 2** (see references [2, 3, 32, 37, 39]). These interactions consist of (multi-)pion exchanges between nucleons, indicated by dashed lines, as well as nucleon contact interactions. The different types of vertices are proportional to the low-energy constants (LECs) of chiral EFT, which encode physics that is not explicitly resolved because it involves either a high momentum scale or excluded degrees of freedom. Eventually, one hopes to calculate these LECs directly from the underlying QCD either through matching or renormalization group evolution of the couplings (see section 2.2), but at present, the LECs are fit to experimental data [3, 4, 39–41].

The power counting scheme shown in **Figure 2** yields consistent two-, three- and higher many-nucleon interactions, and explains their empirical hierarchy, i.e., $V_{\rm NN} > V_{\rm 3N} > V_{\rm 4N} > \ldots$. Moreover, one can readily extend the chiral Lagrangian with couplings to the electroweak sector by gauging the derivatives. In this way, nuclear interactions and electroweak currents depend on the same LECs, and one can use electroweak observables to constrain their values [42–45]. Last but not least, the existence of a power counting scheme offers inherent diagnostics for assessing the theoretical uncertainties that result from working at a given chiral order [34–36]. This is especially useful since issues relating to the regularization and renormalization of these interactions remain (see, e.g., references [2, 46–51] and section 4.4).

2.2. The Similarity Renormalization Group

Renormalization group methods are a natural companion to the hierarchy of EFTs for the strong interaction. They provide the means to systematically dial the resolution scales and cutoffs of these theories, and this makes it possible, at least in principle, to connect the different levels in our hierarchy of EFTs. The RGs also expand the diagnostic toolkit for assessing the inherent consistency of EFT power counting schemes, e.g., by tracing the enhancement or suppression of specific operators, or by identifying important missing operators.

In nuclear many-body theory, the SRG has become the method of choice. In contrast to Wilsonian RG [52], which is based on *decimation*, i.e., integrating out high-momentum degrees of freedom, SRGs decouple low- and high-momentum physics using continuous unitary transformations. Note that this concept is not limited to RG applications: we can construct

[1] This exhausts my contractually allowed contingent of 2020 vision puns, I swear.

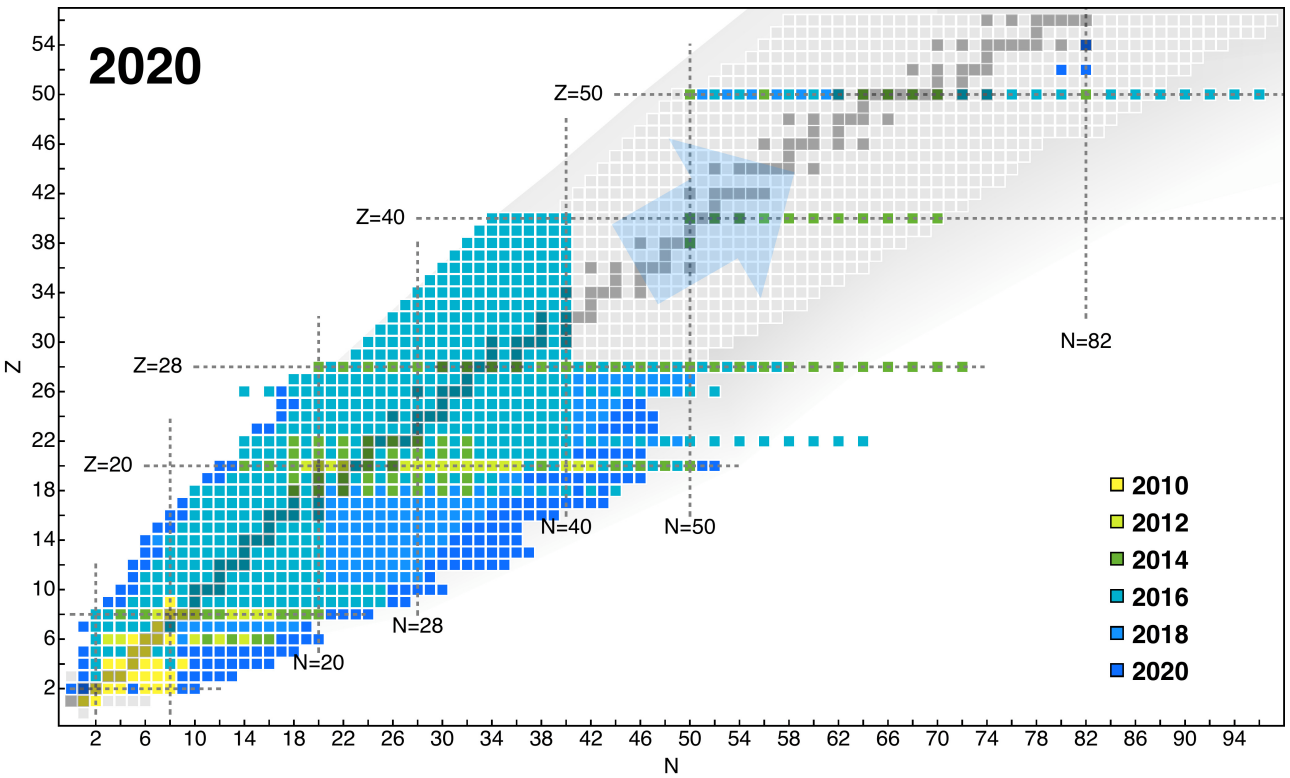

FIGURE 1 | Progress in *ab initio* nuclear structure calculations over the past decade. The blue arrow indicates nuclei that will become accessible with new advances for open-shell nuclei in the very near term (see section 2.3).

transformations that adapt a many-body Hamiltonian or other observables of interest to our needs, e.g., to extract eigenvalues [11, 53], or impose specific structures on the operator [1, 26, 27, 54, 55].

We define the flowing Hamiltonian

$$H(s) = U(s)H(0)U^\dagger(s)\,, \tag{1}$$

where $H(s = 0)$ is the starting Hamiltonian, and the flow parameter s parameterizes the unitary transformation. Instead of making an ansatz for $U(s)$, we take the derivative of Equation (1) and obtain the operator flow equation

$$\frac{d}{ds}H(s) = [\eta(s), H(s)]\,, \tag{2}$$

where the anti-Hermitian generator $\eta(s)$ is related to $U(s)$ by

$$\eta(s) = \frac{dU(s)}{ds}U^\dagger(s) = -\eta^\dagger(s)\,. \tag{3}$$

We can choose $\eta(s)$ to achieve the desired transformation of the Hamiltonian as we integrate the flow Equation (2) for $s \to \infty$. Wegner [56] originally proposed a class of generators of the form

$$\eta(s) \equiv [H_d(s), H_{od}(s)]\,, \tag{4}$$

that is widely used in applications, although it gives rise to stiff flow equations, and more efficient alternatives exist for specific applications [1, 11, 53]. Wegner generators are constructed by splitting the Hamiltonian into suitably chosen *diagonal* ($H_d(s)$) and *off-diagonal* ($H_{od}(s)$) parts. These labels are a legacy of applying this generator to drive finite-dimensional matrices toward diagonality. For our purposes, they reflect the desired structure of the operator in the limit $s \to \infty$: We want to keep the diagonal part and drive $H_{od}(s)$ to zero by evolving it via Equation (2) (see references [1, 11, 53, 56, 57]).

To implement the operator flow equation (23), we need to express $\eta(s)$ and $H(s)$ in a basis of suitable operators $\{O_i\}_{i\in\mathbb{N}}$,

$$\eta(s) = \sum_i \eta_i(s)O_i\,, \tag{5}$$

$$H(s) = \sum_i H_i(s)O_i(s)\,, \tag{6}$$

where $\eta_i(s)$ and $H_i(s)$ are the running couplings of the operators. If the algebra of the operators O_i is closed naturally or with some truncation, we have

$$[O_i, O_j] = \sum_k c_{ijk}O_k \;\; (+\ldots) \tag{7}$$

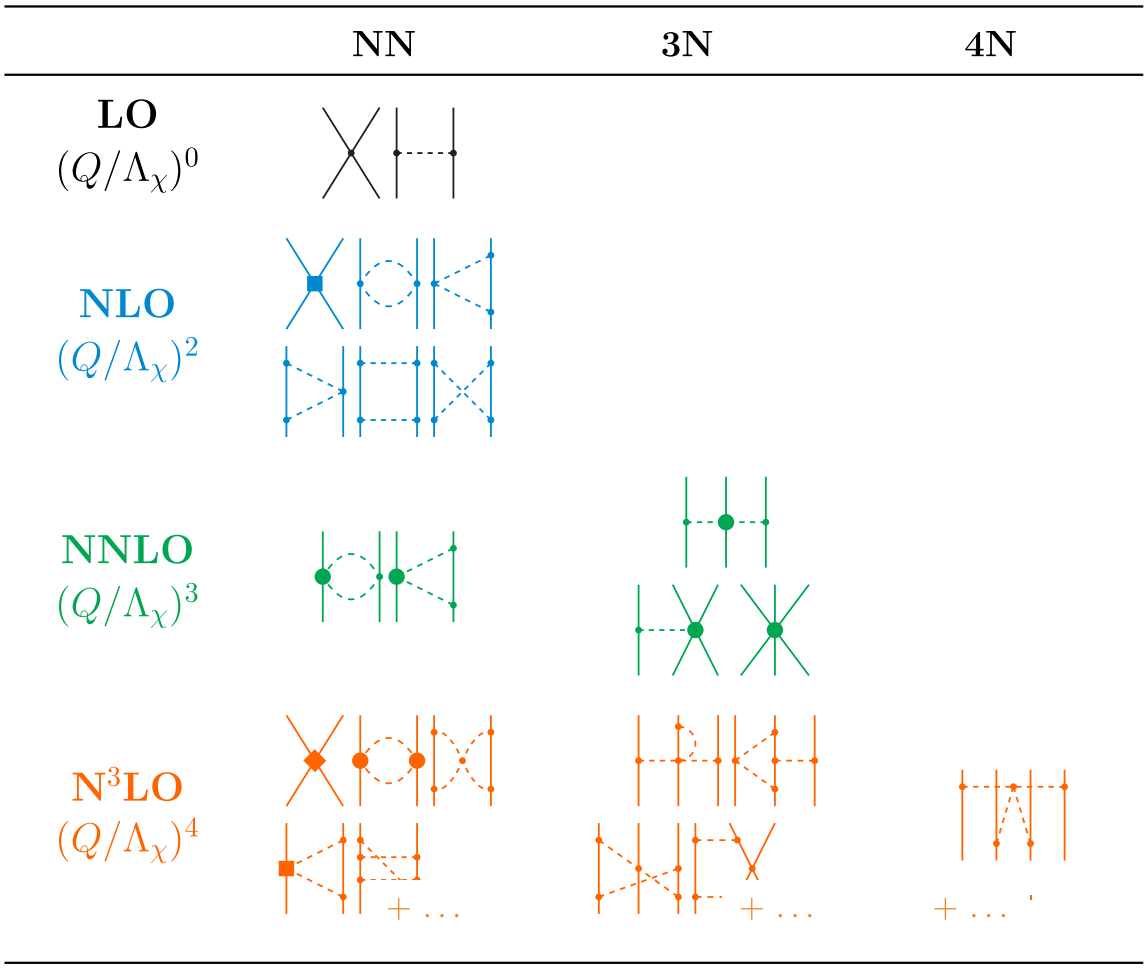

FIGURE 2 | Chiral two-, three-, and four nucleon forces through next-to-next-to-next-to-leading order (N^{3}LO) (see, e.g., [2, 37, 38]). Dashed lines represent pion exchanges between nucleons. The large solid circles, boxes and diamonds represent vertices that are proportional to low-energy constants (LECs) of the theory (see text).

and Equation (2) becomes a system of flow equations for the coupling coefficients:

$$\frac{d}{ds}H_i(s) = f_i(\boldsymbol{c}, \boldsymbol{\eta}(s), \boldsymbol{H}(s))\,, \tag{8}$$

where the bold quantities collect the algebra's structure constants and the running couplings, respectively. From this discussion, it is clear that the choice of the O_i can have a significant effect on the size of the system of flow equations, as well as the quality of any introduced truncations.

An important application of the SRG in nuclear many-body theory is the dialing of the operators' resolution scales. This is achieved by using the Wegner-type generator

$$\eta(\lambda) = [T, H(\lambda)] \tag{9}$$

to band-diagonalize the Hamiltonian in momentum space, and thereby decouple low- and high-momentum physics in the operators and eigenstates. As indicated in Equation (9) the flow is typically re-parameterized by $\lambda = s^{-1/4}$, which characterizes the width of the band in momentum space and controls the magnitude of the momentum transferred in an interaction process. For example, $|\boldsymbol{k}_i - \boldsymbol{k}_f| \lesssim \lambda$ in a two-nucleon system [1, 58].

Nowadays, the momentum space evolution is regularly performed for two- and three-nucleon forces [1, 59–62]. In light of the previous discussion, it can be understood as choosing the operator basis

$$\mathcal{B} = \{a_p^\dagger a_q,\ a_p^\dagger a_q^\dagger a_s a_r,\ a_p^\dagger a_q^\dagger a_r^\dagger a_u a_t a_s,\ \ldots\}_{pqrstu\ldots\in\mathbb{N}}\,, \tag{10}$$

with creation and annihilation operators referring to (discretized) single-particle momentum modes, and truncating four- and higher-body terms that appear when the commutators of the basis operators are evaluated. Since the commutator of an M-body and an N-body operator in the basis (10) acts at least on $K = \max(M, N)$ particles, the SRG evolution is exact for $A \leq 3$ systems under this truncation [59, 61]. It is implemented

by working with the matrix representations of $H(s)$ in two- and three-nucleon systems, whose entries correspond to the coupling constants in our chosen operator basis (cf. Equation 6). For efficiency, an additional basis change is made to center-of-mass and relative coordinates.

In principle, the strategy for evolving nuclear interactions toward some form of "diagonality" could be used to determine eigenvalues of many-body Hamiltonians, but the computational cost for dealing either with exponentially growing matrix representations or induced terms of high particle rank is prohibitive. This motivates the implementation of the flow equation with a different choice of basis operators in the In-Medium SRG (see section 2.3.3).

2.3. Many-Body Methods

Let us now discuss commonly used many-body methods for solving the nuclear Schrödinger equation. Roughly speaking, they fall into two categories: configuration space methods that expand the nuclear eigenstates on a basis of known many-body states, or coordinate-space methods that work directly with the wave function and optimize them in some fashion. Our goal is to use approaches that systematically converge to an exact result, e.g., by adding more and more particle-hole excitations of a selected reference state to the many-body basis of a configuration space, or by exhausting the distribution of meaningful wave function parameters.

The discussion in the following sections will be light on mathematical details, which can be found in more specialized articles and reviews, including other contributions to the present volume. The goal is to review only certain ideas that will become relevant later on.

2.3.1. The Many-Body Problem in Configuration Space

Let us briefly discuss the general setup of the configuration-space approaches. We choose a single-particle basis, e.g., the eigenstates of a harmonic oscillator, and use it to construct a basis of Slater determinants for the many-body Hilbert space. Usually, the many-body basis is organized by selecting a reference state $|\Phi\rangle$ and constructing its particle-hole excitations in order to account for the natural energy scales of the system under consideration. For further use, we define

$$|\Phi^{a\cdots}_{i\cdots}\rangle \equiv \{a^\dagger_a \ldots a_i \ldots\}\,|\Phi\rangle\,, \tag{11}$$

where particle $(a, b, \ldots)$ and hole $(i, j, \ldots)$ indices run over unoccupied and occupied single-particle states, respectively[2]. The parentheses indicate that the strings of creation and annihilation operators are *normal ordered* with respect to the reference state. They are related to the original operators by

$$a^\dagger_p a_q = \{a^\dagger_p a_q\} + C_{qp}\,, \tag{12}$$

$$\begin{aligned} a^\dagger_p a^\dagger_q a_s a_r = {} & \{a^\dagger_p a^\dagger_q a_s a_r\} + C_{rp}\{a^\dagger_q a_s\} - C_{sp}\{a^\dagger_q a_r\} \\ & + C_{sq}\{a^\dagger_p a_r\} - C_{rq}\{a^\dagger_p a_s\} + C_{rp}C_{sq} - C_{sp}C_{rq}\,, \end{aligned} \tag{13}$$

where the indices $p, q, \ldots$ run over all single-particle states, and the *contractions* are defined as

$$C_{qp} \equiv \langle\Phi|\, a^\dagger_p a_q\,|\Phi\rangle = \rho_{qp} \tag{14}$$

(see, e.g., references [11, 53] for more details).

Let us now consider a Hamiltonian containing up to two-body interactions, for simplicity. In normal-ordered form, it is given by

$$H = E_0 + \sum_{pq} f_{pq}\{a^\dagger_p a_q\} + \frac{1}{4}\sum_{pqrs}\Gamma_{pqrs}\{a^\dagger_p a^\dagger_q a_s a_r\}\,, \tag{15}$$

where E is the energy expectation value of the reference state, while f and Γ are the mean-field Hamiltonian and residual two-body interaction, respectively [11, 53]. Our task is to solve the many-body Schrödinger equation for this Hamiltonian to determine its eigenvalues and eigenstates, either in an approximate fashion or by exactly diagonalizing its matrix representation, which is shown in **Figure 3A**.

2.3.2. Many-Body Perturbation Theory

Many-Body Perturbation Theory (MBPT) is the simplest configuration-space approach for capturing correlations in interacting quantum many-body systems. It has enjoyed widespread popularity in treatments of the many-electron system since the early days of quantum mechanics, and it comes in a myriad of flavors (see, e.g., reference [64] and references therein). A major factor in its success is that the Coulomb interaction is sufficiently weak to make perturbative treatments feasible. Applications in nuclear physics had long been hindered by the strong short-range repulsion and tensor interactions in realistic nuclear forces, despite the introduction of techniques like Brueckner's G matrix formalism that were meant to resum the strong correlations from these contributions [65–68]. These issues were overcome with the introduction of the SRG evolution to low resolution scales, which makes nuclear interactions genuinely perturbative, albeit at the cost of inducing three-and higher many-body interactions [1]. As a consequence, MBPT has undergone a renaissance in nuclear physics in the past decade [69], leading to efficient applications for the computation of ground-state properties [5, 6, 70] and the construction of effective Shell Model interactions and operators (see, e.g., references [71–74], or the reviews [75, 76], and references therein). These successes have also motivated the development of novel types of MBPTs [69, 77, 78].

In a nutshell, MBPT assumes that the Hamiltonian can be partitioned into a solvable part H_0 and a perturbation H_I,

$$H = H_0 + H_I\,, \tag{16}$$

which then allows an order-by-order expansion of its eigenvalues and eigenstates in powers of H_I, usually starting from a mean-field solution. In the Rayleigh-Schrödinger formulation of MBPT,

[2]This labeling scheme is commonly used in chemistry [63], and it is used with increasing frequency in nuclear physics as well.

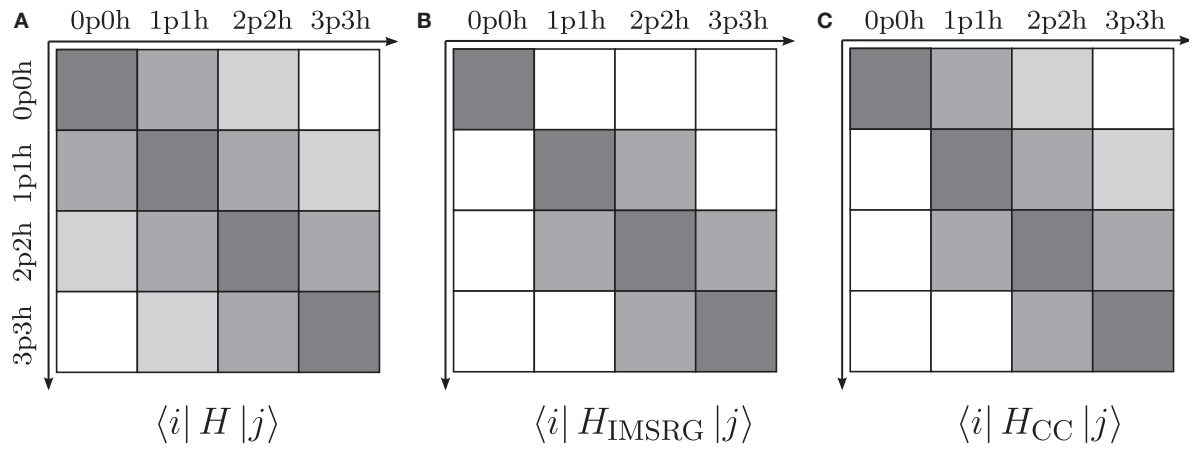

FIGURE 3 | Decoupling of particle-hole excitations from a 0p0h reference state: the schematic matrix representation of the initial Hamiltonian H_0 **(A)** and the transformed Hamiltonians obtained from IMSRG **(B)** and CC **(C)**, respectively (see text for details).

which is widely used for its convenience,

$$|\Psi\rangle = |\Phi\rangle + \sum_{n=1}^{\infty} \left(\frac{H_I}{H_0 - E^{(0)}} \right)^n |\Phi\rangle \,, \tag{17}$$

$$E = E^{(0)} + \sum_{n=0}^{\infty} \langle \Phi | H_I \left(\frac{H_I}{H_0 - E^{(0)}} \right)^n |\Phi\rangle \,, \tag{18}$$

where $E^{(0)}$ is the unperturbed energy. If we assume that the reference Slater determinant $|\Phi\rangle$ has been variationally optimized by solving the Hartree-Fock equations, E_0 in Equation (15) is the Hartree-Fock energy and f is diagonal. Then we can introduce the so-called Møller-Plesset partitioning,

$$H_0 = E_0 + \sum_p f_p \{a_p^\dagger a_p\} \,, \quad H_I = \frac{1}{4} \sum_{pqrs} \Gamma_{pqrs} \{a_p^\dagger a_q^\dagger a_s a_r\} \,, \tag{19}$$

and note that the Slater determinants of the basis introduced in section 2.3.1 are eigenstates of H_0:

$$H_0 \, |\Phi_{i\ldots}^{a\ldots}\rangle = (E_0 + f_a + \ldots - f_i - \ldots) \, |\Phi_{i\ldots}^{a\ldots}\rangle \,. \tag{20}$$

The eigenvalues of H_0 then become the unperturbed energies appearing in Equations (17), (18), and the energy including a finite number of correction terms can be evaluated straightforwardly. For example, the ground-state energy through second order is given by

$$E = E_0 - \frac{1}{4} \sum_{abij} \frac{|\Gamma_{abij}|^2}{f_a + f_b - f_i - f_j} \,. \tag{21}$$

For a more detailed discussion, we refer to reference [69] and references therein.

The expression (21) can serve to illustrate both advantages and drawbacks of an MBPT treatment of nuclei. We see that the second-order energy can be evaluated very efficiently, since it requires a non-iterative calculation whose computational effort scales polynomially in the single-particle basis size N, namely as $\mathcal{O}(N^4)$. The reason is that the construction of the Hamiltonian matrix (**Figure 3A**) can be avoided. In fact, the computational scaling is even more favorable, because we can distinguish particle and hole states and achieve $\mathcal{O}(N_p^2 N_h^2)$, and we typically have $N_h \sim A \ll N_p$. Although there is a proliferation of terms with increasing order [63, 69, 79], MBPT is still fundamentally polynomial and therefore more efficient than an exact diagonalization, whose cost scales exponentially with N. It is also clear from Equation (21) that the expansion of the exact eigenvalue will break down if one (or more) of the energy denominators become small due to (near-)degeneracies of the unperturbed energies. Thus, MBPT works best for ground states in systems with a strong energy gap, i.e., closed-shell nuclei, although extensions for more complex scenarios exist (see references [63, 68, 69] and references therein). A noteworthy new development is Bogoliubov MBPT, in which particle number symmetry is broken and eventually restored [77, 80, 81].

As mentioned at the beginning of this section, MBPT can be used to derive effective interactions and operators. The primary tool for such efforts is the $\hat{Q}$-box or folded-diagram resummation of the perturbative series (see references [75, 76, 82] and references therein).

2.3.3. In-Medium Similarity Renormalization Group

As already mentioned in our discussion of the SRG in section 2.2, we could envision applying SRG techniques not only to preprocess the nuclear interactions, but also to compute eigenvalues and eigenstates. For all but the lightest nuclei, applying the SRG to the Hamiltonian matrix is hopeless, so we work with the operators instead.

Let us again consider the matrix representation shown in **Figure 3A**. We want to design a transformation that will decouple the one-dimensional 0p0h block in the Hamiltonian matrix, spanned by a reference state Slater determinant $|\Phi\rangle$, from all excitations as the flow equation (2) is integrated. The matrix

element in this block will then be driven toward an eigenvalue (up to truncation errors), and the unitary transformation becomes a mapping between the reference Slater determinant and the exact eigenstate (see below). In principle, we could use a suitably chosen reference to target different eigenstates, e.g., by taking references which are expected to have a large overlap with the target state (see section 10.3 in reference [58]). In practice, we usually target the ground state by using a Hartree-Fock Slater determinant as our reference.

To implement the operator flow, we need to choose an operator basis to express $H(s)$ and the generator $\eta(s)$. Instead of using the basis (10), we switch to operators that are normal ordered with respect to the reference state $|\Phi\rangle$:

$$\mathcal{B} = \left\{ \{a_p^\dagger a_q\}, \{a_p^\dagger a_q^\dagger a_s a_r\}, \{a_p^\dagger a_q^\dagger a_r^\dagger a_u a_t a_s\}, \ldots \right\}_{pqrstu\ldots\in\mathbb{N}} . \quad (22)$$

Commutators of these operators can feed into terms of *lower* particle rank: For instance, a commutator of M-body and $N-$body operators generates $|M-N|$-body through $(M+N-1)$-body operators, while the lower bound for the basis (10) is $\max(M,N)$ (cf. section 2.2). As a result, the complexity of the flow equations for the operators' coupling coefficients increases due to the appearance of additional terms that depend on the contractions introduced in Equations (12) and (13). These contractions translate into density matrices (or occupation numbers)—hence the name In-Medium SRG. At the same time, we achieve a reduction of the truncation error because only the *residual*, contraction-independent parts of the operators (12) and (13) are omitted. In the majority of applications to date, we truncate all operators and their commutators at the two-body level, defining the IMSRG(2) truncation scheme. More details can be found in references [11, 53, 58, 76].

In the chosen basis we now identify the parts of the Hamiltonian that are responsible for coupling the reference state to 1p1h and 2p2h excitations, and define the off-diagonal Hamiltonian (cf. 2.2) as

$$H_{od} \equiv \sum_{ai} f_{ai}\{a_a^\dagger a_i\} + \frac{1}{4}\sum_{abij} \Gamma_{abij}\{a_a^\dagger a_b^\dagger a_j a_i\} + \text{H. c.}\,. \quad (23)$$

We use this H_{od} to construct a generator, either using Wegner's ansatz (4) or an alternative choice [11, 53]. Plugging the generator into the operator flow equation (2), we obtain a system of flow equations for the energy $E(s)$ and the coefficients $f_{pq}(s), \Gamma_{pqrs}(s), \ldots$ (cf. Equation 8 and references [11, 53, 76]). By integrating these flow equations, we evolve the Hamiltonian operator so that its matrix representation assumes the shape shown in **Figure 3B**. We note that the suppression of H_{od} not only leads to the desired ground-state decoupling, but also eliminates the outermost band in the Hamiltonian matrix. This simplification makes the evolved Hamiltonian an attractive input for other approaches, e.g., configuration interaction (CI) or equation-of-motion methods (see references [27, 29, 76, 83–86] and discussion below).

Valence-space IMSRG. Soon after introducing the IMSRG in nuclear physics [87], Tsukiyama, Bogner, and Schwenk proposed the use of the IMSRG flow to derive Hamiltonians (and other effective operators) for use in nuclear Shell Model calculations [88]. This is achieved by partitioning the single-particle basis into core, valence, and beyond-valence states, normal ordering all operators with respect to a Slater determinant describing the closed-shell core, and extending the definition of the off-diagonal Hamiltonian (23) to include all terms that couple valence and non-valence states. The eigenvalue problem for the evolved Hamiltonian can then be solved in the valence space with widely available Shell model codes [89–93]. After a study of the oxygen isotopic chain revealed an increasing overbinding away from the chosen core [26], we adopted a normal-ordering scheme that uses an ensemble of Slater determinants to account for partially filled shells in open-shell nuclei [27, 54]. This improved operator basis, along with the valence decoupling procedure and subsequent Shell Model diagonalization defines what is nowadays called the valence-space IMSRG (VS-IMSRG)—see reference [76] for a recent review.

Correlated reference states and multi-reference IMSRG. Another important development was the extension of the IMSRG formalism to correlated reference states, in the so-called Multi-Reference IMSRG (MR-IMSRG) [20, 53, 58]. The unitarity of the IMSRG transformation allows us to control to what extent correlations are described by either the Hamiltonian or the reference state. We can see this by considering the stationary Schrödinger equation and applying $U(s)$:

$$\left[U(s)HU^\dagger(s)\right] U(s)\,|\Psi_k\rangle = E_k U(s)\,|\Psi_k\rangle\,. \quad (24)$$

The transformation shifts correlations from the wave function into the evolved, RG-improved Hamiltonian $H(s) = U(s)HU^\dagger(s)$, and any many-body method that uses this Hamiltonian as input now needs to describe $U(s)\,|\Psi_k\rangle$, which should be less correlated than the exact eigenstate $|\Psi_k\rangle$. In the extreme cases, $U(s) = 1$ and the wave function carries all correlations, or $U(s)$ has shifted all correlations into the Hamiltonian and $|\Phi\rangle = U(s)\,|\Psi\rangle$ is a simple Slater determinant.

Correlated reference states can be particularly useful for the description of systems with strong *static* or *collective* correlations, like open-shell nuclei with strong intrinsic deformation or shape coexistence. Reference states that describe these types of correlations efficiently, e.g., through symmetry breaking and restoration (also see section 2.3.4), are an ideal complement to the IMSRG transformation, which excels at capturing *dynamic* correlations, involving the excitation of a few particles up to high energies. This complementarity is schematically illustrated in **Figure 4**: Collective correlations that would require as much as an IMSRG(A) calculation in the conventional approach are built into the reference state, and an MR-IMSRG(2) calculation is sufficient to treat the bulk of the dynamical correlations in the system.

Reference state correlations are built into the MR-IMSRG framework by using a generalized normal ordering [53, 94, 95] that is extended with contractions of higher rank, namely the

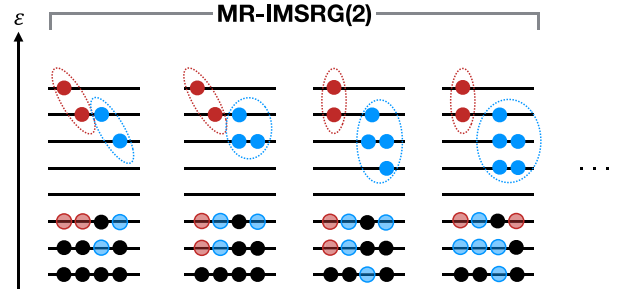

FIGURE 4 | Schematic view of correlations in nuclei. Solid circles indicate nucleons, transparent circles hole states, and dashed ellipses indicate correlations between nucleons. Certain 2p2h, 3p3h and higher correlations (indicated in blue) are built into a correlated wave function that then serves as the reference state for an MR-IMSRG(2) calculation (capturing correlations indicated in red), while up to an IMSRG(A) calculation would be needed for an equivalent description in the conventional framework.

irreducible k-body density matrices $\lambda^{(k)}$:

$$\lambda_{pq} \equiv \rho_{pq}\,, \tag{25}$$

$$\lambda_{pqrs} \equiv \rho_{pqrs} - \rho_{pr}\rho_{qs} + \rho_{qr}\rho_{ps}\,, \tag{26}$$

etc. The irreducible densities matrices encode the correlation content of an arbitrary reference state $|\Phi\rangle$, hence they vanish for Slater determinants. While the basis of normal-ordered operators superficially is the same as in the conventional IMSRG, shown in Equation (22), the inclusion of the irreducible densities (cf. Equations 12 and 13) equips the basis with the capability to describe the correlations that are present in the reference state, which in turn should help to reduce MR-IMSRG truncation errors. To understand this, let us assume that we know the ground state of our system, and we normal order the Hamiltonian with respect to this correlated state. Then the zero-body part of the normal ordered Hamiltonian already is the exact ground-state energy, and the normal-ordered one-, two-, and higher-body parts do not matter at all for our result, and neither does their evolution under an exact or truncated MR-IMSRG flow. Thus, the better the reference state matches the ground state, the less work the MR-IMSRG evolution and any subsequent many-body method have to do to obtain the correct ground-state energy.

Computational scaling and Magnus expansion. The computational scaling of all three IMSRG flavors discussed here—traditional, VS-IMSRG, and MR-IMSRG—is governed by the truncation scheme. If we truncate operators and commutators at the two-body level, as briefly mentioned above, the number of flow equations scales as $\mathcal{O}(N^4)$ with the single-particle basis size N, and the computational effort for evaluating the right-hand sides as $\mathcal{O}(N^6)$. This holds despite the greater complexity of the MR-IMSRG flow equations, which contain terms containing irreducible two- and higher-body density matrices.

Any observables of interest must, in principle, be evolved alongside the Hamiltonian for consistency, which would create a significant overhead. In practice, we can address this issue by using the so-called Magnus formulation of the IMSRG [58, 76, 83, 96]: Assuming that the IMSRG transformation can be written as an explicit exponential, $U(s) = \exp\Omega(s)$, we can solve a single set of flow equations for the anti-Hermitian operator $\Omega(s)$ instead of evolving observables separately. All operators of interest can then be computed by applying the Baker-Campbell-Hausdorff expansion to $O(s) = \exp[\Omega(s)]O\exp[-\Omega(s)]$.

IMSRG hybrid methods. As noted earlier in this section, the conventional IMSRG evolution makes the matrix representation of the Hamiltonian more diagonal by suppressing couplings between the npnh excitations of the reference state. This implies a decoupling of energy scales of the many-body system, analogous to the decoupling of momentum scales by the free-space SRG, although there are differences in detail that are associated with the operator bases in which the flow is expressed (cf. Equations 10 and 22).

From this realization, it is not a big step to consider using the IMSRG to construct RG-improved Hamiltonians for applications in other methods, defining novel hybrid approaches. In fact, even the original IMSRG formulation can be understood from this perspective: The evolution generates a Hamiltonian that yields the exact ground-state energy (up to truncations) in a Hartree-Fock calculation, except the HF equations are automatically satisfied for the evolved H, and we can read off the ground-state energy directly. The same Hamiltonian can then be used as input for EOM methods to compute excitation spectra [83]. Likewise, the VS-IMSRG produces an RG-improved Hamiltonian that serves as input for a Shell Model diagonalization.

Applying the same logic as in the VS-IMSRG case, the IMSRG has been merged with the No-Core Shell Model (NCSM, see section 2.3.6) into the In-Medium NCSM [84, 97]. In this approach, the IMSRG improves the Hamiltonian with dynamical correlations from high-energy few-nucleon excitations that would require enormously large model spaces in the conventional NCSM, and the exact diagonalization in a small model space describes the dynamics of many-nucleon excitations. The NCSM as the "host" method is rooted in the same particle-hole expansion picture as the IMSRG itself, but this is not a requirement. Another new hybrid method is the In-Medium Generator Coordinate Method (IM-GCM), which relies on the GCM as a host method to capture collective correlations [29, 85, 86]. In this approach, a many-body basis is generated by restoring the symmetries of mean field solutions with various types of shape and gauge configuration constraints, which is very different from the particle-hole excitation basis discussed so far.

2.3.4. Coupled Cluster Methods

The Coupled Cluster (CC) method [12, 63] is an older cousin of the IMSRG approach. It can also be understood as a decoupling transformation of the Hamiltonian, but in contrast to the IMSRG, it relies on a non-unitary similarity transformation (see **Figure 3**). Traditionally, CC is motivated by an exponential ansatz for the exact wave function of a system,

$$|\Psi_{CC}\rangle = e^{T}\,|\Phi\rangle\,, \tag{27}$$

where $|\Phi\rangle$ is a reference Slater determinant, and T is the so-called *cluster operator*. This operator is expanded on particle-hole excitations,

$$T = \sum_{ph} t_{ai}\{a_a^\dagger a_i\} + \frac{1}{4}\sum_{abij} t_{abij}\{a_a^\dagger a_b^\dagger a_j a_i\} + \dots\,, \qquad (28)$$

with the *cluster amplitudes* $t_{ai}, t_{abij}, \dots$. In practical applications, the T is truncated to include up to 2p2h (CC with Singles and Doubles, or CCSD) or 3p3h terms (CCSDT, including Triples). Various schemes exist for iteratively or non-iteratively including subsets of Triples [12, 63, 98–100]. When it acts on the reference state $|\Phi\rangle$, e^T admixes arbitrary powers of few-particle, few-hole excitations. Note, however, that the cluster operator T is not anti-Hermitian because it lacks de-excitation operators, and therefore e^T is not unitary.

The cluster amplitudes are determined by demanding that the transformed Hamiltonian,

$$H_{CC} \equiv e^{-T} H e^T\,, \qquad (29)$$

does not couple the reference to 1p1h and 2p2h states (see **Figure 3**). Using notation introduced in section 2.3.1, the decoupling conditions lead to the following system of non-linear equations:

$$\langle\Phi|\, e^{-T} H e^T\, |\Phi\rangle = E_{CC}\,, \qquad (30)$$

$$\langle\Phi_i^a|\, e^{-T} H e^T\, |\Phi\rangle = 0\,, \qquad (31)$$

$$\langle\Phi_{ij}^{ab}|\, e^{-T} H e^T\, |\Phi\rangle = 0\,. \qquad (32)$$

Here, E_{CC} is the CC ground-state energy, which corresponds to the one-dimensional block in the upper left of **Figure 3C** and is analogous to the zero-body part of the IMSRG-evolved Hamiltonian, as discussed in the previous section. The other blocks in the first column of the matrix vanish because of the CC Equations (30)–(32).

Since the CC transformation is non-unitary, one needs to be careful when one evaluates observables using the CC wave function, or uses H_{CC} as input for equation-of-motion calculations or other applications [12, 63]. For instance, the non-Hermiticity of H_{CC} forces us to consider left and right eigenstates separately. This is a drawback compared to unitary transformation methods like the IMSRG. Coupled Cluster also has advantages, though: For instance, the Baker-Campbell-Hausdorff expansion appearing in Equations (30)–(32) automatically terminates at finite order because the cluster operator only contains excitation operators. For the same reason, Equation (31) will automatically solve the Hartree-Fock equations, so any Slater determinant is equally well-suited as a reference state, while MBPT, IMSRG, and even exact diagonalization approaches exhibit (some) reference-state dependence.

Symmetry breaking and collective correlations. While most applications of CC theory in nuclear physics have enforced and exploited spherical symmetry, the capabilities for performing M-scheme calculations that allow nuclei to develop intrinsic deformation have existed for more than a decade. This is a more natural approach for capturing collective correlations than the construction of Triples, Quadruples (4p4h), and ever higher particle-hole excitations of a spherical reference (cf. section 2.3.3). Converging such calculations is challenging because the single-particle basis typically grows by an order of magnitude or more, and the broken symmetries must eventually be restored. The formalism for symmetry restoration in CC has been developed in references [101–104]. In fact, the work of Duguet et al. forms the basis of recent works on symmetry breaking and restoration in MBPT [77, 80, 81]. Applications are currently underway.

Shell-model CC. Like the IMSRG, the CC framework can be used to construct effective interactions and operators for Shell model calculations. Initial work in that direction applied Hilbert space projection techniques (cf. section 2.3.6) to construct a so-called CC effective interaction (CCEI) [24, 105], but the construction of the model spaces via Equation-of-Motion CC methods proved to be computationally expensive. The CCEI approach is now superseded by the Shell Model CC method [25], which applies a second similarity transformation to H_{CC} in Fock space, similar to VS-IMSRG decoupling (cf. section 2.3.3).

Unitary CC. While almost all applications of CC in nuclear physics use the traditional ansatz (27), unitary CC (UCC) approaches that parameterize the wave function as $|\Psi_{UCC}\rangle = e^{T-T^\dagger}|\Phi\rangle$ have been used in numerous studies in quantum chemistry (see, e.g., [106, 107]). Unitary CC wave functions have also become a popular ansatz for the Variational Quantum Eigensolver (VQE) algorithm on current and near-term quantum devices [108, 109]. It is also worth noting that the recently revived Unitary Model Operator Approach (UMOA) is closely related to UCC [110, 111].

2.3.5. Self-Consistent Green's Functions

Self-Consistent Green's Function (SCGF) theory is another prominent approach for solving the nuclear many-body problem with systematic approximations [112–115]. The Green's Functions in question are correlation functions of the form

$$g_{pq\dots rs} \equiv \langle\Psi_0^A|\, \mathcal{T}[a_p(t_p)a_q(t_q)\dots a_s^\dagger(t_s)a_r^\dagger(t_r)]\, |\Psi_0^A\rangle\,, \qquad (33)$$

which describe the propagation of nucleons in the exact ground state $|\Psi_0^A\rangle$ of the system. Using Wick's theorem, the exact A-body propagator (33) can be factorized into products of irreducible one-, two-, etc. propagators, similar to the decomposition of density matrices briefly touched upon in section 2.3.3. One can then formulate coupled equations of motion for propagators, and introduce truncations to obtain polynomially scaling methods, again somewhat analogous to IMSRG and CC. We must remain aware that the propagators of SCGF, the induced operators of IMSRG, and the CC amplitudes are all different objects, and while their definitions may make the seem complementary to each other, there are subtle distinctions. One of these is that the $g^{(k)}$ are formally defined with respect to the exact wave function, while IMSRG and CC use definitions with respect to a reference state.

Practical implementations of the SCGF technique usually work with the Fourier transforms of the propagators to the energy domain. One needs to solve integral equations of motion of the form

$$g = g_0 + g_0 \Sigma g \,, \tag{34}$$

where g_0 is the propagator of the non-interacting system and Σ a kernel that encodes the particles' interactions, which is constructed using diagrammatic techniques. For example, the one-body propagator is obtained by solving

$$g_{pq}(\omega) = g^{(0)}_{pq}(\omega) + \sum_{rs} g^{(0)}_{pr} \Sigma_{rs}(\omega) g_{sq} \,, \tag{35}$$

the so-called Dyson equation. From this propagator, one can compute the one-body density matrix

$$\rho_{pq} = \langle \Psi^A_0 | \, a^\dagger_q a_p \, | \Psi^A_0 \rangle = \int_{C^+} \frac{d\omega}{2\pi i} g_{pq}(\omega) \,, \tag{36}$$

where C^+ indicates an integration contour in the complex upper half plane. Higher-body density matrices are connected to the corresponding higher-body propagators in analogous fashion. Using the density matrices, one can then evaluate any operator expectation values of interest. For more details, we refer to the contributions [10, 115] to the present volume, and the works cited therein.

Current applications of SCGF techniques in nuclear physics make use of the so-called Algebraic Diagrammatic Construction (ADC) scheme, with increasing orders, denoted by ADC(n), converging to an exact solution. For closed-shell nuclei, calculations up to ADC(3) are be performed regularly, which contain correlations that are roughly comparable to IMSRG(2) with a perturbative 3p3h correction (see section 2.3.3 and references [83, 86, 116]) and CCSD(T) (cf. section 2.3.4). Somà and collaborators have extended the ADC scheme to open-shell nuclei by using Gor'kov Green's Functions with explicitly broken particle number symmetry [117, 118]. Applications of this framework have used a self-consistent second-order scheme, denoted Gor'kov-ADC(2), and the extension to Gor'kov-ADC(3) as well the integration of particle-number projection to restore the broken number symmetry are in progress [80, 114].

While the computation of the Green's Functions tends to be a more involved task than solving the IMSRG flow equations or CC amplitude equations, the propagator contains more information from a single computation than these other methods. For instance, one can immediately extract spectral information about the neighboring nuclei and the response of the system [119, 120], which requires the application of additional techniques in the IMSRG [83] and CC approaches [12, 121, 122], or, indeed, the computation of the Green's Function using similarity-transformed operators. Furthermore, the kernels of the equations of motion (34) are energy-dependent effective interactions that govern the dynamics of (few-)nucleon-nucleus interactions. For example, the one-nucleon self-energy in Equation (35) is an *ab initio* version of an optical potential, as used in reaction theory [123–125]. We will return to this discussion in section 4.5.

2.3.6. Configuration Interaction Approaches

No-core configuration interaction methods. The most straightforward but also most computationally expensive approach to solving the many-body Schrödinger equation is to exactly diagonalize the Hamiltonian in a basis of many-body states. In general, we refer to such approaches as No-Core Configuration Interaction (NCCI). "No core" makes it explicitly clear that all nucleons are treated as active degrees of freedom, in contrast to the nuclear Shell model discussed below.

In light nuclei, the exact diagonalization can be directly formulated in Jacobi coordinates, using translationally invariant harmonic oscillator [126] or hyperspherical harmonic wave functions [127, 128]. Since the construction of the basis states themselves and the matrix representation of the Hamiltonian becomes increasingly complicated and computationally expensive as the particle number grows, one eventually has to switch to Slater determinants in the laboratory system, using a construction along the lines discussed in section 2.3.1.

A common choice for the single-particle basis in the laboratory system are spherical harmonic oscillator (SHO) states, because they allow an exact separation of center-of-mass and intrinsic degrees of freedom provided one uses an energy-based truncation for the model space [129, 130]. These choices define what we specifically call the No-Core Shell Model (NCSM). A disadvantage of using SHO orbitals is that they are not optimized to the energy scales of specific nuclei, and they are poorly suited for describing physical features like extended exponential wave function tails. Other popular choices are Hartree-Fock single-particle states, and perturbatively [131] or non-perturbatively enhanced natural orbitals [132–134]. Model spaces built on these bases no longer guarantee the separation of center-of-mass and intrinsic coordinates, but fortunately, center-of-mass contaminations either remain small automatically [135], or they can be suppressed using techniques like the Lawson method [136].

Importance truncation and symmetry adaptation. As indicated above, the main issue with exact diagonalization approaches is the exponential (or greater) growth of the Hilbert space dimension, which is proportional to $\binom{N}{A}$ with single particle basis size N and particle number A. A variety of strategies can be used to address this often-quoted "explosion" of the basis size. One direction is to avoid the construction of the full model space basis by applying importance-based truncation or sampling methods, leading to the Importance-Truncated NCSM [9] or Monte-Carlo (No-Core) CI approaches [137, 138].

Another important research program is the exploration of many-body states that are constructed from the irreducible representations (irreps) of the symplectic group Sp(3,$\mathbb{R}$), which describes an approximate emergent symmetry of finite nuclei [139, 140]. An exact diagonalization in such a symmetry-adapted basis will offer a much more efficient description of nuclear states with intrinsic deformation than the conventional NCSM, which would need to use massive model spaces with many-particle-many-hole excitations. This reduction of the model space dimensions also allows such symmetry-adapted NCSM [139, 140] and NCCI approaches [141] to reach heavier nuclei than the conventional versions.

Interacting nuclear shell model with a core (valence CI). Instead of treating all of the nucleons as active, one can also factorize the nuclear wave function by introducing an inert core and only treat the interactions of a smaller number of valence nucleons via appropriately transformed interactions:

$$|\Psi\rangle = |\Psi\rangle_{\text{core}} \otimes |\Psi\rangle_{\text{valence}} \,. \tag{37}$$

This, of course, is the traditional nuclear Shell model approach. Even with the substantial reduction of the single-particle basis to a relatively small number of valence orbitals, the numerical cost for an exact diagonalization quickly becomes unfeasible for many medium-mass and heavy nuclei, especially if one needs multi-shell valence-spaces to capture complex nuclear structure features like coexisting intrinsic shapes.

In previous sections, we have discussed how a variety of many-body methods can be used to derive valence-space interactions, hence it is not a surprise that this is possible in NCCI approaches as well. One strategy is to project solutions of no-core calculations for the core and its neighboring nuclei onto a valence-configuration space to extract the effective Hamiltonian. The viability of this approach has been demonstrated in several publications [142–145], although there are ambiguities in the extraction of the valence-space Hamiltonian, and the initial NCCI calculations that serve as input for the projection rapidly become expensive.

Description of continuum effects and nuclear dynamics. An important breakthrough in *ab initio* calculations for light nuclei has been the merging of the NCSM with resonating group method (RGM) techniques [130, 146]. This makes it possible to describe clustered states as well as reactions between light projectile(s) and targets. In the original NCSM/RGM approach, compact clusters of nucleons are described by NCSM states, which are then used to construct a basis of configurations $|\chi_i\rangle$ that place such clusters at different relative distances. In this basis, one can then solve the generalized eigenvalue problem, known as the Griffin-Hill-Wheeler equation [147] in the RGM context:

$$\mathcal{H}\,|\Psi\rangle = E\mathcal{N}\,|\Psi\rangle \,, \tag{38}$$

where $\mathcal{H}$ and $\mathcal{N}$ are the so-called Hamiltonian and norm kernels. The latter appears because the chosen basis configurations are not orthogonal in general. The dimension of Equation (38) is typically small, certainly compared to the NCSM model space, but the computation of the kernels is computationally expensive since it relies on the construction of up to three-body transition density matrices. In recent years, the NCSM/RGM has been extended to the NCSM with Continuum (NCSMC), which accounts for the coupling between the NCSM and RGM sectors of the many-body basis [130]. It requires solving the generalized eigenvalue problem

$$\begin{pmatrix} h & \bar{h} \\ \bar{h} & \mathcal{H} \end{pmatrix} \begin{pmatrix} \Phi \\ \chi \end{pmatrix} = E \begin{pmatrix} \mathbb{1} & \bar{n} \\ \bar{n} & \mathcal{N} \end{pmatrix} \begin{pmatrix} \Phi \\ \chi \end{pmatrix} , \tag{39}$$

where h and $\mathbb{1}$ are the Hamiltonian and norm kernel in the NCSM sector (the latter being diagonal), $\mathcal{H}$ and $\mathcal{N}$ the corresponding kernels in the RGM sector (cf. Equation 38), and $\bar{h}$ and $\bar{n}$ encode the coupling between the sectors of the basis.

Alternative approaches to the description of continuum effects in the NCSM are the Single-State HORSE (Harmonic Oscillator Representation of Scattering Equations) method [148–150], for which the nomen is omen, as well as the No-Core Gamow Shell Model (GSM), a no-core CI approach that constructs Slater determinants from a single-particle Berggren basis [151] consisting of bound, resonant and scattering states [152–155].

2.3.7. Quantum Monte Carlo

The most commonly used Quantum Monte Carlo (QMC) techniques in nuclear physics make use of many-body wave functions in coordinate space representation [156–159]. As such, they are well-suited for the description of nuclear states with complex intrinsic structures, and they can readily use interactions with a high momentum cutoff, as opposed to the configuration space methods which would exhibit poor convergence in such cases. This allows QMC calculations to explore physics across the interfaces of the hierarchy of EFTs for the strong interaction (cf. sections 2.1 and 4.4), e.g., for processes that explore energies approaching the breakdown scale of chiral EFT [160–163].

A typical ansatz for a QMC trial state is

$$|\Phi_T\rangle \equiv \mathcal{F}(\boldsymbol{a})\,|\Phi(\boldsymbol{b})\rangle \,, \tag{40}$$

where $\mathcal{F}(\boldsymbol{a})$ is an operator that explicitly imprints correlations on the mean-field like state $|\Phi(\boldsymbol{b})\rangle$, and $\boldsymbol{a}, \boldsymbol{b}$ are vectors of tunable parameters. The first step of most QMC calculations is a variational minimization of the energy in the trial state ,

$$\min_{\boldsymbol{a},\boldsymbol{b}} \frac{\langle\Phi_T|\,H\,|\Phi_T\rangle}{\langle\Phi_T|\Phi_T\rangle} \geq E_0 \,, \tag{41}$$

followed by an imaginary-time evolution to project out the true ground state in a quasi-exact fashion:

$$|\Psi_0\rangle \propto \lim_{\tau\to\infty} e^{-(H-E_T)\tau}\,|\Phi_T\rangle \,. \tag{42}$$

This projection can be implemented using Monte Carlo techniques in a variety of ways, which gives rise to different approaches like Green's Function Monte Carlo (GFMC) or Auxiliary-Field Diffusion Monte Carlo (AFDMC) [156, 158].

A major challenge in QMC calculations is that most commonly used algorithms suffer from some form of sign problem [156, 158]. Many quantities of interest like the wave functions or local operator expectation values in these wave functions are not positive definite across their entire domain, which means that they cannot be immediately interpreted as probability distributions that the algorithms sample. This is one of the main reasons why QMC methods can only be used with Hamiltonians that are either completely local, or have a non-locality that is at most quadratic in the momenta, e.g., $\boldsymbol{p}^2$ or $\boldsymbol{l}^2$.

While QMC applications in *ab initio* nuclear structure have been focused on coordinate space, there *are* a wide variety of approaches that merge QMC techniques with the configuration space approaches discussed in previous sections. Examples

include sampling the intermediate-state summations in MBPT [164], diagrammatic expansions [165–167], or the coefficients of correlated CC [168] or (No-Core) CI wave functions [137, 138, 169–171].

2.3.8. Lattice Effective Field Theory

Lattice methods are nowadays widely used to simulate the dynamics of non-perturbative field theories on finite space-time lattices. The most prominent example is Lattice QCD, but implementations of various Effective Field Theories on the Lattice have been developed and applied with impressive outcomes in the past two decades—see, for example, references [172–175] and references therein, which also provide pedagogical introductions to Lattice EFT for nuclear systems.

Lattice EFT simulations are built around the partition function, which is defined for a pure state $|\Psi\rangle$ as

$$\mathcal{Z}(\tau) = \langle \Psi(\tau = 0)| \exp(-H\tau) |\Psi(\tau = 0)\rangle . \tag{43}$$

Here, H is an EFT Hamiltonian, typically truncated at a given order of the EFT's power counting scheme. In practice, the partition function is evaluated as a path integral in which field configurations are sampled using Monte Carlo techniques. At large τ, one can extract information about the ground state and low-lying excited states of the system directly from $\mathcal{Z}$ (cf. section 2.3.7), and general expectation values can be evaluated using

$$\langle O\rangle_\tau = \frac{1}{Z(\tau)} \langle \Psi_0| \exp(-H\tau/2)\, O\, \exp(-H\tau/2) |\Psi_0\rangle . \tag{44}$$

The use of discretized spatial lattices makes Lattice EFT particularly suited for the description of nuclear states with complex geometries like cluster structures [176–178]. Depending on the size of the lattices, it will also typically require less computational effort than the imaginary-time evolution of states that are formulated in continuum coordinates, as in AFDMC or GFMC (see section 2.3.7). Moreover, the development of the so-called adiabatic projection method (APM) [179, 180] in recent years has made it possible to compute scattering cross sections for reactions of (light) clusters on the lattice. Conceptually, the APM is reminiscent of the resonating-group method used to describe reactions in the NCSMC framework discussed in section 2.3.6.

Of course, Lattice EFT is not free of disadvantages, which are usually caused by the discretization of space(time). The finite size and lattice spacing are related to infrared (long-range, low-momentum) and ultraviolet (short-range, high-momentum) cutoffs of a calculation, which need to be carefully considered. Since the recognition of cutoff scales is an inherent aspect of EFTs, one can systematically correct for these effects [181, 182]. The discrete lattice also breaks continuous spatial symmetries that may need to be restored approximately or exactly before comparisons with experimental data are made [172, 182].

3. THE PAST IS PROLOGUE: ACHIEVEMENTS IN THE LAST DECADE

In this section, I will discuss selected achievements of the *ab initio* nuclear many-body community in the past decade, and the issues that were encountered in the process. As stated in the introduction, this selection is subjective, and giving full justice to the breadth of research accomplishments is beyond the scope of this work. I hope that the present discussion will serve as an invitation for further exploration, for which the cited literature may serve as a useful starting point.

3.1. Benchmarking Nuclear Forces

One of the biggest issues in nuclear theory was the lack of comparability between different approaches for describing the structure of medium-mass or heavy nuclei. These nuclei were well in reach of the Shell Model and nuclear Density Functional Theory (DFT), but whenever issues emerged, it was unclear whether they resulted from approximations in the many-body method, or deficiencies in the effective interactions, i.e., the valence-space Hamiltonians or energy density functionals (EDF). Moreover, one cannot simply perform a valence CI calculation with an EDF, or a DFT calculation with a Shell Model interaction, because the interactions are tailored to their specific many-body method.

The development of the RG/EFT and many-body methods discussed in section 2 has opened up a new era for benchmarking the same nuclear interactions across multiple approaches, and on top of that, these methods provide a systematic framework for analyzing, and eventually quantifying, the reasons for differences between the obtained results.

One of the earliest testing grounds for *ab initio* calculations of medium-mass nuclei was the oxygen isotopic chain, which was accessible to all of the approaches that emerged at the beginning of the past decade. **Figure 5** shows the ground-state energies of even oxygen isotopes for the same chiral NN+3N interaction, obtained with several of the configuration space approaches introduced in section 2.3. In addition, results for applying various types of MBPT to the same interaction and nuclei are presented in reference [69]—I only refrained from including them here to avoid overloading the figure. As we can see, the ground-state energies obtained from the different approaches are in good agreement with each other and with experiment. Since our results include quasi-exact IT-NCSM values, the deviation of the other methods' energies from these values provide us with an estimate of the theoretical uncertainties due to any employed truncations, which is on the order of 1–2%. As we can see from **Figure 5**, essentially all of the used many-body methods place the drip line in the oxygen isotopic chain at ^{24}O, although the signal is exaggerated. Continuum effects that have been omitted in these calculations would lower the energy of the ^{26}O resonance, which is experimentally constrained to be a mere 18(7) keV above the two-neutron threshold [185], and produce a very flat trend in the energies toward ^{28}O. Similar features were found in calculations for other isotopic chains and other chiral interactions [21, 114, 118, 186]. The ^{16}O ground state energies obtained for the employed chiral NN+3N Hamiltonian are also compatible with a Lattice EFT result that was obtained at a similar resolution scale [177].

This last comparison shows that some obstacles to the ideal cross-validation scenario still remain. Since coordinate-space approaches like Lattice EFT or QMC are truly complementary

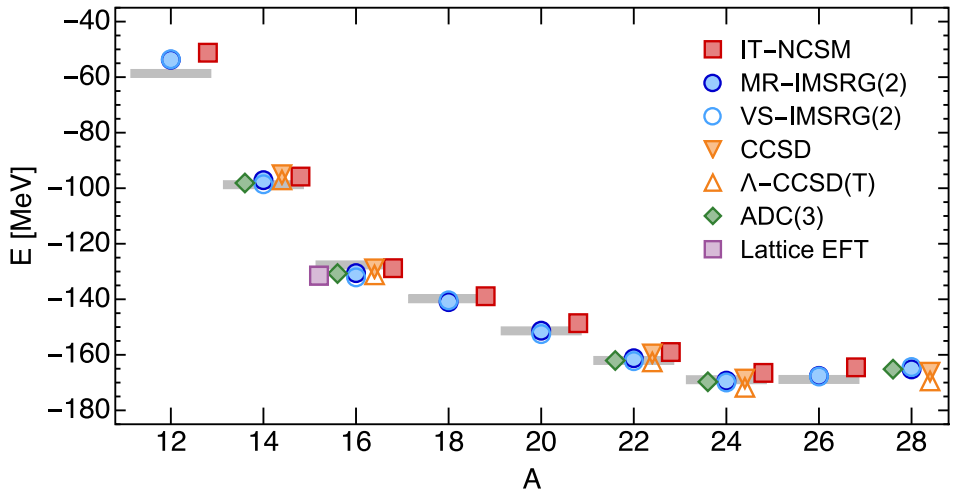

FIGURE 5 | Ground-state energies of the oxygen isotopes for various many-body approaches, using the chiral NN+3N(400) interaction at $\lambda = 1.88\,\mathrm{fm}^{-1}$ [183]. Details on the Lattice EFT calculation can be found in reference [177]. Gray bars indicate experimental data [184].

to configuration-space methods, it would be highly desirable to test the same chiral NN+3N Hamiltonians in both types of calculations. However, the Hamiltonians used in configuration space are typically given in terms of harmonic oscillator matrix elements (especially if SRG evolved) instead of the coordinate-space operators required by Lattice EFT or QMC calculations. Furthermore, Lattice EFT and QMC cannot handle all possible types of non-locality in the Hamiltonian (cf. section 2.3.7), including the forms generated by the non-local regulators that are favored for configuration-space Hamiltonians. Conversely, local chiral interactions that have been constructed explicitly for QMC applications [4, 158, 187–190] exhibit slow model-space convergence in configuration-space calculations because they still tend to require a significant repulsive core at short distance to describe nucleon-nucleon scattering data, albeit a far weaker one than interactions like Argonne V18 [191].

3.2. Extending the Reach of *ab initio* Theory

The reach of *ab initio* many-body theory has increased dramatically over the past decade. **Figure 1** illustrates this growing coverage of the nuclear chart, but it tells only part of the story. The expansion has happened in many "dimensions" besides the mass number A, namely by pushing toward exotic nuclei via improved treatments of the continuum degrees of freedom, filling in gaps in the coverage that are occupied by doubly open-shell nuclei with strong intrinsic deformation, and expanding the types of observables that can be computed from first principles. Recalling section 3.1, the ongoing push against the limitations of our many-body approaches will continue to grow the opportunities for benchmarking current- and next-generation chiral Hamiltonians.

3.2.1. Pushing the Mass Boundaries

First calculations for selected nuclei and semi-magic isotopic chains up to tin were already published in the first half of the last decade [19, 21, 23]. For the most part, they were using a family of chiral NN+3N interactions that gave a good description of the oxygen ground-state energies (cf. **Figure 5**) as well as the spectroscopy of the lower *sd*-shell region [24, 26]. However, the same interactions underpredict nuclear charge radii [192], and start to overbind as we approached the calcium chain (cf. **Figure 7**), eventually leading to an overbinding of 1 MeV per nucleon in tin. While model-space convergence in CC, IMSRG and SCGF calculations suggested that calculations for heavier nuclei would have been technically possible, it made little sense to pursue them.

The growing number of results for medium-mass nuclei and the problems they revealed motivated a new wave of efforts to refine chiral interactions. One direction of research aimed to achieve a simultaneous description of nuclear energies and radii up to ^{48}Ca by including selected many-body data in the optimization protocol of the chiral LECs. This work resulted in the so-called $\mathrm{NNLO_{sat}}$ interaction [194]. While $\mathrm{NNLO_{sat}}$ definitely improved radii [195], its model-space convergence was found to become problematically slow already in lower *pf*-shell nuclei [114, 196, 197].

Simultaneously with the efforts to develop new interactions, attention also turned toward an older, less consistently constructed family of chiral NN+3N interactions that exhibited reasonable saturation properties in nuclear matter calculations [198, 199]. These forces are referred to as EMλ/Λ, where λ indicates the resolution scale of the NN interaction, the SRG-evolved N^{3}LO potential of Entem and Machleidt [200], and Λ is the cutoff of an NNLO three-nucleon interaction whose low-energy constants have been adjusted to fit the triton binding energy and ^{4}He charge radius [198, 199]. In CC calculations for the nickel isotopes, Hagen et al. demonstrated that the EM1.8/2.0 interaction, in particular, allowed a good description of the energies of nuclei in the vicinity of ^{78}Ni [196]. As shown in **Figure 6**, these findings have been reinforced by subsequent VS-IMSRG calculations, as well as the experimental observation of the first excited 2^+ state in this nucleus [201].

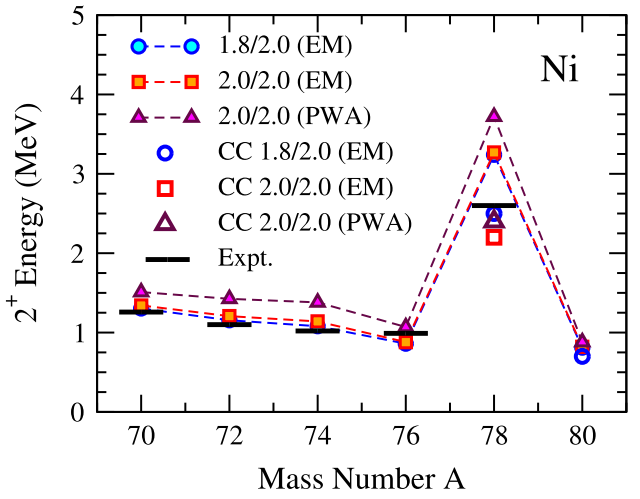

FIGURE 6 | Energies of the first excited 2^+ states from VS-IMSRG [201] and Equation-of-Motion CC [196] calculations for several chiral two- plus three-nucleon interactions. Experimental values [201, 202] are indicated as black bars. Data courtesy of J. D. Holt, J. Menéndez, and G. Hagen.

Since this initial application in medium-mass nuclei, the EMλ/Λ family has seen widespread use in *ab initio* calculations due to its empirical quality, although the Hamiltonian's theoretical uncertainties are less well-defined than for interactions that obey the chiral power counting more rigorously. Indeed the EM1.8/2.0 interaction was used in VS-IMSRG calculations to produce what is to my knowledge the first attempt at producing an *ab initio* mass table for nuclei up to the iron isotopes [186]. For selected nuclei up to the tin region, it also yields converged energies for ground and low-lying states that are in good agreement with experimental data [203, 204]. It also yields slightly larger radii than previous interactions, although the underprediction is not eliminated entirely (see references [195, 203] and section 3.2.3).

Multiple applications of the EMλ/Λ Hamiltonians in support of spectroscopy experiments have been published in recent years (see, e.g., [197, 205–208]), and additional studies are underway, including an effort to better understand what makes the EM1.8/2.0 Hamiltonian so successful. Furthermore, a new generation of chiral NN+3N interactions is now available for applications in medium-mass and heavy nuclei [46, 114, 209–211].

3.2.2. Toward the Drip Lines

Neutron-rich nuclei are excellent laboratories for disentangling the interplay of nuclear interactions, many-body correlations and the continuum. Thus, data from the experimental push toward the drip line can offer important constraints for the refinement of chiral interactions if the many-body truncations and continuum effects are under control.

In practice, *ab initio* results for observables like the absolute energies of states still exhibit significant scale and scheme dependence due to truncations that are made in the EFT, the potential implementation of SRG evolutions, and the many-body methods. Since such variations tend to be systematic within families of interactions (and sometimes even across multiple families), differential quantities like separation and excitation energies or transition matrix elements often exhibit a weaker scale and scheme dependence—note, for example, the small systematic variation of the first excited 2^+ states of the neutron-rich nickel isotopes for EMλ/Λ interactions. This makes energy differences an ideal observable for confronting *ab initio* results with experimental data.

Let us consider two-neutron separation energies as a concrete example. Sudden drops in these observables are a signal of (sub)shell closures (albeit not universally [195]) and in the neutron-rich domain, they are important indicators for the proximity of the drip line. **Figure 7** shows MR-IMSRG ground-state and two-neutron separation energies of the calcium isotopes, obtained with the NN+3N(400) interaction used in **Figure 5**, as well as the NNLO_{sat} and EM1.8/2.0 interactions briefly discussed in the previous section. We note the overbinding produced by NN+3N(400) and the baffling accuracy of the EM1.8/2.0 results, given the approximations that went into the construction of this force, as well as the MR-IMSRG truncation. Common to all three interactions is the emergence of a very flat trend in the ground-state and separation energies in neutron-rich calcium isotopes, which will likely be further enhanced by the inclusion of continuum effects, and extended beyond the shown mass range. Similar flat trends emerge in many isotopic chains, as shown both in *ab initio* surveys based on chiral interactions [10, 114, 186] as well as a sophisticated Bayesian analysis of empirical EDF models [212]. Naturally, this will make the precise determination of the neutron drip line in the medium-mass region a challenging task, but also suggests that interesting features like alternating patterns of unbound odd nuclei and weakly-bound even nuclei with multi-neutron halos could emerge. This is an exciting prospect for the experimental programs at rare-isotope facilities.

With the exception of the NCSMC and HORSE methods discussed in section 2.3.6, the inclusion of continuum degrees in configuration-space techniques has been focused on the use of the Berggren basis [151]. While such calculations are challenging due to the significantly increased single-particle basis size and the difficulties of handling the resulting complex symmetric Hamiltonians, applications in CC (see references [12, 213] and references therein), both valence and No-Core Gamow Shell Model [153–155, 214, 215] and IMSRG [216] calculations have been published. Common to all these approaches is that a configuration space interaction that is given in terms of SHO matrix elements is expanded on a basis containing SHO and Berggren states, hence it is still an open question how a direct implementation of the interactions in a basis with continuum degrees of freedom might modify existing results. It is worth noting that such a construction has been achieved for phenomenological GSM interactions that have been tuned for light nuclei [217–222].

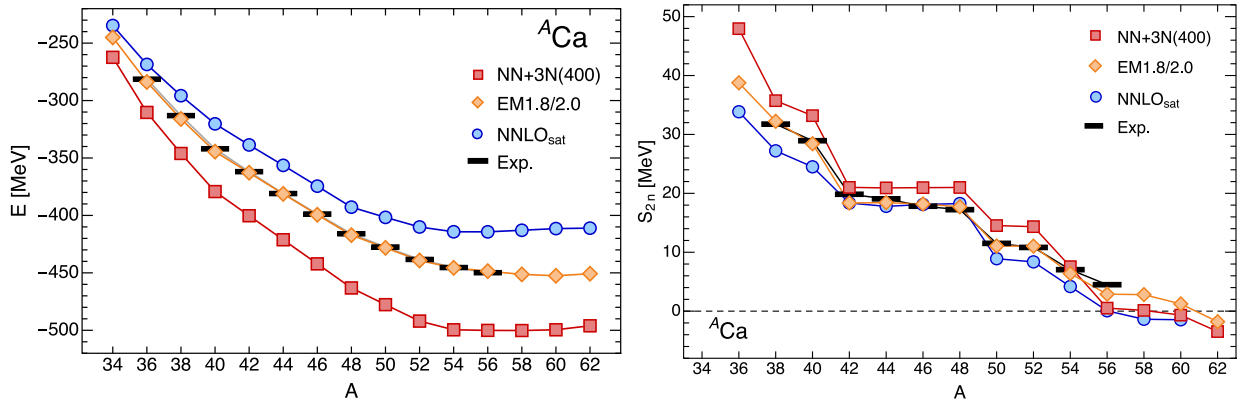

FIGURE 7 | Ground-state and two-neutron separation energies for several chiral NN+3N interactions from MR-IMSRG(2) calculations. Experimental data are indicated by black bars [184, 193].

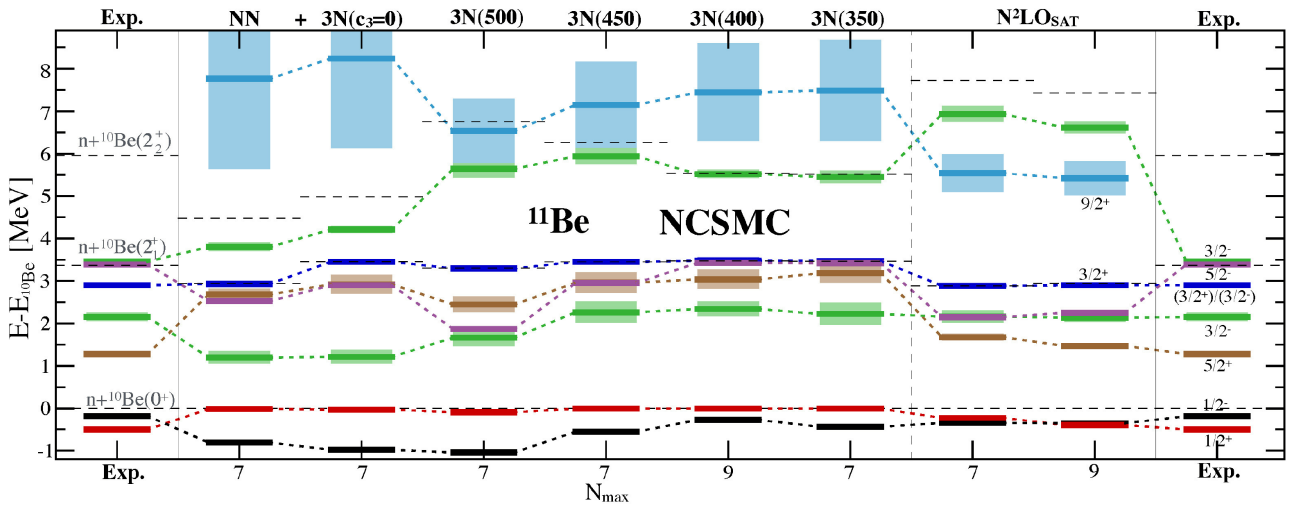

FIGURE 8 | NCSMC spectrum of ^{11}Be with respect to the $n+^{10}$ Be threshold. Dashed black lines indicate the energies of the ^{10}Be states. Light boxes indicate resonance widths. See reference [223] for details. Figure reprinted with permission from the American Physical Society.

In light nuclei, the NCSMC has been applied with impressive success to describe a variety of exotic nuclei with up to three-cluster structures. For example, Calci et al. [223] carried out NCSMC calculations for ^{11}Be with several chiral NN+3N interactions to investigate the parity inversion of the ground and first-excited states in this nucleus from first principles. The authors found that the coupling between the NCSM and RGM sectors of the generalized eigenvalue has strong effects, but that among the tested interactions, only NNLO$_{sat}$ can produce the experimentally observed ordering of the states (see **Figure 8**). However, it still underpredicts the splitting of these levels and as a result, overestimates the cross section for the photodisintegration ^{11}Be$(\gamma, n)^{10}$Be. Additional applications of the NCSMC for exotic nuclei can be found in the review [130] and references therein, as well as the more recent works [224–226].

3.2.3. Accessing More Observables

The capabilities of *ab initio* approaches have also significantly expanded when it comes to the evaluation of observables other than the energies.

Nuclear radii. **Figure 9** shows MR-IMSRG results for the charge radii of calcium isotopes. The left panel illustrates the reasonable reproduction of the ^{40}Ca and ^{48}Ca charge radii that can be obtained for NNLO$_{sat}$. The MR-IMSRG(2) results are slightly smaller than the experimental data due to differences in the truncations from the CCSD charge radius calculations that were used in the NNLO$_{sat}$ optimization protocol [194]. Note the steep increase in the experimental charge radii beyond ^{48}Ca: At the time of the measurement, NNLO$_{sat}$ was the only chiral NN+3N interaction exhibiting this feature, although other more recent interactions can replicate this trend as well [10, 114]. Also note that none of the calculations are able to reproduce the

inverted arc of the charge radii between ^{40}Ca and ^{48}Ca. In a CI picture, it is caused by strong mixing with 4p4h excitations into the *pf*-shell [229]. Since the MR-IMSRG(2) calculations shown here included only up to (generalized) 2p2h excitations and used particle-number projected Hartree-Fock Bogoliubov vacua as reference states that do not contain collective correlations (cf. section 2.3.3), it is not surprising that the inverted arc cannot be reproduced. We will return to this issue of missing collectivity later.

While the EMλ/Λ interactions underpredict the absolute charge radii, they fare quite well in the description of radius differences, as suggested in the previous section. **Figure 9B** is adapted from a recent study that suggests a correlation between the charge radius difference of mirror nuclei, $\Delta R_{\rm ch}$, and the slope of the symmetry energy in the nuclear matter equation of state [228]. We see that the MR-IMSRG results for $\Delta R_{\rm ch}$ are actually compatible with results from a multitude of Skyrme EDFs, and the value for the magic EM1.8/2.0 interaction falls into the uncertainty band of the experimental result.

Electromagnetic transitions. Since the second half of the past decade, *ab initio* calculations for transitions in medium-mass nuclei have become more frequent, owing to the appropriate extensions of the IMSRG, CC and SCGF methods [205, 230, 231]. While results for transitions that are dominated by a few nucleons, e.g., $M1$ transitions [230] or β decays (see reference [232] and the discussion below) can be quite good, the description of collective transitions is hampered by inherent truncations of these many-body methods, which are better suited for dynamical, few-particle correlations (see sections 2.3.3 and 2.3.4). Results from the SA-NCSM [139, 140] and the IM-GCM discussed in section 2.3.3 show that the modern chiral interactions themselves adequately support the emergence of nuclear collectivity.

Consider for example **Figure 10**, which shows VS-IMSRG(2) results for the quadrupole transition from the first excited 2^+ state to the ground state in ^{14}C, ^{22}O and ^{32}S [230]. The picture is fairly consistent for all four chiral NN+3N interactions that were used in the study: The 2^+ energies are described quite well, but energies are not very sensitive to the details of the nuclear wave functions. In ^{14}C, the $E2$ transition is weakly collective, so the $E2$ matrix element is reasonably reproduced, while the matrix element for the collective transition in ^{32}S is underpredicted by 25–50%. The NN+3N(400) interaction gives a particularly poor result, but this is also related to the significant underestimation of the point-proton radius we obtain for this Hamiltonian, as discussed earlier.

The result for ^{22}O deserves special attention. The $E2$ transition matrix element is only a third of the experimental value, although the transition is only weakly collective. However, ^{22}O only has neutrons in an *sd* valence space, so the $E2$ matrix element would vanish in a conventional Shell Model calculation unless the neutrons have an effective charge. Such effective charges must be introduced by hand and fit to data in phenomenological Shell Model calculations. Here, we see that the VS-IMSRG decoupling naturally induces a non-vanishing quadrupole moment through an effective neutron charge in the one-body transition operator as well as an induced two-body contribution (see reference [230], and reference [231] for an analogous effort in SCGF theory). It is likely that the $E2$ strength could be improved by performing the VS-IMSRG calculation in a *psd* valence space, so that the proton dynamics is treated explicitly instead of implicitly by valence-space decoupling. Until recently, we were unable to perform such a multi-shell decoupling because of the IMSRG version of the intruder-state problem, but a promising workaround was introduced in reference [28].

Gamow-Teller transitions. In recent years, there have been concerted efforts to understand the mechanisms behind the empirically observed quenching of Gamow-Teller (GT) transitions in medium-mass nuclei, in part due to its relevance to neutrinoless double-beta decay searches (see below). In reference [232], the authors show that this issue is largely resolved by properly accounting for the scale and scheme dependence of configuration-space calculations. By dialing the resolution scale to typical values favored by approaches like NCSM, CC, and VS-IMSRG, correlations are shifted from the wave functions into induced two- and higher-body contributions to the renormalized transition operator, just as in the quadrupole case discussed above.

The transition operator, including two-body currents, is consistently evolved to lower resolution scale alongside the nuclear interactions, keeping the induced contributions. The transition matrix elements of the evolved operator are then computed with the NCSM in light nuclei, and VS-IMSRG in *sd*- and *pf*-shell nuclei, leading to agreement with experimental GT strengths within a few %. In contrast, the bare GT operator must be quenched by 20–25% via the introduction of an effective axial coupling, $g_A^{\rm eff} < g_A$, to yield agreement with experimental beta decay rates.

The GT transitions in light nuclei have also been evaluated in the GFMC, most recently with consistently constructed local chiral interactions and currents [234, 235]. Interestingly, the inclusion of two-body currents seems to consistently enhance the GT matrix elements, while it tends to quench the matrix element in NCSM calculations. Since this is almost certainly related to the differences in the resolution scale and calculation scheme, the disentanglement of these observables might yield further insights into the interplay of wave function correlations and the renormalization of the transition operators.

Neutrinoless double beta decay. Due to the high impact the observation of neutrinoless double beta decay (or lack thereof) would have on particle physics and cosmology, the computation of nuclear matrix elements (NMEs) for neutrinoless double beta decay is a high priority for nuclear structure theory. Precise knowledge of the NMEs for various candidate nuclei is required to extract key observables like the absolute neutrino mass scale from the measured lifetimes (or at least, any new bounds that would be provided by experiment). Most calculations of the NME to date were subject to the lack of comparability between phenomenological nuclear structure results that was discussed in section 3.1, hence a new generation of *ab initio* calculations with quantified uncertainties is required.

A major step in that direction was the first calculation of the NME for the decay ^{48}Ca $\rightarrow^{48}$ Ti based on chiral interactions

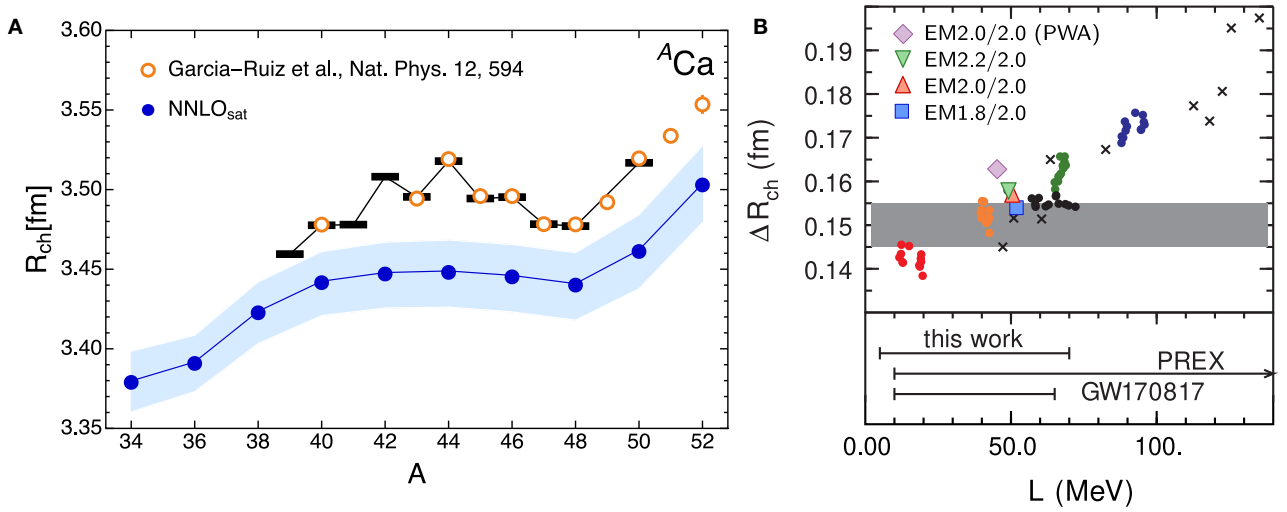

FIGURE 9 | (A) Calcium charge radii from MR-IMSRG(2) calculations with $NNLO_{sat}$ The shaded area indicates uncertainties from basis convergence. Black bars and orange circles indicate experimental data [195, 227]. **(B)** Mirror charge radius difference of ^{36}Ca and ^{36}S vs. the slope of the symmetry energy, L, at nuclear saturation, for the EMλ/Λ interactions (symbols as indicated in the legend), compared to Skyrme functionals (solid circles) and Relativistic Mean Field models (crosses). The band indicates the experimental result from the BECOLA facility at NSCL. See reference [228] for details.

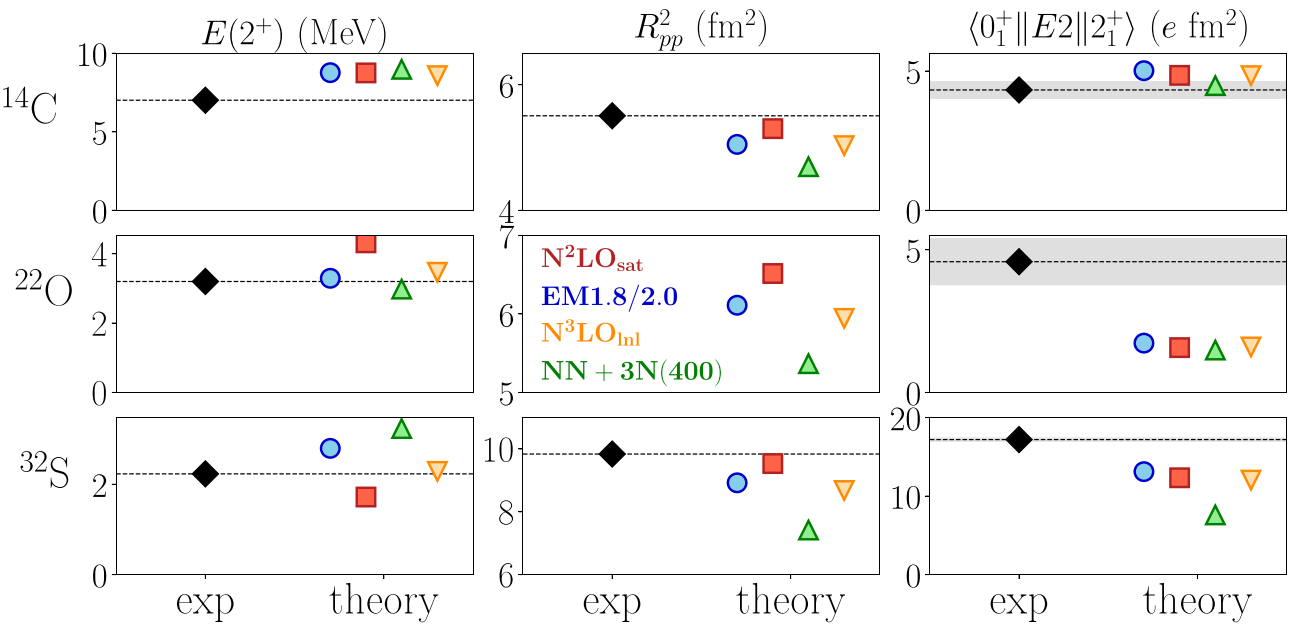

FIGURE 10 | Energies of the first excited 2^+ state, proton mean square radius and quadrupole transition matrix elements for selected nuclei, based on VS-IMSRG(2) calculations with multiple chiral NN+3N interactions. See references [76] and [230] for more details. Experimental values (with uncertainties indicated by bands) are taken from [227, 233]. Figure courtesy of R. Stroberg.

[29]. The IM-GCM approach discussed in section 2.3.3 was used to describe the structure of the intrinsically deformed daughter nucleus ^{48}Ti, achieving a satisfactory reproduction of the low-lying states and their quadrupole transitions (see **Figure 11**). Since the initial publication (blue spectra in **Figure 11A**), the description of the excited states has been improved further through the admixing of cranked configurations (red spectra), without affecting the NME (**Figure 11B**). Work on quantifying the uncertainties due to the many-body method, the Hamiltonian, and the transition operator is underway, in preparation for the computation of the NMEs of more realistic candidate nuclei like ^{76}Ge and ^{136}Xe.

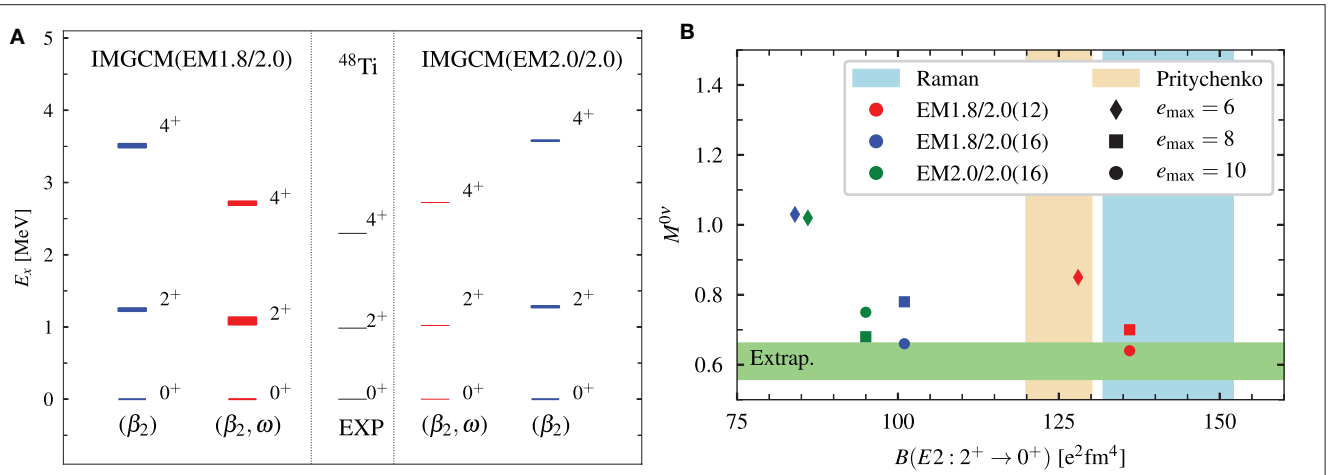

FIGURE 11 | IM-GCM description of the neutrinoless double beta decay ^{48}Ca $\rightarrow^{48}$ Ti, using EMλ/Λ interactions: Low-lying spectrum of ^{48}Ti and its compression through the admixing of cranked configurations **(A)** and the nuclear matrix element vs. B(E2) transition probability **(B)**. See text and reference [29] for details. **(A)** courtesy of J. M. Yao, **(B)** reprinted with permission from the American Physical Society.

3.2.4. Response and Scattering

From the computation of transitions between low-lying levels, it is only a small step to the computation of nuclear response functions and cross sections, although the implementation can be challenging and the applications are often computationally expensive.

Nuclear response functions. In light nuclei, GFMC is a powerful yet numerically heavy tool for computing exact nuclear response functions (see, e.g., references [236, 237]). In medium-mass nuclei, applications of SCGF and CC techniques to the computation of the nuclear response have been published in recent years. As mentioned in section 2.3.5, the Green's functions computed in the standard or Gor'kov ADC Green's function schemes inherently contain information about the nuclear response that has been used to study both electromagnetic and weak processes of medium-mass nuclei [119, 120, 238–240].

In the Coupled Cluster framework, response functions have been computed by merging CC with up to Triples excitations with the Lorentz Integral Transformation (LIT) technique [241–245]. Immediately after its inception, this approach was used to for the first *ab initio* calculations of dipole response and the related photodisassociation cross section of medium-mass closed-shell nuclei [241, 242]. More recently, it was used to compute the electric dipole polarizability α_D of nuclei like ^{48}Ca [243, 244, 246] and ^{68}Ni [247]. Together with measurements of the charge radius, this quantity can be used to constrain *ab initio* calculations that will in turn allow the theoretical extraction of the neutron point radius as well as the thickness of the neutron skin.

An important application for nuclear response calculations is to map out the neutrino response of ^{40}Ar, the primary target material in detectors for the short-baseline [248] and long-baseline neutrino experiments, like the Deep Underground Neutrino Experiment (DUNE) Far Detector [249, 250]. At low energies, the cross section for coherent neutrino elastic scattering is essentially determined by the weak form factor of ^{40}Ar, which has recently been computed using CC techniques [251]. This work is complementary to SCGF calculations of the neutrino response in the region of the quasi-elastic peak by Barbieri et al. [238].

Nuclear reactions. As discussed in section 2.3, there has been enormous progress in the development of unified treatments of *ab initio* nuclear structure and reactions. Here, I want to highlight two among a bevy of impressive results. **Figure 12A** shows $S-$ and $D-$wave phase shifts for $\alpha - \alpha$ scattering, computed order by order in Lattice EFT [179, 180]. These calculations are made possible by the lattice's capability to describe clustered states (also see references [176–178]), as well the development of the APM and associated algorithms. The results for the phase shifts show the desired order-by-order improvement, and the inclusion of higher-order terms of the chiral expansion is expected to improve agreement with experimental data. The near identical NLO and NNLO phase shifts in the $S-$wave appear to be the result of an accidental cancellation that is not occurring in the $D-$wave phase shifts.

In reference [252], the authors studied deuterium-tritium (D-T) fusion using the NCSMC. One of the main results of this work is shown in **Figure 12B**, which compares the NCSMC D–T reaction rates for polarized and unpolarized fuels to each other, as well as rates obtained with several widely used parameterizations of the D–T fusion cross section. The NCSMC calculations indicate that for an experimentally realizable polarized fuel with aligned spins, a reaction rate of the same magnitude as for unpolarized fuel can be achieved at about half the temperature. Naturally, this suggests that polarized D-T fuels will allow a more efficient power generation in thermonuclear reactors.

3.3. Emergence of Empirical Nuclear Structure Models From *ab initio* Calculations

The progress in *ab initio* calculations over the past decade has not only led to impressive results for nuclear observables, but also

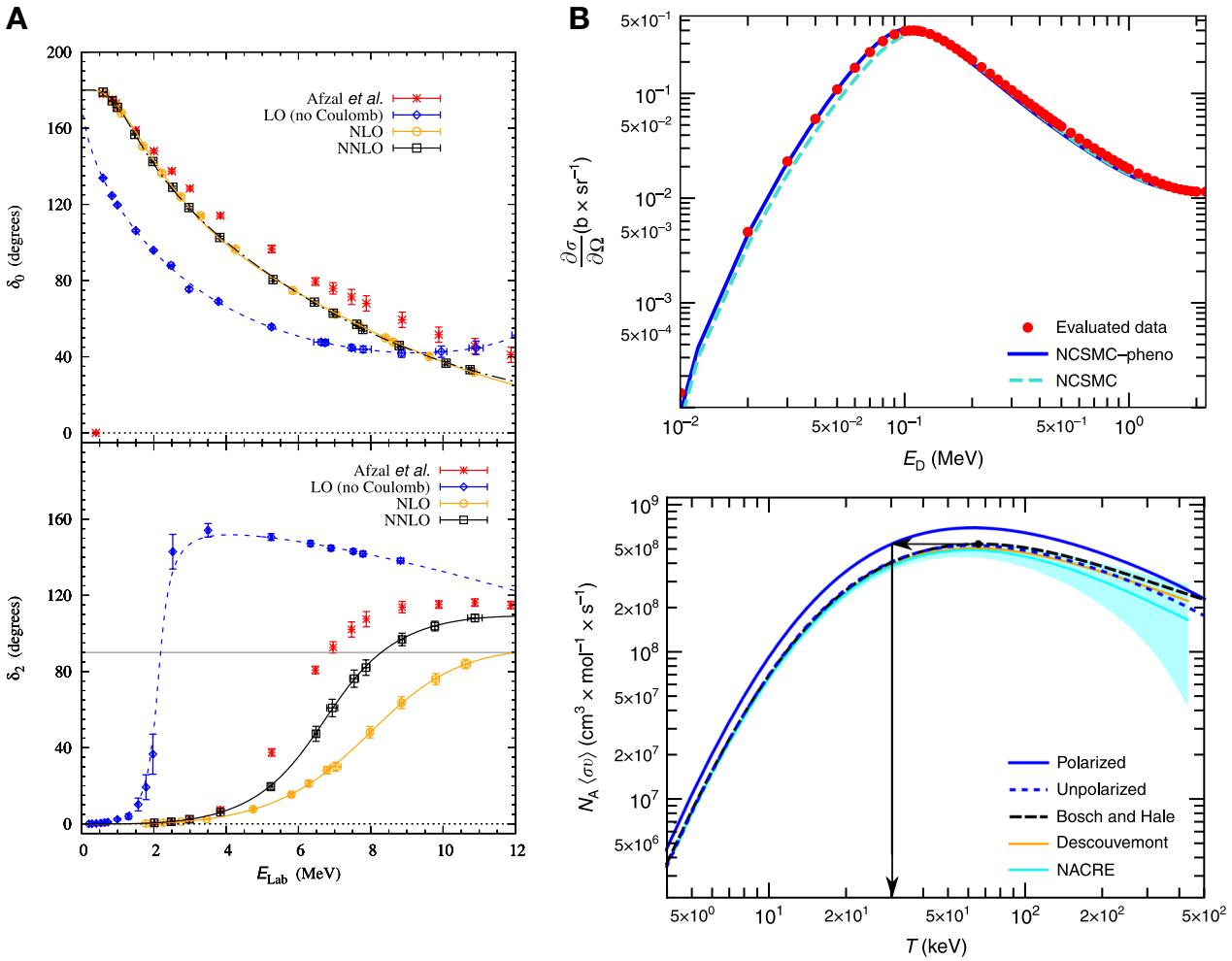

FIGURE 12 | *Ab initio* calculations of nuclear reactions. **(A)** S (δ_0) and D-wave phase shifts (δ_2) for α-α scattering at various orders in Lattice EFT. For details, see references [179, 180]. Figure courtesy of S. Elhatisari. **(B)** NCSMC results for the deuterium-tritium (D–T) fusion cross section (top) and reaction rate (bottom). The figure compares the rates for unpolarized and polarized fuel, as well as rates obtained from widely adopted parametrization of the fusion cross section (see reference [252] for details). The arrows are included to the guide the reader's eye (see text). Figure reprinted from Hupin et al. [252] under a CC BY 4.0 license.

revealed the long-surmised underpinnings of empirical models of nuclear structure. In many cases, the ideas that led to the formulation of such models were shown to be correct, but they could not be verified at the time because RG and EFT techniques or sufficient computing power for a more thorough exploration were not available.

The Nuclear Shell Model. The first prominent example I want to discuss is the nuclear Shell Model and some of the "folklore" surrounding it. We can immediately make the observation that the Shell model picture is inherently a low-momentum description of nuclear structure. It is based on the assumption that nucleons are able to move (almost) independently in a mean field potential, and that nuclear spectra can be explained by the mixing of a few valence configurations above an inert core via the residual interaction. As we know now, the existence of a bound mean-field solution and a weak, possibly perturbative residual interaction relies on the decoupling of low and high momenta in the nuclear Hamiltonian [1, 6, 253], e.g., by an SRG transformation. Historical approaches to exploit this connection to construct the Shell model from realistic nuclear forces [254–256] failed in part because the decoupling of the momentum scales via Brueckner's G−matrix formalism [65–67] was not as good as believed [1].

In addition to the momentum-space decoupling, one must also decouple the valence space configurations from the excluded space. This can be achieved using a variety of techniques (cf. sections 2.3.3–2.3.6), and either by performing transformations in sequence, or designing a single procedure that achieves both types of decoupling simultaneously. In practice, the former strategy tends to be more efficient and less prone to truncation errors—an example is the VS-IMSRG decoupling of Hamiltonians that have been evolved to a low resolution

scale by means of a prior SRG evolution (see sections 2.2 and 2.3.3, as well as reference [76]). An added benefit of using low-momentum interactions is that the Shell Model wave functions will qualitatively resemble those obtained by a no-core method using the same Hamiltonian without valence decoupling. This facilitates qualitative comparisons and allow us to apply the same intuitive picture. For quantitative comparisons, the effects of all unitary transformations must be carefully taken into account [257].

Figure 13 illustrates the effect of the discussed transformations via the deviations between the computed and experimental energies of close to 400 levels in the *sd*-shell. Since the EM1.8/2.0 interaction used in these calculations has a low resolution scale, simply using the valence-space matrix elements of the input Hamiltonian without any further valence-space decoupling yields a root-mean-square (rms) deviation of "only" about 1.7 MeV, which is not outright disastrous. When we apply the VS-IMRSG to decouple the valence space, the newly evolved interaction yields a much improved rms deviation of $\sim$ 650 keV, which is better than for some of the older *sd*-shell interactions, albeit not as good as the USDB Hamiltonian, which is shown for comparison [258, 259]. This is not really surprising: USDB essentially represents the best possible fit to experimental data under the model assumptions, i.e., the choice of a pure *sd*-shell valence space, the restriction to a two-body Hamiltonian, the omission of isospin-breaking effects from the Coulomb interaction and the nuclear interactions, and the empirical A-dependence multiplying the two-body matrix elements (TBMEs). The accuracy of the VS-IMSRG results, on the other hand, is affected by possible deficiencies in the input Hamiltonian and the use of the VS-IMSRG(2) truncation. Naturally, both of these aspects will be improved systematically in future calculations.

Phenomenological adjustments of effective Shell Model interactions like the A-dependent scaling factors in the USD Hamiltonians or Zuker's monopole shift [260] are typically attributed to the changes in the nuclear mean field away from the core, as well as missing three-body interactions. In reference [76], the VS-IMSRG is used to *demonstrate* that this is indeed the case. As described in section 2.3.3, upon normal ordering, the three-body force gives contributions to operators of equal and lower particle rank, which in the Shell Model case amounts to the core energy, single-particle energy, and two-body matrix elements. All of these contributions become A-dependent in the VS-IMSRG, but one can shift the A-dependent parts completely into the TBMEs, like in phenomenological interactions, without changing the Hamiltonian matrix in the many-body Hilbert space or its eigenvalues.

Procedures like the VS-IMSRG decoupling also let us track in detail how operators besides the nuclear interactions evolve when they are subject to the valence-decoupling transformation. Recall from the discussion in section 3.2.3 that this can even *quantitatively* explain the quenching of the Gamow-Teller strength in phenomenological Shell Model calculations, provided two-body current contributions to the initial transition operator are taken into account as well. For electromagnetic transitions, the renormalization of the one-body transition operator and the appearance of induced terms generate at least some part of the usual phenomenological effective charges, but a more complete treatment of nuclear collectivity (cf. section 2.3.3) as well the inclusion of current contributions to these operators are developments that need to be undertaken in the coming years.

Emergence of collectivity. Both NCCI and VS-IMSRG calculations with chiral NN+3N interactions have demonstrated that these interactions do indeed produce the telltale features of collective behavior in nuclear spectra [26, 141, 213, 261, 262]. Upon a bit of reflection, it is not surprising that reasonable results on rotational bands, for instance, should be found in these approaches: While they rely on particle-hole type expansions, the exact diagonalization is done in a complete model space of up to $A_v\mathrm{h}A_v\mathrm{p}$ excitations, where A_v is the number of valence nucleons. In contrast, equation-of-motion methods that typically employ 1p1h or 2p2h truncations struggle with the description of collectivity in low-lying states [83, 122, 204], but they do work reasonably well for giant resonances [241, 242].

As argued in sections 2.3.3 and 2.3.6, bases built on particle-hole type expansions are not ideally suited to the description of collective correlations. The SA-NCSM [139] instead uses irreducible representations of SU(3) or Sp(3,), the dynamical symmetry groups of collective models [263], to achieve a much more efficient description of collective behavior in nuclei. This is illustrated for the case of ^{20}Ne in **Figure 14**. The SA-NCSM calculations [140] based on the two-nucleon $NNLO_{opt}$ potential [264] describe the ground-state rotational band extremely well, all the way to the $J = 8^+$ state. It is dominated by a single SU(3) irrep, associated with the axially elongated shape of the computed intrinsic density profile that is also shown in the figure.

4. THE FUTURE TO BE WRITTEN: A LOOK AT THE CHALLENGES AHEAD

4.1. Rethinking the Many-Body Expansion

A substantial part of the appeal of methods like CC, IMSRG and SCGF is their polynomial scaling. For the purposes of uncertainty quantification (UQ), we need to be able to evaluate at least two consecutive truncation levels to assess the convergence of the many-body expansion in nuclei for which exact calculations are not feasible. Efforts in that direction have been in progress for some time, and while some methods are at a more advanced stage than others, the improved truncations should be available for regular use within the next couple of years [10, 12, 86, 100, 116, 244, 265]. In part, this is owing to the development of computer tools that automate tasks like diagrammatic evaluation or angular momentum coupling [266, 267]. The computational scaling of these approaches will be of order $\mathcal{O}(N^8)$ or $\mathcal{O}(N^9)$, which makes applications a task for leadership-class computing resources for the foreseeable future. It is clear that it will not be feasible to just push the calculations further, since we would then face a (naive) $\mathcal{O}(N^{12})$ scaling.

Applications where we would expect to need high-order truncations involve nuclear states with strong collective correlations, provided we work from a spherical reference state. As explained in section 2.3, this issue can likely be

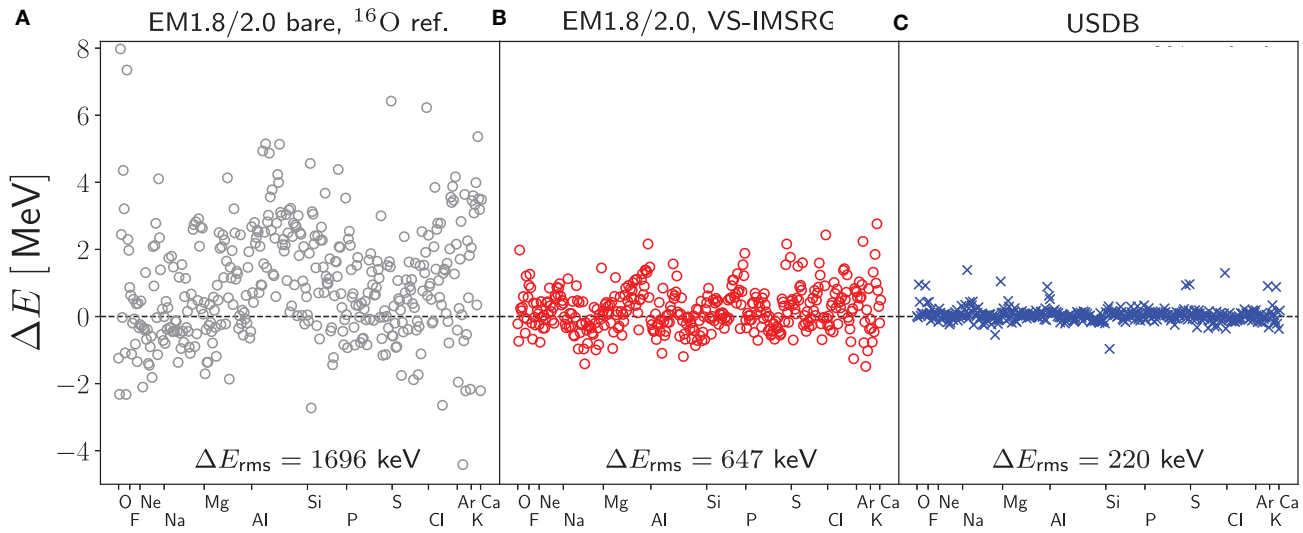

FIGURE 13 | Deviations between theoretical and experimental excitation energies of 391 *sd*-shell states, for **(A)** the EM1.8/2.0 interaction without valence decoupling, **(B)** the same interaction transformed with VS-IMSRG, and **(C)** the USDB interaction [258]. The points correspond to the respective root-mean-square deviations for each interaction. Figure courtesy of R. Stroberg.

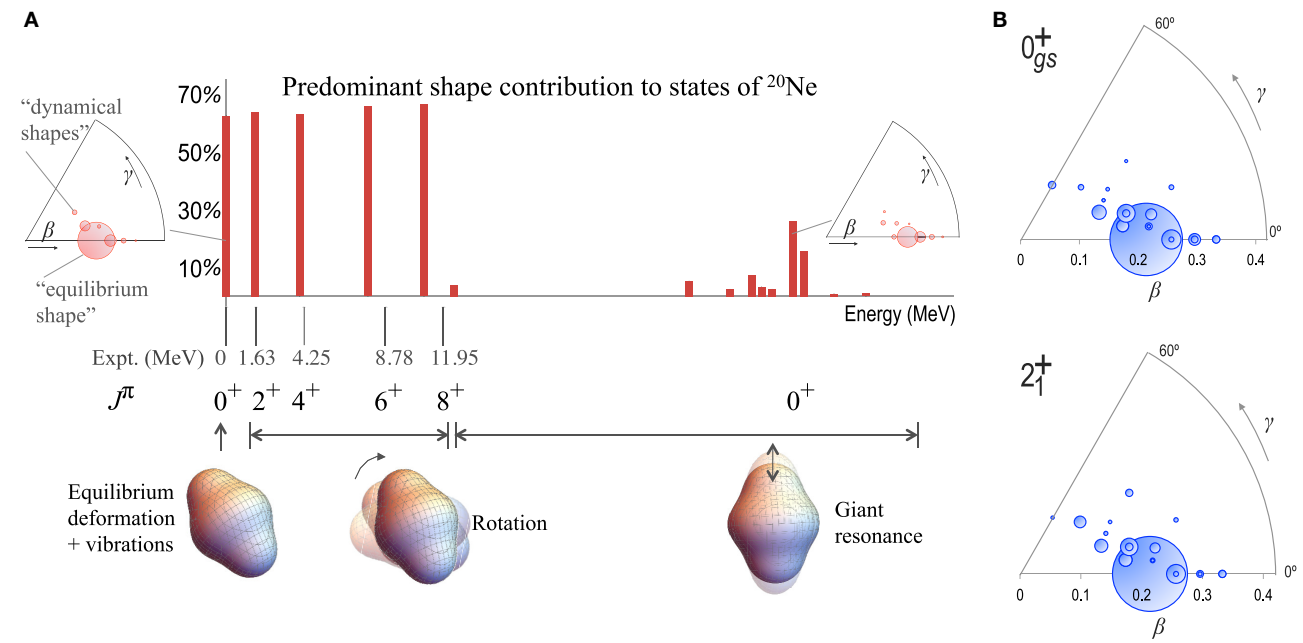

FIGURE 14 | SA-NCSM results for ^{20}Ne in an SU(3)-adapted basis, using the two-nucleon interaction [264]. **(A)** Excitation energies (horizontal axis) of the ground-state rotational band ($J^\pi = 0^+$ through 8^+) and 0^+ states, and the dominant shape in each state (vertical axis), indicated using the *ab initio* one-body density profiles in the intrinsic (body-fixed) frame. **(B)** Distribution of the equilibrium shapes that contribute to the ground state and first excited 2^+ state, indicated by the average deformation parameters (β, γ). See reference [140] for additional details. Figure reprinted with permission from the American Physical Society.

addressed either by using mean-field reference states with spontaneously broken symmetries (cf. section 2.3.4) or using correlated reference states in the first place (cf. section 2.3.3), and the first applications of the IM-GCM give credence to that idea. Moreover, there is first evidence that the CC and IMSRG truncations converge much more rapidly for observables that are sensitive to collectivity [268], i.e., the current state-of-the-art truncations may be sufficiently precise.

The IMSRG framework also offers perspectives for the construction of further IMSRG hybrid methods (cf. section

2.3.3). Based on the successes of both the IM-NCSM and IM-GCM it would be worthwhile to use IMSRG-evolved Hamiltonians in the SA-NCSM or techniques like the Density Matrix Renormalization Group, which is also capable of efficiently describing strong collective correlations under certain conditions [269, 270].

4.2. Leveraging Computational and Algorithmic Advances

The progress in *ab initio* many-body calculations is not simply due to the availability of increasingly powerful computational resources, but also due to dedicated collaborations with computer scientists to ensure that the available high-performance computers are used efficiently. Such collaborations will only grow more important as hardware architectures change rapidly and a growing demand for computing time requires users to demonstrate sufficient efficiency to be granted access to supercomputers.

Measures to boost the numerical efficiency can also be taken at the many-body theory level. Efficient calculations rely on finding optimal representations of the relevant physical information that is encoded in the Hamiltonian. Algorithmic gains are possible whenever there is a mismatch, either because we made convenient choices, e.g., by expanding many-body states in terms of simple Slater determinants, or because we were not able to recognize simplifications beforehand, e.g., due to hidden or dynamical symmetries.

The SRG has played a key role in addressing the first points at the level of the nuclear interaction over the past two decades, and SRG and IMSRG can be applied in novel ways to explore dynamical symmetries [55]. In the construction of a configuration space, the selection of the single-particle basis leaves room for optimization. Indeed, the natural orbitals introduced in reference [131] lead to faster model-space convergence in NCSM and CC calculations, implying a more compact Hamiltonian matrix in natural orbital representation. The efficiency of this representation can be leveraged further by making robust importance truncations based on analytical measures, e.g., in MBPT, CC, or IT-NCSM [9, 271].

The aforementioned steps make use of prior theoretical knowledge, e.g., to identify desired decoupling patterns in interactions, or define analytical measures for the importance of basis states. If such knowledge is not available, or we want to avoid bias, we can leverage a myriad of Principal Component Analysis (PCA) methods to factorize interactions or intermediate quantities in many-body calculations [271, 272]. This can potentially even give us control over the computational scaling of nuclear many-body methods (see, e.g., [273–277]).

A very noteworthy development with origins in nuclear physics is Eigenvector Continuation (EVC) [278, 279], a method for learning manifolds of eigenvector trajectories of parameter-dependent Hamiltonians. The method has been employed in several contexts, e.g., to stabilize high-order MBPT expansions [81] and to construct emulators for nuclear few- and many-body calculations [280, 281]. As an example, **Figure 15** shows a global sensitivity analysis of CC results for ^{16}O under variations of the chiral LECs [281]. Eigenvector continuation was used to learn representations of the CCSD Hamiltonian and charge radius operators in a 64-dimensional subspace of the space of CCSD ground-state wave functions for interactions with 16 varying LECs. The subspace-projected Hamiltonian was then sampled more than a million times on laptop, while full CCSD calculations of the same ensemble would be completely unfeasible. The successful applications of EVC suggest that the method should be further explored as a tool for improvement, emulation and UQ in other many-body methods in the (near) future.

4.3. Uncertainty Quantification

In typical nuclear many-body calculations as discussed in sections 2 and 3 the main sources of theoretical uncertainties are the EFT truncation of the observables and the many-body wave function, either due to many-body expansion and/or model space truncations in configuration space approaches, lattice discretization effects in Lattice EFT, or the specific form of the wave function ansatz in QMC. If an SRG evolution is applied, there is an additional uncertainty associated with the truncation of induced operators (see section 2.2).

The application of Bayesian methods has led to enormous progress in the quantification of the EFT uncertainties [34–36, 282–285], and it would be highly desirable to apply the same approach to the many-body uncertainties as well. The most challenging amongst these are the truncation of the many-body expansion in methods like CC, IMSRG or SCGF, and the truncation of the free-space SRG flow of observables. In contrast, the infrared effects of finite-basis size truncations in HO bases—or general orbitals that are at some point expanded in an HO basis—are well-understood for the energy and other observables, and they can be systematically corrected for [286–290]. The situation is less clear for ultraviolet basis-size errors [291], but this error can be suppressed by working at appropriate values of the HO frequency.

An ideal uncertainty analysis would combine the exploration of EFT and many-body uncertainties for nuclear observables of interest, using EC or Machine Learning (ML) to construct emulators that allow an efficient sampling of the parameter space. In such an effort, the generation of sufficient training data poses a significant challenge, because it would require calculations at several truncation levels (see section 4.1). A possible strategy for mitigating this issue is to combine non-perturbative methods with cheaper high-order MBPT in Bayesian mixed models (see references [212, 292, 293] for applications in nuclear physics). The successful application of factorization methods to the nuclear many-body problem could likely resolve the issue once and for all by reducing the computational scaling of high-order truncations, at the cost of introducing an additional uncertainty from the factorization procedure.

On the road toward the destination represented by such a "complete" UQ framework, the intermediate milestones will already provide valuable insights into open issues in the EFTs of the strong interactions, and enable the design of better protocols for constraining and refining EFT-based interactions and operators (see, e.g., references [294, 295] and references therein).

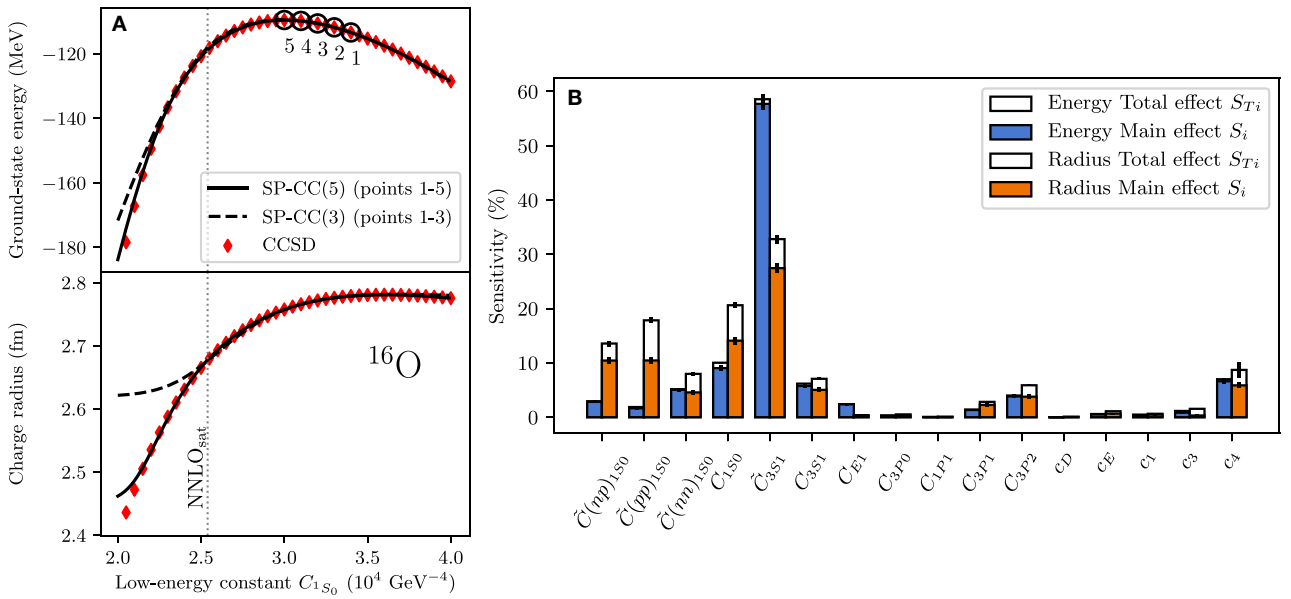

FIGURE 15 | Sensitivity analysis using subspace-projected CC (SPCC) method [281]. **(A)** illustrates the capability of the SPCC Hamiltonian constructed from 3 to 5 sample points to predict full CCSD ground-state energies and charge radii for ^{16}O over a wide range of values of the chiral LEC $C_{^1S_0}$. **(B)** Shows the global sensitivity of the ^{16}O ground-state energy and charge radius to chiral LECs, determined by evaluating over 1,000,000 quasi-MC samples from a 64-dimensional SPCC Hamiltonian. Vertical bars indicate 95% confidence intervals. For details, see reference [281]. Figure reprinted with permission from the American Physical Society.

4.4. Strengthening and Employing the Hierarchy of Strong Interaction EFTs

Strong interaction physics is a multi-scale problem, and there are good reasons for making better use of the hierarchy of Effective (Field) Theories at our disposal. At the top level, we have QCD, followed by EFTs involving hyperons that can be eliminated progressively until we arrive at the "traditional" pionful and pionless chiral EFTs (see references [296, 297] and references therein). At even lower scales, one can formulate an EFT for nuclear halos (or clusters) [297] and make the connection to nuclear DFT and collective models, which can be understood as EFTs as well [298–305].

At least in principle, the different levels of this hierarchy can be connected either by computing observables with different theories and matching the LECs, or using RG flows to track in detail how the theories evolve from one into another. While matching procedures have been applied successfully to modern EFts in nuclear physics [306–311] as well as efforts to match more traditional models of nuclear structure to *ab initio* calculations [312–314], making the connection through RG methods is a more daunting task. While I must admit to bias in this regard, I still consider this an effort worth undertaking. The success of SRG techniques in nuclear physics demonstrate how these methods reveal the most effective degrees of freedom even in situations were the separation of scales is not perfectly clear. Moreover, RGs would also reveal unexpected features of the power counting schemes, like the enhancement or inadvertent omission of certain operators (see reference [51] and references therein).

Tackling power counting issues. Throughout this work, I have alluded to shortcomings and issues of the current generation of chiral interactions, like the struggle to achieve a good simultaneous description of nuclear binding energies and radii (see section 3.1). Recent efforts to construct new, accurate chiral interactions have revealed that this issue is connected to the use of local or non-local regulators, with the latter being favored for better descriptions [114, 209]. In another exploration of non-locally regularized chiral forces [210, 211], a tension between the simultaneous description of nuclear matter and finite was observed in the attempts to fit the chiral LECs. In QMC calculations, it was demonstrated that the use of local regulators breaks the equivalence of parameterizations of the interaction that are connected by Fierz identities, in certain cases with disastrous consequences [188]. Meanwhile, Epelbaum et al. have proposed the use of a more nuanced semilocal regularization scheme that applies local regulators to the long-range pion exchange and non-local regulators to the short-range contact terms [3, 46]. While physical arguments can be made in favor of different regularization schemes, perhaps especially the semilocal one, the significant scheme dependence is at odds with the principles of EFT, which would predict regulator artifacts to be pushed beyond the order at which one currently works.

It has also been suggested that the scales of the chiral EFT interaction and the inherent scales of the many-body configuration space (e.g., IR and UV cutoffs inherited from a HO basis, see section 4.3) or coordinate space wave functions should not be treated independently, and that by doing so, current many-body approaches might at least contribute to power counting

issues. There have been a few efforts to explore this problem, but more work is clearly required [315–320].

Application needs. Aside from the formal need to make progress on the power counting issue, there are also concrete application needs that call for a tighter coupling between QCD and the nuclear EFTs. For example, the chiral EFT transition operator for neutrinoless double-beta decay (see section 3.2.3) contains counter terms whose LECs can only be determined from Lattice QCD [321–324].

The dawning of a new age in our understanding of neutron stars, heralded by the detection of gravitational waves from the neutron-star merger GW170817, has taken the demand for accurate neutron and nuclear matter equations of state to a new level (see, e.g., reference [159] and references therein). While *ab initio* calculations of infinite matter up to the saturation region based on chiral interactions are reasonably well-controlled [159, 190, 285, 325], the supranuclear densities probed in merger events are beyond the range of validity of regular pionful chiral EFT. To increase its validity, hyperons must be taken into account as dynamical degrees of freedom (see [296] and references therein), and the entire set of nuclear and hyperon LECs must be readjusted at the increased breakdown scale. For the NN sector, this is unproblematic due to the plethora of available scattering data. Since no direct experiments on three-neutron or three-proton systems are feasible, the only available experimental constraints come from finite nuclei, which implies that the corresponding channels of the 3N interaction are only constrained at sub-saturation densities. The world database of hyperon-nucleon scattering data is also quite limited. Thus, a high-precision interaction for describing the equation of state at high density can only be constructed with the help of Lattice QCD constraints on the 3N and hypernucleon LECs.

4.5. Interfacing With Reaction Theory

The final important research direction for the coming decade I want to discuss here are efforts to interface the advanced *ab initio* nuclear structure methods at our disposal with reaction theory [326].

As discussed in sections 2.3.6 and 3.2.4, the NCSMC has been applied with great success to the reactions of light nuclei at low energies, but its computational complexity makes this approach unfeasible for nuclei beyond $A \approx 10 - 20$. Work has begun on a similar approach that combines SA-NCSM with the RGM, leveraging the efficiency of the symmetry-adapted basis to reach medium-mass nuclei [327] (cf. sections 2.3.6 and 3.3). Since the RGM is just a special case of a Generator Coordinate Method, the IM-GCM discussed in sections 2.3.3 and 3.2.3 is a promising candidate for extending this type of reaction calculations to even heavier nuclei.

Methods that are similar in spirit to these combinations of structure approaches with the RGM are the APM, which can provide an interface between structure and scattering in Lattice EFT (cf. sections 2.3.8 and 3.2.4), as well as the GSM Coupled Channel (GSM-CC) approach, which was developed to describe reactions between light projectiles and targets that are treated in the GSM with a core [221, 328, 329]. Thus far, applications of the GSM-CC have been based on phenomenological valence-space interactions, but new efforts are underway to directly construct suitable Hamiltonians based on EFT principles [220, 330], or derive the effective interactions from chiral forces with the techniques discussed in section 2.3 (see [214, 215]). Of course, the GSM-CC ideas could also be applied to the No-Core GSM [153, 155, 218], although the computational complexity would limit such an approach to light nuclei.

A complementary strategy for bridging nuclear structure and reactions for medium-mass nuclei is the construction of optical potentials for use in traditional reaction calculations. In SCGF theory, the optical potential for elastic nucleon-nucleus scattering is given by the one-body self energy, which is obtained as a byproduct of a nuclear structure calculation, and can be used with little effort in reaction codes [125]. Similarly, Rotureau et al. constructed optical potentials by extracting the self-energy from the Coupled Cluster Green's Function [123, 124, 331]. One can roughly view this procedure as performing a GF calculation with the similarity-transformed CC Hamiltonian, which does not require self-consistent iterations because of the CC decoupling (cf. section 2.3.4). Optical potentials can also be constructed by folding scattering T-matrices with *ab initio* density matrices. This technique was applied for NCSM density matrices by two collaborations in references [332, 333] and [334, 335], respectively, and more applications are underway.

While the published results from the optical-potential based approaches are promising, an important aspect of these calculations *must* be checked carefully in the near term: The optical potential depends on the resolution scale of the used chiral interactions, and the calculation scheme, which encompasses the truncations in the operators and many-body method, as well as the choice of regulator in the interaction [257, 336]. To produce scale- and scheme-independent observables, these choices must be matched by the reaction theory. Matching the resolution scales is probably the easier of the two checks, but it will require the analysis of free-space SRG transformations on the reaction theory side. Once structure and theory are defined at a matching resolution scale, any residual scheme dependence of the observables will give rise to the remaining theoretical uncertainty of the combined calculation.

5. EPILOGUE

Thus concludes our little excursion through the landscape of state-of-the-art *ab initio* nuclear many-body theory, but of course, the road goes ever on. I hope that this guided tour has contributed to your appreciation of the immense progress the community has made in the last 10 years, as well as the challenges that we are facing on the next stage of the road. None of the obstacles in our path are unsurmountable, and while we chip away at them, results from *ab initio* calculations can make meaningful contributions to the analysis and planning of nuclear physics and fundamental symmetry experiments. With new facilities launching in the next couple of years, the fun will begin in earnest, so here's looking forward to the next decade!

AUTHOR CONTRIBUTIONS

The author confirms being the sole contributor of this work and has approved it for publication.

FUNDING

The preparation of this work has been supported by the U.S. Department of Energy, Office of Science, Office of Nuclear Physics under Awards No. DE-SC0017887, DE-SC0018083 (NUCLEI2 SciDAC-4 Collaboration), and DE-SC0015376 (DBD Topical Theory Collaboration).

ACKNOWLEDGMENTS

This work has been shaped by an enormous amount of discussions over the past decade, and naming all discussion partners would likely require multiple pages—it is safe to say that if your work is cited here, we have likely talked in person at some point. I am deeply grateful for these conversations, and the spirit of the *ab initio* nuclear structure and reactions community that fosters such exchanges.

I would like to thank the current (and former) members of my research group as well as colleagues at NSCL/FRIB, who had the most immediate impact on this work by virtue of being a short walk away. Particular thanks go out to S. Bogner, K. Fossez, M. Hjorth-Jensen, R. Wirth, and J. M. Yao. Special thanks are owed to R. Stroberg and S. Elhatisari, who helped out with sudden requests for figures.

I am also grateful to the Institute of Nuclear Theory for its hospitality, which was the venue for many of the aforementioned discussions, most recently during the program INT-19-2a, Nuclear Structure at the Crossroads.

REFERENCES

1. Bogner SK, Furnstahl RJ, Schwenk A. From low-momentum interactions to nuclear structure. *Prog Part Nucl Phys.* (2010) **65**:94–147. doi: 10.1016/j.ppnp.2010.03.001
2. Machleidt R, Sammarruca F. Chiral EFT based nuclear forces: achievements and challenges. *Phys Scripta.* (2016) **91**:083007. doi: 10.1088/0031-8949/91/8/083007
3. Epelbaum E, Krebs H, Reinert P. High-precision nuclear forces from chiral EFT: state-of-the-art, challenges, and outlook. *Front Phys.* (2020) **8**:98. doi: 10.3389/fphy.2020.00098
4. Piarulli M, Tews I. Local nucleon-nucleon and three-nucleon interactions within chiral effective field theory. *Front Phys.* (2020) **7**:245. doi: 10.3389/fphy.2019.00245
5. Roth R, Langhammer J. Padé-resummed high-order perturbation theory for nuclear structure calculations. *Phys Lett B.* (2010) **683**:272–7. doi: 10.1016/j.physletb.2009.12.046
6. Tichai A, Langhammer J, Binder S, Roth R. Hartree-Fock many-body perturbation theory for nuclear ground-states. *Phys Lett B.* (2016) **756**:283–8. doi: 10.1016/j.physletb.2016.03.029
7. Navrátil P, Gueorguiev VG, Vary JP, Ormand WE, Nogga A. Structure of $A = 10$–13 nuclei with two- plus three-nucleon interactions from chiral effective field theory. *Phys Rev Lett.* (2007) **99**:042501. doi: 10.1103/PhysRevLett.99.042501
8. Roth R, Navrátil P. *Ab initio* study of ^{40}Ca with an importance-truncated No-core shell model. *Phys Rev Lett.* (2007) **99**:092501. doi: 10.1103/PhysRevLett.99.092501
9. Roth R. Importance truncation for large-scale configuration interaction approaches. *Phys Rev C.* (2009) **79**:064324. doi: 10.1103/PhysRevC.79.064324
10. Somà V. Self-consistent Green's function theory for atomic nuclei. *arXiv.* (2020) *arxiv [Preprint] arXiv:*2003.11321.
11. Hergert H, Bogner SK, Morris TD, Schwenk A, Tsukiyama K. The in-medium similarity renormalization group: a novel *ab initio* method for nuclei. *Phys Rep.* (2016) **621**:165–222. doi: 10.1016/j.physrep.2015.12.007
12. Hagen G, Papenbrock T, Hjorth-Jensen M, Dean DJ. Coupled-cluster computations of atomic nuclei. *Rept Prog Phys.* (2014) **77**:096302. doi: 10.1088/0034-4885/77/9/096302
13. Coester F. Bound states of a many-particle system. *Nucl Phys.* (1958) **7**:421–4. doi: 10.1016/0029-5582(58)90280-3
14. Coester F, Kümmel H. Short-range correlations in nuclear wave functions. *Nucl Phys.* (1960) **17**:477–85. doi: 10.1016/0029-5582(60)90140-1
15. Hagen G, Hjorth-Jensen M, Jansen GR, Machleidt R, Papenbrock T. Continuum effects and three-nucleon forces in neutron-rich oxygen isotopes. *Phys Rev Lett.* (2012) **108**:242501. doi: 10.1103/PhysRevLett.108.242501
16. Hagen G, Hjorth-Jensen M, Jansen GR, Machleidt R, Papenbrock T. Evolution of shell structure in neutron-rich calcium isotopes. *Phys Rev Lett.* (2012) **109**:032502. doi: 10.1103/PhysRevLett.109.032502
17. Hergert H, Bogner SK, Binder S, Calci A, Langhammer J, Roth R, et al. In-medium similarity renormalization group with chiral two- plus three-nucleon interactions. *Phys Rev C.* (2013) **87**:034307. doi: 10.1103/PhysRevC.87.034307
18. Cipollone A, Barbieri C, Navrátil P. Isotopic chains around oxygen from evolved chiral two- and three-nucleon interactions. *Phys Rev Lett.* (2013) **111**:062501. doi: 10.1103/PhysRevLett.111.062501
19. Binder S, Langhammer J, Calci A, Roth R. *Ab initio* path to heavy nuclei. *Phys Lett B.* (2014) **736**:119–23. doi: 10.1016/j.physletb.2014.07.010
20. Hergert H, Binder S, Calci A, Langhammer J, Roth R. *Ab initio* calculations of even oxygen isotopes with chiral two-plus-three-nucleon interactions. *Phys Rev Lett.* (2013) **110**:242501. doi: 10.1103/PhysRevLett.110.242501
21. Hergert H, Bogner SK, Morris TD, Binder S, Calci A, Langhammer J, et al. *Ab initio* multi-reference in-medium similarity renormalization group calculations of even calcium and nickel isotopes. *Phys Rev C.* (2014) **90**:041302. doi: 10.1103/PhysRevC.90.041302
22. Somà V, Barbieri C, Duguet T. *Ab initio* Gorkov-Green's function calculations of open-shell nuclei. *Phys Rev C.* (2013) **87**:011303. doi: 10.1103/PhysRevC.87.011303
23. Somà V, Cipollone A, Barbieri C, Navrátil P, Duguet T. Chiral two- and three-nucleon forces along medium-mass isotope chains. *Phys Rev C.* (2014) **89**:061301. doi: 10.1103/PhysRevC.89.061301
24. Jansen GR, Engel J, Hagen G, Navratil P, Signoracci A. Ab-initio coupled-cluster effective interactions for the shell model: application to neutron-rich oxygen and carbon isotopes. *Phys Rev Lett.* (2014) **113**:142502. doi: 10.1103/PhysRevLett.113.142502
25. Sun ZH, Morris TD, Hagen G, Jansen GR, Papenbrock T. Shell-model coupled-cluster method for open-shell nuclei. *Phys Rev C.* (2018) **98**:054320. doi: 10.1103/PhysRevC.98.054320
26. Bogner SK, Hergert H, Holt JD, Schwenk A, Binder S, Calci A, et al. Nonperturbative shell-model interactions from the in-medium similarity renormalization group. *Phys Rev Lett.* (2014) **113**:142501. doi: 10.1103/PhysRevLett.113.142501
27. Stroberg SR, Calci A, Hergert H, Holt JD, Bogner SK, Roth R, et al. Nucleus-dependent valence-space approach to nuclear structure. *Phys Rev Lett.* (2017) **118**:032502. doi: 10.1103/PhysRevLett.118.032502
28. Miyagi T, Stroberg SR, Holt JD, Shimizu N. *Ab initio* multi-shell valence-space Hamiltonians and the island of inversion. *arXiv.* (2020) *arxiv [Preprint] arXiv:*2004.12969.
29. Yao JM, Bally B, Engel J, Wirth R, Rodríguez TR, Hergert H. *Ab initio* treatment of collective correlations and the neutrinoless

double beta decay of ^{48}Ca. *Phys Rev Lett.* (2020) **124**:232501. doi: 10.1103/PhysRevLett.124.232501
30. Gross DJ, Wilczek F. Ultraviolet behavior of non-Abelian gauge theories. *Phys Rev Lett.* (1973) **30**:1343–6. doi: 10.1103/PhysRevLett.30.1343
31. Politzer HD. Reliable perturbative results for strong interactions? *Phys Rev Lett.* (1973) **30**:1346–9. doi: 10.1103/PhysRevLett.30.1346
32. Weinberg S. Effective chiral lagrangians for nucleon-pion interactions and nuclear forces. *Nucl Phys B.* (1991) **363**:3–18. doi: 10.1016/0550-3213(91)90231-L
33. Weinberg S. *The Quantum Theory of Fields, Vol. II. Modern Applications*. 2nd ed. Cambridge: Cambridge University Press (1996).
34. Melendez JA, Wesolowski S, Furnstahl RJ. Bayesian truncation errors in chiral effective field theory: nucleon-nucleon observables. *Phys Rev C.* (2017) **96**:024003. doi: 10.1103/PhysRevC.96.024003
35. Melendez JA, Furnstahl RJ, Phillips DR, Pratola MT, Wesolowski S. Quantifying correlated truncation errors in effective field theory. *Phys Rev C.* (2019) **100**:044001. doi: 10.1103/PhysRevC.100.044001
36. Wesolowski S, Furnstahl RJ, Melendez JA, Phillips DR. Exploring Bayesian parameter estimation for chiral effective field theory using nucleon-nucleon phase shifts. *J Phys G Nucl Part Phys.* (2019) **46**:045102. doi: 10.1088/1361-6471/aaf5fc
37. Epelbaum E, Hammer HW, Meißner UG. Modern theory of nuclear forces. *Rev Mod Phys.* (2009) **81**:1773–825. doi: 10.1103/RevModPhys.81.1773
38. Machleidt R, Entem DR. Chiral effective field theory and nuclear forces. *Phys Rept.* (2011) **503**:1–75. doi: 10.1016/j.physrep.2011.02.001
39. Rodriguez Entem D, Machleidt R, Nosyk Y. Nucleon-nucleon scattering up to N5LO in chiral effective field theory. *Front Phys.* (2020) **8**:57. doi: 10.3389/fphy.2020.00057
40. Ekström A. Analyzing the nuclear interaction: challenges and new ideas. *Front Phys.* (2020) **8**:29. doi: 10.3389/fphy.2020.00029
41. Ruiz Arriola E, Amaro JE, Navarro Pérez R. NN scattering and nuclear uncertainties. *Front Phys.* (2020) **8**:1. doi: 10.3389/fphy.2020.00001
42. Gazit D, Quaglioni S, Navrátil P. Three-nucleon low-energy constants from the consistency of interactions and currents in chiral effective field theory. *Phys Rev Lett.* (2009) **103**:102502. doi: 10.1103/PhysRevLett.103.102502
43. Pastore S, Girlanda L, Schiavilla R, Viviani M. Two-nucleon electromagnetic charge operator in chiral effective field theory (χEFT) up to one loop. *Phys Rev C.* (2011) **84**:024001. doi: 10.1103/PhysRevC.84.024001
44. Kölling S, Epelbaum E, Krebs H, Meißner UG. Two-nucleon electromagnetic current in chiral effective field theory: one-pion exchange and short-range contributions. *Phys Rev C.* (2011) **84**:054008. doi: 10.1103/PhysRevC.84.054008
45. Piarulli M, Girlanda L, Marcucci LE, Pastore S, Schiavilla R, Viviani M. Electromagnetic structure of A=2 and 3 nuclei in chiral effective field theory. *Phys Rev C.* (2013) **87**:014006. doi: 10.1103/PhysRevC.87.014006
46. Reinert P, Krebs H, Epelbaum E. Semilocal momentum-space regularized chiral two-nucleon potentials up to fifth order. *Eur Phys J A.* (2018) **54**:86. doi: 10.1140/epja/i2018-12516-4
47. Lynn JE, Tews I, Carlson J, Gandolfi S, Gezerlis A, Schmidt KE, et al. Chiral three-nucleon interactions in light nuclei, neutron-α scattering, and neutron matter. *Phys Rev Lett.* (2016) **116**:062501. doi: 10.1103/PhysRevLett.116.062501
48. Lynn JE, Tews I, Carlson J, Gandolfi S, Gezerlis A, Schmidt KE, et al. Quantum Monte Carlo calculations of light nuclei with local chiral two- and three-nucleon interactions. *Phys Rev C.* (2017) **96**:054007. doi: 10.1103/PhysRevC.96.054007
49. Valderrama MP, Sánchez MS, Yang CJ, Long B, Carbonell J, van Kolck U. Power counting in peripheral partial waves: the singlet channels. *Phys Rev C.* (2017) **95**:054001. doi: 10.1103/PhysRevC.95.054001
50. Sánchez MS, Yang CJ, Long B, van Kolck U. Two-nucleon $^1S_0$ amplitude zero in chiral effective field theory. *Phys Rev C.* (2018) **97**:024001. doi: 10.1103/PhysRevC.97.024001
51. van Kolck U. The problem of renormalization of chiral nuclear forces. *Front Phys.* (2020) **8**:79. doi: 10.3389/fphy.2020.00079
52. Wilson KG. The renormalization group: critical phenomena and the Kondo problem. *Rev Mod Phys.* (1975) **47**:773–840. doi: 10.1103/RevModPhys.47.773
53. Hergert H. In-medium similarity renormalization group for closed and open-shell nuclei. *Phys Scripta.* (2017) **92**:023002. doi: 10.1088/1402-4896/92/2/023002
54. Stroberg SR, Hergert H, Holt JD, Bogner SK, Schwenk A. Ground and excited states of doubly open-shell nuclei from *ab initio* valence-space Hamiltonians. *Phys Rev C.* (2016) **93**:051301. doi: 10.1103/PhysRevC.93.051301
55. Johnson CW. Unmixing symmetries. *Phys Rev Lett.* (2020) **124**:172502. doi: 10.1103/PhysRevLett.124.172502
56. Wegner F. Flow equations for Hamiltonians. *Ann Phys (Leipzig).* (1994) **3**:77. doi: 10.1002/andp.19945060203
57. Kehrein S. *The Flow Equation Approach to Many-Particle Systems. Vol. 237 of Springer Tracts in Modern Physics*. Berlin; Heidelberg: Springer Berlin Heidelberg (2006).
58. Hergert H, Bogner SK, Lietz JG, Morris TD, Novario SJ, Parzuchowski NM, et al. In-medium similarity renormalization group approach to the nuclear many-body problem. In: Hjorth-Jensen M, Lombardo MP, van Kolck U, editors. *An Advanced Course in Computational Nuclear Physics: Bridging the Scales from Quarks to Neutron Stars*. Cham: Springer International Publishing (2017). p. 477–570. doi: 10.1007/978-3-319-53336-0_10
59. Jurgenson ED, Navrátil P, Furnstahl RJ. Evolution of nuclear many-body forces with the similarity renormalization group. *Phys Rev Lett.* (2009) **103**:082501. doi: 10.1103/PhysRevLett.103.082501
60. Hebeler K. Momentum-space evolution of chiral three-nucleon forces. *Phys Rev C.* (2012) **85**:021002. doi: 10.1103/PhysRevC.85.021002
61. Wendt KA. Similarity renormalization group evolution of three-nucleon forces in a hyperspherical momentum representation. *Phys Rev C.* (2013) **87**:061001. doi: 10.1103/PhysRevC.87.061001
62. Calci A. *Evolved Chiral Hamiltonians at the Three-Body Level and Beyond*. Darmstadt: TU Darmstadt (2014).
63. Shavitt I, Bartlett RJ. *Many-Body Methods in Chemistry and Physics: MBPT and Coupled-Cluster Theory*. Cambridge: Cambridge University Press (2009).
64. Kutzelnigg W. How many-body perturbation theory (MBPT) has changed quantum chemistry. *Int J Quantum Chem.* (2009) **109**:3858–84. doi: 10.1002/qua.22384
65. Brueckner KA, Levinson CA, Mahmoud HM. Two-body forces and nuclear saturation. I. Central forces. *Phys Rev.* (1954) **95**:217–28. doi: 10.1103/PhysRev.95.217
66. Brueckner KA, Levinson CA. Approximate reduction of the many-body problem for strongly interacting particles to a problem of self-consistent fields. *Phys Rev.* (1955) **97**:1344–52. doi: 10.1103/PhysRev.97.1344
67. Day BD. Elements of the Brueckner-Goldstone theory of nuclear matter. *Rev Mod Phys.* (1967) **39**:719–44. doi: 10.1103/RevModPhys.39.719
68. Brandow BH. Linked-cluster expansions for the nuclear many-body problem. *Rev Mod Phys.* (1967) **39**:771–828. doi: 10.1103/RevModPhys.39.771
69. Tichai A, Roth R, Duguet T. Many-body perturbation theories for finite nuclei. *Front Phys.* (2020) **8**:164. doi: 10.3389/fphy.2020.00164
70. Langhammer J, Roth R, Stumpf C. Spectra of open-shell nuclei with Padé-resummed degenerate perturbation theory. *Phys Rev C.* (2012) **86**:054315. doi: 10.1103/PhysRevC.86.054315
71. Otsuka T, Suzuki T, Holt JD, Schwenk A, Akaishi Y. Three-body forces and the limit of oxygen isotopes. *Phys Rev Lett.* (2010) **105**:032501. doi: 10.1103/PhysRevLett.105.032501
72. Holt JD, Engel J. Effective double-β-decay operator for ^{76}Ge and ^{82}Se. *Phys Rev C.* (2013) **87**:064315. doi: 10.1103/PhysRevC.87.064315
73. Tsunoda N, Takayanagi K, Hjorth-Jensen M, Otsuka T. Multi-shell effective interactions. *Phys Rev C.* (2014) **89**:024313. doi: 10.1103/PhysRevC.89.024313
74. Holt JD, Menéndez J, Simonis J, Schwenk A. Three-nucleon forces and spectroscopy of neutron-rich calcium isotopes. *Phys Rev C.* (2014) **90**:024312. doi: 10.1103/PhysRevC.90.024312
75. Coraggio L, Covello A, Gargano A, Itaco N, Kuo TTS. Shell-model calculations and realistic effective interactions. *Prog Part Nucl Phys.* (2009) **62**:135–82. doi: 10.1016/j.ppnp.2008.06.001
76. Stroberg SR, Hergert H, Bogner SK, Holt JD. Nonempirical interactions for the nuclear shell model: an update. *Annu Rev Nucl Part Sci.* (2019) 69:307–62. doi: 10.1146/annurev-nucl-101917-021120

77. Tichai A, Arthuis P, Duguet T, Hergert H, Somà V, Roth R. Bogoliubov many-body perturbation theory for open-shell nuclei. *Phys Lett B.* (2018) **786**:195–200. doi: 10.1016/j.physletb.2018.09.044
78. Tichai A, Gebrerufael E, Vobig K, Roth R. Open-shell nuclei from No-core shell model with perturbative improvement. *Phys Lett B.* (2018) **786**:448–52. doi: 10.1016/j.physletb.2018.10.029
79. Kucharski SA, Bartlett RJ. Fifth-order many-body perturbation theory and its relationship to various coupled-cluster approaches. *Adv Quantum Chem.* (1986) **18**, 281–344. doi: 10.1016/S0065-3276(08)60051-9
80. Ripoche J, Tichai A, Duguet T. Normal-ordered k-body approximation in particle-number-breaking theories. *Eur Phys J A.* (2020) **56**:40. doi: 10.1140/epja/s10050-020-00045-8
81. Demol P, Duguet T, Ekström A, Frosini M, Hebeler K, König S, et al. Improved many-body expansions from eigenvector continuation. *Phys Rev C.* (2020) **101**:041302. doi: 10.1103/PhysRevC.101.041302
82. Hjorth-Jensen M, Kuo TTS, Osnes E. Realistic effective interactions for nuclear systems. *Phys Rept.* (1995) **261**:125–270. doi: 10.1016/0370-1573(95)00012-6
83. Parzuchowski NM, Morris TD, Bogner SK. *Ab initio* excited states from the in-medium similarity renormalization group. *Phys Rev C.* (2017) **95**:044304. doi: 10.1103/PhysRevC.95.044304
84. Gebrerufael E, Vobig K, Hergert H, Roth R. *Ab initio* description of open-shell nuclei: merging No-core shell model and in-medium similarity renormalization group. *Phys Rev Lett.* (2017) **118**:152503. doi: 10.1103/PhysRevLett.118.152503
85. Yao JM, Engel J, Wang LJ, Jiao CF, Hergert H. Generator-coordinate reference states for spectra and $0\nu\beta\beta$ decay in the in-medium similarity renormalization group. *Phys Rev C.* (2018) **98**:054311. doi: 10.1103/PhysRevC.98.054311
86. Hergert H, Yao JM, Morris TD, Parzuchowski NM, Bogner SK, Engel J. Nuclear structure from the in-medium similarity renormalization group. *J Phys Conf Series.* (2018) **1041**:012007. doi: 10.1088/1742-6596/1041/1/012007
87. Tsukiyama K, Bogner SK, Schwenk A. In-medium similarity renormalization group for nuclei. *Phys Rev Lett.* (2011) **106**:222502. doi: 10.1103/PhysRevLett.106.222502
88. Tsukiyama K, Bogner SK, Schwenk A. In-medium similarity renormalization group for open-shell nuclei. *Phys Rev C.* (2012) **85**:061304. doi: 10.1103/PhysRevC.85.061304
89. Caurier E, Martínez-Pinedo G, Nowacki F, Poves A, Zuker AP. The shell model as a unified view of nuclear structure. *Rev Mod Phys.* (2005) **77**:427–88. doi: 10.1103/RevModPhys.77.427
90. Brown BA, Rae WDM. The shell-model code NuShellX@MSU. *Nucl Data Sheets.* (2014) **120**:115–8. doi: 10.1016/j.nds.2014.07.022
91. Engeland T, Hjorth-Jensen M. *The Oslo FCI Code.* (2017). Available online at: https://github.com/ManyBodyPhysics/ManybodyCodes
92. Johnson CW, Ormand WE, McElvain KS, Shan H. BIGSTICK: a flexible configuration-interaction shell-model code. *arXiv*. (2018) *arxiv [Preprint] arXiv*:180108432.
93. Shimizu N, Mizusaki T, Utsuno Y, Tsunoda Y. Thick-restart block Lanczos method for large-scale shell-model calculations. *Comput Phys Commun.* (2019) **244**:372–84. doi: 10.1016/j.cpc.2019.06.011
94. Kutzelnigg W, Mukherjee D. Normal order and extended Wick theorem for a multiconfiguration reference wave function. *J Chem Phys.* (1997) **107**:432–49. doi: 10.1063/1.474405
95. Kong L, Nooijen M, Mukherjee D. An algebraic proof of generalized Wick theorem. *J Chem Phys.* (2010) **132**:234107. doi: 10.1063/1.3439395
96. Morris TD, Parzuchowski NM, Bogner SK. Magnus expansion and in-medium similarity renormalization group. *Phys Rev C.* (2015) **92**:034331. doi: 10.1103/PhysRevC.92.034331
97. D'Alessio A, et al. Precision measurement of the *E*2 transition strength to the 2_1^+ state of ^{12}C. *arXiv*. (2020) *arxiv [Preprint] arXiv*:2005.04072.
98. Taube AG, Bartlett RJ. Improving upon CCSD(T): Lambda CCSD(T). I. Potential energy surfaces. *J Chem Phys.* (2008) **128**:044110. doi: 10.1063/1.2830236
99. Taube AG, Bartlett RJ. Improving upon CCSD(T): Lambda CCSD(T). II. Stationary formulation and derivatives. *J Chem Phys.* (2008) **128**:044111. doi: 10.1063/1.2830237
100. Binder S, Piecuch P, Calci A, Langhammer J, Navrátil P, Roth R. Extension of coupled-cluster theory with a noniterative treatment of connected triply excited clusters to three-body Hamiltonians. *Phys Rev C.* (2013) **88**:054319. doi: 10.1103/PhysRevC.88.054319
101. Duguet T. Symmetry broken and restored coupled-cluster theory: I. Rotational symmetry and angular momentum. *J Phys G.* (2015) **42**:025107. doi: 10.1088/0954-3899/42/2/025107
102. Signoracci A, Duguet T, Hagen G, Jansen GR. *Ab initio* Bogoliubov coupled cluster theory for open-shell nuclei. *Phys Rev C.* (2015) **91**:064320. doi: 10.1103/PhysRevC.91.064320
103. Duguet T, Signoracci A. Symmetry broken and restored coupled-cluster theory: II. Global gauge symmetry and particle number. *J Phys G Nucl Part Phys.* (2017) **44**:015103. doi: 10.1088/0954-3899/44/1/015103
104. Qiu Y, Henderson TM, Duguet T, Scuseria GE. Particle-number projected Bogoliubov-coupled-cluster theory: application to the pairing Hamiltonian. *Phys Rev C.* (2019) **99**:044301. doi: 10.1103/PhysRevC.99.044301
105. Jansen GR, Schuster MD, Signoracci A, Hagen G, Navrátil P. Open *sd*-shell nuclei from first principles. *Phys Rev C.* (2016) **94**:011301. doi: 10.1103/PhysRevC.94.011301
106. Taube AG, Bartlett RJ. New perspectives on unitary coupled-cluster theory. *Int J Quantum Chem.* (2006) **106**:3393–401. doi: 10.1002/qua.21198
107. Bartlett RJ, Musiał M. Coupled-cluster theory in quantum chemistry. *Rev Mod Phys.* (2007) **79**:291–352. doi: 10.1103/RevModPhys.79.291
108. Dumitrescu EF, McCaskey AJ, Hagen G, Jansen GR, Morris TD, Papenbrock T, et al. Cloud quantum computing of an atomic nucleus. *Phys Rev Lett.* (2018) **120**:210501. doi: 10.1103/PhysRevLett.120.210501
109. Lu HH, Klco N, Lukens JM, Morris TD, Bansal A, Ekström A, et al. Simulations of subatomic many-body physics on a quantum frequency processor. *Phys Rev A.* (2019) **100**:012320. doi: 10.1103/PhysRevA.100.012320
110. Miyagi T, Abe T, Okamoto R, Otsuka T. Introduction of the one-body correlation operator in the unitary-model-operator approach. *Phys Rev C.* (2017) **96**:054312. doi: 10.1103/PhysRevC.96.054312
111. Miyagi T, Abe T, Kohno M, Navrátil P, Okamoto R, Otsuka T, et al. Ground-state properties of doubly magic nuclei from the unitary-model-operator approach with chiral two- and three-nucleon forces. *Phys Rev C.* (2019) **100**:034310. doi: 10.1103/PhysRevC.100.034310
112. Dickhoff WH, Barbieri C. Self-consistent Green's function method for nuclei and nuclear matter. *Prog Part Nucl Phys.* (2004) **52**:377–496. doi: 10.1016/j.ppnp.2004.02.038
113. Barbieri C, Carbone A. Self-consistent Green's function approaches. In: Hjorth-Jensen M, Lombardo M, van Kolck U, editors. *An Advanced Course in Computational Nuclear Physics. No. 936 in Lecture Notes in Physics*. Springer. (2017).
114. Somà V, Navrátil P, Raimondi F, Barbieri C, Duguet T. Novel chiral Hamiltonian and observables in light and medium-mass nuclei. *Phys Rev C.* (2020) **101**:014318. doi: 10.1103/PhysRevC.101.014318
115. Rios A. Green's functions techniques for extended nuclear systems. *arXiv*. (2020) *arxiv [Preprint] arXiv*:2006.10610.
116. Morris TD. *Systematic Improvements of Ab Initio In-Medium Similarity Renormalization Group Calculations*. East Lansing, MI: Michigan State University (2016).
117. Somà V, Duguet T, Barbieri C. *Ab initio* self-consistent Gorkov-Green's function calculations of semimagic nuclei: Formalism at second order with a two-nucleon interaction. *Phys Rev C.* (2011) **84**:064317. doi: 10.1103/PhysRevC.84.064317
118. Somà V, Barbieri C, Duguet T. *Ab initio* self-consistent Gorkov-Green's function calculations of semi-magic nuclei: numerical implementation at second order with a two-nucleon interaction. *Phys Rev C.* (2014) **89**:024323. doi: 10.1103/PhysRevC.89.024323
119. Raimondi F, Barbieri C. Nuclear electromagnetic dipole response with the self-consistent Green's function formalism. *Phys Rev C.* (2019) **99**:054327. doi: 10.1103/PhysRevC.99.054327
120. Rocco N, Barbieri C. Inclusive electron-nucleus cross section within the self-consistent Green's function approach. *Phys Rev C.* (2018) **98**:025501. doi: 10.1103/PhysRevC.98.025501

121. Jansen GR, Hjorth-Jensen M, Hagen G, Papenbrock T. Toward open-shell nuclei with coupled-cluster theory. *Phys Rev C.* (2011) **83**:054306. doi: 10.1103/PhysRevC.83.054306
122. Jansen GR. Spherical coupled-cluster theory for open-shell nuclei. *Phys Rev C.* (2013) **88**:024305. doi: 10.1103/PhysRevC.88.024305
123. Rotureau J, Danielewicz P, Hagen G, Nunes FM, Papenbrock T. Optical potential from first principles. *Phys Rev C.* (2017) **95**:024315. doi: 10.1103/PhysRevC.95.024315
124. Rotureau J, Danielewicz P, Hagen G, Jansen GR, Nunes FM. Microscopic optical potentials for calcium isotopes. *Phys Rev C.* (2018) **98**:044625. doi: 10.1103/PhysRevC.98.044625
125. Idini A, Barbieri C, Navrátil P. *Ab initio* optical potentials and nucleon scattering on medium mass nuclei. *Phys Rev Lett.* (2019) **123**:092501. doi: 10.1103/PhysRevLett.123.092501
126. Navrátil P, Kamuntavicius GP, Barrett BR. Few-nucleon systems in translationally invariant harmonic oscillator basis. *Phys Rev C.* (2000) **61**:044001. doi: 10.1103/PhysRevC.61.044001
127. Barnea N, Leidemann W, Orlandini G. State-dependent effective interaction for the hyperspherical formalism with noncentral forces. *Nucl Phys A.* (2001) **693**:565–78. doi: 10.1016/S0375-9474(01)00794-1
128. Barnea N, Efros VD, Leidemann W, Orlandini G. Incorporation of three-nucleon force in the effective-interaction hyperspherical-harmonic approach. *Few Body Syst.* (2004) **35**:155–67. doi: 10.1007/s00601-004-0066-y
129. Barrett BR, Navrátil P, Vary JP. *Ab initio* no core shell model. *Prog Part Nucl Phys.* (2013) **69**:131–81. doi: 10.1016/j.ppnp.2012.10.003
130. Navrátil P, Quaglioni S, Hupin G, Romero-Redondo C, Calci A. Unified *ab initio* approaches to nuclear structure and reactions. *Phys Scripta.* (2016) **91**:053002. doi: 10.1088/0031-8949/91/5/053002
131. Tichai A, Müller J, Vobig K, Roth R. Natural orbitals for *ab initio* no-core shell model calculations. *Phys Rev C.* (2019) **99**:034321. doi: 10.1103/PhysRevC.99.034321
132. Robin C, Pillet N, Peña Arteaga D, Berger JF. Description of nuclear systems with a self-consistent configuration-mixing approach: theory, algorithm, and application to the ^{12}C test nucleus. *Phys Rev C.* (2016) **93**:024302. doi: 10.1103/PhysRevC.93.024302
133. Robin C, Pillet N, Dupuis M, Le Bloas J, Peña Arteaga D, Berger JF. Description of nuclear systems with a self-consistent configuration-mixing approach. II. Application to structure and reactions in even-even *sd*-shell nuclei. *Phys Rev C.* (2017) **95**:044315. doi: 10.1103/PhysRevC.95.044315
134. Pillet N, Robin C, Dupuis M, Hupin G, Berger JF. The self-consistent multiparticle-multihole configuration mixing. *Eur Phys J A.* (2017) **53**:49. doi: 10.1140/epja/i2017-12232-7
135. Roth R, Gour JR, Piecuch P. Center-of-mass problem in truncated configuration interaction and coupled-cluster calculations. *Phys Lett B.* (2009) **679**:334–9. doi: 10.1016/j.physletb.2009.07.071
136. Gloeckner DH, Lawson RD. Spurious center-of-mass motion. *Phys Lett B.* (1974) **53**:313–8. doi: 10.1016/0370-2693(74)90390-6
137. Otsuka T, Honma M, Mizusaki T, Shimizu N, Utsuno Y. Monte Carlo shell model for atomic nuclei. *Prog Part Nucl Phys.* (2001) **47**:319–400. doi: 10.1016/S0146-6410(01)00157-0
138. Shimizu N, Abe T, Honma M, Otsuka T, Togashi T, Tsunoda Y, et al. Monte Carlo shell model studies with massively parallel supercomputers. *Phys Scripta.* (2017) **92**:063001. doi: 10.1088/1402-4896/aa65e4
139. Launey KD, Dytrych T, Draayer JP. Symmetry-guided large-scale shell-model theory. *Prog Part Nucl Phys.* (2016) **89**:101–36. doi: 10.1016/j.ppnp.2016.02.001
140. Dytrych T, Launey KD, Draayer JP, Rowe DJ, Wood JL, Rosensteel G, et al. Physics of nuclei: key role of an emergent symmetry. *Phys Rev Lett.* (2020) **124**:042501. doi: 10.1103/PhysRevLett.124.042501
141. Caprio MA, Fasano PJ, Maris P, McCoy AE, Vary JP. Probing *ab initio* emergence of nuclear rotation. *Eur Phys J A.* (2020) **56**:120. doi: 10.1140/epja/s10050-020-00112-0
142. Lisetskiy AF, Barrett BR, Kruse MKG, Navrátil P, Stetcu I, Vary JP. *Ab-initio* shell model with a core. *Phys Rev C.* (2008) **78**:044302. doi: 10.1103/PhysRevC.78.044302
143. Lisetskiy AF, Kruse MKG, Barrett BR, Navrátil P, Stetcu I, Vary JP. Effective operators from exact many-body renormalization. *Phys Rev C.* (2009) **80**:024315. doi: 10.1103/PhysRevC.80.024315
144. Dikmen E, Lisetskiy AF, Barrett BR, Maris P, Shirokov AM, Vary JP. *Ab initio* effective interactions for *sd*-shell valence nucleons. *Phys Rev C.* (2015) **91**:064301. doi: 10.1103/PhysRevC.91.064301
145. Smirnova NA, Barrett BR, Kim Y, Shin IJ, Shirokov AM, Dikmen E, et al. Effective interactions in the *sd* shell. *Phys Rev C.* (2019) **100**:054329. doi: 10.1103/PhysRevC.100.054329
146. Kravvaris K, Volya A. Study of nuclear clustering from an *ab initio* perspective. *Phys Rev Lett.* (2017) **119**:062501. doi: 10.1103/PhysRevLett.119.062501
147. Ring P, Schuck P. *The Nuclear Many-Body Problem*. 1st ed. Springer (1980).
148. Shirokov AM, Mazur AI, Mazur IA, Vary JP. Shell model states in the continuum. *Phys Rev C.* (2016) **94**:064320. doi: 10.1103/PhysRevC.94.064320
149. Shirokov AM, Mazur AI, Mazur IA, Mazur EA, Shin IJ, Kim Y, et al. Nucleon-α scattering and resonances in ^{5}*He* and ^{5}*Li* with JISP16 and Daejeon16 *NN* interactions. *Phys Rev C.* (2018) **98**:044624. doi: 10.1103/PhysRevC.98.044624
150. Bang JM, Mazur AI, Shirokov AM, Smirnov YF, Zaytsev SA. P-matrix and J-matrix approaches: coulomb asymptotics in the harmonic oscillator representation of scattering theory. *Ann Phys.* (2000) **280**:299–335. doi: 10.1006/aphy.1999.5992
151. Berggren T. On the use of resonant states in eigenfunction expansions of scattering and reaction amplitudes. *Nucl Phys A.* (1968) **109**:265–87. doi: 10.1016/0375-9474(68)90593-9
152. Michel N, Nazarewicz W, Płoszajczak M, Vertse T. Shell model in the complex energy plane. *J Phys G.* (2009) **36**:013101. doi: 10.1088/0954-3899/36/1/013101
153. Papadimitriou G, Rotureau J, Michel N, Płoszajczak M, Barrett BR. *Ab initio* no-core Gamow shell model calculations with realistic interactions. *Phys Rev C.* (2013) **88**:044318. doi: 10.1103/PhysRevC.88.044318
154. Rotureau J, van Kolck U. Effective field theory and the Gamow shell model. *Few Body Syst.* (2013) **54**:725–35. doi: 10.1007/s00601-012-0455-6
155. Shin IJ, Kim Y, Maris P, Vary JP, Forssén C, Rotureau J, et al. *Ab initio* no-core solutions for ^{6}Li. *J Phys G Nucl Part Phys.* (2017) **44**:075103. doi: 10.1088/1361-6471/aa6cb7
156. Carlson J, Gandolfi S, Pederiva F, Pieper SC, Schiavilla R, Schmidt KE, et al. Quantum Monte Carlo methods for nuclear physics. *Rev Mod Phys.* (2015) **87**:1067–18. doi: 10.1103/RevModPhys.87.1067
157. Lynn JE, Tews I, Gandolfi S, Lovato A. Quantum Monte Carlo methods in nuclear physics: recent advances. *Annu Rev Nucl Part Sci.* (2019) **69**:279–305. doi: 10.1146/annurev-nucl-101918-023600
158. Gandolfi S, Lonardoni D, Lovato A, Piarulli M. Atomic nuclei from quantum Monte Carlo calculations with chiral EFT interactions. *Front Phys.* (2020) **8**:117. doi: 10.3389/fphy.2020.00117
159. Tews I. Quantum Monte Carlo methods for astrophysical applications. *Front Phys.* (2020) **8**:153. doi: 10.3389/fphy.2020.00153
160. Lonardoni D, Lovato A, Gandolfi S, Pederiva F. Hyperon puzzle: hints from quantum Monte Carlo calculations. *Phys Rev Lett.* (2015) **114**:092301. doi: 10.1103/PhysRevLett.114.092301
161. Madeira L, Lovato A, Pederiva F, Schmidt KE. Quantum Monte Carlo formalism for dynamical pions and nucleons. *Phys Rev C.* (2018) **98**:034005. doi: 10.1103/PhysRevC.98.034005
162. Cruz-Torres R, Lonardoni D, Weiss R, Barnea N, Higinbotham DW, Piasetzky E, et al. Scale and scheme independence and position-momentum equivalence of nuclear short-range correlations. *arXiv.* (2019) *arxiv [Preprint] arXiv:*1907.03658.
163. Lynn JE, Lonardoni D, Carlson J, Chen JW, Detmold W, Gandolfi S, et al. *Ab initio* short-range-correlation scaling factors from light to medium-mass nuclei. *J Phys G Nucl Part Phys.* (2020) **47**:045109. doi: 10.1088/1361-6471/ab6af7
164. Hirata S, He X, Hermes MR, Willow SY. Second-order many-body perturbation theory: an eternal frontier. *J Phys Chem A.* (2014) **118**:655–72. doi: 10.1021/jp410587b
165. Prokof'ev N, Svistunov B. Bold diagrammatic Monte Carlo technique: when the sign problem is welcome. *Phys Rev Lett.* (2007) **99**:250201. doi: 10.1103/PhysRevLett.99.250201
166. Van Houcke K, Werner F, Kozik E, Prokof'ev N, Svistunov B, Ku MJH, et al. Feynman diagrams versus Fermi-gas Feynman emulator. *Nat Phys.* (2012) **8**:366–70. doi: 10.1038/nphys2273

167. Scott CJC, Di Remigio R, Crawford TD, Thom AJW. Diagrammatic coupled cluster Monte Carlo. *J Phys Chem Lett.* (2019) **10**:925–35. doi: 10.1021/acs.jpclett.9b00067
168. Roggero A, Mukherjee A, Pederiva F. Quantum Monte Carlo calculations of neutron matter with nonlocal chiral interactions. *Phys Rev Lett.* (2014) **112**:221103. doi: 10.1103/PhysRevLett.112.221103
169. Booth GH, Thom AJW, Alavi A. Fermion Monte Carlo without fixed nodes: a game of life, death, and annihilation in Slater determinant space. *J Chem Phys*. (2009) **131**:054106. doi: 10.1063/1.3193710
170. Blunt NS, Thom AJW, Scott CJC. Preconditioning and perturbative estimators in full configuration interaction quantum Monte Carlo. *J Chem Theory Comput.* (2019) **15**:3537–51. doi: 10.1021/acs.jctc.9b00049
171. Ten-no S. Stochastic determination of effective Hamiltonian for the full configuration interaction solution of quasi-degenerate electronic states. *J Chem Phys*. (2013) **138**:164126. doi: 10.1063/1.4802766
172. Nicholson AN. Lattice methods and effective field theory. In: Hjorth-Jensen M, Lombardo M, van Kolck U, editors. *An Advanced Course in Computational Nuclear Physics. No. 936 in Lecture Notes in Physics*. Springer. (2017). p. 155–236. doi: 10.1007/978-3-319-53336-0_5
173. Lee D. Recent progress in nuclear lattice simulations. *Front Phys.* (2020) **8**:174. doi: 10.3389/fphy.2020.00174
174. Lähde TA, Meißner UG. *Nuclear Lattice Effective Field Theory. No. 957 in Lecture Notes in Physics*. Cham: Springer (2019).
175. Lee D. Lattice methods and the nuclear few- and many-body problem. In: Hjorth-Jensen M, Lombardo M, van Kolck U, editors. *An Advanced Course in Computational Nuclear Physics. No. 936 in Lecture Notes in Physics*. Springer (2017).
176. Epelbaum E, Krebs H, Lähde TA, Lee D, Meißner UG. Structure and rotations of the Hoyle State. *Phys Rev Lett.* (2012) **109**:252501. doi: 10.1103/PhysRevLett.109.252501
177. Epelbaum E, Krebs H, Lähde TA, Lee D, Meißner UG, Rupak G. *Ab initio* calculation of the spectrum and structure of O16. *Phys Rev Lett.* (2014) **112**:102501. doi: 10.1103/PhysRevLett.112.102501
178. Elhatisari S, Epelbaum E, Krebs H, Lähde TA, Lee D, Li N, et al. *Ab initio* calculations of the isotopic dependence of nuclear clustering. *Phys Rev Lett.* (2017) **119**:222505. doi: 10.1103/PhysRevLett.119.222505
179. Elhatisari S, Lee D, Rupak G, Epelbaum E, Krebs H, Lähde TA, et al. *Ab initio* alpha-alpha scattering. *Nature.* (2015) **528**:111–4. doi: 10.1038/nature16067
180. Elhatisari S. Adiabatic projection method with Euclidean time subspace projection. *Eur Phys J A.* (2019) **55**:144. doi: 10.1140/epja/i2019-12844-9
181. Klein N, Lee D, Meißner UG. Lattice improvement in lattice effective field theory. *Eur Phys J A.* (2018) **54**:233. doi: 10.1140/epja/i2018-12676-1
182. Klein N, Elhatisari S, Lähde TA, Lee D, Meißner UG. The Tjon band in nuclear lattice effective field theory. *Eur Phys J A.* (2018) **54**:121. doi: 10.1140/epja/i2018-12553-y
183. Roth R, Langhammer J, Calci A, Binder S, Navrátil P. Similarity-transformed chiral $NN+3N$ interactions for the *ab initio* description of ^{12}**C** and ^{16}**O**. *Phys Rev Lett.* (2011) **107**:072501. doi: 10.1103/PhysRevLett.107.072501
184. Huang WJ, Audi G, Wang M, Kondev FG, Naimi S, Xu X. The AME2016 atomic mass evaluation (I). Evaluation of input data; and adjustment procedures. *Chin Phys C.* (2017) **41**:030002. doi: 10.1088/1674-1137/41/3/030002
185. Kondo Y, Nakamura T, Tanaka R, Minakata R, Ogoshi S, Orr NA, et al. Nucleus ^{26}O: a barely unbound system beyond the drip line. *Phys Rev Lett.* (2016) **116**:102503. doi: 10.1103/PhysRevLett.116.102503
186. Holt JD, Stroberg SR, Schwenk A, Simonis J. *Ab initio* limits of atomic nuclei. *arXiv*. (2019) *arxiv [Preprint] arXiv:*1905.10475.
187. Gezerlis A, Tews I, Epelbaum E, Freunek M, Gandolfi S, Hebeler K, et al. Local chiral effective field theory interactions and quantum Monte Carlo applications. *Phys Rev C.* (2014) **90**:054323. doi: 10.1103/PhysRevC.90.054323
188. Lonardoni D, Gandolfi S, Lynn JE, Petrie C, Carlson J, Schmidt KE, et al. Auxiliary field diffusion Monte Carlo calculations of light and medium-mass nuclei with local chiral interactions. *Phys Rev C.* (2018) **97**:044318. doi: 10.1103/PhysRevC.97.044318
189. Piarulli M, Baroni A, Girlanda L, Kievsky A, Lovato A, Lusk E, et al. Light-nuclei spectra from chiral dynamics. *Phys Rev Lett.* (2018) **120**:052503. doi: 10.1103/PhysRevLett.120.052503
190. Lonardoni D, Tews I, Gandolfi S, Carlson J. Nuclear and neutron-star matter from local chiral interactions. *Phys Rev Res.* (2020) **2**:022033. doi: 10.1103/PhysRevResearch.2.022033
191. Wiringa RB, Stoks VGJ, Schiavilla R. Accurate nucleon-nucleon potential with charge-independence breaking. *Phys Rev C.* (1995) **51**:38–51. doi: 10.1103/PhysRevC.51.38
192. Lapoux V, Somà V, Barbieri C, Hergert H, Holt JD, Stroberg SR. Radii and binding energies in oxygen isotopes: a challenge for nuclear forces. *Phys Rev Lett.* (2016) **117**:052501. doi: 10.1103/PhysRevLett.117.052501
193. Michimasa S, Kobayashi M, Kiyokawa Y, Ota S, Ahn DS, Baba H, et al. Magic nature of neutrons in ^{54}Ca: first mass measurements of $^{55-57}Ca$. *Phys Rev Lett.* (2018) **121**:022506. doi: 10.1103/PhysRevLett.121.022506
194. Ekström A, Jansen GR, Wendt KA, Hagen G, Papenbrock T, Carlsson BD, et al. Accurate nuclear radii and binding energies from a chiral interaction. *Phys Rev C.* (2015) **91**:051301. doi: 10.1103/PhysRevC.91.051301
195. Garcia Ruiz RF, Bissell ML, Blaum K, Ekstrom A, Frommgen N, Hagen G, et al. Unexpectedly large charge radii of neutron-rich calcium isotopes. *Nat Phys.* (2016) **12**:594–8. doi: 10.1038/nphys3645
196. Hagen G, Jansen GR, Papenbrock T. Structure of ^{78}Ni from first-principles computations. *Phys Rev Lett.* (2016) **117**:172501. doi: 10.1103/PhysRevLett.117.172501
197. Leistenschneider E, Reiter MP, Ayet San Andrés S, Kootte B, Holt JD, Navrátil P, et al. Dawning of the $N = 32$ shell closure seen through precision mass measurements of neutron-rich titanium isotopes. *Phys Rev Lett.* (2018) **120**:062503. doi: 10.1103/PhysRevLett.120.062503
198. Nogga A, Bogner SK, Schwenk A. Low-momentum interaction in few-nucleon systems. *Phys Rev C.* (2004) **70**:061002. doi: 10.1103/PhysRevC.70.061002
199. Hebeler K, Bogner SK, Furnstahl RJ, Nogga A, Schwenk A. Improved nuclear matter calculations from chiral low-momentum interactions. *Phys Rev C.* (2011) **83**:031301. doi: 10.1103/PhysRevC.83.031301
200. Entem DR, Machleidt R. Accurate charge-dependent nucleon-nucleon potential at fourth order of chiral perturbation theory. *Phys Rev C.* (2003) **68**:041001. doi: 10.1103/PhysRevC.68.041001
201. Taniuchi R, Santamaria C, Doornenbal P, Obertelli A, Yoneda K, Authelet G, et al. 78Ni revealed as a doubly magic stronghold against nuclear deformation. *Nature.* (2019) **569**:53–8. doi: 10.1038/s41586-019-1155-x
202. National Nuclear Data Center. *NuDat 2 Database*. Available online at: https://www.nndc.bnl.gov/nudat2
203. Simonis J, Stroberg SR, Hebeler K, Holt JD, Schwenk A. Saturation with chiral interactions and consequences for finite nuclei. *Phys Rev C.* (2017) **96**:014303. doi: 10.1103/PhysRevC.96.014303
204. Morris TD, Simonis J, Stroberg SR, Stumpf C, Hagen G, Holt JD, et al. Structure of the lightest tin isotopes. *Phys Rev Lett.* (2018) **120**:152503. doi: 10.1103/PhysRevLett.120.152503
205. Henderson J, Hackman G, Ruotsalainen P, Stroberg SR, Launey KD, Holt JD, et al. Testing microscopically derived descriptions of nuclear collectivity: Coulomb excitation of ^{22}Mg. *Phys Lett B.* (2018) **782**:468–73. doi: 10.1016/j.physletb.2018.05.064
206. Evitts LJ, Garnsworthy AB, Kibédi T, Smallcombe J, Reed MW, Stuchbery AE, et al. $E0$ transition strength in stable Ni isotopes. *Phys Rev C.* (2019) **99**:024306. doi: 10.1103/PhysRevC.99.024306
207. Liu HN, Obertelli A, Doornenbal P, Bertulani CA, Hagen G, Holt JD, et al. How robust is the $N = 34$ subshell closure? First Spectroscopy of ^{52}Ar. *Phys Rev Lett.* (2019) **122**:072502. doi: 10.1103/PhysRevLett.122.072502
208. Xu X, Wang M, Blaum K, Holt JD, Litvinov YA, Schwenk A, et al. Masses of neutron-rich $^{52-54}Sc$ and $^{54,56}Ti$ nuclides: The $N = 32$ subshell closure in scandium. *Phys Rev C.* (2019) **99**:064303. doi: 10.1103/PhysRevC.99.064303
209. Hüther T, Vobig K, Hebeler K, Machleidt R, Roth R. Family of chiral two-plus three-nucleon interactions for accurate nuclear structure studies. *arXiv*. (2019) arXiv:1911.04955. doi: 10.1016/j.physletb.2020.135651
210. Drischler C, Hebeler K, Schwenk A. Chiral interactions up to next-to-next-to-next-to-leading order and nuclear saturation. *Phys Rev Lett.* (2019) **122**:042501. doi: 10.1103/PhysRevLett.122.042501
211. Hoppe J, Drischler C, Hebeler K, Schwenk A, Simonis J. Probing chiral interactions up to next-to-next-to-next-to-leading order in medium-mass nuclei. *Phys Rev C.* (2019) **100**:024318. doi: 10.1103/PhysRevC.100.024318

212. Neufcourt L, Cao Y, Nazarewicz W, Olsen E, Viens F. Neutron drip line in the Ca region from Bayesian model averaging. *Phys Rev Lett.* (2019) **122**:062502. doi: 10.1103/PhysRevLett.122.062502
213. Hagen G, Hjorth-Jensen M, Jansen GR, Papenbrock T. Emergent properties of nuclei from ab initio coupled-cluster calculations. *Phys Scripta.* (2016) **91**:063006. doi: 10.1088/0031-8949/91/6/063006
214. Sun ZH, Wu Q, Zhao ZH, Hu BS, Dai SJ, Xu FR. Resonance and continuum Gamow shell model with realistic nuclear forces. *Phys Lett B.* (2017) **769**:227–32. doi: 10.1016/j.physletb.2017.03.054
215. Hu BS, Wu Q, Li JG, Ma YZ, Sun ZH, Michel N, et al. An *ab-initio* Gamow shell model approach with a core. *Phys Lett B.* (2020) **802**:135206. doi: 10.1016/j.physletb.2020.135206
216. Hu BS, Wu Q, Sun ZH, Xu FR. *Ab initio* Gamow in-medium similarity renormalization group with resonance and continuum. *Phys Rev C.* (2019) **99**:061302. doi: 10.1103/PhysRevC.99.061302
217. Jaganathen Y, Betan RMI, Michel N, Nazarewicz W, Płoszajczak M. Quantified Gamow shell model interaction for *psd*-shell nuclei. *Phys Rev C.* (2017) **96**:054316. doi: 10.1103/PhysRevC.96.054316
218. Fossez K, Rotureau J, Michel N, Płoszajczak M. Can tetraneutron be a narrow resonance? *Phys Rev Lett.* (2017) **119**:032501. doi: 10.1103/PhysRevLett.119.032501
219. Fossez K, Rotureau J, Michel N, Nazarewicz W. Continuum effects in neutron-drip-line oxygen isotopes. *Phys Rev C.* (2017) **96**:024308. doi: 10.1103/PhysRevC.96.024308
220. Fossez K, Rotureau J, Nazarewicz W. Energy spectrum of neutron-rich helium isotopes: complex made simple. *Phys Rev C.* (2018) **98**:061302. doi: 10.1103/PhysRevC.98.061302
221. Wang SM, Nazarewicz W, Charity RJ, Sobotka LG. Structure and decay of the extremely proton-rich nuclei $^{11,12}O$. *Phys Rev C.* (2019) **99**:054302. doi: 10.1103/PhysRevC.99.054302
222. Mao X, Rotureau J, Nazarewicz W, Michel N, Betan RMI, Jaganathen Y. Gamow shell model description of Li isotopes and their mirror partners. *arXiv*. (2020) arXiv:2004.02981. doi: 10.1103/PhysRevC.102.024309
223. Calci A, Navrátil P, Roth R, Dohet-Eraly J, Quaglioni S, Hupin G. Can *Ab Initio* theory explain the phenomenon of parity inversion in ^{11}Be? *Phys Rev Lett.* (2016) **117**:242501. doi: 10.1103/PhysRevLett.117.242501
224. Kumar A, Kanungo R, Calci A, Navrátil P, Sanetullaev A, Alcorta M, et al. Nuclear force imprints revealed on the elastic scattering of protons with ^{10}C. *Phys Rev Lett.* (2017) **118**:262502. doi: 10.1103/PhysRevLett.118.262502
225. Vorabbi M, Calci A, Navrátil P, Kruse MKG, Quaglioni S, Hupin G. Structure of the exotic ^{9}He nucleus from the no-core shell model with continuum. *Phys Rev C.* (2018) **97**:034314. doi: 10.1103/PhysRevC.97.034314
226. Vorabbi M, Navrátil P, Quaglioni S, Hupin G. ^{7}Be and ^{7}Li nuclei within the no-core shell model with continuum. *Phys Rev C.* (2019) **100**:024304. doi: 10.1103/PhysRevC.100.024304
227. Angeli I, Marinova KP. Table of experimental nuclear ground state charge radii: an update. *Atomic Data Nucl Data Tables.* (2013) **99**:69–95. doi: 10.1016/j.adt.2011.12.006
228. Brown BA, Minamisono K, Piekarewicz J, Hergert H, Garand D, Klose A, et al. Implications of the $^{36}Ca-^{36}S$ and $^{38}Ca-^{38}$ Ar difference in mirror charge radii on the neutron matter equation of state. *Phys Rev Res.* (2020) **2**:022035. doi: 10.1103/PhysRevResearch.2.022035
229. Caurier E, Langanke K, Martínez-Pinedo G, Nowacki F, Vogel P. Shell model description of isotope shifts in calcium. *Phys Lett B.* (2001) **522**:240–4. doi: 10.1016/S0370-2693(01)01246-1
230. Parzuchowski NM, Stroberg SR, Navrátil P, Hergert H, Bogner SK. *Ab initio* electromagnetic observables with the in-medium similarity renormalization group. *Phys Rev C.* (2017) **96**:034324. doi: 10.1103/PhysRevC.96.034324
231. Raimondi F, Barbieri C. Core-polarization effects and effective charges in O and Ni isotopes from chiral interactions. *Phys Rev C.* (2019) **100**:024317. doi: 10.1103/PhysRevC.100.024317
232. Gysbers P, Hagen G, Holt JD, Jansen GR, Morris TD, Navrátil P, et al. Discrepancy between experimental and theoretical Îš-decay rates resolved from first principles. *Nat Phys.* (2019) **15**:428. doi: 10.1038/s41567-019-0450-7
233. Pritychenko B, Birch M, Singh B, Horoi M. Tables of E2 transition probabilities from the first 2+ states in even-even nuclei. *Atomic Data Nucl Data Tables.* (2016) **107**:1–139. doi: 10.1016/j.adt.2015.10.001
234. Pastore S, Baroni A, Carlson J, Gandolfi S, Pieper SC, Schiavilla R, et al. Quantum Monte Carlo calculations of weak transitions in $A = 6 - -10$ nuclei. *Phys Rev C.* (2018) **97**:022501. doi: 10.1103/PhysRevC.97.022501
235. King GB, Andreoli L, Pastore S, Piarulli M, Schiavilla R, Wiringa RB, et al. Chiral effective field theory calculations of weak transitions in light nuclei. *arXiv*. (2020) arXiv:2004.05263. doi: 10.1103/PhysRevC.102.025501
236. Lovato A, Gandolfi S, Carlson J, Pieper SC, Schiavilla R. Neutral weak current two-body contributions in inclusive scattering from ^{12}C. *Phys Rev Lett.* (2014) **112**:182502. doi: 10.1103/PhysRevLett.112.182502
237. Lovato A, Gandolfi S, Carlson J, Lusk E, Pieper SC, Schiavilla R. Quantum Monte Carlo calculation of neutral-current $\nu -^{12}$ C inclusive quasielastic scattering. *Phys Rev C.* (2018) **97**:022502. doi: 10.1103/PhysRevC.97.022502
238. Barbieri C, Rocco N, Somà V. Lepton scattering from ^{40}Ar and ^{48}Ti in the quasielastic peak region. *Phys Rev C.* (2019) **100**:062501. doi: 10.1103/PhysRevC.100.062501
239. Rocco N, Barbieri C, Benhar O, De Pace A, Lovato A. Neutrino-nucleus cross section within the extended factorization scheme. *Phys Rev C.* (2019) **99**:025502. doi: 10.1103/PhysRevC.99.025502
240. Rocco N. *Ab initio* calculations of lepton-nucleus scattering. *Front Phys.* (2020) **8**:116. doi: 10.3389/fphy.2020.00116
241. Bacca S, Barnea N, Hagen G, Orlandini G, Papenbrock T. First principles description of the giant dipole resonance in ^{16}**O**. *Phys Rev Lett.* (2013) **111**:122502. doi: 10.1103/PhysRevLett.111.122502
242. Bacca S, Barnea N, Hagen G, Miorelli M, Orlandini G, Papenbrock T. Giant and pigmy dipole resonances in ^{4}He, $^{16,22}O$, and ^{40}Ca from chiral nucleon-nucleon interactions. *Phys Rev C.* (2014) **90**:064619. doi: 10.1103/PhysRevC.90.064619
243. Miorelli M, Bacca S, Barnea N, Hagen G, Jansen GR, Orlandini G, et al. Electric dipole polarizability from first principles calculations. *Phys Rev C.* (2016) **94**:034317. doi: 10.1103/PhysRevC.94.034317
244. Miorelli M, Bacca S, Hagen G, Papenbrock T. Computing the dipole polarizability of ^{48}Ca with increased precision. *Phys Rev C.* (2018) **98**:014324. doi: 10.1103/PhysRevC.98.014324
245. Simonis J, Bacca S, Hagen G. First principles electromagnetic responses in medium-mass nuclei. *Eur Phys J A.* (2019) **55**:241. doi: 10.1140/epja/i2019-12825-0
246. Birkhan J, Miorelli M, Bacca S, Bassauer S, Bertulani CA, Hagen G, et al. Electric dipole polarizability of ^{48}Ca and implications for the neutron skin. *Phys Rev Lett.* (2017) **118**:252501. doi: 10.1103/PhysRevLett.118.252501
247. Kaufmann S, Simonis J, Bacca S, Billowes J, Bissell ML, Blaum K, et al. Charge radius of the short-lived ^{68}Ni and correlation with the dipole polarizability. *Phys Rev Lett.* (2020) **124**:132502. doi: 10.1103/PhysRevLett.124.132502
248. Antonello M, et al. A proposal for a three detector short-baseline neutrino oscillation program in the fermilab booster neutrino beam. *arXiv*. (2015) *arxiv [Preprint] arXiv*:1503.01520.
249. Abi B, Acciarri R, Acero M, Adamov G, Adams D, Adinolfi M, et al. Deep underground neutrino experiment (DUNE), far detector technical design report, volume I: introduction to DUNE. *arXiv*. (2020) *arxiv [Preprint] arXiv:*2002.02967.
250. Abi B, Acciarri R, Acero M, Adamov G, Adams D, Adinolfi M, et al. Deep underground neutrino experiment (DUNE), far detector technical design report, volume II: DUNE physics. *arXiv*. (2020) *arxiv [Preprint] arXiv:*2002.03005.
251. Payne CG, Bacca S, Hagen G, Jiang WG, Papenbrock T. Coherent elastic neutrino-nucleus scattering on ^{40}Ar from first principles. *Phys Rev C.* (2019) **100**:061304. doi: 10.1103/PhysRevC.100.061304
252. Hupin G, Quaglioni S, Navrátil P. *Ab initio* predictions for polarized deuterium-tritium thermonuclear fusion. *Nat Commun.* (2019) **10**:351. doi: 10.1038/s41467-018-08052-6
253. Hoppe J, Drischler C, Furnstahl RJ, Hebeler K, Schwenk A. Weinberg eigenvalues for chiral nucleon-nucleon interactions. *Phys Rev C.* (2017) **96**:054002. doi: 10.1103/PhysRevC.96.054002
254. Bertsch GF. Role of core polarization in two-body interaction. *Nucl Phys.* (1965) **74**:234–40. doi: 10.1016/0029-5582(65)90262-2

255. Kuo TTS, Brown GE. Structure of finite nuclei and the free nucleon-nucleon interaction: an application to 18O and 18F. *Nucl Phys.* (1966) **85**:40–86. doi: 10.1016/0029-5582(66)90131-3
256. Kuo TTS. Structure of finite nuclei and the free nucleon-nucleon interactions. *Nucl Phys A.* (1967) **90**:199–208. doi: 10.1016/0375-9474(67)90749-X
257. Duguet T, Hergert H, Holt JD, Somà V. Nonobservable nature of the nuclear shell structure: meaning, illustrations, and consequences. *Phys Rev C.* (2015) **92**:034313. doi: 10.1103/PhysRevC.92.034313
258. Brown BA, Richter WA. New "USD" Hamiltonians for the sd-shell. *Phys Rev C.* (2006) **74**:034315. doi: 10.1103/PhysRevC.74.034315
259. Magilligan A, Brown BA. New isospin-breaking "USD" Hamiltonians for the sd shell. *Phys Rev C.* (2020) **101**:064312. doi: 10.1103/PhysRevC.101.064312
260. Zuker A. Three-body monopole corrections to realistic interactions. *Phys Rev Lett.* (2003) **90**:042502. doi: 10.1103/PhysRevLett.90.042502
261. Caprio MA, Maris P, Vary JP. Emergence of rotational bands in *ab initio* no-core configuration interaction calculations of light nuclei. *Phys Lett B.* (2013) **719**:179–84. doi: 10.1016/j.physletb.2012.12.064
262. Caprio MA, Maris P, Vary JP, Smith R. Collective rotation from *ab initio* theory. *Int J Mod Phys E.* (2015) **24**:1541002. doi: 10.1142/S0218301315410025
263. Rowe DJ, McCoy AE, Caprio MA. The many-nucleon theory of nuclear collective structure and its macroscopic limits: an algebraic perspective. *Phys Scripta.* (2016) **91**:033003. doi: 10.1088/0031-8949/91/3/033003
264. Ekström A, Baardsen G, Forssén C, Hagen G, Hjorth-Jensen M, Jansen GR, et al. Optimized chiral nucleon-nucleon interaction at next-to-next-to-leading order. *Phys Rev Lett.* (2013) **110**:192502. doi: 10.1103/PhysRevLett.110.192502
265. Raimondi F, Barbieri C. Algebraic diagrammatic construction formalism with three-body interactions. *Phys Rev C.* (2018) **97**:054308. doi: 10.1103/PhysRevC.97.054308
266. Arthuis P, Duguet T, Tichai A, Lasseri RD, Ebran JP. ADG: automated generation and evaluation of many-body diagrams I. Bogoliubov many-body perturbation theory. *Comput Phys Commun.* (2019) **240**:202–27. doi: 10.1016/j.cpc.2018.11.023
267. Tichai A, Wirth R, Ripoche J, Duguet T. Symmetry reduction of tensor networks in many-body theory I. Automated symbolic evaluation of *SU*(2) algebra. *arXiv*. (2020) *arxiv [Preprint] arXiv:*2002.05011.
268. Novario SJ. *Private Communication. arXiv [Preprint]* (2020). Available online at: https://arxiv.org/abs/2008.09696
269. Rotureau J, Michel N, Nazarewicz W, Płoszajczak M, Dukelsky J. Density matrix renormalization group approach to two-fluid open many-fermion systems. *Phys Rev C.* (2009) **79**:014304. doi: 10.1103/PhysRevC.79.014304
270. Legeza O, Veis L, Poves A, Dukelsky J. Advanced density matrix renormalization group method for nuclear structure calculations. *Phys Rev C.* (2015) **92**:051303. doi: 10.1103/PhysRevC.92.051303
271. Tichai A, Ripoche J, Duguet T. Pre-processing the nuclear many-body problem. *Eur Phys J A.* (2019) **55**:90. doi: 10.1140/epja/i2019-12758-6
272. Tichai A, Schutski R, Scuseria GE, Duguet T. Tensor-decomposition techniques for ab initio nuclear structure calculations: From chiral nuclear potentials to ground-state energies. *Phys Rev C.* (2019) **99**:034320. doi: 10.1103/PhysRevC.99.034320
273. Hohenstein EG, Parrish RM, Martínez TJ. Tensor hypercontraction density fitting. I. Quartic scaling second- and third-order Møller-Plesset perturbation theory. *J Chem Phys.* (2012) **137**:044103. doi: 10.1063/1.4732310
274. Parrish RM, Hohenstein EG, Martínez TJ, Sherrill CD. Tensor hypercontraction. II. Least-squares renormalization. *J Chem Phys.* (2012) **137**:224106. doi: 10.1063/1.4768233
275. Hohenstein EG, Parrish RM, Sherrill CD, Martínez TJ. Communication: Tensor hypercontraction. III. Least-squares tensor hypercontraction for the determination of correlated wavefunctions. *J Chem Phys.* (2012) **137**:221101. doi: 10.1063/1.4768241
276. Parrish RM, Sherrill CD, Hohenstein EG, Kokkila SIL, Martínez TJ. Communication: acceleration of coupled cluster singles and doubles via orbital-weighted least-squares tensor hypercontraction. *J Chem Phys.* (2014) **140**:181102. doi: 10.1063/1.4876016
277. Parrish RM, Hohenstein EG, Schunck NF, Sherrill CD, Martínez TJ. Exact tensor hypercontraction: a universal technique for the resolution of matrix elements of local finite-range *N*-body potentials in many-body quantum problems. *Phys Rev Lett.* (2013) **111**:132505. doi: 10.1103/PhysRevLett.111.132505
278. Frame D, He R, Ipsen I, Lee D, Lee D, Rrapaj E. Eigenvector continuation with subspace learning. *Phys Rev Lett.* (2018) **121**:032501. doi: 10.1103/PhysRevLett.121.032501
279. Sarkar A, Lee D. Convergence of eigenvector continuation. *arXiv*. (2020) *arxiv [Preprint] arXiv:*2004.07651.
280. König S, Ekström A, Hebeler K, Lee D, Schwenk A. Eigenvector continuation as an efficient and accurate emulator for uncertainty quantification. *arXiv*. (2019) *arxiv [Preprint] arXiv:*1909.08446.
281. Ekström A, Hagen G. Global sensitivity analysis of bulk properties of an atomic nucleus. *Phys Rev Lett.* (2019) **123**:252501. doi: 10.1103/PhysRevLett.123.252501
282. Furnstahl RJ, Phillips DR, Wesolowski S. A recipe for EFT uncertainty quantification in nuclear physics. *arXiv*. (2014) *arxiv [Preprint] arXiv:*1407.0657. doi: 10.1088/0954-3899/42/3/034028
283. Furnstahl RJ, Klco N, Phillips DR, Wesolowski S. Quantifying truncation errors in effective field theory. *Phys Rev C.* (2015) **92**:024005. doi: 10.1103/PhysRevC.92.024005
284. Wesolowski S, Klco N, Furnstahl RJ, Phillips DR, Thapaliya A. Bayesian parameter estimation for effective field theories. *J Phys G Nucl Part Phys.* (2016) **43**:074001. doi: 10.1088/0954-3899/43/7/074001
285. Drischler C, Melendez JA, Furnstahl RJ, Phillips DR. Quantifying uncertainties and correlations in the nuclear-matter equation of state. *arXiv*. (2020) *arxiv [Preprint] arXiv:*2004.07805.
286. More SN, Ekström A, Furnstahl RJ, Hagen G, Papenbrock T. Universal properties of infrared oscillator basis extrapolations. *Phys Rev C.* (2013) **87**:044326. doi: 10.1103/PhysRevC.87.044326
287. Furnstahl RJ, More SN, Papenbrock T. Systematic expansion for infrared oscillator basis extrapolations. *Phys Rev C.* (2014) **89**:044301. doi: 10.1103/PhysRevC.89.044301
288. Wendt KA, Forssén C, Papenbrock T, Sääf D. Infrared length scale and extrapolations for the no-core shell model. *Phys Rev C.* (2015) **91**:061301. doi: 10.1103/PhysRevC.91.061301
289. Odell D, Papenbrock T, Platter L. Infrared extrapolations of quadrupole moments and transitions. *Phys Rev C.* (2016) **93**:044331. doi: 10.1103/PhysRevC.93.044331
290. Forssén C, Carlsson BD, Johansson HT, Sääf D, Bansal A, Hagen G, et al. Large-scale exact diagonalizations reveal low-momentum scales of nuclei. *Phys Rev C.* (2018) **97**:034328. doi: 10.1103/PhysRevC.97.034328
291. König S, Bogner SK, Furnstahl RJ, More SN, Papenbrock T. Ultraviolet extrapolations in finite oscillator bases. *Phys Rev C.* (2014) **90**:064007. doi: 10.1103/PhysRevC.90.064007
292. Kejzlar V, Neufcourt L, Maiti T, Viens F. Bayesian averaging of computer models with domain discrepancies: a nuclear physics perspective. *arXiv*. (2019) *arxiv [Preprint] arXiv:*1904.04793.
293. Neufcourt L, Cao Y, Giuliani SA, Nazarewicz W, Olsen E, Tarasov OB. Quantified limits of the nuclear landscape. *Phys Rev C.* (2020) **101**:044307. doi: 10.1103/PhysRevC.101.044307
294. Ekström A, Forssén C, Dimitrakakis C, Dubhashi D, Johansson HT, Muhammad AS, et al. Bayesian optimization in *ab initio* nuclear physics. *J Phys G Nucl Part Phys.* (2019) **46**:095101. doi: 10.1088/1361-6471/ab2b14
295. Melendez JA, Furnstahl RJ, Grießhammer HW, McGovern JA, Phillips DR, Pratola MT. Designing optimal experiments: an application to proton compton scattering. *arXiv*. (2020) *arxiv [Preprint] arXiv:*2004.11307.
296. Haidenbauer J, Meißner UG, Nogga A. Hyperon-nucleon interaction within chiral effective field theory revisited. *Eur Phys J A.* (2020) **56**:91. doi: 10.1140/epja/s10050-020-00100-4
297. Hammer HW, König S, van Kolck U. Nuclear effective field theory: status and perspectives. *Rev Mod Phys.* (2020) **92**:025004. doi: 10.1103/RevModPhys.92.025004
298. Furnstahl RJ. EFT for DFT. In: Schwenk A, Polonyi J, editors. Renormalization Group and Effective Field Theory Approaches to

Many-Body Systems. *Lecture Notes in Physics*, Vol. 852. Berlin; Heidelberg: Springer (2012). doi: 10.1007/978-3-642-27320-9_3
299. Furnstahl RJ. Turning the nuclear energy density functional method into a proper effective field theory: reflections. *Eur Phys J A.* (2020) **56**:85. doi: 10.1140/epja/s10050-020-00095-y
300. Papenbrock T, Weidenmüller HA. Effective field theory for finite systems with spontaneously broken symmetry. *Phys Rev C.* (2014) **89**:014334. doi: 10.1103/PhysRevC.89.014334
301. Papenbrock T, Weidenmüller HA. Effective field theory of emergent symmetry breaking in deformed atomic nuclei. *J Phys G Nucl Part Phys.* (2015) **42**:105103. doi: 10.1088/0954-3899/42/10/105103
302. Coello Pérez EA, Papenbrock T. Effective field theory for nuclear vibrations with quantified uncertainties. *Phys Rev C.* (2015) **92**:064309. doi: 10.1103/PhysRevC.92.064309
303. Coello Pérez EA, Papenbrock T. Effective theory for the nonrigid rotor in an electromagnetic field: toward accurate and precise calculations of *E*2 transitions in deformed nuclei. *Phys Rev C.* (2015) **92**:014323. doi: 10.1103/PhysRevC.92.014323
304. Coello Pérez EA, Papenbrock T. Effective field theory for vibrations in odd-mass nuclei. *Phys Rev C.* (2016) **94**:054316. doi: 10.1103/PhysRevC.94.054316
305. Papenbrock T, Weidenmüller HA. Effective field theory for deformed odd-mass nuclei. *arXiv*. (2020) *arxiv [Preprint] arXiv:*2005.11865.
306. Contessi L, Lovato A, Pederiva F, Roggero A, Kirscher J, van Kolck U. Ground-state properties of 4He and 16O extrapolated from lattice QCD with pionless EFT. *Phys Lett B.* (2017) **772**:839–48. doi: 10.1016/j.physletb.2017.07.048
307. Hagen G, Hagen P, Hammer HW, Platter L. Efimov physics around the neutron-rich Ca60 isotope. *Phys Rev Lett.* (2013) **111**:132501. doi: 10.1103/PhysRevLett.111.132501
308. Bogner SK, Furnstahl RJ, Hergert H, Kortelainen M, Maris P, Stoitsov M, et al. Testing the density matrix expansion against *ab initio* calculations of trapped neutron drops. *Phys Rev C.* (2011) **84**:044306. doi: 10.1103/PhysRevC.84.044306
309. Dyhdalo A, Bogner SK, Furnstahl RJ. Applying the density matrix expansion with coordinate-space chiral interactions. *Phys Rev C.* (2017) **95**:054314. doi: 10.1103/PhysRevC.95.054314
310. Navarro Pérez R, Schunck N, Dyhdalo A, Furnstahl RJ, Bogner SK. Microscopically based energy density functionals for nuclei using the density matrix expansion. II. Full optimization and validation. *Phys Rev C.* (2018) **97**:054304. doi: 10.1103/PhysRevC.97.054304
311. Zhang YN, Bogner SK, Furnstahl RJ. Incorporating Brueckner-Hartree-Fock correlations in energy density functionals. *Phys Rev C.* (2018) **98**:064306. doi: 10.1103/PhysRevC.98.064306
312. Pudliner BS, Smerzi A, Carlson J, Pandharipande VR, Pieper SC, Ravenhall DG. Neutron drops and Skyrme energy-density functionals. *Phys Rev Lett.* (1996) **76**:2416–9. doi: 10.1103/PhysRevLett.76.2416
313. Duguet T, Lesinski T. Non-empirical pairing functional. *Eur Phys J.* (2008) **156**:207–15. doi: 10.1140/epjst/e2008-00618-x
314. Shen S, Colò G, Roca-Maza X. Skyrme functional with tensor terms from ab initio calculations of neutron-proton drops. *Phys Rev C.* (2019) **99**:034322. doi: 10.1103/PhysRevC.99.034322
315. Yang CJ. Chiral potential renormalized in harmonic-oscillator space. *Phys Rev C.* (2016) **94**:064004. doi: 10.1103/PhysRevC.94.064004
316. Yang CJ. Do we know how to count powers in pionless and pionful effective field theory? *Eur Phys J A.* (2020) **56**:96. doi: 10.1140/epja/s10050-020-00104-0
317. Binder S, Ekström A, Hagen G, Papenbrock T, Wendt KA. Effective field theory in the harmonic oscillator basis. *Phys Rev C.* (2016) **93**:044332. doi: 10.1103/PhysRevC.93.044332
318. Bansal A, Binder S, Ekström A, Hagen G, Jansen GR, Papenbrock T. Pion-less effective field theory for atomic nuclei and lattice nuclei. *Phys Rev C.* (2018) **98**:054301. doi: 10.1103/PhysRevC.98.054301
319. McElvain KS, Haxton WC. Nuclear physics without high-momentum potentials: constructing the nuclear effective interaction directly from scattering observables. *Phys Lett B.* (2019) **797**:134880. doi: 10.1016/j.physletb.2019.134880
320. Drissi M, Duguet T, Somà V. Renormalization of pionless effective field theory in the A-body sector. *Eur Phys J A.* (2020) **56**:119. doi: 10.1140/epja/s10050-020-00097-w
321. Cirigliano V, Dekens W, de Vries J, Graesser ML, Mereghetti E. A neutrinoless double beta decay master formula from effective field theory. *J High Energy Phys.* (2018) **2018**:97. doi: 10.1007/JHEP12(2018)097
322. Cirigliano V, Dekens W, de Vries J, Graesser ML, Mereghetti E, Pastore S, et al. New leading contribution to neutrinoless double-β decay. *Phys Rev Lett.* (2018) **120**:202001. doi: 10.1103/PhysRevLett.120.202001
323. Cirigliano V, Dekens W, Mereghetti E, Walker-Loud A. Neutrinoless double-β decay in effective field theory: the light-Majorana neutrino-exchange mechanism. *Phys Rev C.* (2018) **97**:065501. doi: 10.1103/PhysRevC.97.065501
324. Cirigliano V, Dekens W, de Vries J, Graesser ML, Mereghetti E, Pastore S, et al. Renormalized approach to neutrinoless double-β decay. *Phys Rev C.* (2019) **100**:055504. doi: 10.1103/PhysRevC.100.055504
325. Drischler C, Furnstahl RJ, Melendez JA, Phillips DR. How well do we know the neutron-matter equation of state at the densities inside neutron stars? A Bayesian approach with correlated uncertainties. *arXiv*. (2020) *arxiv [Preprint] arXiv:*2004.07232.
326. Johnson CW, et al. From bound states to the continuum. *arXiv*. (2019) *arxiv [Preprint] arXiv:*1912.00451.
327. Mercenne A, Launey KD, Escher JE, Dytrych T, Draayer JP. New symmetry-adapted *ab initio* approach to nuclear reactions for intermediate-mass nuclei. *arXiv*. (2019) *arxiv [Preprint] arXiv:*1910.00638.
328. Jaganathen Y, Michel N, Płoszajczak M. Gamow shell model description of proton scattering on ^{18}Ne. *Phys Rev C.* (2014) **89**:034624. doi: 10.1103/PhysRevC.89.034624
329. Mercenne A, Michel N, Płoszajczak M. Gamow shell model description of ^{4}He(d, d) elastic scattering reactions. *Phys Rev C.* (2019) **99**:044606. doi: 10.1103/PhysRevC.99.044606
330. Huth L, Durant V, Simonis J, Schwenk A. Shell-model interactions from chiral effective field theory. *Phys Rev C.* (2018) **98**:044301. doi: 10.1103/PhysRevC.98.044301
331. Rotureau J, Potel G, Li W, Nunes FM. Merging *ab initio* theory and few-body approach for (d, p) reactions. *J Phys G.* (2020) **47**:065103. doi: 10.1088/1361-6471/ab8530
332. Burrows M, Elster C, Popa G, Launey KD, Nogga A, Maris P. *Ab initio* translationally invariant nonlocal one-body densities from no-core shell-model theory. *Phys Rev C.* (2018) **97**:024325. doi: 10.1103/PhysRevC.97.024325
333. Burrows M, Elster C, Weppner SP, Launey KD, Maris P, Nogga A, et al. *Ab initio* folding potentials for nucleon-nucleus scattering based on no-core shell-model one-body densities. *Phys Rev C.* (2019) **99**:044603. doi: 10.1103/PhysRevC.99.044603
334. Gennari M, Vorabbi M, Calci A, Navrátil P. Microscopic optical potentials derived from *ab initio* translationally invariant nonlocal one-body densities. *Phys Rev C.* (2018) **97**:034619. doi: 10.1103/PhysRevC.97.034619
335. Gennari M, Navrátil P. Nuclear kinetic density from *ab initio* theory. *Phys Rev C.* (2019) **99**:024305. doi: 10.1103/PhysRevC.99.024305
336. Furnstahl RJ, Hebeler K. New applications of renormalization group methods in nuclear physics. *Rept Prog Phys.* (2013) **76**:126301. doi: 10.1088/0034-4885/76/12/126301

Conflict of Interest: The author declares that the research was conducted in the absence of any commercial or financial relationships that could be construed as a potential conflict of interest.

GLOSSARY

ADC	*Algebraic Diagrammatic Construction (for Self-Consistent Green's Functions)*
AFDMC	*Auxiliary Field Diffusion Monte Carlo*
APM	*Adiabatic Projection Method (in Lattice EFT)*
BMBPT	*Bogoliubov Many-Body Perturbation Theory*
CI	*Configuration Interaction*
CC	*Coupled Cluster*
CCSD	*Coupled Cluster with Singles and Doubles excitations*
CCSDT	*Coupled Cluster with Singles, Doubles and Triples excitations*
CCSD(T)	*Coupled Cluster with Singles, Doubles and perturbative Triples excitations*
χEFT	*Chiral Effective Field Theory*
DFT	*Density Functional Theory*
EVC	*Eigenvector Continuation*
EDF	*Energy Density Functional*
EFT	*Effective Field Theory*
GCM	*Generator Coordinate Method*
GFMC	*Green's Function Monte Carlo*
GHW	*Griffin-Hill-Wheeler (equation)*
HF	*Hartree-Fock*
HFB	*Hartree-Fock-Bogoliubov*
IM-GCM	*In-Medium Generator Coordinate Method (a combination of IMSRG and GCM)*
IM-NCSM	*In-Medium No-Core Shell Model (a combination of IMSRG and NCSM)*
IMSRG	*In-Medium Similarity Renormalization Group*
LEFT	*Lattice Effective Field Theory*
LO	*Leading Order (Effective Field Theory)*
MBPT	*Many-Body Perturbation Theory*
MR-IMSRG	*Multi-Reference In-Medium Similarity Renormalization Group*
NCCI	*No-Core Configuration Interaction*
NCSM	*No-Core Shell Model*
NCSMC	*No-Core Shell Model with Continuum*
NLO	*Next-to-Leading Order (EFT)*
NNLO	*Next-to-Next-to-Leading Order (EFT)*
N^3LO	*Next-to-Next-to-Next-to-Leading Order (EFT)*
N^4LO	*Next-to-Next-to-Next-to-Next-to-Leading Order (EFT)*
QCD	*Quantum Chromodynamics*
QMC	*Quantum Monte Carlo*
RG	*Renormalization Group*
RGM	*Resonating Group Method*
SCGF	*Self-Consistent Green's Functions*
SRG	*Similarity Renormalization Group*
TBME	*two-body matrix elements (typically in the discussion of Shell Model interactions)*
UCC	*Unitary Coupled Cluster*
UMOA	*Unitary Model Operator Approach*
UQ	*Uncertainty Quantification*
VMC	*Variational Monte Carlo*
VS-IMSRG	*Valence-Space In-Medium Similarity Renormalization Group*

frontiers in Physics

REVIEW
published: 24 April 2020
doi: 10.3389/fphy.2020.00117

Atomic Nuclei From Quantum Monte Carlo Calculations With Chiral EFT Interactions

Stefano Gandolfi[1]*, *Diego Lonardoni*[1,2], *Alessandro Lovato*[3,4] and *Maria Piarulli*[5]

[1] Theoretical Division, Los Alamos National Laboratory, Los Alamos, NM, United States, [2] Facility for Rare Isotope Beams, Michigan State University, East Lansing, MI, United States, [3] Physics Division, Argonne National Laboratory, Argonne, IL, United States, [4] Trento Institute of Fundamental Physics and Applications (TIFPA), National Institute for Nuclear Physics (INFN), Trento, Italy, [5] Physics Department, Washington University, St. Louis, MO, United States

Quantum Monte Carlo methods are powerful numerical tools to accurately solve the Schrödinger equation for nuclear systems, a necessary step to describe the structure and reactions of nuclei and nucleonic matter starting from realistic interactions and currents. These *ab-initio* methods have been used to accurately compute properties of light nuclei—including their spectra, moments, and transitions—and the equation of state of neutron and nuclear matter. In this work we review selected results obtained by combining quantum Monte Carlo methods and recent Hamiltonians constructed within chiral effective field theory.

Keywords: quantum Monte Carlo methods, variational Monte Carlo, Green's function Monte Carlo, auxiliary field diffusion Monte Carlo, chiral effective field theory, nuclear Hamiltonians, nuclear structure

OPEN ACCESS

Edited by:
Carlo Barbieri,
University of Surrey, United Kingdom

Reviewed by:
Andrea Celentano,
Istituto Nazionale di Fisica Nucleare (INFN), Sezione di Genova, Italy
Marco La Cognata,
Laboratori Nazionali del Sud (INFN), Catania, Italy

***Correspondence:**
Stefano Gandolfi
stefano@lanl.gov

Specialty section:
This article was submitted to Nuclear Physics, a section of the journal Frontiers in Physics

Received: *06 January 2020*
Accepted: *25 March 2020*
Published: *24 April 2020*

Citation:
Gandolfi S, Lonardoni D, Lovato A and Piarulli M (2020) Atomic Nuclei From Quantum Monte Carlo Calculations With Chiral EFT Interactions. Front. Phys. 8:117. doi: 10.3389/fphy.2020.00117

1. INTRODUCTION

The study of nuclear properties as they emerge from the individual interactions among protons and neutrons is a fascinating long-standing problem, subject of both theoretically and experimentally research activities. From a theoretical point of view, a truly *ab-initio* description of nuclei is still very challenging at present. The underlying theory of strong interactions, Quantum Chromodynamics (QCD), that describes how quarks and gluons interact to form nucleons and nuclei, in the low-energy regime is non-perturbative in its coupling constant. Despite remarkable progresses [1, 2], realistic computations of many-body nuclear systems in terms of the fundamental degrees of freedom of QCD—quarks and gluons—are still extremely challenging.

A more feasible approach to the problem consists in assuming that at the energy regime relevant to the description of atomic nuclei, quarks, and gluons are confined within hadrons. The latter are the active degrees of freedom at soft scales, and they interact among themselves through non-relativistic effective potentials that are consistent with the symmetries of QCD. The solution of nuclear many-body problems requires two main ingredients: an Hamiltonian that accurately models the interactions among the nucleons, and reliable numerical many-body methods to solve the corresponding Schrödinger equation.

Microscopic nuclear Hamiltonians, capable of reproducing nucleon-nucleon scattering data and the properties of few-body systems, have been successfully used to describe light nuclei. For example, the highly-realistic Argonne v_{18} two-body potential [3] combined with the phenomenological Illinois-7 three-body force have been employed to predict several properties of nuclei up to $A = 12$ with great accuracy [4]. Several calculations of energies, rms radii, transitions, and densities turn out to be in excellent agreement with experimental data. The main limitation of these phenomenological Hamiltonians is that it is not clear how they can be systematically

improved, and how to quantify theoretical, i.e., systematic, uncertainties related to the specific interaction model. Another approach that became very popular in the last two decades consist in deriving nuclear interactions within the framework of chiral Effective Field Theory (χEFT). The advantage of this approach is that it provides the necessary tools to systematically improve the interaction models, to estimate uncertainties related to the truncation of the chiral expansion, and to consistently derive electroweak currents.

Several many-body methods have been developed to numerical solve the many-body Schrödinger equation. Most of them rely on basis expansions, for example the coupled cluster method [5, 6], the no core shell model [7], the similarity renormalization group [8], and the self consistent Green's function [9]. Each of these methods has distinct advantages, and many are able to treat a wider variety of nuclear interaction models. These many-body techniques are very effective and achieve a good convergence only when relatively soft potentials are used.

Quantum Monte Carlo (QMC) methods are ideally suited to study strongly correlated many-body systems, and have no difficulties in treating "stiff" nuclear interactions, but are limited to nearly local nuclear potentials. For this reason, until fairly recently, the applicability of QMC methods was limited to phenomenological interactions, as χEFT Hamiltonians were typically written in momentum space. Over the past few years, the situation has drastically changed with the development of local χEFT potentials, both with [10, 11] and without explicit delta degrees of freedom [12, 13], that have provided a way to combine an EFT-based description of nuclear dynamics with precise QMC techniques. In this work we will review selected results of nuclei obtained using QMC methods and chiral Hamiltonians.

2. NUCLEAR INTERACTIONS

The microscopic model of nuclear theory assumes that nuclear systems can be described as point-like nucleons, whose dynamics is characterized by a non-relativistic Hamiltonian

$$H = \sum_i T_i + \sum_{i<j} v_{ij} + \sum_{i<j<k} V_{ijk} + \cdots , \tag{1}$$

where T_i is the one-body kinetic energy operator, v_{ij} is the nucleon-nucleon (NN) interaction between particles i and j, V_{ijk} is the three-nucleon ($3N$) interaction between particles i, j, and k, and the ellipsis indicate interactions involving more than three particles. There are indications that four-nucleon interactions may contribute at the level of only $\sim$ 100 keV in ^{4}He [14] or pure neutron matter [15], and therefore are negligible compared to NN and $3N$ components. Hence, current formulations of the microscopic model do not typically include them (see, for example, reference [4]).

The NN interaction term in the nuclear Hamiltonian is the most studied of all, with thousands of experimental data points at laboratory energies ($E_{\rm lab}$) from essentially zero to hundreds of MeV. It consists of a long-range component, for inter-nucleon separation $r \gtrsim 2$ fm, due to one-pion exchange (OPE) [16], and intermediate- and short-range components, for, respectively, 1 fm $\lesssim r \lesssim$ 2 fm and $r \lesssim 1$ fm, derived, up to the mid 1990's, almost exclusively from meson-exchange phenomenology [3, 17, 18]. These models fit the large amount of empirical information about NN scattering data contained in the Nijmegen database [19], available at the time, with a χ^2/datum $\simeq$ 1 for $E_{\rm lab}$ up to pion-production threshold. Two well-known and still widely used examples in this class of NN interactions are the CD-Bonn [18] and the Argonne v_{18} (AV18) [3] potentials.

The AV18 interaction is a local, configuration-space NN potential that has been extensively and successfully used in a number of QMC calculations. It is expressed as a sum of electromagnetic and OPE terms and phenomenological intermediate- and short-range parts:

$$v_{ij} = v_{ij}^{\gamma} + v_{ij}^{\pi} + v_{ij}^{I} + v_{ij}^{S} . \tag{2}$$

The electromagnetic term v_{ij}^{γ} has one- and two-photon exchange Coulomb interaction, vacuum polarization, Darwin-Foldy, and magnetic moment terms, with appropriate form factors that keep terms finite at $r = 0$ (see reference [3] for more details). The OPE part includes the charge-dependent (CD) terms due to the difference in neutral (m_{π_0}) and charged pion ($m_{\pi_\pm}$) masses, and in coordinate-space it reads

$$v_{ij}^{\pi} = \left[v_{\sigma\tau}^{\pi}(r)\, \boldsymbol{\sigma}_i \cdot \boldsymbol{\sigma}_j + v_{t\tau}^{\pi}(r)\, S_{ij} \right] \boldsymbol{\tau}_i \cdot \boldsymbol{\tau}_j + \left[v_{\sigma T}^{\pi}(r)\, \boldsymbol{\sigma}_i \cdot \boldsymbol{\sigma}_j + v_{tT}^{\pi}(r)\, S_{ij} \right] T_{ij} , \tag{3}$$

where $\boldsymbol{\sigma}$ adn $\boldsymbol{\tau}$ are the Pauli matrices that operate over the spin and isospin of particles, and $S_{ij} = 3\, \boldsymbol{\sigma}_i \cdot \hat{\mathbf{r}}_{ij}\, \boldsymbol{\sigma}_j \cdot \hat{\mathbf{r}}_{ij} - \boldsymbol{\sigma}_i \cdot \boldsymbol{\sigma}_j$ and $T_{ij} = 3\, \tau_{iz} \tau_{jz} - \boldsymbol{\tau}_i \cdot \boldsymbol{\tau}_j$ are the tensor and isotensor operators, respectively. The functions, $v_{\sigma\tau}^{\pi}(r)$, $v_{t\tau}^{\pi}(r)$, $v_{\sigma T}^{\pi}(r)$, and $v_{tT}^{\pi}(r)$ are defined as

$$\begin{aligned} v_{\sigma\tau}^{\pi}(r) &= \frac{Y_0(r) + 2\, Y_+(r)}{3} , \qquad v_{t\tau}^{\pi}(r) = \frac{T_0(r) + 2\, T_+(r)}{3} , \\ v_{\sigma T}^{\pi}(r) &= \frac{Y_0(q) - Y_+(r)}{3} , \qquad v_{tT}^{\pi}(r) = \frac{T_0(r) - T_+(r)}{3} , \end{aligned} \tag{4}$$

where $Y_\alpha(r)$ and $T_\alpha(r)$ are the Yukawa and tensor functions given by

$$Y_\alpha(r) = \frac{g_A^2}{12\,\pi} \frac{m_{\pi_\alpha}^3}{(2 f_\pi)^2} \frac{e^{-x_\alpha}}{x_\alpha} , \quad T_\alpha(r) = Y_\alpha(r) \left(1 + \frac{3}{x_\alpha} + \frac{3}{x_\alpha^2} \right) , \tag{5}$$

with $x_\alpha = m_{\pi_\alpha} r$, and $g_A = 1.267$, $f_\pi = 92.4$ MeV being the axial-vector coupling constant of the nucleon and the pion decay constant, respectively.

The intermediate-range region, v_{ij}^{I}, is parametrized in terms of two-pion exchange (TPE), based on, but not consistently derived from, a field-theory analysis of box diagrams with intermediate nucleons and Δ isobars [20]. The short-range region, v_{ij}^{S}, is instead represented by spin-isospin and momentum-dependent operators multiplied by Woods-Saxon radial functions [3].

The AV18 model can be written as an overall sum of eighteen operators ($\mathcal{N} = 18$)

$$v_{ij} = \sum_{p=1}^{\mathcal{N}} v^p(r_{ij})\mathcal{O}_{ij}^p, \tag{6}$$

where the first eight are given by

$$\mathcal{O}_{ij}^{p=1-8} = \left[1, \boldsymbol{\sigma}_i \cdot \boldsymbol{\sigma}_j, S_{ij}, \mathbf{L}\cdot\mathbf{S}\right] \otimes \left[1, \boldsymbol{\tau}_i \cdot \boldsymbol{\tau}_j\right], \tag{7}$$

with the spin-orbit contribution expressed in terms of the relative angular momentum $\mathbf{L} = \frac{1}{2i}(\mathbf{r}_i - \mathbf{r}_j) \times (\boldsymbol{\nabla}_i - \boldsymbol{\nabla}_j)$ and the total spin $\mathbf{S} = \frac{1}{2}(\boldsymbol{\sigma}_i + \boldsymbol{\sigma}_j)$ of the pair. There are six additional charge-independent operators corresponding to $p = 9 - 14$ that are quadratic in L

$$\mathcal{O}_{ij}^{p=9-14} = \left[\mathbf{L}^2, \mathbf{L}^2\,\boldsymbol{\sigma}_i \cdot \boldsymbol{\sigma}_j, (\mathbf{L}\cdot\mathbf{S})^2\right] \otimes \left[1, \boldsymbol{\tau}_i \cdot \boldsymbol{\tau}_j\right], \tag{8}$$

while the $p = 15 - 18$ are charge-independence breaking terms

$$\mathcal{O}_{ij}^{p=15-18} = \left[T_{ij}, T_{ij}\,\boldsymbol{\sigma}_i \cdot \boldsymbol{\sigma}_j, T_{ij}\,S_{ij}, \tau_{i,z} + \tau_{j,z}\right]. \tag{9}$$

The AV18 model has a total of 42 independent parameters. A simplex routine [21] was used to make an initial fit to the phase shifts of the Nijmegen partial-wave analysis (PWA) [19], followed by a final fit direct to the database, which contains 1,787 *pp* and 2,514 *np* observables for E_{lab} up to 350 MeV. The *nn* scattering length and deuteron binding energy were also fit. The final χ^2/datum = 1.1 [3]. While the fit was made up to 350 MeV, the phase shifts are qualitatively good up to much larger energies, $E \leq 600$ MeV [22].

Simplified versions of these interactions, including only a subset of the operators in Equation (7), are available. For instance, the Argonne v_8' (AV8′) contains a charge-independent eight-operator projection, $\mathcal{O}_{ij}^{p=1-8} = \left[1, \boldsymbol{\sigma}_i \cdot \boldsymbol{\sigma}_j, S_{ij}, \mathbf{L}\cdot\mathbf{S}\right] \otimes \left[1, \boldsymbol{\tau}_i \cdot \boldsymbol{\tau}_j\right]$, of the full *NN* potential, constructed to preserve the potential in all *S* and *P* waves as well as the $^3D_1$ and its coupling to the $^3S_1$, while over-binding the deuteron by 18 keV due to the omission of electromagnetic terms [23]. The main missing features of these simplified interactions is the lack of terms describing charge and isospin symmetry breaking, as well as a slightly poorer description of nucleon-nucleon scattering data in higher partial waves. However, these contributions are very small, as outlined in reference [23].

Already in the 1980s, accurate three-body calculations showed that contemporary *NN* interactions did not provide enough binding for the three-body nuclei, ^{3}H and ^{3}He [24]. In the late 1990s and early 2000s this realization was also extended to the spectra (ground and low-lying excited states) of light *p*-shell nuclei, for instance, in calculations based on QMC methods [25] and in no-core shell-model studies [26]. Consequently, the microscopic model with only *NN* interactions fit to scattering data, without the inclusion of a 3*N* interaction, is no longer considered realistic.

In addition to *NN* forces, sophisticated phenomenological 3*N* interactions have been then developed. They are generally expressed as a sum of a TPE *P*-wave term, a TPE *S*-wave contribution, a three-pion-exchange contribution, and a 3*N* contact [4]. More specifically, two families of 3*N* interactions were obtained in combination with the AV18 potential: the Urbana IX (UIX) [27] and Illinois 7 (IL7) [28] models. The UIX potential contains two parameters fit to reproduce the ground-state energy of ^{3}H and the saturation-point of symmetric nuclear matter, while the IL7 potential involves five parameters constrained on the low-lying spectra of nuclei in the mass range $A = 3 - 10$.

Despite their success in predicting a wide range of nuclear properties [4], the phenomenological potentials suffer from several drawbacks. For example, the resulting AV18+IL7 Hamiltonian leads to predictions of $\approx$ 100 ground- and excited-state energies up to $A = 12$ in good agreement with the corresponding empirical values. However, when used to compute the neutron-star equation of state, such Hamiltonian does not provide sufficient repulsion to guarantee the stability of the observed stars against gravitational collapse [29]. On the other end, the AV18+UIX model, while providing a reasonable description of *s*-shell nuclei and nuclear matter properties, it somewhat underbinds light *p*-shell nuclei.

Thus, in the context of the phenomenological nuclear interactions, we do not have a Hamiltonian that can explain the properties of all nuclear systems, from *NN* scattering to dense nuclear and neutron matter. Furthermore, this phenomenological approach does not provide a rigorous scheme to consistently derive two- and many-body forces and compatible electroweak currents. In addition, there is no clear way to properly assess the theoretical uncertainty associated with the nuclear potentials and currents.

These shortcomings were addressed when a new phase in the evolution of microscopic models began in the early 1990's with the emergence of χEFT [30–32]. χEFT is a low-energy effective theory of QCD and provides the most general scheme accommodating all possible interactions among nucleons and pions (Δ-less χEFT) compatible with the relevant symmetries and symmetry breakings—in particular chiral symmetry—of low-energy QCD. In some modern approaches, the choice of degrees of freedom also includes the Δ isobar (Δ-full χEFT), because the Δ-nucleon mass splitting is only 300 MeV $\sim 2m_\pi$.

By its own nature, the χEFT formulation has an expansion in powers of pion momenta as its organizing principle. Most chiral interactions employed in recent nuclear structure and reaction calculations are based on Weinberg power counting. Within Weinberg power counting, the interactions are expanded in powers of the typical momentum p over the breakdown scale $\Lambda_b \sim$ GeV, $Q = p/\Lambda_b$, where the breakdown scale denotes momenta at which the short distance structure becomes important and cannot be neglected and absorbed into contact interactions anymore (see references [33–36] for recent review articles). It is important mentioning that alternative power-counting schemes have been also suggested [37–42] but not fully explored.

This expansion introduces an order by order scheme, defined by the power ν of the expansion scale Q associated with each interaction terms: leading order (LO) for $\nu = 0$, next-to-leading

order (NLO) for $\nu = 2$, next-to-next-to-leading order (N^2LO) for $\nu = 3$ and so on. Similarly as for nuclear interactions, such a scheme can also be developed for electroweak currents. Therefore, χEFT provides a rigorous scheme to systematically construct many-body forces and consistent electroweak currents, and tools to estimate their uncertainties [43–48].

Chiral nuclear forces are comprised of both pion-exchange contributions and contact terms. Pion-exchange contributions represent the long-range part of nuclear interactions and some of the pion-nucleon (πN) couplings entering sub-leading diagrams can consistently be obtained from low-energy πN scattering data [49–54, 54–56]. On the other end, contact terms encode the short-range physics, and their strength is specified by unknown low-energy constants (LECs), obtained by fitting experimental data. Similarly to the phenomenological interactions, the LECs entering the *NN* component are obtained by fitting *NN* scattering data up to 300 MeV lab energies, while the LECs involved in the 3*N* terms are fixed by reproducing properties of light-nuclei. This optimization procedure involves separate fit of the *NN* and 3*N* terms. Recently, a different strategy has been introduced by Ekström *et al.* [57]. This new approach is based on a simultaneous fit of the *NN* and 3*N* forces to low-energy *NN* data, deuteron binding energy, and binding energies and charge radii of hydrogen, helium, carbon, and oxygen isotopes.

Within χEFT, many studies have been carried out dealing with the construction and optimization of *NN* and 3*N* interactions [34, 42, 44, 49, 57–81] and accompanying isospin-symmetry-breaking corrections [82–84]. These interactions are typically formulated in momentum space, and include cutoff functions to regularize their behavior at large momenta. This makes them strongly non-local when Fourier-transformed in configuration space, and therefore unsuitable for use with QMC methods. In this context, an interaction is local if it depends solely on the momentum transfer $\mathbf{q} = \mathbf{p} - \mathbf{p}'$ ($\mathbf{p}$ and $\mathbf{p}'$ are the initial and final relative momenta of the two nucleons), which, upon Fourier transform, leads to dependencies solely on $\mathbf{r}$. However, interactions in momentum-space can also depend on the momentum scale $\mathbf{k} = (\mathbf{p}' + \mathbf{p})/2$, whose Fourier transform introduces derivatives in coordinate space. These $\mathbf{k}$ dependencies, and thus non-localities, come about because of (i) the specific functional choice made to regularize the momentum space potentials in terms of the two momentum scales $\mathbf{p}$ and $\mathbf{p}'$, and (ii) contact interactions that explicitly depend on $\mathbf{k}$.

In recent years, local configuration-space chiral *NN* interactions have been derived by two groups. On the one side, the authors of references [12, 85] constructed *NN* local chiral potentials within Δ-less χEFT by including one- and two-pion exchange contributions and contact terms up to N^2LO in the chiral expansion. The contact terms are regularized in coordinate space by a cutoff function depending only on the relative distance between the two nucleons, and use Fierz identities [86] to remove completely the dependence on the relative momentum of the two nucleons, by selecting appropriate combinations of contact operators. Their strength is characterized by 11 LECs, fixed by performing order by order χ^2 fit to *NN* phase shifts from the Nijmegen PWA up to 150 MeV lab energy. The fitting procedure is carried out for different values of the cutoff R_0 in the range of $R_0 = 1.0 - 1.2$ fm. The motivations why the authors of references [12, 85] truncated the chiral expansion of these local potentials at N^2LO is because at this order it is (i) possible to have a fully local representation of the *NN* chiral interactions and (ii) the inclusion of consistent 3*N* force is straightforward. In their models, the unknown 3*N* LECs are obtained by reproducing the binding energy of ^{4}He as well as the *P*-wave $n - \alpha$ elastic scattering phase shifts. In addition, they explore different parametrization for the 3*N*, force accordingly to Fierz identities [87–89]. In the present work, we are referring to a set of these local chiral interactions, specifically the $(D2, E\tau)$ model with $R_0 = 1.0$ fm of reference [89], as GT+Eτ-1.0.

On the other side, the authors of references [10, 90] developed a different set of *NN* local chiral interactions by (i) including diagrams with the virtual excitation of Δ-isobars in the TPE contributions up to N^2LO (Δ-full χEFT), ii) retaining contact terms up to N^3LO. The LECs entering the *NN* contact interactions in this model are constrained to reproduce *NN* scattering data from the most recent and up-to-date database collected by the Granada group [91–93]. The contact terms are implemented via a Gaussian representation of the three-dimensional delta function with R_S as the Gaussian parameter [10, 90, 94]. The pion-range operators are regularized at high-value of momentum transfer via a special radial function characterized by the cutoff R_L [10, 90, 94]. There are two classes of these potentials. Class I (II) are fit to data up to 125 MeV (200 MeV). For each class, two combinations of short- and long-range regulators have been used, namely $(R_S, R_L) = (0.8, 1.2)$ fm (models NV2-Ia and NV2-IIa) and $(R_S, R_L) = (0.7, 1.0)$ fm (models NV2-Ib and NV2-IIb). Class I (II) fits about 2,700 (3,700) data points with a χ^2/datum $\lesssim$ 1.1 ($\lesssim$ 1.4) [10, 90]. In conjunction with these models, two distinct sets of Δ-full 3*N* interactions have also been constructed up to N^2LO. In the first, the 3*N* unknown LECs were determined by simultaneously reproducing the experimental trinucleon ground-state energies and neutron-deuteron (*nd*) doublet scattering length for each of the NN models considered, namely NV2-Ia/b and NV2-IIa/b [11, 95]. In the second set, these LECs were constrained by fitting, in addition to the trinucleon energies, the empirical value of the Gamow-Teller matrix element in tritium β-decay [94]. The resulting Hamiltonians were labeled as NV2+3-Ia/b and NV2+3-IIa/b (or Ia/b and IIa/b for short) in the first case, and as NV2+3-Ia*/b* and NV2+3-IIa*/b* (or Ia*/b* and IIa*/b*) in the second.

The interactions between external electroweak probes—electrons and neutrinos—and interacting nuclear systems is described by a set of effective nuclear currents and charge operators. Analogously to the nuclear interactions, electroweak currents can also be expressed as an expansion in many-body operators that act on nucleonic degrees of freedom. Electroweak currents have been developed in both meson-exchange and χEFT approaches. We refrain to discuss them in this work, redirecting the interested reader to dedicated reviews [4, 96–98] and references therein.

3. QUANTUM MONTE CARLO METHODS

The χEFT Hamiltonians and the consistent electroweak currents discussed in the previous section are the main

input of sophisticated many-body methods aimed at solving with controlled approximations the nuclear many-body Schrödinger equation

$$H|\Psi_n\rangle = E_n|\Psi_n\rangle\,. \tag{10}$$

This is a highly non-trivial problem, mainly because of the non-perturbative nature and the strong spin-isospin dependence of realistic nuclear forces. In this work, we will focus on QMC techniques, namely the variational Monte Carlo (VMC), the Green's function Monte Carlo (GFMC), and the auxiliary-field diffusion Monte Carlo (AFDMC) methods.

3.1. Variational Monte Carlo

The variational Monte Carlo method is routinely used to obtain approximate solutions to the many-body Schrödinger equation for a wide range of strongly interacting nuclear systems, including few-body nuclei, light closed-shell nuclei, and nuclear and neutron matter [4]. The VMC algorithm relies on the Rayleigh-Ritz variational principle

$$\frac{\langle\Psi_T|H|\Psi_T\rangle}{\langle\Psi_T|\Psi_T\rangle} = E_T \geq E_0 \tag{11}$$

to find the optimal set of variational parameters defining the trial wave function Ψ_T. As far as the nuclear many-body problem is concerned, it is customary to assume that the trial state factorizes into long- and short-range components

$$|\Psi_T\rangle = \Big(1 - \sum_{i<j<k} F_{ijk}\Big)\Big(\mathcal{S}\prod_{i<j} F_{ij}\Big)|\Phi_J\rangle\,, \tag{12}$$

where F_{ij} and F_{ijk} are two- and three-body correlations, respectively. The symbol $\mathcal{S}$ indicates a symmetrized product over nucleon pairs since, in general, the F_{ij} do not commute. VMC calculations explicitly account for the underlying strong alpha-cluster structure of light nuclei. For instance, the totally antisymmetric Jastrow wave function of p-shell nuclei is constructed from a sum over independent-particle terms, Φ_A, each having four nucleons in an α-like core and the remaining $(A-4)$ nucleons in p-shell orbitals [99]:

$$|\Phi_J\rangle = \mathcal{A}\left[\prod_{i<j<k} f^c_{ijk}\prod_{i<j\leq 4} f_{ss}(r_{ij})\prod_{k\leq 4<l\leq A} f_{sp}(r_{kl})\right.$$
$$\left.\times\sum_{LS[n]}\Big(\beta_{LS[n]}\prod_{4<l<m\leq A} f^{[n]}_{pp}(r_{lm})\,|\Phi_A(LS[n]JJ_zT_z)_{1234:5\ldots A}\rangle\Big)\right]. \tag{13}$$

The operator $\mathcal{A}$ stands for an antisymmetric sum over all possible $\binom{A}{4}$ partitions of the A particles into four s-shell and $(A-4)$ p-shell states. As suggested by standard shell-model studies, the independent-particle wave function $|\Phi_A(LS[n]JJ_zT_z)_{1234:5\ldots A}\rangle$ with the desired JM value of a given nuclear state is obtained using LS coupling, which is most efficient for nuclei with up to $A = 12$. The symbol $[n]$ is the Young pattern that indicates the spatial symmetry of the angular momentum coupling of the p-shell nucleons [25]. Note that $|\Phi_A(LS[n]JJ_zT_z)_{1234:5\ldots A}\rangle$ is chosen to be independent of the center of mass as it is expressed in terms of the intrinsic coordinates

$$\mathbf{r}_i \to \mathbf{r}_i - \mathbf{R}_{\rm CM}\,, \qquad \mathbf{R}_{\rm CM} = \frac{1}{A}\sum_{i=1}^{A}\mathbf{r}_i\,. \tag{14}$$

The pair correlation for particles within the s-shell, f_{ss}, arises from the structure of the α particle. The f_{sp} is similar to the f_{ss} at short range, but with a long-range tail that goes to unity at large distances, allowing the wave function to develop a cluster structure. Finally, f_{pp} is set to give the appropriate cluster structure outside the α core. The three-body central correlations, induced by the two-body potential has the following operator independent form

$$f^c_{ijk} = 1 - q^c_1(\mathbf{r}_{ij}\cdot\mathbf{r}_{ik})(\mathbf{r}_{ij}\cdot\mathbf{r}_{jk})(\mathbf{r}_{ik}\cdot\mathbf{r}_{jk})e^{-q^c_2(r_{ij}+r_{ik}+r_{jk})}\,, \tag{15}$$

where q^c_1 and q^c_2 are variational parameters. In addition the scalar correlations of Equation (13), VMC trial wave functions include spin-dependent nuclear correlations, whose operator structure reflects the one of the NN potential of Equation (6)

$$F_{ij} = \big(1 + U_{ij}\big) = \Big(1 + \sum_{p=2}^{6} u^p(r_{ij})\mathcal{O}^p_{ij}\Big)\,. \tag{16}$$

More sophisticated trial wave functions can be constructed by explicitly accounting for spin-orbit correlations, as, for instance, in the cluster variational Monte Carlo calculations of reference [100]. However, the computational cost of these additional terms is significant, while the gain in the variational energy is relatively small [101]. The radial functions $u^p(r_{ij})$ are generated by minimizing the two-body cluster energy of the interaction $\bar{v} - \lambda$, with

$$\bar{v} - \lambda = \sum_{p=1}^{18}\Big(\alpha_p v^p(r_{ij})\mathcal{O}^p_{ij} - \lambda_p(r_{ij})\Big)\,. \tag{17}$$

The variational parameters α_p simulate the quenching of spin-isospin interactions between particles i and j due to interactions of these particles with others in the system. The Lagrange multipliers $\lambda_p(r_{ij})$ account for short-range screening effects, and are fixed at large distances by the asymptotic behavior of the correlation functions, which is encoded by an additional set of variational parameters. The quality of the trial wave function is improved by reducing the strength of the spin- and isospin-dependent correlation functions $u^p(r_{ij})$ when a particle k comes close to the pair ij [102]

$$u^p(r_{ij}) \to \left[\prod_{k\neq i\neq j} f^p_{ijk}(\mathbf{r}_{ij},\mathbf{r}_{ik})\right]u^p(r_{ij})\,, \tag{18}$$

where the three-body operator-dependent correlation induced by the NN interaction is usually expressed as

$$f^p_{ijk}(\mathbf{r}_{ij},\mathbf{r}_{ik}) = 1 - q^p_1(1 - \hat{\mathbf{r}}_{ik}\cdot\hat{\mathbf{r}}_{jk})e^{-q^p_2(r_{ij}+r_{ik}+r_{jk})}\,, \tag{19}$$

with q_1^p and q_2^p being variational parameters [25]. The three-body correlation operator F_{ijk} turns out to be particularly relevant for when $3N$ interactions are present in the nuclear Hamiltonian. In this case, its form is suggested by perturbation theory

$$F_{ijk} = \sum_q \epsilon_q V_{ijk}^q(y_q r_{ij}, y_q r_{ik}, y_q r_{jk}) , \tag{20}$$

where y_q is a scaling parameter, and ϵ_q a small, constant. The superscript q indicates the various terms of the $3N$ force. It has been shown that the vast majority of the $3N$ correlations can be recovered by omitting the commutator term $\epsilon_C V_{ijk}^C$, provided that the strength of the anticommutator term ϵ_A is opportunely adjusted. This allows to save a significant amount of computing time, since anticommutators involving pairs ij and jk can be expressed as a generalized tensor operators involving the spins of nucleons i and k only. Hence, the computing time scales as the number of pairs rather than the number of triplets [25].

The expectation values of the form of Equation (11) contain multi-dimensional integrals over all particle positions

$$\langle \mathcal{O} \rangle = \frac{\int d\mathbf{R} \Psi_T^\dagger(\mathbf{R}) \mathcal{O} \Psi_T(\mathbf{R})}{\int d\mathbf{R} \Psi_T^\dagger(\mathbf{R}) \Psi_T(\mathbf{R})} . \tag{21}$$

A deterministic integration of the above integral is computationally prohibitive, therefore Metropolis Monte Carlo techniques are employed to stochastically evaluate it. The order of operators in the symmetrized product of Equation (12), denoted by p and q for the left and right hand side wave functions, respectively, is also sampled. The $3A$-dimensional integration is facilitated by introducing a probability distribution, $W_{pq}(\mathbf{R})$, such that

$$\langle \mathcal{O} \rangle = \frac{\sum_{p,q} \int d\mathbf{R} \frac{\Psi_{T,p}^\dagger(\mathbf{R}) \mathcal{O} \Psi_{T,q}(\mathbf{R})}{W_{pq}(\mathbf{R})} W_{pq}(\mathbf{R})}{\sum_{p,q} \int d\mathbf{R} \frac{\Psi_{T,p}^\dagger(\mathbf{R}) \Psi_{T,q}(\mathbf{R})}{W_{pq}(\mathbf{R})} W_{pq}(\mathbf{R})} . \tag{22}$$

In standard VMC calculations, one usually takes $W_{pq}(\mathbf{R}) = |\mathrm{Re}(\Psi_{T,p}^\dagger(\mathbf{R}) \Psi_{T,q}(\mathbf{R}))|$, even though simpler choices might be used to reduce the computational cost. The Metropolis algorithm is used to stochastically sample the probability distribution $W_{pq}(\mathbf{R})$ and obtain a collection of uncorrelated or independent configurations.

Since the nuclear interaction is spin-isospin dependent, the trial state is a sum of complex amplitudes for each spin-isospin state of the system

$$|\Psi_T\rangle = \sum_{i_s \le n_s, i_t \le n_t} a(i_s, i_t; \mathbf{R}) |\chi_{i_s}\, \chi_{i_t}\rangle . \tag{23}$$

The $n_s = 2^A$ many-body spin states can be written as

$$\begin{aligned} |\chi_1\rangle &= |\downarrow_1, \downarrow_2, \ldots, \downarrow_A\rangle \\ |\chi_2\rangle &= |\uparrow_1, \downarrow_2, \ldots, \downarrow_A\rangle \\ |\chi_3\rangle &= |\downarrow_1, \uparrow_2, \ldots, \downarrow_A\rangle \\ &\cdots \\ |\chi_{n_s}\rangle &= |\uparrow_1, \uparrow_2, \ldots, \uparrow_A\rangle \end{aligned} \tag{24}$$

and the isospin ones can be recovered by replacing $\downarrow$ with n and $\uparrow$ with p. Note that, because of charge conservation, the number of isospin states reduces to $n_t = \binom{A}{Z}$. To construct the trial state, one starts from the mean-field component $|\Phi_A(LS[n]JJ_zT_z)_{1234:5\ldots A}\rangle$. For fixed spatial coordinates $\mathbf{R}$, the spin-isospin independent correlations needed to retrieve $|\Phi_J\rangle$ are simple multiplicative factors, common to all spin amplitudes. The symmetrized product of pair correlation operators is evaluated by successive operations for each pair, sampling their ordering as alluded to earlier. As an example, consider the application of the operator $\boldsymbol{\sigma}_1 \cdot \boldsymbol{\sigma}_2$ on a three-body spin state (for simplicity we neglect the isospin components). Noting that $\boldsymbol{\sigma}_i \cdot \boldsymbol{\sigma}_j = 2\,\mathcal{P}_{ij}^\sigma - 1$, where $2\,\mathcal{P}_{ij}^\sigma$ exchanges the spin of particles i and j, we obtain:

$$\boldsymbol{\sigma}_1 \cdot \boldsymbol{\sigma}_2 \begin{pmatrix} a_{\uparrow\uparrow\uparrow} \\ a_{\uparrow\uparrow\downarrow} \\ a_{\uparrow\downarrow\uparrow} \\ a_{\uparrow\downarrow\downarrow} \\ a_{\downarrow\uparrow\uparrow} \\ a_{\downarrow\uparrow\downarrow} \\ a_{\downarrow\downarrow\uparrow} \\ a_{\downarrow\downarrow\downarrow} \end{pmatrix} = \begin{pmatrix} a_{\uparrow\uparrow\uparrow} \\ a_{\uparrow\uparrow\downarrow} \\ 2a_{\downarrow\uparrow\uparrow} - a_{\uparrow\downarrow\uparrow} \\ 2a_{\downarrow\uparrow\downarrow} - a_{\uparrow\downarrow\downarrow} \\ 2a_{\uparrow\downarrow\uparrow} - a_{\downarrow\uparrow\uparrow} \\ 2a_{\uparrow\downarrow\downarrow} - a_{\downarrow\uparrow\downarrow} \\ a_{\downarrow\downarrow\uparrow} \\ a_{\downarrow\downarrow\downarrow} \end{pmatrix} . \tag{25}$$

Hence, the many-body spin-isospin basis is closed under the action of the operators contained in the nuclear Hamiltonian.

Most of the computing time is spent on spin-isospin operations like the one just described. They amount to an iterative sequence of large sparse complex matrix multiplications that are performed on-the-fly using explicitly coded subroutines, which mainly rely on three useful matrices. The first matrix $m(i, i_s)$ gives the z-component of the spin of particle i associated to the many-body spin-state i_s. A second useful matrix is $n_{\mathrm{exch}}(k_{ij}, i_s)$, that provides the number of the many-body spin state obtained by exchanging the spins of particles i and j, belonging to the pair labeled k_{ij} in the state i_s. The matrix $n_{\mathrm{flip}}(i, i_s)$ yields the number of the spin state obtained by flipping the spin of particle i in the spin state. The action of the operator $\boldsymbol{\sigma}_1 \cdot \boldsymbol{\sigma}_2$ can then be expressed as

$$\begin{aligned} &\boldsymbol{\sigma}_1 \cdot \boldsymbol{\sigma}_2 \sum_{i_s, i_t} a(i_s, i_t; \mathbf{R}) |\chi_{i_s}\, \chi_{i_t}\rangle \\ &= \sum_{i_s, i_t} \left[2a(i_s, i_t; \mathbf{R}) - a(n_{\mathrm{exch}}(k_{ij}, i_s), i_t; \mathbf{R}) \right] |\chi_{i_s}\, \chi_{i_t}\rangle . \end{aligned} \tag{26}$$

By utilizing this representation, we only need to evaluate 2^A operations for each pair, instead of the $2^A \times 2^A$ operations that are required using a simple matrix representation in spin space. The tensor operator is slightly more complicated to evaluate and requires both matrices $m(i, i_s)$ and $n_{\mathrm{flip}}(i, i_s)$ [103]. Analogous matrices are employed to perform operations in the isospin space, as the two representations are practically identical.

The expectation values of Equation (21) are evaluated by having the operators act entirely on the right hand side of the trial wave function. The matrix machinery used to apply the spin-dependent correlation operators is also used to evaluate $\mathcal{O}|\Psi_{T,p}\rangle$. A simple scalar product of this quantity with $\langle \Psi_{T,q}|$, provides the numerator of the local estimate $\Psi_{T,q}^\dagger(\mathbf{R}) \mathcal{O} \Psi_{T,p}(\mathbf{R}) / W_{pq}(\mathbf{R})$ and

$W_{pq}(\mathbf{R})$ is computed in a similar fashion. The first and second derivatives of the wave function are numerically computed by means of the two- and three-point stencil, respectively. Hence, to determine the kinetic energy, $6A + 1$ evaluations of $\Psi_T(\mathbf{R})$ are needed. Finally, using the trick described in reference [104], we can evaluate the action of the angular momentum dependent terms in the potential evaluating $\Psi_T(\mathbf{R})$ an additional $3A(A-1)/2$ times.

Not only does the size of the wave vector grows exponentially with the number of nucleons, but so does the number of evaluations necessary to calculate the energy, limiting the applicability of the VMC method to $A \leq 12$ nuclei. Sampling the spin-isospin state and evaluating the trial wave function's amplitude for that sampled state still requires a number of operations exponential in the particle number, bringing little savings in terms of computing time. Extending VMC calculations to larger nuclear systems requires devising trial wave functions that can capture most of physics of the system while requiring computational time that scales polynomially with A.

3.2. Green's Function Monte Carlo

Green's function Monte Carlo overcomes the limitations intrinsic to the variational ansatz by using an imaginary-time projection technique to enhance the true ground-state component of a starting trial wave function

$$|\Psi_0\rangle \propto \lim_{\tau\to\infty} e^{-(H-E_T)\tau}|\Psi_T\rangle\,. \tag{27}$$

In the above equation, τ is the imaginary time, and E_T is a parameter used to control the normalization. In addition to ground-states properties, excited states can be computed within GFMC. The imaginary-time diffusion yields the lowest-energy eigenstate with the same quantum numbers as $|\Psi_T\rangle$. Thus, to obtain an excited state with distinct quantum numbers from the ground state, one only needs to construct a trial wave function with the appropriate quantum numbers. If the excited-state quantum numbers coincide with those of the ground state, more care is needed, but precise results for such states can still be obtained [105].

Except for some specific cases, the direct computation of the propagator $e^{-H\tau}$ for arbitrary values of τ is typically not possible. For small imaginary times $\delta\tau = \tau/N$ with N large, the calculation is tractable, and the full propagation to large imaginary times τ can be recovered through the following path integral

$$\Psi(\tau,\mathbf{R}_N) = \int \prod_{i=0}^{N-1} \mathrm{d}\mathbf{R}_i \left\langle \mathbf{R}_N \left| e^{-(H-E_T)\delta\tau} \right| \mathbf{R}_{N-1} \right\rangle \cdots \left\langle \mathbf{R}_1 \left| e^{-(H-E_T)\delta\tau} \right| \mathbf{R}_0 \right\rangle \langle \mathbf{R}_0 \rangle\, \Psi_T\,. \tag{28}$$

The GFMC wave function at imaginary time $\tau+\delta\tau$ can be written in an integral form

$$\Psi(\tau+\delta\tau,\mathbf{R}_{i+1}) = \int d\mathbf{R}_i G_{\delta\tau}(\mathbf{R}_{i+1},\mathbf{R}_i)\Psi(\tau,\mathbf{R}_i)\,, \tag{29}$$

where we defined the short-time propagator, or Green's function,

$$G_{\delta\tau}(\mathbf{R}_{i+1},\mathbf{R}_i) = \left\langle \mathbf{R}_{i+1} \left| e^{-H\delta\tau} \right| \mathbf{R}_i \right\rangle\,. \tag{30}$$

Monte Carlo techniques are used to sample the paths by simultaneously evolving a set of configurations—dubbed *walkers*—in imaginary time, until the distribution converges to the ground-state wave function [106]. To avoid the large statistical errors arising from configurations that diffuse into regions where they make very little contribution to the ground-state wave function, the diffusion process is guided by introducing an importance-sampling function $\Psi_I(\mathbf{R})$, which has the same quantum numbers as the ground-state. The importance function is typically taken to coincide with the variational wave function, but different choices are possible. Multiplying Equation (29) on the left by $\Psi_I^\dagger(\mathbf{R}_{i+1})$ yields

$$\Psi_I^\dagger(\mathbf{R}_{i+1})\Psi(\tau+\delta\tau,\mathbf{R}_{i+1}) = \int d\mathbf{R}_i \left[\Psi_I^\dagger(\mathbf{R}_{i+1}) G_{\delta\tau}(\mathbf{R}_{i+1},\mathbf{R}_i) \frac{1}{\Psi_I^\dagger(\mathbf{R}_i)} \right] \Psi_I^\dagger(\mathbf{R}_i)\Psi(\tau,\mathbf{R}_i)\,. \tag{31}$$

The quantity within squared brackets is the importance-sampled propagator $G^I_{\delta\tau}(\mathbf{R}_{i+1},\mathbf{R}_i)$. Note that a set of walkers can be sampled from $\Psi_I^\dagger(\mathbf{R}_i)\Psi(\tau+\delta\tau,\mathbf{R}_i)$ only if this density is positive definite. In this case, the latter can be interpreted as a probability density distribution and its integral determines the size of the population, i.e., the number of walkers. In Fermion systems, however, the positiveness of $\Psi_I^\dagger(\mathbf{R}_i)\Psi(\tau+\delta\tau,\mathbf{R}_i)$ is only granted for exact importance-sampling functions. In general, the nodal surface of the ground state can be different from that of Ψ_I. We will return to this point later on. The importance function can be expanded in terms of eigenstates of the Hamiltonian as

$$\Psi_I(\mathbf{R}_i) = \sum_n c_n \Psi_n(\mathbf{R})\,. \tag{32}$$

The Green's function can also be expressed in terms of the same eigenstates:

$$G_{\delta\tau}(\mathbf{R}_{i+1},\mathbf{R}_i) = \sum_n \Psi_n(\mathbf{R}_{i+1}) e^{-(E_n-E_T)\delta\tau} \Psi_n^\dagger(\mathbf{R})\,. \tag{33}$$

Inserting the last two relations into Equation (29) and integrating over $\mathbf{R}_{i+1}$, we get

$$\sum_n c_n^* \int d\mathbf{R}_{i+1} \Psi_n^\dagger(\mathbf{R}_{i+1})\Psi(\tau+\delta\tau,\mathbf{R}_{i+1}) = \sum_n c_n^* \int d\mathbf{R}_i \Psi_n^\dagger(\mathbf{R}_i)\, e^{-(E_n-E_T)\delta\tau}\Psi(\tau,\mathbf{R}_i)\,. \tag{34}$$

If the importance-sampling function closely resembles the ground-state wave function, then $c_n^* \simeq \delta_{n0}$ and $E_T \simeq E_0$, implying

$$\int d\mathbf{R}_{i+1} \Psi_0^\dagger(\mathbf{R}_{i+1})\Psi(\tau+\delta\tau,\mathbf{R}_{i+1}) \simeq \int d\mathbf{R}_i \Psi_0^\dagger(\mathbf{R}_i)\Psi(\tau,\mathbf{R}_i)\,. \tag{35}$$

Therefore, having accurate importance function reduces the fluctuations in the population size from one time step to the next, thereby reducing the statistical errors in the calculation.

A common approximation for the short-time propagator is based upon the Trotter-Suzuki expansion

$$G_{\delta\tau}(\mathbf{R}_{i+1},\mathbf{R}_i) = e^{-V(\mathbf{R}_{i+1})\delta\tau/2}\langle \mathbf{R}_{i+1}|e^{-T\delta\tau}|\mathbf{R}_i\rangle e^{-V(\mathbf{R}_i)\delta\tau/2} + o(\delta\tau^3). \tag{36}$$

Here, T is the kinetic energy giving rise to the free-particle propagator that, for non-relativistic systems, can be expressed as a simple Gaussian in configuration space

$$\langle \mathbf{R}_{i+1}|e^{-T\delta\tau}|\mathbf{R}_i\rangle = G^0_{\delta\tau}(\mathbf{R}_{i+1},\mathbf{R}_i) = \left[\frac{1}{\lambda^3\pi^{3/2}}\right]^A e^{-(\mathbf{R}_{i+1}-\mathbf{R}_i)^2/\lambda^2}, \tag{37}$$

with $\lambda^2 = 4\frac{\hbar^2}{2m}\delta\tau$. The exponentials of the two-body potentials can be approximated to first order by turning the sums over pairs in the exponent into a symmetrized product of exponentials of the individual pair potentials. The first six terms of the potential can be easily exponentiated, while momentum dependent terms cannot be treated this way. A simple way to include them consists in expanding the exponential of the momentum dependent terms to first order in $\delta\tau$ and use integration by parts to let the derivatives act on the free-particle Green's function. This approach can only be successfully applied to the terms in the potential that are linear in momentum, such as $\mathbf{L}\cdot\mathbf{S}$ and $(\mathbf{L}\cdot\mathbf{S})\,\boldsymbol{\tau}_i\cdot\boldsymbol{\tau}_j$ [107]. On the other hand, contributions to the potential that are quadratic in the momentum cannot be evaluated to first order in this manner. For this reason we use approximations to the full *NN* potentials, such as the AV8′ interaction, that only contain the first eight operators. The difference between AV18 and AV8′ is treated in perturbation theory.

More sophisticated alternatives of reducing the time-step error exist and are routinely used in GFMC calculations. The most common one consists in building the Green's function operator as a product of exact two-body propagators

$$G_{\delta\tau}(\mathbf{R}_{i+1},\mathbf{R}_i) = \left(\mathcal{S}\prod_{j<k}\frac{g_{jk}(\mathbf{r}_{jk,i},\mathbf{r}_{jk,i+1})}{g^0_{jk}(\mathbf{r}_{jk,i},\mathbf{r}_{jk,i+1})}\right) G^0_{\delta\tau}(\mathbf{R}_{i+1},\mathbf{R}_i), \tag{38}$$

where $g_{jk}(\mathbf{r}_{jk,i},\mathbf{r}_{jk,i+1})$ is the exact two-body propagator and $g^0_{jk}(\mathbf{r}_{jk,i},\mathbf{r}_{jk,i+1})$ is the two-body free- particle propagator [108]. At variance with the propagator of Equation (36), terms quadratic in the angular momentum can in principle be accounted for into the exact pair propagator. However, the inclusion of these terms requires the sampled distribution to have the same locality structure to keep statistical errors under control. Thus, simplified AV8′ potentials are also used in the pair propagator, even though in this case no approximations in treating $\mathbf{L}\cdot\mathbf{S}$ and $(\mathbf{L}\cdot\mathbf{S})\,\boldsymbol{\tau}_i\cdot\boldsymbol{\tau}_j$ terms are necessary.

Since the matrix V is the spin/isospin-dependent interaction, the propagator is in turn a matrix in spin-isospin space. To deal with it, first a scalar approximation to the importance sampled Green's function, denoted as $\tilde{G}^I_{\delta\tau}(\mathbf{R}_{i+1},\mathbf{R}_i)$, is introduced. Recalling the form of the importance sampled Green's function

$$G^I_{\delta\tau}(\mathbf{R}_{i+1},\mathbf{R}_i) = \frac{\Psi^\dagger_I(\mathbf{R}_{i+1})}{\Psi^\dagger_I(\mathbf{R}_i)}G_{\delta\tau}(\mathbf{R}_{i+1},\mathbf{R}_i), \tag{39}$$

constructing its scalar counterpart requires defining a scalar approximation for the importance-sampling function, which can be taken to be $\tilde{\Psi}_I(\mathbf{R}) = \sqrt{\Psi^\dagger_J(\mathbf{R})\Psi_J(\mathbf{R})}$. As for the potential, we can use the average of the central parts in the $^1S_0$ and $^3S_1$ channels, thus

$$\tilde{G}^I_{\delta\tau}(\mathbf{R}_{i+1},\mathbf{R}_i) = \frac{\tilde{\Psi}_I(\mathbf{R}_{i+1})}{\tilde{\Psi}_I(\mathbf{R}_i)}e^{-[V_{10}(\mathbf{R}_{i+1})+V_{01}(\mathbf{R}_{i+1})]\delta\tau/4}G^0_{\delta\tau}(\mathbf{R}_{i+1},\mathbf{R}_i)e^{-[V_{10}(\mathbf{R}_i)+V_{01}(\mathbf{R}_i]\delta\tau/4}. \tag{40}$$

At each time-step, the walkers are propagated with $G^0_{\delta\tau}(\mathbf{R}_{i+1},\mathbf{R}_i)$ by sampling a $3A$-dimensional vector from a gaussian distribution to shift the spatial coordinates. To remove the linear terms coming from the exponential of Equation (37), we use two mirror points $\mathbf{R}_{i+1} = \mathbf{R}_i \pm \delta\mathbf{R}$ and we consider the corresponding two weights

$$w_\pm = \frac{\tilde{\Psi}_I(\mathbf{R}_i \pm \delta\mathbf{R})}{\tilde{\Psi}_I(\mathbf{R}_i)}e^{-[V_{10}(\mathbf{R}_i\pm\delta\mathbf{R})+V_{01}(\mathbf{R}_i\pm\delta\mathbf{R})+V_{10}(\mathbf{R}_i)+V_{01}(\mathbf{R}_i]\delta\tau/4}e^{E_T\delta\tau}. \tag{41}$$

One of the two walkers is kept in the propagation according to a heat-bath sampling among the two normalized weights $w_\pm/(\sum_\pm w_\pm)$ and the average weight $\sum_\pm w_\pm/2$ is associated to the propagated configuration.

In terms of the scalar Green's function, the propagation of Equation (29) reads

$$\Psi(\tau+\delta\tau,\mathbf{R}_{i+1}) = \int d\mathbf{R}_i\left[\frac{G_{\delta\tau}(\mathbf{R}_{i+1},\mathbf{R}_i)}{\tilde{G}^I_{\delta\tau}(\mathbf{R}_{i+1},\mathbf{R}_i)}\right]\tilde{G}^I_{\delta\tau}(\mathbf{R}_{i+1},\mathbf{R}_i)\Psi(\tau,\mathbf{R}_i). \tag{42}$$

Since the new positions are sampled according to $\tilde{G}^I_{\delta\tau}(\mathbf{R}_{i+1},\mathbf{R}_i)$, we can conveniently define

$$\Psi(\tau+\delta\tau,\mathbf{R}_{i+1}) = \frac{G_{\delta\tau}(\mathbf{R}_{i+1},\mathbf{R}_i)}{\tilde{G}^I_{\delta\tau}(\mathbf{R}_{i+1},\mathbf{R}_i)}\Psi(\tau,\mathbf{R}_i). \tag{43}$$

The imaginary-time evolution of the walker density is given by

$$\Psi^\dagger_I(\mathbf{R}_{i+1})\Psi(\tau+\delta\tau,\mathbf{R}_{i+1}) = \int d\mathbf{R}_i\left[\frac{\Psi^\dagger_I(\mathbf{R}_{i+1})G_{\delta\tau}(\mathbf{R}_{i+1},\mathbf{R}_i)\Psi(\tau,\mathbf{R}_i)}{\Psi^\dagger_I(\mathbf{R}_i)\tilde{G}^I_{\delta\tau}(\mathbf{R}_{i+1},\mathbf{R}_i)\Psi(\tau,\mathbf{R}_i)}\right]\tilde{G}^I_{\delta\tau}(\mathbf{R}_{i+1},\mathbf{R}_i)\Psi^\dagger_I(\mathbf{R}_i)\Psi(\tau,\mathbf{R}_i). \tag{44}$$

Iterations of Equation (44) amount to multiple matrix multiplications

$$\Psi(\tau,\mathbf{R}_N)=\left[\frac{G_{\delta\tau}(\mathbf{R}_N,\mathbf{R}_{N-1})}{\tilde{G}^I_{\delta\tau}(\mathbf{R}_N,\mathbf{R}_{N-1})}\right]\left[\frac{G_{\delta\tau}(\mathbf{R}_{N-1},\mathbf{R}_{N-2})}{\tilde{G}^I_{\delta\tau}(\mathbf{R}_{N-1},\mathbf{R}_{N-2})}\right]\cdots\left[\frac{G_{\delta\tau}(\mathbf{R}_1,\mathbf{R}_0)}{\tilde{G}^I_{\delta\tau}(\mathbf{R}_1,\mathbf{R}_0)}\right]\Psi_T(\mathbf{R}_0)\,, \tag{45}$$

that are performed using the same matrices used to construct $|\Psi_T\rangle$. It has to be stressed that $\Psi(\tau,\mathbf{R}_N)$ is *not* the ground-state wave function. It rather represents a spin-isospin set of amplitudes that, when taken in product with the Hermitian conjugate of the importance function, gives an overlap for each component of the wave function. Are the changes in these overlaps that drive the distribution of walkers toward that of the true ground state.

To avoid sign fluctuations in $\Psi^\dagger_I(\mathbf{R}_i)\Psi(\tau,\mathbf{R}_i)$, we sample the walkers from the positive-definite density distribution

$$I(\mathbf{R}_i)=\left|\sum_{i_s,i_t}\langle\Psi_I(\mathbf{R}_i)|\chi_{i_s}\,\chi_{i_t}\rangle\langle\chi_{i_s}\,\chi_{i_t}|\Psi(\tau,\mathbf{R}_i)\rangle\right| +\epsilon\sum_{i_s,i_t}\left|\langle\Psi_I(\mathbf{R}_i)|\chi_{i_s}\,\chi_{i_t}\rangle\langle\chi_{i_s}\,\chi_{i_t}|\Psi(\tau,\mathbf{R}_i)\rangle\right|. \tag{46}$$

The first term simply measures the magnitude of the overlap of the wave functions, while the second, with a small coefficient $\epsilon \simeq 0.01$, ensures a positive definite importance function to allow diffusion across nodal surfaces. This choice for the sampling distribution is monitored by checking how much this estimate of the population size deviates from the actual number of configurations. Since the configurations are distributed according to $I(\mathbf{R}_i)$ defined in Equation (46), the expectation values of observables that commute with the Hamiltonian are estimated as

$$\langle\mathcal{O}(\tau)\rangle=\frac{\langle\Psi_T|\mathcal{O}|\Psi(\tau)\rangle}{\langle\Psi_T|\Psi(\tau)\rangle}=\frac{\sum_{R_i}\langle\Psi_T(\mathbf{R}_i)|O|\Psi(\tau,\mathbf{R}_i)\rangle/I(\mathbf{R}_i)}{\sum_{R_i}\langle\Psi_T(\mathbf{R}_i)|\Psi(\tau,\mathbf{R}_i)\rangle/I(\mathbf{R}_i)}\,. \tag{47}$$

For all other observables, we compute the mixed estimates

$$\langle\mathcal{O}(\tau)\rangle\simeq 2\frac{\langle\Psi_T|\mathcal{O}|\Psi(\tau)\rangle}{\langle\Psi_T|\Psi(\tau)\rangle}-\frac{\langle\Psi_T|\mathcal{O}|\Psi_T\rangle}{\langle\Psi_T|\Psi_T\rangle}\,, \tag{48}$$

where the first and the second term correspond to the DMC and VMC expectation value, respectively.

As in standard Fermion diffusion Monte Carlo algorithms, the GFMC method suffers from the Fermion sign problem that arises from stochastically evaluating the matrix elements in Equation (47). The imaginary-time propagator is a local operator, while antisymmetry is a global property of the system. As a consequence, $|\Psi(\tau)\rangle$ can contain bosonic components that have much lower energy than the Fermionic ones and are exponentially amplified during the propagation. When the dot product with the antisymmetric Ψ_T is taken, the desired Fermionic component is projected out in the expectation values, but the variance—and hence the statistical error—grows exponentially with τ. Because the number of pairs that can be exchanged grows with A, the sign problem also grows exponentially with the number of nucleons. Already for $A = 8$, the statistical errors grow so fast that convergence cannot be achieved.

To control the sign problem, we adopt the so-called "contrained-path" method [101], originally developed to study condensed matter systems [109]. This method is based on discarding those configurations that in future generations will contribute only noise to expectations values. If we knew the exact ground state, we could discard any walker for which

$$\Psi^\dagger_0(\mathbf{R}_i)\Psi(\tau,\mathbf{R}_i)=0\,, \tag{49}$$

where a sum over spin-isospin states is implied. The sum of these discarded configurations can be written as a state $|\Psi_d\rangle$, which has zero overlap with the ground state. Disregarding $|\Psi_d\rangle$ is justified because it only contains excited-states components and should decay away as $\tau\to\infty$. However, in general, the exact ground state is not known, and the constraint is approximately imposed using Ψ_T in place of Ψ_0:

$$\langle\Psi_T|\Psi_d\rangle=0\,. \tag{50}$$

The GFMC wave function evolves smoothly in imaginary time and changes can be made arbitrarily small by reducing $\delta\tau$. Hence, if the wave function is purely scalar, any configuration which yields a negative overlap must first pass through a point at which Ψ_T—and hence the overlap—is zero. Discarding these configurations is then sufficient to stabilize the simulation and produce "fixed-node" variational solutions, to the many-Fermion problem. However, the GFMC trial wave function is a vector in spin-isospin space, and there are no coordinates for which all the spin-isospin amplitudes vanish. In addition, the overlap $\Psi^\dagger_{T,p}(\mathbf{R}_i)\Psi(\tau,\mathbf{R}_i)$ is complex and depends on the particular sampled order p. As a consequence, it does not evolve smoothly and can pass through zero. The constraint of Equation (50) cannot be satisfied for individual configurations, but rather only on average for the sum of discarded configurations. To circumvent these difficulties, we define the overlap

$$O_{T,p}=\Re[\Psi^\dagger_{T,p}(\mathbf{R}_i)\Psi(\tau,\mathbf{R}_i)]\,. \tag{51}$$

We can then introduce a probability for discarding a configuration in terms of the ratio $O_{T,p}/I_{T,p}$ where $I_{T,p}$ corresponds to choosing the ordering p in Ψ_I as defined in Equation (46)

$$P[\Psi^\dagger_{T,p}(\mathbf{R}_i),\Psi(\tau,\mathbf{R}_i)]=\begin{cases}0 & O/I>\alpha_c\\ \frac{\alpha_C-O/I}{\alpha_c-\beta_c} & \alpha_c>O/I>\beta_c\\ 1 & O/I<\beta_c\end{cases}$$

The constants α_c and β_c are adjusted such that the average of the overlap $O_{T,p}/I_{T,P}$ is zero within statistical errors.

In a few cases the constrained propagation converges to the wrong energy (either above or below the correct energy). Therefore, a small number, $n_u = 10$–80, of unconstrained steps are made before evaluating expectation values. These few unconstrained steps appear to be sufficient to remove the bias introduced by the constraint but do not greatly increase the statistical error.

3.3. Auxiliary Field Diffusion Monte Carlo

Over the last two decades, the auxiliary field diffusion Monte Carlo method [110] has become a mainstay for studying atomic nuclei [89, 111–113] and infinite neutron matter [13, 87, 114]. The AFDMC overcomes the exponential scaling with the number of nucleons of the GFMC by using a spin-isospin basis given by the outer product of single-nucleon spinors

$$|\chi_{i_s}\,\chi_{i_t}\rangle \rightarrow |S\rangle \equiv |s_1\rangle \otimes |s_2\rangle \otimes \cdots \otimes |s_A\rangle\,, \tag{52}$$

where

$$|s_i\rangle = a_{i,\uparrow p}|\uparrow p\rangle + a_{i,\downarrow p}|\downarrow p\rangle + a_{i,\uparrow n}|\uparrow n\rangle + a_{i,\downarrow n}|\downarrow n\rangle\,. \tag{53}$$

The state vector is fully specified by a set of $4A$ complex coefficients. As opposed to the many-body spin-isospin basis defined in Equation (23), the single-particle one is not closed under the action of two-body operators. To see this, lets apply again the operator $\boldsymbol{\sigma}_1 \cdot \boldsymbol{\sigma}_2$ on a three-body spin state

$$\begin{aligned}
&\boldsymbol{\sigma}_1 \cdot \boldsymbol{\sigma}_2 \Big[\big(a_{1,\uparrow}|\uparrow\rangle + a_{1,\downarrow}|\downarrow\rangle\big) \otimes \big(a_{2,\uparrow}|\uparrow\rangle + a_{2,\downarrow}|\downarrow\rangle\big) \otimes \\
&\big(a_{3,\uparrow}|\uparrow\rangle + a_{3,\downarrow}|\downarrow\rangle\big) \Big] = 2\Big[\big(a_{2,\uparrow}|\uparrow\rangle + a_{2,\downarrow}|\downarrow\rangle\big) \otimes \\
&\big(a_{1,\uparrow}|\uparrow\rangle + a_{1,\downarrow}|\downarrow\rangle\big) \otimes \big(a_{3,\uparrow}|\uparrow\rangle + a_{3,\downarrow}|\downarrow\rangle\big) \Big] \\
&- \Big[\big(a_{1,\uparrow}|\uparrow\rangle + a_{1,\downarrow}|\downarrow\rangle\big) \otimes \big(a_{2,\uparrow}|\uparrow\rangle + a_{2,\downarrow}|\downarrow\rangle\big) \otimes \\
&\big(a_{3,\uparrow}|\uparrow\rangle + a_{3,\downarrow}|\downarrow\rangle\big) \Big]\,.
\end{aligned} \tag{54}$$

In general, the action of all pairwise spin/isospin operators needed to construct the trial state defined in Equation (12) generates all the $2^A\binom{A}{Z}$ amplitudes of the many-body spin-isospin basis. For this reason, the trial wave function typically used in AFDMC calculations [89, 115] is simpler than the one of the GFMC and takes the form

$$|\Psi_T\rangle = \Big(1 - \sum_{i<j} F_{ij} - \sum_{i<j<k} F_{ijk}\Big)|\Phi_J\rangle\,, \tag{55}$$

where F_{ij} and F_{ijk} are defined in Equations (16) and (20), respectively. Since it contains a linearized version of spin/isospin-dependent two-body correlations, this wave function is significantly cheaper to evaluate than the one used in GFMC, as it scales polynomially with the number of nucleons rather than exponentially. However, because only pairs of nucleons are correlated at a time, the cluster property is violated. Nevertheless, the use of these linearized spin-dependent correlations has enabled a number of remarkably accurate AFDMC calculations, in which properties of atomic nuclei up to $A = 16$ [89, 111, 112] have been investigated utilizing the local χEFT interactions of references [12, 87]. Very recently, the AFDMC trial wave function has been improved by including quadratic pair correlations [89, 116].

The Jastrow component of $|\Psi_T\rangle$ is also simpler than the one of Equation (13),

$$|\Phi_J\rangle = \prod_{i<j} f^c_{ij} \prod_{i<j<k} f^c_{ijk} |\Phi_A(J^\pi, J_z, T_z)\rangle\,, \tag{56}$$

where the two-body scalar correlation are obtained consistently with the $u^p(r_{ij})$ minimizing the two-body cluster energy. The three-body scalar correlation is the one defined in Equation (15). The mean-field component is modeled by a sum of Slater determinants,

$$\langle X|\Phi(J^\pi, J_z, T_z)\rangle = \sum_n c_n \left[\sum_{JJ_z} C_{JJ_z} \mathcal{A}\big[\,\phi_{\alpha_1}(x_1)\ldots\phi_{\alpha_A}(x_A)\,\big] \right]_{JJ_z}\,. \tag{57}$$

In the above equation we have introduced $X = \{x_1, \ldots, x_A\}$, where the generalized coordinate $x_i \equiv \{\mathbf{r}_i, s_i\}$ represents both the position $\mathbf{R} = \mathbf{r}_1, \ldots, \mathbf{r}_A$ and the spin-isospin coordinates $S = s_1, \ldots, s_A$ of the A nucleons. The determinants are coupled with Clebsch-Gordan coefficients C_{JJ_z} in order to reproduce the total angular momentum, total isospin, and parity. The single-particle orbitals are given by

$$\phi_\alpha(x_i) = R_{nl}(r_i)\, Y_{ll_z}(\hat{r}_i)\, \chi_{ss_z}(\sigma)\, \chi_{tt_z}(\tau), \tag{58}$$

where $R_{nl}(r)$ is the radial function, Y_{ll_z} is the spherical harmonic, and $\chi_{ss_z}(\sigma)$ and $\chi_{tt_z}(\tau)$ are the complex spinors describing the spin and isospin of the single-particle state.

The AFDMC imaginary-time propagation can be broken up in small time steps similarly to what is done in Equation (28) for the GFMC method. This time however, the generalized coordinate X is used instead of $\mathbf{R}$ and the spin-isospin degrees of freedom are also sampled. The AFDMC wave function at imaginary time $\tau + \delta\tau$ can be written in an integral form analogous to the one of Equation (29)

$$\Psi(\tau + \delta\tau, X_{i+1}) = \sum_{S_i} \int d\mathbf{R}_i G_{\delta\tau}(X_{i+1}, X_i) \Psi(\tau, X_i)\,. \tag{59}$$

Using the Trotter decomposition of Equation (36), the short-time Green's function factorizes as

$$\begin{aligned}
G_{\delta\tau}(X_{i+1}, X_i) = G^0_{\delta\tau}(\mathbf{R}_{i+1}, \mathbf{R}_i) \langle S_{i+1}| e^{-(V(\mathbf{R}_{i+1})/2 + V(\mathbf{R}_i)/2 - E_T)\delta\tau} |S_i\rangle \\
+ o(\delta\tau^3)\,.
\end{aligned} \tag{60}$$

Quadratic spin-isospin operators contained in the nuclear potential can connect a single spin-isospin state $|S_i\rangle$ to all possible $|S_{i+1}\rangle$ states. In order to preserve the single-particle representation, the short-time propagator is linearized utilizing the Hubbard-Stratonovich transformation

$$e^{-\lambda\mathcal{O}^2\delta\tau/2} = \frac{1}{\sqrt{2\pi}} \int_{-\infty}^{\infty} dx\, e^{-x^2/2}\, e^{x\sqrt{-\lambda\delta\tau}\,\mathcal{O}}\,, \tag{61}$$

where x are the *auxiliary fields* and the operators $\mathcal{O}$ are obtained as follows. The first six terms defining the *NN* potential can be conveniently separated in a spin/isospin-dependent V_{SD} and spin/isospin-independent V_{SI} contributions. To see this in more details, lets consider purely neutron systems, where $\boldsymbol{\tau}_i \cdot \boldsymbol{\tau}_j = 1$, since the extension to isospin-dependent terms is trivial [89]. In this case, V_{SD} can be cast in the form

$$V_{SD} = \frac{1}{2} \sum_{i\alpha j\beta} A_{i\alpha,j\beta}\, \sigma_i^\alpha\, \sigma_j^\beta = \frac{1}{2} \sum_{n=1}^{3A} \mathcal{O}_n^2\, \lambda_n\,, \tag{62}$$

where the operators $\mathcal{O}_n$ are defined as

$$\mathcal{O}_n = \sum_{i,\alpha} \sigma_i^\alpha\, \psi_{i\alpha}^n\,. \tag{63}$$

In the above equations λ_n and $\psi_{i\alpha}^n$ are the eigenvalues and eigenvectors of the matrix A. Hence, applying the exponential of the spin-dependent terms of the *NN* interaction amounts to rotating the spin-isospin states of nucleons

$$e^{-V(\mathbf{R}_i)\delta\tau/2}|S_i\rangle = \prod_n \frac{1}{\sqrt{2\pi}} \int dx_n e^{-x_n^2/2} e^{x_n\sqrt{-\lambda\delta\tau}\, O_n}|S_i\rangle\,, \tag{64}$$

and the imaginary-time propagation is performed by sampling the auxiliary fields $\bar{x}_n$ from the Gaussian probability distribution

$$|S_{i+1}\rangle = \prod_n e^{\bar{x}_n\sqrt{-\lambda\delta\tau}\, O_n}|S_i\rangle\,. \tag{65}$$

The spin-orbit term of the *NN* potential—$p = 7$ in Equation (6)—is implemented in the propagator as described in reference [117], and appropriate counter terms are included to remove the spurious contributions of order $\delta\tau$. Presently, the isospin-dependent spin-orbit term of the *NN* potential, corresponding to $p = 8$ in Equation (6), cannot be properly treated within the AFDMC algorithm, as its counter term contains cubic spin-isospin operators, preventing the straightforward use of the Hubbard-Stratonovich transformation.

Importance sampling techniques are also routinely implemented in the AFDMC method—in both the spatial coordinates and spin-isospin configurations—to drastically improve the efficiency of the algorithm. To this aim, the propagator of Equation (60) is modified as

$$G_{\delta\tau}^I(X_{i+1}, X_i) = G_{\delta\tau}(X_{i+1}, X_i) \frac{\Psi_I(X_{i+1})}{\Psi_I(X_i)}\,, \tag{66}$$

and we typically take $\Psi_I(X) = \Psi_T(X)$. At each time step, each walker is propagated sampling a $3A$-dimensional vector to shift the spatial coordinates and a set of auxiliary fields $\mathcal{X}$ from Gaussian distributions. To remove the linear terms coming from the exponential of both Equations (37) and (64), in analogy to the GFMC method, we consider four weights, corresponding to separately flipping the sign of the spatial moves and spin-isospin rotations

$$w_i = \frac{\Psi_I(\pm\mathbf{R}_{i+1}, S_{i+1}(\pm\mathcal{X}))}{\Psi_I(\mathbf{R}_i, S_i)}\,. \tag{67}$$

In the same spirit as the GFMC algorithm, only one of the four configurations is kept according to a heat-bath sampling among the four normalized weights w_i/W, with $W = \sum_{i=1}^4 w_i/4$ being the cumulative weight. The latter is then rescaled by

$$W \to We^{-[V_{SI}(\mathbf{R}_i)/2 + V_{SI}(\mathbf{R}_{i+1})/2 - E_T]\delta\tau}\,, \tag{68}$$

and associated to this new configuration for branching and computing observables. This "plus and minus" procedure, first implemented in the AFDMC method in reference [115] significantly reduces the dependence of the results on $\delta\tau$.

Expectation values are estimated during the imaginary-time propagation in a similar fashion as for the GFMC

$$\langle\mathcal{O}(\tau)\rangle = \frac{\langle\Psi_T|\mathcal{O}|\Psi(\tau)\rangle}{\langle\Psi_T|\Psi(\tau)\rangle} = \frac{\sum_{X_i}\langle\Psi_T(X_i)|\mathcal{O}|\Psi(\tau, X_i)\rangle/\Psi_I(X_i)}{\sum_{X_i}\langle\Psi_T(X_i)|\Psi(\tau, X_i)\rangle/\Psi_I(X_i)}\,, \tag{69}$$

To alleviate the sign problem, as in reference [118], we implement an algorithm similar to the constrained-path approximation [119], but applicable to complex wave functions and propagators. The weights w_i of Equation (67) are evaluated with

$$\frac{\Psi_I(X_{i+1})}{\Psi_I(X_i)} \to \mathrm{Re}\left\{\frac{\Psi_I(X_{i+1})}{\Psi_I(X_i)}\right\}\,, \tag{70}$$

and they are set to zero if the ratio is negative. Unlike the fixed-node approximation, which is applicable for scalar potentials and for cases in which a real wave function can be used, the solution obtained from the constrained propagation is not a rigorous upper-bound to the true ground-state energy [101]. To remove the bias associated with this procedure, the configurations obtained from a constrained propagation are further evolved using the following positive-definite importance sampling function [89, 120]

$$\Psi_I(X) = \left|\mathrm{Re}\{\Psi_T(X)\}\right| + \alpha\left|\mathrm{Im}\{\Psi_T(X)\}\right|\,, \tag{71}$$

where we typically take $0.1 < \alpha < 0.5$. Along this unconstrained propagation, the expectation value of the energy is estimated according to Equation (69). The asymptotic value is found by fitting the imaginary-time behavior of the unconstrained energy with a single-exponential function, as in reference [25]. Unconstrained propagations have been performed in the latest AFDMC studies of atomic nuclei [89, 111] and infinite nucleonic matter [116, 121]. An example of unconstrained propagation in ^{6}Li for the GT+Eτ-1.0 local chiral Hamiltonian is reported in **Figure 1**, where the blue dots with error bars are the AFDMC unconstrained energies, the red curve is the exponential fit, and the green band represents the final result including the uncertainty coming from the fitting procedure.

In summary, the VMC method is used to find the best possible guess for the wave function for a given nucleus, i.e., it is used to optimize the wave function variational parameters. VMC energies are usually above the ones coming from GFMC and AFDMC calculations, while other observables, such as

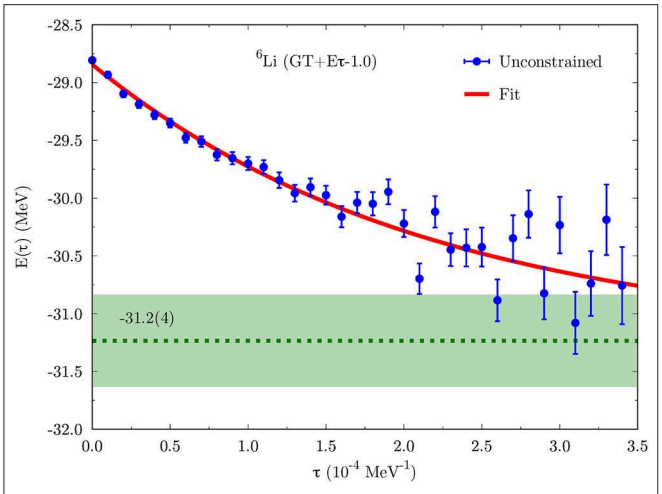

FIGURE 1 | Unconstrained evolution in ^{6}Li for the GT+Eτ-1.0 local chiral Hamiltonian. Blue dots with error bars bands are AFDMC energies. The red curve is a single-exponential function fit to the AFDMC results. The green band represents the final energy result including the uncertainty coming from the fitting procedure.

radii and density distributions are in closer agreement. The variationally optimized wave function is then used as input for the (statistically) exact GFMC and AFDMC algorithms. The difference between these two methods relies in their accuracy and limitations. The GFMC method is very accurate in predicting several observables with very small statistical error bars, but its applicability is limited up to 12 nucleons. The AFDMC method can tackle larger systems, but its precision is somewhat reduced and it is currently limited to somewhat simplified interactions [4].

4. NUCLEAR STRUCTURE RESULTS

GFMC and AFDMC are complimentary methods that have been extensively used in the past to accurately calculate ground-state properties of light nuclei ($A \lesssim 16$). In the following we will present results obtained using the GFMC method for Δ-full χEFT potentials, and using the AFDMC method for Δ-less χEFT interactions. In **Figure 2** we show the binding energies of nuclei up to ^{16}O as calculated with GFMC for the NV2+3-Ia potential (red, left) [11], and with AFDMC for the GT+Eτ-1.0 interaction (blue, right) [89, 111]. The central green bars are the experimental data. GFMC results only carry Monte Carlo statistical uncertainties, while for AFDMC results, theoretical uncertainties coming from the truncation of the chiral expansion are also included. For an observable $X^{(i)}$ at order $i = 0, 2, 3, \ldots$, the theoretical uncertainty $\delta X^{(i)}$ is estimated according to the prescription of Epelbaum *et al.* [74]:

$$\begin{aligned}
\delta X^{(0)} &= Q^2 \left| X^{(0)} \right|, \\
\delta X^{(i)} &= \max_{2 \le j \le i} \left(Q^{i+1} \left| X^{(0)} \right|, \, Q^{i+1-j} \left| \Delta X^{(j)} \right| \right) \quad \text{for } i \ge 2, \\
\delta X^{(i)} &\ge \max \left(\left| X^{(j \ge i)} - X^{(k \ge i)} \right| \right),
\end{aligned} \tag{72}$$

where

$$\begin{aligned}
\Delta X^{(2)} &\equiv X^{(2)} - X^{(0)}, \\
\Delta X^{(i)} &\equiv X^{(i)} - X^{(i-1)} \quad \text{for } i \ge 3.
\end{aligned} \tag{73}$$

For the local chiral interaction GT+Eτ-1.0, results are presented at N^{2}LO ($i = 3$) considering $Q = m_\pi / \Lambda_b$, with $m_\pi \approx 140$ MeV and $\Lambda_b = 600$ MeV [89, 111].

The NV2+3-Ia interaction provides an overall good description of the ground-state energy of light nuclei, including neutron-rich systems with isospin asymmetry as large as 0.6 (^{10}He). This can be appreciated even more by looking at **Figure 3**, where the ratio between QMC results and experimental data is shown. Above $A = 8$, the NV2+3-Ia description of binding energies looks slightly less accurate, with some nuclei slightly underbound (^{10}He, ^{11}B) and some other sightly overbound (^{9}Be, ^{10}B, ^{12}C). However, the difference with the experimental values is always < 0.2 MeV/A, discrepancy that we expect to be fully covered by the uncertainty coming from the truncation of the chiral expansion (i.e., theoretical uncertainty from the interaction model), currently not available for the NV2+3-Ia potential.

The binding energy of very light nuclei is also well-reproduced by the GT+Eτ-1.0 interaction, with ^{8}He slightly underbound (0.37 MeV/A difference compared to the experimental value), but compatible with observations within the estimated statistical plus systematic uncertainties (see **Figure 3**). Differently from GFMC calculations, AFDMC results for $8 \le A \le 11$ open-shell nuclei are currently not available. The ground-state energy of heavier closed-shell systems, such as ^{12}C and ^{16}O, for the GT+Eτ-1.0 potential is higher than the expected result. However, the binding energy of ^{16}O is still compatible with the experimental value within the fully uncertainty estimate. As discussed in reference [89], the discrepancy found for ^{12}C is due to the somewhat too simplistic $A = 12$ AFDMC wave function, that only includes couplings in the p-shells, rather than a deficiency of the interaction itself. It has to be noted that AFDMC results for the GT+Eτ-1.0 interaction carry larger overall uncertainties compared to GFMC results for the NV2+3-Ia potential. This is because the full uncertainty evaluation includes both statistical and theoretical errors. Both QMC methods imply statistical uncertainties of the order of few percent. For the Δ-less potential, the theoretical errors coming from the truncation of the chiral expansion dominate compared to the statistical errors. Considering the next order in the chiral expansion should reduce theoretical uncertainties, and work is currently being done in developing such potentials.

Figure 4 shows the charge radii of $A \le 16$ nuclei for the NV2+3-Ia and GT+Eτ-1.0 potentials, with respect to the available experimental data. The expectation value of the charge radius is derived from the point-proton radius $r_{\rm pt}$ using the relation

$$\left\langle r_{\rm ch}^2 \right\rangle = \left\langle r_{\rm pt}^2 \right\rangle + \left\langle R_p^2 \right\rangle + \frac{A-Z}{Z} \left\langle R_n^2 \right\rangle + \frac{3\hbar^2}{4M_p^2 c^2} + \left\langle r_{\rm so}^2 \right\rangle, \tag{74}$$

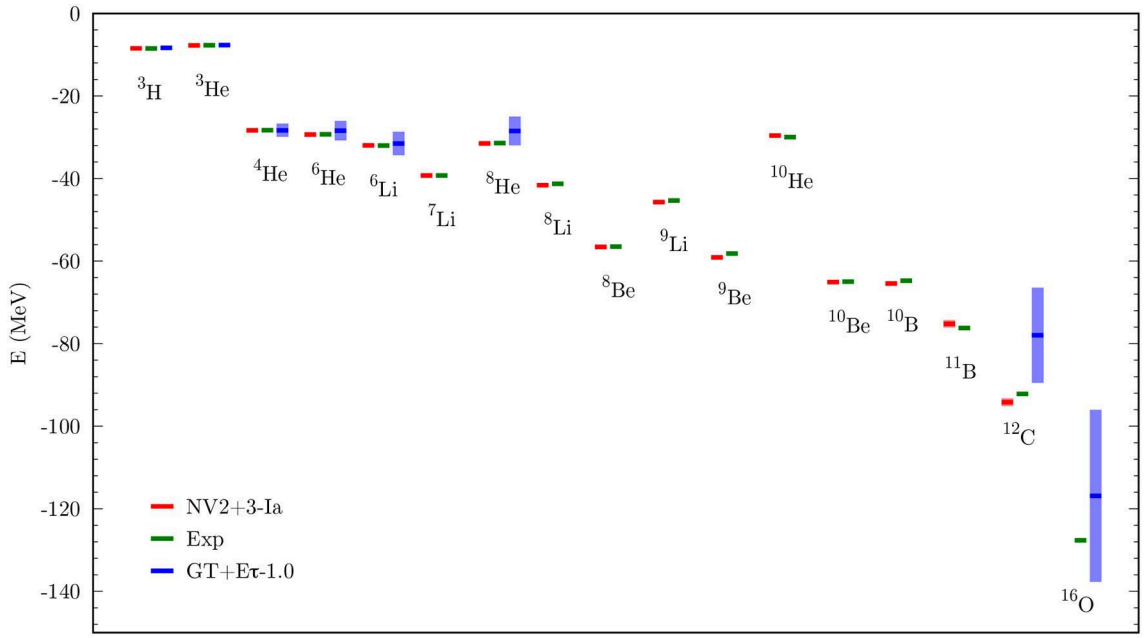

FIGURE 2 | Ground-state energies in $A \leq 16$ nuclei. For each nucleus, experimental results [122] are shown in green at the center. GFMC (AFDMC) results for the NV2+3-Ia [11] (GT+Eτ-1.0 [89]) potential are shown in red (blue) to the left (right) of the experimental values. For the NV2+3-Ia (GT+Eτ-1.0) potential, the colored bands include statistical (statistical plus systematic) uncertainties.

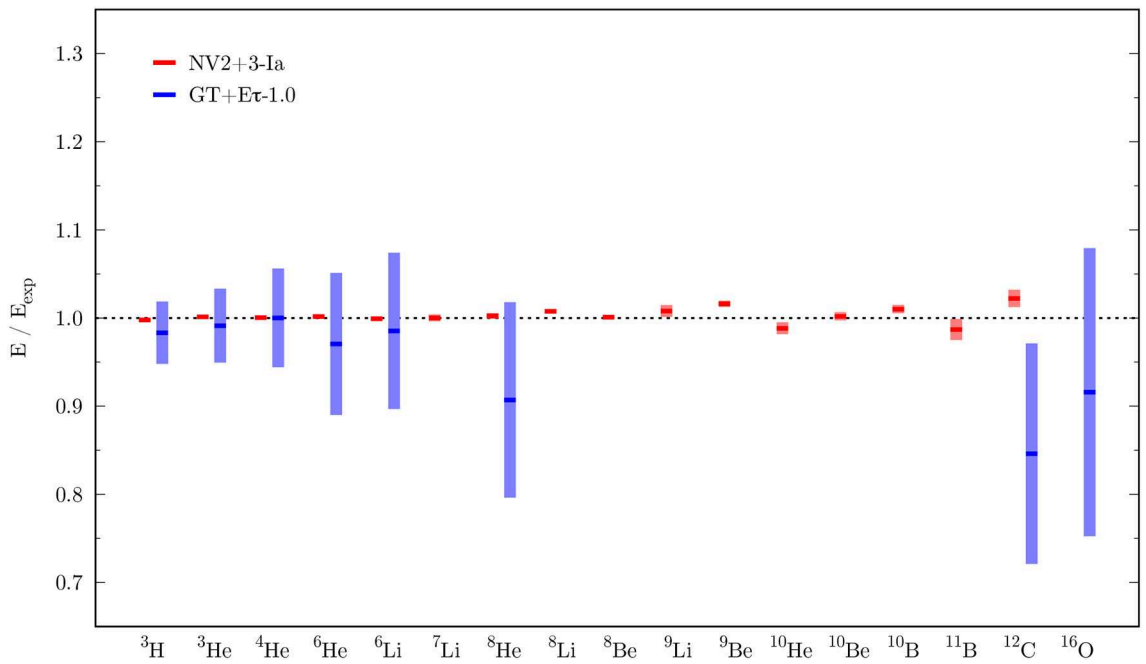

FIGURE 3 | Energy ratio between the calculated binding energies and the experimental data. The color scheme is the same as **Figure 2**.

where $\langle R_p^2 \rangle = 0.770(9)\,\mathrm{fm}^2$ is the proton radius [127], $\langle R_n^2 \rangle = -0.116(2)\,\mathrm{fm}^2$ is the neutron radius [127], $(3\hbar^2)/(4M_p^2c^2) \approx 0.033\,\mathrm{fm}^2$ is the Darwin-Foldy correction [128], and $\langle r_{\mathrm{so}}^2 \rangle$ is a spin-orbit correction due to the anomalous magnetic moment in halo nuclei [129]. The point-nucleon radius r_{pt} is calculated as

$$\langle r_N^2 \rangle = \frac{1}{\mathcal{N}} \langle \Psi | \sum_i \mathcal{P}_{N_i} |\mathbf{r}_i|^2 | \Psi \rangle, \tag{75}$$

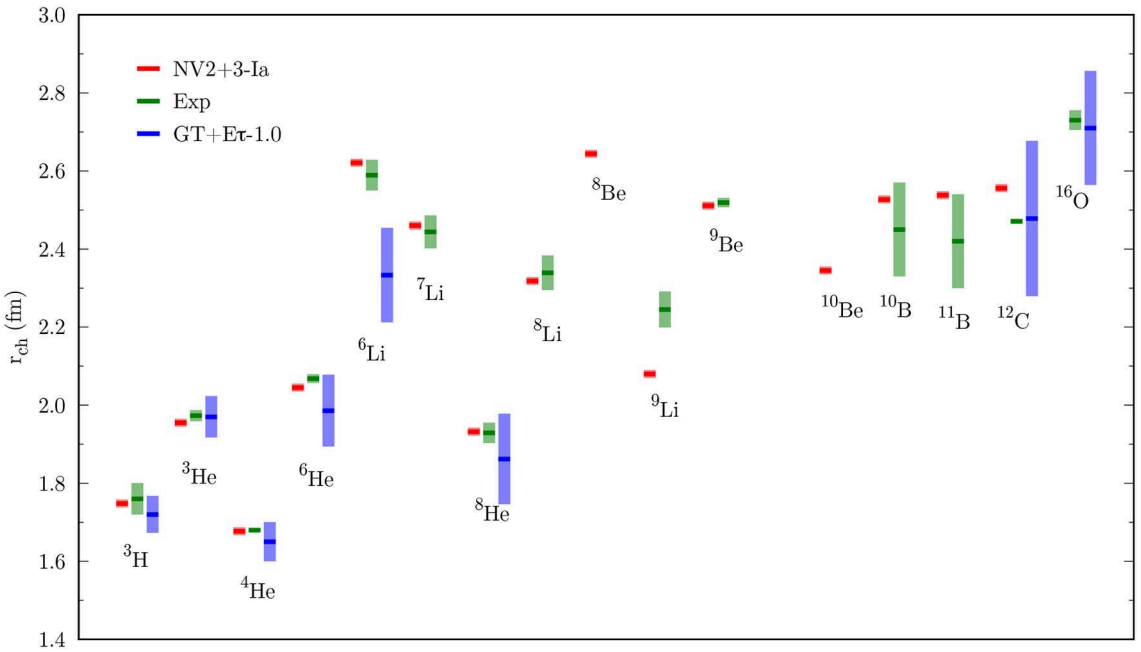

FIGURE 4 | Same as **Figure 2** but for charge radii. Experimental data are from references [123–126].

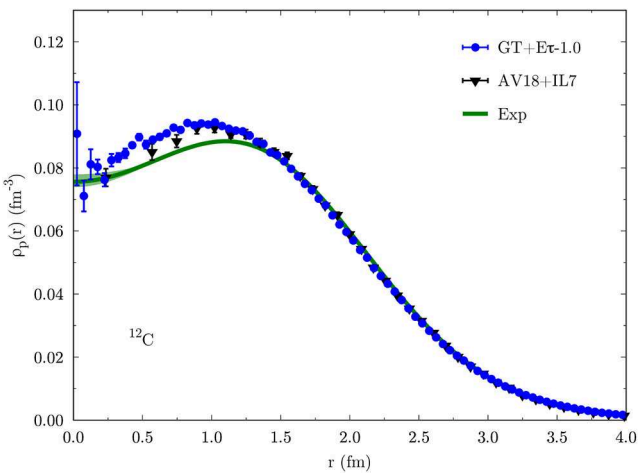

FIGURE 5 | Proton density in ^{12}C. Black triangles are GFMC results for the AV18+IL7 potential [130]. Blue dots are AFDMC results for the GT+Eτ-1.0 interaction [89]. The green band corresponds to the experimental results, unfolded from electron scattering data (see text for details).

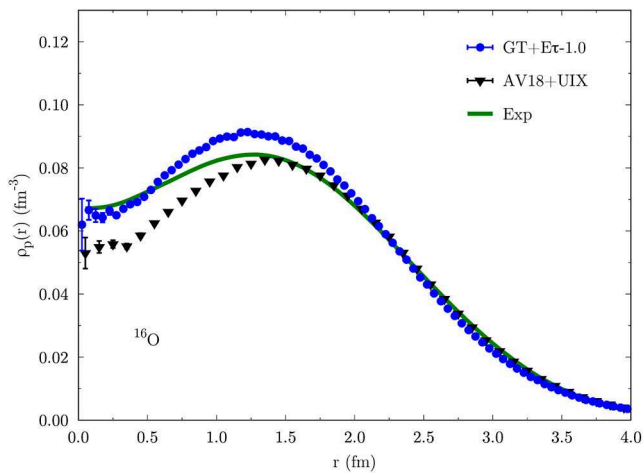

FIGURE 6 | Same as **Figure 5** but for ^{16}O. Black triangles are cluster VMC results for the AV18+UIX potential [100]. Blue dots are AFDMC results for the GT+Eτ-1.0 interaction [89].

where $\mathbf{r}_i$ is the intrinsic coordinate of Equation (14), $\mathcal{N}$ is the number of protons or neutrons, and

$$\mathcal{P}_{N_i} = \frac{1 \pm \tau_{z_i}}{2} \tag{76}$$

is the projector operator onto protons (+) or neutrons (−). The charge radius is a mixed expectation value, and it requires the calculation of both VMC and DMC point-proton radii, according to Equation (48). Even though mixed expectation values typically depend on the quality of the employed trial wave functions, for the highly-accurate wave functions employed in the GFMC and AFDMC methods, the extrapolation of the mixed estimate $\langle r^2_{\rm ch} \rangle$ is always small.

Both chiral interactions nicely reproduce the charge radius of helium isotopes. The NV2+3-Ia potential also reproduces the radius of lithium, beryllium, and boron isotopes, with new predictions for ^{8}Be and ^{10}Be. The charge radius of

^{9}Li is underpredicted, whereas that of ^{12}C is overestimated. The GT+Eτ-1.0 potential works remarkably well in predicting the charge radius of ^{12}C and ^{16}O, even though theoretical uncertainties, that dominate over the statistical one, are large. As discussed in the previous paragraphs, going to the next order in the chiral expansion will reduce such theoretical uncertainties. For the GT+Eτ-1.0 interaction, the charge radius of ^{6}Li turns out to be smaller compared to the experimental value. Once again, this is not a feature of the employed interaction, rather a deficiency of the AFDMC wave function. In fact, differently from GFMC, the current AFDMC wave function does not include dedicated α-deuteron-like correlations, necessary to capture the structural properties of ^{6}Li.

In QMC methods, single-nucleon densities are calculated as

$$\rho_N(r) = \frac{1}{4\pi r^2}\left\langle \Psi \right| \sum_i \mathcal{P}_{N_i} \delta(r - |\mathbf{r}_i|) \left| \Psi \right\rangle, \qquad (77)$$

where $\mathcal{P}_{N_i}$ is the projector operator of Equation (76) and ρ_N integrates to the number of nucleons. In **Figures 5**, **6** we show the QMC proton density in ^{12}C and ^{16}O for the available phenomenological (black) and chiral EFT (blue) potentials. Error bars correspond to statistical uncertainties only. The green bands are the experimental single-nucleon densities, obtained from the "sum-of-Gaussians" parametrization of the charge densities given in reference [132] by unfolding the nucleon form factors and subtracting the small contribution of the neutrons. As can be seen, both phenomenological and chiral EFT interactions provide a good description of the proton density in ^{12}C. The small discrepancy with the experimental curve at short distance is due to two-body meson exchange currents, not included in the proton density presented here. As shown in reference [130], such currents have little effect on the single-nucleon density for $A \geq 12$, slightly reducing its value at small r. The phenomenological AV18+UIX potential underestimates the proton density a short distance in ^{16}O. As indicated by the cluster VMC analysis of reference [100], the three-body potential UIX introduces repulsion in the system, pushing nucleons far away from the nucleus center of mass, and thus resulting in larger radius and smaller central density. The ^{16}O AFDMC density for the GT+Eτ-1.0 potential is instead in better agreement with the experimental curve.

As opposed to the charge radius, densities are not observables themselves. However, the single-nucleon density can be related to the longitudinal elastic (charge) form factor, physical quantity experimentally accessible via electron-nucleon scattering

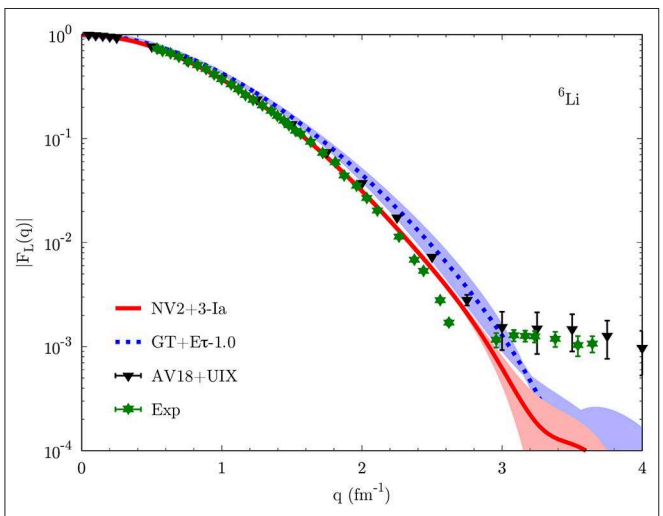

FIGURE 7 | Longitudinal elastic form factor in ^{6}Li for different nuclear potentials. For the NV2+3-Ia (solid red line) and AV18+UIX (black triangles) potentials, errors correspond to statistical Monte Carlo uncertainties. The blue band for the GT+Eτ-1.0 potential also includes the uncertainties coming from the truncation of the chiral expansion. Green stars are the experimental values [131]. Adapted from reference [89].

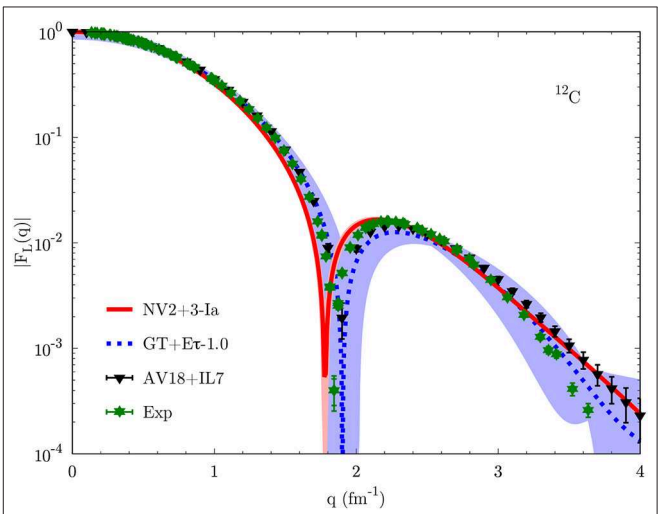

FIGURE 8 | Same as **Figure 7** but for ^{12}C. Experimental data are taken from reference [132]. Adapted from reference [89].

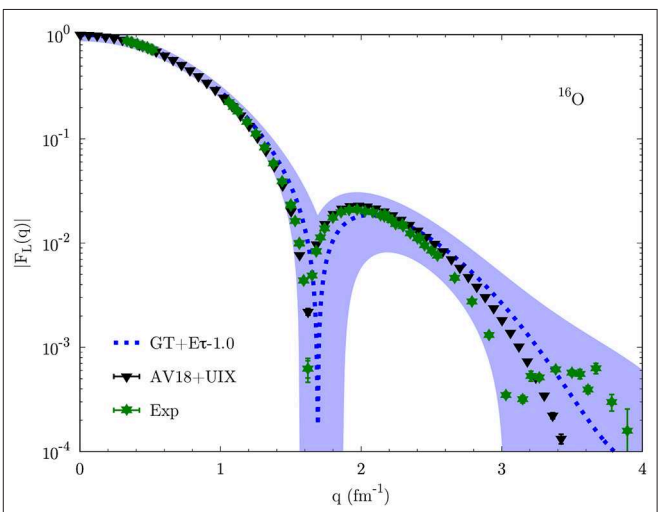

FIGURE 9 | Same as **Figure 7** but for ^{16}O. Experimental data are from Sick, based on references [136–138]. Adapted from reference [89].

processes. In fact, the charge form factor can be expressed as the ground-state expectation value of the one-body charge operator [133], which, ignoring small spin-orbit contributions in the one-body current, results in the following expression:

$$F_L(q) = \frac{1}{Z} \frac{G_E^p(Q_{\rm el}^2)\,\tilde{\rho}_p(q) + G_E^n(Q_{\rm el}^2)\,\tilde{\rho}_n(q)}{\sqrt{1 + Q_{\rm el}^2/(4m_N^2)}}, \qquad (78)$$

where $\tilde{\rho}_N(q)$ is the Fourier transform of the single-nucleon density defined in Equation (77), and $Q_{\rm el}^2 = \mathbf{q}^2 - \omega_{\rm el}^2$ is the four-momentum squared, with $\omega_{\rm el} = \sqrt{q^2 + m_A^2} - m_A$ the energy transfer corresponding to the electron scattering elastic peak, m_A being the mass of the target nucleus. $G_E^N(Q^2)$ are the nucleon electric form factors, for which we adopt Kelly's parametrization [134].

In **Figures 7–9** we show the charge form factor in ^{6}Li, ^{12}C, and ^{16}O. Lines with bands correspond to chiral interactions, solid red for NV2+3-Ia from GFMC calculations and dotted blue for GT+Eτ-1.0 from AFDMC calculations. The black triangles are the results for the phenomenological potentials: AV18+UIX in ^{6}Li from VMC calculations [135], AV18+IL7 in ^{12}C from GFMC calculations [130], and AV18+UIX in ^{16}O from cluster VMC calculations [100]. Green stars are the available experimental results [131, 132, 136–138]. Note that for all QMC calculations of the charge form factor only one-body charge operators are considered, i.e., no two-body electromagnetic currents are included. However, as shown in references [130, 135, 139], such operators give a non-negligible contribution only for $q > 2\,\mathrm{fm}^{-1}$, as they basically include relativistic corrections.

In ^{6}Li all interactions provide a consistent description of the charge form factor, with NV2+3-Ia and AV18+UIX compatible with the experimental results up to $q \approx 2\,\mathrm{fm}^{-1}$, where two-body currents start playing a role. In the same range, the GT+Eτ-1.0 results are slightly higher, as already indicated by the too small charge radius (see **Figure 4**). Interestingly, only the phenomenological potential is capable of reproducing the kink in the experimental data, while chiral interactions predict a smooth charge form factor also above $q \approx 3\,\mathrm{fm}^{-1}$. The inclusion of two-body currents could improve the description of the charge form factor at high momentum. However, this is a momentum range roughly corresponding to the characteristic cut-off of chiral potentials, hence their description of observables in such regime is not supposed to hold. Similar conclusions can be drawn for the charge form factor in ^{12}C and ^{16}O, where chiral forces produce results compatible with the experimental data, in particular for the position of the first diffraction peak. This is slightly underestimated for ^{12}C with the NV2+3-Ia potential, but we expect it to be consistent with the experimental results once the uncertainties coming from the truncation of the chiral expansion are taken into consideration.

Note that the "zero" in the form factor is due to the presence of a term like $\sin^2(qR)$, where R is related to the nucleus charge radius. The zero is obtained when $qR = \pi$. Therefore, a smaller (larger) q value for the zero compared to the experimental data suggests a larger (smaller) R value, i.e., a larger (smaller) $r_{\rm ch}$ value. This is indeed verified by QMC calculations. For instance, in **Figure 8**, the NV2+3-Ia potential predicts a smaller q value for the zero of the charge form factor in ^{12}C, hence a larger value for the charge radius, as confirmed by **Figure 4**.

5. CONCLUSIONS

In this work we have reviewed recent advancements in the development of realistic nuclear interactions and of *ab-initio* many-body methods for nuclear physics. In particular, we have discussed the recent integration of nearly-local interactions derived within chiral effective field theory, both with and without the inclusion of Δ degrees of freedom, in quantum Monte Carlo methods, namely variational Monte Carlo, Green's function Monte Carlo, and auxiliary field diffusion Monte Carlo. Such a successful combination lead to accurate and realistic calculations of ground- and excited-state properties of nuclei, that include but is not limited to spectra, charge radii, and longitudinal elastic form factors. Even though the chiral interactions discussed in this work have been constructed using few-body observables only, nucleon-nucleon scattering data and properties of nuclei up to $A = 5$, they provide a remarkable description of the physics of nuclei up to, at least, $A = 16$, with excellent agreement with experimental data.

The same techniques and nuclear potentials reviewed here have also been used to calculate the equation of state of infinite nuclear and neutron matter [116, 121], and to infer properties of neutron stars, with results compatible with astrophysical observations including constraints extracted from gravitational waves of the neutron-star merger GW170817 by the LIGO-Virgo detection [140].

Future efforts will be dedicated to i) further improve the employed local chiral interactions, by extending to higher order in the chiral expansion, ii) calculate electroweak properties in nuclear systems, by consistently deriving electroweak currents, and iii) extend the calculations to heavier nuclei, by improving the AFDMC variational wave functions and the scaling of the algorithm.

AUTHOR CONTRIBUTIONS

All authors listed have made a substantial, direct and intellectual contribution to the work, and approved it for publication.

FUNDING

The work of SG was supported by the U.S. Department of Energy, Office of Science, Office of Nuclear Physics, under contract No. DE-AC52-06NA25396, by the NUCLEI SciDAC program, by the LDRD program at LANL, and by the DOE Early Career research Program. The work of DL was supported by the U.S. Department of Energy, Office of Science, Office of Nuclear Physics, under Contract No. DE-SC0013617, and by the NUCLEI SciDAC program. The work of AL was supported by the U.S. Department of Energy, Office of Science, Office of Nuclear Physics, under contract No. DE-AC02-06CH11357. The work of MP was supported by

the U.S. Department of Energy, Office of Science, Office of Nuclear Physics, under the FRIB Theory Alliance award DE-SC0013617. Computational resources have been provided by the Los Alamos National Laboratory Institutional Computing Program, which is supported by the U.S. Department of Energy National Nuclear Security Administration under Contract No. 89233218CNA000001, and by the National Energy Research Scientific Computing Center (NERSC), which is supported by the U.S. Department of Energy, Office of Science, under contract No. DE-AC02-05CH11231.

REFERENCES

1. Winter F, Detmold W, Gambhir AS, Orginos K, Savage MJ, Shanahan PE, et al. First lattice QCD study of the gluonic structure of light nuclei. *Phys Rev D*. (2017) **96**:094512. doi: 10.1103/PhysRevD.96.094512
2. Chang E, Davoudi Z, Detmold W, Gambhir AS, Orginos K, Savage MJ, et al. Scalar, axial, and tensor interactions of light nuclei from lattice QCD. *Phys Rev Lett*. (2018) **120**:152002. doi: 10.1103/PhysRevLett.120.152002
3. Wiringa RB, Stoks VGJ, Schiavilla R. An Accurate nucleon-nucleon potential with charge independence breaking. *Phys Rev C*. (1995) **51**:38–51. doi: 10.1103/PhysRevC.51.38
4. Carlson J, Gandolfi S, Pederiva F, Pieper SC, Schiavilla R, Schmidt KE, et al. Quantum Monte Carlo methods for nuclear physics. *Rev Mod Phys*. (2015) **87**:1067–118. doi: 10.1103/RevModPhys.87.1067
5. Hagen G, Papenbrock T, Hjorth-Jensen M, Dean DJ. Coupled-cluster computations of atomic nuclei. *Rep Progr Phys*. (2014) **77**:096302. doi: 10.1088/0034-4885/77/9/096302
6. Hagen G, Papenbrock T, Ekström A, Wendt KA, Baardsen G, Gandolfi S, et al. Coupled-cluster calculations of nucleonic matter. *Phys Rev C*. (2014) **89**:014319. doi: 10.1103/PhysRevC.89.014319
7. Barrett BR, Navrátil P, Vary JP. *Ab initio* no core shell model. *Prog Part Nucl Phys*. (2013) **69**:131–81. doi: 10.1016/j.ppnp.2012.10.003
8. Bogner S, Furnstahl R, Schwenk A. From low-momentum interactions to nuclear structure. *Prog Part Nucl Phys*. (2010) **65**:94–147. doi: 10.1016/j.ppnp.2010.03.001
9. Dickhoff WH, Barbieri C. Self-consistent Green's function method for nuclei and nuclear matter. *Prog Part Nucl Phys*. (2004) **52**:377–496. doi: 10.1016/j.ppnp.2004.02.038
10. Piarulli M, Girlanda L, Schiavilla R, Navarro Pérez R, Amaro JE, Ruiz Arriola E. Minimally nonlocal nucleon-nucleon potentials with chiral two-pion exchange including Δ resonances. *Phys Rev C*. (2015) **91**:024003. doi: 10.1103/PhysRevC.91.024003
11. Piarulli M, Baroni A, Girlanda L, Kievsky A, Lovato A, Lusk E, et al. Light-nuclei spectra from chiral dynamics. *Phys Rev Lett*. (2018) **120**:052503. doi: 10.1103/PhysRevLett.120.052503
12. Gezerlis A, Tews I, Epelbaum E, Gandolfi S, Hebeler K, Nogga A, et al. Quantum Monte Carlo calculations with chiral effective field theory interactions. *Phys Rev Lett*. (2013) **111**:032501. doi: 10.1103/PhysRevLett.111.032501
13. Tews I, Gandolfi S, Gezerlis A, Schwenk A. Quantum Monte Carlo calculations of neutron matter with chiral three-body forces. *Phys Rev C*. (2016) **93**:024305. doi: 10.1103/PhysRevC.93.024305
14. Rozpedzik D, Golak J, Skibinski R, Witala H, Glockle W, Epelbaum E, et al. A first estimation of chiral four-nucleon force effects in He-4. *Acta Phys Polon B*. (2006) **37**:2889–904.
15. Krüger T, Tews I, Hebeler K, Schwenk A. Neutron matter from chiral effective field theory interactions. *Phys Rev C*. (2013) **88**:025802. doi: 10.1103/PhysRevC.88.025802
16. Yukawa H. On the interaction of elementary particles I. *Proc Phys Math Soc Jap*. (1935) **17**:48–57.
17. Stoks VGJ, Klomp RAM, Terheggen CPF, de Swart JJ. Construction of high quality N N potential models. *Phys Rev C*. (1994) **49**:2950–62. doi: 10.1103/PhysRevC.49.2950
18. Machleidt R. The High precision, charge dependent Bonn nucleon-nucleon potential (CD-Bonn). *Phys Rev C*. (2001) **63**:024001. doi: 10.1103/PhysRevC.63.024001
19. Stoks VGJ, Klomp RAM, Rentmeester MCM, de Swart JJ. Partial wave analaysis of all nucleon-nucleon scattering data below 350-MeV. *Phys Rev C*. (1993) **48**:792–815. doi: 10.1103/PhysRevC.48.792
20. Smith RA, Pandharipande VR. Nucleon-nucleon potentials including pi n delta coupling effects. *Nucl Phys A*. (1976) **256**:327–48. doi: 10.1016/0375-9474(76)90376-6
21. Nelder JA, Mead R. A simplex method for function minimization. *Comput J*. (1965) **7**:308–13. doi: 10.1093/comjnl/7.4.308
22. Gandolfi S, Carlson J, Reddy S, Steiner AW, Wiringa RB. The equation of state of neutron matter, symmetry energy, and neutron star structure. *Eur Phys J A*. (2014) **50**:10. doi: 10.1140/epja/i2014-14010-5
23. Wiringa RB, Pieper SC. Evolution of nuclear spectra with nuclear forces. *Phys Rev Lett*. (2002) **89**:182501. doi: 10.1103/PhysRevLett.89.182501
24. Friar JL, Gibson BF, Payne GL. Recent progress in understanding trinucleon properties. *Ann Rev Nucl Part Sci*. (1984) **34**:403–33. doi: 10.1146/annurev.ns.34.120184.002155
25. Pudliner BS, Pandharipande VR, Carlson J, Pieper SC, Wiringa RB. Quantum Monte Carlo calculations of nuclei with A <= 7. *Phys Rev C*. (1997) **56**:1720–50. doi: 10.1103/PhysRevC.56.1720
26. Navratil P, Vary JP, Barrett BR. Large basis ab initio no-core shell model and its application to C-12. *Phys Rev C*. (2000) **62**:054311. doi: 10.1103/PhysRevC.62.054311
27. Carlson J, Pandharipande VR, Wiringa RB. Three-nucleon interaction in 3-body, 4-body, and infinite-body systems. *Nucl Phys A*. (1983) **401**:59–85. doi: 10.1016/0375-9474(83)90336-6
28. Pieper SC, Pandharipande VR, Wiringa RB, Carlson J. Realistic models of pion exchange three nucleon interactions. *Phys Rev C*. (2001) **64**:014001. doi: 10.1103/PhysRevC.64.014001
29. Maris P, Vary JP, Gandolfi S, Carlson J, Pieper SC. Properties of trapped neutrons interacting with realistic nuclear Hamiltonians. *Phys Rev C*. (2013) **87**:054318. doi: 10.1103/PhysRevC.87.054318
30. Weinberg S. Nuclear forces from chiral Lagrangians. *Phys Lett B*. (1990) **251**:288–92. doi: 10.1016/0370-2693(90)90938-3
31. Weinberg S. Effective chiral Lagrangians for nucleon–pion interactions and nuclear forces. *Nucl Phys B*. (1991) **363**:3–18. doi: 10.1016/0550-3213(91)90231-L
32. Weinberg S. Three body interactions among nucleons and pions. *Phys Lett B*. (1992) **295**:114–21. doi: 10.1016/0370-2693(92)90099-P
33. Epelbaum E, Hammer HW, Meissner UG. Modern theory of nuclear forces. *Rev Mod Phys*. (2009) **81**:1773–825. doi: 10.1103/RevModPhys.81.1773
34. Machleidt R, Entem DR. Chiral effective field theory and nuclear forces. *Phys Rept*. (2011) **503**:1–75. doi: 10.1016/j.physrep.2011.02.001
35. Machleidt R, Sammarruca F. Chiral EFT based nuclear forces: achievements and challenges. *Phys Scripta*. (2016) **91**:083007. doi: 10.1088/0031-8949/91/8/083007
36. Machleidt R. Historical perspective and future prospects for nuclear interactions. *Int J Mod Phys E*. (2017) **26**:1730005. doi: 10.1142/S0218301317300053
37. Kaplan DB, Savage MJ, Wise MB. A new expansion for nucleon-nucleon interactions. *Phys Lett B*. (1998) **424**:390–6. doi: 10.1016/S0370-2693(98)00210-X
38. Kaplan DB, Savage MJ, Wise MB. Two nucleon systems from effective field theory. *Nucl Phys B*. (1998) **534**:329–55. doi: 10.1016/S0550-3213(98)00440-4
39. Nogga A, Timmermans RGE, van Kolck U. Renormalization of one-pion exchange and power counting. *Phys Rev C*. (2005) **72**:054006. doi: 10.1103/PhysRevC.72.054006

40. Pavon Valderrama M, Ruiz Arriola E. Renormalization of NN interaction with chiral two pion exchange potential. central phases and the deuteron. *Phys Rev C*. (2006) **74**:054001. doi: 10.1103/PhysRevC.74.054001
41. Long B, Yang CJ. Renormalizing chiral nuclear forces: triplet channels. *Phys Rev C*. (2012) **85**:034002. doi: 10.1103/PhysRevC.85.034002
42. van Kolck U. Few nucleon forces from chiral Lagrangians. *Phys Rev C*. (1994) **49**:2932–41. doi: 10.1103/PhysRevC.49.2932
43. Furnstahl RJ, Phillips DR, Wesolowski S. A recipe for EFT uncertainty quantification in nuclear physics. *J. Phys. G Nucl. Part. Phys*. (2015) **42**:034028. doi: 10.1088/0954-3899/42/3/034028
44. Epelbaum E, Krebs H, Meissner UG. Improved chiral nucleon-nucleon potential up to next-to-next-to-next-to-leading order. *Eur Phys J A*. (2015) **51**:53. doi: 10.1140/epja/i2015-15053-8
45. Furnstahl RJ, Klco N, Phillips DR, Wesolowski S. Quantifying truncation errors in effective field theory. *Phys Rev C*. (2015) **92**:024005. doi: 10.1103/PhysRevC.92.024005
46. Wesolowski S, Klco N, Furnstahl RJ, Phillips DR, Thapaliya A. Bayesian parameter estimation for effective field theories. *J. Phys. G Nucl. Part. Phys*. (2016) **43**:074001. doi: 10.1088/0954-3899/43/7/074001
47. Melendez JA, Wesolowski S, Furnstahl RJ. Bayesian truncation errors in chiral effective field theory: nucleon-nucleon observables. *Phys Rev C*. (2017) **96**:024003. doi: 10.1103/PhysRevC.96.024003
48. Wesolowski S, Furnstahl RJ, Melendez JA, Phillips DR. Exploring Bayesian parameter estimation for chiral effective field theory using nucleon-nucleon phase shifts. *J Phys G Nucl Part Phys*. (2018) **46**:045102. doi: 10.1088/1361-6471/aaf5fc
49. Krebs H, Epelbaum E, Meissner UG. Nuclear forces with delta-excitations up to next-to-next-to-leading order. I. Peripheral nucleon-nucleon waves. *Eur Phys J A*. (2007) **32**:127–37. doi: 10.1140/epja/i2007-10372-y
50. Ditsche C, Hoferichter M, Kubis B, Meissner UG. Roy-Steiner equations for pion-nucleon scattering. *J. High Energ. Phys*. (2012) **6**:043. doi: 10.1007/JHEP06(2012)043
51. Hoferichter M, Ruiz de Elvira J, Kubis B, Meissner UG. High-precision determination of the pion-nucleon σ term from Roy-Steiner equations. *Phys Rev Lett*. (2015) **115**:092301. doi: 10.1103/PhysRevLett.115.092301
52. Hoferichter M, Ruiz de Elvira J, Kubis B, Meissner UG. Roy-Steiner-equation analysis of pion-nucleon scattering. *Phys Rept*. (2016) **625**:1–88. doi: 10.1016/j.physrep.2016.02.002
53. Hoferichter M, Ruiz de Elvira J, Kubis B, Meissner UG. Matching pion-nucleon Roy-Steiner equations to chiral perturbation theory. *Phys Rev Lett*. (2015) **115**:192301. doi: 10.1103/PhysRevLett.115.192301
54. Siemens D, Bernard V, Epelbaum E, Gasparyan A, Krebs H, Meissner UG. Elastic pion-nucleon scattering in chiral perturbation theory: a fresh look. *Phys Rev C*. (2016) **94**:014620. doi: 10.1103/PhysRevC.94.014620
55. Siemens D, Ruiz de Elvira J, Epelbaum E, Hoferichter M, Krebs H, Kubis B, et al. Reconciling threshold and subthreshold expansions for pion-nucleon scattering. *Phys Lett B*. (2017) **770**:27–34. doi: 10.1016/j.physletb.2017.04.039
56. Yao DL, Siemens D, Bernard V, Epelbaum E, Gasparyan AM, Gegelia J, et al. Pion-nucleon scattering in covariant baryon chiral perturbation theory with explicit Delta resonances. *JHEP*. (2016) **5**:038. doi: 10.1007/JHEP05(2016)038
57. Ekström A, Jansen GR, Wendt KA, Hagen G, Papenbrock T, Carlsson BD, et al. Accurate nuclear radii and binding energies from a chiral interaction. *Phys Rev C*. (2015) **91**:051301. doi: 10.1103/PhysRevC.91.051301
58. Ordonez C, Ray L, van Kolck U. The two nucleon potential from chiral Lagrangians. *Phys Rev C*. (1996) **53**:2086–105. doi: 10.1103/PhysRevC.53.2086
59. Kaiser N, Brockmann R, Weise W. Peripheral nucleon-nucleon phase shifts and chiral symmetry. *Nucl Phys A*. (1997) **625**:758–88. doi: 10.1016/S0375-9474(97)00586-1
60. Kaiser N, Gerstendorfer S, Weise W. Peripheral NN scattering: role of delta excitation, correlated two pion and vector meson exchange. *Nucl Phys A*. (1998) **637**:395–420. doi: 10.1016/S0375-9474(98)00234-6
61. Epelbaum E, Gloeckle W, Meissner UG. Nuclear forces from chiral Lagrangians using the method of unitary transformation. 1. Formalism. *Nucl Phys A*. (1998) **637**:107–34. doi: 10.1016/S0375-9474(98)00220-6
62. Epelbaum E, Gloeckle W, Meissner UG. Nuclear forces from chiral Lagrangians using the method of unitary transformation. 2. The two nucleon system. *Nucl Phys A*. (2000) **671**:295–331. doi: 10.1016/S0375-9474(99)00821-0
63. Kaiser N. Chiral 3 pi exchange N N potentials: Results for representation invariant classes of diagrams. *Phys Rev C*. (2000) **61**:014003. doi: 10.1103/PhysRevC.61.014003
64. Kaiser N. Chiral three pi exchange N N potentials: results for diagrams proportional to $g(A)^4$ and $g(A)^6$. *Phys Rev C*. (2000) **62**:024001. doi: 10.1103/PhysRevC.62.024001
65. Kaiser N. Chiral 3 pi exchange N N potentials: results for dominant next-to-leading order contributions. *Phys Rev C*. (2001) **63**:044010. doi: 10.1103/PhysRevC.63.044010
66. Kaiser N. Chiral 2 pi exchange N N potentials: two loop contributions. *Phys Rev C*. (2001) **64**:057001. doi: 10.1103/PhysRevC.64.057001
67. Kaiser N. Chiral 2 pi exchange NN potentials: relativistic $1/M^2$ corrections. *Phys Rev C*. (2002) **65**:017001. doi: 10.1103/PhysRevC.65.017001
68. Entem DR, Machleidt R. Accurate charge dependent nucleon nucleon potential at fourth order of chiral perturbation theory. *Phys Rev C*. (2003) **68**:041001. doi: 10.1103/PhysRevC.68.041001
69. Epelbaum E, Nogga A, Gloeckle W, Kamada H, Meissner UG, Witala H. Three nucleon forces from chiral effective field theory. *Phys Rev C*. (2002) **66**:064001. doi: 10.1103/PhysRevC.66.064001
70. Navratil P. Local three-nucleon interaction from chiral effective field theory. *Few Body Syst*. (2007) **41**:117–40. doi: 10.1007/s00601-007-0193-3
71. Bernard V, Epelbaum E, Krebs H, Meissner UG. Subleading contributions to the chiral three-nucleon force II: short-range terms and relativistic corrections. *Phys Rev C*. (2011) **84**:054001. doi: 10.1103/PhysRevC.84.054001
72. Girlanda L, Kievsky A, Viviani M. Subleading contributions to the three-nucleon contact interaction. *Phys Rev C*. (2011) **84**:014001. doi: 10.1103/PhysRevC.84.014001
73. Krebs H, Gasparyan A, Epelbaum E. Chiral three-nucleon force at N^4LO I: longest-range contributions. *Phys Rev C*. (2012) **85**:054006. doi: 10.1103/PhysRevC.85.054006
74. Epelbaum E, Krebs H, Meissner UG. Precision nucleon-nucleon potential at fifth order in the chiral expansion. *Phys Rev Lett*. (2015) **115**:122301. doi: 10.1103/PhysRevLett.115.122301
75. Entem DR, Kaiser N, Machleidt R, Nosyk Y. Peripheral nucleon-nucleon scattering at fifth order of chiral perturbation theory. *Phys Rev C*. (2015) **91**:014002. doi: 10.1103/PhysRevC.91.014002
76. Entem DR, Kaiser N, Machleidt R, Nosyk Y. Dominant contributions to the nucleon-nucleon interaction at sixth order of chiral perturbation theory. *Phys Rev C*. (2015) **92**:064001. doi: 10.1103/PhysRevC.92.064001
77. Ekström A, Baardsen G, Forssén C, Hagen G, Hjorth-Jensen M, Jansen GR, et al. Optimized chiral nucleon-nucleon interaction at next-to-next-to-leading order. *Phys Rev Lett*. (2013) **110**:192502. doi: 10.1103/PhysRevLett.110.192502
78. Ekström A, Hagen G, Morris TD, Papenbrock T, Schwartz PD. Δ isobars and nuclear saturation. *Phys Rev C*. (2018) **97**:024332. doi: 10.1103/PhysRevC.97.024332
79. Reinert P, Krebs H, Epelbaum E. Semilocal momentum-space regularized chiral two-nucleon potentials up to fifth order. *Eur Phys J A*. (2018) **54**:86. doi: 10.1140/epja/i2018-12516-4
80. Binder S, et al. Few-nucleon and many-nucleon systems with semilocal coordinate-space regularized chiral nucleon-nucleon forces. *Phys Rev C*. (2018) **98**:014002. doi: 10.1103/PhysRevC.98.014002
81. Krebs H, Gasparyan AM, Epelbaum E. Three-nucleon force in chiral EFT with explicit $\Delta(1232)$ degrees of freedom: longest-range contributions at fourth order. *Phys Rev C*. (2018) **98**:014003. doi: 10.1103/PhysRevC.98.014003
82. Friar JL, van Kolck U. Charge independence breaking in the two pion exchange nucleon-nucleon force. *Phys Rev C*. (1999) **60**:034006. doi: 10.1103/PhysRevC.60.034006
83. Friar JL, van Kolck U, Rentmeester MCM, Timmermans RGE. The nucleon-mass difference in chiral perturbation theory and nuclear forces. *Phys Rev C*. (2004) **70**:044001. doi: 10.1103/PhysRevC.70.044001
84. Friar JL, Payne GL, van Kolck U. Charge-symmetry-breaking three-nucleon forces. *Phys Rev C*. (2005) **71**:024003. doi: 10.1103/PhysRevC.71.024003
85. Gezerlis A, Tews I, Epelbaum E, Freunek M, Gandolfi S, Hebeler K, et al. Local chiral effective field theory interactions and

quantum Monte Carlo applications. *Phys Rev C*. (2014) **90**:054323. doi: 10.1103/PhysRevC.90.054323
86. Fierz M. Zur Fermischen Theorie des β-Zerfalls. *Z Phys*. (1937) **104**:553–65. doi: 10.1007/BF01330070
87. Lynn JE, Tews I, Carlson J, Gandolfi S, Gezerlis A, Schmidt KE, et al. Chiral three-nucleon interactions in light nuclei, neutron-α scattering, and neutron matter. *Phys Rev Lett*. (2016) **116**:062501. doi: 10.1103/PhysRevLett.116.062501
88. Lynn JE, Tews I, Carlson J, Gandolfi S, Gezerlis A, Schmidt KE, et al. Quantum Monte Carlo calculations of light nuclei with local chiral two- and three-nucleon interactions. *Phys Rev C*. (2017) **96**:054007. doi: 10.1103/PhysRevC.96.054007
89. Lonardoni D, Gandolfi S, Lynn JE, Petrie C, Carlson J, Schmidt KE, et al. Auxiliary field diffusion Monte Carlo calculations of light and medium-mass nuclei with local chiral interactions. *Phys Rev C*. (2018) **97**:044318. doi: 10.1103/PhysRevC.97.044318
90. Piarulli M, Girlanda L, Schiavilla R, Kievsky A, Lovato A, Marcucci LE, et al. Local chiral potentials with Δ-intermediate states and the structure of light nuclei. *Phys Rev C*. (2016) **94**:054007. doi: 10.1103/PhysRevC.94.054007
91. Navarro Pérez R, Amaro JE, Ruiz Arriola E. Coarse-grained potential analysis of neutron-proton and proton-proton scattering below the pion production threshold. *Phys Rev C*. (2013) **88**:064002.. doi: 10.1103/PhysRevC.88.064002
92. Navarro Pérez R, Amaro JE, Ruiz Arriola E. Coarse grained NN potential with chiral two pion exchange. *Phys Rev C*. (2014) **89**:024004. doi: 10.1103/PhysRevC.89.024004
93. Navarro Pérez R, Amaro JE, Ruiz Arriola E. Statistical error analysis for phenomenological nucleon-nucleon potentials. *Phys Rev C*. (2014) **89**:064006. doi: 10.1103/PhysRevC.89.064006
94. Baroni A, et al. Local chiral interactions, the tritium Gamow-Teller matrix element, and the three-nucleon contact term. *Phys Rev C*. (2018) **98**:044003. doi: 10.1103/PhysRevC.98.044003
95. Baroni A, Girlanda L, Kievsky A, Marcucci LE, Schiavilla R, Viviani M. Tritium β-decay in chiral effective field theory. *Phys Rev C*. (2016) **94**:024003. doi: 10.1103/PhysRevC.94.024003
96. Bacca S, Pastore S. Electromagnetic reactions on light nuclei. *J. Phys. G Nucl. Part. Phys*. (2014) **41**:123002. doi: 10.1088/0954-3899/41/12/123002
97. Marcucci LE, Gross F, Pena MT, Piarulli M, Schiavilla R, Sick I, et al. Electromagnetic structure of few-nucleon ground states. *J. Phys. G Nucl. Part. Phys*. (2016) **43**:023002. doi: 10.1088/0954-3899/43/2/023002
98. Lynn JE, Tews I, Gandolfi S, Lovato A. Quantum Monte Carlo methods in nuclear physics: recent advances. *Annu Rev*. (2019) **69**:279–305. doi: 10.1146/annurev-nucl-101918-023600
99. Pieper SC, Varga K, Wiringa RB. Quantum Monte Carlo calculations of A = 9, A = 10 nuclei. *Phys Rev C*. (2002) **66**:044310. doi: 10.1103/PhysRevC.66.044310
100. Lonardoni D, Lovato A, Pieper SC, Wiringa RB. Variational calculation of the ground state of closed-shell nuclei up to $A = 40$. *Phys Rev C*. (2017) **96**:024326. doi: 10.1103/PhysRevC.96.024326
101. Wiringa RB, Pieper SC, Carlson J, Pandharipande VR. Quantum Monte Carlo calculations of A = 8 nuclei. *Phys Rev C*. (2000) **62**:014001. doi: 10.1103/PhysRevC.62.014001
102. Lomnitz-Adler J, Pandharipande VR, Smith RA. Monte Carlo calculations of triton and 4 He nuclei with the Reid potential. *Nucl Phys A*. (1981) **361**:399–411. doi: 10.1016/0375-9474(81)90642-4
103. Pudliner BS. *Green's Function Monte Carlo Calculations of Few-Nucleon Systems*. Champaign, IL: University of Illinois at Urbana-Champaign (1996).
104. Schiavilla R, Pandharipande VR, Wiringa RB. Momentum distributions in a A = 3 and 4 nuclei. *Nucl Phys A*. (1986) **449**:219–42. doi: 10.1016/0375-9474(86)90003-5
105. Carlsson BD, Ekström A, Forssen C, Stromberg DF, Jansen GR, Lilja O, et al. Uncertainty analysis and order-by-order optimization of chiral nuclear interactions. *Phys Rev X*. (2016) **6**:011019. doi: 10.1103/PhysRevX.6.011019
106. Foulkes WMC, Mitas L, Needs RJ, Rajagopal G. Quantum Monte Carlo simulations of solids. *Rev Mod Phys*. (2001) **73**:33–83. doi: 10.1103/RevModPhys.73.33
107. Carlson J. Alpha particle structure. *Phys Rev C*. (1988) **38**:1879–85. doi: 10.1103/PhysRevC.38.1879
108. Schmidt KE, Lee MA. High-accuracy Trotter-formula method for path integrals. *Phys Rev E*. (1995) **51**:5495–8. doi: 10.1103/PhysRevE.51.5495
109. Zhang S, Carlson J, Gubernatis JE. Constrained Path Quantum Monte Carlo method for fermion ground states. *Phys Rev Lett*. (1995) **74**:3652–5. doi: 10.1103/PhysRevLett.74.3652
110. Schmidt KE, Fantoni S. A quantum Monte Carlo method for nucleon systems. *Phys Lett B*. (1999) **446**:99–103. doi: 10.1016/S0370-2693(98)01522-6
111. Lonardoni D, Carlson J, Gandolfi S, Lynn JE, Schmidt KE, Schwenk A, et al. Properties of nuclei up to $A = 16$ using local chiral interactions. *Phys Rev Lett*. (2018) **120**:122502. doi: 10.1103/PhysRevLett.120.122502
112. Lonardoni D, Gandolfi S, Wang XB, Carlson J. Single- and two-nucleon momentum distributions for local chiral interactions. *Phys Rev C*. (2018) **98**:014322. doi: 10.1103/PhysRevC.98.014322
113. Lynn JE, Lonardoni D, Carlson J, Chen JW, Detmold W, Gandolfi S, et al. *Ab initio* short-range-correlation scaling factors from light to medium-mass nuclei. *J Phys G Nucl Part Phys*. (2020) **47**:045109. doi: 10.1088/1361-6471/ab6af7
114. Tews I, Carlson J, Gandolfi S, Reddy S. Constraining the speed of sound inside neutron stars with chiral effective field theory interactions and observations. *Astrophys J*. (2018) **860**:149. doi: 10.3847/1538-4357/aac267
115. Gandolfi S, Lovato A, Carlson J, Schmidt KE. From the lightest nuclei to the equation of state of asymmetric nuclear matter with realistic nuclear interactions. *Phys Rev C*. (2014) **90**:061306. doi: 10.1103/PhysRevC.90.061306
116. Lonardoni D, Tews I, Gandolfi S, Carlson J. Nuclear and neutron-star matter from local chiral interactions. *arXiv*. (2019) 1912.09411 nucl-th.
117. Sarsa A, Fantoni S, Schmidt KE, Pederiva F. Neutron matter at zero temperature with auxiliary field diffusion Monte Carlo. *Phys Rev C*. (2003) **68**:024308. doi: 10.1103/PhysRevC.68.024308
118. Zhang S, Krakauer H. Quantum Monte Carlo method using phase-free random walks with Slater determinants. *Phys Rev Lett*. (2003) **90**:136401. doi: 10.1103/PhysRevLett.90.136401
119. Zhang S, Carlson J, Gubernatis JE. A Constrained path Monte Carlo method for fermion ground states. *Phys Rev B*. (1997) **55**:7464. doi: 10.1103/PhysRevB.55.7464
120. Pederiva F, Sarsa A, Schmidt KE, Fantoni S. Auxiliary field diffusion Monte Carlo calculation of ground state properties of neutron drops. *Nucl Phys A*. (2004) **742**:255–68. doi: 10.1016/j.nuclphysa.2004.06.030
121. Piarulli M, Bombaci I, Logoteta D, Lovato A, Wiringa RB. Benchmark calculations of pure neutron matter with realistic nucleon-nucleon interactions. *arXiv*. (2019) 1908.04426 nucl-th.
122. Wang M, Audi G, Kondev FG, Huang WJ, Naimi S, Xu X. The AME2016 atomic mass evaluation (II). Tables, graphs and references. *Chinese Phys C*. (2017) **41**:030003. doi: 10.1088/1674-1137/41/3/030003
123. Fricke G, Heilig K. Nuclear charge radii.1 In: Schopper H, editor. *Elementary Particles, Nuclei and Atoms*. Springer (2004).
124. Sick I. Precise radii of light nuclei from electron scattering. *Lect Notes Phys*. (2008) **745**:57–77. doi: 10.1007/978-3-540-75479-4_4
125. Mueller P, Sulai IA, Villari ACC, Alcántara-Núñez JA, Alves-Condé R, Bailey K, et al. Nuclear charge radius of ^{8}He. *Phys Rev Lett*. (2007) **99**:252501. doi: 10.1103/PhysRevLett.99.252501
126. Nörtershäuser W, Neff T, Sánchez R, Sick I. Charge radii and ground state structure of lithium isotopes: experiment and theory reexamined. *Phys Rev C*. (2011) **84**:024307. doi: 10.1103/PhysRevC.84.024307
127. Beringer J, Arguin JF, Barnett RM, Copic K, Dahl O, Groom DE, et al. Review of particle physics. *Phys Rev D*. (2012) **86**:010001. doi: 10.1103/PhysRevD.86.010001
128. Friar JL, Martorell J, Sprung DWL. Nuclear sizes and the isotope shift. *Phys Rev A*. (1997) **56**:4579–86. doi: 10.1103/PhysRevA.56.4579
129. Ong A, Berengut JC, Flambaum VV. Effect of spin-orbit nuclear charge density corrections due to the anomalous magnetic moment on halonuclei. *Phys Rev C*. (2010) **82**:014320. doi: 10.1103/PhysRevC.82.014320
130. Lovato A, Gandolfi S, Butler R, Carlson J, Lusk E, Pieper SC, et al. Charge form factor and sum rules of electromagnetic response functions in ^{1}2C. *Phys Rev Lett*. (2013) **111**:092501. doi: 10.1103/PhysRevLett.111.092501

131. Li GC, Sick I, Whitney RR, Yearian MR. High-energy electron scattering from ^{6}Li. *Nucl Phys A*. (1971) **162**:583–92. doi: 10.1016/0375-9474(71)90257-0
132. de Vries H, de Jager CW, de Vries C. Nuclear charge-density-distribution parameters from elastic electron scattering. *At Data Nucl Data Tables*. (1987) **36**:495. doi: 10.1016/0092-640X(87)90013-1
133. McVoy KW, Van Hove L. Inelastic electron-nucleus scattering and nucleon-nucleon correlations. *Phys Rev*. (1962) **125**:1034–43. doi: 10.1103/PhysRev.125.1034
134. Kelly JJ. Simple parametrization of nucleon form factors. *Phys Rev C*. (2004) **70**:068202. doi: 10.1103/PhysRevC.70.068202
135. Wiringa RB, Schiavilla R. Microscopic calculation of ^{6}Li elastic and transition form factors. *Phys Rev Lett*. (1998) **81**:4317–20. doi: 10.1103/PhysRevLett.81.4317
136. Sick I, McCarthy JS. Elastic electron scattering from ^{1}2C and ^{1}6O. *Nucl Phys A*. (1970) **150**:631–54. doi: 10.1016/0375-9474(70)90423-9
137. Schütz W. Elastische Elektronenstreuung an14N,15N,16O und18O bei kleiner Impulsübertragung. *Z Phys A*. (1975) **273**:69–75. doi: 10.1007/BF01435760
138. Sick I. (1975).
139. Mihaila B, Heisenberg JH. Microscopic calculation of the inclusive electron scattering structure function in ^{1}6O. *Phys Rev Lett*. (2000) **84**:1403–6. doi: 10.1103/PhysRevLett.84.1403
140. Abbott BP, Abbott R, Abbott TD, Acernese F, Ackley K, Adams C, et al. GW170817: Measurements of neutron star radii and equation of state. *Phys Rev Lett*. (2018) **121**:161101. doi: 10.1103/PhysRevLett.121.161101

Conflict of Interest: The authors declare that the research was conducted in the absence of any commercial or financial relationships that could be construed as a potential conflict of interest.

frontiers in Physics

PERSPECTIVE
published: 21 May 2020
doi: 10.3389/fphy.2020.00174

Recent Progress in Nuclear Lattice Simulations

*Dean Lee**

Facility for Rare Isotope Beams and Department of Physics & Astronomy, Michigan State University, East Lansing, MI, United States

We review several recent results on lattice simulations by the Nuclear Lattice Effective Field Theory Collaboration. In the first part we discuss the implementation of nuclear forces on the lattice using chiral effective field theory. The new development we highlight is the use of non-local lattice operators to achieve a simpler spin channel decomposition, in contrast with previous studies that considered only local interactions. In the second part, we present evidence that nuclear physics is close to a quantum phase transition. This development is also linked to the study of the differences between local and non-local interactions. In the final part we further explore the link between the nuclear forces and nuclear structure. We consider the simplest possible nuclear interaction which can accurately reproduce the ground state energies of neutron matter, light nuclei, and medium-mass nuclei. We discuss what these recent developments say about the emergence of nuclear structure from nuclear forces and the road ahead for nuclear lattice simulations.

Keywords: nuclear structure, nuclear forces, lattice effective field theory, nuclear lattice simulations, quantum phase transition

OPEN ACCESS

Edited by:
Saori Pastore, Los Alamos National Laboratory (DOE), United States

Reviewed by:
Robert B. Wiringa, Argonne National Laboratory (DOE), United States
Roelof Bijker, National Autonomous University of Mexico, Mexico

***Correspondence:**
Dean Lee
leed@frib.msu.edu

Specialty section:
This article was submitted to Nuclear Physics, a section of the journal Frontiers in Physics

Received: *26 December 2019*
Accepted: *24 April 2020*
Published: *21 May 2020*

Citation:
Lee D (2020) Recent Progress in Nuclear Lattice Simulations. Front. Phys. 8:174. doi: 10.3389/fphy.2020.00174

1. INTRODUCTION

In this article we review several recent advances by the Nuclear Lattice Effective Field Theory Collaboration that combine of chiral effective field theory with lattice methods, an approach that we call nuclear lattice effective field theory. See Epelbaum et al. [1] and Machleidt and Entem [2] for reviews of chiral effective field theory (EFT) and Lee [3] and Lähde and Meißner [4] for reviews of nuclear lattice EFT. We begin the article by presenting some technical developments regarding the nuclear lattice interactions. The new technology that makes this possible is the use of non-local smearing for the operator interactions. These are important for producing interactions that can give accurate reproductions of the empirical nucleon-nucleon phase shifts.

In the second part of the article we consider the features of the nuclear interactions which are responsible for the bulk binding properties of atomic nuclei. From *ab initio* lattice simulations we present numerical data showing that nature sits near a quantum phase transition. It turns out that the differences between local and non-local interactions will again be important. In the last part of the review we continue with our first principles investigations of nuclear forces and nuclear structure. This time we discuss a simple nuclear interaction which gives the correct ground state energies of neutron matter, light nuclei, and medium-mass nuclei with no more than a few percent error. We then conclude by discussing the connection between nuclear structure and nuclear forces and some possible future directions for nuclear lattice simulations.

2. IMPROVED LATTICE INTERACTIONS

Simulations using lattice chiral EFT have been applied to predict the scattering and structure of nuclei [5–7]. The application of nuclear forces at higher chiral orders are problematic on the lattice due to the breaking of rotational invariance produced by the lattice regularization [8, 9]. In this review we focus only on the short-range interactions since this is where the new developments have been made. We use the terms leading order (LO), next-to-leading order (NLO), next-to-next-to-leading order (N^2LO), and next-to-next-to-next-to-leading order (N^3LO) for the successive orders in chiral EFT.

In Li et al. [10], we introduce a set of short-range interactions in lattice chiral EFT that decompose more naturally into spin channels. In the following we explain how to construct two-nucleon operators on the lattice with intrinsic spin S, S_z, orbital angular momentum L, L_z, and isospin I, I_z. Since orbital angular momentum is not exactly conserved on the lattice, we enforce the required orbital angular momentum projection by hand using smeared distributions of annihilation and creation operators whose angular dependence are given by spherical harmonics. The use of these smeared annihilation and creation operators has the effect of controlling the range of the interaction as well as reducing lattice artifacts. Since the annihilation and creation operators are no longer at the same point in space, the resulting interaction depends on the particle velocities and is therefore a non-local interaction. This is in contrast with local interactions, where the annhiliation and creation operators are at the same point in space. Previous lattice studies had only considered local interactions [8].

We will work with lattice units where quantities are multiplied by the corresponding power of the spatial lattice spacing a to make the object dimensionless. Let $\langle \mathbf{n}'\mathbf{n}\rangle$ denote the nearest neighbors $\mathbf{n}'$ of lattice site $\mathbf{n}$. Our starting point is $a_{i,j}(\mathbf{n})$, the nucleon annihilation operator for lattice site $\mathbf{n}$ with spin i and isospin j. We then add lattice operators on neighboring lattice sites with coefficient, $s_{\rm NL}$. This defines the smeared annihilation operator

$$a_{{\rm NL},i,j}(\mathbf{n}) = a_{i,j}(\mathbf{n}) + s_{\rm NL}\sum_{\langle \mathbf{n}'\mathbf{n}\rangle} a_{i,j}(\mathbf{n}'). \tag{1}$$

The overall normalization of the smeared annihilation operators is not important since any normalization factors can be absorbed into the definition of the interaction coefficients that we build with these smeared operators.

This process can easily be extended to lattice sites beyond the nearest neighbors of $\mathbf{n}$. After this we construct combinations with spin S, S_z, and isospin I, I_z,

$$\begin{aligned}&[a(\mathbf{n})a(\mathbf{n}')]^{s_{\rm NL}}_{S,S_z,I,I_z}\\ &= \sum_{i,j,i',j'} a_{{\rm NL},i,j}(\mathbf{n})M_{ii'}(S,S_z)M_{jj'}(I,I_z)a_{{\rm NL},i',j'}(\mathbf{n}').\end{aligned} \tag{2}$$

Let us define the lattice derivative ∇_l along the l spatial direction as

$$\nabla_l f(\mathbf{n}) = \frac{1}{2}f(\mathbf{n}+\hat{\mathbf{l}}) - \frac{1}{2}f(\mathbf{n}-\hat{\mathbf{l}}). \tag{3}$$

We can also define the lattice derivative $\nabla_{1/2,l}$ with half steps in the forward and backward directions,

$$\nabla_{1/2,l} f(\mathbf{n}) = f(\mathbf{n}+\frac{1}{2}\hat{\mathbf{l}}) - f(\mathbf{n}-\frac{1}{2}\hat{\mathbf{l}}). \tag{4}$$

This yields a well-defined function on the lattice sites when we take double derivatives,

$$\nabla^2_{1/2,l} f(\mathbf{n}) = f(\mathbf{n}+\hat{\mathbf{l}}) - 2f(\mathbf{n}) + f(\mathbf{n}-\hat{\mathbf{l}}). \tag{5}$$

The lattice Laplacian operator is defined as

$$\nabla^2_{1/2} f(\mathbf{n}) = \sum_l \nabla^2_{1/2,l} f(\mathbf{n}). \tag{6}$$

We select orbital angular momenta with the help of solid spherical harmonics,

$$R_{L,L_z}(\mathbf{r}) = \sqrt{\frac{4\pi}{2L+1}} r^L Y_{L,L_z}(\theta,\phi). \tag{7}$$

We work with polynomials of the lattice derivatives that act on one of the annihilation operators, with coefficients prescribed by the solid spherical harmonics,

$$P^{2M,s_{\rm NL}}_{S,S_z,L,L_z,I,I_z}(\mathbf{n}) = [a(\mathbf{n})\nabla^{2M}_{1/2}R^*_{L,L_z}(\nabla)a(\mathbf{n})]^{s_{\rm NL}}_{S,S_z,I,I_z}. \tag{8}$$

This ensures the lattice operators have the correct rotational properties in the continuum limit. We use Clebsch-Gordan coefficients to put together the required spin and orbital angular momentum combinations,

$$\begin{aligned}&O^{2M,s_{\rm NL}}_{S,L,J,J_z,I,I_z}(\mathbf{n})\\ &\quad= \sum_{S_z,L_z}\langle SS_zLL_z|JJ_z\rangle P^{2M,s_{\rm NL}}_{S,S_z,L,L_z,I,I_z}(\mathbf{n}).\end{aligned} \tag{9}$$

In Li et al. [10], we consider the neutron-proton system up to N^3LO. The chosen lattice spacings are 1.97, 1.64, 1.32, and 0.99 fm. In **Figure S1** we show the phase shifts and mixing angles for neutron-proton scattering vs. relative momenta for lattice spacing $a = 1.32$ fm. In **Figure S2** we show the phase shifts and mixing angles for neutron-proton scattering for lattice spacing $a = 0.99$ fm. The estimated uncertainties at NLO, N^2LO, and N^3LO are labeled with the blue, green, and red bands, respectively. The Nijmegen partial wave analysis results are shown with black solid lines, and the lattice results at N^3LO are shown with diamonds. These results show marked improvement over previous studies of the lattice chiral EFT interactions [8]. We see that in most cases the error bands at LO, NLO, N^2LO, and N^3LO are overlapping with each other and decreasing in width with each successive order. This indicates the consistency of the effective field theory expansion as well as its convergence rate. There are however some exceptions such as the high-momentum region of the $^3P_2$ and $^3D_2$ phase shifts where the convergence is not yet optimal. We have work in progress now that indicates these problems are resolved with a better lattice treatment of

the tensor force in the one-pion exchange potential and will be discussed in a forthcoming publication. As one would expect, we also see a general improvement of the lattice phase shifts as we decrease the lattice spacing. We see both better agreement with the empirical data as well as smaller error bands.

3. NUCLEAR PHYSICS NEAR A QUANTUM PHASE TRANSITION

In Elhatisari et al. [11], we investigate two different LO interactions in chiral EFT, which we call interactions A and B. Both are defined with lattice spacing $a = 1.97$ fm and have nearly the same nucleon-nucleon scattering phase shifts and binding energies for the three- and four-nucleon systems. However, for heavier nuclei the binding energies are very different. Interactions A and B each have the same one-pion exchange interaction as well as the same Coulomb potential between protons. The only distinction between the interactions A and B is the form of the short-range interactions, and we limit our discussion here to the short-range interactions.

We write σ_S with $S = 1, 2, 3$ for the spin Pauli matrices, and τ_I with $I = 1, 2, 3$ for the isospin Pauli matrices. We will write $a(\mathbf{n})$ for the column vector of annihilation operators $a_{i,j}(\mathbf{n})$, and we will write $a^\dagger(\mathbf{n})$ for the row vector of creation operators $a^\dagger_{i,j}(\mathbf{n})$. For our chosen non-local smearing parameter $s_{\rm NL}$, we construct the smeared operators as in Equation (1),

$$a_{\rm NL}(\mathbf{n}) = a(\mathbf{n}) + s_{\rm NL} \sum_{\langle \mathbf{n}'\mathbf{n}\rangle} a(\mathbf{n}'), \tag{10}$$

$$a^\dagger_{\rm NL}(\mathbf{n}) = a^\dagger(\mathbf{n}) + s_{\rm NL} \sum_{\langle \mathbf{n}'\mathbf{n}\rangle} a^\dagger(\mathbf{n}'). \tag{11}$$

The point-like density operators are defined as

$$\rho(\mathbf{n}) = a^\dagger(\mathbf{n})a(\mathbf{n}), \tag{12}$$

$$\rho_S(\mathbf{n}) = a^\dagger(\mathbf{n})[\sigma_S]a(\mathbf{n}), \tag{13}$$

$$\rho_I(\mathbf{n}) = a^\dagger(\mathbf{n})[\tau_I]a(\mathbf{n}), \tag{14}$$

$$\rho_{S,I}(\mathbf{n}) = a^\dagger(\mathbf{n})[\sigma_S \otimes \tau_I]a(\mathbf{n}). \tag{15}$$

The smeared non-local densities are defined as

$$\rho_{\rm NL}(\mathbf{n}) = a^\dagger_{\rm NL}(\mathbf{n})a_{\rm NL}(\mathbf{n}), \tag{16}$$

$$\rho_{S,{\rm NL}}(\mathbf{n}) = a^\dagger_{\rm NL}(\mathbf{n})[\sigma_S]a_{\rm NL}(\mathbf{n}), \tag{17}$$

$$\rho_{I,{\rm NL}}(\mathbf{n}) = a^\dagger_{\rm NL}(\mathbf{n})[\tau_I]a_{\rm NL}(\mathbf{n}), \tag{18}$$

$$\rho_{S,I,{\rm NL}}(\mathbf{n}) = a^\dagger_{\rm NL}(\mathbf{n})[\sigma_S \otimes \tau_I]a_{\rm NL}(\mathbf{n}), \tag{19}$$

while the smeared local densities for local smearing parameter $s_{\rm L}$ are

$$\rho_{\rm L}(\mathbf{n}) = a^\dagger(\mathbf{n})a(\mathbf{n}) + s_{\rm L} \sum_{\langle \mathbf{n}'\,\mathbf{n}\rangle} a^\dagger(\mathbf{n}')a(\mathbf{n}'), \tag{20}$$

$$\rho_{S,{\rm L}}(\mathbf{n}) = a^\dagger(\mathbf{n})[\sigma_S]a(\mathbf{n}) + s_{\rm L} \sum_{\langle \mathbf{n}'\,\mathbf{n}\rangle} a^\dagger(\mathbf{n}')[\sigma_S]a(\mathbf{n}'), \tag{21}$$

$$\rho_{I,{\rm L}}(\mathbf{n}) = a^\dagger(\mathbf{n})[\tau_I]a(\mathbf{n}) + s_{\rm L} \sum_{\langle \mathbf{n}'\,\mathbf{n}\rangle} a^\dagger(\mathbf{n}')[\tau_I]a(\mathbf{n}'), \tag{22}$$

$$\rho_{S,I,{\rm L}}(\mathbf{n}) = a^\dagger(\mathbf{n})[\sigma_S \otimes \tau_I]a(\mathbf{n}) + s_{\rm L} \sum_{\langle \mathbf{n}'\,\mathbf{n}\rangle} a^\dagger(\mathbf{n}')[\sigma_S \otimes \tau_I]a(\mathbf{n}'). \tag{23}$$

The non-local short-range interactions have the form

$$V_{\rm NL} = \frac{c_{\rm NL}}{2} \sum_{\mathbf{n}} :\rho_{\rm NL}(\mathbf{n})\rho_{\rm NL}(\mathbf{n}): + \frac{c_{I,{\rm NL}}}{2} \sum_{\mathbf{n},I} :\rho_{I,{\rm NL}}(\mathbf{n})\rho_{I,{\rm NL}}(\mathbf{n}):, \tag{24}$$

while the local short-range interactions are given by

$$\begin{aligned} V_{\rm L} =& \frac{c_{\rm L}}{2} \sum_{\mathbf{n}} :\rho_{\rm L}(\mathbf{n})\rho_{\rm L}(\mathbf{n}): + \frac{c_{S,{\rm L}}}{2} \sum_{\mathbf{n},S} :\rho_{S,{\rm L}}(\mathbf{n})\rho_{S,{\rm L}}(\mathbf{n}): \\ &+ \frac{c_{I,{\rm L}}}{2} \sum_{\mathbf{n},I} :\rho_{I,{\rm L}}(\mathbf{n})\rho_{I,{\rm L}}(\mathbf{n}): + \frac{c_{S,I,{\rm L}}}{2} \sum_{\mathbf{n},S,I} :\rho_{S,I,{\rm L}}(\mathbf{n})\rho_{S,I,{\rm L}}(\mathbf{n}):. \end{aligned} \tag{25}$$

The : : symbol indicates normal ordering where the annihilation operators are pushed to the right and the creation operators are pulled to the left.

For interaction A we take the short-range interaction to have the purely non-local form described in Equation (24). For interaction B we take the short-range interaction to have a combination of the non-local and local forms described in Equations (24), (25), respectively. In **Table 1**, we show results for the ground state energies of ^{8}Be, ^{12}C, ^{16}O, and ^{20}Ne. We present results for interactions A and B at LO, including Coulomb interactions, and the comparison with experimental data. While the ground state energies for B are close to the experimental data, the binding energies for A are not.

To identify the reason for the disagreement, we compute the ground state energies of ^{8}Be, ^{12}C, ^{16}O, and ^{20}Ne for interaction A with the Coulomb interactions turned off. When we turn off Coulomb and divide the ground state energy for each nucleus with that of ^{4}He, we find the ratios

$$\frac{E_{^8{\rm Be}}}{E_{^4{\rm He}}} = 1.997(6), \quad \frac{E_{^{12}{\rm C}}}{E_{^4{\rm He}}} = 3.00(1), \tag{26}$$

$$\frac{E_{^{16}{\rm O}}}{E_{^4{\rm He}}} = 4.00(2), \quad \frac{E_{^{20}{\rm Ne}}}{E_{^4{\rm He}}} = 5.03(3). \tag{27}$$

TABLE 1 | Results for the ground energies of ^{8}Be, ^{12}C, ^{16}O, and ^{20}Ne using interactions A and B at LO with Coulomb interactions and the comparison with experimental data.

Nucleus	A (LO + Coulomb)	B (LO + Coulomb)	Experiment
^{8}Be	−56.51(14)	−57.29(7)	−56.591
^{12}C	−84.0(3)	−89.9(5)	−92.162
^{16}O	−110.5(6)	−126.0(7)	−127.619
^{20}Ne	−137(1)	−164(1)	−160.645

These consecutive integer numbers are an indication of a Bose condensate of alpha particles filling the periodic box. In Elhatisari et al. [11] this interpretation is confirmed by showing that the alpha-alpha interactions are indeed very weak for interaction A.

These results shows that nature sits near a quantum phase transition. Along the $N = Z$ line where the number of neutrons equals the number of protons, there is a first-order quantum transition separating a Bose gas of alpha particles from a nuclear liquid. The strength of the alpha-alpha interactions determines whether one has a Bose gas of alpha particles or a nuclear liquid. In turn, the alpha-alpha interactions are impacted by the strength and range of the local part of the nucleon-nucleon interactions. The local part of interaction B is stronger than the local part of interaction A, and hence the different behaviors that we see.

The phase diagram of nuclear matter at zero temperature is in **Figure S3**. The parameter λ indicates the strength of the local part of the nucleon-nucleon interactions. This can be constructed explicitly by taking a linear combination of the interactions used for interactions A and B. Nuclear matter is in a Bose gas phase of alpha particles when λ is below the critical value, and nuclear matter is in a nuclear liquid phase if λ crosses above the critical value. When λ increases even further, finite A-body nuclei become stable as their energy fall below the threshold value $E_\alpha A/4$ associated with multi-alpha continuum states.

4. ESSENTIAL ELEMENTS FOR NUCLEAR BINDING

In Lu et al. [12], we investigate a basic question connecting nuclear forces and nuclear structure. What are the essential elements for nuclear binding? For this analysis we work with a simple leading order effective field theory without pions. This simple pionless EFT theory is SU(4)-invariant, where the SU(4) is Wigner's approximate symmetry where the four nucleon degrees of freedom can be rotated into each other [13]. The lattice Hamiltonian has the form

$$H_{\mathrm{SU(4)}} = H_{\mathrm{free}} + \frac{1}{2!}C_2 \sum_{\boldsymbol{n}} \tilde{\rho}^2(\mathbf{n}) + \frac{1}{3!}C_3 \sum_{\mathbf{n}} \tilde{\rho}^3(\mathbf{n}), \qquad (28)$$

where H_{free} is the free nucleon Hamiltonian and

$$\tilde{\rho}(\mathbf{n}) = \rho_{\mathrm{NL}}(\mathbf{n}) + s_{\mathrm{L}} \sum_{\langle \mathbf{n}'\mathbf{n} \rangle} \rho_{\mathrm{NL}}(\mathbf{n}), \qquad (29)$$

and $\rho_{\mathrm{NL}}(\mathbf{n})$ was defined in Equation (16). The local part of the interaction is adjusted using the parameter s_{L}, while the non-local part of the interaction is controlled by the parameter s_{NL}, which appears implicitly in the definition of $\rho_{\mathrm{NL}}(\mathbf{n})$. The parameter C_2 controls the strength of the two-nucleon interaction, and C_3 controls the three-nucleon interaction. For these calculations the lattice spacing is $a = 1.32$ fm.

The two-nucleon interaction coefficient C_2 and interaction range, controlled jointly by s_{NL} and s_{L}, are set by fitting the scattering length a_0 and effective range r_0 averaged over the two S-wave channels, $^1S_0$ and $^3S_1$. The three-nucleon coupling strength C_3 is set according to the binding energy of ^{3}H. At the empirical binding energy $B(^3\mathrm{H}) = 8.48$ MeV, the ^{4}He binding energy is 28.9 MeV, and this is near the empirical value $B(^4\mathrm{He}) = 28.3$ MeV. This fitting process is carried out for several pairs of values for s_{NL} and s_{L}. We calculate several nuclear ground states for each pair using auxiliary-field lattice Monte Carlo simulations. We find that $s_{\mathrm{NL}} = 0.5$ and $s_{\mathrm{L}} = 0.061$ gives the best agreement overall. We note that the rather large value of s_{L} as compared with s_{NL} is an indication that the local interaction plays an important role in nuclear binding. The corresponding couplings are $C_2 = -3.41 \times 10^{-7}$ MeV^{-2} and $C_3 = -1.4 \times 10^{-14}$ MeV^{-5}. Overall about 20% of the binding is coming from the three-body interaction. This is consistent with the expected hierarchy of forces in effective field theory, with three-body forces being less important than two-body forces.

We present binding energies and charge radii in **Table 2** for selected nuclei together with the experimental values and the computed Coulomb energy. Although the ^{3}H energy is a constraint in the fitting process, the other values are predictions. We have included the charge radius of the proton for calculations of the nuclear charge radii, but have not included smaller effects arising from the charge distribution of the neutron, relativistic corrections, and spin-orbit terms. In **Figure S4** we show the binding energies for 86 bound nuclei with up to $A = 48$ nucleons in comparison with empirical data. The Monte Carlo error bars are not visible as they are smaller than the symbol size. The errors associated with Euclidean time extrapolation and volume extrapolation are less than 1% relative error, and these errors are not shown. In **Figure S4** one can see that the agreement with empirical results is fairly good. The remaining discrepancies are a sign of missing effects such as interactions which are spin dependent.

In **Figure S5** we show the charge densities of ^{16}O and ^{40}Ca. These densities are calculated using the pinhole algorithm [16] where a barrier is placed in the middle of the Euclidean time evolution, and the amplitude vanishes unless each nucleon passes through a pinhole. As the number of pinholes are set to equal the number of nucleons, the sampling over pinholes yields a classical distribution of the nucleon positions. We show the comparison

TABLE 2 | *Left side:* Computed binding energies of several nuclei compared with experimental values.

	B	Exp.	Coulomb	B/Exp.	R_{ch}	Exp.	R_{ch}/Exp.
^{3}H	8.48 (2)(0)	8.48	0.0	1.00	1.90 (1)(1)	1.76	1.08
^{3}He	7.75 (2)(0)	7.72	0.73 (1)(0)	1.00	1.99 (1)(1)	1.97	1.01
^{4}He	28.89 (1)(1)	28.3	0.80 (1)(1)	1.02	1.72 (1)(3)	1.68	1.02
^{16}O	121.9 (1)(3)	127.6	13.9 (1)(2)	0.96	2.74 (1)(1)	2.70	1.01
^{20}Ne	161.6 (1)(1)	160.6	20.2 (1)(1)	1.01	2.95 (1)(1)	3.01	0.98
^{24}Mg	193.5 (02)(17)	198.3	28.0 (1)(2)	0.98	3.13 (1)(2)	3.06	1.02
^{28}Si	235.8 (04)(17)	236.5	37.1 (2)(3)	1.00	3.26 (1)(1)	3.12	1.04
^{40}Ca	346.8 (6)(5)	342.1	71.7 (4)(4)	1.01	3.42 (1)(3)	3.48	0.98

Right side: Computed charge radii of several nuclei compared with empirical values. The first parenthesis denotes the Monte Carlo error, and the second parenthesis is the time extrapolation error. All energies are in MeV, and all lengths are in fm. Experimental data is from Wang et al. [14]. Table from Lu et al. [12].

with electron scattering data, as well as the lattice results with the Coulomb interaction included via first order perturbation theory. The Coulomb force suppresses the densities near the nucleus center, bringing the results in better agreement with the experimental data. The results are surprisingly accurate in view of the simple nuclear interaction.

The ground state energy of pure neutron matter is shown in **Figure S6** as a function of the neutron density. We show the results of several other calculations for comparison. For the lattice results the number of neutrons ranges from 14 to 66. The calculations are done with three box sizes $L = 5, 6, 7$. Our lattice results, shown as the filled red polygons, are generally in good agreement with the other calculations for densities higher than 0.05 fm^{-3}. For lower densities the disagreement is larger due to the neutron-neutron scattering length being incorrect. The open red polygons correspond to an improved calculation where a contact interaction is included to give the correct neutron-neutron scattering length. There is also a correction included to restore invariance with respect to Galilean boosts [17]. In spite of the simplicity of the interaction, the results are quite good.

5. DISCUSSION

We have reviewed several recent results by the Nuclear Lattice EFT Collaboration. We presented the improved description of scattering phase shifts in chiral effective field theory up to N^{3}LO. We then showed evidence that nuclear physics is close to a quantum phase transition. After this we described the minimal nuclear interaction that can accurately reproduce the ground state energies of neutron matter, light nuclei, and medium-mass nuclei. A common theme flowing through all aspects of our review was the notable difference between local and non-local interactions. We now put some of these findings into context.

Numerous calculations show the reliability of chiral EFT for the properties of light nuclei [18–22]. However, the binding energies as well as the charge radii of medium mass nuclei are sometimes not well reproduced [20, 23–29]. One notable case is that the charge radius of ^{16}O, which is often too small [23, 25–28]. Without further input, chiral EFT calculations do not yet provide accurate predictions at higher nuclear densities.

One practical approach is to put constraints on the nuclear force by fitting the properties of medium mass nuclei and nuclear matter saturation [29]. This strategy has been used in several calculations [30–33]. The approach we have pursued in nuclear lattice studies is to focus on the microscopic origins of the problem. In Elhatisari et al. [11], we find that nuclear matter resides near a quantum phase transition that lies at the boundary between a Bose condensate of alpha particles and a nuclear liquid. There we show that local interactions are especially important for nuclear binding. In Lu et al. [12], we construct a simple nuclear interaction that can produce, with no more than a few percent error, the ground state energies of neutron matter, light nuclei, and medium-mass nuclei. From that analysis we see the importance of the range and locality of the SU(4)-invariant forces in determining the bulk properties of nuclei.

The dominance of SU(4)-invariant interactions can be explained in terms of coherent enhancement. Upon summation over nucleonic spin configurations, much of the effect of spin-dependent forces cancel. In a similar manner, isospin-dependent forces will cancel in symmetric nuclear matter due to the protons and neutrons being equal in number. One important exception though is the Coulomb interaction. SU(4) symmetry and large scattering length universality have a long history in nuclear physics. It is well-known that the Tjon line connecting ^{3}H and ^{4}He binding energies is a manifestation of universality in nuclear systems [9, 34–36].

SU(4)-symmetric short-range interactions are now being used with local and non-local smearing and one-pion exchange. These improved calculations of light and medium-mass nuclei will use chiral forces up to N^{3}LO. One of the central questions that we seek to address is why the straightforward application of chiral EFT does not give reliable and accurate predictions at higher nuclear densities. While more investigations are needed, it seems that part of the answer to this question is related to the emergence of a physical length scale relevant to many-body nuclear systems, the size of the alpha particle. The amount of fine tuning needed to reproduce the alpha-alpha and alpha-nucleon scattering phase shifts can be understood as the competition between Pauli repulsion and attractive nucleon-nucleon interactions. This important and delicate balance is amplified by the fact that the range of the nucleon-nucleon interaction is comparable to the size of the alpha particle. Hence small differences in the range or locality of the interaction can have a large impact on the interactions of the alpha particle. This is turn has consequences for nuclear systems with increasing numbers of nucleons.

DATA AVAILABILITY STATEMENT

The datasets analyzed in this article are not publicly available. Requests to access the datasets should be directed to leed@frib.msu.edu.

AUTHOR CONTRIBUTIONS

The author confirms being the sole contributor of this work and has approved it for publication.

ACKNOWLEDGMENTS

I thank my wonderful collaborators Serdar Elhatisari, Evgeny Epelbaum, Hermann Krebs, Timo A. Lähde, Ning Li, Bing-Nan Lu, Thomas Luu, Ulf-G. Meißner, Gautam Rupak, for their insight, work, and determination that made on the collaborative work reported here possible. Partial support provided by the U.S. Department of Energy (DE-SC0018638 and DE-AC52-06NA25396). The computational resources were provided by the Julich Supercomputing Centre at Forschungszentrum Jülich, Oak Ridge Leadership Computing Facility, RWTH Aachen, and Michigan State University.

SUPPLEMENTARY MATERIAL

The Supplementary Material for this article can be found online at: https://www.frontiersin.org/articles/10.3389/fphy.2020.00174/full#supplementary-material

Figure S1 | Results for the neutron-proton scattering phase shifts and mixing angles vs. the relative momenta for lattice spacing a = 1.32 fm. The blue, green and red bands show the estimated uncertainties at NLO, N^2LO and N^3LO respectively. The black solid line and diamonds denote phase shift or mixing angle from the Nijmegen partial wave analysis and lattice calculation at N^3LO, respectively. Figure from Li et al. [10].

Figure S2 | Results for the neutron-proton scattering phase shifts and mixing angles vs. the relative momenta for lattice spacing a = 0.99 fm. The blue, green and red bands show the estimated uncertainties at NLO, N^2LO and N^3LO respectively. The black solid line and diamonds denote phase shift or mixing angle from the Nijmegen partial wave analysis and lattice calculation at N^3LO, respectively. Figure from Li et al. [10].

Figure S3 | Phase diagram of nuclear matter at zero temperature. λ controls the strength of the local part of the interactions. Figure from Elhatisari et al. [11].

Figure S4 | Calculated binding energies from ^{3}H to ^{48}Ca. The solid symbols are lattice results and the open symbols are experimental values. The experimental values are from Wang et al. [14]. Figure adapted from Lu et al. [12].

Figure S5 | Computed ^{16}O and ^{40}Ca charge densities compared with experimental results. The circles denote the results without Coulomb interaction. The squares are the results with the Coulomb interaction included perturbatively. Experimental results are from De Vries et al. [15]. Figure adapted from Lu et al. [12].

Figure S6 | Ground state energy of pure neutron matter as a function of neutron density for box sizes L = 5 (upright triangles), L = 6 (squares), L = 7 (right-pointing triangles). The filled red polygons are results for the leading-order interaction. The open red polygons show an improved calculation with a short-range interaction tuned to the physical neutron-neutron scattering length as well as a correction to restore Galilean invariance. Also shown are results calculated with N^3LO chiral interactions (EM 500 MeV, EGM 450/500 MeV and EGM 450/700 MeV) [37], as well as results from variational (APR) [38] and auxiliary-field diffusion MC calculations (GCR) [39]. Figure adapted from Lu et al. [12].

REFERENCES

1. Epelbaum E, Hammer HW, Meißner U-G. Modern theory of nuclear forces. *Rev Mod Phys.* (2009) **81**:1773. doi: 10.1103/RevModPhys.81.1773
2. Machleidt R, Entem DR. Chiral effective field theory and nuclear forces. *Phys Rept.* (2011) **503**:1–75. doi: 10.1016/j.physrep.2011.02.001
3. Lee D. Lattice simulations for few- and many-body systems. *Prog Part Nuclear Phys.* (2009) **63**:117–74. doi: 10.1016/j.ppnp.2008.12.001
4. Lähde TA, Meißner UG. *Nuclear Lattice Effective Field Theory : An Introduction.* Cham: Springer (2019).
5. Epelbaum E, Krebs H, Lee D, Meißner UG. *Ab initio* calculation of the Hoyle state. *Phys Rev Lett.* (2011) **106**:192501. doi: 10.1103/PhysRevLett.106.192501
6. Epelbaum E, Krebs H, Lähde TA, Lee D, Meißner UG. Structure and rotations of the Hoyle state. *Phys Rev Lett.* (2012) **109**:252501. doi: 10.1103/PhysRevLett.109.252501
7. Elhatisari S, Lee D, Rupak G, Epelbaum E, Krebs H, Lähde TA, et al. *Ab initio* alpha-alpha scattering. *Nature* (2015) **528**:111. doi: 10.1038/nature16067
8. Alarcón JM. Du D, Klein N, Lähde TA, Lee D, Li N, et al. Neutron-proton scattering at next-to-next-to-leading order in Nuclear Lattice Effective Field Theory. *Eur Phys J A.* (2017) **53**:83. doi: 10.1140/epja/i2017-12273-x
9. Klein N, Elhatisari S, Lähde TA, Lee D, Meißner UG. The Tjon band in nuclear lattice effective field theory. *Eur Phys J A.* (2018) **54**:121. doi: 10.1140/epja/i2018-12553-y
10. Li N, Elhatisari S, Epelbaum E, Lee D, Lu BN, Meißner UG. Neutron-proton scattering with lattice chiral effective field theory at next-to-next-to-next-to-leading order. *Phys Rev C.* (2018) **98**:044002. doi: 10.1103/PhysRevC.98.044002
11. Elhatisari S, Li N, Rokash A, Alarcón JM, Du D, Klein N, et al. Nuclear binding near a quantum phase transition. *Phys Rev Lett.* (2016) **117**:132501. doi: 10.1103/PhysRevLett.117.132501
12. Lu BN, Li N, Elhatisari S, Lee D, Epelbaum E and Meißner UG. Essential elements for nuclear binding. *Phys Lett B.* (2019) **797**:134863. doi: 10.1016/j.physletb.2019.134863
13. Wigner E. On the consequences of the symmetry of the nuclear Hamiltonian on the spectroscopy of nuclei. *Phys Rev.* (1937) **51**:106. doi: 10.1103/PhysRev.51.106
14. Wang M, Audi G, Kondev FG, Huang WJ, Naimi S, Xu X. The AME2016 atomic mass evaluation (II). Tables, graphs and references. *Chin Phys C.* (2017) **41**:030003. doi: 10.1088/1674-1137/41/3/030003
15. De Vries H, De Jager CW, De Vries C. Nuclear charge-density-distribution parameters from elastic electron scattering. *Atom Data Nuclear Data Tabl.* (1987) **36**:495–536. doi: 10.1016/0092-640X(87)90013-1
16. Elhatisari S, Epelbaum E, Krebs H, Lähde TA, Lee D, Li N, et al. *Ab initio* calculations of the isotopic dependence of nuclear clustering. *Phys Rev Lett.* (2017) **119**:222505. doi: 10.1103/PhysRevLett.119.222505
17. Li N, Elhatisari S, Epelbaum E, Lee D, Lu B, Meißner UG. Galilean invariance restoration on the lattice. *Phys Rev C.* (2019) **99**:064001. doi: 10.1103/PhysRevC.99.064001
18. Hupin G, Quaglioni S, Navrátil P. Unified description of ^{6}Li structure and deuterium-^{4}He dynamics with chiral two- and three-nucleon forces. *Phys Rev Lett.* (2015) **114**:212502. doi: 10.1103/PhysRevLett.114.212502
19. Navrátil P, Gueorguiev VG, Vary JP, Ormand WE, Nogga A, Quaglioni S. Light nuclei from chiral EFT interactions. *Few Body Syst.* (2008) **43**:129–35. doi: 10.1007/s00601-008-0221-y
20. Lonardoni D, Carlson J, Gandolfi S, Lynn JE, Schmidt KE, Schwenk A, et al. Properties of nuclei up to $A = 16$ using local chiral interactions. *Phys Rev Lett.* (2018) **120**:122502. doi: 10.1103/PhysRevLett.120.122502
21. Piarulli M, Baroni A, Girlanda L, Kievsky A, Lovato A, Lusk E, et al. Light-nuclei spectra from chiral dynamics. *Phys Rev Lett.* (2018) **120**:052503. doi: 10.1103/PhysRevLett.120.052503
22. Epelbaum E, Golak J, Hebeler K, Hüther T, Kamada H, Krebs H, Maris P, et al. Few- and many-nucleon systems with semilocal coordinate-space regularized chiral two- and three-body forces. *Phys Rev C.* (2019) **99**:024313. doi: 10.1103/PhysRevC.99.024313
23. Wloch M, Dean DJ, Gour JR, Hjorth-Jensen M, Kowalski K, Papenbrock T, et al. *Ab initio* coupled-cluster study of O-16. *Phys Rev Lett.* (2005) **94**:212501. doi: 10.1103/PhysRevLett.94.212501
24. Hagen G, Papenbrock T, Dean DJ, Hjorth-Jensen M. Medium-mass nuclei from chiral nucleon-nucleon interactions. *Phys Rev Lett.* (2008) **101**:092502. doi: 10.1103/PhysRevLett.101.092502
25. Hagen G, Hjorth-Jensen M, Jansen GR, Machleidt R, Papenbrock T. Continuum effects and three-nucleon forces in neutron-rich oxygen isotopes. *Phys Rev Lett.* (2012) **108**:242501. doi: 10.1103/PhysRevLett.108.242501
26. Binder S, Langhammer J, Calci A, Roth R. *Ab initio* path to heavy nuclei. *Phys Lett B.* (2014) **736**:119. doi: 10.1016/j.physletb.2014.07.010
27. Epelbaum E, Krebs H, Lähde TA, Lee D, Meißner UG, Rupak G. *Ab initio* calculation of the spectrum and structure of ^{16}O. *Phys Rev Lett.* (2014) **112**:102501. doi: 10.1103/PhysRevLett.112.102501
28. Cipollone A, Barbieri C, Navrátil P. Chiral three-nucleon forces and the evolution of correlations along the oxygen isotopic chain. *Phys Rev C.* (2015) **92**:014306. doi: 10.1103/PhysRevC.92.014306
29. Ekström A, Jansen JR, Wendt KA, Hagen G, Papenbrock T, Carlsson BD, et al. Accurate nuclear radii and binding energies from a chiral interaction. *Phys Rev C.* (2015) **91**:051301. doi: 10.1103/PhysRevC.91.051301
30. Hagen G, Ekström A, Forssén C, Jansen GR, Nazarewicz W, Papenbrock T, et al. Neutron and weak-charge distributions of the ^{48}Ca nucleus. *Nat Phys.* (2015) **12**:186–90. doi: 10.1038/nphys3529

31. Hagen G, Jansen GR, Papenbrock T. Structure of ^{78}Ni from first principles computations. *Phys Rev Lett.* (2016) **117**:172501. doi: 10.1103/PhysRevLett.117.172501
32. Simonis J, Stroberg SR, Hebeler K, Holt JD, Schwenk A. Saturation with chiral interactions and consequences for finite nuclei. *Phys Rev C.* (2017) **96**:014303. doi: 10.1103/PhysRevC.96.014303
33. Morris TD, Simonis J, Stroberg SR, Stumpf C, Hagen G, Holt JD, et al. Structure of the lightest tin isotopes. *Phys Rev Lett.* (2018) **120**:152503. doi: 10.1103/PhysRevLett.120.152503
34. Platter L, Hammer HW, Meißner UG. On the correlation between the binding energies of the triton and the alpha-particle. *Phys Lett B.* (2005) **607**:254. doi: 10.1016/j.physletb.2004.12.068
35. König S, Grießhammer HW, Hammer HW, van Kolck U. Nuclear physics around the unitarity limit. *Phys Rev Lett.* (2017) **118**:202501. doi: 10.1103/PhysRevLett.118.202501
36. Kievsky A, Gattobigio M. Efimov physics with 1/2 spin-isospin fermions. *Few Body Syst.* (2016) **57**:217–27. doi: 10.1007/s00601-016-1049-5
37. Tews I, Krüger T, Hebeler K, Schwenk A. Neutron matter at next-to-next-to-next-to-leading order in chiral effective field theory. *Phys Rev Lett.* (2013) **110**:032504. doi: 10.1103/PhysRevLett.110.032504
38. Akmal A, Pandharipande VR, Ravenhall DG. The Equation of state of nucleon matter and neutron star structure. *Phys Rev C.* (1998) **58**:1804. doi: 10.1103/PhysRevC.58.1804
39. Gandolfi S, Carlson J, Reddy S. The maximum mass and radius of neutron stars and the nuclear symmetry energy. *Phys Rev C.* (2012) **85**:032801. doi: 10.1103/PhysRevC.85.032801

Conflict of Interest: The author declares that the research was conducted in the absence of any commercial or financial relationships that could be construed as a potential conflict of interest.

frontiers in Physics

REVIEW
published: 24 September 2020
doi: 10.3389/fphy.2020.00340

Self-Consistent Green's Function Theory for Atomic Nuclei

*Vittorio Somà**

IRFU, CEA, Université Paris-Saclay, Gif-sur-Yvette, France

Nuclear structure theory has recently gone through a major renewal with the development of *ab initio* techniques that can be applied to a large number of atomic nuclei, well-beyond the light sector that had been traditionally targeted in the past. Self-consistent Green's function theory is one among these techniques. The present work aims to give an overview of the self-consistent Green's function approach for atomic nuclei, including examples of recent applications and a discussion on the perspectives for extending the method to nuclear reactions, doubly open-shell systems, and heavy nuclei.

Keywords: nuclear theory, many-body theory, *ab initio* nuclear structure, Green's function theory, open-shell nuclei

1. INTRODUCTION

The theoretical description of atomic nuclei is particularly challenging, for several reasons. First, different energy scales are at play, which is manifest in the rich set of observables and phenomena one is confronted with[1]. As a consequence, the choice of relevant degrees of freedom might not be universal but depend on the particular properties one is interested in. The standard description in terms of nucleons, i.e., protons and neutrons, leads to a many-body Schrödinger equation for up to a few hundred particles, which are too many to be easily treated exactly but too few to be amenable to a statistical treatment[2]. Furthermore, interactions between nucleons should be derived from quantum chromodynamics (QCD) in its nonperturbative regime, which prevents direct calculations and requires an additional modelization effort[3]. In the past, all these features have hindered full solutions of the many-body Schrödinger equation and favored the development of a plentitude of models, following different strategies and characterized by different ranges of application. Although successful in reproducing experimental observations, these models are not always comparable to each other and do not provide a coherent and unified description of nuclear systems.

Only relatively recently so-called *ab initio* calculations of atomic nuclei, i.e., systematically improvable solutions of the many-body Schrödinger equation that start solely from the knowledge of inter-nucleon interactions, have become available for a large number of isotopes. These advances were made possible by the concomitance of different factors. First, new formal developments of many-body techniques were carried out. Second, chiral effective field theory (χ-EFT) was introduced in nuclear physics [3–5], providing a systematic and consistent framework in which the nuclear Hamiltonian can be modeled. Third, similarity renormalization group (SRG) techniques were applied to χ-EFT Hamiltonians [6], which largely improves the convergence of actual

[1]One could further recall the large variety of experimental probes used to study nuclear properties, as well as the diversity of processes that can concern atomic nuclei, for which three of the four fundamental interactions (strong, electromagnetic and weak) are involved.

[2]This characteristic is usually associated to the definition of nuclei as *mesoscopic* systems.

[3]Recently, pioneering lattice QCD calculations have produced the first usable nucleon-nucleon potentials [1, 2]. However, complications still exist in the derivation of three-nucleon forces such that the systematic implementation of lattice QCD interactions is not envisaged in the very near future.

OPEN ACCESS

Edited by:
Saori Pastore,
Washington University in St. Louis,
United States

Reviewed by:
Pieter Maris,
Iowa State University, United States
Mack Atkinson,
TRIUMF, Canada

***Correspondence:**
Vittorio Somà
vittorio.soma@cea.fr

Specialty section:
This article was submitted to Nuclear Physics, a section of the journal Frontiers in Physics

Received: *18 March 2020*
Accepted: *22 July 2020*
Published: *24 September 2020*

Citation:
Somà V (2020) Self-Consistent Green's Function Theory for Atomic Nuclei. Front. Phys. 8:340. doi: 10.3389/fphy.2020.00340

calculations with respect to basis truncations, thus enabling the handling of heavier nuclei. Finally, the availability of computational tools and in particular high-performance computing resources largely increased. As a result, at present, *ab initio* calculations (with two- and three-nucleon interactions) can be performed for a considerable fraction of the nuclei with mass number $A \lesssim 100$.

Among the techniques applicable to the nuclear many-body problem, one can distinguish "virtually exact" and "approximate" approaches. Approaches in the first category do not impose any *formal* approximation on the solution of the many-body Schrödinger equation, which is thus affected only by basis truncation and numerical errors. Typical examples of such methods are Quantum Monte Carlo [7, 8], no-core shell model (or configuration interaction) [9] or nuclear lattice EFT [10]. The second category includes techniques that do approximate the solution of the Schrödinger equation in a systematic way. This solution can be improved, in principle, up to the recovery of the exact one. This is typically achieved by first selecting a reference state and then defining an expansion on top of it, usually in terms of particle-hole correlations (whence the denomination *correlation-expansion* methods). In doing so, the main advantage resides in the scaling with the basis size: while exact methods scale factorially or exponentially with the system size, correlation-expansion methods only scale polynomially and can be thus applied to a much wider set of nuclei.

The simplest (and most inexpensive) among correlation-expansion approaches is many-body perturbation theory (MBPT) [11]. Following the belief that the nuclear many-body problem is intrinsically non-perturbative, MBPT was put aside for several decades after its development in the 1950s. Only relatively recently, with the advent of EFTs and, specially, SRG techniques applied to nuclear Hamiltonians, MBPT was revived [12, 13] and it is now considered as a convenient approach for large-scale systematic calculations. Moreover, it can be easily complemented with resummation techniques like Padé or eigenvector continuation [14, 15] (see [16] for a recent review). Other methods rely on the MBPT concept but are built such that infinite subsets of MBPT contributions are resummed by construction. The three typical examples employed in the nuclear context are in-medium similarity renormalization group (IMSRG), coupled-cluster (CC) and self-consistent Green's function (SCGF) methods. While IMSRG has been originally designed for the nuclear many-body problem not long ago [17, 18], CC and SCGF, although initially proposed for nuclear systems, have been largely developed in quantum chemistry and solid-state physics before being reimported into nuclear physics starting from the 1990s [19, 20] (see [21] for a recent CC review). IMSRG [22], CC [23], as well as no-core shell model [24] have also been adapted to derive a valence-space interaction that can be used in standard shell-model codes, thus further enlarging the reach of *ab initio* calculations.

The present manuscript deals with one of such correlation-expansion approaches, the self-consistent Green's function method. Although GFs have been and are implemented in different ways in the context of atomic nuclei (see e.g., [25]), here the focus is on *ab initio* SCGFs. Early SCGF calculations with realistic nucleon-nucleon potentials dealt mainly with infinite nuclear matter [19]. Formal developments setting the bases for modern implementations in finite nuclei date back to the early 2000s [26–28]. By the end of the decade advanced SCGF implementations were routinely applied [29, 30]. In 2011, standard (i.e., Dyson) SCGF theory was generalized to a particle-number-breaking (i.e., Gorkov) framework [31, 32]. In 2013 the inclusion of three-body interactions was formalized in Dyson theory [33]. In 2018, working equations for the state-of-the-art many-body truncation used in nuclear structure calculations (algebraic diagrammatic construction at third order, see section 3.1) were derived [34].

Building on these formal advances, several applications (based on either Dyson or Gorkov frameworks) have been carried out in the past decade. Typical examples are ground-state properties of medium-mass nuclei, going from the oxygen region [35, 36] to silicon and sulfur [37], calcium [38, 39], and nickel [40] regions, up to the very recent computation of tin and xenon isotopes [41]. As discussed in sections 2 and 4.2, excited spectra of odd-even nuclei are also easily accessible in SCGF theory and were studied in particular in [36, 37, 40]. Excited states of even-even systems were addressed in the form of the electromagnetic dipole response in [42]. In [43], *ab initio* optical potentials were computed and applied in elastic scattering off ^{16}O and ^{40}Ca. Barbieri et al. [44] instead discussed lepton-nucleus scattering, with particular attention to neutrino scattering off ^{40}Ar. Dedicated applications studied effective charges (typically employed in shell-model calculations) [45] and the scale dependence of effective single-particle energies and other non-observable quantities [46]. The possibility of using nucleon-nucleon interactions derived from lattice QCD calculations was also explored in [2]. Last but not least, several collaborations with experimental groups have led to testing the method on e.g., state-of-the-art measurements of nuclear masses [47, 48], energies and spins of excited states [49–52], charge and matter radii [53].

The present article discusses a few of these examples, without any pretension of exhaustivity but with the aim of giving the reader a perception of the reach and versatility of SCGF method, as well we the great deal of possible applications to atomic nuclei. A short introduction to the formalism and implementation in finite nuclei is presented beforehand; however, again, it is far from being complete. The reader interested in a comprehensive treatment of GF theory in a modern form is referred e.g., to the book of Dickhoff and Van Neck [54]. Older, yet valuable sources are the books of Nozières [55] and Abrikosov et al. [56]. An interesting work, although tailored to solid-state physics, is the one of Economou [57]. An extensive review covering SCGF applications to nuclear physics appeared in 2004 [28]. A more recent pedagogical introduction to the basics of SCGF formalism and implementation in both finite nuclei and infinite nuclear matter (including computational details and examples of numerical codes) can be found in [58]. A numerical code including a second-order evaluation of the self-energy in the Dyson framework is publicly available [59].

This manuscript is organized as follows. In section 2, the most important concepts and equations of GF theory are

introduced. Section 3 describes the actual implementation of the methods in calculations of finite nuclei, briefly reviewing the most commonly used self-energy truncations, the working equations, the choice of basis and interaction. In section 4, some representative applications to ground-state properties, excitation spectra, and lepton-nucleus collisions are discussed. Finally, section 5 addresses perspectives and present as well as future challenges, focusing on three directions of research: the consistent treatment of nuclear structure and reactions, the generalization to doubly open-shell systems and the extension to heavy nuclei.

2. BASIC CONCEPTS AND EQUATIONS

Many-body Green's function[4] theory comprises a set of techniques that originated in quantum field theory (QFT) and have been subsequently imported in the (non-relativistic) quantum many-body problem. The late 1950's and the 1960's marked the beginning of the field, with flow of QFT ideas and development of formalism. Since the 1970's technical developments were realized and the approach was applied throughout several disciplines and types of many-body problems, ranging from many-electron systems such as crystals, molecules, and atoms to many-nucleon systems such as nuclei and nuclear matter. Starting from the 1990's such techniques were implemented as an *ab initio* method in nuclear physics.

As for other many-body methods, the purpose of such techniques is to achieve an approximate (yet systematically improvable) solution of the A-body Schrödinger equation. In standard (or *Dyson*) many-body Green's function theory, this is realized by rewriting the Schrödinger equation in terms of one-, two-, ..., A-body objects $g^I(=g), g^{II}, ..., g^A$ named propagators or, indeed, Green's functions (GFs). Each of these objects is then expanded in a perturbation series, which in practical applications is truncated to include a subset of all possible contributions. In *self-consistent* schemes such series are themselves expressed in terms of the exact GFs, which requires an iterative solution and makes the method intrinsically non-perturbative, effectively resumming an infinite subsets of perturbative terms. The x-body GF g^x allows one to compute all x-body observables in the A-body ground state[5]. Therefore, for most applications one is mainly interested in the one-body GF.

Formally g is defined as the expectation value of a time-ordered product of annihilation and creation operators in the A-body ground state $|\Psi_0^A\rangle$

$$g_{\alpha\beta}(t_\alpha, t_\beta) \equiv -i\,\langle\Psi_0^A|\mathcal{T}[a_\alpha(t_\alpha)a_\beta^\dagger(t_\beta)]|\Psi_0^A\rangle\,, \tag{1}$$

with Greek indices labeling basis states of the one-body Hilbert space $\mathcal{H}_1$. One usually works with the Fourier transform of Equation (1) in the energy domain and recasts its perturbation series into the Dyson equation

$$g_{\alpha\beta}(\omega) = g^{(0)}_{\alpha\beta}(\omega) + \sum_{\gamma\delta} g^{(0)}_{\alpha\gamma}(\omega)\,\Sigma^\star_{\gamma\delta}(\omega)\,g_{\delta\beta}(\omega)\,, \tag{2}$$

where $g^{(0)}$ represents some initial ansatz for g, e.g., stemming from the solution of Hartree-Fock (HF) equations. The (irreducible) self-energy $\Sigma^\star$ encodes all terms of the expansion, which is truncated in actual calculations.

Once the one-body GF is obtained as the solution of Equation (2), the expectation value of any one-body operator $\hat{O}^{1B} \equiv \sum_{\alpha\beta} O^{1B}_{\alpha\beta} a^\dagger_\alpha a_\beta$ can be computed as

$$\langle\hat{O}^{1B}\rangle = \sum_{\alpha\beta}\int_{C\uparrow}\frac{d\omega}{2\pi i}\,O^{1B}_{\alpha\beta}\,g_{\beta\alpha}(\omega) = \sum_{\alpha\beta} O^{1B}_{\alpha\beta}\;\rho_{\beta\alpha}\,, \tag{3}$$

where $C\uparrow$ denotes an integral closed on the upper imaginary plane and the one-body density matrix

$$\rho_{\alpha\beta} \equiv \langle\Psi_0^A|a^\dagger_\beta a_\alpha|\Psi_0^A\rangle = \int_{C\uparrow}\frac{d\omega}{2\pi i}\,g_{\alpha\beta}(\omega) \tag{4}$$

has been introduced.

Additionally, for a Hamiltonian with one- and two-body operators, the one-body propagator gives access to the total energy by means of the Galitski-Migdal-Koltun (GMK) sum-rule [60, 61]

$$E_0^A = \sum_{\alpha\beta}\frac{1}{2}\int_{C\uparrow}\frac{d\omega}{2\pi i}\,[\,T_{\alpha\beta} + \omega\,\delta_{\alpha\beta}\,]\,g_{\beta\alpha}(\omega)\,, \tag{5}$$

where $T_{\alpha\beta}$ denote the matrix elements of the one-body operator. Nowadays, realistic nuclear structure calculations require the inclusion of at least a three-body interaction in the starting Hamiltonian. In this case, the GMK sum rule needs to be generalized to [33]

$$E_0^A = \sum_{\alpha\beta}\frac{1}{2}\int_{C\uparrow}\frac{d\omega}{2\pi i}\,[\,T_{\alpha\beta} + \omega\,\delta_{\alpha\beta}\,]\,g_{\beta\alpha}(\omega) - \frac{1}{2}\langle W\rangle\,, \tag{6}$$

where the ground-state expectation value of the three-nucleon operator $\hat{W}$ has to be evaluated. Such a term requires in principle the knowledge of the three-body propagator g^{III}. This is however currently out of reach and in most of practical applications the last term in Equation (6) is computed as

$$\langle W\rangle \simeq \frac{1}{6}\sum_{\alpha\beta\mu\gamma\delta\nu} W_{\alpha\beta\mu,\gamma\delta\nu}\;\rho_{\gamma\alpha}\;\rho_{\delta\beta}\;\rho_{\nu\mu}\,, \tag{7}$$

i.e., by approximating the full three-body density matrix with the antisymmetrized product of the one-body one. In [35], this was shown to introduce errors smaller than 250 keV for the binding energy of oxygen isotopes.

In addition to giving access to the ground-state properties of the A-body system, the one-body GF contains information on

[4]Let us remark that *many-body Green's functions* and *Green's function Monte Carlo* are *not* the same thing. The latter refers to a (virtually exact) technique that aims at projecting out the ground-state wave function typically from a variational solution of the Schrödinger equation [7, 8].

[5]One notable exception is the ground-state energy E_0^A: for a Hamiltonian containing up to y-body operators the knowledge of one- up to $(y-1)$-body Green's functions is sufficient (see Equations 5, 6).

neighboring ($A \pm 1$) nuclei. It becomes evident when rewriting the propagator (Equation 1) in the Lehmann representation

$$g_{\alpha\beta}(\omega) = \sum_n \frac{\langle \Psi_0^A | a_\alpha | \Psi_n^{A+1} \rangle \langle \Psi_n^{A+1} | a_\beta^\dagger | \Psi_0^A \rangle}{\omega - E_n^+ + \mathrm{i}\eta} + \sum_k \frac{\langle \Psi_0^A | a_\beta^\dagger | \Psi_k^{A-1} \rangle \langle \Psi_k^{A-1} | a_\alpha | \Psi_0^A \rangle}{\omega - E_k^- - \mathrm{i}\eta} , \quad (8)$$

where $|\Psi_i^{A\pm1}\rangle$ represent eigenstates of $(A\pm1)$-body systems while $E_n^+ \equiv (E_n^{A+1} - E_0^A)$ and $E_k^- \equiv (E_0^A - E_k^{A-1})$ are one-nucleon addition and removal energies, respectively.

In Dyson GF theory the expansion starts from a particle-number conserving (e.g., a Hartree-Fock) reference state providing $g^{(0)}$. On top of this, spherical symmetry is typically imposed. While such an expansion can suitably address closed-shell systems, it becomes inefficient or even breaks down as soon as pairing and/or quadrupole correlations become important. If one wishes to stick with a single-reference method, a possible solution consists in working, from the outset, with a symmetry-breaking reference state. In particular, breaking U(1) symmetry associated with particle number conservation[6] while maintaining spherical symmetry allows one to efficiently capture pairing correlations, thus gaining access to singly open-shell nuclei.

Dyson GFs were thus generalized to a U(1) symmetry-breaking (typically Hartree-Fock-Bogolyubov) reference state originally by [62]. The formalism was then adapted and implemented for applications to finite nuclei in [31]. Technically, the extension is achieved by working with an A-body ground state that is a linear combination of states with different particle numbers

$$\Psi_0^A \longrightarrow \Psi_0 = \sum_{A'} c_{A'} \Psi_0^{A'} . \quad (9)$$

This leads to the definition of four one-body propagators

$$g_{\alpha\beta}^{11}(t,t') \equiv -i \langle \Psi_0 | \mathcal{T}[a_\alpha(t) a_\beta^\dagger(t')] | \Psi_0 \rangle , \quad (10a)$$

$$g_{\alpha\beta}^{12}(t,t') \equiv -i \langle \Psi_0 | \mathcal{T}[a_\alpha(t) \bar{a}_\beta(t')] | \Psi_0 \rangle , \quad (10b)$$

$$g_{\alpha\beta}^{21}(t,t') \equiv -i \langle \Psi_0 | \mathcal{T}[\bar{a}_\alpha^\dagger(t) a_\beta^\dagger(t')] | \Psi_0 \rangle , \quad (10c)$$

$$g_{\alpha\beta}^{22}(t,t') \equiv -i \langle \Psi_0 | \mathcal{T}[\bar{a}_\alpha^\dagger(t) \bar{a}_\beta(t')] | \Psi_0 \rangle , \quad (10d)$$

two of which (g^{11} and g^{22}) involve *normal* combinations of a and $a^\dagger$ and are associated to the standard density matrix (Equation 3). The remaining two propagators (g^{12} and g^{21}) invoke so-called *anomalous* contributions of a and $a^\dagger$ (interpreted as the annihilation or the creation of a nucleon pair) and lead to the definition of an anomalous (or pairing) density matrix

$$\tilde{\rho}_{\alpha\beta} \equiv \langle \Psi_0 | \bar{a}_\beta a_\alpha | \Psi_0 \rangle = \int_{C\uparrow} \frac{d\omega}{2\pi i} g_{\alpha\bar{\beta}}^{12}(\omega) . \quad (11)$$

In Equation (10), creation operators $\{\bar{a}_\alpha^\dagger\}$ define a one-body basis dual to $\{a_\alpha^\dagger\}$ and are obtained via

$$\bar{a}_a^\dagger(t) \equiv \eta_a a_{\tilde{a}}^\dagger(t) , \qquad \bar{a}_a(t) \equiv \eta_a a_{\tilde{a}}(t) , \quad (12)$$

which correspond to exchanging the state a with its time-reversal partner $\tilde{a}$ up to the phase η_a [31]. The four Gorkov propagators (Equation 10) can be conveniently recast in a 2×2 matrix notation via Nambu's formalism [63]

$$\mathbf{g}_{\alpha\beta}(t,t') \equiv \begin{pmatrix} g_{\alpha\beta}^{11}(t,t') & g_{\alpha\beta}^{12}(t,t') \\ g_{\alpha\beta}^{21}(t,t') & g_{\alpha\beta}^{22}(t,t') \end{pmatrix} . \quad (13)$$

All quantities (operators, self-energy, ...) can be generalized in an analogous fashion such that one ends up with the Gorkov equation

$$\mathbf{g}_{\alpha\beta}(\omega) = \mathbf{g}_{\alpha\beta}^{(0)}(\omega) + \sum_{\gamma\delta} \mathbf{g}_{\alpha\gamma}^{(0)}(\omega) \, \boldsymbol{\Sigma}_{\gamma\delta}^\star(\omega) \, \mathbf{g}_{\delta\beta}(\omega) . \quad (14)$$

Similarly, all standard GF equations including Equations (3)–(8) are rewritten in a matrix form. Last but not least, a chemical potential λ needs to be introduced to guarantee that the number of particles is the correct one *on average*. This amounts to replacing the Hamiltonian $\hat{H}$ with the grand potential

$$\hat{\Omega} \equiv \hat{H} - \lambda \hat{A} . \quad (15)$$

As a consequence of the symmetry breaking, observables might be contaminated by components associated to different particle numbers. Even if in practice the variance is expected to remain small[7], the broken symmetry has to be eventually restored. While symmetry-restored formalism has been developed for other (post-Hartree-Fock-Bogolyubov) many-body methods [64, 65], it remains to be formulated for Gorkov GFs.

3. IMPLEMENTATION FOR ATOMIC NUCLEI

3.1. Choice of Approximation Scheme

Self-consistent GF approximation schemes are defined by the content of the irreducible self-energy, which is expressed as a function of the exact GFs and encodes its perturbative expansion. There exist several ways of approximating the self-energy. The most basic one simply amounts to truncating

[6] In the case of atomic nuclei proton and neutron numbers are conserved individually, therefore it is always intended $U(1)_N \otimes U(1)_Z$ where one of the two or both are broken.

[7] Away from closed-shell systems, contributions from components with $A' \neq A$ are assumed to cancel out to some extent. The largest contamination is expected in differential observables across closed shells, where one of the two systems does not spontaneously break particle-number symmetry.

the perturbative expansion at a certain order. More refined techniques resort to including infinite subsets of perturbation-theory terms via the definition of implicit equations. This is the case, e.g., of the so called *ladder* or *in-medium T-matrix* approximation that resums all multiple particle-particle scattering contributions[8]. This approximation scheme gained considerable attention in early *ab initio* applications because of its ability of tackling nucleon-nucleon interactions with strong short-range components [67–72]. These truncations and resummations are typically conveniently expressed in terms of Feynman diagrams, which facilitate the manipulation of the various terms and give an insight in their physical content.

An alternative, although not orthogonal, route was proposed in the context of quantum chemistry [73, 74] and instead exploits the analytical structure of the self-energy. Similarly to the one-body GF, the exact (dynamical, i.e., energy-dependent, part of the) self-energy displays a Lehmann representation

$$\Sigma^{\star}_{\alpha\beta}(\omega) = \sum_{nn'} M^{\dagger}_{\alpha n} \left[\frac{1}{\omega - (E^{>} + C) + i\eta} \right]_{nn'} M_{n'\beta} + \sum_{kk'} N^{\dagger}_{\alpha k} \left[\frac{1}{\omega - (E^{<} + D) - i\eta} \right]_{kk'} N^{\dagger}_{k'\beta} \,, \qquad (16)$$

where the matrices M, N couple the single-particle motion of the nucleons (i.e., the one-body propagator in which the self-energy is inserted) to intermediate multiparticle-multihole configurations, whose energies ("bare" and resulting from the interference between them) are encoded in the matrices $E^{>}, E^{<}$, and C, D, respectively. The algebraic diagrammatic construction at order n [ADC(n)] is built by demanding that, in addition to including all perturbation-theory contributions up to a given order n, the approximated self-energy has the same analytical structure as the exact one, i.e., in particular, is the same function of the energy. The latter condition requires the self-energy to contain additional sets of contributions, e.g., infinite resummations that would necessitate *ad-hoc* procedures are in this way automatically included in the ADC formalism. The first order, ADC(1), is simply the standard Hartree-Fock (or Hartree-Fock-Bogolyubov, in the case of Gorkov GFs) approximation. ADC(2) introduces lowest-order dynamical correlations in terms of two particle-one hole and two hole-one particle contributions. ADC(3) builds couplings between such configurations and, as a result, includes infinite-order resummations of both particle-particle/hole-hole and particle-hole ladders. Higher orders build on higher-rank particle-hole excitations in a similar but not identical fashion as in other popular many-body methods like coupled-cluster (CC) or in-medium SRG (see e.g., [75] for a connection between GF and CC formalisms). Importantly, by preserving at each order the analytical properties of the exact self-energy, the ADC expansion ensure that causality is not violated. Moreover, this form allows the derivation of an energy-independent auxiliary eigenvalue problem that significantly simplifies the numerical solution of Dyson and Gorkov equations, as discussed in section 3.2.

The ADC scheme has been developed in the context of finite nuclei in the past few years. At present, ADC(1), ADC(2), and ADC(3) self-energies are implemented in the Dyson framework [35, 37], while ADC(1) and ADC(2) are available in the Gorkov case [31, 32]. Gorkov-ADC(3) is under construction within a project whose goal is to automatize the generation of the associated self-energy diagrams. In Dyson theory, the ADC formalism has been recently generalized to the presence of three-body interactions [34].

Generally speaking, ADC(n) defines a truncation scheme that is systematically improvable in the sense that going to higher orders should provide results closer and closer to the exact solution, recovered in the limit of ADC(∞). Nevertheless, in the case of perturbation theory (and, by consequence, resummation methods building on MBPT), there does not exist a well-defined expansion parameter informing on the accuracy associated to a certain truncation level. Hence, there are two ways of assessing the accuracy of a given approximation: (i) by comparing successive orders in the expansion and (ii) via benchmarks with exact methods. Concerning the first possibility, a typical convergence behavior for ADC(1-3) is shown in **Figure 1** for ground-state energies and root-mean-square (rms) charge radii of two representative medium-mass nuclei. Two different interactions are used, the "soft" *NN*+3*N*(lnl) and the "harder" NNLO$_{\rm sat}$(see section 3.4 for details). One observes a clear pattern going from ADC(1) to ADC(3) for all quantities. For total energies, while ADC(2) already yields a qualitatively

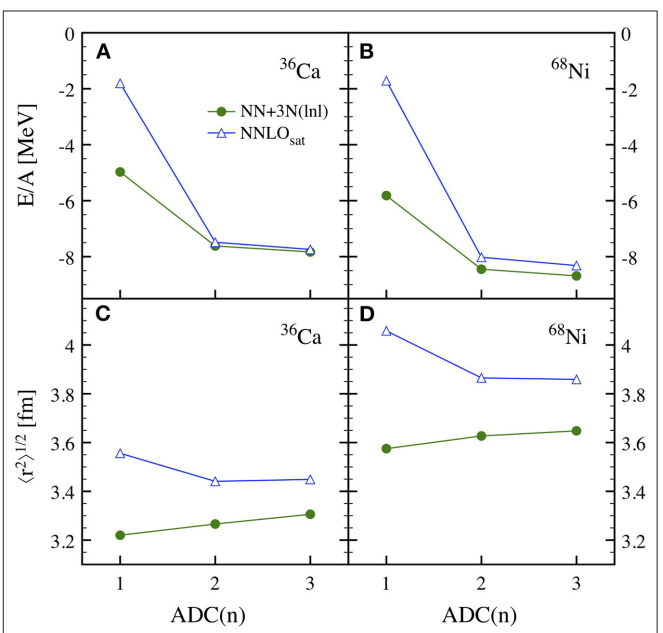

FIGURE 1 | Ground-state energies **(top)** and rms charge radii **(bottom)** of ^{36}Ca and ^{68}Ni computed within different ADC(n) truncation schemes. Results for the NNLO$_{\rm sat}$ and *NN*+3*N*(lnl) interactions are displayed. Reprinted figure with permission from [40], copyright (2020) by the American Physical Society.

[8]Other types of resummation are employed in other domains. For instance, in solid-state physics the resummation of particle-hole (i.e., ring) diagrams (typically in the so-called *GW* approximation) allows resolving the long-range features of the Coulomb force [66].

good account, additional correlations introduced at the ADC(3) level are deemed necessary for an accurate description. In contrast, charge radii are already largely converged at the ADC(2) level. After analysing the ADC convergence behavior, one expects ADC(4) corrections to be small for total energies and negligible for charge radii. The accuracy of the ADC(3) scheme is also confirmed by a direct benchmark against no-core shell model in ^{16}O, with total energies computed in the two approaches differing by less than 1% for any tested interaction [40].

3.2. Working Equations

In practice, solving Dyson or Gorkov equations in their forms Equations (2) and (14) is problematic, specially for finite systems where a solution has to be achieved for numerous (discrete) values of the energy ω. A method to overcome the problem was proposed once again in quantum chemistry [76], and consists of two steps. In the first one, after exploiting the analytical energy dependence of the propagator, Equation (2) is transformed into an eigenvalue equation where the (energy-dependent) self-energy acts as an effective one-body potential. The second steps makes use of the analytical energy dependence of the self-energy in the form of Equation (16) and rewrites the problem as an energy-independent eigenvalue equation. The latter constitutes the working equation to be solved iteratively, and whose solutions directly provide amplitudes and energies entering Equation (8) for the one-body propagator (see [58] for a more detailed discussion). The derivation of this energy-independent eigenvalue problem has been generalized to Gorkov theory in [31].

One disadvantage of the energy-independent formulation is that the number of energy poles, i.e., the eigenvalues and the dimensionality of the energy-independent Dyson or Gorkov matrix, increases at each self-consistent iteration. In practice, this growth is reduced via the application of Krylov projection techniques [76, 77], typically implemented by means of a Lanczos algorithm (see [32] for a detailed discussion and a numerical study).

3.3. Choice of Basis

Equations presented in section 2 are general, i.e., are valid in any basis of choice[9]. In an actual calculation, one needs to specify a basis in which operators, together with all relevant quantities, are expanded on. In the case of atomic nuclei one typically employs a one-body spherical harmonic oscillator (HO) basis, whose eigenfunctions are well suited to the description of a confined system[10]. A HO basis is characterized by two parameters: the oscillator inverse length $\hbar\Omega$ and the number of considered HO wave functions. The latter is usually determined by the parameter $e_{\max} \equiv \max(2n + l)$, which sets the energy threshold of a basis eigenfunction. Many-body bases are subsequently built as direct products of one-body bases. While naturally for a k-body operator one would set $e_{k\max} = k \cdot e_{\max}$, the storage of three-body matrix elements for realistic values of $e_{\max}$ presently constitutes an issue and obliges one to work with $e_{3\max} \lll 3 \cdot e_{\max}$. In current state-of-the-art implementations, typical values of $e_{\max} = 12 - 15$, $e_{2\max} = 2 \cdot e_{\max}$, and $e_{3\max} = 14 - 18$ are used.

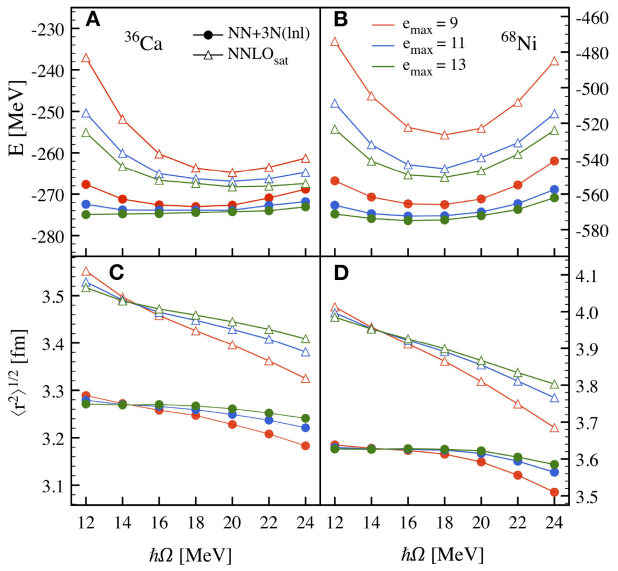

FIGURE 2 | Ground-state energies **(top)** and rms charge radii **(bottom)** of ^{36}Ca and ^{68}Ni computed with the *NN*+3*N*(lnl) and NNLO$_{sat}$ Hamiltonians as a function of the harmonic oscillator parameter $\hbar\Omega$ and for increasing size $e_{\max}$ of the one-body basis. In all cases $e_{3\max} = 16$ was used. Reprinted figure with permission from [40], copyright (2020) by the American Physical Society.

The first step of a calculation consists in studying the convergence properties (of the observables of interest) with respect to the basis size and oscillator parameter. An example is shown in **Figure 2**, where the basis dependence of ground-state energy and charge radius is investigated for two different nuclei and two different Hamiltonians with ADC(2) calculations. One sees that in ^{36}Ca an $e_{\max} = 13$ model space guarantees sufficiently converged results. In ^{68}Ni and for the higher-cutoff Hamiltonian NNLO$_{sat}$ (see next section for details) the convergence is not yet optimal.

Combining uncertainties from basis truncation, discussed here, and from many-body expansion, discussed in section 3.1,

[9]Since the present formalism is written in single-nucleon coordinates, the appearance of center-of-mass (c.o.m.) contributions might pollute the computation of different quantities/observables and must be taken care of. As for energies, the c.o.m. kinetic energy $\hat{T}_{\text{c.o.m.}}$ is subtracted from the total Hamiltonian from the outset, such that one eventually works with the intrinsic Hamiltonian $\hat{H}_{\text{int}} \equiv \hat{H} - \hat{T}_{\text{c.o.m.}}$. Although in the present truncation scheme this does not lead to an exact factorization of c.o.m. and intrinsic wave functions, it has been demonstrated in similar correlation-expansion methods [18, 78] that such an approximate c.o.m. correction is sufficient for all practical purposes. Furthermore, specific *a posteriori* corrections are applied for radii and densities [see discussion in section 4.1 and, e.g., [36] for more details].

[10]On the other hand, the asymptotic behavior of HO wave functions do not correctly account for the fall-off of the nuclear wave function. As a consequence, a HO basis is not well-suited to describe states near the particle continuum, where the long-range part of the wave function is particularly important. In this case, a possibility consists in complementing the HO with a basis specifically designed to account for resonances and non-resonant continuum, e.g., the Berggren basis [79, 80].

one can evaluate the total theoretical error of the method for a given input interaction. To give an example [40], for soft potentials, like the *NN*+3*N*(400) and the *NN*+3*N*(lnl) Hamiltonians presented in the next section, one estimates an error of about 2% ($< 0.5\%$) associated to ground-state energies (radii) of medium-mass nuclei. For harder potentials, like the NNLO_{sat} Hamiltonian, the errors rise to 4 and 1% for energies and radii, respectively. To a good extent, these uncertainties cancel out when differential observables are considered, as in the case of one- or two-nucleon separation energies. In the results presented in the following such systematic uncertainties are not explicitly reported in the figures (except for **Figures 8**, **10**) and should be kept in mind by the reader.

3.4. Choice of Input Interaction

Like most of *ab initio* techniques, self-consistent GFs can take in principle any nucleon-nucleon plus three-nucleon (NN+3N) Hamiltonian as input. In the early 2000s, nearly all applications were performed using semi-phenomenological[11] potentials like CD-Bonn [84] or Nijmegen [85], possibly complemented with three-nucleon forces [72, 86]. Although these interactions had proven successful in the description of light nuclei, their "hard" character, i.e., the associated large momentum cutoff, required the use of sophisticated resummation schemes, thus hindering applications in medium-mass nuclei. Starting from 2010, the use of Hamiltonians derived in the context of chiral effective field theory (χ-EFT) [5] began to spread. Compared to the previous phenomenological models, χ-EFT interactions present several advantages:

1. By explicitly taking into account only low-energy degrees of freedom, they have a much smaller associated cutoff;
2. All many-body (i.e., 2N, 3N, 4N, ...) operators and currents are derived consistently without any *ad-hoc* assumption, which augments the predictive power;
3. A theoretical error can be associated to a given χ-EFT Hamiltonian (which relates to the employed truncation in the EFT expansion).

Nowadays, χ-EFT interactions constitute the standard for *ab initio* nuclear structure calculations. The first feature, i.e., their "softness," is often further amplified by the use of similarity renormalization group (SRG) techniques [6], i.e., unitary transformations of the Hamiltonian that further decouple low- and high-momentum modes, leading to much improved convergence properties. The third point implies that the EFT error can (and should) be subsequently propagated to many-body observables. This has been done in practice only very recently (see e.g., [16, 87–92]) and more formal and technical developments along these lines will be required in the future.

Mainly three different χ-EFT Hamiltonians have been employed in recent GF calculations, all of which are discussed here. The first one, labeled *NN*+3*N*(400), is based on the next-to-next-to-next-to-leading order (N^3LO) nucleon-nucleon potential from Entem and Machleidt [4, 93] combined with the N^2LO 3*N* interaction with a local regulator [94]. The 2*N* interaction of [93] was built with a cutoff of 500 MeV/c, however, a 400 MeV/c regulator was used for the 3*N* sector [95]. This Hamiltonian has been systematically applied to *p*- and *sd*-shell nuclei and yields a good reproduction of oxygen, nitrogen and fluorine binding energies [35, 36, 96]. Nevertheless, it leads to overbinding in medium-mass nuclei starting in the calcium chain and underpredicts nuclear radii even for O isotopes [39, 53, 97].

With the main objective of improving on the description of radii, a chiral Hamiltonian with terms up to N^2LO was developed in [98]. It is characterized by a simultaneous fit of 2*N* and 3*N* LECs that does not rely solely on two-nucleon and $A = 3, 4$ data, but also on binding energies of ^{14}C and ^{16,22,24,25}O as well as charge radii of ^{14}C and ^{16}O. The resulting interaction, named NNLO_{sat}, successfully describes the saturation of infinite nuclear matter [98] as well as various observables in mid-mass nuclei, including charge radii [42–44, 53]. Unlike the *NN*+3*N*(400) interaction, NNLO_{sat} employs a non-local regulator.

Motivated by the success of NNLO_{sat}, a novel interaction named *NN*+3*N*(lnl) was presented recently [40]. The goal was to amend the original *NN*+3*N*(400) interaction, and in particular its 3*N* part. While the latter has been shown to be problematic, its 2*N* part is instead believed to perform relatively well and thus is kept unchanged. Being based on the N^3LO potential, which provides a better description of nucleon-nucleon data compared to the lower-order NNLO_{sat}, it yields superior features in light systems, e.g., a better reproduction of spectroscopy of natural parity states in *p*- and light *sd*-shell nuclei. *NN*+3*N*(lnl) has been also shown to provide a very good description of energy observables (ground-state energies and energy spectra) in medium-mass nuclei up to mass $A \sim 60$ [40].

3.5. Computational Requirements

As any other state-of-the-art *ab initio* nuclear structure approach, the SCGF method requires the development of an advanced numerical code. The computational cost of a simulation strongly depends on (i) the size of the model space, (ii) the chosen level of approximation[12], and (iii) the two- or three-body character of the input Hamiltonian. ADC(1) calculations with only NN forces can be easily performed on a laptop also in large bases (in few CPU minutes). Going to ADC(2) limits a laptop calculation to a small, yet (semi-)realistic model space, typically $e_{\max} = 8 - 9$ (doable in a few CPU hours). If larger bases are needed (to ensure model-space convergence, e.g., typically $e_{\max} = 12 - 13$), then one has to resort to a dedicated computer cluster (with a corresponding cost of few hundred CPU hours). ADC(3) is doable on a laptop only for very small model spaces and any realistic calculation requires the implementation of MPI parallelization and the use of a high-performance computing center (with running times of several thousand CPU hours).

The inclusion of 3N forces results into an increase of both CPU time (due to the higher rank of the tensors at play) and

[11] For example, based on a one-boson exchange model plus phenomenological corrections.

[12] For a given approximation, a Gorkov calculation is more costly than a Dyson one because of the increased dimensionality of the quasiparticle space. Estimates presented in this section refer to Dyson calculations of typical medium-mass nuclei.

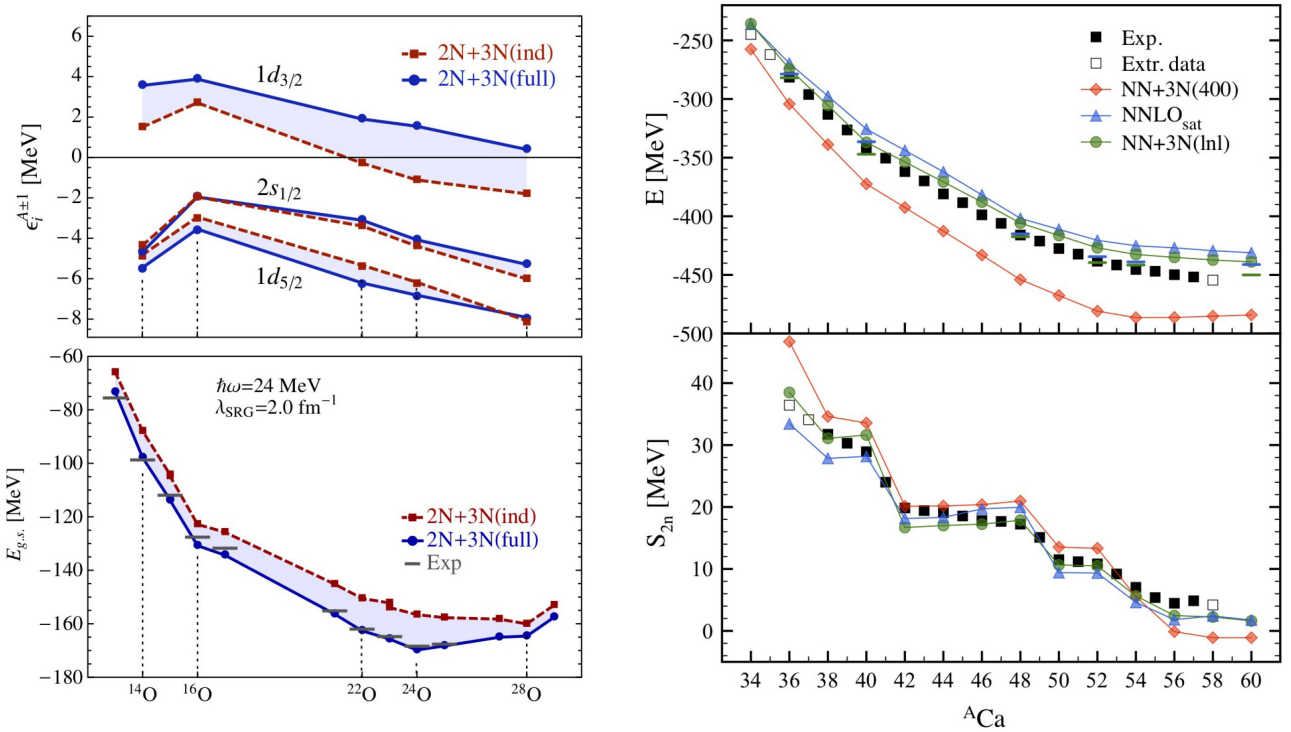

FIGURE 3 | (Left) ADC(3) calculations of closed-shell oxygen isotopes performed with the *NN*+3*N*(400) Hamiltonian (blue points and lines). For reference, results with only original 2*N* operators are displayed (red points and lines). (Top) One-neutron addition and removal energies associated to dominant quasiparticle peaks. (Bottom) Ground-state energies compared with experimental values (gray bars). Adapted figure with permission from [35], copyright (2013) by the American Physical Society. **(Right)** ADC(2) calculations of even-even calcium isotopes performed with the *NN*+3*N*(400), NNLO$_{sat}$, and *NN*+3*N*(lnl) Hamiltonians (colored points and lines), compared with measured and extrapolated data (black points). ADC(3) results are depicted as horizontal lines when available. (Top) Total ground-state energies. (Bottom) Two-neutron separation energies. Adapted figure with permission from [40], copyright (2020) by the American Physical Society.

memory usage (due to the larger amount of matrix elements to be stored). As a consequence, on a laptop and for realistic bases, even an ADC(1) calculation becomes heavy in terms of CPU and one quickly reaches the limits in terms of available RAM[13]. ADC(2) and ADC(3) calculations require optimized implementations and the use of a high-performance computing center, with typical running times of a few thousand and tens of thousands CPU hours, respectively.

4. RECENT APPLICATIONS

4.1. Ground-State Properties

The total ground-state energy, or binding energy, of a nucleus constitutes the most basic nuclear structure observable. In Green's function theory, total energies are preferably computed via the generalized GMK sum-rule (Equation 6). While earlier applications made use of a 2*N*-only Hamiltonian, possibly complemented by a phenomenological correction to compensate for missing 3*N* [29, 30, 38], starting from 2013 calculations with realistic $2N + 3N$ interactions could be routinely performed. A representative example concerns the oxygen chain [35] and is shown in **Figure 3** (left). In the bottom panel, ADC(3) ground-state energies are displayed for closed-shell oxygen isotopes, computed with the *NN*+3*N*(400) interaction, respectively excluding and including original 3*N* operators[14]. One notices that the addition of 3*N* forces is crucial for a quantitative reproduction of experimental data. In particular, when only a 2*N* interaction is considered, the neutron dripline is wrongly located at $N = 20$, while it is correctly reproduced at ^{24}O in the presence of 3*N* forces.

In such a context it can be instructive to inspect one-neutron addition and removal energies associated to dominant quasiparticle peaks, see top-left panel of **Figure 3**. One sees that the $3/2^+$ fragment becomes bound in neutron-rich isotopes when the 2*N*-only Hamiltonian is employed. When 3*N* interactions are switched on, it is instead pushed up and remains unbound all the way to ^{28}O, thus explaining the position of the dripline. This observation confirmed the repulsive character of the Fujita-Miyazawa 3*N* interaction, as previously discussed in [99].

This result was one of the first successful applications of *ab initio* techniques beyond light nuclei. The oxygen

[13]See also discussion in section 5.3 on storage of 3N matrix elements.

[14]The SRG evolution described in section 3.4 and standardly applied to nuclear Hamiltonians induces additional many-body operators that need to be taken into account [6]. Hence, one has to distinguish between *original* and *induced* e.g., 3*N* forces.

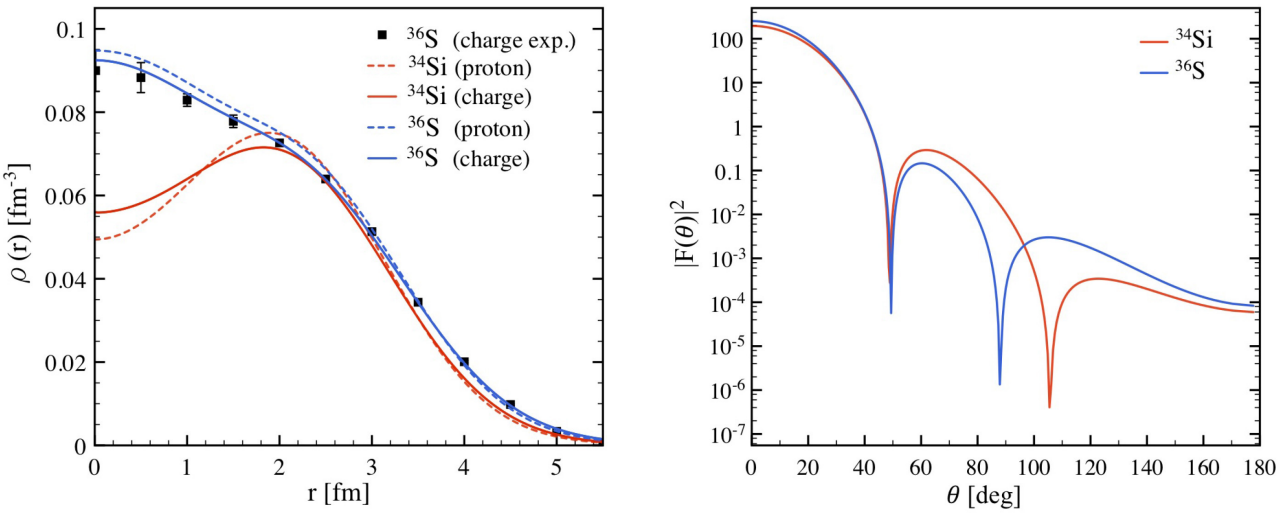

FIGURE 4 | (Left) Point-proton and charge densities of ^{34}Si and ^{36}S computed at the ADC(3) level with the NNLO$_{sat}$ interaction. The experimental charge density of ^{36}S is taken from [114]. **(Right)** Angular dependence of the charge form factor computed for 300 MeV electron scattering. Modified figure with permission from [37], copyright (2017) by the American Physical Society.

chain also constituted, for a few years, a testbed where calculations from various approaches could be benchmarked, demonstrating the reliability of the different many-body truncations [23, 96, 100, 101]. More recently, the availability of new Hamiltonians prompted calculations of heavier systems, from calcium up to the nickel chain. An example is constituted by Gorkov GF calculations exploring the performance of three interactions along few semi-magic chains, as reported in [40]. A typical outcome is the one displayed in **Figure 3** (right), where ground-state energies of calcium isotopes as well as their differences, two-neutron separation energies, are shown as a function of neutron number. The overbinding generated by the older *NN*+3*N*(400) clearly stands out. In contrast, the newer Hamiltonians NNLO$_{sat}$ and *NN*+3*N*(lnl) yield an excellent reproduction of total as well as differential ground-state energies, specially once ADC(3) corrections are taken into account. A good performance is found also in the nickel chain, up to the point where current computational limitations hinder a complete model-space convergence of the calculations [40]. In addition to semi-magic chains, the theory was tested in relation to novel experimental measurements in potassium [47], titanium [48], and argon [102] chains.

The performance of these three Hamiltonians was further investigated on nuclear radii in [40]. It was found that NNLO$_{sat}$ provides a good account of rms charge radii all the way up to nickel. Specifically, the bulk contributions are well-described already at the ADC(2) level, while finer details (e.g., the parabolic behavior observed between ^{40}Ca and ^{48}Ca) need further improvement of the many-body truncation and/or the interaction. Density distributions provide even further insight into the way nucleons arrange themselves in the correlated nuclear medium. The nuclear charge density distribution is typically obtained as a sum of three contributions [103],

$$\rho_{\rm ch}(r) = \rho^{\rm p}_{\rm ch}(r) + \rho^{\rm n}_{\rm ch}(r) + \rho^{\rm ls}_{\rm ch}(r), \tag{17}$$

where $\rho^{\rm p}_{\rm ch}$ ($\rho^{\rm n}_{\rm ch}$) is determined by folding the point-proton (point-neutron) density with the finite charge distribution of the proton (neutron) and $\rho^{\rm ls}_{\rm ch}$ is a relativistic correction that depends on spin-orbit terms. In addition, center-of-mass and relativistic Darwin-Foldy corrections are taken into account by employing an effective position variable [104]. Finite nucleon charge distributions can be expressed as a sum of Gaussians, with the parameters adjusted to reproduce form factors from electron scattering data [105]. The relativistic spin-orbit correction is usually computed within the factorization approximation introduced in [106]. Even though $\rho^{\rm p}_{\rm ch}$ largely dominates, the other two contributions can visibly alter the total charge distribution in some cases.

As for radii, densities are computed directly from the one-body GF and can therefore be routinely evaluated for medium-mass systems. An interesting example relates to the possible presence of a depletion in the central part of the charge density profile, usually referred to as *bubble*. One of the most likely candidates has been identified in the nucleus ^{34}Si [107–113]. In [37] this system, together with its $Z+2$ partner ^{36}S, has been thoroughly investigated by means of both Dyson and Gorkov GF calculations. The resulting point-proton and charge density distributions are shown in **Figure 4** (left). The effect of folding with the finite size of the proton is specially visible in the center, with an attenuation of oscillations in the charge profiles. The agreement between the computed and the measured charge distribution for the stable nucleus ^{36}S is excellent, which gives confidence in the prediction for the unstable ^{34}Si, yet unknown experimentally. For the latter, a depletion in the region below 2

fm is indeed found. Its magnitude is comparable or even larger than what previously obtained in EDF [111, 112] or shell model calculations [110].

A measurement of the charge distribution of ^{34}Si would require electron scattering on radioactive ions. These experiments are becoming feasible only now [115], with first results on the heavier ^{132}Xe obtained by the SCRIT collaboration [83]. In the coming years, the case of ^{34}Si will thus constitute an interesting objective for electron-nucleus scattering facilities. Such a measurement would extract the electromagnetic charge form factor, related to the charge profile via

$$F(q) = \int d\vec{r}\rho_{\rm ch}(r)e^{-i\vec{q}\cdot\vec{r}}\,, \tag{18}$$

where $\vec{q}$ is the transferred momentum, itself related to the incident momentum $\vec{p}$ and the scattering angle θ via $q = 2p\sin\theta/2$. The calculated charge form factors for 300 MeV electron scattering on ^{34}Si and ^{36}Si are displayed in **Figure 4** (right). Clear differences appear in the angular dependence for the two systems, with a higher magnitude and a displaced position of the second minimum for ^{34}Si. This analysis gives indications on what range of transferred momenta, and consequently which luminosities, are necessary for identifying possible depleted density profiles in this mass region.

4.2. Excited-State Properties

An asset of GF theory resides in the rich content of the one-body propagator, which does not solely provide information on the targeted (even-even) system with mass number A but also on the four neighboring (odd-even) $A \pm 1$ nuclei. This information is explicit in the Lehmann representation of the GF (Equation 8). The poles $E_i^{\pm}$ of the function correspond to one-nucleon addition and removal energies, as schematically depicted in **Figure 5** (top left). In addition, the associated amplitudes in the numerator represent the probabilities to reach a specific eigenstate $|\Psi_n^{A+1}\rangle$ ($|\Psi_k^{A-1}\rangle$) of the $A+1$ ($A-1$) system by adding (removing) a nucleon in a single-particle state to (from) the ground state $|\Psi_0^A\rangle$ of the even-even system. Those amplitudes

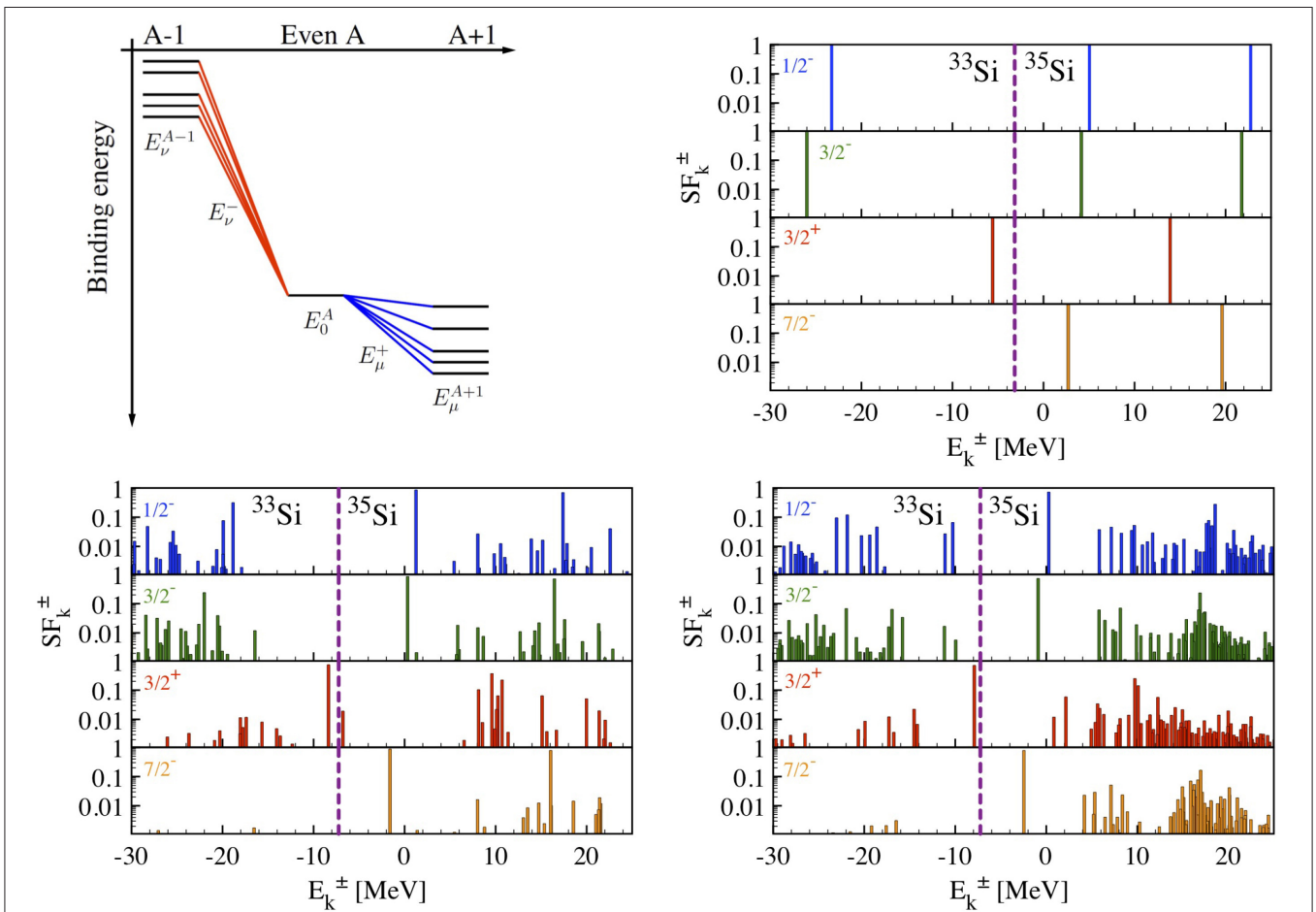

FIGURE 5 | (Top left) Schematic view of the $A \pm 1$ states (and associated energies) reached via one-nucleon addition and removal. **(Top right)** Neutron spectral strength distribution in ^{34}Si computed at the ADC(1) level with the NNLO$_{\rm sat}$ interaction. The four panels display different angular momentum and parity channels. The dashed vertical line represents the Fermi energy, separating the spectra of ^{33}Si and ^{35}Si. **(Bottom)** Same as above but for ADC(2) and ADC(3) calculations. Data originates from the results of [37].

can be expanded in a single-particle basis $\{a^\dagger_\alpha\}$ according to

$$U^\alpha_n \equiv \langle \Psi^{\rm A}_0 | a_\alpha | \Psi^{\rm A+1}_n \rangle \,, \tag{19a}$$
$$V^\alpha_k \equiv \langle \Psi^{\rm A}_0 | a^\dagger_\alpha | \Psi^{\rm A-1}_k \rangle \,. \tag{19b}$$

Next, spectroscopic probability matrices for the nucleon addition and removal can be built[15], $\mathbf{S}^+_n \equiv \mathbf{U}_n\mathbf{U}^\dagger_n$ and $\mathbf{S}^-_k \equiv \mathbf{V}^*_k\mathbf{V}^T_k$, respectively. Their elements read as

$$S^{+\alpha\beta}_n \equiv \langle \Psi^{\rm A}_0 | a_\alpha | \Psi^{\rm A+1}_n \rangle \langle \Psi^{\rm A+1}_n | a^\dagger_\beta | \Psi^{\rm A}_0 \rangle \,, \tag{20a}$$
$$S^{-\alpha\beta}_k \equiv \langle \Psi^{\rm A}_0 | a^\dagger_\beta | \Psi^{\rm A-1}_k \rangle \langle \Psi^{\rm A-1}_k | a_\alpha | \Psi^{\rm A}_0 \rangle \,. \tag{20b}$$

Taking the trace over the one-body Hilbert space $\mathcal{H}_1$ leads to spectroscopic factors

$$SF^+_n \equiv {\rm Tr}_{\mathcal{H}_1}\big[\mathbf{S}^+_n\big] = \sum_{\alpha\in\mathcal{H}_1} \big|U^\alpha_n\big|^2 \,, \tag{21a}$$
$$SF^-_k \equiv {\rm Tr}_{\mathcal{H}_1}\big[\mathbf{S}^-_k\big] = \sum_{\alpha\in\mathcal{H}_1} \big|V^\alpha_k\big|^2 \,, \tag{21b}$$

which are the norms of the spectroscopic amplitudes. A spectroscopic factor thus sums the probabilities that an eigenstate of the $A+1$ ($A-1$) system can be described as a nucleon added to (removed from) a single-particle state on top of the ground state of the A-nucleon system.

The complete spectroscopic information associated with one-nucleon addition and removal processes can be collected into the spectral function $\mathbf{S}(\omega)$, defined as the energy-*dependent* matrix on $\mathcal{H}_1$

$$\mathbf{S}(\omega) \equiv \sum_{n\in\mathcal{H}_{A+1}} \mathbf{S}^+_n \,\delta(\omega - E^+_n) + \sum_{k\in\mathcal{H}_{A-1}} \mathbf{S}^-_k \,\delta(\omega - E^-_k), \tag{22}$$

where the first (second) sum runs over eigenstates of H in the Hilbert space $\mathcal{H}_{A+1}$ ($\mathcal{H}_{A-1}$) associated with the $A+1$ ($A-1$) system. Taking the trace of $\mathbf{S}(\omega)$ gives the spectral strength distribution (SDD)

$$\begin{aligned}\mathcal{S}(\omega) &\equiv {\rm Tr}_{\mathcal{H}_1}\big[\mathbf{S}(\omega)\big] \\ &= \sum_{n\in\mathcal{H}_{A+1}} SF^+_n \,\delta(\omega - E^+_n) + \sum_{k\in\mathcal{H}_{A-1}} SF^-_k \,\delta(\omega - E^-_k)\,,\end{aligned} \tag{23}$$

which is a basis-independent function of the energy. Equations (19)–(23) can be generalized to the Gorkov formalism [31].

An example of SDD computed at three different levels of approximation, ADC(1-3), is shown in **Figure 5** for the nucleus ^{34}Si. ADC(1), i.e., Hartree-Fock, is a mean-field (or independent-particle) approximation, which translates into a series of quasiparticle peaks with unity spectroscopic factors, i.e., there is a one-to-one correspondence between the single-particle basis $\{a^\dagger_\alpha\}$ and the many-body states $|\Psi^{\rm A\pm1}_i\rangle$ accessible via the process of adding or removing a nucleon. One can nevertheless identify the main qualitative features of the SDD, e.g., associate the ground state of ^{33}Si (^{35}Si) with the first peak on the left (right) of the Fermi energy characterized by spin and parity $3/2^+$ ($7/2^-$). ADC(2) introduces the lowest-order dynamical correlations that lead to a first fragmentation of the spectral distribution. A number of fragments with small spectroscopic factors appear in the vicinity of the ADC(1) peak, which is now shifted in energy and reduced in strength, i.e., it has $SF^\pm_i < 1$. ADC(3) correlations further fragment the quasiparticle strength, giving rise to a large number of small peaks and a further reduction of the main-peak spectroscopic factor. One notices that, around the Fermi energy, fragments with a good quasiparticle character, i.e., large spectroscopic factors, survive, in accordance to Landau's Fermi liquid theory. In contrast, away from the Fermi level the strength is spread over a wide energy interval and one can hardly identify single-particle-like excitations.

From the SDD depicted in **Figure 5** one can extract an excitation spectrum of the $A-1$ ($A+1$) system, by looking at increasingly negative (increasingly positive) energies on the left (right) of the Fermi surface (see top-left panel for a schematic representation). By comparing ADC(2) and ADC(3) truncations, one concludes that the latter is necessary for an accurate description of the main energy peaks [37, 40], in accordance with analogous calculations in quantum chemistry [116–119]. Conservatively, one can associate uncertainty bands with ADC(2)-ADC(3) differences, as done in **Figure 6** where spectra resulting from one-nucleon addition and removal from and to ^{54}Ca are displayed. These four systems sit at the limits of what can be presently studied in radioactive ion beam facilities. Yet, not many experimental data are available, such that these calculations mostly represent predictions that can be presumably tested in the near future. In ^{53}Ca, where the ground state and two excited states are identified, *NN*+3*N*(lnl) GF calculations succeed in reproducing the measured spectrum in with good accuracy. NNLO$_{\rm sat}$ instead mildly overestimates the splitting between the two excited states. In ^{53}K, the difference between the two interactions is even more striking. While *NN*+3*N*(lnl) reproduces the measured first excited state with good precision, NNLO$_{\rm sat}$ predicts a wrong ordering of the $3/2^+$ and $1/2^+$ states, resulting in a ground state with incorrect spin. The potassium chain indeed constitutes an interesting case because of an unusual inversion (at $N=28$) and re-inversion (at $N=32$) of the spins of the ground- and first excited states [50, 120]. As discussed in [40, 52], Gorkov GF calculations with the *NN*+3*N*(lnl) Hamiltonian yield ax excellent reproduction of the whole trend, from ^{37}K to ^{53}K. Such studies, complementary to those focusing on ground-state observables, are not only relevant in relation to current experimental programs, but also provide a unique testing ground for the development of nuclear interactions.

The spectral representation of the one-body GF thus gives access to spectroscopic studies of odd-even nuclei. If one is interested in the excitations of an even-even system, the two-body GF (in one of its possible time orderings) has to be considered instead. A typical example is the polarization propagator, which provides the response of the nuclear system to an external

[15]Here bold symbols denote matrices in the one-body Hilbert space $\mathcal{H}_1$.

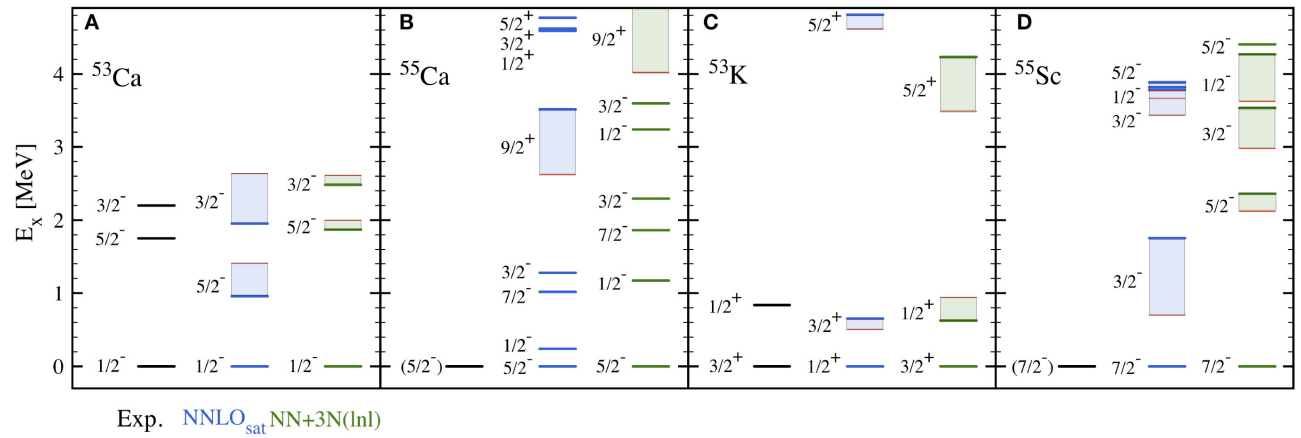

FIGURE 6 | One-nucleon addition (panels **B** and **D**) and removal (panels **A** and **C**) spectra starting from ^{54}Ca. Available experimental data appear in the left column of each panel. GF calculations performed with the NNLO$_{sat}$ and *NN*+3*N*(lnl) interactions are displayed in the central and right column of each panel, respectively. Red lines constitute results obtained at the ADC(3) level. Shaded areas connect ADC(2) and ADC(3) where available. In all panels, states with $E_x < 5$ MeV and $SF < 10\%$ are shown. Modified figure with permission from [40], copyright (2020) by the American Physical Society. Additional new experimental data are from [51, 52].

operator. In analogy to Equation (8), its Lehmann representation reads as

$$\Pi_{\gamma\delta,\alpha\beta}(\omega) = \sum_{n_\pi \neq 0} \frac{\langle \Psi_0^A | a_\delta^\dagger a_\gamma | \Psi_{n_\pi}^A \rangle \langle \Psi_{n_\pi}^A | a_\alpha^\dagger a_\beta | \Psi_0^A \rangle}{\omega - (E_{n_\pi}^A - E_0^A) + i\eta} - \sum_{n_\pi \neq 0} \frac{\langle \Psi_0^A | a_\alpha^\dagger a_\beta | \Psi_{n_\pi}^A \rangle \langle \Psi_{n_\pi}^A | a_\delta^\dagger a_\gamma | \Psi_0^A \rangle}{\omega + (E_{n_\pi}^A - E_0^A) - i\eta} , \quad (24)$$

where n_π label the excited states of the A-body system. In the numerators, the residues

$$\mathcal{Z}_{\alpha\beta}^{n_\pi} \equiv \langle \Psi_{n_\pi}^A | a_\alpha^\dagger a_\beta | \Psi_0^A \rangle . \quad (25)$$

represent particle-hole matrix elements between excited states of the A-nucleon system. The poles appearing in the denominator

$$\epsilon_{n_\pi}^\pi \equiv E_{n_\pi}^A - E_0^A \quad (26)$$

instead constitute energy differences between excited states of the A-nucleon system and its ground-state. The polarization propagator (Equation 24) is obtained as a solution of the Bethe-Salpeter equation,

$$\Pi_{\gamma\delta,\alpha\beta}(\omega) = \Pi^{(0)}_{\gamma\delta,\alpha\beta}(\omega) + \sum_{\mu\rho\nu\sigma} \Pi^{(0)}_{\gamma\delta,\mu\rho}(\omega) K^{(ph)}_{\mu\rho,\nu\sigma}(\omega) \Pi_{\nu\sigma,\alpha\beta}(\omega) , \quad (27)$$

where $\Pi^{(0)}(\omega)$ is the free polarization propagator, and the particle-hole irreducible interaction $K^{(ph)}$ plays a similar role as that of the self-energy in Equation (2) for the single-particle propagator. While the corresponding formalism has been developed and implemented for Dyson GFs, the generalization to the Gorkov framework remains to be carried out.

In [42, 121], the polarization propagator was calculated with the aim of accessing the nuclear isovector electric dipole (E1) response. A dressed random phase approximation (DRPA) was adopted for the computation of $\Pi(\omega)$. The scheme makes use of a correlated, e.g., ADC(3), one-body propagator as the starting point for the RPA equations, thus going beyond a simple HF-based particle-hole resummation. **Figure 7** shows results for the integrated isovector E1 photoabsorption cross section, which is directly obtained from the polarization propagator [42]. Two representative examples are shown here, ^{16}O and ^{48}Ca. Calculations make use of the NNLO$_{sat}$ interaction, ensuring that nuclei have the correct size, which is a crucial property for this application. In ^{16}O the peak associated to the giant dipole resonance (GDR) is well-reproduced. At higher excitation energies, the calculation underestimates the experimental spectrum, presumably due to missing correlations beyond the simple RPA. A similar picture emerges for ^{48}Ca, with the GDR peak in good agreement with recent experimental measurements [124] and the high-energy tail missing some strength. Several other closed-shell nuclei, for some of which experimental data are not yet available, are discussed in [42]. A generalization of this formalism to the Gorkov framework would allow us to extend these promising results to a large number of open-shell nuclei.

4.3. Lepton-Nucleus Scattering

The spectral function introduced in Equations (22)–(23) carries information about the energy-momentum distribution of the correlated nucleons. Certain scattering processes, where an external probe scatters off the nucleus, under certain kinematical conditions (e.g., characterized by a sufficiently large momentum transfer), can be described as an incoherent sum of scattering amplitudes on bound nucleons. Then, the cross section can be computed in the so-called impulse approximation and expressed as a sum of one-body terms containing a convolution with the nucleon spectral function.

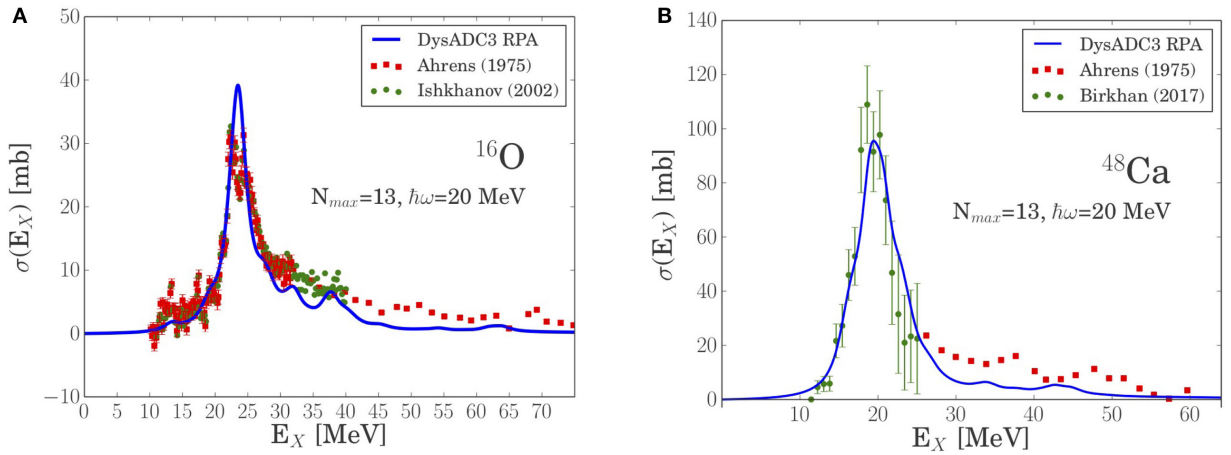

FIGURE 7 | Isovector E1 photoabsorbption cross section of ^{16}O **(A)** and ^{48}Ca **(B)** computed with the NNLO$_{sat}$ interaction. Theoretical curves are obtained by folding the discrete spectra with Lorentzian widths $\Gamma = 3$ MeV. Experimental data are from [122–124]. Adapted figure with permission from [42], copyright (2019) by the American Physical Society.

This is the case, e.g., of electron and neutrino scattering in the region of the quasielastic peak. Here the double differential cross section for inclusive lepton-nucleus scattering can be written as [125]

$$\left(\frac{d\sigma}{dE'd\Omega'}\right)_\ell = C_\ell \frac{E'_k}{E_k} L_{\mu\nu} W^{\mu\nu}, \tag{28}$$

where $L_{\mu\nu}$ is the leptonic tensor and $k = (E_k, \mathbf{k})$ and $k' = (E'_k, \mathbf{k}')$ are the laboratory four-momenta of the incoming and outgoing leptons, respectively. The factor $C_\ell = \alpha/(k-k')^4$ for electrons and $C_\ell = G/8\pi^2$ for neutrinos, where $G = G_F$ for neutral current (NC) and $G = G_F \cos\theta_c$ for charged current (CC) processes. The electroweak coupling constants are $\alpha \simeq 1/137$, $G_F = 1.1803 \times 10^{-5}\,\text{GeV}^{-2}$ [126] and $\cos\theta_c = 0.97425$ [127]. The hadron tensor $W^{\mu\nu}$ incorporates the transition matrix elements from the target ground state $|\Psi_0^A\rangle$ to the final states $|\Psi_f^A\rangle$ due to the hadronic currents, including additional axial terms for neutrino scattering. The impulse approximation consists in factorizing $|\Psi_f^A\rangle \rightarrow |\mathbf{p}'\rangle \otimes |\Psi_n^{A-1}\rangle$, i.e. it allows to work with the outgoing nucleon of momentum $\mathbf{p}'$ and the residual nucleus, left in a state $|\Psi_n^{A-1}\rangle$. This leads to [128, 129]

$$W^{\mu\nu}_{1b}(\mathbf{q},\omega) = \int \frac{d^3\mathbf{p}'\,dE}{(2\pi)^3} \frac{m_N^2}{e(\mathbf{p}')e(\mathbf{p}'-\mathbf{q})} \delta(\omega + E - e(\mathbf{p}')) \times \sum_s S_s^h(\mathbf{p}'-\mathbf{q}, E) \langle p'|j_s^{\mu\dagger}|p'-q\rangle \langle p'-q|j_s^\nu|p'\rangle, \tag{29}$$

where ω represents the energy transfer, M_N is the nucleon mass, $e(\mathbf{p})$ the energy of a nucleon with momentum $\mathbf{p}$. The one-body current operators j_s^μ depend on the spin-isospin degrees of freedom s and $S_s^h(\mathbf{p}, E)$ is the one-body spectral function normalized to the total number of nucleons. For two-body currents and hadron production, Equation (29) extends non trivially in terms of one- and two-body spectral functions [129–132].

Following the above formalism, electron and neutrino scattering off argon and titanium isotopes was investigated in [44]. The interest in studying lepton scattering off these nuclei resides in the fact that future-generation neutrino experiments (e.g., DUNE [133]) will use liquid-argon time-projection chambers, which rely on scattering of neutrinos off ^{40}Ar. The nuclear component of the cross section has to be well determined for a meaningful interpretation of the measured events, in particular to reconstruct the neutrino energy with sufficient accuracy. In this respect, a tailored electron scattering experiment[16] was designed and recently performed at JLab [81, 82, 134]. In [44], nuclear spectral functions of stable argon, calcium and titanium isotopes were computed at the ADC(2) level with the NNLO$_{sat}$ interactions. A good reproduction of available charge radii and density distributions was found. Starting from these spectral functions, inclusive electron-^{48}Ti and electron-^{40}Ar cross sections were computed. They are shown in **Figure 8** (left) as a function of the energy transfer and compared to the recent experimental data from the JLab E12-14-012 collaboration [81, 82]. Calculations closely follow the quasi elastic peak, thus validating the theoretical approach and the impulse approximation in particular. Next, the quasielastic neutral and charged current cross sections were studied for 1 GeV neutrino scattering. Results are displayed in the right panel of **Figure 8**, also compared to scattering off ^{12}C. The quasielastic peak is found at a similar energy, with an increase in the magnitude of the cross section consistent with super scaling properties of inclusive reactions. The use of a Ti *proton* spectral function instead of an Ar *neutron* spectral function was also tested and found to be an excellent approximation. Further studies will be needed to thoroughly assess theoretical uncertainties.

[16]Since the neutron spectral function is not easily accessed by electrons, a complementary study with titanium, which has as many protons (22) as the neutrons in ^{40}Ar, was carried out.

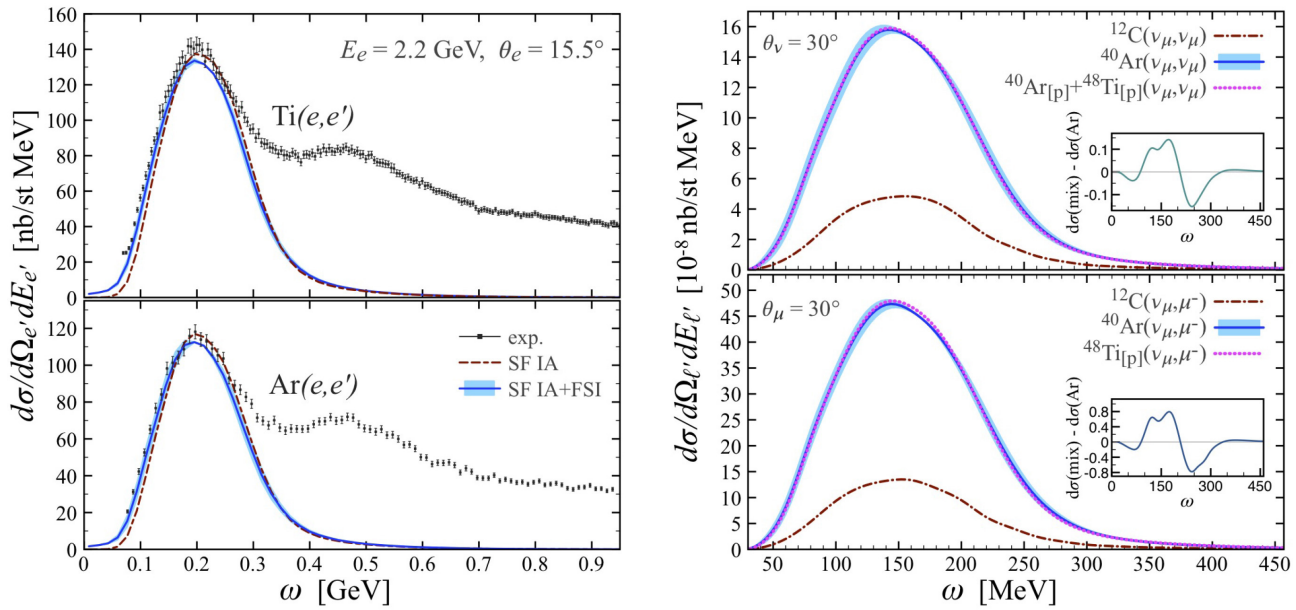

FIGURE 8 | (Left) Inclusive Ti(e, e′) (top) and Ar(e, e′) (bottom) cross sections at 2.2 GeV and 15.5° scattering angle. The solid (dashed) line shows the quasielastic cross section with (without) the inclusion of finals-state interactions (FSI, see [44] for details). For the FSI results, the theoretical uncertainties coming from model-space convergence are also shown as a shaded band. Experimental data are taken from [81, 82] and show both the quasielastic peak and the contribution from meson production at larger missing energies. **(Right)** Quasielastic neutral (top) and charged current (bottom) cross sections for 1 GeV neutrino scattering. Dot-dashed lines refer to a ^{12}C target and solid lines refer to ^{40}Ar. The colored band represents theoretical uncertainties due to model-space convergence. The dotted lines result from using the ^{48}Ti proton spectral function as an approximation for neutrons in ^{40}Ar. The insets show the difference between the latter and calculations where the full spectral distribution of ^{40}Ar is used. Adapted figure with permission from [44], copyright (2019) by the American Physical Society.

5. PERSPECTIVES AND CHALLENGES

5.1. Toward the Description of Nuclear Reactions

While the good knowledge of electro(weak) interactions facilitate the modeling of lepton-nucleus scattering, nuclear reactions, because of the complexity of strong interactions, require a more involved theoretical description. As a consequence, very few *ab initio* methods are presently capable of going beyond structure properties and directly computing reaction observables. Nevertheless, nucleon-nucleus and nucleus-nucleus reactions constitute nowadays the tools of choice to study the properties of atomic nuclei, such that progress on their *ab initio* description would be highly valuable.

A relatively clean process that can be used as a training field for *ab initio* reaction theory is quasifree nucleon knockout [135]. Quasifree scattering represents a process in which an incident nucleon (typically a proton[17]) with an energy of few hundred MeV knocks out a bound nucleon from the isotope of interest (see **Figure 9**, left panel, for a schematic illustration). Kinematical conditions are chosen such that the process can be preferentially described by a single, localized interaction between the incident and the struck nucleons, thus minimizing multiple collisions for the incoming nucleon. This sudden removal mechanism suggests that the remaining $A-1$ nucleons can be treated as spectators, which translates into an impulse approximation analogous to the one discussed in section 4.3. As a result, the total cross section can be separated into a structure and a reaction part. The latter involves nucleons that are usually described in terms of distorted waves to account for their propagation under the influence of the nuclear medium. Under these assumptions the differential cross section, labeled distorted-wave impulse approximation (DWIA), can be schematically written as

$$\left(\frac{d\sigma}{d^3Q}\right)_{\rm DWIA} = SF_N \times \left\langle \frac{d\sigma_{pN}}{d\Omega} \right\rangle \times \left\langle S_{pA} S_{p(A-1)} S_{N(A-1)} \Psi_N \right\rangle \ . \quad (30)$$

The first factor on the right-hand side is the spectroscopic factor of the struck nucleon, encoding the structure properties of the nucleus. The second term represents an in-medium proton-nucleon cross section, determining the probability of the collision between the projectile and one of the bound nucleons. The third term contains the scattering matrices for the (effective) degrees of freedom at play, i.e., respectively (i) proton and initial A-body system, (ii) proton and final $(A-1)$-body system, (iii) struck nucleon and final $(A-1)$-body system, plus the scattering wave function of the outgoing nucleon.

An *ab initio* calculations for some of the above quantities was recently performed within the GF formalism, in connection with a quasifree neutron knockout study on ^{54}Ca [51]. Specifically,

[17] Since many current experiments concern unstable nuclei, they are performed in inverse kinematics, whence the use of a proton target. In the following, the case of an incident proton will be thus considered.

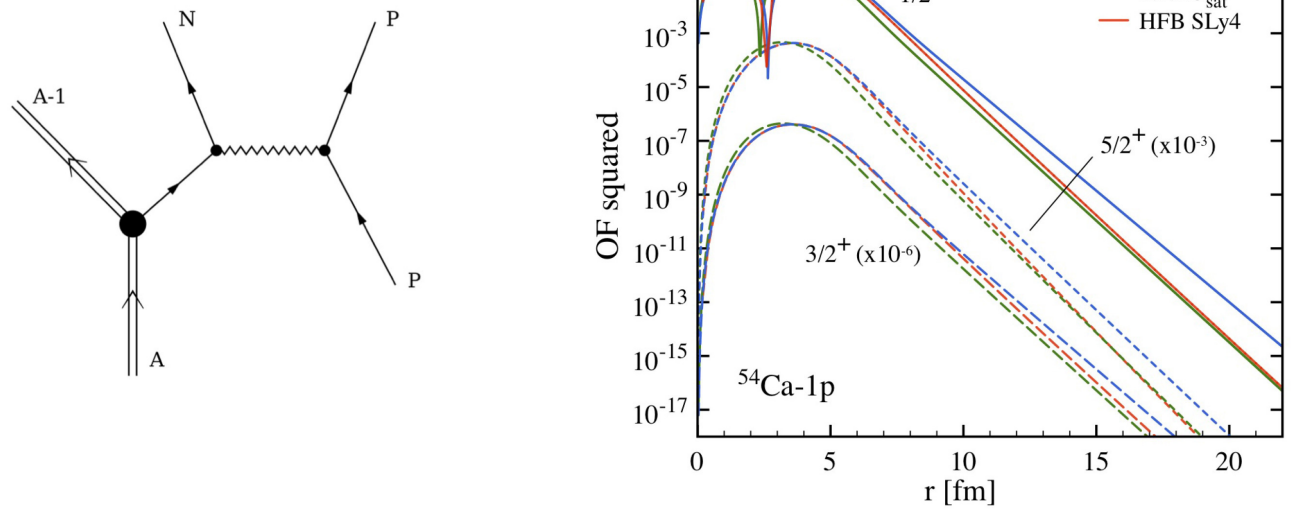

FIGURE 9 | (Left) Schematic representation of quasifree nucleon knockout: an incoming proton p scatters off an A-body nucleus, knocking out a nucleon N. **(Right)** One-proton overlap functions (squared) computed at the ADC(3) level using NNLO$_{sat}$ and NN+3N(lnl) interactions [136]. OFs corresponding to the main quasiparticle fragments for three angular momentum and parity channels $J^\pi = 1/2^+, 3/2^+, 5/2^+$ are shown. For comparison, EDF calculations [137, 138] performed with the SLy4 parameterization are displayed. These OFs were employed in the calculation of one-proton knockout cross sections in [52].

spectroscopic factors and one-body overlap functions for the struck neutron were computed. The latter enter the evaluation of the scattering matrices, where they are convoluted with nucleon-nucleus optical potentials. Overlaps functions (OFs) for three different neutron states, corresponding to the first three (ground and excited) states in ^{53}Ca, are shown in **Figure 9** (right). GF calculations were performed at the ADC(3) level with two different interactions, NNLO$_{sat}$ and NN+3N(lnl). For comparison, OFs from an EDF calculation with the SLy4 Skyrme parameterization are displayed. An overall good agreement is found between the three sets of calculations. Looking more in detail, one notices that NNLO$_{sat}$ better reproduces the maximum of the overlap at around 2–5 fm, i.e., the region of the nuclear surface. This clearly relates to the ability of this interaction to well describe nuclear sizes (cf. discussion in section 4.1). In contrast, NN+3N(lnl) is in better agreement in the tail of the OF. This is in line with the more accurate description of the low-lying spectrum of ^{53}Ca (cf. **Figure 6**).

In order to compute the cross section (Equation 30) for the ^{54}Ca$(p, pn)^{53}$Ca reaction, in [51] the GF input was complemented by phenomenological optical potentials and in-medium nucleon-nucleon cross sections, yielding results in good agreement with shell model calculations. An analogous study had been performed previously for the ^{14}O$(d, t)^{13}$O and ^{14}O$(d,^3 He)^{13}$N reactions, leading to similar conclusions [49]. These applications might be seen as a first step toward a consistent approach to structure and reaction, and show that *ab initio* ingredients can be as efficient as phenomenological ones. In fact, the in-medium nucleon-nucleon cross section could be already extracted from nuclear matter calculations (see e.g., [139]). Moreover, a nucleon-nucleus potential can be directly computed from the one-body self-energy (see [43]), for the first applications to oxygen and calcium isotopes. Thus, in the future the full *ab initio* calculation of the cross section (30) can be envisaged.

5.2. Toward Doubly Open-Shell Nuclei

The development of Gorkov GF theory [31], and its subsequent implementation to finite nuclei [32, 38] proved that symmetry breaking can be a powerful tool in the context of *ab initio* calculations. The generalization of other many-body techniques to a symmetry-breaking scheme [13, 96, 140] further confirmed the validity of this strategy. Such advances have allowed to extend the reach of *ab initio* calculations in mid-mass systems from a few closed-shell nuclei to a large number of open-shell isotopes, e.g., to complete semi-magic isotopic or isotonic chains. In their current implementation, however, these methods do not break rotational symmetry. This results in an inefficient account of quadrupole correlations, such that the description of (doubly) open-shell systems displaying significant deformation can be problematic.

As opposed to pairing, where the strong static correlations at the Fermi surface cause the breakdown of the particle-hole expansion, in the presence of deformation one can usually produce converged calculations, i.e., compute few orders in the many-body expansion. Nevertheless, one expects the accuracy to deteriorate with the strength of the deformation. This has been indeed observed in Gorkov GF calculations around the calcium chain, in particular for titanium and chromium isotopes

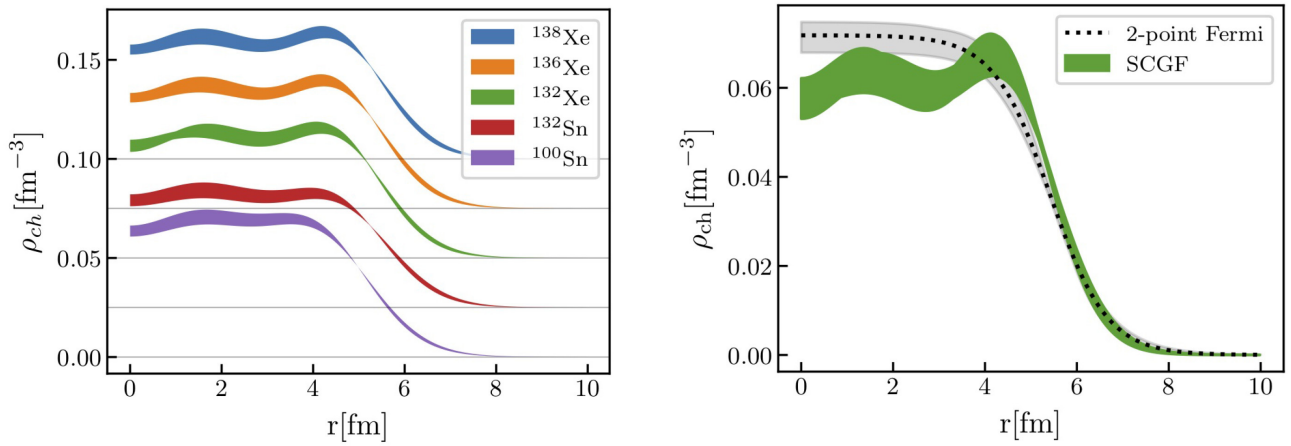

FIGURE 10 | (Left) Charge density distributions of selected Sn and Xe isotopes computed with the NNLO$_{\rm sat}$ interaction in Gorkov GF theory at the ADC(2) level. Each curve is shifted upwards with respect to the one below by 0.025 fm^{-3} for clarity purposes. Colored band account for uncertainties stemming from model-space convergence. **(Right)** Charge density distributions of ^{132}Xe computed with the NNLO$_{\rm sat}$ interaction in Gorkov GF theory at the ADC(2) level. The dotted line with gray band corresponds to the two-point Fermi distribution with parameter and error bars extracted from [83]. Adapted figure with permission from [41].

characterized by mid-shell protons. For instance, by studying neutron gaps[18] at the neutron traditional magic number $N = 28$ one finds an excellent agreement with experiment up to $Z = 22$, after which symmetry-restricted GF calculations clearly depart from data [102]. Furthermore, one can identify a correlation between the deviation to experimental data and the amount of deformation (e.g., estimated by EDF calculations [141]). This situation suggests that the additional breaking of the SU(2) symmetry associated to rotational invariance will be needed in the extension of correlation-expansion methods to doubly open-shell nuclei. Some of the existing approaches are indeed being generalized along these lines [142]. In the case of Gorkov GF such an extension will presumably require the use of importance truncation [143] and/or tensor factorization techniques [144].

5.3. Toward Heavy Nuclei

Over the past years, GF *ab initio* calculations have extended their reach across the Segrè chart, going from the first application to the oxygen chain ($A \sim 20$) [35] to recent computations of nickel isotopes ($A \sim 70$) [40]. Such calculations rely on sophisticated numerical codes that make extensive use of available high-performance computing resources. Although the management of the computing time[19] could be problematic, the bottleneck that currently prevents (converged) calculations beyond $A \sim 100$ is related to the storage of the matrix elements of $3N$ operators. Indeed, presently employed truncations on the three-body basis of $e_{3\rm max} = 14 - 18$ allow keeping the size of $3N$ matrix elements below 100 GB, which is roughly the order of magnitude of the available memory on a single node of a state-of-the-art supercomputer. Going considerably beyond this size thus constitutes an issue. At the same time, such values of $e_{3\rm max}$ are enough to achieve reasonably converged results in the ($A \sim 60 - 70$), while they become insufficient for larger isotopes [40, 145].

Different strategies are being explored to overcome this issue. One possibility would be to discard beforehand, for a given $e_{3\rm max}$, a subset of the initial $3N$ matrix elements. While performing a selection[20] directly on the original set might be problematic, a promising technique based on tensor factorization algorithms has been put forward recently [143]. Since in the majority of applications $3N$ forces are included in the normal-ordered two-body approximation[21], another option could consist in performing the normal ordering procedure in a different (smaller) basis than the HO one, e.g., in momentum space.

Even with current limitations, however, some meaningful results can be produced for nuclei above mass $A = 100$. Indeed, as discussed in section 3.3, not all observables show the same convergence pattern. In particular, while ground-state energy curves get lower and lower as the basis size is increased, radii tilt around a fixed point that can be assumed to correspond to the infinite-basis result. This allow to provide an estimate of the radius (and, correspondingly, of the density distribution) in bases for which the energy is far from being converged. Based on this observation, charge densities of closed- and open-shell tin and xenon isotopes have been recently calculated within GF theory [41]. Examples are reported in **Figure 10**, where the NNLO$_{\rm sat}$ interaction has been employed. In the left panel, the charge distribution of several nuclei is shown, exemplifying

[18]Neutron gaps, defined as differences of two-neutron separation energies, are one of possible observables that meaningfully estimate the "magic" character of a neutron number.

[19]In this respect, while the numerical cost of Dyson GF calculations grows with the mass number, the one of Gorkov GFs solely depend on the basis dimension [32].

[20]That is, using a different truncation than the $e_{3\rm max}$ truncation.

[21]It consists of two steps: (i) a normal ordering of the ($3N$) Hamiltonian with respect to a reference state and (ii) the disregard of operators of rank higher than two (see [146] for a pedagogical description and the generalization to the case of symmetry-breaking reference states).

the typical range of system that can be presently accessed. In the right panel, the charge density of ^{132}Xe is displayed and compared to a two-point Fermi distribution fitted on the recent experimental data from the SCRIT collaboration [83]. The two are in very good agreement at the surface and in the tail of the distribution. In the interior, the two-point Fermi distribution and the lack of high-momentum transfer data lead to flat behavior for the experimental distribution, whereas the computed density shows a well defined oscillation pattern. This example shows that even in present implementations of GF calculations it is possible to provide relevant predictions in the region $A = 100 - 150$.

AUTHOR CONTRIBUTIONS

The author confirms being the sole contributor of this work and has approved it for publication.

ACKNOWLEDGMENTS

The author wishes to thank F. Raimondi and Y. L. Sun for providing the results appearing in **Figure 9**, all collaborators that contributed to the results presented in this work, and additionally C. Barbieri and T. Duguet for useful remarks on the manuscript.

REFERENCES

1. Ishii N, Aoki S, Hatsuda T. Nuclear force from lattice QCD. *Phys Rev Lett*. (2007) **99**:022001. doi: 10.1103/PhysRevLett.99.022001
2. McIlroy C, Barbieri C, Inoue T, Doi T, Hatsuda T. Doubly magic nuclei from lattice QCD forces at M_PS =469 MeV/c^2. *Phys Rev C*. (2018) **97**:021303. doi: 10.1103/PhysRevC.97.021303
3. Epelbaum E, Hammer HW, Meißner UG. Modern theory of nuclear forces. *Rev Mod Phys*. (2009) **81**:1773. doi: 10.1103/RevModPhys.81.1773
4. Machleidt R, Entem D. Chiral effective field theory and nuclear forces. *Phys Rep*. (2011) **503**:1. doi: 10.1016/j.physrep.2011.02.001
5. Hammer HW, König S, van Kolck U. Nuclear effective field theory: status and perspectives. *Rev Mod Phys*. (2020) **92**:025004. doi: 10.1103/RevModPhys.92.025004
6. Bogner SK, Furnstahl RJ, Schwenk A. From low-momentum interactions to nuclear structure. *Prog Part Nucl Phys*. (2010) **65**:94–147. doi: 10.1016/j.ppnp.2010.03.001
7. Carlson J, Gandolfi S, Pederiva F, Pieper SC, Schiavilla R, Schmidt KE, et al. Quantum Monte Carlo methods for nuclear physics. *Rev Mod Phys*. (2015) **87**:1067–118. doi: 10.1103/RevModPhys.87.1067
8. Gandolfi S, Lonardoni D, Lovato A, Piarulli M. Atomic nuclei from quantum Monte Carlo calculations with chiral EFT interactions. *Front Phys*. (2020) **8**:117. doi: 10.3389/fphy.2020.00117
9. Barrett BR, Navratil P, Vary JP. *Ab initio* no core shell model. *Prog Part Nucl Phys*. (2013) **69**:131–81. doi: 10.1016/j.ppnp.2012.10.003
10. Lähde TA, Epelbaum E, Krebs H, Lee D, Meißner UG, Rupak G. Lattice effective field theory for medium-mass nuclei. *Phys Lett B*. (2014) **732**:110–5. doi: 10.1016/j.physletb.2014.03.023
11. Shavitt I, Bartlett RJ. *Many-Body Methods in Chemistry and Physics*. New York, NY: Cambridge University Press (2009). doi: 10.1017/CBO9780511596834
12. Tichai A, Langhammer J, Binder S, Roth R. Hartree-Fock many-body perturbation theory for nuclear ground-states. *Phys Lett B*. (2016) **756**:283–8. doi: 10.1016/j.physletb.2016.03.029
13. Tichai A, Arthuis P, Duguet T, Hergert H, Somá V, Roth R. Bogoliubov many-body perturbation theory for open-shell nuclei. *Phys Lett B*. (2018) **786**:195–200. doi: 10.1016/j.physletb.2018.09.044
14. Demol P, Duguet T, Ekström A, Frosini M, Hebeler K, König S, et al. Improved many-body expansions from eigenvector continuation. *Phys Rev C*. (2020) **101**:041302. doi: 10.1103/PhysRevC.101.041302
15. Demol P, Frosini M, Tichai A, Somá V, Duguet T. Bogoliubov many-body perturbation theory under constraint. (2020) *arXiv:2002.02724*.
16. Tichai A, Roth R, Duguet T. Many-body perturbation theories for finite nuclei. *Front Phys*. (2020) **8**:164. doi: 10.3389/fphy.2020.00164
17. Tsukiyama K, Bogner SK, Schwenk A. In-medium similarity renormalization group for nuclei. *Phys Rev Lett*. (2011) **106**:222502. doi: 10.1103/PhysRevLett.106.222502
18. Hergert H, Bogner SK, Morris TD, Schwenk A, Tsukiyama K. The in-medium similarity renormalization group: a novel ab initio method for nuclei. *Phys Rep*. (2016) **621**:165–222. doi: 10.1016/j.physrep.2015.12.007
19. Dickhoff WH, Muther H. Nucleon properties in the nuclear medium. *Rept Prog Phys*. (1992) **55**:1947–2023. doi: 10.1088/0034-4885/55/11/002
20. Kowalski K, Dean DJ, Hjorth-Jensen M, Papenbrock T, Piecuch P. Coupled cluster calculations of ground and excited states of nuclei. *Phys Rev Lett*. (2004) **92**:132501. doi: 10.1103/PhysRevLett.92.132501
21. Hagen G, Papenbrock T, Hjorth-Jensen M, Dean DJ. Coupled-cluster computations of atomic nuclei. *Rep Prog Phys*. (2014) **77**:096302. doi: 10.1088/0034-4885/77/9/096302
22. Bogner SK, Hergert H, Holt JD, Schwenk A, Binder S, Calci A, et al. Nonperturbative shell-model interactions from the in-medium similarity renormalization group. *Phys Rev Lett*. (2014) **113**:142501. doi: 10.1103/PhysRevLett.113.142501
23. Jansen GR, Engel J, Hagen G, Navratil P, Signoracci A. *Ab initio* coupled-cluster effective interactions for the shell model: application to neutron-rich oxygen and carbon isotopes. *Phys Rev Lett*. (2014) **113**:142502. doi: 10.1103/PhysRevLett.113.142502
24. Smirnova NA, Barrett BR, Kim Y, Shin IJ, Shirokov AM, Dikmen E, et al. Effective interactions in the *sd* shell. *Phys Rev C*. (2019) **100**:054329. doi: 10.1103/PhysRevC.100.054329
25. Broglia RA, Bortignon PF, Barranco F, Vigezzi E, Idini A, Potel G. Unified description of structure and reactions: implementing the nuclear field theory program. *Phys Scripta*. (2016) **91**:063012. doi: 10.1088/0031-8949/91/6/063012
26. Barbieri C, Dickhoff WH. Faddeev description of two-hole-one-particle motion and the single-particle spectral function. *Phys Rev C*. (2001) **63**:034313. doi: 10.1103/PhysRevC.63.034313
27. Barbieri C, Dickhoff WH. Faddeev treatment of long-range correlations and the one-hole spectral function of ^{16}O. *Phys Rev C*. (2002) **65**:064313. doi: 10.1103/PhysRevC.65.064313
28. Dickhoff WH, Barbieri C. Self-consistent Green's function method for nuclei and nuclear matter. *Prog Part Nucl Phys*. (2004) **52**:377. doi: 10.1016/j.ppnp.2004.02.038
29. Barbieri C, Hjorth-Jensen M. Quasiparticle and quasihole states of nuclei around ^{56}Ni. *Phys Rev C*. (2009) **79**:064313. doi: 10.1103/PhysRevC.79.064313
30. Barbieri C. Role of long-range correlations in the quenching of spectroscopic factors. *Phys Rev Lett*. (2009) **103**:202502. doi: 10.1103/PhysRevLett.103.202502
31. Somá V, Duguet T, Barbieri C. *Ab initio* self-consistent Gorkov-Green's function calculations of semimagic nuclei: formalism at second order with a two-nucleon interaction. *Phys Rev C*. (2011) **84**:064317. doi: 10.1103/PhysRevC.84.064317
32. Somá V, Barbieri C, Duguet T. *Ab initio* self-consistent Gorkov-Green's function calculations of semi-magic nuclei: numerical implementation at second order with a two-nucleon interaction. *Phys Rev C*. (2014) **89**:024323. doi: 10.1103/PhysRevC.89.024323

33. Carbone A, Cipollone A, Barbieri C, Rios A, Polls A. Self-consistent Green's functions formalism with three-body interactions. *Phys Rev C*. (2013) **88**:054326. doi: 10.1103/PhysRevC.88.054326
34. Raimondi F, Barbieri C. Algebraic diagrammatic construction formalism with three-body interactions. *Phys Rev C*. (2018) **97**:054308. doi: 10.1103/PhysRevC.97.054308
35. Cipollone A, Barbieri C, Navrátil P. Isotopic chains around oxygen from evolved chiral two- and three-nucleon interactions. *Phys Rev Lett*. (2013) **111**:062501. doi: 10.1103/PhysRevLett.111.062501
36. Cipollone A, Barbieri C, Navrátil P. Chiral three-nucleon forces and the evolution of correlations along the oxygen isotopic chain. *Phys Rev C*. (2015) **92**:014306. doi: 10.1103/PhysRevC.92.014306
37. Duguet T, Somá V, Lecluse S, Barbieri C, Navrátil P. *Ab initio* calculation of the potential bubble nucleus ^{34}Si. *Phys Rev C*. (2017) **95**:034319. doi: 10.1103/PhysRevC.95.034319
38. Somá V, Barbieri C, Duguet T. *Ab initio* Gorkov-Green's function calculations of open-shell nuclei. *Phys Rev C*. (2013) **87**:011303. doi: 10.1103/PhysRevC.87.011303
39. Somá V, Cipollone A, Barbieri C, Navrátil P, Duguet T. Chiral two- and three-nucleon forces along medium-mass isotope chains. *Phys Rev C*. (2014) **89**:061301. doi: 10.1103/PhysRevC.89.061301
40. Somá V, Navrátil P, Raimondi F, Barbieri C, Duguet T. Novel chiral Hamiltonian and observables in light and medium-mass nuclei. *Phys Rev C*. (2020) **101**:014318. doi: 10.1103/PhysRevC.101.014318
41. Arthuis P, Barbieri C, Vorabbi M, Finelli P. Ab initio computation of charge densities for Sn and Xe isotopes. (2020) *arXiv:2002.02214*.
42. Raimondi F, Barbieri C. Nuclear electromagnetic dipole response with the self-consistent Green's function formalism. *Phys Rev C*. (2019) **99**:054327. doi: 10.1103/PhysRevC.99.054327
43. Idini A, Barbieri C, Navrátil P. *Ab initio* optical potentials and nucleon scattering on medium mass nuclei. *Phys Rev Lett*. (2019) **123**:092501. doi: 10.1103/PhysRevLett.123.092501
44. Barbieri C, Rocco N, Somá V. Lepton scattering from ^{40}Ar and ^{48}Ti in the quasielastic peak region. *Phys Rev C*. (2019) **100**:062501. doi: 10.1103/PhysRevC.100.062501
45. Raimondi F, Barbieri C. Core-polarization effects and effective charges in O and Ni isotopes from chiral interactions. *Phys Rev C*. (2019) **100**:024317. doi: 10.1103/PhysRevC.100.024317
46. Duguet T, Hergert H, Holt JD, Somá V. Nonobservable nature of the nuclear shell structure: meaning, illustrations, and consequences. *Phys Rev C*. (2015) **92**:034313. doi: 10.1103/PhysRevC.92.034313
47. Rosenbusch M, Ascher P, Atanasov D, Barbieri C, Beck D, Blaum K, et al. Probing the $N = 32$ shell closure below the magic proton number $Z = 20$: mass measurements of the exotic isotopes ^{52,53}K. *Phys Rev Lett*. (2015) **114**:202501. doi: 10.1103/PhysRevLett.114.202501
48. Leistenschneider E, Reiter MP, Ayet San Andrés S, Kootte B, Holt JD, Navrátil P, et al. Dawning of the $N = 32$ shell closure seen through precision mass measurements of neutron-rich titanium isotopes. *Phys Rev Lett*. (2018) **120**:062503. doi: 10.1103/PhysRevLett.120.062503
49. Flavigny F, Gillibert A, Nalpas L, Obertelli A, Keeley N, Barbieri C, et al. Limited asymmetry dependence of correlations from single nucleon transfer. *Phys Rev Lett*. (2013) **110**:122503. doi: 10.1103/PhysRevLett.110.122503
50. Papuga J, Bissell ML, Kreim K, Barbieri C, Blaum K, Rydt MD, et al. Shell structure of potassium isotopes deduced from their magnetic moments. *Phys Rev C*. (2014) **90**:034321. doi: 10.1103/PhysRevC.90.034321
51. Chen S, Lee J, Doornenbal P, Obertelli A, Barbieri C, Chazono Y, et al. Quasifree neutron knockout from ^{54}Ca corroborates arising $N = 34$ neutron magic number. *Phys Rev Lett*. (2019) **123**:142501. doi: 10.1103/PhysRevLett.123.142501
52. Sun YL, et al. Restoration of the natural $E(1/2_1^+) - E(3/2_1^+)$ energy splitting in odd-K isotopes towards $N = 40$. *Phys Lett B*. (2020) **802**:135215. doi: 10.1016/j.physletb.2020.135215
53. Lapoux V, Somá V, Barbieri C, Hergert H, Holt JD, Stroberg SR. Radii and binding energies in oxygen isotopes: a challenge for nuclear forces. *Phys Rev Lett*. (2016) **117**:052501. doi: 10.1103/PhysRevLett.117.052501
54. Dickhoff WH, Van Neck D. *Many-Body Theory Exposed*! Singapore: World Scientific (2005). doi: 10.1142/5804
55. Noziéres P. *Theory of Interacting Fermi Sytems*. Boulder: Westview Press (1964).
56. Abrikosov AA, Gorkov LP, Dzyaloshinski IE. *Methods of Quantum Field Theory in Statistical Physics*. Lowell, MA: Courier Corporation (1975).
57. Economou EN. *Green's Functions in Quantum Physics*. Berlin: Springer (2006). doi: 10.1007/3-540-28841-4
58. Barbieri C, Carbone A. Self-consistent green's function approaches. In: Hjorth-Jensen M, Lombardo M, van Kolck U, editors. *An Advanced Course in Computational Nuclear Physics*. Vol. 936 of Lecture Notes in Physics. Cham: Springer (2017). p. 571–644.
59. Barbieri C. *Computational Many-Body Physics*. Available online at: http://personal.ph.surrey.ac.uk/$\sim$cb0023/bcdor/bcdor/Comp_Many-Body_Phys.html
60. Galitskii VM, Migdal AB. Applications of quantum field theory methods to the many body problem. *Z Eksp Teor Fiz*. (1958) **34**:139.
61. Koltun DS. Total binding energies of nuclei, and particle-removal experiments. *Phys Rev Lett*. (1972) **28**:182. doi: 10.1103/PhysRevLett.28.182
62. Gorkov LP. On the energy spectrum of superconductors. *Sov Phys JETP*. (1958) **34**:505. doi: 10.2307/2607987
63. Nambu Y. Quasi-particles and gauge invariance in the theory of superconductivity. *Phys Rev*. (1960) **117**:648. doi: 10.1103/PhysRev.117.648
64. Duguet T. Symmetry broken and restored coupled-cluster theory: I. Rotational symmetry and angular momentum. *J Phys G*. (2015) **42**:025107. doi: 10.1088/0954-3899/42/2/025107
65. Duguet T, Signoracci A. Symmetry broken and restored coupled-cluster theory: II. Global gauge symmetry and particle number. *J Phys G*. (2017) **44**:015103. doi: 10.1088/0954-3899/44/1/015103
66. Onida G, Reining L, Rubio A. Electronic excitations: density-functional versus many-body Green's-function approaches. *Rev Mod Phys*. (2002) **74**:601–59. doi: 10.1103/RevModPhys.74.601
67. Bożek P. Self-consistent solution of Galitskii-Feynman equations at finite temperature. *Phys Rev C*. (1999) **59**:2619–26. doi: 10.1103/PhysRevC.59.2619
68. Frick T, Müther H. Self-consistent solution to the nuclear many-body problem at finite temperature. *Phys Rev C*. (2003) **68**:034310. doi: 10.1103/PhysRevC.68.034310
69. Somá V, Bożek P. Diagrammatic calculation of thermodynamical quantities in nuclear matter. *Phys Rev C*. (2006) **74**:045809. doi: 10.1103/PhysRevC.74.045809
70. Rios A, Polls A, Ramos A, Müther H. Entropy of a correlated system of nucleons. *Phys Rev C*. (2006) **74**:054317. doi: 10.1103/PhysRevC.74.054317
71. Rios A, Polls A, Ramos A, Müther H. Liquid-gas phase transition in nuclear matter from realistic many-body approaches. *Phys Rev C*. (2008) **78**:044314. doi: 10.1103/PhysRevC.78.044314
72. Somá V, Bożek P. In-medium T-matrix for nuclear matter with three-body forces: binding energy and single-particle properties. *Phys Rev C*. (2008) **78**:054003. doi: 10.1103/PhysRevC.78.054003
73. Schirmer J. Beyond the random-phase approximation: a new approximation scheme for the polarization propagator. *Phys Rev A*. (1982) **26**:2395–416. doi: 10.1103/PhysRevA.26.2395
74. Schirmer J, Cederbaum LS, Walter O. New approach to the one-particle Green's function for finite Fermi systems. *Phys Rev A*. (1983) **28**:1237–59. doi: 10.1103/PhysRevA.28.1237
75. Nooijen M, Snijders JG. Coupled cluster approach to the single-particle Green's function. *Int J Quant Chem*. (1992) **26**:55. doi: 10.1002/qua.560440808
76. Schirmer J, Angonoa G. On Green's function calculations of the static self-energy part, the ground state energy and expectation values. *J Chem Phys*. (1989) **91**:1754. doi: 10.1063/1.457081
77. Dewulf Y, Neck DV, Daele LV, Waroquier M. Long-range correlations in finite nuclei: comparison of two self-consistent treatments. *Phys Lett B*. (1997) **396**:7–14. doi: 10.1016/S0370-2693(97)00135-4
78. Hagen G, Papenbrock T, Dean DJ. Solution of the center-of-mass problem in nuclear structure calculations. *Phys Rev Lett*. (2009) **103**:062503. doi: 10.1103/PhysRevLett.103.062503

79. Berggren T. On the use of resonant states in eigenfunction expansions of scattering and reaction amplitudes. *Nucl Phys A*. (1968) **109**:265–87. doi: 10.1016/0375-9474(68)90593-9
80. Berggren T. On the treatment of resonant final states in direct reactions. *Nucl Phys A*. (1971) **169**:353–62. doi: 10.1016/0375-9474(71)90889-X
81. Dai H, Murphy M, Pandey V, Abrams D, Nguyen D, Aljawrneh B, et al. First measurement of the $Ti(e,e')X$ cross section at Jefferson Lab. *Phys Rev C*. (2018) **98**:014617. doi: 10.1103/PhysRevC.98.014617
82. Dai H, Murphy M, Pandey V, Abrams D, Nguyen D, Aljawrneh B, et al. First measurement of the $Ar(e,e')X$ cross section at Jefferson Laboratory. *Phys Rev C*. (2019) **99**:054608. doi: 10.1103/PhysRevC.99.054608
83. Tsukada K, Enokizono A, Ohnishi T, Adachi K, Fujita T, Hara M, et al. First elastic electron scattering from ^{132}Xe at the SCRIT facility. *Phys Rev Lett*. (2017) **118**:262501. doi: 10.1103/PhysRevLett.118.262501
84. Machleidt R. The high-precision, charge-dependent Bonn nucleon-nucleon potential (CD-Bonn). *Phys Rev C*. (2001) **63**:024001. doi: 10.1103/PhysRevC.63.024001
85. Stoks VGJ, Klomp RAM, Terheggen CPF, de Swart JJ. Construction of high quality NN potential models. *Phys Rev C*. (1994) **49**:2950. doi: 10.1103/PhysRevC.49.2950
86. Somá V, Bożek P. Thermodynamic properties of nuclear matter with three-body forces. *Phys Rev C*. (2009) **80**:025803. doi: 10.1103/PhysRevC.80.025803
87. Epelbaum E, Krebs H, Meißner UG. Improved chiral nucleon-nucleon potential up to next-to-next-to-next-to-leading order. *Eur Phys J A*. (2015) **51**:53. doi: 10.1140/epja/i2015-15053-8
88. Binder S, Calci A, Epelbaum E, Furnstahl RJ, Golak J, Hebeler K, et al. Few-nucleon and many-nucleon systems with semilocal coordinate-space regularized chiral nucleon-nucleon forces. *Phys Rev C*. (2018) **98**:014002. doi: 10.1103/PhysRevC.98.014002
89. Drischler C, Hebeler K, Schwenk A. Chiral interactions up to next-to-next-to-next-to-leading order and nuclear saturation. *Phys Rev Lett*. (2019) **122**:042501. doi: 10.1103/PhysRevLett.122.042501
90. Hüther T, Vobig K, Hebeler K, Machleidt R, Roth R. Family of chiral two- plus three-nucleon interactions for accurate nuclear structure studies. (2019) *arXiv:1911.04955*. doi: 10.1016/j.physletb.2020.135651
91. Epelbaum E, Golak J, Hebeler K, Hüther T, Kamada H, Krebs H, et al. Few- and many-nucleon systems with semilocal coordinate-space regularized chiral two- and three-body forces. *Phys Rev C*. (2019) **99**:024313. doi: 10.1103/PhysRevC.99.024313
92. Epelbaum E, Krebs H, Reinert P. High-precision nuclear forces from chiral EFT: state-of-the-art, challenges and outlook. *Front Phys*. (2020) **8**:98. doi: 10.3389/fphy.2020.00098
93. Entem DR, Machleidt R. Accurate charge-dependent nucleon-nucleon potential at fourth order of chiral perturbation theory. *Phys Rev C*. (2003) **68**:041001. doi: 10.1103/PhysRevC.68.041001
94. Navrátil P. Local three-nucleon interaction from chiral effective field theory. *Few-Body Syst*. (2007) **41**:117–40. doi: 10.1007/s00601-007-0193-3
95. Roth R, Binder S, Vobig K, Calci A, Langhammer J, Navrátil P. Medium-mass nuclei with normal-ordered chiral $NN+3N$ interactions. *Phys Rev Lett*. (2012) **109**:052501. doi: 10.1103/PhysRevLett.109.052501
96. Hergert H, Binder S, Calci A, Langhammer J, Roth R. *Ab initio* calculations of even oxygen isotopes with chiral two- plus three-nucleon interactions. *Phys Rev Lett*. (2013) **110**:242501. doi: 10.1103/PhysRevLett.110.242501
97. Binder S, Langhammer J, Calci A, Roth R. *Ab initio* path to heavy nuclei. *Phys Lett B*. (2014) **736**:119–23. doi: 10.1016/j.physletb.2014.07.010
98. Ekström A, Jansen GR, Wendt KA, Hagen G, Papenbrock T, Carlsson BD, et al. Accurate nuclear radii and binding energies from a chiral interaction. *Phys Rev C*. (2015) **91**:051301. doi: 10.1103/PhysRevC.91.051301
99. Otsuka T, Suzuki T, Holt JD, Schwenk A, Akaishi Y. Three-body forces and the limit of oxygen isotopes. *Phys Rev Lett*. (2010) **105**:032501. doi: 10.1103/PhysRevLett.105.032501
100. Epelbaum E, Krebs H, Lähde TA, Lee D, Meißner UG, Rupak G. *Ab initio* calculation of the spectrum and structure of ^{16}O. *Phys Rev Lett*. (2014) **112**:102501. doi: 10.1103/PhysRevLett.112.102501
101. Hebeler K, Holt JD, Menéndez J, Schwenk A. Nuclear forces and their impact on neutron-rich nuclei and neutron-rich matter. *Annu Rev Nucl Part Sci*. (2015) **65**:457–84. doi: 10.1146/annurev-nucl-102313-025446
102. Mougeot M, Atanasov D, Barbieri C, Blaum K, Breitenfeld M, de Roubin A, et al. Examining the $N = 28$ shell closure through high-precision mass measurements of $^{46-48}$Ar. *Phys Rev C*. (2020) **102**:014301. doi: 10.1103/PhysRevC.102.014301
103. Brown BA, Massen SE, Hodgson PE. The charge distributions of the oxygen and calcium isotopes. *Phys Lett B*. (1979) **85**:167–71. doi: 10.1016/0370-2693(79)90569-0
104. Negele JW. Structure of finite nuclei in the local-density approximation. *Phys Rev C*. (1970) **1**:1260–321. doi: 10.1103/PhysRevC.1.1260
105. Chandra H, Sauer G. Relativistic corrections to the elastic electron scattering from ^{208}Pb. *Phys Rev C*. (1976) **13**:245–52. doi: 10.1103/PhysRevC.13.245
106. Bertozzi W, Friar J, Heisenberg J, Negele JW. Contributions of neutrons to elastic electron scattering from nuclei. *Phys Lett B*. (1972) **41**:408–14. doi: 10.1016/0370-2693(72)90662-4
107. Richter WA, Brown BA. Nuclear charge densities with the Skyrme Hartree-Fock method. *Phys Rev C*. (2003) **67**:034317. doi: 10.1103/PhysRevC.67.034317
108. Todd-Rutel BG, Piekarewicz J, Cottle PD. Spin orbit splitting in low j neutron orbits and proton densities in the nuclear interior. *Phys Rev C*. (2004) **69**:021301. doi: 10.1103/PhysRevC.69.021301
109. Khan E, Grasso M, Margueron J, Van Giai N. Detecting bubbles in exotic nuclei. *Nucl Phys A*. (2008) **800**:37–46. doi: 10.1016/j.nuclphysa.2007.11.012
110. Grasso M, Gaudefroy L, Khan E, Niksic T, Piekarewicz J, Sorlin O, et al. Nuclear 'bubble' structure in Si-34. *Phys Rev C*. (2009) **79**:034318. doi: 10.1103/PhysRevC.79.034318
111. Yao JM, Baroni S, Bender M, Heenen PH. Beyond-mean-field study of the possible "bubble" structure of ^{3}4Si. *Phys Rev C*. (2012) **86**:014310. doi: 10.1103/PhysRevC.86.014310
112. Yao JM, Mei H, Li ZP. Does a proton "bubble" structure exist in the low-lying states of 34Si? *Phys Lett B*. (2013) **723**:459–63. doi: 10.1016/j.physletb.2013.05.049
113. Wu XY, Yao JM, Li ZP. Low-energy structure and anti-bubble effect of dynamical correlations in ^{4}6Ar. *Phys Rev C*. (2014) **89**:017304. doi: 10.1103/PhysRevC.89.017304
114. Rychel D, Emrich HJ, Miska H, Gyufko R, Wiedner CA. Charge distribution of the neven sulphur isotopes from elastic electron scattering. *Phys Lett*. (1983) 130B:5–8. doi: 10.1016/0370-2693(83)91051-1
115. Suda T, Simon H. Prospects for electron scattering on unstable, exotic nuclei. *Prog Part Nucl Phys*. (2017) **96**:1–31. doi: 10.1016/j.ppnp.2017.04.002
116. von Niessen W, Schirmer J, Cederbaum LS. Computational methods for the one-particle Green's function. *Comput Phys Rep*. (1984) **1**:57–125. doi: 10.1016/0167-7977(84)90002-9
117. Danovich D. Green's function methods for calculating ionization potentials, electron affinities, and excitation energies. *Wiley Interdisc Rev*. (2011) **1**:377–87. doi: 10.1002/wcms.38
118. Degroote M, Van Neck D, Barbieri C. Faddeev random-phase approximation for molecules. *Phys Rev A*. (2011) **83**:042517. doi: 10.1103/PhysRevA.83.042517
119. Barbieri C, Van Neck D, Degroote M. Accuracy of the Faddeev random phase approximation for light atoms. *Phys Rev A*. (2012) **85**:012501. doi: 10.1103/PhysRevA.85.012501
120. Papuga J, Bissell ML, Kreim K, Blaum K, Brown BA, De Rydt M, et al. Spins and magnetic moments of ^{49}K and ^{51}K: establishing the $1/2^+$ and $3/2^+$ level ordering beyond N=28. *Phys Rev Lett*. (2013) **110**:172503. doi: 10.1103/PhysRevLett.110.172503
121. Barbieri C, Raimondi F, McIlroy C. Recent applications of self-consistent Green's function theory to nuclei. *J Phys*. (2018) **966**:012015. doi: 10.1088/1742-6596/966/1/012015
122. Ahrens J, Borchert H, Czock KH, Eppler HB, Gimm H, Gundrum H, et al. Total nuclear photon absorption cross sections for some light elements. *Nucl Phys A*. (1975) **251**:479–92. doi: 10.1016/0375-9474(75)90543-6
123. Ishkhanov B, Kapitonov I, Lileeva E, Shirokov E, Erokhova V, Elkin M, et al. *Cross Sections of Photon Absorption by Nuclei With Nucleon Numbers*. Moscow: Institute of Nuclear Physics, Moscow State University (2002).

124. Birkhan J, Miorelli M, Bacca S, Bassauer S, Bertulani CA, Hagen G, et al. Electric dipole polarizability of ^{48}Ca and implications for the neutron skin. *Phys Rev Lett*. (2017) **118**:252501. doi: 10.1103/PhysRevLett.118.252501
125. Boffi S, Giusti C, Pacati Fd, Radici M. *Electromagnetic Response of Atomic Nuclei*. Vol. 20 of Oxford Studies in Nuclear Physics. Oxford: Clarendon Press (1996).
126. Herczeg P, Hoffman CM, Klapdor-Kleingrothaus HV. *Physics Beyond the Standard Model*. Singapore: World Scientific (1999). doi: 10.1142/9789814527514
127. Nakamura K, et al. Review of particle physics. *J Phys G*. (2010) **37**:075021. doi: 10.1088/0954-3899/37/7A/075021
128. Rocco N, Barbieri C. Inclusive electron-nucleus cross section within the self-consistent Green's function approach. *Phys Rev C*. (2018) **98**:025501. doi: 10.1103/PhysRevC.98.025501
129. Rocco N, Barbieri C, Benhar O, De Pace A, Lovato A. Neutrino-nucleus cross section within the extended factorization scheme. *Phys Rev C*. (2019) **99**:025502. doi: 10.1103/PhysRevC.99.025502
130. Giusti C, Pacati FD, Schwamb M, Boffi S. On the treatment of the Δ-contributions in electromagnetic pp-knockout reactions. *Eur Phys J A*. (2005) **26**:209–20. doi: 10.1140/epja/i2005-10162-7
131. Barbieri C, Giusti C, Pacati FD, Dickhoff WH. Effects of nuclear correlations on the ^{1}6O$(e, e'pN)$ reactions to discrete final states. *Phys Rev C*. (2004) **70**:014606. doi: 10.1103/PhysRevC.70.014606
132. Barbieri C. Final state interactions in electron scattering at high missing energies and momenta. *Nucl Phys B*. (2006) **159**:174–9. doi: 10.1016/j.nuclphysbps.2006.08.035
133. Acciarri R, et al. Long-baseline neutrino facility (LBNF) and deep underground neutrino experiment (DUNE). (2015) *arXiv:1601.05471*. doi: 10.2172/1250878
134. Benhar O, et al. Measurement of the spectral function of 40Ar through the (e,e'p) reaction. (2014).
135. Aumann T, Bertulani CA, Ryckebusch J. Quasifree $(p,2p)$ and (p,pn) reactions with unstable nuclei. *Phys Rev C*. (2013) **88**:064610. doi: 10.1103/PhysRevC.88.064610
136. Raimondi F. Private communication (2019).
137. Bennaceur K, Dobaczewski J. *Comp Phys Comm*. (2005) **168**:96. doi: 10.1016/j.cpc.2005.02.002
138. Sun YL (2019). Private communication.
139. Rios A, Somá V. Self-consistent Green's function calculation of the nucleon mean free path. *Phys Rev Lett*. (2012) **108**:012501. doi: 10.1103/PhysRevLett.108.012501
140. Signoracci A, Duguet T, Hagen G, Jansen G. *Ab initio* Bogoliubov coupled cluster theory for open-shell nuclei. *Phys Rev C*. (2015) **91**:064320. doi: 10.1103/PhysRevC.91.064320
141. Bender M, Bertsch GF, Heenen PH. Global study of quadrupole correlation effects. *Phys Rev C*. (2006) **73**:034322. doi: 10.1103/PhysRevC.73.034322
142. Yao JM, Bally B, Engel J, Wirth R, Rodríguez TR, Hergert H. *Ab initio* treatment of collective correlations and the neutrinoless double beta decay of ^{4}8Ca. (2019) *Phys Rev Lett*. 124:232501. doi: 10.1103/PhysRevLett.124.232501
143. Tichai A, Ripoche J, Duguet T. Pre-processing the nuclear many-body problem: importance truncation versus tensor factorization techniques. *Eur Phys J A*. (2019) **55**:90. doi: 10.1140/epja/i2019-12758-6
144. Tichai A, Schutski R, Scuseria GE, Duguet T. Tensor-decomposition techniques for ab initio nuclear structure calculations. From chiral nuclear potentials to ground-state energies. *Phys Rev C*. (2019) **99**:034320. doi: 10.1103/PhysRevC.99.034320
145. Hagen G, Jansen GR, Papenbrock T. Structure of ^{78}Ni from first-principles computations. *Phys Rev Lett*. (2016) **117**:172501. doi: 10.1103/PhysRevLett.117.172501
146. Ripoche J, Tichai A, Duguet T. Normal-ordered k-body approximation in particle-number-breaking theories. *Eur Phys J A*. (2020) **56**:40. doi: 10.1140/epja/s10050-020-00045-8

Conflict of Interest: The author declares that the research was conducted in the absence of any commercial or financial relationships that could be construed as a potential conflict of interest.

frontiers in Physics

REVIEW
published: 15 October 2020
doi: 10.3389/fphy.2020.00345

Perturbative Approach to Effective Shell-Model Hamiltonians and Operators

Luigi Coraggio[1]* *and Nunzio Itaco*[1,2]*

[1] Istituto Nazionale di Fisica Nucleare, Sezione di Napoli, Naples, Italy, [2] Dipartimento di Matematica e Fisica, Università degli Studi della Campania "Luigi Vanvitelli", Caserta, Italy

This article presents an overview of the derivation of effective shell-model Hamiltonian and decay operators within the framework of many-body perturbation theory, and discusses the results of selected shell-model studies based on these operators. More precisely, we give technical details that non-experts will need in order to derive shell-model Hamiltonians and operators starting from realistic nuclear potentials, and provide some guidance for shell-model calculations where the single-particle energies, two-body matrix elements of the residual interaction, effective charges, and decay matrix elements are all obtained without resorting to empirical adjustments. We report results of studies of double-β decay of heavy-mass nuclei where the shell-model ingredients are derived from theory, so as to assess the reliability of such an approach to shell-model investigations. Attention will be also focused on aspects relating to the behavior of the perturbative expansion, knowledge of which is needed for establishing limits and applying this approach to nuclear structure calculations.

Keywords: nuclear shell model, effective interactions, many-body perturbation theory, nuclear forces, double-beta decay

OPEN ACCESS

Edited by:
Michele Viviani,
National Institute of Nuclear Physics of Pisa, Italy

Reviewed by:
Artur Polls,
University of Barcelona, Spain
Daniel Phillips,
Ohio University, United States

***Correspondence:**
Luigi Coraggio
luigi.coraggio@na.infn.it
Nunzio Itaco
nunzio.itaco@unicampania.it

Specialty section:
This article was submitted to Nuclear Physics, a section of the journal Frontiers in Physics

Received: *15 May 2020*
Accepted: *22 July 2020*
Published: *15 October 2020*

Citation:
Coraggio L and Itaco N (2020) Perturbative Approach to Effective Shell-Model Hamiltonians and Operators. Front. Phys. 8:345. doi: 10.3389/fphy.2020.00345

1. INTRODUCTION

This article presents formal details of the derivation of effective shell-model Hamiltonians ($H_{\rm eff}$) and decay operators by a perturbative approach, and reviews a large sample of recent applications to the study of spectroscopic properties of atomic nuclei. The goal of this work is to provide a useful tool for practitioners who are interested in using shell-model single-particle energies, two-body matrix elements, effective charges, and magnetic-dipole and β-decay operators, which are derived from many-body theory, to reproduce a selection of observables without resorting to parameters that are empirically adjusted.

The well-known nuclear shell model (SM) is widely considered a basic theoretical tool for the microscopic description of nuclear structure properties. The nuclear SM is based on the ansatz that each nucleon inside the nucleus moves independently of other nucleons, in a spherically symmetric mean field plus a strong spin-orbit term. This first-approximation depiction of a nucleus is supported by the observation of "magic numbers" of protons and/or neutrons, corresponding to nuclei which are more tightly bound than their neighbors.

These considerations have led to depictions of nucleons arranging themselves into groups of energy levels, called "shells," that are well-separated from each other. The main result of the SM scheme is the reduction of the complex nuclear many-body problem to a very simplified setting where only a few valence nucleons interact in a reduced model space spanned by a single major shell situated above an inert core.

The cost of such a simplification is that shell-model wave functions, which describe the independent motions of individual nucleons, do not include the correlations induced by the strong short-range bare interaction, and therefore could be very different from the real wave functions of the nuclei. The SM Hamiltonian, which will be introduced in the next section, contains one- and two-body components whose characterizing parameters, namely the single-particle (SP) energies and two-body matrix elements (TBMEs) of the residual interaction, account for the degrees of freedom that are not explicitly included in the truncated Hilbert space of the configurations. As a matter of fact, SP energies and TBMEs should be determined to include, in an effective way, the excitations of both the core nucleons and the valence nucleons in the shells above the model space.

Derivation of the effective SM Hamiltonian may follow two distinct paths. One approach is phenomenological: that is, the one- and two-body components of the Hamiltonian are adjusted to reproduce a selected set of experimental data. This can be done either by using an analytical expression for the residual interaction with adjustable parameters, or by treating the Hamiltonian matrix elements directly as free parameters (see [1, 2]).

Over more than 70 years of SM calculations, this approach has been very successful at reproducing a huge amount of data and describing some of the most fundamental physical properties of the structure of atomic nuclei. In this regard, it is worth mentioning the review by Caurier et al. [3], which contains an interesting discussion about the properties of the effective SM Hamiltonian; additional references will be given in the following section.

Another way of constructing H_{eff} is to start from realistic nuclear forces—two- and three-body potentials if possible—and derive the effective Hamiltonian in the framework of many-body theory, i.e., obtain an H_{eff} whose eigenvalues belong to the set of eigenvalues of the full nuclear Hamiltonian defined in the whole Hilbert space.

To do this, one needs a similarity transformation which, within the full Hilbert space of the configurations, leads to a decoupling of the model space P, where the valence nucleons are constrained, from its complement $Q = 1 - P$. Nowadays this can be achieved within the framework of *ab initio* methods, which aim to solve the full Hamiltonian of A nucleons by employing controlled truncations of the accessible degrees of freedom. However, this approach is strictly limited by the computational power available and, even if successful, is currently confined to just a few nuclear mass regions. A comprehensive survey of possible ways to tackle the problem of deriving H_{eff} starting from *ab initio* methods can be found in reference [4], where some SM applications and results are also reviewed.

The present work focuses on perturbative expansion of the effective SM Hamiltonian, grounded in the energy-independent linked-diagram perturbation theory [5], which has been extensively used in SM calculations over the past 50 years (see also the review papers [6, 7]).

An earlier attempt along this line was made by Bertsch [8], who employed as interaction vertices the matrix elements of the reaction matrix G derived from the Kallio-Kolltveit potential [9] to study the role played by the core-polarization diagram at second order in perturbation theory, accounting for one-particle-one-hole ($1p$-$1h$) excitations above the Fermi level of the core nucleons. The results of this work showed that the contribution of such a diagram to H_{eff} was about 30% of the first-order two-body matrix element, when considering the open-shell nuclei ^{18}O and ^{42}Sc outside doubly closed cores ^{16}O and ^{40}Ca, respectively.

Then came the seminal paper by Tom Kuo and Gerry Brown [10], which represents a true turning point in nuclear structure theory. It includes the first successful attempt at performing a shell-model calculation starting from the free nucleon-nucleon (NN) Hamada-Johnston (HJ) potential [11], and resulted in a quantitative description of the spectroscopic properties of sd-shell nuclei.

The TBMEs of the sd-shell effective interaction in reference [10] were derived starting from the HJ potential, with the hard-core component renormalized via calculation of the reaction matrix G. The matrix elements of G were then used as interaction vertices in the perturbative expansion of H_{eff}, including terms up to second order in G.

The TBMEs obtained by this approach were used to calculate the energy spectra of ^{18}O and ^{18}F and yielded results in good agreement with experiments. Moreover, these matrix elements, as well as those derived 2 years later for SM calculations in the fp-shell [12], have become the backbone of the fine-tuning of successful empirical SM Hamiltonians, such as the USD [13] and the KB3G potentials [3, 14].

Between the late 1960s and early 1970s the theoretical framework evolved thanks to the introduction of the folded-diagrams expansion, which formally defined the correct procedure for the perturbative expansion of effective SM Hamiltonians [15, 16].

In the forthcoming sections we will present in detail the derivation of H_{eff} and consistent effective SM decay operators, within the theoretical framework of many-body perturbation theory. At the core of our approach is the perturbative expansion of two vertex functions, the so-called $\hat{Q}$-box and $\hat{\Theta}$-box, in terms of irreducible valence-linked Goldstone diagrams. The $\hat{Q}$-box is then employed to solve non-linear matrix equations in order to obtain H_{eff} by way of iterative techniques [17], and the latter together with the $\hat{\Theta}$-box are the main ingredients for deriving the effective decay operators [18].

This paper is organized as follows. In the next section we present a general overview of the SM eigenvalue problem and the derivation of the effective SM Hamiltonian. In section 3 we tackle the problem on the basis of the Lee-Suzuki similarity transformation [17, 19] and introduce the iterative procedures for solving the decoupling equation that provides this similarity transformation into H_{eff}, for both degenerate and non-degenerate model spaces. Two subsections are devoted to the perturbative expansion of the $\hat{Q}$-box vertex function and the derivation of effective SM decay operators. In section 4 we summarize results of investigations into the double-β decay of ^{130}Te and ^{136}Xe, and discuss the perturbative properties of H_{eff} and effective SM decay operators. The final section gives a summary of the present work.

2. GENERAL OVERVIEW

As mentioned in the Introduction, the SM, introduced 70 years ago [20, 21], is based on the assumption that, as a first approximation, each nucleon (proton or neutron) inside the nucleus moves independently in a spherically symmetric potential representing the average interaction with the other nucleons. This potential is usually described by a Woods-Saxon or harmonic oscillator potential plus a strong spin-orbit term. Inclusion of the latter term is crucial to producing single-particle states clustered in groups of orbits that are close in energy (shells). Each shell is well-separated in energy from the other shells, and this enables the nucleus to be schematized as an inert core, made up of shells filled with neutrons and protons paired to give a total angular momentum of $J = 0^+$, plus a certain number of external nucleons, the so-called "valence" nucleons. This extreme single-particle SM is able to successfully describe various nuclear properties [22], such as the angular momentum and parity of the ground states in odd-mass nuclei. However, it is clear that in order to describe the low-energy structure of nuclei with two or more valence nucleons, the "residual" interaction between the valence nucleons has to be considered explicitly, where the term "residual" refers to that part of the interaction which is not taken into account by the central potential. The inclusion of the residual interaction removes the degeneracy of states belonging to the same configuration and produces a mixing of different configurations.

Let us now use the simple nucleus ^{18}O to introduce some common terminology used in effective interaction theories.

Suppose we want to calculate the properties of the low-lying states in ^{18}O. Then we must solve the Schrödinger equation

$$H|\Psi_\nu\rangle = E_\nu|\Psi_\nu\rangle, \tag{1}$$

where

$$H = H_0 + H_1 \tag{2}$$

with

$$H_0 = \sum_{i=1}^{A}\left(\frac{p_i^2}{2m} + U_i\right) \tag{3}$$

and

$$H_1 = \sum_{i<j=1}^{A} V_{ij}^{NN} - \sum_{i=1}^{A} U_i. \tag{4}$$

An auxiliary one-body potential U_i has been introduced to decompose the nuclear Hamiltonian as the sum of a one-body term H_0, which describes the independent motion of the nucleons, and the residual interaction H_1. It is worth pointing out that in the following, for the sake of simplicity and without any loss of generality, we will assume that the interaction between the nucleons is described by a two-body force only, neglecting three-body contributions. The generalization of the formalism to include three-nucleon forces may be found in references [23, 24].

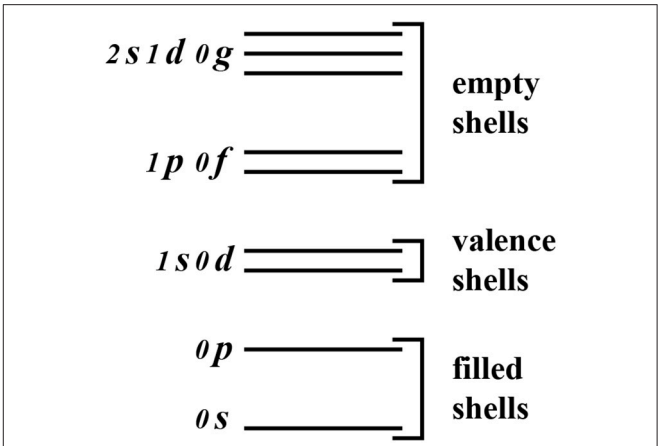

FIGURE 1 | Energy shells that characterize the core, valence space, and empty orbitals for ^{18}O.

It is customary to choose an auxiliary one-body potential U of convenient mathematical form, such as the harmonic oscillator potential

$$U = \sum_{i=1}^{A} \frac{1}{2} m\omega r_i^2. \tag{5}$$

In **Figure 1** we show the relevant portion of the H_0 spectrum for ^{18}O.

We expect the wave functions of the low-lying states in ^{18}O to be dominated by components with a closed ^{16}O core (i.e., the 0*s* and 0*p* orbits are filled) and two neutrons in the valence orbits 1*s* and 0*d*. Hence, we choose a model space spanned by the vectors

$$|\Phi_i\rangle = \sum_{\alpha,\beta\in\text{valence space}} C^i_{\alpha\beta}[a^\dagger_\alpha a^\dagger_\beta]_i|c\rangle, \quad i = 1,\ldots,d, \tag{6}$$

where $|c\rangle$ represents the unperturbed ^{16}O core obtained by completely filling the 0*s* and 0*p* orbits,

$$|c\rangle = \prod_{\alpha\in\text{filled shells}} a^\dagger_\alpha|0\rangle, \tag{7}$$

and the index *i* stands for all the other quantum numbers needed to specify the state (e.g., the total angular momentum).

To illustrate the situation, we show in **Figure 2** some SM configurations labeled in terms of particles and holes with respect to the ^{16}O core.

Solving Equation (1) using basis vectors like those shown in **Figure 2** amounts to diagonalizing the infinite matrix H in **Figure 3**. This is infeasible, so we seek to reduce this huge matrix to a smaller one, H_{eff}, with the requirement that the eigenvalues of the latter should belong to the set of eigenvalues of the former. The notation $|2\text{p}'\,0\text{h}\rangle$ represents a configuration with a closed ^{16}O core plus two particles constrained to interact in the *sd*-shell.

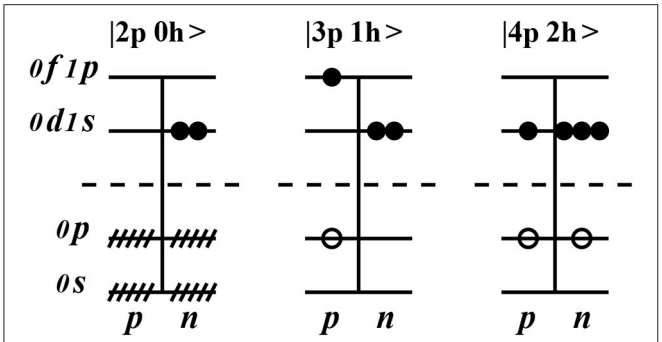

FIGURE 2 | Some ^{18}O shell-model configurations.

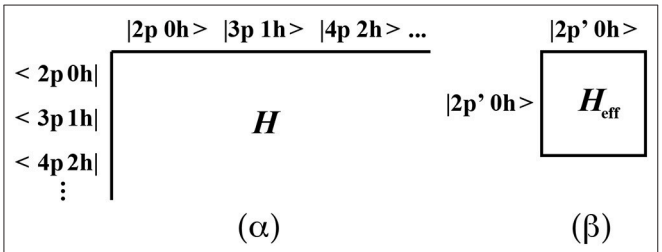

FIGURE 3 | Representation of the matrices H and H_{eff} for ^{18}O.

More formally, it is convenient to define the projection operators P and $Q = 1 - P$, which project from the complete Hilbert space onto the model space and its complementary space (excluded space), respectively. The operator P can be expressed in terms of the vectors in Equation (6) as

$$P = \sum_{i=1}^{d} |\Phi_i\rangle\langle\Phi_i|. \tag{8}$$

The projection operators P and Q satisfy the properties

$$P^2 = P, \quad Q^2 = Q, \quad PQ = QP = 0. \tag{9}$$

The key idea of the effective SM interaction theory is to transform the eigenvalue problem of Equation (1) into a reduced model-space eigenvalue problem

$$PH_{\text{eff}}P|\Psi_\alpha\rangle = (E_\alpha - E_C)P|\Psi_\alpha\rangle, \tag{10}$$

where E_C is the true energy of the core, i.e., the true ground-state energy of ^{16}O in the present case.

As mentioned in the Introduction, there are two main approaches to deriving H_{eff}:

- a phenomenological approach;
- an approach that starts from the bare nuclear interactions and makes use of an appropriate many-body theory.

In the phenomenological approach, empirical effective interactions containing adjustable parameters are introduced and modified to fit a certain set of experimental data, or the two-body matrix elements themselves are treated as free parameters. This approach has been very successful, and we refer to several excellent reviews [2, 3, 25–27] for a comprehensive discussion of the topic.

Currently there are several ways to derive an effective SM Hamiltonian starting from the bare interactions between nucleons. In fact, besides the well-established approaches based on many-body perturbation theory [5] or the Lee-Suzuki transformation [17, 19], novel non-perturbative methods, such as valence-space in-medium similarity renormalization group (VS-IMSRG) [28], shell-model coupled cluster (SMCC) [29], or the no-core shell model (NCSM) with a core based on the Lee-Suzuki similarity transformation [30–33], are now available. These non-perturbative approaches are firmly rooted in many-body theory and provide somewhat different paths to H_{eff}. They can be derived in the same general theoretical framework by expressing H_{eff} as the result of a similarity transformation acting on the original Hamiltonian,

$$H_{\text{eff}} = e^{\mathcal{G}} H e^{-\mathcal{G}}, \tag{11}$$

where the transformation is parameterized as the exponential of a generator $\mathcal{G}$, such that the decoupling condition

$$QH_{\text{eff}}P = 0 \tag{12}$$

is satisfied. Reference [4] contains a very detailed discussion of how the different methods (perturbative and non-perturbative) can be derived within such a general framework, as well as descriptions of the corresponding approximation schemes employed in each approach.

As stated in the Introduction, the present review aims to describe in detail the perturbative approach to the derivation of H_{eff}; this is the focus of the next section. We refer to the already cited review paper by Stroberg et al. [4] for an exhaustive description of alternative methods.

3. PERTURBATIVE EXPANSION OF EFFECTIVE SHELL-MODEL OPERATORS

3.1. The Lee-Suzuki Similarity Transformation

In this subsection we present the formalism of the derivation of the effective SM Hamiltonian based on the similarity transformation introduced by Lee and Suzuki [19]. It is worth noting that this approach has been very successful since it makes a straightforward perturbative expansion of H_{eff} possible for open-shell systems outside a closed core, whereas in other approaches, such as the oscillator-based effective theory (HOBET) proposed by Haxton and Song [34] or the coupled-cluster similarity transformation [35], factorization of the core configurations with respect to the valence nucleons is far more complicated to perform.

We start from the Schrödinger equation for the A-nucleon system, defined in the whole Hilbert space:

$$H|\Psi_\nu\rangle = E_\nu|\Psi_\nu\rangle. \tag{13}$$

As already mentioned, within the SM framework an auxiliary one-body potential U is introduced to express the nuclear Hamiltonian as the sum of an unperturbed one-body mean-field term H_0 and the residual interaction Hamiltonian H_1. The full Hamiltonian H is then rewritten in terms of H_0 and H_1, as in Equations (2)–(4).

According to the nuclear SM described in the previous section, the nucleus may be thought of as a frozen core, composed of a number of nucleons which fill a certain number of energy shells generated by the spectrum of the one-body Hamiltonian H_0, plus a remainder of n interacting valence nucleons moving in the mean field H_0.

The large energy gap between the shells allows us to regard the $A - n$ core nucleons, which completely fill the shells that are lowest in energy, as inert. The SP states accessible to the valence nucleons are those belonging to the major shell situated (in energy) just above the closed core. The configurations allowed by the valence nucleons within this major shell define a reduced Hilbert space, the model space, in terms of a finite subset of d eigenvectors of H_0, as expressed in Equation (6).

We then consider the projection operators P (see Equation 8) and $Q = 1 - P$, which project from the complete Hilbert space onto the model space and its complementary space, respectively, and satisfy the properties in Equation (9).

The goal of an SM calculation is to reduce the eigenvalue problem of Equation (13) to the model-space eigenvalue problem

$$H_{\rm eff}P|\Psi_\alpha\rangle = E_\alpha P|\Psi_\alpha\rangle, \quad \alpha = 1,\ldots,d, \tag{14}$$

where $H_{\rm eff}$ is defined only in the model space.

This means that we are looking for a new Hamiltonian $\mathcal{H}$ whose eigenvalues are the same as those of the Hamiltonian H for the A-nucleon system but which satisfies the decoupling equation between the model space P and its complement Q:

$$Q\mathcal{H}P = 0, \tag{15}$$

which guarantees that the desired effective Hamiltonian is $H_{\rm eff} = P\mathcal{H}P$.

The Hamiltonian $\mathcal{H}$ should be obtained by way of a similarity transformation defined in the whole Hilbert space:

$$\mathcal{H} = X^{-1}HX. \tag{16}$$

Of course, the class of transformation operators X that satisfy the decoupling Equation (15) is infinite, and Lee and Suzuki [17, 19] proposed an operator X defined as $X = e^{\omega}$. Without loss of generality, ω can be chosen to satisfy the following properties:

$$\omega = Q\omega P, \tag{17}$$

$$P\omega P = Q\omega Q = P\omega Q = 0. \tag{18}$$

Equation (17) implies that

$$\omega^2 = \omega^3 = \cdots = 0. \tag{19}$$

According to the above equation, X may be written as $X = 1 + \omega$, and consequently we have the following expression for $H_{\rm eff}$:

$$H_{\rm eff} = P\mathcal{H}P = PHP + PHQ\omega. \tag{20}$$

The operator ω may be calculated by solving the decoupling Equation (15), and the latter can be rewritten as

$$QHP + QHQ\omega - \omega PHP - \omega PHQ\omega = 0. \tag{21}$$

This matrix equation is non-linear, and once the Hamiltonian H is expressed explicitly in the whole Hilbert space, it can be easily solved. Actually, this is not an easy task for nuclei with mass $A > 2$, and, as mentioned in the previous section, this approach has been employed only for light nuclei within the *ab initio* framework.

A successful way to solve Equation (21) for SM calculations is to use a vertex function, the $\hat{Q}$-box, which is suitable for a perturbative expansion. We now explain the $\hat{Q}$-box approach to deriving $H_{\rm eff}$. It is important to note that in the following we assume our model space to be degenerate:

$$PH_0P = \epsilon_0 P. \tag{22}$$

Then, thanks to the decoupling Equation (15), the effective Hamiltonian $H_1^{\rm eff} = H_{\rm eff} - PH_0P$ can be expressed as a function of ω:

$$H_1^{\rm eff} = P\mathcal{H}P - PH_0P = PH_1P + PH_1Q\omega. \tag{23}$$

The above identity, the decoupling Equation (21), and the properties of H_0 and H_1 allow us to define recursively the effective Hamiltonian $H_1^{\rm eff}$. First, since H_0 is diagonal, we can write the following identity:

$$QHP = QH_1P + QH_0P = QH_1P. \tag{24}$$

Then, the decoupling Equation (21) can be rewritten in the form

$$\begin{aligned} &QH_1P + QHQ\omega - \omega(PH_0P + PH_1P + PH_1Q\omega) \\ &\quad = QH_1P + QHQ\omega - \omega(\epsilon_0 P + H_1^{\rm eff}) = 0. \end{aligned} \tag{25}$$

Using this expression for the decoupling equation, we can write a new identity for the operator ω:

$$\omega = Q\frac{1}{\epsilon_0 - QHQ}QH_1P - Q\frac{1}{\epsilon_0 - QHQ}\omega H_1^{\rm eff}. \tag{26}$$

Finally, we obtain a recursive equation by substituting Equation (26) into the identity (23):

$$\begin{aligned} H_1^{\rm eff}(\omega) \;=\; & PH_1P + PH_1Q\frac{1}{\epsilon_0 - QHQ}QH_1P \\ & -PH_1Q\frac{1}{\epsilon_0 - QHQ}\omega H_1^{\rm eff}(\omega). \end{aligned} \tag{27}$$

We now define the $\hat{Q}$-box vertex function as

$$\hat{Q}(\epsilon) = PH_1P + PH_1Q\frac{1}{\epsilon - QHQ}QH_1P, \tag{28}$$

and this allows us to express the recursive Equation (27) as

$$H_1^{\text{eff}}(\omega) = \hat{Q}(\epsilon_0) - PH_1Q\frac{1}{\epsilon_0 - QHQ}\,\omega H_1^{\text{eff}}(\omega). \tag{29}$$

As can be seen from both of the Equations (28) and (29), configurations belonging to the Q space that have energy close to the unperturbed energy of model-space configurations (intruder states) may give unstable solutions of Equation (29). This is the so-called "intruder-state problem" as pointed out in references [36, 37] by Schucan and Weidenmüller. In the following we first present two possible iterative techniques for solving Equation (29), as suggested by Lee and Suzuki [17]. These methods, which are based on calculation of the $\hat{Q}$-box and its derivatives, are known as the Krenciglowa-Kuo and Lee-Suzuki techniques. In particular, we point out that in reference [17] it is shown that the Lee-Suzuki iterative procedure is convergent even when there are some intruder states. We will then present some other approaches that generalize the derivation of H_{eff}, based on calculation of the $\hat{Q}$-box, to unperturbed Hamiltonians H_0 which provide non-degenerate model spaces.

3.1.1. The Krenciglowa-Kuo Iterative Technique

The Krenciglowa-Kuo (KK) iterative technique for solving the recursive Equation (29) is based on the coupling of Equations (29) and (26), which gives the iterative equation

$$H_1^{\text{eff}}(\omega_n) = \sum_{m=0}^{\infty}\left[-PH_1Q\left(\frac{-1}{\epsilon_0 - QHQ}\right)^{m+1}QH_1P\right]\left[H_1^{\text{eff}}(\omega_{n-1})\right]^m. \tag{30}$$

The quantity inside the first set of square brackets in Equation (30), which will be denoted by $\hat{Q}_m(\epsilon_0)$ from now on, is proportional to the mth derivative of the $\hat{Q}$-box calculated at $\epsilon = \epsilon_0$:

$$\hat{Q}_m(\epsilon_0) = -PH_1Q\left(\frac{-1}{\epsilon_0 - QHQ}\right)^{m+1}$$
$$QH_1P = \frac{1}{m!}\left[\frac{d^m\hat{Q}(\epsilon)}{d\epsilon^m}\right]_{\epsilon=\epsilon_0}. \tag{31}$$

We may then rewrite Equation (30) according to the above identity as

$$H_1^{\text{eff}}(\omega_n) = \sum_{m=0}^{\infty}\frac{1}{m!}\left[\frac{d^m\hat{Q}(\epsilon)}{d\epsilon^m}\right]_{\epsilon=\epsilon_0}\left[H_1^{\text{eff}}(\omega_{n-1})\right]^m = \sum_{m=0}^{\infty}\hat{Q}_m(\epsilon_0)\left[H_1^{\text{eff}}(\omega_{n-1})\right]^m. \tag{32}$$

The starting point of the KK iterative method is the assumption that $H_1^{\text{eff}}(\omega_0) = \hat{Q}(\epsilon_0)$, which enables us to rewrite Equation (32) in the form

$$H^{\text{eff}} = \sum_{i=0}^{\infty}F_i, \tag{33}$$

where

$$\begin{aligned} F_0 &= \hat{Q}(\epsilon_0),\\ F_1 &= \hat{Q}_1(\epsilon_0)\hat{Q}(\epsilon_0),\\ F_2 &= \hat{Q}_2(\epsilon_0)\hat{Q}(\epsilon_0)\hat{Q}(\epsilon_0) + \hat{Q}_1(\epsilon_0)\hat{Q}_1(\epsilon_0)\hat{Q}(\epsilon_0),\\ &\vdots \end{aligned} \tag{34}$$

Expression (33) is the well-known folded-diagram expansion of the effective Hamiltonian introduced by Kuo and Krenciglowa. In reference [38] they demonstrated the following operatorial identity:

$$\hat{Q}_1\hat{Q} = -\hat{Q}\int\hat{Q}, \tag{35}$$

where the integral sign corresponds to the so-called folding operation introduced by Brandow in reference [15].

3.1.2. The Lee-Suzuki Iterative Technique

The Lee-Suzuki (LS) technique is another iterative procedure, which is carried out by rearranging Equation (29) to obtain an explicit expression for the effective Hamiltonian H_1^{eff} in terms of the operators ω and $\hat{Q}$ [17]:

$$H_1^{\text{eff}}(\omega) = \left(1 + PH_1Q\frac{1}{\epsilon_0 - QHQ}\omega\right)^{-1}\hat{Q}(\epsilon_0). \tag{36}$$

The iterative form of the above equation is

$$H_1^{\text{eff}}(\omega_n) = \left(1 + PH_1Q\frac{1}{\epsilon_0 - QHQ}\,\omega_{n-1}\right)^{-1}\hat{Q}(\epsilon_0), \tag{37}$$

and we may also write an iterative expression for Equation (26):

$$\omega_n = Q\frac{1}{\epsilon_0 - QHQ}QH_1P - Q\frac{1}{\epsilon_0 - QHQ}\,\omega_{n-1}H_1^{\text{eff}}(\omega_n). \tag{38}$$

The standard procedure is to start the iteration by choosing $\omega_0 = 0$, so that we may write

$$H_1^{\text{eff}}(\omega_1) = \hat{Q}(\epsilon_0),$$
$$\omega_1 = Q\frac{1}{\epsilon_0 - QHQ}QH_1P.$$

After some algebra, the following identity can be established:

$$\hat{Q}_1(\epsilon_0) = -PH_1Q\frac{1}{\epsilon_0 - QHQ}Q\frac{1}{\epsilon_0 - QHQ}$$
$$QH_1P = -PH_1Q\frac{1}{\epsilon_0 - QHQ}\,\omega_1. \tag{39}$$

Then for the $n = 2$ iteration we have

$$H_1^{\text{eff}}(\omega_2) = \left(1 + PH_1\frac{1}{\epsilon_0 - QHQ}\,\omega_1\right)^{-1}\hat{Q}(\epsilon_0) = \frac{1}{1 - \hat{Q}_1(\epsilon_0)}\,\hat{Q}(\epsilon_0),$$

$$\omega_2 = Q\frac{1}{\epsilon_0 - QHQ}QH_1P - Q\frac{1}{\epsilon_0 - QHQ}\omega_1 H_1^{\text{eff}}(\omega_2). \tag{40}$$

Finally, the LS iterative expression for H_{eff} is

$$H_1^{\text{eff}}(\omega_n) = \left[1 - \hat{Q}_1(\epsilon_0)\sum_{m=2}^{n-1}\hat{Q}_m(\epsilon_0)\prod_{k=n-m+1}^{n-1}H_1^{\text{eff}}(\omega_k)\right]^{-1}\hat{Q}(\epsilon_0). \tag{41}$$

It is important to realize that the KK and LS iterative techniques, which allow the solution of the decoupling Equation (25), do not in principle provide the same H_{eff}. Suzuki and Lee have shown that the KK iterative approach provides an effective Hamiltonian whose eigenstates have the largest overlap with the eigenstates of the model space, and that H_{eff} obtained from the LS technique has eigenvalues that are lowest in energy among those belonging to the set of the full Hamiltonian H [17].

Both the KK and the LS procedures are limited to employing an unperturbed Hamiltonian H_0 whose model-space eigenstates are degenerate in energy. However, reference [39] introduced an alternative approach to the KK and LS techniques, which extends these methods to the case of non-degenerate H_0 by using multi-energy $\hat{Q}$-boxes. This approach is quite involved in practice, and the only existing application in the literature is that in reference [40].

We next outline two methods [41, 42] for deriving effective SM Hamiltonians which may be implemented straightforwardly with H_0's that are non-degenerate in the model space.

3.1.3. The Kuo-Krenciglowa Technique Extended to Non-degenerate Model Spaces

The extended Kuo-Krenciglowa (EKK) method is an extension of the KK iterative technique that can be used to derive an H_{eff} within non-degenerate model spaces [41, 43]. We summarize the EKK method as follows.

First, a shifted Hamiltonian $\tilde{H}$ is defined in terms of an energy parameter E:

$$\tilde{H} = H - E. \tag{42}$$

Then we rewrite Equation (25) in terms of $\tilde{H}$:

$$(E - QHQ)\omega = QH_1P - \omega P\tilde{H}P - \omega PH_1Q\omega = QH_1P - \omega\tilde{H}_{\text{eff}}. \tag{43}$$

Equation (43) may be solved by an iterative procedure analogous to the KK technique, in terms of the $\hat{Q}$-box and its derivatives as defined in Equations (28) and (31), respectively.

The effective Hamiltonian $\tilde{H}_{\text{eff}}$ at the nth step of the iterative procedure may then be expressed as [41]

$$\tilde{H}_{\text{eff}}^{(n)} = \tilde{H}_{\text{BH}}(0) + \sum_{k=1}^{\infty}\hat{Q}_k(0)\left[\tilde{H}_{\text{eff}}^{(n-1)}\right]^k, \tag{44}$$

where $\tilde{H}_{\text{BH}}$ is the solution of the Bloch-Horowitz equation [44]:

$$\tilde{H}_{\text{BH}}(E) = P\tilde{H}P + PH_1Q\frac{1}{E - QHQ}QH_1P. \tag{45}$$

We note that the EKK method does not require H_0 to be degenerate within the model space; it has therefore been applied to derive H_{eff} in a multi-shell valence space [45, 46] and in Gamow SM calculations with realistic NN potentials [47, 48].

It is worth pointing out that, since $\tilde{H}_{\text{eff}} = \lim_{n\to\infty}\tilde{H}_{\text{eff}}^{(n)}$, we can write

$$\tilde{H}_{\text{eff}} = \tilde{H}_{\text{BH}}(0) + \sum_{k=1}^{\infty}\hat{Q}_k(0)\left[\tilde{H}_{\text{eff}}\right]^k. \tag{46}$$

Equation (46) may be interpreted as a Taylor series expansion of $\tilde{H}_{\text{eff}}$ about $\tilde{H}_{\text{BH}}$, and the parameter E corresponds to a shift of the origin of the expansion and a resummation of the series [45]. In fact, by virtue of Equation (42) we may express H_{eff} as

$$H_{\text{eff}} = \tilde{H}_{\text{eff}} + E = H_{\text{BH}}(0) + \sum_{k=1}^{\infty}\hat{Q}_k(0)\left[\tilde{H}_{\text{eff}}\right]^k. \tag{47}$$

Now, both sides of the above equation are independent of E provided that the summation is carried out at infinity, and the parameter E may be tuned to accelerate the convergence of the series when in practical applications a numerical partial summation needs to be employed and a perturbative expansion of the $\hat{Q}$-box is carried out [45].

3.1.4. The $\hat{Z}(\epsilon)$ Vertex Function

Suzuki and coworkers proposed in reference [42] an approach to the derivation of H_{eff} that aims to avoid the divergences of the $\hat{Q}$-box vertex function when a non-degenerate model space is considered. In fact, the definition of the $\hat{Q}$-box in Equation (28) shows that if ϵ approaches one of the eigenvalues of QHQ, then instabilities may arise if one employs a numerical derivation, since these eigenvalues are poles of $\hat{Q}(\epsilon)$.

We now sketch the procedure described in reference [42] and, for the sake of simplicity, consider the case of a degenerate unperturbed model space (i.e., $PH_0P = \epsilon_0 P$).

A new vertex function $\hat{Z}(\epsilon)$ is introduced and defined in terms of $\hat{Q}(\epsilon)$ and its first derivative as

$$\hat{Z}(\epsilon) \equiv \frac{1}{1 - \hat{Q}_1(\epsilon)}\left[\hat{Q}(\epsilon) - \hat{Q}_1(\epsilon)(\epsilon - \epsilon_0)P\right]. \tag{48}$$

It can be demonstrated that $\hat{Z}(\epsilon)$ satisfies the equation [42]

$$\left[\epsilon_0 + \hat{Z}(E_\alpha)\right]P|\Psi_\alpha\rangle = E_\alpha P|\Psi_\alpha\rangle, \quad \alpha = 1, \ldots, d. \tag{49}$$

Consequently, H_1^{eff} may be obtained by calculating the $\hat{Z}$-box for those values of the energy, determined self-consistently, that correspond to the "true" eigenvalues E_α.

To calculate E_α, we solve the eigenvalue problem

$$\left[\epsilon_0 + \hat{Z}(\epsilon)\right]|\phi_k\rangle = F_k(\epsilon)|\phi_k\rangle, \quad k = 1, 2, \ldots, d, \tag{50}$$

where $F_k(\epsilon)$ are d eigenvalues that depend on ϵ. Then, the true eigenvalues E_α can be obtained by solving the d equations

$$\epsilon = F_k(\epsilon), \quad k = 1, 2, \ldots, d. \tag{51}$$

First, it is worth pointing out some fundamental properties of $\hat{Z}(\epsilon)$ and the associated functions $F_k(\epsilon)$. We then proceed to discuss the solution of the Equations (50) and (51).

The behavior of $\hat{Z}(\epsilon)$ near the poles of $\hat{Q}(\epsilon)$ is dominated by $\hat{Q}_1(\epsilon)$, and we may write $\hat{Z}(\epsilon) \approx (\epsilon - \epsilon_0)P$. This means that $\hat{Z}(\epsilon)$ has no poles and so the $F_k(\epsilon)$'s are continuous and differentiable functions for any value of ϵ.

The Equations (51) may have solutions that do not correspond to the true eigenvalues E_α, i.e., spurious solutions. In reference [42] it is shown that since the energy derivative of $F_k(\epsilon)$ approaches zero at $\epsilon = E_\alpha$, study of this derivative provides a criterion for locating and rejecting spurious solutions. The solution of Equations (50) and (51), which is necessary for deriving the effective interaction, may be achieved through both iterative and non-iterative methods.

We describe here a graphical non-iterative method for solving Equation (51). As mentioned before, the $F_k(\epsilon)$'s are continuous functions of the energy, and hence the solutions of Equation (51) may be determined as intersections of the graphs $y = \epsilon$ and $y = F_k(\epsilon)$, using one of the well-known algorithms for solving non-linear equations.

More precisely, if we define the functions $f_k(\epsilon)$ as $f_k(\epsilon) = F_k(\epsilon) - \epsilon$, the solutions of Equation (51) can obtained by finding the roots of the equations $f_k(\epsilon) = 0$. From inspection of the graphs $y = \epsilon$ and $y = F_k(\epsilon)$, we can locate for each intersection a small surrounding interval $[\epsilon_a, \epsilon_b]$ where $f_k(\epsilon_a) f_k(\epsilon_b) < 0$. The assumption that $f_k(\epsilon)$ is a monotone function within this interval implies the existence of a unique root, which can be accurately determined by means of the secant algorithm (see e.g., reference [49]).

After we have determined the true eigenvalues E_α, the effective Hamiltonian H_1^{eff} is constructed as

$$H_1^{\text{eff}} = \sum_{\alpha=1}^{d} \hat{Z}(E_\alpha)|\phi_\alpha\rangle\langle\tilde{\phi}_\alpha|, \tag{52}$$

where $|\phi_\alpha\rangle$ is the eigenvector obtained from Equation (50) and $\langle\tilde{\phi}_\alpha|$ is the corresponding biorthogonal state (such that $\langle\tilde{\phi}_\alpha|\phi_{\alpha'}\rangle = \delta_{\alpha\alpha'}$).

As mentioned at the beginning of this subsection, we focus on the case of a degenerate unperturbed model space (i.e., $PH_0P = \epsilon_0 P$), but the above formalism can easily be generalized to the non-degenerate case by replacing $\epsilon_0 P$ with PH_0P in Equations (48)–(50).

3.2. Diagrammatic Expansion of the $\hat{Q}$-box Vertex Function

The methods of deriving H_{eff} presented in the preceding sections require the calculation of the $\hat{Q}$-box vertex function

$$\hat{Q}(\epsilon) = PH_1P + PH_1Q \frac{1}{\epsilon - QHQ} QH_1P.$$

For our purposes, the term $1/(\epsilon - QHQ)$ is expanded as a power series

$$\frac{1}{\epsilon - QHQ} = \sum_{n=0}^{\infty} \frac{1}{\epsilon - QH_0Q} \left(\frac{QH_1Q}{\epsilon - QH_0Q}\right)^n, \tag{53}$$

leading to a perturbative expansion of the $\hat{Q}$-box. It is useful to employ a diagrammatic representation of this perturbative expansion, which is a collection of Goldstone diagrams that have at least one H_1-vertex, are irreducible (i.e., at least one line between two successive vertices does not belong to the model space), and are linked to at least one external valence line (valence-linked) [16].

The standard procedure for most perturbative derivations of H_{eff} is to deal with systems that have one and two valence nucleons, but later we will show how include contributions from three-body diagrams, which come into play when more than two valence nucleons are considered. The H_{eff}^{1b} of single-valence-nucleon nuclei provides the theoretical effective SP energies, while TBMEs of the residual interaction V^{eff} are obtained from the H_{eff}^{2b} for systems with two valence nucleons. This can be achieved by a subtraction procedure [50], namely removing from H_{eff}^{2b} the diagonal component of the effective SP energies derived from the H_{eff}^{1b} of the one-valence-nucleon systems.

A useful resource for practitioners who want to acquire sufficient knowledge about the calculation of $\hat{Q}$-box diagrams in an angular-momentum coupled representation is the paper by Kuo and coworkers [51].

It is worth pointing out that in the current literature effective SM Hamiltonians are derived accounting for $\hat{Q}$-box diagrams up to at most third order in perturbation theory, as it is computationally highly demanding to perform calculations including higher-order sets of diagrams. A complete list of diagrams can be found in reference [52], Appendix B, and consists of 43 one-body and 135 two-body diagrams. We remark that lists of diagrams can easily be obtained using algorithms which generate order-by-order Hugenholtz diagrams for perturbation theory applications (see e.g., reference [53]).

Because the aim of this article is to provide practitioners with useful tips for deriving effective SM Hamiltonians within the perturbative approach, we give some examples of $\hat{Q}$-box diagrams and their analytical expressions. Our first example is the third-order ladder diagram V_{ladder} shown in **Figure 4**. To obtain an explicit expression for it, we will use the proton-neutron angular-momentum coupled representation for the TBMEs of the input potential V_{NN}:

$$\langle 1,2;J|V_{NN}|3,4;J\rangle \equiv \langle n_1 l_1 j_1 t_{z_1}, n_2 l_2 j_2 t_{z_2}; J|V_{NN}|n_3 l_3 j_3 t_{z_3}, n_4 l_4 j_4 t_{z_4}; J\rangle. \tag{54}$$

The TBMEs of V_{NN} are antisymmetrized but not normalized to ease the calculation of the $\hat{Q}$-box diagrams; n_m, l_m, j_m, and t_{z_m} indicate the orbital and isospin quantum numbers of the SP state m.

The analytical expression for V_{ladder} is

$$\begin{aligned}&\langle a,b;J|V_{\text{ladder}}|c,d;J\rangle \\ &= +\frac{1}{4}\sum_{p_1,p_2,p_3,p_4} \frac{\langle a,b;J|V_{NN}|p_1,p_2;J\rangle\langle p_1,p_2;J|V_{NN}|p_3,p_4;J\rangle\langle p_3,p_4;J|V_{NN}|c,d;J\rangle}{[\epsilon_0 - (\epsilon_{p_1} + \epsilon_{p_2})][\epsilon_0 - (\epsilon_{p_3} + \epsilon_{p_4})]},\end{aligned} \tag{55}$$

where ϵ_m denotes the unperturbed SP energy of the orbital j_m and ϵ_0 is the so-called starting energy, i.e., the unperturbed energy of the incoming particles, $\epsilon_0 = \epsilon_c + \epsilon_d$.

We point out that the factor $+1/4$ is related to rules that characterize the calculation of overall factors in $\hat{Q}$-box Goldstone diagrams; for any diagram we have a phase factor

$$(-1)^{(n_{\rm h}+n_{\rm l}+n_{\rm c}+n_{\rm exh})}$$

whose value is determined by the total number of hole lines ($n_{\rm h}$), the total number of closed loops ($n_{\rm l}$), the total number of crossings of different external lines as they trace through the diagrams ($n_{\rm c}$), and the total number of external hole lines that continuously trace through the diagrams ($n_{\rm exh}$) [51]. There is also a factor of $(1/2)^{n_{\rm ep}}$, which accounts for the pairs of lines that start together from one interaction vertex and end together at another one ($n_{\rm ep}$).

The diagram in **Figure 4** has $n_{\rm h} = n_{\rm l} = n_{\rm c} = n_{\rm exh} = 0$, and consequently the phase is positive. The number of pairs of particles starting and ending together at the same vertices is $n_{\rm ep} = 2$, and so the overall factor is $+1/4$.

The factorization of Goldstone diagrams, such as the ladder diagram in **Figure 4** in terms of their interaction vertices is quite simple. There is a large class of diagrams, like the three-particle-one-hole diagram ($3p$-$1h$) in **Figure 5**, which require some additional considerations to obtain a straightforward factorization.

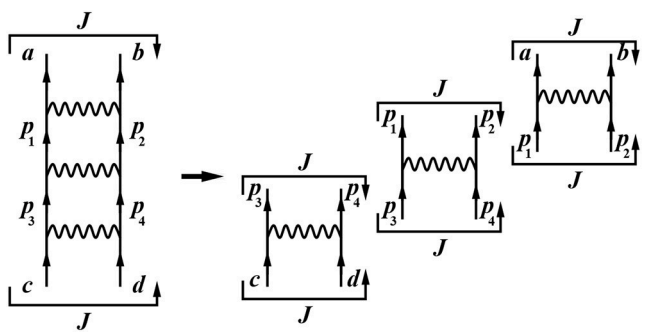

FIGURE 4 | Two-body ladder diagram at third order in perturbation theory: lines with arrows represent incoming/outgoing and intermediate particle states; wavy lines represent interaction vertices.

The factorization can easily be performed by taking into account the fact that the interaction operator V_{NN} transforms as a scalar under rotation, and so we introduce the following cross-coupling transformation of the TBMEs:

$$\langle a,b;J|V_{NN}|c,d;J\rangle_{\rm CC} = \frac{1}{\hat{J}}\sum_{J'}\hat{J}'X\begin{pmatrix} j_c & j_a & J \\ j_d & j_b & J \\ J' & J' & 0\end{pmatrix} \langle a,b;J'|V_{NN}|c,d;J'\rangle, \tag{56}$$

where $\hat{x} = (2x+1)^{1/2}$ and X is the so-called standard normalized 9-j symbol, expressed in terms of the Wigner 9-j symbol [54] as

$$X\begin{pmatrix} r & s & t \\ u & v & w \\ x & y & z\end{pmatrix} = \hat{t}\,\hat{w}\,\hat{x}\,\hat{y}\begin{Bmatrix} r & s & t \\ u & v & w \\ x & y & z\end{Bmatrix}.$$

The orthonormalization properties of X allow us to then write the direct-coupled TBMEs in terms of the cross-coupled TBMEs:

$$\langle a,b;J|V_{NN}|c,d;J\rangle = \frac{1}{\hat{J}}\sum_{J'}\hat{J}'X\begin{pmatrix} j_c & j_d & J \\ j_a & j_b & J \\ J' & J' & 0\end{pmatrix} \langle a,b;J'|V_{NN}|c,d;J'\rangle_{\rm CC}. \tag{57}$$

Equations (56) and (57) help us to perform the factorization of the diagram in **Figure 5**. First, a rotation according to Equation (57) transforms the direct coupling to the total angular momentum J into the cross-coupled one J' (diagram A going to diagram A_1 in **Figure 5**). This allows us to cut the inner loop and factorize the diagram into two terms, a ladder component (α) and a cross-coupled matrix element (β) (diagram A_2 in **Figure 5**):

$$(\alpha) = \langle a,p_3;J'|{\rm A}|c,h;J'\rangle_{\rm CC},$$
$$(\beta) = \langle h,b;J'|V_{NN}|p_3,d;J'\rangle_{\rm CC}.$$

Next, we transform the ladder diagram (A) back to a direct coupling to J'' by way of Equation (56), and factorize it into the TBMEs (I) and (II) (diagram A_3 in **Figure 5**):

$$({\rm I}) = \langle a,p_3;J''|V_{NN}|p_1,p_2;J''\rangle,$$

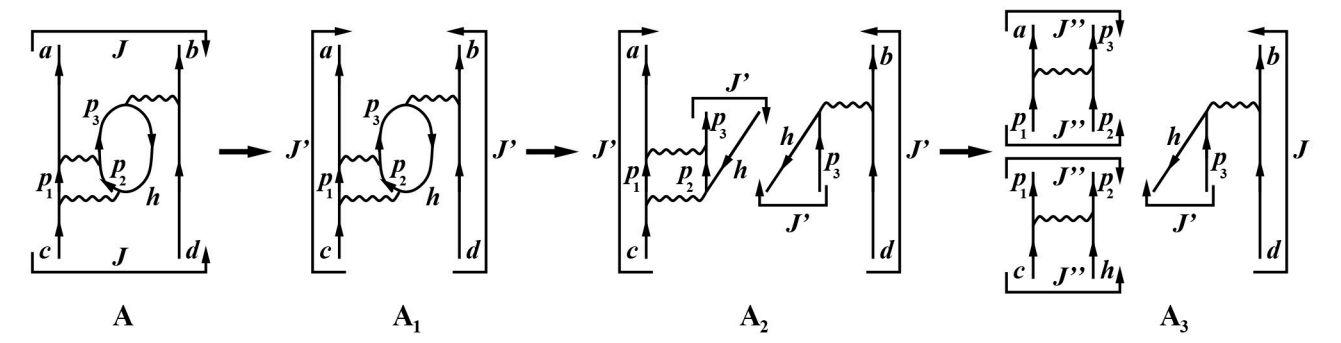

FIGURE 5 | Two-body $3p$-$1h$ diagram at third order in perturbation theory: lines with arrows represent incoming/outgoing and intermediate particle/hole states; wavy lines indicate interaction vertices.

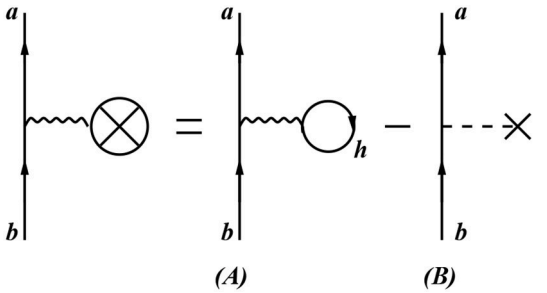

FIGURE 6 | (*V*-*U*)-insertion diagram: graph *A* is the self-energy diagram, and graph *B* represents the matrix element of the harmonic oscillator potential $U = \frac{1}{2}m\omega^2 r^2$.

$$(\mathrm{II}) = \langle p_1, p_2; J''|V_{NN}|c, h; J''\rangle.$$

The analytical expression for the diagram in **Figure 5** is then

$$\langle a, b; J|V_{3p1h}|c, d; J\rangle = -\frac{1}{2}\frac{1}{\hat{J}}\sum_{h,p_1,p_2,p_3}\sum_{J',J''}\hat{J''}X\begin{pmatrix} j_c & j_d & J \\ j_a & j_b & J \\ J' & J' & 0\end{pmatrix}X\begin{pmatrix} j_c & j_a & J' \\ j_h & j_p & J' \\ J'' & J'' & 0\end{pmatrix} \times \frac{\langle h, b; J'|V_{NN}|p_3, d; J'\rangle_{\mathrm{CC}}\langle a, p_3; J''|V_{NN}|p_1, p_2; J''\rangle\langle p_1, p_2; J''|V_{NN}|c, h; J''\rangle}{[\epsilon_0 - (\epsilon_{p_1} + \epsilon_{p_2})][\epsilon_0 - (\epsilon_{p_3} + \epsilon_{p_4})]}, \tag{58}$$

The factor of $-1/2$ accounts for the facts that $n_{\mathrm{ep}} = 1$, $n_{\mathrm{h}} = n_{\mathrm{l}} = 1$, and an extra phase factor $(-1)^{n_{\mathrm{ph}}}$ is needed for the total number of cuts of particle-hole pairs (n_{ph}) [51], since in order to factorize the diagram we have to cut the inner loop.

We remark that there are another three diagrams with the same topology as the one in **Figure 5**, which corresponds to the exchange of external incoming and outgoing particles.

Let us now turn our attention to one-body diagrams. First, we consider the contribution of diagrams, such as the one in **Figure 6**.

The diagram in **Figure 6** is the so-called (*V*-*U*)-insertion diagram and is composed of the self-energy diagram (*V*-insertion diagram) minus the auxiliary potential *U*-insertion. The *U*-insertion diagrams are due to the presence of the *U* term in H_1. The analytical expression for this diagram is

$$\begin{aligned}\langle a||(V\text{-}U)||b\rangle &= \frac{\delta_{j_a j_b}}{2j_a+1}\sum_{J,h}(2J+1)\langle j_a, h; J|V|j_b, h; J\rangle - \langle a||U||b\rangle \\ &= \frac{\delta_{j_a j_b}}{2j_a+1}\sum_{J,h}(2J+1)\langle j_a, h; J|V|j_b, h; J\rangle - \langle a||\frac{1}{2}m\omega^2 r^2||b\rangle.\end{aligned} \tag{59}$$

The calculation of the self-energy diagram *A* is performed by coupling the external lines to a scalar, which leads to the SP total angular momentum and the parity of j_a, j_b being identical. Then we cut the inner hole line and, since the SP states *a* and *b* are coupled to $J = 0^+$, apply the transformation in Equation (56) with $J = 0^+$.

Since the standard choice for the auxiliary potential is the harmonic oscillator potential, we also have the reduced matrix element of $U = \frac{1}{2}m\omega^2 r^2$ between the SP states *a* and *b* (graph *B* in **Figure 6**).

It is worth pointing out that the diagonal contributions of (*V*-*U*)-insertion diagrams, for SP states belonging to the model space, correspond to first-order contributions of the perturbative expansion of the effective SM Hamiltonian H_{eff}^{1b} of single-valence-nucleon systems.

Moreover, (*V*-*U*)-insertion diagrams turn out to be identically zero if a self-consistent Hartree-Fock (HF) auxiliary potential is used [40], and reference [52] discusses the important role played by these terms, comparing different effective Hamiltonians derived by starting from $\hat{Q}$-boxes with and without contributions from (*V*-*U*)-insertion diagrams.

Now we will give an example of a one-body diagram and comment briefly on its analytical calculation. We consider the diagram in **Figure 7**; the complete list of third-order one-body diagrams can be found in reference [52], Figure B.19.

We call this diagram V_{2p1h}, since between the upper interaction vertices two particles and one hole appear as intermediate states. This diagram belongs to the group of non-symmetric diagrams, which always occur in pairs that give equal contributions. Its analytical expression is

$$\langle j||V_{2p1h}||j\rangle = -\frac{1}{2}\frac{1}{2j+1} \sum_{\substack{J,p_1,p_2,\\ h_1,h_2}}(2J+1)\frac{\langle j, h_2; J|V_{NN}|p_1, p_2; J\rangle\langle p_1, p_2; J|V_{NN}|h_1, h_2; J\rangle\langle h_1||V\text{-}U||j\rangle}{[\epsilon_0 - (\epsilon_{p_1} + \epsilon_{p_2} - \epsilon_{h_2})][\epsilon_0 - (\epsilon_j + \epsilon_{p_1} + \epsilon_{p_2} - \epsilon_{h_1} - \epsilon_{h_2})]} \tag{60}$$

where $\epsilon_0 = \epsilon_j$ is the unperturbed SP energy of the incoming particle *j*.

To factorize the diagram, we first cross-couple the incoming and outgoing model-space states *j* to $J' = 0^+$ (diagram A_1 in **Figure 7**). Then we cut the hole line h_2 and, by way of Equation (56), obtain a sum of two-body diagrams which are direct-coupled to the total angular momentum *J* [51] (diagram A_2 in **Figure 7**). These operations are responsible for the factors $1/(2j+1)$ and $(2J+1)$; the overall factor $1/2$ is due to the pair of particle lines (p_1, p_2) starting and ending at the same vertices, while the minus sign comes from the two hole lines and one loop appearing in the diagram. The factorization also takes into account the (*V*-*U*)-insertion $\langle h_1||V\text{-}U|j\rangle$.

As mentioned before, this diagrammatic approach is valid for deriving H_{eff} for one- and two-valence-nucleon systems; the situation is different and more complicated if one wishes to derive H_{eff} for systems with three or more valence nucleons.

Actually, none of the available SM codes can perform diagonalization of SM Hamiltonians with three-body components; the exception is the BIGSTICK SM code [55], but it works only for light nuclei.

In order to incorporate the contribution to H_{eff} of $\hat{Q}$-box diagrams with at least three incoming and outgoing valence particles, we resort to the so-called normal-ordering decomposition of the three-body component of a many-body Hamiltonian [56]. To this end, we also include in the calculation of the $\hat{Q}$-box second-order three-body diagrams, which, for those nuclei with more than two valence nucleons, account for the interaction via the two-body force of the valence nucleons with core excitations as well as virtual intermediate nucleons scattered above the model space (see **Figure 8**).

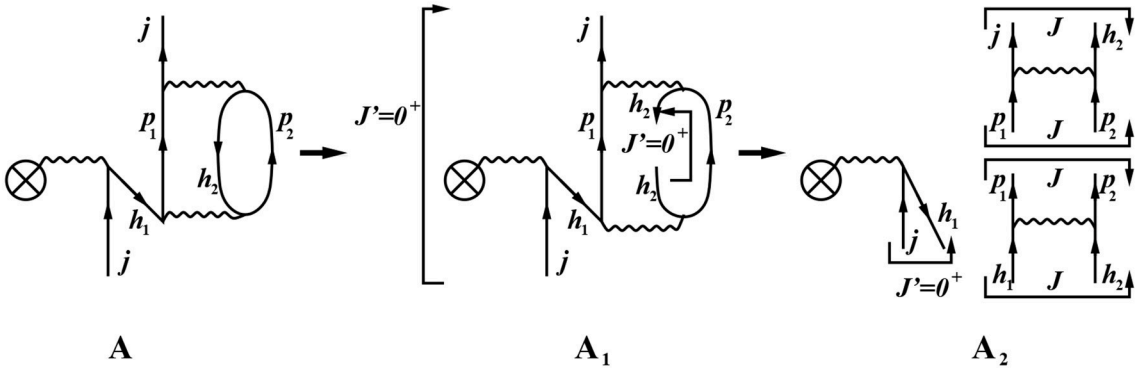

FIGURE 7 | An example of a one-body diagram (see text for details).

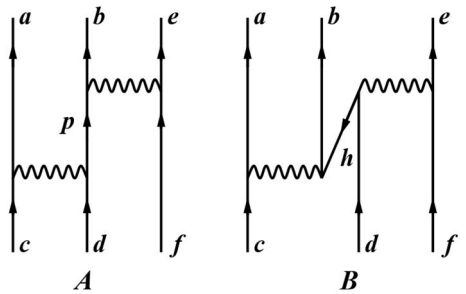

FIGURE 8 | Second-order three-body diagrams. The sum over the intermediate lines runs over particle and hole states outside the model space, shown in *A* and *B*, respectively. For the sake of simplicity, for each topology we show only one of the diagrams which correspond to permutations of the external lines.

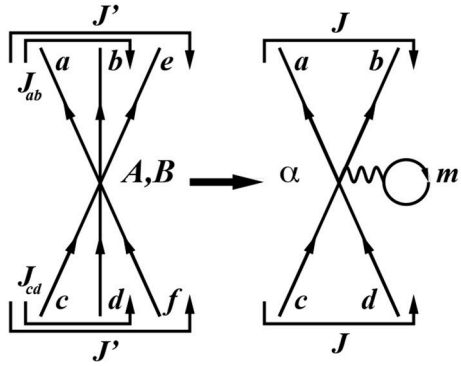

FIGURE 9 | Density-dependent two-body contribution obtained from a three-body one; α is obtained by summing over one incoming and one outgoing particle of the three-body graphs *A* in **Figure 8**.

For each topology shown in **Figure 8** there are nine diagrams, corresponding to the possible permutations of the external lines. The analytical expressions for the second-order three-body contributions are reported in reference [57], and we derive from those expressions a density-dependent two-body term.

To this end, for each (A, B) topology we calculate nine one-loop diagrams, i.e., graphs of the form α in **Figure 9**. Their explicit form, in terms of the three-body graphs (A, B), is

$$\langle (j_a j_b)_J | V^{\alpha} | (j_c j_d)_J \rangle = \sum_{m,J'} \rho_m \frac{\hat{J'}^2}{\hat{J}^2} \langle \left[(j_a j_b)_J, j_m \right]_{J'} | V^{A,B} | \left[(j_c j_d)_J, j_m \right]_{J'} \rangle, \qquad (61)$$

where the summation over the index m runs over the model space and ρ_m is the unperturbed occupation density of the orbital m according to the number of valence nucleons.

Finally, the perturbative expansion of the $\hat{Q}$-box contains one- and two-body diagrams up to third order in V_{NN}, along with a density-dependent two-body contribution that accounts for three-body second-order diagrams [57, 58]. We point out that the latter term depends on the number of valence protons and neutrons, thus leading to the derivation of specific effective SM Hamiltonians that differ only in the two-body matrix elements.

3.3. Effective Shell-Model Decay Operators

In the SM approach, we are interested not only in calculating energies but also in finding the matrix elements of operators Θ that represent physical observables (such as electromagnetic transition rates, multipole moments, etc.).

Since the wave functions $|\psi_\alpha\rangle$ obtained from diagonalizing $H_{\rm eff}$ are not the true ones $|\Psi_\alpha\rangle$ but their projections onto the chosen model space ($|\psi_\alpha\rangle = P|\Psi_\alpha\rangle$), it is obvious that one has to renormalize Θ to take into account the neglected degrees of freedom corresponding to the Q-space. In other words, one needs to consider the short-range correlation "wounds" inflicted by the bare interaction on the SM wave functions. Formally, one seeks to derive an effective operator $\Theta_{\rm eff}$ such that

$$\langle \tilde{\Psi}_\alpha | \Theta | \Psi_\beta \rangle = \langle \tilde{\psi}_\alpha | \Theta_{\rm eff} | \psi_\beta \rangle. \qquad (62)$$

The perturbative expansion of effective operators has been studied since the earliest attempts to employ realistic potentials for SM calculations; among the many studies we mention the

fundamental and pioneering work carried out by L. Zamick on the problem of electromagnetic transitions [59–61] and by I. S. Towner on the quenching of spin-operator matrix elements [62, 63].

In this subsection we discuss the formal structure of non-Hermitian effective operators, as introduced by Suzuki and Okamoto in reference [18]. More precisely, we give an expansion formula for the effective operators in terms of the $\hat{\Theta}$-box, which, analogous to the $\hat{Q}$-box in the effective interaction theory (see section 3), is the building block for constructing effective operators.

According to Equation (20) (and keeping in mind that $\omega \equiv Q\omega P$), we may write $H_{\rm eff}$ as

$$H_{\rm eff} = PH(P+\omega), \tag{63}$$

so that we can express the true eigenstates $|\Psi_\alpha\rangle$ and their orthonormal counterparts $\langle\tilde{\Psi}_\alpha|$ as

$$|\Psi_\alpha\rangle = (P+\omega)|\psi_\alpha\rangle, \quad \langle\tilde{\Psi}_\alpha| = \langle\tilde{\psi}_\alpha|(P+\omega^\dagger\omega)(P+\omega^\dagger). \tag{64}$$

On the other hand, a general effective operator expression in the bra-ket representation is

$$\Theta_{\rm eff} = \sum_{\alpha,\beta} |\psi_\alpha\rangle\langle\tilde{\Psi}_\alpha|\Theta|\Psi_\beta\rangle\langle\tilde{\psi}_\beta|, \tag{65}$$

where Θ is a general time-independent Hermitian operator. Therefore, we can write $\Theta_{\rm eff}$ in operator form as

$$\Theta_{\rm eff} = (P+\omega^\dagger\omega)^{-1}(P+\omega^\dagger)\Theta(P+\omega). \tag{66}$$

It is worth noting that Equation (62) holds independently of the normalization of $|\Psi_\alpha\rangle$ and $|\psi_\alpha\rangle$, but if the true eigenvectors are normalized, then $\langle\tilde{\Psi}_\alpha| = \langle\Psi_\alpha|$ and the $|\psi_\alpha\rangle$ should be normalized in the following way:

$$\langle\tilde{\psi}_\alpha|(P+\omega^\dagger\omega)|\psi_\alpha\rangle = 1. \tag{67}$$

To explicitly calculate $\Theta_{\rm eff}$, we introduce the $\hat{\Theta}$-box, defined as

$$\hat{\Theta} = (P+\omega^\dagger)\Theta(P+\omega), \tag{68}$$

so that $\Theta_{\rm eff}$ can be factorized as

$$\Theta_{\rm eff} = (P+\omega^\dagger\omega)^{-1}\hat{\Theta}. \tag{69}$$

The derivation of $\Theta_{\rm eff}$ is divided into two steps: the calculation of $\hat{\Theta}$ and the calculation of $\omega^\dagger\omega$.

According to Equation (68) and taking into account the expression for ω in terms of $H_{\rm eff}$, i.e.,

$$\omega = \sum_{n=0}^{\infty}(-1)^n\left(\frac{1}{\epsilon_0 - QHQ}\right)^{n+1} QH_1P(H_1^{\rm eff})^n, \tag{70}$$

we can write

$$\hat{\Theta} = \hat{\Theta}_{PP} + (\hat{\Theta}_{PQ} + \text{h.c.}) + \hat{\Theta}_{QQ}, \tag{71}$$

where

$$\hat{\Theta}_{PP} = P\Theta P, \tag{72}$$

$$\hat{\Theta}_{PQ} = P\Theta\omega P = \sum_{n=0}^{\infty}\hat{\Theta}_n(H_1^{\rm eff})^n, \tag{73}$$

$$\hat{\Theta}_{QQ} = P\omega^\dagger\Theta\omega P = \sum_{n,m=0}^{\infty}(H_1^{\rm eff})^n\hat{\Theta}_{nm}(H_1^{\rm eff})^m, \tag{74}$$

and $\hat{\Theta}_m$ and $\hat{\Theta}_{mn}$ are given by

$$\hat{\Theta}_m = \frac{1}{m!}\frac{d^m\hat{\Theta}(\epsilon)}{d\epsilon^m}\bigg|_{\epsilon=\epsilon_0}, \tag{75}$$

$$\hat{\Theta}_{mn} = \frac{1}{m!n!}\frac{d^m}{d\epsilon_1^m}\frac{d^n}{d\epsilon_2^n}\hat{\Theta}(\epsilon_1;\epsilon_2)\bigg|_{\epsilon_1=\epsilon_0,\epsilon_2=\epsilon_0} \tag{76}$$

with

$$\hat{\Theta}(\epsilon) = P\Theta P + P\Theta Q\frac{1}{\epsilon - QHQ}QH_1P, \tag{77}$$

$$\hat{\Theta}(\epsilon_1;\epsilon_2) = PH_1Q\frac{1}{\epsilon_1 - QHQ}Q\Theta Q\frac{1}{\epsilon_2 - QHQ}QH_1P. \tag{78}$$

As regards the product $\omega^\dagger\omega$, using the definition (31) we can write

$$\omega^\dagger\omega = -\sum_{n=1}^{\infty}\sum_{m=1}^{\infty}((H_1^{\rm eff})^\dagger)^{n-1}\hat{Q}(\epsilon_0)_{n+m-1}(H_1^{\rm eff})^{m-1}. \tag{79}$$

Upon expressing $H_1^{\rm eff}$ in terms of the $\hat{Q}$-box and its derivatives (see Equations 33 and 34), the above quantity may be rewritten as

$$\begin{aligned}\omega^\dagger\omega \;=\; &-\hat{Q}_1 + (\hat{Q}_2\hat{Q} + \text{h.c.}) + (\hat{Q}_3\hat{Q}\hat{Q} + \text{h.c.})\\ &+(\hat{Q}_2\hat{Q}_1\hat{Q} + \text{h.c.}) + \cdots.\end{aligned} \tag{80}$$

Putting together Equations (77) and (80), we can write the final perturbative expansion of the effective operator $\Theta_{\rm eff}$:

$$\Theta_{\rm eff} = (P+\hat{Q}_1+\hat{Q}_1\hat{Q}_1+\hat{Q}_2\hat{Q}+\hat{Q}\hat{Q}_2+\cdots)\times(\chi_0+\chi_1+\chi_2+\cdots), \tag{81}$$

where

$$\chi_0 = (\hat{\Theta}_0 + \text{h.c.}) + \hat{\Theta}_{00}\,, \tag{82}$$

$$\chi_1 = (\hat{\Theta}_1\hat{Q} + \text{h.c.}) + (\hat{\Theta}_{01}\hat{Q} + \text{h.c.}), \tag{83}$$

$$\begin{aligned}\chi_2 = &(\hat{\Theta}_1\hat{Q}_1\hat{Q} + \text{h.c.}) + (\hat{\Theta}_2\hat{Q}\hat{Q} + \text{h.c.})\\ &+ (\hat{\Theta}_{02}\hat{Q}\hat{Q} + \text{h.c.}) + \hat{Q}\hat{\Theta}_{11}\hat{Q}\,.\end{aligned} \tag{84}$$

$$\vdots$$

It is worth elucidating the strong link that exists between $H_{\rm eff}$ and any effective operator. This is achieved by inserting the identity $\hat{Q}\hat{Q}^{-1} = \mathbf{1}$ into Equation (81) to obtain the following expression:

$$\Theta_{\rm eff} = (P + \hat{Q}_1 + \hat{Q}_1\hat{Q}_1 + \hat{Q}_2\hat{Q} + \hat{Q}\hat{Q}_2 + \cdots)\hat{Q}\hat{Q}^{-1}$$

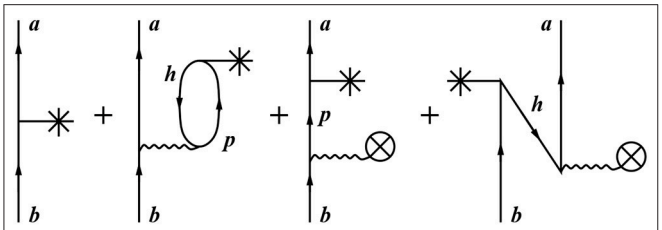

FIGURE 10 | One-body second-order diagrams included in the perturbative expansion of $\hat{\Theta}_0$; an asterisk indicates the bare operator Θ.

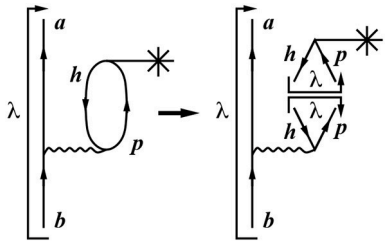

FIGURE 11 | One-body second-order 2*p*-1*h* diagram included in the perturbative expansion of $\hat{\Theta}_0$; an asterisk indicates the bare operator Θ.

$$\times (\chi_0 + \chi_1 + \chi_2 + \cdots)$$
$$= H_{\rm eff}\hat{Q}^{-1}(\chi_0 + \chi_1 + \chi_2 + \cdots). \quad (85)$$

In actual calculations the χ_n series is truncated to a finite order and the starting point is the derivation of perturbative expansions for $\hat{\Theta}_0 \equiv \hat{\Theta}(\epsilon_0)$ and $\hat{\Theta}_{00} \equiv \hat{\Theta}(\epsilon_0;\epsilon_0)$, including diagrams up to a finite order in the perturbation theory, consistently with the expansion of the $\hat{Q}$-box. The issue of convergence of the χ_n series and of the perturbative expansions of $\hat{\Theta}_0$ and $\hat{\Theta}_{00}$ will be treated extensively in section 4.1.

In **Figure 10** we display all the diagrams up to second order appearing in the $\hat{\Theta}_0$ expansion for a one-body operator Θ.

The evaluation of the diagrams involved in the derivation of $\Theta_{\rm eff}$ follows the same procedure as described in the previous section. Therefore, in the following we will just outline the procedure for calculating such diagrams with one Θ vertex.

Let us suppose that the operator Θ transforms like a spherical tensor of rank λ and with component μ:

$$\Theta \equiv T^{\lambda}_{\mu}, \quad (86)$$

with

$$(T^{\lambda}_{\mu})^{\dagger} = (-1)^{\lambda-\mu} T^{\lambda}_{-\mu}. \quad (87)$$

By using the Wigner-Eckart theorem, it is possible to express any transition matrix element in terms of a reduced transition element:

$$\langle j_a||T^{\lambda}||j_b\rangle = (-1)^{\lambda-\mu}\langle j_a|T^{\lambda}_{\mu}|j_b\rangle, \quad (88)$$

where in the right-hand side j_b and j_a are coupled to a total angular momentum and projection equal to λ and $-\mu$, respectively, and we have assumed without lack of generality that we are dealing with single-particle states.

Therefore, we evaluate each diagram as a contribution to the reduced matrix element of the effective operator. To be more explicit, we consider as an example the calculation of the following second-order diagram that takes into account the renormalization of the operator due to 1*p*-1*h* core excitations.

The first step is to couple j_b and j_a to a total angular momentum equal to λ. This enables us to factorize the diagram as the product of a cross-coupled matrix element of the interaction and the reduced matrix element of the operator (see the right-hand part of **Figure 11**).

Explicitly, we can evaluate the diagram as

$$\langle j_a||\Theta_{2p1h}||j_b\rangle$$
$$= -\sum_{p,h}(-1)^{j_p+j_h-\lambda}\frac{\langle j_a,p;\lambda|V_{NN}|j_b,h;\lambda\rangle_{\rm CC}\langle h||T^{\lambda}||p\rangle}{\epsilon_0-(\epsilon_a+\epsilon_b-\epsilon_{\rm h})}. \quad (89)$$

The minus sign in front is due to the fact that $n_{\rm h} = n_{\rm l} = 1$ and that an extra phase factor $(-1)^{n_{\rm ph}}$ is needed for the total number of cuts of particle-hole pairs ($n_{\rm ph}$) [51], since we have to cut the inner loop to factorize the diagram.

4. APPLICATIONS

In this section we present a specific example of SM calculations performed by employing effective SM Hamiltonian and decay operators derived from realistic nuclear potentials within the many-body perturbation theory.

These kinds of calculations have actually been carried out since the mid-1960s, but they mostly involved retaining only the TBMEs, since the single-body components of $H_{\rm eff}$ were not considered accurate enough to provide SM results that would agree well with experiments. A large sample of calculations performed in that successful framework can be found in previous reviews of the topic [6, 7].

Here we present results of a calculation where both the SP energies and the TBMEs that are needed to diagonalize the SM Hamiltonian have been obtained by deriving $H_{\rm eff}$ according to the procedures described in the previous section. Besides $H_{\rm eff}$, the many-body perturbation theory has been used to derive consistently effective operators to calculate electromagnetic transition rates and Gamow-Teller (GT) strengths without resorting to the use of empirical effective charges or quenching factors for the axial coupling constant g_A.

The following are some motivations for performing SM calculations by deriving and employing all SM parameters—SP energies, TBMEs, and effective transition and decay operators—starting from realistic nuclear forces:

- the need to study the soundness of many-body perturbation theory so as to provide reliable SM parameters;
- the need to determine the ability of classes of nuclear potentials to describe nuclear structure observables;

- the opportunity to compare and benchmark SM calculations against other nuclear structure methods that employ realistic potentials.

The goal of these studies is to assess the reliability of such an approach to investigating the nuclear SM, especially its predictiveness, which is crucial for describing physical phenomena that are not yet accessible experimentally.

4.1. The Double-β Decay Around Doubly Closed ^{132}Sn

Neutrinoless double-β ($0\nu\beta\beta$) decay is an exotic second-order electroweak process predicted by extensions of the Standard Model of particle physics. Observation of such a process would demonstrate the non-conservation of the lepton number and provide evidence that neutrinos have a Majorana mass component (see references [64, 65] and references therein).

In the framework of light-neutrino exchange, the half-life of the $0\nu\beta\beta$ decay is inversely proportional to the square of the effective Majorana neutrino mass $\langle m_\nu \rangle$:

$$\left[T^{0\nu}_{1/2}\right]^{-1} = G^{0\nu}\left|M^{0\nu}\right|^2 g_A^4 \left|\frac{\langle m_\nu \rangle}{m_e}\right|^2, \tag{90}$$

where g_A is the axial coupling constant, m_e is the electron mass, $G^{0\nu}$ is the so-called phase-space factor (or kinematic factor), and $M^{0\nu}$ is the nuclear matrix element (NME), which is related to the wave functions of the nuclei involved in the decay.

At present, the phase-space factors for nuclei that are possible candidates for $0\nu\beta\beta$ decay can be calculated with great accuracy [66, 67]. It is therefore crucial to have precise values for the NME, both to improve the reliability of the $0\nu\beta\beta$ lifetime predictions—a fundamental ingredient in the design of new experiments—and to extract neutrino properties from the experimental results, when they become available.

Several nuclear structure models have been exploited to provide NME values that are as precise as possible, the most commonly used being the interacting boson model [68–70], the quasiparticle random-phase approximation [71–74], energy density functional methods [75], the covariant density functional theory [76–78], the generator-coordinate method [79–82], and the shell model [83–87].

All of the above models use a truncated Hilbert space to reduce the computational complexity, and each can be more efficient than the others for a specific class of nuclei. However, when comparing the calculated NMEs obtained via different approaches, it is seen that, at present, the results can differ by a factor of two or three (see for instance the review in reference [88]).

Reference [89] reports on the calculation of the $0\nu\beta\beta$-decay NME for ^{48}Ca, ^{76}Ge, ^{82}Se, ^{130}Te, and ^{136}Xe in the framework of the realistic SM, where the $H_{\rm eff}$'s and $0\nu\beta\beta$-decay effective operators are consistently derived starting from a realistic *NN* potential, the high-precision CD-Bonn potential [90].

We remark that the above work is not the first example of such an approach, which was pioneered by Kuo and coworkers [91, 92] and more recently pursued by Holt and Engel [93].

Here we restrict ourselves to the results obtained in reference [89] for the heavy-mass nuclei around ^{132}Sn, ^{130}Te, and ^{136}Xe. At present, these nuclei are under investigation as $0\nu\beta\beta$-decay candidates by some large experimental collaborations. The possible $0\nu\beta\beta$ decay of ^{130}Te is being studied by the CUORE collaboration at the INFN Laboratori Nazionali del Gran Sasso in Italy [94], while ^{136}Xe is being investigated by both the EXO-200 collaboration at the Waste Isolation Pilot Plant in Carlsbad, New Mexico [95], and the KamLAND-Zen collaboration at the Kamioka mine in Japan [96].

The starting point of the SM calculation is the high-precision CD-Bonn *NN* potential [90], whose non-perturbative behavior induced by its repulsive high-momentum components is treated with the so-called $V_{\text{low-}k}$ approach [97]. This yields a smooth potential which exactly preserves the onshell properties of the original *NN* potential up to a chosen cutoff momentum Λ. As in other SM studies [98–101], the value of the cutoff has been chosen as $\Lambda = 2.6$ fm^{-1}, since the role of the missing three-nucleon force (3NF) decreases as the $V_{\text{low-}k}$ cutoff is increased [99]. In fact, in reference [99] it is shown that $H_{\rm eff}$'s derived from $V_{\text{low-}k}$'s with small cutoffs ($\Lambda = 2.1$ fm^{-1}) have SP energies that are in worse agreement with experiments, as well as unrealistic shell-evolution behavior. This may be attributed to a greater impact of the induced 3NF, which becomes less important with a larger cutoff.

In our experience, $\Lambda = 2.6$ fm^{-1}, within a perturbative expansion of the $\hat{Q}$-box, is an upper limit, since a larger cutoff worsens the order-by-order behavior of the perturbative expansion; at the end of this section we report a study of the perturbative properties of $H_{\rm eff}$ and of the effective decay operators derived using this $V_{\text{low-}k}$ potential.

The Coulomb potential is explicitly taken into account in the proton-proton channel.

The SM effective Hamiltonian $H_{\rm eff}$ is derived within the framework of the many-body perturbation theory as described in section 3, including diagrams up to third order in H_1 in the $\hat{Q}$-box-expansion, while all the effective operators, both one- and two-body, are obtained consistently using the approach described in section 3.3, including diagrams up to third order in perturbation theory in the evaluation of the $\hat{\Theta}$-box and truncating the χ_n series in Equation (81) to χ_2.

The effective Hamiltonian and operators are defined in a model space spanned by the five proton and neutron orbitals, $0g_{7/2}$, $1d_{5/2}$, $1d_{3/2}$, $2s_{1/2}$, and $0h_{11/2}$, outside the doubly closed ^{100}Sn core. The SP energies and TBMEs of $H_{\rm eff}$ can be found in reference [101].

Before showing the results for the $0\nu\beta\beta$ NME obtained in reference [89], it is worth checking the reliability of the approach we have adopted. To this end, we present some results obtained from the calculation of quantities for which there exist experimental counterparts to compare with. In particular, we show selected results for the electromagnetic properties, GT strength distributions, and $2\nu\beta\beta$ decays in ^{130}Te and ^{136}Xe, which have been reported in references [101, 102].

Figures 12, **13** show experimental [103, 104] and calculated low-energy spectra and $B(E2)$ strengths of parent and

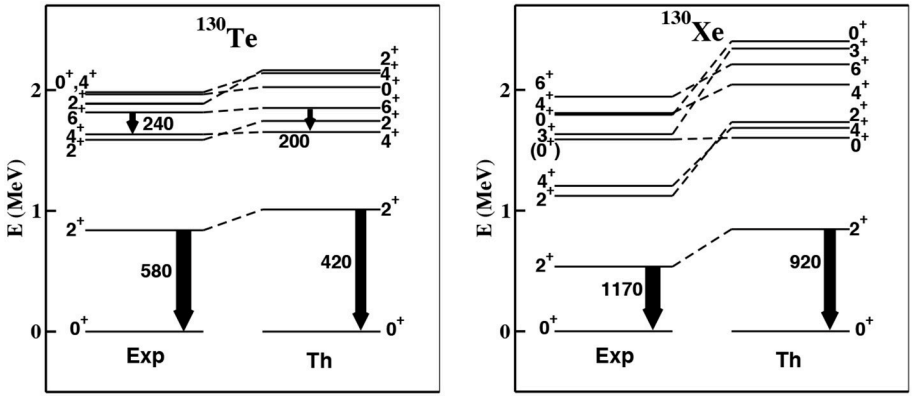

FIGURE 12 | Experimental and calculated spectra of ^{130}Te and ^{130}Xe; the arrows are proportional to the $B(E2)$ strengths, whose values are reported in e^2fm^4. Reproduced from reference [102].

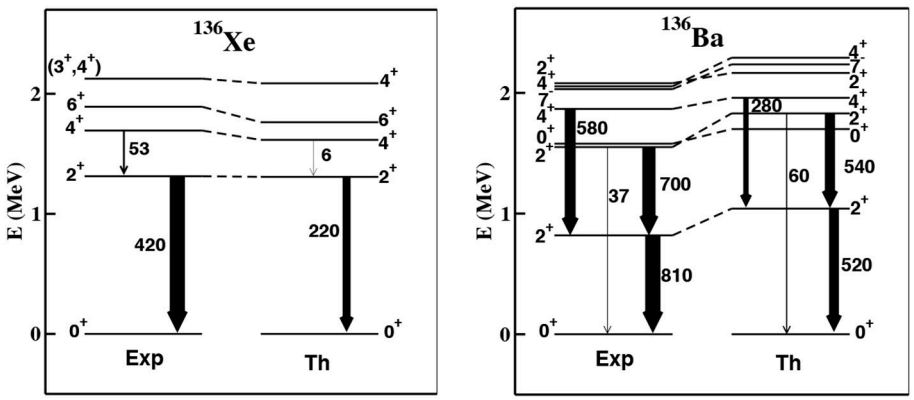

FIGURE 13 | Same as **Figure 12** but for ^{136}Xe and ^{136}Ba. Reproduced from reference [102].

granddaughter nuclei involved in double-β decay of ^{130}Te and ^{136}Xe, respectively.

By inspection of **Figures 12**, **13** it can be seen that, as regards the low-lying excited states and the $B(E2)$ transition rates, theory and experiment agree quite well for ^{130}Te, ^{136}Xe, and ^{136}Ba, but less so for ^{130}Xe, whose theoretical spectrum is expanded compared with the observed one. As regards the electromagnetic properties, in reference [102] they are calculated along with some $B(M1)$ strengths and magnetic dipole moments using an effective spin-dependent $M1$ operator, and comparison with the available data (see Tables VII and IX in reference [102]) shows good agreement.

Two kinds of experimental data related to GT decay are available for ^{130}Te and ^{136}Xe: GT strength distributions and the NMEs involved in $2\nu\beta\beta$ decays. The GT strength B(GT) can be extracted from the GT component of the cross-section at zero degrees of intermediate energy charge-exchange reactions, following the standard approach in the distorted-wave Born approximation [105, 106]:

$$\frac{d\sigma^{\rm GT}(0^\circ)}{d\Omega} = \left(\frac{\mu}{\pi\hbar^2}\right)^2 \frac{k_f}{k_i} N_{\rm D}^{\sigma\tau} |J_{\sigma\tau}|^2 B({\rm GT}), \tag{91}$$

where $N_{\rm D}^{\sigma\tau}$ is the distortion factor, $|J_{\sigma\tau}|$ is the volume integral of the effective NN interaction, k_i and k_f are the initial and final momenta, respectively, and μ is the reduced mass.

On the other hand, the experimental $2\nu\beta\beta$ NME $M^{2\nu}_{\rm GT}$ can be extracted from the observed half-life $T^{2\nu}_{1/2}$ of the parent nucleus as follows:

$$\left[T^{2\nu}_{1/2}\right]^{-1} = G^{2\nu} \left|M^{2\nu}_{\rm GT}\right|^2 . \tag{92}$$

Both of the above quantities can be calculated in terms of the matrix elements of the GT$^-$ operator $\vec{\sigma}\tau^-$:

$$B({\rm GT}) = \frac{\left|\langle\Phi_f||\sum_j \vec{\sigma}_j \tau_j^- ||\Phi_i\rangle\right|^2}{2J_i+1}, \tag{93}$$

$$M^{2\nu}_{\rm GT} = \sum_n \frac{\langle 0_f^+||\vec{\sigma}\tau^-||1_n^+\rangle\langle 1_n^+||\vec{\sigma}\tau^-||0_i^+\rangle}{E_n + E_0}, \tag{94}$$

where E_n is the excitation energy of the $J^\pi = 1_n^+$ intermediate state and $E_0 = \frac{1}{2}Q_{\beta\beta}(0^+) + \Delta M$, with $Q_{\beta\beta}(0^+)$ and ΔM being the Q-value of the $\beta\beta$ decay and the mass difference between the daughter and parent nuclei, respectively. The nuclear

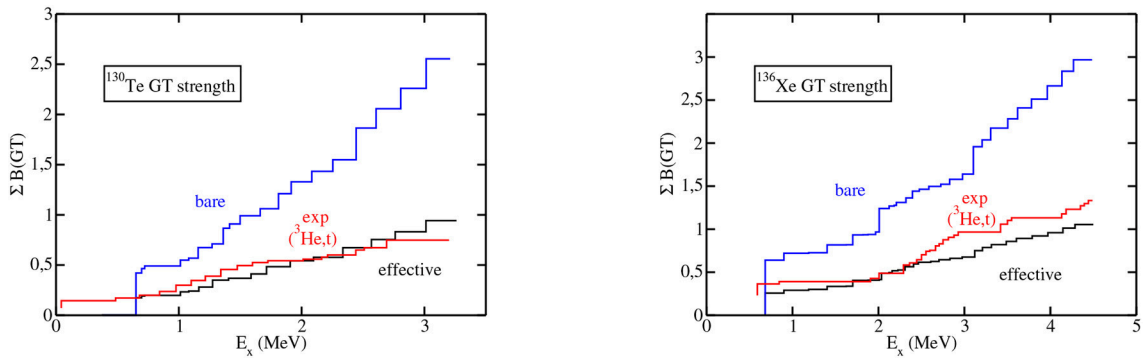

FIGURE 14 | Running sums of the B(GT) strengths as a function of the excitation energy E_x up to 3 and 4.5 MeV, respectively, for ^{130}Te and ^{136}Xe. Reproduced from reference [102].

TABLE 1 | Experimental [109] and calculated NMEs (in MeV^{-1}) of the $2\nu\beta\beta$ decay for ^{130}Te and ^{136}Xe.

Decay	NME_{Expt}	Bare	Effective
^{130}Te $\rightarrow$ ^{130}Xe	0.031 ± 0.004	0.131	0.061
^{136}Xe $\rightarrow$ ^{136}Ba	0.0181 ± 0.0007	0.0910	0.0341

matrix elements in Equations (93) and (94) are calculated within the long-wavelength approximation, including only the leading order of the GT operator in a non-relativistic reduction of the hadronic current.

In reference [102] the GT strength distributions and $2\nu\beta\beta$ NMEs were calculated for ^{130}Te and ^{136}Xe using an effective spin-isospin-dependent GT operator, derived in a manner consistent with $H_{\rm eff}$ by following the procedure described in section 3.3.

Figure 14 shows the theoretical running sums of the GT strengths ΣB(GT), calculated with both bare and effective GT operators, plotted against the excitation energy and compared with the available data extracted from (^{3}He, t) charge-exchange experiments [107, 108] for ^{130}Te and ^{136}Xe. It can be seen that in both nuclei, the GT strength distributions calculated using the bare GT operator overestimate the experimental ones by more than a factor of two. Including the many-body renormalization of the GT operator brings the predicted GT strength distribution into much better agreement with that extracted from experimental data.

In reference [102] the NMEs $M^{2\nu}_{\rm GT}$ involved in the decay of ^{130}Te and ^{136}Xe are calculated using the definition in Equation (94), by means of the Lanczos strength function method as in reference [3]. The results obtained with the bare GT operator and with the effective one are reported in **Table 1** and compared with experimental values [109].

The effective operator induces a relevant quenching of the calculated NME, 47% for ^{130}Te and 37% for ^{136}Xe decay, leading to fairly good agreement with the experimental value for both nuclei, of the same quality as for other SM calculations where all parameters (SP energies and TBMEs) were fitted to experimental values and a quenching factor q was introduced to reproduce GT data (see, for example, reference [110]). The overall agreement between theory and experiment shows that the many-body perturbation theory can be used to derive consistently effective Hamiltonians and transition operators that are able to reproduce quantitatively the observed spectroscopic and decay properties, without having to resort to any empirical adjustments, such as quenching of the axial coupling constant g_A. This supports the reliability of this approach to calculating the NMEs involved in $0\nu\beta\beta$, the results of which were reported in reference [89] and are briefly summarized in the following.

The $0\nu\beta\beta$ two-body operator for the light-neutrino scenario can be expressed in the closure approximation (see e.g., references [111, 112]) in terms of the neutrino potentials H_α and form functions $h_\alpha(q)$ ($\alpha =$ F, GT, or T) as

$$\Theta_{\rm GT} = \vec{\sigma}_1 \cdot \vec{\sigma}_2 H_{\rm GT}(r)\tau_1^- \tau_2^-, \tag{95}$$

$$\Theta_{\rm F} = H_{\rm F}(r)\tau_1^- \tau_2^-, \tag{96}$$

$$\Theta_{\rm T} = \left[3\left(\vec{\sigma}_1 \cdot \hat{r}\right)\left(\vec{\sigma}_1 \cdot \hat{r}\right) - \vec{\sigma}_1 \cdot \vec{\sigma}_2\right] H_{\rm T}(r)\tau_1^- \tau_2^-, \tag{97}$$

where

$$H_\alpha(r) = \frac{2R}{\pi}\int_0^\infty \frac{j_{n_\alpha}(qr)h_\alpha(q^2)q\,dq}{q + \langle E\rangle}. \tag{98}$$

The value of the parameter R is $1.2\,A^{1/3}$ fm, and the $j_{n_\alpha}(qr)$ are the spherical Bessel functions, with $n_\alpha = 0$ for the Fermi and GT components and $n_\alpha = 2$ for the tensor one. The explicit expressions for the neutrino form functions $h_\alpha(q)$ can be found in reference [89], and the average energies $\langle E\rangle$ are evaluated as in references [111, 112].

Apart from effects related to sub-nucleonic degrees of freedom, which were not accounted for in reference [89], the $0\nu\beta\beta$-decay operator has to be renormalized to take into account both the degrees of freedom that are neglected in the adopted model space and the contribution of short-range correlations (SRCs). The latter arise because the action of a two-body decay operator on an unperturbed (uncorrelated) wave function, such as the one used in the perturbative expansion of $\Theta_{\rm eff}$, differs from the action of the same operator on the real (correlated) nuclear wave function.

TABLE 2 | Calculated values of $M^{0\nu}$ for ^{130}Te and ^{136}Xe decay.

Decay	Bare operator	Θ_{eff}
$^{130}\text{Te} \rightarrow {}^{130}\text{Xe}$	3.27	3.16
$^{136}\text{Xe} \rightarrow {}^{136}\text{Ba}$	2.47	2.39

The first column of values correspond to results obtained using the bare $0\nu\beta\beta$-decay operator, and the second column to results calculated with Θ_{eff}.

It is worth pointing out that the calculations for $2\nu\beta\beta$ decay are not affected by this renormalization, since, as mentioned before, we retain only the leading order of the long-wavelength approximation, which corresponds to a zero-momentum-exchange ($q = 0$) process. On the other hand, the inclusion of higher-order contributions or corrections due to the sub-nucleonic structure of the nucleons [113–116] would connect high- and low-momentum configurations, and this renormalization should be carried out for the two-neutrino emission decay too.

In reference [117] the inclusion of SRCs was realized by means of an original approach [117] that is consistent with the $V_{\text{low-}k}$ procedure. The $0\nu\beta\beta$ operator Θ, expressed in the momentum space, is renormalized by the same similarity transformation operator $\Omega_{\text{low-}k}$ that defines the $V_{\text{low-}k}$ potential. This enables us to effectively take into account the high-momentum (short-range) components of the *NN* potential, in a framework where their direct contribution is not explicitly considered above a cutoff Λ. The resulting $\Theta_{\text{low-}k}$ vertices are then employed in the perturbative expansion of the $\hat{\Theta}$-box to calculate Θ_{eff} using Equation (85). More precisely, the perturbative expansion considers diagrams up to third order in perturbation theory, including those related to the so-called Pauli blocking effect (see **Figure 2** in reference [89]), and the χ_n series is truncated to χ_2.

In reference [89] the contribution of the tensor component of the neutrino potential (Equation 97) is neglected, and therefore the total NME $M^{0\nu}$ is expressed as

$$M^{0\nu} = M^{0\nu}_{\text{GT}} - \left(\frac{g_V}{g_A}\right)^2 M^{0\nu}_{\text{F}}, \tag{99}$$

where $g_A = 1.2723$, $g_V = 1$ [118], and the matrix elements between the initial and final states $M^{0\nu}_{\alpha}$ are calculated within the closure approximation

$$M^{0\nu}_{\alpha} = \sum_{j_n j_{n'} j_p j_{p'}} \langle f | a^{\dagger}_p a_n a^{\dagger}_{p'} a_{n'} | i \rangle \times \langle j_p j_{p'} \mid \Theta_{\alpha} \mid j_n j_{n'} \rangle. \tag{100}$$

The NMEs calculated using the $0\nu\beta\beta$-decay effective operator are reported in **Table 2** and compared with the values obtained using the bare operator without any renormalization.

The most striking feature that can be inferred from inspection of **Table 2** is that the effects of the renormalization of the $0\nu\beta\beta$-decay operator are far less relevant than those observed in the $2\nu\beta\beta$-decay case.

A long-standing issue related to the calculation of $M^{0\nu}$ is possible interplay between the derivation of the effective one-body GT operator and the renormalization of the two-body GT component of the $0\nu\beta\beta$ operator, with some authors assuming that the same empirical quenching used to reproduce the observed GT-decay properties (single-β decay strengths, $M^{2\nu}_{\text{GT}}$'s, etc.) should also be employed to calculate $M^{0\nu}$ (see for instance references [119, 120]). In fact, comparison of the results in **Tables 1**, **2** shows that the mechanisms underlying the microscopic derivation of the one-body single-β and the two-body $0\nu\beta\beta$-decay effective operators lead to a considerably different renormalization, at variance with the above hypothesis.

The SM calculations of this section have been performed by employing, as interaction vertices of the perturbative expansion of the $\hat{Q}$-box, a realistic potential derived from the high-precision CD-Bonn *NN* potential [90]. This potential is characterized by strong repulsive behavior in the high-momentum regime, so, as mentioned before, it is renormalized by deriving a low-momentum *NN* potential using the $V_{\text{low-}k}$ approach [97].

As in other SM studies [98–101], the value of the cutoff is chosen as $\Lambda = 2.6$ fm^{-1}, since the role of the missing 3NF decreases as the $V_{\text{low-}k}$ cutoff is increased [99]. This value, within a perturbative expansion of the $\hat{Q}$-box, is an upper limit, since a larger cutoff worsens the order-by-order behavior of the perturbative expansion. Here, we discuss some implications for the properties of the perturbative expansion of H_{eff} and the SM effective transition operator when this "hard" $V_{\text{low-}k}$ is employed to derive the SM Hamiltonian and operators.

Studies of the perturbative properties of the SP energy spacings and TBMEs are reported in references [99, 121], where H_{eff} is derived within the model space outside ^{132}Sn starting from the "hard" $V_{\text{low-}k}$. reference [122] contains a systematic investigation of the convergence properties of theoretical SP energy spectra, TBMEs, and $2\nu\beta\beta$ NMEs as functions of both the dimension of the intermediate state space and the order of the perturbative expansion. Moreover, reference [89] discusses convergence properties of the perturbative expansion of the effective $0\nu\beta\beta$-decay operator with respect to the number of intermediate states and the truncation of both the order of the χ_n operators and the perturbative order of the diagrams. Here, we briefly sketch these results in order to assess the reliability of realistic SM calculations performed starting from a "hard" $V_{\text{low-}k}$.

The model space employed for the SM calculations in reference [122] is spanned by the five proton and neutron orbitals outside the doubly closed ^{100}Sn, namely $0g_{7/2}$, $1d_{5/2}$, $1d_{3/2}$, $2s_{1/2}$, and $0h_{11/2}$, to study the $2\nu\beta\beta$ decay of ^{130}Te and ^{136}Xe.

The left panel of **Figure 15** shows the behavior of the calculated SP spectrum of ^{101}Sn with respect to the $0g_{7/2}$ SP energy as a function of the maximum allowed excitation energy of the intermediate states expressed in terms of the oscillator quanta N_{max}. It is clear that convergence is achieved at $N_{\text{max}} = 14$, which, for the perturbative expansion of the effective SM Hamiltonian and decay operators, justifies the decision to include intermediate states with an unperturbed excitation energy of up to $E_{\text{max}} = N_{\text{max}}\hbar\omega$ where $N_{\text{max}} = 16$ [89, 101, 102, 122].

As regards the order-by-order convergence of the SP energies, the right panel of **Figure 15** plots the calculated neutron SP energies, using a number of intermediate states corresponding

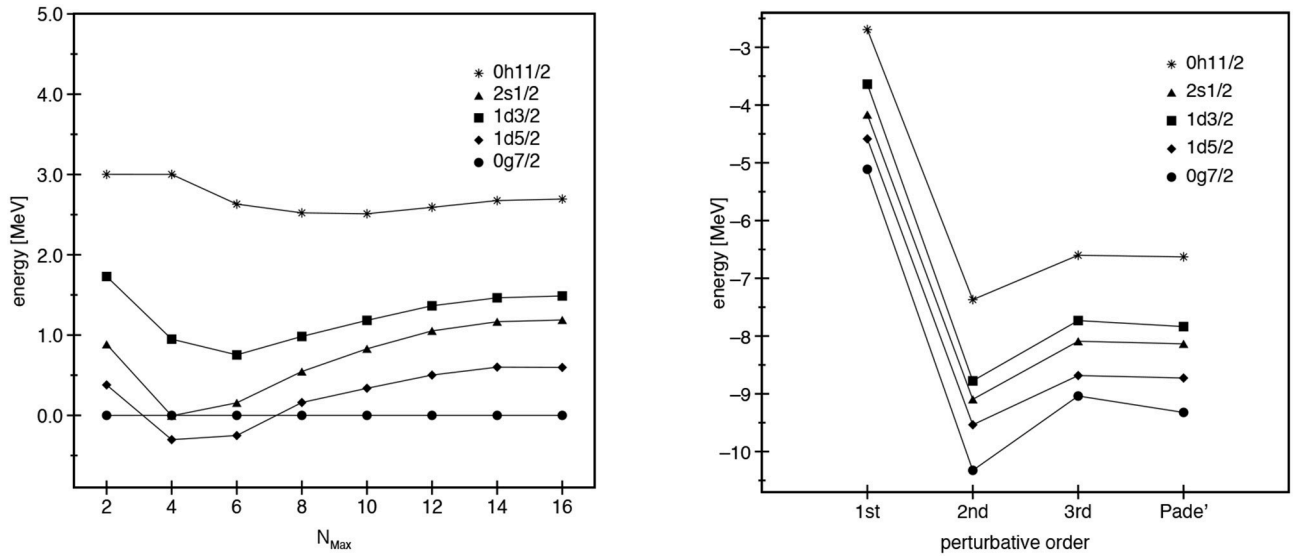

FIGURE 15 | Neutron SP energies as a function of N_{max} (left) and of the perturbative order (right). Reproduced from reference [122] under the Creative Commons CC BY license.

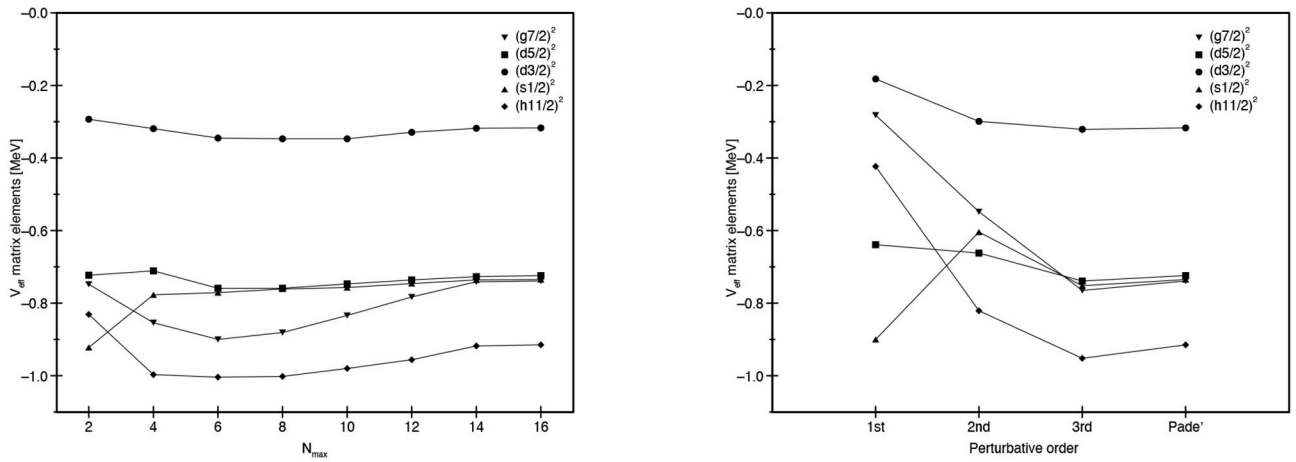

FIGURE 16 | Neutron-neutron diagonal $J^{\pi} = 0^{+}$ TBMEs as a function of N_{max} (left) and of the perturbative order (right). Reproduced from reference [122] under the Creative Commons CC BY license.

to $N_{\max} = 16$, against the order of the perturbative expansion up to third order. The calculated neutron SP energies are also compared with the Padé approximant [2|1] of the $\hat{Q}$-box, which estimates the value to which the perturbative series may converge. The results at third order are very close to those obtained with the Padé approximant, indicating that the truncation to third order should provide a reasonable estimate for the sum of the series.

As regards the TBMEs, we plot in **Figure 16** the neutron-neutron diagonal $J^{\pi} = 0^{+}$ TBMEs as a function both of $N_{\max}$ and of the perturbative order. These TBMEs, which contain the pairing properties of the effective Hamiltonian, are the largest in size of the calculated matrix elements and the most sensitive to the behavior of the perturbative expansion.

From **Figure 16**, the convergence with respect to $N_{\max}$ seems to be very fast for the diagonal matrix elements $(1d_{5/2})^2$, $(1d_{3/2})^2$, and $(2s_{1/2})^2$, whereas elements corresponding to orbitals that lack their own spin-orbit partner, i.e., $(0g_{7/2})^2$ and $(0h_{11/2})^2$, show slower convergence. The order-by-order convergence seen in **Figure 16** is quite satisfactory, and again the results at third order are very close to those obtained with the Padé approximant. Therefore, we can conclude that H_{eff} calculated from a $V_{\text{low-}k}$ with cutoff equal to 2.6 fm^{-1} by way of a perturbative expansion truncated at third order is a good estimate of the sum of its perturbative expansion, for both the one-body and the two-body components.

We now turn our attention to the perturbative expansion of the GT effective operator GT_{eff}. The selection rules of the GT operator that characterize a spin-isospin-dependent decay drive fast convergence of the matrix elements of its SM effective operator with respect to N_{max}. In fact, if the perturbative expansion is truncated at second order, their values do not change from $N_{max} = 2$ onward [62]; and at third order in perturbation theory, their third decimal digit values do not change from $N_{max} = 12$ onward.

TABLE 3 | Order-by-order $M^{2\nu}_{GT}$'s (in MeV^{-1}) for ^{130}Te and ^{136}Xe [122].

Decay	1st order $M^{2\nu}_{GT}$	2nd order $M^{2\nu}_{GT}$	3rd order $M^{2\nu}_{GT}$	Experiment
^{130}Te → ^{130}Xe	0.142	0.040	0.044	0.031 ± 0.004
^{136}Xe → ^{136}Ba	0.0975	0.0272	0.0285	0.0181 ± 0.0007

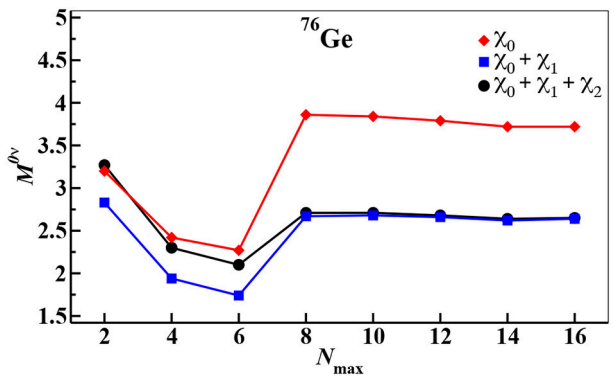

FIGURE 17 | Calculated $M^{0\nu}$ values for the ^{76}Ge → ^{76}Se decay as a function of N_{max}: shown are truncations of the χ_n expansion up to χ_0 (red diamonds), up to χ_1 (blue squares), and up to χ_2 (black dots). Reproduced from reference [89].

Table 3 reports the calculated NMEs of the $2\nu\beta\beta$ decays $^{130}Te_{g.s.} \rightarrow ^{130}Xe_{g.s.}$ and $^{136}Xe_{g.s.} \rightarrow ^{136}Ba_{g.s.}$ obtained with effective operators at first, second, and third order in perturbation theory [with the χ_n series in Equation (85) truncated to χ_0] and compares them with experimental results [109].

As can be seen, the order-by-order convergence of the $M^{2\nu}_{GT}$'s is also very satisfactory; for both transitions the results change by about 260% from the first- to the second-order calculations, while the changes are 9 and 5% from the second- to third-order results for the ^{130}Te and ^{136}Xe decays, respectively. This suppression of the third-order contributions relative to the second-order ones is favored by the mutual cancelation of third-order diagrams.

In reference [89] a study was also conducted on the convergence properties of the effective decay operator Θ_{eff} for the $0\nu\beta\beta$ decay with respect to the truncation of the χ_n operators, the number of intermediate states accounted for in the perturbative expansion, and the order-by-order behavior up to third order in perturbation theory.

Figure 17 displays the calculated values of $M^{0\nu}$ for the $^{76}Ge \rightarrow {}^{76}Se$ decay as a function of the maximum allowed excitation energy of the intermediate states expressed in terms of the oscillator quanta N_{max}, including χ_n contributions up to $n = 2$. We can see that the $M^{0\nu}$ values are convergent from $N_{max} = 12$ onward and that contributions from χ_1 are quite relevant, whereas those from χ_2 can be considered negligible.

We point out that, according to expression (84), χ_3 is defined in terms of the first, second, and third derivatives of $\hat{\Theta}_0$ and $\hat{\Theta}_{00}$, as well as the first and second derivatives of the $\hat{Q}$-box. This means that one could estimate χ_3 as being about one order of magnitude smaller than the χ_2 contribution.

On the above grounds, in reference [89] the effective SM $0\nu\beta\beta$-decay operator was obtained by including in the perturbative expansion diagrams of up to third order, with the number of intermediate states corresponding to oscillator quanta of up to $N_{max} = 14$, and up to χ_2 contributions.

Now, to examine the order-by-order convergence behavior, in **Figure 18** we plot the calculated values of $M^{0\nu}$, $M^{0\nu}_{GT}$, and $M^{0\nu}_{F}$ for ^{130}Te and ^{136}Xe$0\nu\beta\beta$ decay at first, second, and third order in perturbation theory. We also compare the order-by-order results

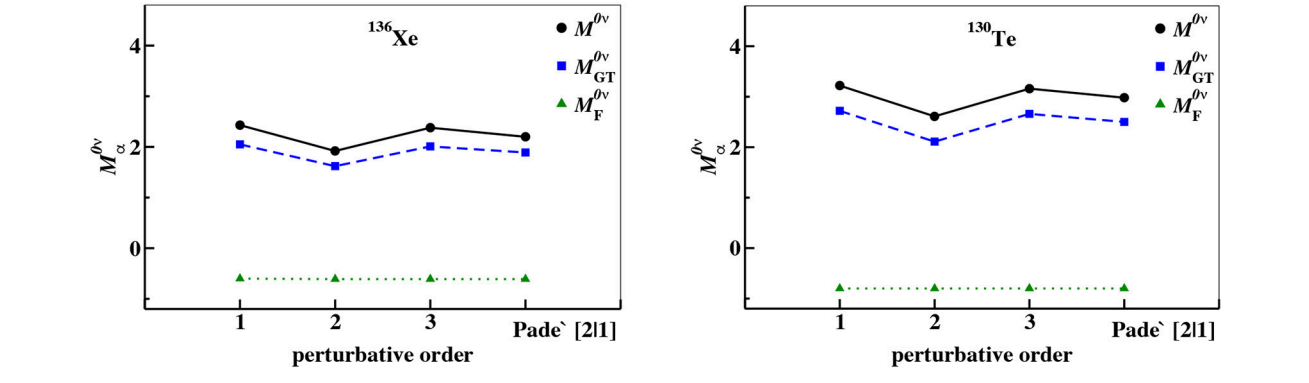

FIGURE 18 | Calculated $M^{0\nu}$ values for the ^{136}Xe → ^{136}Ba decay (left) and the ^{130}Te → ^{130}Xe decay (right) as a function of the perturbative order. The green triangles correspond to $M^{0\nu}_{F}$, the blue squares to $M^{0\nu}_{GT}$, and the black dots to the full $M^{0\nu}$. Reproduced from reference [89].

with their Padé approximant [2|1], to get an idea of the quality of the perturbative behavior [123].

It is worth noting that the perturbative behavior is dominated by the GT component, with the Fermi matrix element $M_{\rm F}^{0\nu}$ being only slightly affected by the renormalization procedure. Moreover, if the order-by-order perturbative behavior of the effective SM $0\nu\beta\beta$-decay operator is compared with that of the single β-decay operator, we observe less satisfactory perturbative behavior for the calculation of $M^{0\nu}$, the difference between the second- and third-order results being about 30% for the ^{130}Te and ^{136}Xe $0\nu\beta\beta$ decays.

5. SUMMARY

This paper has presented a general overview of the perturbative approach to deriving effective SM operators, in particular the SM Hamiltonian and decay operators.

First, we described the theoretical framework, which is essentially based on the perturbative expansion of a vertex function—the $\hat{Q}$-box for the effective Hamiltonian and the $\hat{\Theta}$-box for effective decay operators—whose calculation is pivotal in the Lee-Suzuki similarity transformation. The iterative procedures used to solve the recursive equations that yield effective SM Hamiltonians have been presented in detail, along with tips that could be helpful for calculating the Goldstone diagrams that arise in the perturbative expansion of the above-mentioned vertex functions.

We then reported results from an SM study carried out using only single-particle energies, two-body matrix elements of the residual interaction, and effective decay operators derived from a realistic nuclear potential, without any empirical adjustments. This forms part of a large body of investigations that aim to assess the relevance of such an approach to the study of nuclear structure. The versatility of SM calculations comes from their ability to reproduce experimental results for mass regions ranging from light nuclei (^{4}He core [23, 52]) to heavy mass systems (nuclei around ^{132}Sn [121]), as well as to describe exotic and rare phenomena, such as the Borromean structure [124], quadrupole collectivity [98, 100], and the double-β decay process [89, 101, 102] without resorting to empirical adjustments of data.

The results presented in this article testify to the flexibility and usefulness of this theoretical tool, and could provide inspiration for further investigations in the future.

AUTHOR CONTRIBUTIONS

All authors listed have made a substantial, direct and intellectual contribution to the work, and approved it for publication.

REFERENCES

1. Elliott JP. Nuclear forces and the structure of nuclei. In: Jean M, editor. *Cargése Lectures in Physics*, Vol. 3. New York, NY: Gordon and Breach (1969). p. 337.
2. Talmi I. Fifty years of the shell model–the quest for the effective interaction. *Adv Nucl Phys.* (2003) **27**:1. doi: 10.1007/0-306-47916-8_1
3. Caurier E, Martínez-Pinedo G, Nowacki F, Poves A, Zuker AP. The shell model as a unified view of nuclear structure. *Rev Mod Phys.* (2005) **77**:427–88. doi: 10.1103/RevModPhys.77.427
4. Stroberg SR, Hergert H, Bogner SK, Holt JD. Nonempirical interactions for the nuclear shell model: an update. *Annu Rev Nucl Part Sci.* (2019) **69**:307–62. doi: 10.1146/annurev-nucl-101917-021120
5. Kuo TTS, Osnes E. *Lecture Notes in Physics*. Vol. 364. Berlin: Springer-Verlag (1990).
6. Hjorth-Jensen M, Kuo TTS, Osnes E. Realistic effective interactions for nuclear systems. *Phys Rep.* (1995) **261**:125. doi: 10.1016/0370-1573(95)00012-6
7. Coraggio L, Covello A, Gargano A, Itaco N, Kuo TTS. Shell-model calculations and realistic effective interactions. *Prog Part Nucl Phys.* (2009) **62**:135. doi: 10.1016/j.ppnp.2008.06.001
8. Bertsch GF. Role of core polarization in two-body interaction. *Nucl Phys.* (1965) **74**:234. doi: 10.1016/0029-5582(65)90262-2
9. Kallio A, Kolltveit K. An application of the separation method in shell-model calculation. *Nucl Phys.* (1964) **53**:87. doi: 10.1016/0029-5582(64)90588-7
10. Kuo TTS, Brown GE. Structure of finite nuclei and the free nucleon-nucleon interaction: an application to ^{18}O and ^{18}F. *Nucl Phys.* (1966) **85**:40. doi: 10.1016/0029-5582(66)90131-3
11. Hamada T, Johnston ID. A potential model representation of two-nucleon data below 315 MeV. *Nucl Phys.* (1962) **34**:382. doi: 10.1016/0029-5582(62)90228-6
12. Kuo TTS, Brown GE. Reaction matrix elements for the 0*f*-1*p* shell nuclei. *Nucl Phys A.* (1968) **114**:241. doi: 10.1016/0375-9474(68)90353-9
13. Brown BA, Wildenthal BH. Status of the nuclear shell model. *Annu Rev Nucl Part Sci.* (1988) **38**:29. doi: 10.1146/annurev.ns.38.120188.000333
14. Poves A, Sánchez-Solano J, Caurier E, Nowacki F. Shell model study of the isobaric chains A = 50, A = 51 and A = 52. *Nucl Phys A.* (2001) **694**:157. doi: 10.1016/S0375-9474(01)00967-8
15. Brandow BH. Linked-cluster expansions for the nuclear many-body problem. *Rev Mod Phys.* (1967) **39**:771. doi: 10.1103/RevModPhys.39.771
16. Kuo TTS, Lee SY, Ratcliff KF. A folded-diagram expansion of the model-space effective Hamiltonian. *Nucl Phys A.* (1971) **176**:65. doi: 10.1016/0375-9474(71)90731-7
17. Suzuki K, Lee SY. Convergent theory for effective interaction in nuclei. *Prog Theor Phys.* (1980) **64**:2091. doi: 10.1143/PTP.64.2091
18. Suzuki K, Okamoto R. Effective operators in time-independent approach. *Prog Theor Phys.* (1995) **93**:905. doi: 10.1143/ptp/93.5.905
19. Lee SY, Suzuki K. The effective interaction of two nucleons in the *sd* shell. *Phys Lett B.* (1980) **91**:173. doi: 10.1016/0370-2693(80)90423-2
20. Mayer MG. On closed shells in nuclei. II. *Phys Rev.* (1949) **75**:1969–70. doi: 10.1103/PhysRev.75.1969
21. Haxel O, Jensen JHD, Suess HE. On the "magic numbers" in nuclear structure. *Phys Rev.* (1949) **75**:1766. doi: 10.1103/PhysRev.75.1766.2
22. Mayer MG, Jensen JHD. *Elementary Theory of Nuclear Shell Structure*. New York, NY: John Wiley (1955).
23. Fukui T, De Angelis L, Ma YZ, Coraggio L, Gargano A, Itaco N, et al. Realistic shell-model calculations for *p*-shell nuclei including contributions of a chiral three-body force. *Phys Rev C.* (2018) **98**:044305. doi: 10.1103/PhysRevC.98.044305
24. Ma YZ, Coraggio L, De Angelis L, Fukui T, Gargano A, Itaco N, et al. Contribution of chiral three-body forces to the monopole component of the effective shell-model Hamiltonian. *Phys Rev C.* (2019) **100**:034324. doi: 10.1103/PhysRevC.100.034324
25. Brown BA. The nuclear shell model towards the drip lines. *Prog Part Nucl Phys.* (2001) **47**:517. doi: 10.1016/S0146-6410(01)00159-4
26. Alex Brown B. The nuclear configuration interations method. In: García-Ramos JE, Andrés MV, Valera JAL, Moro AM, Pérez-Bernal F, editors. *Basic Concepts in Nuclear Physics: Theory, Experiments and Applications*. RABIDA 2018. Cham: Springer International Publishing (2019). p. 3–31. doi: 10.1007/978-3-030-22204-8_1

27. Otsuka T, Gade A, Sorlin O, Suzuki T, Utsuno Y. Evolution of shell structure in exotic nuclei. *Rev Mod Phys.* (2020) **92**:015002. doi: 10.1103/RevModPhys.92.015002
28. Morris TD, Parzuchowski NM, Bogner SK. Magnus expansion and in-medium similarity renormalization group. *Phys Rev C.* (2015) **92**:034331. doi: 10.1103/PhysRevC.92.034331
29. Sun ZH, Morris TD, Hagen G, Jansen GR, Papenbrock T. Shell-model coupled-cluster method for open-shell nuclei. *Phys Rev C.* (2018) **98**:054320. doi: 10.1103/PhysRevC.98.054320
30. Lisetskiy AF, Barrett BR, Kruse MKG, Navratil P, Stetcu I, Vary JP. *Ab-initio* shell model with a core. *Phys Rev C.* (2008) **78**:044302. doi: 10.1103/PhysRevC.78.044302
31. Lisetskiy AF, Kruse MKG, Barrett BR, Navratil P, Stetcu I, Vary JP. Effective operators from exact many-body renormalization. *Phys Rev C.* (2009) **80**:024315. doi: 10.1103/PhysRevC.80.024315
32. Dikmen E, Lisetskiy AF, Barrett BR, Maris P, Shirokov AM, Vary JP. *Ab initio* effective interactions for *sd*-shell valence nucleons. *Phys Rev C.* (2015) **91**:064301. doi: 10.1103/PhysRevC.91.064301
33. Smirnova NA, Barrett BR, Kim Y, Shin IJ, Shirokov AM, Dikmen E, et al. Effective interactions in the *sd* shell. *Phys Rev C.* (2019) **100**:054329. doi: 10.1103/PhysRevC.100.054329
34. Haxton WC, Song CL. Morphing the ShellModel into an effective theory. *Phys Rev Lett.* (2000) **84**:5484–7. doi: 10.1103/PhysRevLett.84.5484
35. Kümmel H, Lührmann KH, Zabolitzky JG. Many-fermion theory in expS- (or coupled cluster) form. *Phys Rep.* (1978) **36**:1. doi: 10.1016/0370-1573(78)90081-9
36. Schucan TH, Weidenmüller HA. The effective interaction in nuclei and its perturbation expansion: an algebraic approach. *Ann Phys.* (1972) **73**:108. doi: 10.1016/0003-4916(72)90315-6
37. Schucan TH, Weidenmüller HA. Perturbation theory for the effective interaction in nuclei. *Ann Phys.* (1973) **76**:483. doi: 10.1016/0003-4916(73)90044-4
38. Krenciglowa EM, Kuo TTS. Convergence of effective Hamiltonian expansion and partial summations of folded diagrams. *Nucl Phys A.* (1974) **235**:171. doi: 10.1016/0375-9474(74)90184-5
39. Kuo TTS, Krmpotić F, Suzuki K, Okamoto R. Summation of time-dependent folded diagrams for effective interactions with a non-degenerate model space. *Nucl Phys A.* (1995) **582**:205. doi: 10.1016/0375-9474(94)00456-W
40. Coraggio L, Itaco N. Self-consistent nuclear shell-model calculation starting from a realistic *NN* potential. *Phys Lett B.* (2005) **616**:43. doi: 10.1016/j.physletb.2005.04.060
41. Takayanagi K. Effective interaction in non-degenerate model space. *Nucl Phys A.* (2011) **852**:61–81. doi: 10.1016/j.nuclphysa.2011.01.003
42. Suzuki K, Okamoto R, Kumagai H, Fujii S. Graphical method for deriving an effective interaction with a new vertex function. *Phys Rev C.* (2011) **83**:024304. doi: 10.1103/PhysRevC.83.024304
43. Takayanagi K. Effective Hamiltonian in the extended Krenciglowa – Kuo method. *Nucl Phys A.* (2011) **864**:91–112. doi: 10.1016/j.nuclphysa.2011.06.025
44. Bloch C, Horowitz J. Sur la détermination des premiers états d'un systéme de fermions dans le cas dégénéré. *Nucl Phys.* (1958) **8**:91. doi: 10.1016/0029-5582(58)90136-6
45. Tsunoda N, Takayanagi K, Hjorth-Jensen M, Otsuka T. Multi-shell effective interactions. *Phys Rev C.* (2014) **89**:024313. doi: 10.1103/PhysRevC.89.024313
46. Tsunoda N, Otsuka T, Shimizu N, Hjorth-Jensen M, Takayanagi K, Suzuki T. Exotic neutron-rich medium-mass nuclei with realistic nuclear forces. *Phys Rev C.* (2017) **95**:021304. doi: 10.1103/PhysRevC.95.021304
47. Sun ZH, Wu Q, Zhao ZH, Hu BS, Dai SJ, Xu FR. Resonance and continuum Gamow shell model with realistic nuclear forces. *Phys Lett B.* (2017) **769**:227–32. doi: 10.1016/j.physletb.2017.03.054
48. Ma YZ, Xu FR, Coraggio L, Hu BS, Li JG, Fukui T, et al. Chiral three-nucleon force and continuum for dripline nuclei and beyond. *Phys Lett B.* (2020) **802**:135257. doi: 10.1016/j.physletb.2020.135257
49. Press WH, Teukolsky SA, Vetterling WT, Flannery BP. *Fortran Numerical Recipes*. Vol. 1. Cambridge: Cambridge University Press (1992).
50. Shurpin J, Kuo TTS, Strottman D. Folded diagrams and 1*s*-0*d* effective interactions derived from Reid and Paris nucleon-nucleon potentials. *Nucl Phys A.* (1983) **408**:310. doi: 10.1016/0375-9474(83)90586-9
51. Kuo TTS, Shurpin J, Tam KC, Osnes E, Ellis PJ. A simple method for evaluating Goldstone diagrams in an angular momentum coupled representation. *Ann Phys.* (1981) **132**:237. doi: 10.1016/0003-4916(81)90068-3
52. Coraggio L, Covello A, Gargano A, Itaco N, Kuo TTS. Effective shell-model hamiltonians from realistic nucleon-nucleon potentials within a perturbative approach. *Ann Phys.* (2012) **327**:2125. doi: 10.1016/j.aop.2012.04.013
53. Paldus J, Wong HC. Computer generation of Feynman diagrams for perturbation theory I. General algorithm. *Comput Phys Commun.* (1973) **6**:1–7. doi: 10.1016/0010-4655(73)90016-7
54. Edmonds AR. *Angular Momentum in Quantum Mechanics*. Princeton, NJ: Princeton University Press (1957).
55. Johnson CW, Ormand WE, Krastev PG. Factorization in large-scale many-body calculations. *Comput Phys Commun.* (2013) **184**:2761–74. doi: 10.1016/j.cpc.2013.07.022
56. Hjorth-Jensen M, Lombardo MP, van Kolck U, editors. *Lecture Notes in Physics*. Vol. 936. Berlin: Springer (2017).
57. Polls A, Müther H, Faessler A, Kuo TTS, Osnes E. Three-body forces in *sd*-shell nuclei. *Nucl Phys A.* (1983) **401**:124. doi: 10.1016/0375-9474(83)90340-8
58. Ellis PJ, Osnes E. An introductory guide to effective operators in nuclei. *Rev Mod Phys.* (1977) **49**:777. doi: 10.1103/RevModPhys.49.777
59. Mavromatis HA, Zamick L, Brown GE. First and second order corrections to the magnetic moments of nuclei using realistic interactions. *Nucl Phys.* (1966) **80**:545–64. doi: 10.1016/0029-5582(66)90063-0
60. Mavromatis HA, Zamick L. Magnetic moments of nuclei with closed *j-j* shells plus or minus one nucleon. *Nucl Phys A.* (1967) **104**:17–34. doi: 10.1016/0375-9474(67)90754-3
61. Federman P, Zamick L. State-dependent effective charge in the $2p-1f$ shell. *Phys Rev.* (1969) **177**:1534–40. doi: 10.1103/PhysRev.177.1534
62. Towner IS, Khanna KFC. Corrections to the single-particle M1 and Gamow – Teller matrix elements. *Nucl Phys A.* (1983) **399**:334. doi: 10.1016/0375-9474(83)90252-X
63. Towner IS. Quenching of spin matrix elements in nuclei. *Phys Rep.* (1987) **155**:263. doi: 10.1016/0370-1573(87)90138-4
64. Avignone FT, Elliott SR, Engel J. Double beta decay, Majorana neutrinos, and neutrino mass. *Rev Mod Phys.* (2008) **80**:481–516. doi: 10.1103/RevModPhys.80.481
65. Vergados JD, Ejiri H, Šimkovic F. Theory of neutrinoless double beta decay. *Rep Prog Phys.* (2012) **75**:106301. doi: 10.1088/0034-4885/75/10/106301
66. Kotila J, Iachello F. Phase-space factors for double-β decay. *Phys Rev C.* (2012) **85**:034316. doi: 10.1103/PhysRevC.85.034316
67. Stoica S, Mirea M. New calculations for phase space factors involved in double-β decay. *Phys Rev C.* (2013) **88**:037303. doi: 10.1103/PhysRevC.88.037303
68. Barea J, Iachello F. Neutrinoless double-β decay in the microscopic interacting boson model. *Phys Rev C.* (2009) **79**:044301. doi: 10.1103/PhysRevC.79.044301
69. Barea J, Kotila J, Iachello F. Limits on neutrino masses from neutrinoless double-β decay. *Phys Rev Lett.* (2012) **109**:042501. doi: 10.1103/PhysRevLett.109.042501
70. Barea J, Kotila J, Iachello F. Nuclear matrix elements for double-β decay. *Phys Rev C.* (2013) **87**:014315. doi: 10.1103/PhysRevC.87.014315
71. Šimkovic F, Faessler A, Rodin V, Vogel P, Engel J. Anatomy of the $0\nu\beta\beta$ nuclear matrix elements. *Phys Rev C.* (2008) **77**:045503. doi: 10.1103/PhysRevC.77.045503
72. Šimkovic F, Faessler A, Müther H, Rodin V, Stauf M. $0\nu\beta\beta$-decay nuclear matrix elements with self-consistent short-range correlations. *Phys Rev C.* (2009) **79**:055501. doi: 10.1103/PhysRevC.79.055501
73. Fang DL, Faessler A, Rodin V, Šimkovic F. Neutrinoless double-β decay of deformed nuclei within quasiparticle random-phase approximation with a realistic interaction. *Phys Rev C.* (2011) **83**:034320. doi: 10.1103/PhysRevC.83.034320

74. Faessler A, Rodin V, Simkovic F. Nuclear matrix elements for neutrinoless double-beta decay and double-electron capture. *J Phys G.* (2012) **39**:124006. doi: 10.1088/0954-3899/39/12/124006
75. Rodríguez TR, Martínez-Pinedo G. Energy density functional study of nuclear matrix elements for neutrinoless $\beta\beta$ decay. *Phys Rev Lett.* (2010) **105**:252503. doi: 10.1103/PhysRevLett.105.252503
76. Song LS, Yao JM, Ring P, Meng J. Relativistic description of nuclear matrix elements in neutrinoless double-β decay. *Phys Rev C.* (2014) **90**:054309. doi: 10.1103/PhysRevC.90.054309
77. Yao JM, Song LS, Hagino K, Ring P, Meng J. Systematic study of nuclear matrix elements in neutrinoless double-β decay with a beyond-mean-field covariant density functional theory. *Phys Rev C.* (2015) **91**:024316. doi: 10.1103/PhysRevC.91.024316
78. Song LS, Yao JM, Ring P, Meng J. Nuclear matrix element of neutrinoless double-β decay: relativity and short-range correlations. *Phys Rev C.* (2017) **95**:024305. doi: 10.1103/PhysRevC.95.024305
79. Jiao CF, Engel J, Holt JD. Neutrinoless double-β decay matrix elements in large shell-model spaces with the generator-coordinate method. *Phys Rev C.* (2017) **96**:054310. doi: 10.1103/PhysRevC.96.054310
80. Yao JM, Engel J, Wang LJ, Jiao CF, Hergert H. Generator-coordinate reference states for spectra and $0\nu\beta\beta$ decay in the in-medium similarity renormalization group. *Phys Rev C.* (2018) **98**:054311. doi: 10.1103/PhysRevC.98.054311
81. Jiao CF, Horoi M, Neacsu A. Neutrinoless double-β decay of ^{124}Sn, ^{130}Te, and ^{136}Xe in the Hamiltonian-based generator-coordinate method. *Phys Rev C.* (2018) **98**:064324. doi: 10.1103/PhysRevC.98.064324
82. Jiao C, Johnson CW. Union of rotational and vibrational modes in generator-coordinate-type calculations, with application to neutrinoless double-β decay. *Phys Rev C.* (2019) **100**:031303. doi: 10.1103/PhysRevC.100.031303
83. Menéndez J, Poves A, Caurier E, Nowacki F. Occupancies of individual orbits, and the nuclear matrix element of the ^{76}Ge neutrinoless $\beta\beta$ decay. *Phys Rev C.* (2009) **80**:048501. doi: 10.1103/PhysRevC.80.048501
84. Menéndez J, Poves A, Caurier E, Nowacki F. Disassembling the nuclear matrix elements of the neutrinoless $\beta\beta$ decay. *Nucl Phys A.* (2009) **818**:139. doi: 10.1016/j.nuclphysa.2008.12.005
85. Horoi M, Brown BA. Shell-model analysis of the ^{136}Xe double beta decay nuclear matrix elements. *Phys Rev Lett.* (2013) **110**:222502. doi: 10.1103/PhysRevLett.110.222502
86. Neacsu A, Horoi M. Shell model studies of the ^{130}Te neutrinoless double-β decay. *Phys Rev C.* (2015) **91**:024309. doi: 10.1103/PhysRevC.91.024309
87. Brown BA, Fang DL, Horoi M. Evaluation of the theoretical nuclear matrix elements for $\beta\beta$ decay of ^{76}Ge. *Phys Rev C.* (2015) **92**:041301. doi: 10.1103/PhysRevC.92.041301
88. Engel J, Menéndez J. Status and future of nuclear matrix elements for neutrinoless double-beta decay: a review. *Rep Prog Phys.* (2017) **80**:046301. doi: 10.1088/1361-6633/aa5bc5
89. Coraggio L, Gargano A, Itaco N, Mancino R, Nowacki F. Calculation of the neutrinoless double-β decay matrix element within the realistic shell model. *Phys Rev C.* (2020) **101**:044315. doi: 10.1103/PhysRevC.101.044315
90. Machleidt R. High-precision, charge-dependent Bonn nucleon-nucleon potential. *Phys Rev C.* (2001) **63**:024001. doi: 10.1103/PhysRevC.63.024001
91. Song HQ, Wu HF, Kuo TTS. Effect of nuclear core polarization on neutrinoless double beta decay of ^{48}Ca. *Phys Rev C.* (1989) **40**:2260–4. doi: 10.1103/PhysRevC.40.2260
92. Staudt A, Kuo TTS, Klapdor-Kleingrothaus HV. $\beta\beta$ decay of ^{128}Te, ^{130}Te, and ^{76}Ge with renormalized effective interactions derived from Paris and Bonn potentials. *Phys Rev C.* (1992) **46**:871–83. doi: 10.1103/PhysRevC.46.871
93. Holt JD, Engel J. Effective double-β-decay operator for ^{76}Ge and ^{82}Se. *Phys Rev C.* (2013) **87**:064315. doi: 10.1103/PhysRevC.87.064315
94. Alfonso K, Artusa DR, Avignone FT, Azzolini O, Balata M, Banks TI, et al. Search for neutrinoless double-beta decay of ^{130}Te with CUORE − 0. *Phys Rev Lett.* (2015) **115**:102502. doi: 10.1103/PhysRevLett.115.102502
95. Auger M, Auty DJ, Barbeau PS, Beauchamp E, Belov V, Benitez-Medina C, et al. Search for neutrinoless double-beta decay in ^{136}Xe with EXO − 200. *Phys Rev Lett.* (2012) **109**:032505. doi: 10.1103/PhysRevLett.109.032505
96. Gando A, Gando Y, Hachiya T, Hayashi A, Hayashida S, Ikeda H, et al. Search for Majorana neutrinos near the inverted mass hierarchy region with KamLAND − Zen. *Phys Rev Lett.* (2016) **117**:082503. doi: 10.1103/PhysRevLett.117.082503
97. Bogner S, Kuo TTS, Coraggio L, Covello A, Itaco N. Low momentum nucleon-nucleon potential and shell model effective interactions. *Phys Rev C.* (2002) **65**:051301(R). doi: 10.1103/PhysRevC.65.051301
98. Coraggio L, Covello A, Gargano A, Itaco N, Kuo TTS. Shell-model study of quadrupole collectivity in light tin isotopes. *Phys Rev C.* (2015) **91**:041301. doi: 10.1103/PhysRevC.91.041301
99. Coraggio L, Gargano A, Itaco N. Role of three-nucleon forces in neutron-rich nuclei beyond ^{132}Sn. *JPS Conf Proc.* (2015) **6**:020046. doi: 10.7566/JPSCP.6.020046
100. Coraggio L, Gargano A, Itaco N. Double-step truncation procedure for large-scale shell-model calculations. *Phys Rev C.* (2016) **93**:064328. doi: 10.1103/PhysRevC.93.064328
101. Coraggio L, De Angelis L, Fukui T, Gargano A, Itaco N. Calculation of Gamow − Teller and two-neutrino double-β decay properties for ^{130}Te and ^{136}Xe with a realistic nucleon-nucleon potential. *Phys Rev C.* (2017) **95**:064324. doi: 10.1103/PhysRevC.95.064324
102. Coraggio L, De Angelis L, Fukui T, Gargano A, Itaco N, Nowacki F. Renormalization of the Gamow − Teller operator within the realistic shell model. *Phys Rev C.* (2019) **100**:014316. doi: 10.1103/PhysRevC.100.014316
103. Data extracted using the NNDC On-line Data Service from the ENSDF database, file revised as of April 3, 2020 (2020).
104. Data extracted using the NNDC On-line Data Service from the XUNDL database, file revised as of April 6, 2020 (2020).
105. Goodman CD, Goulding CA, Greenfield MB, Rapaport J, Bainum DE, Foster CC, et al. Gamow − Teller matrix elements from 0° (p, n) cross sections. *Phys Rev Lett.* (1980) **44**:1755–9. doi: 10.1103/PhysRevLett.44.1755
106. Taddeucci TN, Goulding CA, Carey TA, Byrd RC, Goodman CD, Gaarde C, et al. The (p, n) reaction as a probe of beta decay strength. *Nucl Phys A.* (1987) **469**:125. doi: 10.1016/0375-9474(87)90089-3
107. Puppe P, Lennarz A, Adachi T, Akimune H, Ejiri H, Frekers D, et al. High resolution (^{3}He,t) experiment on the double-β decaying nuclei ^{128}Te and ^{130}Te. *Phys Rev C.* (2012) **86**:044603. doi: 10.1103/PhysRevC.86.044603
108. Frekers D, Puppe P, Thies JH, Ejiri H. Gamow − Teller strength extraction from (^{3}He,t) reactions. *Nucl Phys A.* (2013) **916**:219. doi: 10.1016/j.nuclphysa.2013.08.006
109. Barabash AS. Average and recommended half-life values for two-neutrino double beta decay. *Nucl Phys A.* (2015) **935**:52. doi: 10.1016/j.nuclphysa.2015.01.001
110. Caurier E, Nowacki F, Poves A. Shell model description of the $\beta\beta$ decay of ^{136}Xe. *Phys Lett B.* (2012) **711**:62. doi: 10.1016/j.physletb.2012.03.076
111. Haxton WC, Stephenson GJ Jr. Double beta decay. *Prog Part Nucl Phys.* (1984) **12**:409. doi: 10.1016/0146-6410(84)90006-1
112. Tomoda T. Double beta decay. *Rep Prog Phys.* (1991) **54**:53. doi: 10.1088/0034-4885/54/1/002
113. Park TS, Min DP, Rho M. Chiral dynamics and heavy-fermion formalism in nuclei: exchange axial currents. *Phys Rep.* (1993) **233**:341. doi: 10.1016/0370-1573(93)90099-Y
114. Pastore S, Girlanda L, Schiavilla R, Viviani M, Wiringa RB. Electromagnetic currents and magnetic moments in chiral effective field theory (χEFT). *Phys Rev C.* (2009) **80**:034004. doi: 10.1103/PhysRevC.80.034004
115. Piarulli M, Girlanda L, Marcucci LE, Pastore S, Schiavilla R, Viviani M. Electromagnetic structure of A = 2 and 3 nuclei in chiral effective field theory. *Phys Rev C.* (2013) **87**:014006. doi: 10.1103/PhysRevC.87.014006
116. Pastore S, Carlson J, Cirigliano V, Dekens W, Mereghetti E, Wiringa RB. Neutrinoless double-β decay matrix elements in light nuclei. *Phys Rev C.* (2018) **97**:014606. doi: 10.1103/PhysRevC.97.014606
117. Coraggio L, Itaco N, Mancino R. Short-range correlations for neutrinoless double-beta decay and low-momentum NN potentials. *arXiv.* (2019) 191004146[nucl-th].
118. Tanabashi M, Hagiwara K, Hikasa K, Nakamura K, Sumino Y, Takahashi F, et al. Review of Particle Physics. *Phys Rev D.* (2018) **98**:030001. doi: 10.1103/PhysRevD.98.030001

119. Suhonen J. Impact of the quenching of g_A on the sensitivity of $0\nu\beta\beta$ experiments. *Phys Rev C.* (2017) **96**:055501. doi: 10.1103/PhysRevC.96.055501
120. Suhonen JT. Value of the axial-vector coupling strength in β and $\beta\beta$ decays: a review. *Front Phys.* (2017) **5**:55. doi: 10.3389/fphy.2017.00055
121. Coraggio L, Covello A, Gargano A, Itaco N, Kuo TTS. Shell-model study of the N = 82 isotonic chain with a realistic effective Hamiltonian. *Phys Rev C.* (2009) **80**:044320. doi: 10.1103/PhysRevC.80.044320
122. Coraggio L, De Angelis L, Fukui T, Gargano A, Itaco N. Two-neutrino double-beta decay within the realistic shell model. *J Phys Conf Ser.* (2018) **1056**:012012. doi: 10.1088/1742-6596/1056/1/012012
123. Baker GA, Gammel JL. *The Padé Approximant in Theoretical Physics. Vol. 71 of Mathematics in Science and Engineering*. New York, NY: Academic Press (1970).
124. Coraggio L, Covello A, Gargano A, Itaco N. Shell-model calculations for neutron-rich carbon isotopes with a chiral nucleon-nucleon potential. *Phys Rev C.* (2010) **81**:064303. doi: 10.1103/PhysRevC.81.064303

Conflict of Interest: The authors declare that the research was conducted in the absence of any commercial or financial relationships that could be construed as a potential conflict of interest.

frontiers in Physics

HYPOTHESIS AND THEORY
published: 05 June 2020
doi: 10.3389/fphy.2020.00164

Many-Body Perturbation Theories for Finite Nuclei

Alexander Tichai[1,2,3,4]*, *Robert Roth*[2] *and Thomas Duguet*[5,6]

[1] *Max-Planck-Institut für Kernphysik, Heidelberg, Germany,* [2] *Institut für Kernphysik, Technische Universität Darmstadt, Darmstadt, Germany,* [3] *ExtreMe Matter Institute EMMI, GSI Helmholtzzentrum für Schwerionenforschung GmbH, Darmstadt, Germany,* [4] *ESNT, Irfu, DPhN, CEA Saclay, Gif-sur-Yvette, France,* [5] *Irfu, DPhN, CEA Saclay, Gif-sure-Yvette, France,* [6] *Instituut voor Kern- en Stralingsfysica, KU Leuven, Leuven, Belgium*

In recent years many-body perturbation theory encountered a renaissance in the field of *ab initio* nuclear structure theory. In various applications it was shown that perturbation theory, including novel flavors of it, constitutes a useful tool to describe atomic nuclei, either as a full-fledged many-body approach or as an auxiliary method to support more sophisticated non-perturbative many-body schemes. In this work the current status of many-body perturbation theory in the field of nuclear structure is discussed and novel results are provided that highlight its power as a efficient and yet accurate (pre-processing) approach to systematically investigate medium-mass nuclei. Eventually a new generation of chiral nuclear Hamiltonians is benchmarked using several state-of-the-art flavors of many-body perturbation theory.

Keywords: many-body theory, *ab initio*, perturbation theory, correlation expansion, open-shell nuclei

OPEN ACCESS

Edited by:
Carlo Barbieri,
University of Surrey, United Kingdom

Reviewed by:
Furong Xu,
Peking University, China
Artur Polls,
University of Barcelona, Spain

***Correspondence:**
Alexander Tichai
alexander.tichai@physik.tu-darmstadt.de

Specialty section:
This article was submitted to Nuclear Physics, a section of the journal Frontiers in Physics

Received: *28 January 2020*
Accepted: *20 April 2020*
Published: *05 June 2020*

Citation:
Tichai A, Roth R and Duguet T (2020) Many-Body Perturbation Theories for Finite Nuclei. Front. Phys. 8:164. doi: 10.3389/fphy.2020.00164

1. INTRODUCTION

A major goal of quantum many-body theory is to provide accurate solutions of the stationary Schrödinger equation

$$H|\Psi_k^{\mathrm{A}}\rangle = E_k^{\mathrm{A}}|\Psi_k^{\mathrm{A}}\rangle \tag{1}$$

for a given input Hamiltonian H, where $|\Psi_k^{\mathrm{A}}\rangle$ denotes the k-th eigenstate of the A-body system with eigenvalue E_k^{A}. As for the study of the atomic nucleus at low energy, the starting point is a realistic Hamiltonian arising from the modeling of the strong interaction

$$H = T + V + W + ..., \tag{2}$$

in terms of nucleonic degrees of freedom. In Equation (2), T denotes the intrinsic kinetic energy, V the two-nucleon (2N) potential, W the three-nucleon (3N) potential, and so on. Nowadays, high-precision Hamiltonians are systematically constructed within the framework of chiral effective field theory (χEFT) [1–6]. Earlier on, more phenomenological models were employed that fitted a somewhat *ad hoc* parametrization to reproduce few-body observables, e.g., 2N scattering data. Examples of such potentials are the Argonne [7] or Bonn [8] potentials. It was recognized in various many-body studies that the inclusion of three-nucleon interactions is mandatory to reproduce nuclear phenomenology, e.g., nuclear saturation properties or the correct prediction of the oxygen neutron dripline [9, 10]. The relevance of three-nucleon interactions constitutes a key difference from other fields of many-body research like atomic physics, molecular structure, or solid-state physics, and poses significant challenges.

Over the past two decades, the range of applicability of *ab initio* nuclear many-body theory has been extended significantly. While 20 years ago first-principle solutions of the quantum many-body problem were restricted to nuclei lighter than $A \approx 12$, formal and computational developments have made it possible to investigate a much wider range of masses. Initially, the *ab initio* treatment employed mostly large-scale diagonalization methods like the no-core shell model (NCSM) [11–13], or quantum Monte Carlo (QMC) [14–17] techniques. In addition, the few-body ($A = 3, 4$) solution could be constructed using the Fadeev approach or its Fadeev-Yakubowski extension [18, 19]. A major breakthrough occurred in the early 2000s when the re-import of so-called *expansion methods* from quantum chemistry provided systematically improvable many-body approximations for medium-mass closed-shell systems up to ^{132}Sn. In such approaches an initial guess for the exact wave function is taken as a reference state and corrections to this starting point are constructed through a chosen expansion scheme. Initially, this was done within the framework of self-consistent Green's function (SCGF) [20–25] and coupled cluster (CC) [26–31] theories that had proven to be extremely efficient at grasping *dynamical correlations* in electronic systems. Later on, the same strategy was transferred to other many-body expansion methods such as many-body perturbation theory (MBPT) [32–37], in-medium similarity renormalization group (IMSRG) [10, 38–44] or the unitary model operator approach (UMOA) [45, 46]. All of these methods provide a consistent description of ground-state energies of closed-shell mid-mass nuclei even though the rationales behind their expansions are not trivially related to one another. For sure, this consistency is a remarkable sign of success for *ab initio* nuclear many-body theory.

While closed-shell systems, dominated by so-called *dynamical correlations*, transparently allow for the use of single-reference techniques, the extension to open-shell systems requires a different strategy due to the degeneracy of single Slater-determinant reference states with respect to elementary excitations. Open-shell systems located in the vicinity of shell closures can be targeted via equation-of-motion (EOM) techniques where one or two nucleons are attached to the correlated ground state of a closed-shell nucleus [47, 48]. In nuclear systems, however, the strong coupling between spin and orbital angular momenta is such that long sequences of nuclei with open-shell character arise as the mass increases. Consequently, EOM approaches do not provide a viable option to tackle most of the open-shell systems that differ from closed-shell ones by more than one or two mass units. Two different routes have been followed in recent years to overcome this difficulty: (i) the construction of *ab initio*-rooted valence-space (VS) interactions used in a subsequent shell-model diagonalization and (ii) the use of correlated reference states capturing so-called *static correlations* and thus lifting from the outset the degeneracy with respect to elementary excitations. The design of VS interactions has been performed in various frameworks, going from simple low-order MBPT approaches [49] to more advanced non-perturbative schemes like IMSRG [39, 44] or CC [30]. While the design of the effective interaction can be performed at low polynomial cost, the final diagonalization, even though taking place in a limited valence space, still exhibits factorial scaling in the number of active nucleons pointing to the *hybrid scaling* of the approach.

In this article, the construction of VS interactions is not discussed and the focus is rather on the alternative strategy to overcome the limitations of single Slater-determinant-based expansions via the use of more general reference states. Reference states handling the bulk of *static correlations* from the outset re-introduce an *energy gap* in open-shell systems such that expanding the exact ground-state via elementary excitations of the reference state becomes well-defined again. In practice, this is done by resorting to either a *multi-determinantal* reference state or to a single *symmetry-broken* determinantal reference state. In an *ab initio* spirit, this was first done within the frame of SCGF theory, i.e., through the Gorkov extension of SCGF (GSCGF) [50] formulated on the basis of a Hartree-Fock-Bogoliubov (HFB) reference state breaking $U(1)$ global-gauge symmetry associated with particle number conservation. Soon after, a multi-reference version of IMSRG (MR-IMSRG) was designed based on a particle-number-projected HFB state [51]. Around 2013, these two methods provided the first *ab initio* description of arbitrary mid-mass singly open-shell nuclei. Later on, expansion methods were merged with configuration interaction (CI) technology by using reference states from a prior NCSM calculation performed in a model space of limited size. In this way, one can systematically improve the many-body solution, either by increasing the size of the reference space or by relaxing the truncation of the many-body expansion. Within the framework of perturbative approaches this strategy yields multi-configurational perturbation theory (MCPT) [36] whereas for IMSRG it leads to the introduction of the in-medium no-core shell model (IM-NCSM) [52].

More recently, the use of particle-number-breaking reference states has been exploited in MBPT and CC theory, thus giving rise to Bogoliubov MBPT (BMBPT) and Bogoliubov CC (BCC). While BCC has only undergone proof-of-principle applications in limited model spaces so far [53], BMBPT has been applied successfully in large-scale applications up to medium-heavy isotopic chains [37]. Next, the additional or alternative breaking of $SU(2)$ rotational symmetry associated with angular-momentum conservation will provide a systematic access to doubly open-shell nuclei [54]. While intensive efforts are already dedicated to this extension, no systematic result are available yet.

Whenever using a symmetry-broken reference state, an additional step must be envisioned to account for the quantum fluctuations eventually responsible for the lifting of the fictitious degeneracy associated with the broken symmetry. Indeed, the latter is only *emergent* in finite systems [55–57] such that it is mandatory to restore good symmetry quantum numbers. Doing so does not only change the energy (dramatically in certain situations) but also allows for the proper handling of transition operators characterized by symmetry selection rules. The formalism to achieve this step was proposed recently [54, 58, 59], but only applied to a schematic solvable model so far in the nuclear context [60] and will thus not be covered in the present article. Another topic of importance not presently covered relates to the benefit of applying so-called resummation methods to

the Taylor expansion associated with perturbation theory. While traditional methods such as Padé resummation [32, 33, 61] can typically be employed with success, the newly formulated eigenvector continuation method [62, 63] was recently applied successfully to BMBPT [64] and show great promises for the future. Last but not least, and since the present document focuses on finite nuclei, the recent efforts made to describe nuclear matter, at zero and finite temperature, on the basis of MBPT are not discussed [65–68].

Eventually, the objective of the present article is to describe the on-going revival of MBPT, both in its basic form and in some of its novel extensions, to describe finite closed-shell and open-shell nuclei. Furthermore, the goal is to demonstrate how MBPT complement non-perturbative methods in two ways, i.e., (i) it can act as an inexpensive pre-processing method to accelerate non-perturbative techniques and (ii) as a post-processing tool to further improve upon non-perturbative many-body approaches.

While the present document discusses in detail many-body perturbation theory for (ground-state) energies, the discussion of other observables is intentionally left out. Targeting other observables via MBPT has never been investigated in depth in nuclear physics. Contrary to the energy that is evaluated projectively, other observables must be computed as the expectation value of the associated operator in the perturbatively-determined many-body state. Within CC theory, this is typically achieved via a linear-response treatment, giving rise to its so-called Λ-CC extension [69]. Employing perturbative CC amplitudes, the Λ-MBPT variant could be obtained to evaluate arbitrary observables. Most recently, various groups identified a resummation method called eigenvector continuation [70–73] (EC) as a powerful tool to robustly extract energies from the MBPT expansion, even in the case of a divergent perturbative expansion. Formally, the EC framework can be straightforwardly extended to deliver an expectation value estimate of arbitrary observables.

The present document is structured as follows. Before actually coming to perturbation theory, its possible sources of breakdown are discussed in section 2. The nuclear Hamiltonian and softening techniques are introduced in section 3. In section 4, formal perturbation theory is laid out. Section 5 is then dedicated to the standard Slater-determinant-based MBPT applicable to closed-shell systems. Multi-configurational perturbation theory and Bogoliubov many-body perturbation theory are discussed as open-shell extensions in sections 6 and 7, respectively. In the next two sections, MBPT is employed as a cheap and efficient *pre-processing* tool for non-perturbative many-body methods. In section 8 MBPT is used to pre-select important configurations, i.e., as a data compression tool, in a non-perturbative calculation whereas in section 9 it is used to pre-optimize single-particle states, thus accelerating the convergence of the non-perturbative calculation with respect to the one-body basis dimension. In section 10, MBPT is eventually employed as an inexpensive method to provide systematic tests of a newly designed family of χEFT nuclear Hamiltonians over a large set of nuclei. Conclusions and outlooks are provided in section 11.

2. PERTURBATIVE VS. NON-PERTURBATIVE PROBLEM

Before actually discussing MBPT, it is useful to consider the possible reasons for the failure of expansion methods. With these considerations at hand, various MBPT flavors can be better understood based on the interplay between the symmetries characterizing the reference state around which the exact eigenstate is expanded, its single- or multi-determinantal character as well as the resolution scale of the employed Hamiltonian.

2.1. Rationale

It has often been argued in the past that the nuclear many-body problem is "intrinsically non-perturbative" such that MBPT is bound to fail to describe correlations between nucleons. The statement is, in such generality, *not true* and the strong disfavor against MBPT techniques is, to a large extent, based on historically grown bias.

It is crucial to understand the basic fact that the "(non-)perturbative" character of a system characterized by a Hamiltonian H has no meaning in absolute and can only be stated with respect to a chosen starting point. This notion relates, at least implicitly, to an "unperturbed problem," defined through an unperturbed Hamiltonian H_0 and its associated eigenstates, with respect to which the targeted solution is meant to be expanded. If the expansion can be written as a converging powers series in $H_1 \equiv H - H_0$, the problem is perturbative. Consequently, the more optimized H_0, the better the chances for the problem of actual interest to be *made* perturbative. For example, taking free particles as a reference point[1], the description of any bound state can only be *non* perturbative with respect to it. However, more optimized choices of H_0, making the description, perturbative might be accessible.

The critical point really resides in the cost required to find an appropriate H_0 and its exact eigensolutions, i.e., if the cost to do so is similar to the one needed to employ a non-perturbative method, the perturbation theory built on top of it is not so appealing. In the end, the question is rather: can one find H_0 and solve for its eigenstates at a moderate cost such that the eigenstates of H are obtained from them through a converging power series in $H_1 \equiv H - H_0$? While success is certainly not guaranteed in general, the search for an optimal, yet simple enough, H_0 must be performed in the most open-minded way. Typically, the statement that the nuclear many-body problem is "intrinsically non-perturbative" has been based on too restrictive assumptions of what H_0 is allowed to be.

2.2. Ultra-Violet and Infra-Red Divergences

Whether a perturbative approach is viable or not certainly depends on the nature of the Hamiltonian, i.e., on the nature of the elementary degrees of freedom at play and of their interactions. As a matter of fact, two characteristics of the 2N interaction make the many-body problem hard to solve, e.g., *possibly* non-perturbative. The first one relates to the strong

[1] The unperturbed Hamiltonian H_0 sums individual kinetic energies in this case.

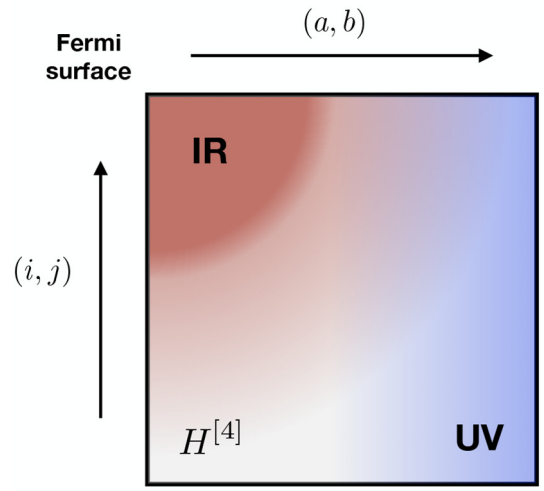

FIGURE 1 | Schematic matrix representation of the residual nuclear two-body interaction at play in perturbation theory. The size of the matrix elements is proportional to the darkness of the pixel while the red (blue) color indicate schematically a negative (positive) sign. In the present case, typically associated to MBPT on top of a closed-shell Slater determinant, the IR (UV) couplings translate into large negative (positive) matrix elements between pairs of unoccupied and occupied states near the Fermi level (between any pairs of occupied and highly excited virtual states).

short-range central and tensor-forces between the nucleons inducing strong correlations in the ultra-violet (UV) regime. The second one relates to the large scattering lengths associated with the existence of a weakly bound proton-neutron state and of a virtual di-neutron state, which induce strong many-body correlations in the infra-red (IR) regime. These characteristics induce typical patterns, i.e., large matrix elements, of the residual interaction as schematically depicted in **Figure 1**: the upper-left corner corresponds to nuclear matrix elements between high-lying occupied and low-lying virtual states, i.e., to physics around the Fermi surface. Those matrix elements involve strong attractive IR couplings that fall off when moving further away from the Fermi surface. Complementary, repulsive UV couplings become more prominent if energetically higher virtual states are considered, independently of the particular pair of occupied states they interact with.

The potential occurrence of a UV-driven divergence is not nucleus specific and concerns all expansion methods, not just MBPT. Still, specific non-perturbative expansions may, at a given truncation order, resum a specific infinite subset of perturbation theory contributions that appropriately handles the divergence driven by the large UV couplings displayed in **Figure 1**. In the end, a pure power series in H_1 is certainly the most sensitive expansion to strong low-to-high momentum couplings in the Hamiltonian that typically make the series to diverge after a few reasonable low-order contributions. It happens, however, that UV-driven divergences can be tamed to a large extent via a pre-processing of the Hamiltonian through renormalization group transformations. These transformations are briefly introduced in section 3.2 and their consequences on the MBPT expansion is illustrated in section 5.6.2.

The potential occurrence of a IR-driven divergence is nucleus specific but concerns all expansion methods, not just MBPT. Infra-red-driven divergences occur whenever the A-body unperturbed reference state, i.e., the ground state of H_0, is (nearly) degenerate with respect to elementary, e.g., particle-hole, excitations. Considering a standard Slater-determinant reference state, and as illustrated in the top panel of **Figure 2**, this situation occurs whenever the number of constituents is such that the highest occupied shell is only partially filled (is too close to the first empty shell), thus defining so-called open-shell (closed-sub-shell) nuclei. Combined with large IR matrix elements (see **Figure 1**), this cancelation (reduction) of the particle-hole gap makes the perturbative expansion (nearly) singular from the outset such that even the few first terms (e.g., Equation 45) are not well behaved. A numerical illustration of the emergence of such a IR divergence is provided in the bottom panel of **Figure 2**. This major difficulty can be controlled to a large extent via the use of more general classes of unperturbed Hamiltonians H_0 and reference states than typically considered in the past. This idea and the corresponding results are discussed in sections 6 and 7.

Of course, even with the use of renormalization group transformations of the Hamiltonian and rather general classes of reference states, the two characteristics of the nucleon-nucleon interaction in the UV and IR regimes may eventually compromise the convergence of *any* practical perturbative expansion and call for resummation techniques or the use of explicitly non-perturbative methods.

3. THE NUCLEAR HAMILTONIAN

3.1. The Bare Operator

As briefly mentioned in the introduction, chiral effective field theory (χEFT) provides a convenient framework to construct systematically improvable nuclear Hamiltonians valid in the low-energy regime relevant to nuclear structure [4, 6]. Starting from nucleons and pions as explicit degrees of freedom, the long- and mid-range parts of the interaction are mediated by multiple-pion exchanges whereas the unresolved short-range part is modeled via contact terms and derivatives of contact terms. In the early 1990's Weinberg paved the way for a systematic treatment of the strong interaction by introducing a power-counting scheme stipulating the *a priori* importance of the infinite number of allowed contributions in the operator expansion [1–3]. Operators with higher particle rank naturally arise at higher orders in this scheme. Eventually, the parameters, i.e., the low-energy constants (LEC's), entering the operator expansion are fitted to low-energy experimental data [74, 75].

Eventually, the second-quantized form of the many-body Hamiltonian takes, in an arbitrary basis $\{|p\rangle \equiv c_p^\dagger|0\rangle\}$ of the one-body Hilbert space $\mathcal{H}_1$, the form

$$\begin{aligned} H &= T + V + W + \dots \\ &\equiv \frac{1}{(1!)^2} \sum_{pq} t_{pq}\, c_p^\dagger c_q \end{aligned} \tag{3}$$

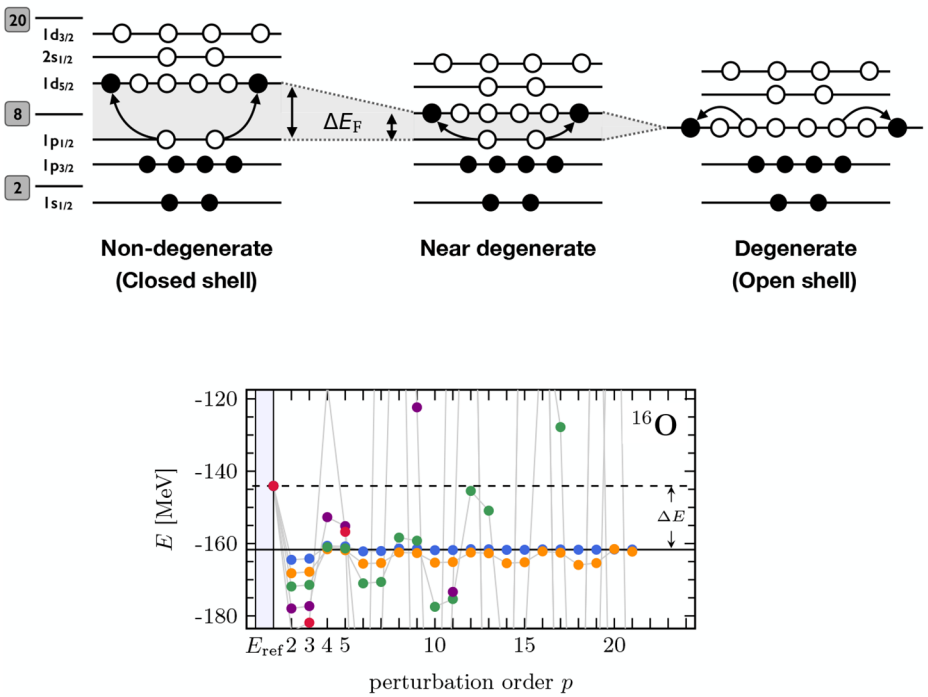

FIGURE 2 | (Top) Schematic representation of neutron or proton energy shells and associated occupations corresponding to a two-particle/two-hole excitation on top of the reference Slater determinant, i.e., the ground state of H_0, appropriate to a ^{16}O-like nucleus (N = Z = 8). The last occupied shell in the reference state is the *Fermi level* and its energy separation to the first empty level is denoted as ΔE_F. Left: closed-shell nucleus for which the number of nucleons is such that (i) the Fermi level is fully occupied and (ii) $\Delta E_F \gg 0$. Center: sub-closed shell nucleus for which the number of nucleons is such that (i) the Fermi level is fully occupied and (ii) ΔE_F is small. Right: open-shell nucleus for which the number of nucleons is such that the Fermi level is only partly occupied such that $\Delta E_F = 0$. **(Bottom)** Emergence of an infra-red divergence in the MBPT expansion of the ground-state energy of ^{16}O induced by a step-wise reduction (going from blue, to yellow, to green, to purple, and to red) of the size of the particle-hole gap in the spectrum of H_0.

$$+\frac{1}{(2!)^2}\sum_{pqrs}\bar{v}_{pqrs}\,c_p^\dagger c_q^\dagger c_s c_r$$
$$+\frac{1}{(3!)^2}\sum_{pqrstu}\bar{w}_{pqrstu}\,c_p^\dagger c_q^\dagger c_r^\dagger c_u c_t c_s$$
$$+\ldots.$$

The Hamiltonian is, thus, represented via a set of one-, two-, and three-body matrix elements t_{pq}, $\bar{v}_{pqrs}$ and $\bar{w}_{pqrstu}$, respectively. In a modern language the above matrix elements define *tensors* of mode $n = 2, 4, 6$, respectively, where the *mode* specifies the number of indices.

3.2. Similarity Renormalization Group

While the tensors defining the Hamiltonian built within χEFT may display large low-to-high momentum couplings, pre-processing tools can be used to tame them. During the past decade the (free-space) similarity renormalization group (SRG) approach has become the standard technique to generate a "softened" basis representation of an operator more amenable to many-body calculations [76].

The SRG approach is based on a unitary transformation of the initial operator O parameterized by a continuous parameter $\alpha \in \mathbb{R}$, i.e.,

$$O(\alpha) = U^\dagger(\alpha) O U(\alpha). \tag{4}$$

Equation (4) can be re-cast into a first-order differential equation

$$\frac{d}{d\alpha}O(\alpha) = [\eta(\alpha), O(\alpha)] \tag{5}$$

involving an anti-Hermitian *generator* $\eta(\alpha)$ that can be chosen freely to achieve a desired decoupling pattern in the transformed operator. A convenient choice employed in many calculations is given by

$$\eta(\alpha) \equiv [T, O(\alpha)], \tag{6}$$

such that the SRG evolution can be interpreted as a *pre-diagonalization* of the operator in momentum space, thus suppressing the coupling between high- and low-momentum modes. This procedure thus drives the Hamiltonian toward a band-diagonal form. Writing $H(\alpha) \equiv T + V(\alpha) + W(\alpha) + \ldots$ in the same single-particle basis as the starting Hamiltonian, the SRG transformation corresponds to generating α-dependent tensors $\bar{v}_{pqrs}(\alpha)$, $\bar{w}_{pqrstu}(\alpha)\ldots$ whose UV elements linking single-particle states corresponding to low and high momenta are strongly suppressed.

In many-body applications SRG-evolved operators display highly improved model-space convergence, thus facilitating studies of mid-mass nuclei. The impact on the convergence properties of the MBPT series will be illustrated in section 5.6.2. However, the numerical improvements come at the price of induced many-body operators, i.e., the unitary transformation shifts information to operators with higher particle ranks. For instance, employing an initial two-body operator O^{2B} leads to

$$O^{2B} \xrightarrow{\text{SRG}} O^{2B}(\alpha) + O^{3B}(\alpha) + O^{4B}(\alpha) + ... \tag{7}$$

In practice, Equation (7) must be truncated at a given operator rank, thus discarding higher-body operators. This approximation formally violates the unitarity of the transformation in Fock space and eventually induces a dependence of many-body observables on the SRG parameter α. A reasonable trade-off must be found for the value of α employed, i.e., it must improve the model-space convergence while keeping the effect of induced many-body operators at a minimum. The optimal parameter range may vary depending on the operator one starts from.

For the evaluation of nuclear properties, it is crucial to consistently transform all other operator representations to the same resolution scale as the Hamiltonian in order to provide a meaningful comparison in terms of a consistent operator basis smoothly connected in terms of the RG flow.

3.3. The "Standard" Hamiltonian

All many-body applications discussed below, except for the novel ones presented in section 10, employ a chiral Hamiltonian containing a 2N interaction at next-to-next-to-next-to-leading-order (N3LO) with a cutoff value of $\Lambda_{2N} = 500\,\text{MeV}/c$ [77, 78]. Three-body forces are included up to next-to-next-to-leading order (N2LO) with a local regulator [78] based on a cutoff value of $\Lambda_{3N} = 400\,\text{MeV}$ [79]. This constitutes a "standard" Hamiltonian used in many recent *ab initio* studies of light and medium-mass nuclei.

Additionally, the intrinsic Hamiltonian is consistently SRG-evolved in the two- and three-body sectors [80, 81]. The particular value of the SRG parameter is specified in each individual application. To avoid the complication of dealing with genuine three-body operators various forms of so-called normal-ordered two-body approximations (NO2B) are employed, depending on the particular nature of the A-body reference state [79, 82, 83].

4. FORMAL PERTURBATION THEORY

The presentation of perturbation theory can be separated into *formal perturbation theory* and *many-body perturbation theory* [69]. Formal perturbation theory allows one to understand the general rationale and most relevant properties of the formalism. This is done by employing abstract Dirac notations and by specifying the initial assumptions via the action of Hilbert or Fock space operators on basis vectors. In particular, many key results can be obtained without specifying the content of the Hamiltonian (e.g., the rank of the operators it contains), the nature of the partitioning (e.g., the symmetries characterizing each contribution) and the associated reference state.

4.1. Partitioning

The starting point of perturbation theory relates to a *partitioning of the Hamiltonian*

$$H \equiv H_0 + H_1, \tag{8}$$

into an unperturbed part H_0 and a perturbation $H_1 \equiv H - H_0$. The main assumption relies on the fact that the eigenvalue equation for H_0 is numerically accessible, i.e.,

$$H_0|\Phi_k\rangle = E_k^{(0)}|\Phi_k\rangle, \tag{9}$$

delivering the set of unperturbed eigenstates and eigenergies $\{|\Phi_k\rangle, E_k^{(0)}; k \in \mathbb{N}\}$ making up an orthonormal, i.e.,

$$\langle\Phi_k|\Phi_l\rangle = \delta_{kl}, \tag{10}$$

basis of the many-body Hilbert space.

Remark: A large part of this document is dedicated to the description of nuclear ground states, i.e., $k = 0$. Consequently, the corresponding index is dropped in the following whenever targeting the ground state, e.g., $|\Psi_0^{\text{A}}\rangle = |\Psi^{\text{A}}\rangle$, $|\Phi_0\rangle = |\Phi\rangle$ or $E_0^{(0)} = E^{(0)}$.

One typically employs *intermediate normalization*, i.e., the ground state $|\Psi^{\text{A}}\rangle$ of H is connected[2] to the unperturbed ground-state $|\Phi\rangle$ of H_0 such that

$$1 = \langle\Phi|\Psi^{\text{A}}\rangle. \tag{11}$$

Associated with the above partitioning are the *projection operators*

$$P \equiv |\Phi\rangle\langle\Phi|, \tag{12a}$$
$$Q \equiv 1 - P, \tag{12b}$$

where $P|\Phi\rangle = |\Phi\rangle$ and $Q|\Phi\rangle = 0$ by orthonormality. It can be shown that P and Q do meet the requirements of projection operators, i.e., Hermiticity and idempotency [69]. The operator Q can be explicitly written as

$$Q \equiv \sum_k{}' |\Phi_k\rangle\langle\Phi_k| \equiv \sum_{|\Phi_k\rangle \neq |\Phi\rangle} |\Phi_k\rangle\langle\Phi_k|, \tag{13}$$

where the primed sum indicates the exclusion of the reference state from the summation. With these operators at hand, the exact ground-state can be written as

$$\begin{aligned} |\Psi^{\text{A}}\rangle &= P|\Psi^{\text{A}}\rangle + Q|\Psi^{\text{A}}\rangle \\ &= |\Phi\rangle + |\chi\rangle, \end{aligned} \tag{14}$$

where the *correlated part* $|\chi\rangle \equiv Q|\Psi^{\text{A}}\rangle$, which is the unknown to be solved for, denotes the *orthogonal complement* of $|\Phi\rangle$.

[2] Both states are supposed to be adiabatically connected when the perturbation H_1 is switched on.

Eventually, the exact ground-state energy is typically accessed in a *projective* way[3] by left-multiplying Equation (1) with the reference state $\langle\Phi|$ such that

$$\begin{aligned} E^{\mathrm{A}} &= \langle\Phi|H|\Psi^{\mathrm{A}}\rangle \\ &= \langle\Phi|H_0|\Phi\rangle + \langle\Phi|H_1|\Phi\rangle + \langle\Phi|H_1|\chi\rangle \\ &= E_{\mathrm{ref}} + \Delta E, \end{aligned} \tag{15}$$

where $E_{\mathrm{ref}} \equiv \langle\Phi|H|\Phi\rangle = E^{(0)} + \langle\Phi|H_1|\Phi\rangle$ and $\Delta E \equiv E^{\mathrm{A}} - E_{\mathrm{ref}} = \langle\Phi|H_1|\chi\rangle$ denote reference and correlation energies, respectively. When using a reference state of product type, e.g., a Slater determinant, ΔE accounts for correlations between the nucleons beyond the mean-field approximation.

4.2. Resolvent Operator

The complete derivation of formal perturbation theory is best performed in terms of the (Rayleigh-Schrödinger) many-body *resolvent operator*

$$R^{\mathrm{RS}} \equiv \sum_k{}' \frac{|\Phi_k\rangle\langle\Phi_k|}{E^{(0)} - E_k^{(0)}}, \tag{16}$$

which, due to orthonormality of the employed many-body basis, annihilates the reference state

$$R^{\mathrm{RS}}|\Phi\rangle = 0. \tag{17}$$

It is possible to employ alternative choices, such as the *Brillouin-Wigner* resolvent

$$R^{\mathrm{BW}} \equiv \sum_k{}' \frac{|\Phi_k\rangle\langle\Phi_k|}{E^{\mathrm{A}} - E_k^{(0)}}, \tag{18}$$

which differs from R^{RS} by the presence of the *exact energy* in the denominator instead of the unperturbed energy $E^{(0)}$. In practice, Brillouin-Wigner perturbation theory requires an (computationally intensive) iterative solution and, additionally, suffers from a lack of size-extensivity[4]. Therefore, this choice is only scarcely used in many-body applications. All of the subsequent results are obtained using a Rayleigh-Schrödinger resolvent. Consequently, the upper-case label "RS" is dropped to avoid notational clutter.

4.3. Power-Series Expansion

After a long but straightforward derivation [69], one obtains the correlated part of many-body ground-state and associated energy under the form [84–86]

$$|\chi\rangle = \sum_{k=1}^{\infty} (RH_1)^k |\Phi\rangle_c, \tag{19a}$$

$$\Delta E = \langle\Phi|H_1 \sum_{k=1}^{\infty} (RH_1)^k |\Phi\rangle_c. \tag{19b}$$

The lower index "c" stipulates the *connected* character of the expansion ensuring its size-extensivity, i.e., proper scaling of observables with system size[5]. Combining Equations (15) and (19b), one obtains the total ground-state wave-function and energy as power series in H_1

$$|\Psi^{\mathrm{A}}\rangle \equiv \sum_{p=0}^{\infty} |\Psi^{(p)}\rangle, \tag{20}$$

$$E^{\mathrm{A}} \equiv \sum_{p=0}^{\infty} E^{(p)}, \tag{21}$$

such that $|\Psi^{(0)}\rangle = |\Phi\rangle$ and $E_{\mathrm{ref}} = E^{(0)} + E^{(1)}$, i.e., the first non-trivial correction contributing to the ground-state correlation energy corresponds to the second-order term of the power series. It reads as

$$E^{(2)} = \langle\Phi|H_1 R H_1|\Phi\rangle_c, \tag{22}$$

and can be re-written more explicitly by expanding the resolvent as

$$E^{(2)} = \sum_k{}' \frac{\langle\Phi|H_1|\Phi_k\rangle\langle\Phi_k|H_1|\Phi\rangle}{E^{(0)} - E_k^{(0)}}. \tag{23}$$

Equation (23) provides a prototypical example of a PT expression associated with ground-state energy corrections involving a resolvent operator connecting the unperturbed reference state (i.e., the P space) to excited states of H_0 (i.e., the Q-space), and then going back to the reference state through the perturbation H_1. As will be seen with explicit MBPT, the nature of the elementary excitations of the reference state effectively involved at a given order depend on the rank, i.e., the k-body character, of the perturbation H_1.

4.4. Recursive Formulation

Equations (19a) and (19b) conveniently provide explicit expressions for the energy and state corrections whenever working at rather low orders. To go to high orders and study the convergence properties of perturbation theory as a power series, a different scheme becomes more useful. It relates to (i) making more explicit that the perturbative expansion relates to the power series expansion of a mathematical function taken at a particular value of its variable and to (ii) computing the coefficient of the series in a recursive way.

On the basis of the partitioning introduced in Equation (8), one defines a one-parameter family of Hamiltonians

$$H(\lambda) \equiv H_0 + \lambda H_1, \tag{24}$$

[3]The projective character of standard MBPT or CC is to be distinguished from an *expectation value* approach, where the correlated state appears both as the bra and the ket in the evaluation of the energy.

[4]A quantum-mechanical method is coined as *size-extensive* if the energy of a systems computed with this method scales linearly in the number of particles.

[5]The first disconnected contribution originally appears at fourth order. It can be shown that the renormalization terms cancel such disconnected contributions at every order [69, 85, 86], thus providing the final connected form.

such that $H(0) = H_0$ and $H(1) = H$. Perturbation theory assumes that the exact eigenstates and eigenenergies of $H(\lambda)$ can be parameterized through the *power series ansatz*

$$E(\lambda) \equiv E^{(0)} + \lambda E^{(1)} + \lambda^2 E^{(2)} + ..., \tag{25a}$$

$$|\Psi(\lambda)\rangle \equiv |\Psi^{(0)}\rangle + \lambda|\Psi^{(1)}\rangle + \lambda^2|\Psi^{(2)}\rangle + ... \tag{25b}$$

Setting $\lambda = 0$, the problem becomes equivalent to Equation (9) while setting $\lambda = 1$, one recovers the expansions of Equations (20) and (21) associated with the fully interacting problem.

Inserting the power series ansatz into the stationary Schrödinger equation for $H(\lambda)$ and grouping together the terms proportional to λ^p leads to

$$E^{(0)}|\Phi\rangle + \sum_{p=1}^{\infty}\lambda^p\Big(H_1|\Psi^{(p-1)}\rangle + H_0|\Psi^{(p)}\rangle\Big) = E^{(0)}|\Phi\rangle + \sum_{p=1}^{\infty}\lambda^p\Big(\sum_{j=0}^{p}E^{(j)}|\Psi^{(p-j)}\rangle\Big). \tag{26}$$

Left multiplying Equation (26) with $\langle\Phi|$ and using intermediate normalization yields

$$\sum_{p=1}^{\infty}\lambda^p\langle\Phi|H_1|\Psi^{(p-1)}\rangle = \sum_{p=1}^{\infty}\lambda^p E^{(p)}, \tag{27}$$

which allows one to write the p-order ground-state energy correction as

$$E^{(p)} = \langle\Phi|H_1|\Psi^{(p-1)}\rangle. \tag{28}$$

Left multiplying Equation (26) with $\langle\Phi_m|$, $m \neq 0$, and matching the terms proportional to λ^p provides the relation

$$\Big(E^{(0)} - E_m^{(0)}\Big)\langle\Phi_m|\Psi^{(p)}\rangle = \langle\Phi_m|H_1|\Psi^{(p-1)}\rangle - \sum_{j=1}^{p}E^{(j)}\langle\Phi_m|\Psi^{(p-j)}\rangle. \tag{29}$$

Introducing the coefficients

$$C_{m0}^{(p)} \equiv \langle\Phi_m|\Psi^{(p)}\rangle = \frac{1}{E^{(0)} - E_m^{(0)}}\left[\langle\Phi_m|H_1|\Psi^{(p-1)}\rangle - \sum_{j=1}^{p}E^{(j)}\langle\Phi_m|\Psi^{(p-j)}\rangle\right], \tag{30}$$

allows one to expand the p-order ground-state correction $|\Psi^{(p)}\rangle$ on the unperturbed basis $\{|\Phi_m\rangle\}$ according to

$$|\Psi^{(p)}\rangle = \sum_m C_{m0}^{(p)}|\Phi_m\rangle, \tag{31}$$

such that Equation (28) becomes

$$E^{(p)} = \sum_m\langle\Phi|H_1|\Phi_m\rangle C_{m0}^{(p-1)}. \tag{32}$$

Inserting Equation (31) into Equation (30) further provides a recursive scheme to compute $C_{m0}^{(p)}$

$$C_{m0}^{(p)} = \frac{1}{E^{(0)} - E_m^{(0)}}\left[\sum_q\langle\Phi_m|H_1|\Phi_q\rangle C_{q0}^{(p-1)} - \sum_{j=1}^{p}E^{(j)}C_{m0}^{(p-j)}\right], \tag{33}$$

with the initial condition $C_{m0}^{(0)} = \delta_{m0}$.

Eventually, Equations (32) and (33) form a set of *recursive relations* from which the ground-state energy and state corrections can be obtained to all orders. In practice, the eigenbasis of H_0 and the associated matrix elements of H_1 are built such that the latter is stored in memory. The recursive steps are then identified as large-scale matrix-vector multiplications, thus, using the same technology as configuration-interaction approaches like the NCSM. While being formally convenient and obviating the explicit algebraic computation of order-p corrections, this approach is limited by the storage of the Hamiltonian due to the extensive size of the many-body basis. Therefore, only proof-of-principle studies in model spaces of limited dimensionality can be performed and realistic calculations of mid-mass nuclei are out of reach in this way.

5. CLOSED-SHELL MANY-BODY PERTURBATION THEORY

With the results of formal perturbation theory at hand, one can envision to apply them to specific many-body systems. To do so, one must further specify the nature of the partitioning and of the associated reference state. In particular, the maximum rank and symmetries of H_0 must be characterized. Additionally, the goal of MBPT is to express all quantities, e.g., many-body matrix elements and unperturbed eigenenergies, entering the formulae at play in terms of the actual inputs to the many-body problem, i.e., the mode-$2k$ tensors defining the k-body contributions to the Hamiltonian (Equation 3).

A series of tools exists to compute the expectation value of products of (many) operators in a vacuum state in an incrementally faster, more flexible and less error-prone way. The first step in this series corresponds to using the second-quantized representation of many-body operators in a chosen single-particle basis and to performing canonical commutations of fermionic operators. Next comes Wick's theorem [87], which is nothing but a procedure to capture the result in a condensed and systematic fashion. Still, the combinatorics associated with the application of Wick's theorem quickly becomes cumbersome whenever a long string of creation and annihilation operators is involved. Furthermore, many terms thus generated give identical contributions to the end result. Many-body diagrams address this issue [69] by providing a pictorial representation of the contributions and, even more importantly, by capturing at once all identical contributions, thus reducing the combinatorics tremendously. While being incredibly useful, the number of diagrams itself grows tremendously when applying MBPT beyond the lowest orders, thus leading to yet another combinatorial challenge. This translates into the difficulty to

both generate all allowed diagrams at a given order without missing any and to evaluate their expression in a quick and error-safe way. Consequently, the last tool introduced to tackle this difficulty consists of an automatized generation and evaluation of diagrams [88–95]. All these technical, yet crucial, aspects of MBPT are not addressed in the present article and the interested reader is referred to the references.

5.1. Reference State

The present chapter is dedicated to the simplest form of MBPT appropriate to closed-shell systems. This first version relies on the use of a symmetry-conserving Slater determinant reference state

$$|\Phi\rangle \equiv \prod_{i=1}^{A} c_i^\dagger |0\rangle, \tag{34}$$

where the set of single-particle creation operators $\{c_p^\dagger\}$ acts on the physical vacuum $|0\rangle$. This constitutes an appropriate starting point of the perturbative expansion as long as $|\Phi\rangle$ denotes a closed-shell Slater determinant in agreement with the left-hand case in **Figure 2**. While, in principle, the single-particle basis is completely arbitrary, applications will reveal its significant impact on the qualitative behavior of the perturbative expansion.

5.2. Normal Ordering

Applying Wick's theorem with respect to $|\Phi\rangle$, the Hamiltonian can be rewritten in terms of normal-ordered contributions

$$H = H^{[0]} + \sum_{pq} H_{pq}^{[2]} \, :c_p^\dagger c_q: + \frac{1}{4} \sum_{pqrs} H_{pqrs}^{[4]} \, :c_p^\dagger c_q^\dagger c_s c_r: + \dots, \tag{35}$$

where $::$ denotes the normal order of the involved creation and annihilation operators. Thus, $H^{[0]}$ is the expectation value of H in $|\Phi\rangle$ whereas $H_{pq}^{[2]}$ and $H_{pqrs}^{[4]}$ define matrix elements of *effective*, i.e., normal-ordered, one-body and two-body operators, respectively. The dots denote normal-ordered operators of higher ranks, up to the maximum rank k_{max} characterizing the initial Hamiltonian (Equation 3). Through the application of Wick's theorem, an effective operator of rank k_{eff} receives contributions from all initial operators with rank k, where $k_{\text{eff}} \leq k \leq k_{\text{max}}$. Using an initial Hamiltonian with up to three-nucleon interactions and working in the normal-ordered two-body approximation (NO2B) [79, 82], the residual three-body part $H^{[6]}$ is presently discarded. For explicit expressions of the matrix elements defining the normal-ordered operator (see [79, 82, 83]).

5.3. Partitioning

To explicitly set up the partitioning of the Hamiltonian (Equation 8), one adds and subtracts a *diagonal* normal-ordered one-body operator

$$\bar{H}^{[2]} \equiv \sum_p e_p \, :c_p^\dagger c_p: \tag{36}$$

such that

$$H_0 = H^{[0]} + \sum_p e_p \, :c_p^\dagger c_p:, \tag{37a}$$

$$H_1 \equiv \check{H}^{[2]} + H^{[4]}, \tag{37b}$$

with

$$\check{H}^{[2]} \equiv H^{[2]} - \bar{H}^{[2]} = \sum_{p \neq q} H_{pq}^{[2]} \, :c_p^\dagger c_q: \, . \tag{38}$$

Introducing the set of Slater determinants obtained from $|\Phi\rangle$ via n-particle/n-hole excitations

$$|\Phi_{ij\dots}^{ab\cdots}\rangle \equiv c_a^\dagger c_b^\dagger \dots c_j c_i |\Phi\rangle, \tag{39}$$

one obtains an orthonormal basis of the A-body Hilbert space

$$\mathcal{H}^A = \{|\Phi\rangle, |\Phi_i^a\rangle, |\Phi_{ij}^{ab}\rangle, |\Phi_{ijk}^{abc}\rangle, \dots\}, \tag{40}$$

which is nothing but the eigenbasis of H_0

$$H_0|\Phi\rangle = H^{[0]}|\Phi\rangle, \tag{41a}$$

$$H_0|\Phi_{ij\dots}^{ab\cdots}\rangle = (H^{[0]} + \epsilon_{ij\dots}^{ab\cdots})|\Phi_{ij\dots}^{ab\cdots}\rangle, \tag{41b}$$

where

$$\epsilon_{ij\dots}^{ab\cdots} \equiv (e_a + e_b + \cdots) - (e_i + e_j + \cdots) \tag{42}$$

sums (subtracts) the n one-body energies of the particle (hole) states the nucleons are excited into (from). Equation (41) corresponds to the explicit form of Equation (9) in the case of a Slater determinant reference state.

Convention: One-body states occupied (unoccupied) in the reference determinant are labeled by $i, j, k, \dots$ ($a, b, c, \dots$) and are referred to as *hole* (*particle*) states. Generic one-body states are denoted by $p, q, r, \dots$.

The single-particle energies $\{\epsilon_p\}$ are parameters of the theory that are fixed by the partitioning, which itself defines the reference state. They can be chosen arbitrarily as long as the A occupied hole states have lower energies than the remaining particle states, such that $\epsilon_{ij\dots}^{ab\cdots} > 0$. A simple choice employed in nuclear physics consists of building $|\Phi\rangle$ by filling up the A lowest single-particle eigenstates of the spherical *harmonic oscillator* Hamiltonian [32, 33], i.e., setting

$$H_0 \equiv \frac{\vec{p}^{\,2}}{2m} + \frac{1}{2} m\omega^2 \vec{r}^{\,2}, \tag{43}$$

where the oscillator frequency ω specifies the width of the potential. A more standard choice throughout various fields of many-body physics and chemistry relates to the so-called Møller-Plesset partitioning that corresponds to taking $\check{H}^{[2]} = 0$, i.e., $H_1 = H^{[4]}$. This is obtained by using the reference Slater determinant $|\Phi\rangle$ solution of the Hartree-Fock (HF) variational problem and by defining $\bar{H}^{[2]}$ from the eigenvalues of the one-body HF Hamiltonian.

5.4. Perturbative Expansion

Given the eigenbasis of H_0 characterized by Equations (34), (39), and (41), the many-body resolvent (Equation 16) takes the form

$$R = -\sum_{ai} \frac{|\Phi_i^a\rangle\langle\Phi_i^a|}{\epsilon_i^a} - \left(\frac{1}{2!}\right)^2 \sum_{abij} \frac{|\Phi_{ij}^{ab}\rangle\langle\Phi_{ij}^{ab}|}{\epsilon_{ij}^{ab}} - \left(\frac{1}{3!}\right)^2 \sum_{abcijk} \frac{|\Phi_{ijk}^{abc}\rangle\langle\Phi_{ijk}^{abc}|}{\epsilon_{ijk}^{abc}} + ..., \tag{44}$$

and is to be fed into Equation (19b) that, once truncated at a given power in H_1, provides the correlation energy at the corresponding perturbative order.

5.5. Low-Order Formulas

As alluded to above, the evaluation of low-order corrections is facilitated by representing the MBPT expansion diagrammatically. This is typically done using either Hugenholtz or (anti-)symmetrized Goldstone diagrams, i.e., the time-ordered counterpart of Feynman diagrams that are used to compute matrix elements in quantum field theory. The interested reader is referred to the literature, e.g., Shavitt and Bartlett [69], for an elaborate discussion of the diagrammatic rules and their relation to Wick's theorem.

Focusing on the first non-trivial correction to the reference energy (Equation 23), the second-order correction takes the algebraic form

$$E^{(2)} = -\sum_{ai} \frac{H_{ai}^{[2]} H_{ia}^{[2]}}{\epsilon_i^a} - \frac{1}{4} \sum_{abij} \frac{H_{abij}^{[4]} H_{ijab}^{[4]}}{\epsilon_{ij}^{ab}}, \tag{45}$$

and is, thus, expressed in terms of the tensors defining the residual interaction H_1 (Equation 37b) in normal-ordered form. The first contribution in Equation (45) relates to a so-called *non-canonical diagram* that vanishes if the reference state is taken to be the HF Slater determinant. The second term constitutes the genuine and dominant second-order correction that contributes for any Slater determinant reference state. Using the HF Slater determinant reference state has the practical benefit of lowering the number of many-body diagrams to be considered. While this feature is not relevant at second-order, the proliferation of non-canonical diagrams at higher order [95] makes the writing of numerical codes more cumbersome. Still, at a given order non-canonical diagrams are always of sub-leading complexity from a computational point of view, i.e., they involve fewer single-particle summations, such that they do not drive the computational cost.

Since $E^{(2)}$ provides the leading contribution to the perturbative expansion, one observes that dynamical correlations are dominated by low-lying 2p2h-contributions. Most importantly, it is clear from Equation (45) that the second-order correction is manifestly negative, i.e., it increases the binding energy. This stems from the fact that the numerators are squared norms of matrix elements contributing to H_1 and that the denominators are positive as long as the Slater determinant reference state displays a non-zero shell gap between occupied and unoccupied states, i.e., as long as one deals with a closed-shell nucleus.

5.6. Results

The first goal of the present analysis is to study the convergence characteristics of the perturbative expansion. In absence of analytical knowledge, this study must be based on empirical observations of high-order corrections, which is achieved through the recursive formulation of section 4.4 in small model spaces. Following this analysis, results of low-order MBPT calculations in realistic model spaces are presented to illustrate state-of-the-art *ab initio* applications to doubly closed-shell nuclei [34].

5.6.1. Impact of Partitioning

While perturbation theory defines a general framework to access nuclear observables, the performance strongly depends on the choice of the partitioning $H = H_0 + H_1$ or, equivalently, on the underlying vacuum fixing the starting point for the expansion. Subsequently, two choices for H_0 are presently compared in the calculation of the ground-state energy of ^{16}O, i.e., the one-body (i) spherical harmonic oscillator (HO) and (ii) self-consistent HF[6] Hamiltonians (cf. section 5.3). The model space is truncated employing the $N_{\max}$-truncation similar to the NCSM. **Figure 3A** shows the sequence of partials sums using a HO partitioning for a set of model spaces. The partial sums are divergent in all cases, which can equally be seen from the exponential divergence of high-order energy corrections in **Figure 3C**. On the other hand, using a HF reference state yields a rapidly converging perturbation series (**Figure 3B**) and the energy corrections are exponentially suppressed as a function of the perturbative order (**Figure 3D**), indicating robust convergence. In all cases the converged results agree up to numerical accuracy with the exact CI diagonalization.

Obviously, the reference state heavily affects the performance of MBPT. In the above case, this can be understood by the poor quality of the HO reference, e.g., the wrong asymptotic radial dependence of single-particle HO eigenstates (Gaussian instead of exponential suppression). Consequently, in the following a HF determinant is used as a reference state when results are reported for closed-shell nuclei.

5.6.2. SRG Dependence

Using a HF partitioning, the impact of the SRG transformation of the Hamiltonian on the perturbative series is now illustrated. In **Figure 4**, the ground-state energy of ^{4}He, ^{16}O, and ^{24}O is displayed while varying the value of the flow parameter α defining the SRG transformation. The left-hand panels show that the perturbative series converge in all cases thus demonstrating the reliability of HF-MBPT. For the light ^{4}He, the results are independent of the flow parameter and the MBPT expansion converges rapidly in all cases. For ^{16}O and ^{24}O, the rate of convergence is slower for harder interactions, i.e., for lower values of α. Furthermore, the partial sums admit a damped

[6]The HF problem is solved in a symmetry-restricted way, enforcing rotational invariance of the resulting single-particle basis.

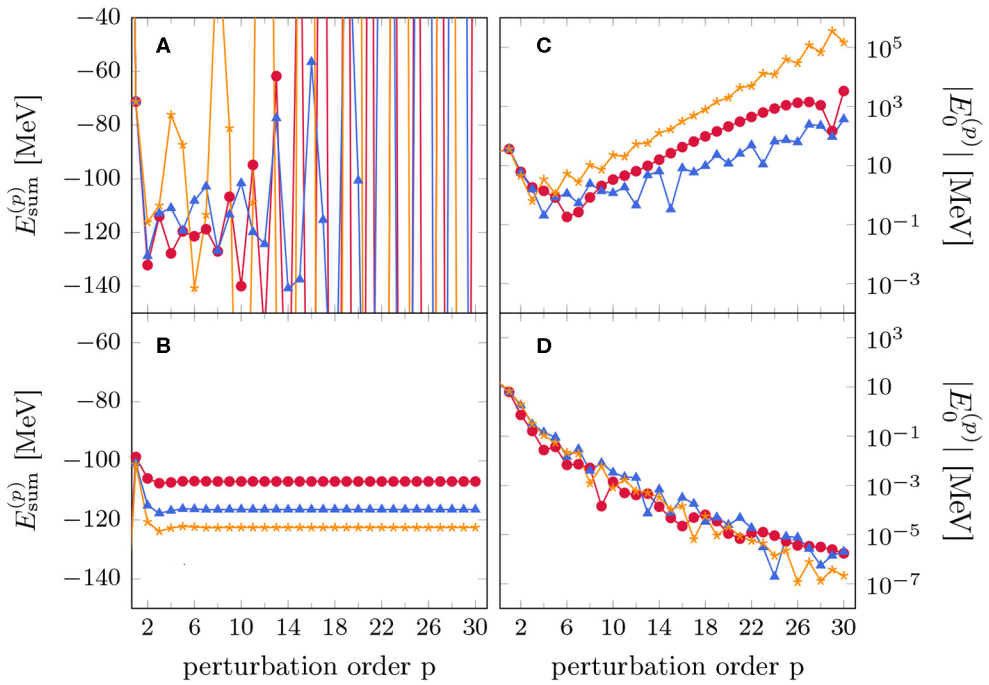

FIGURE 3 | Partial sums **(A,B)** and order-by-order corrections **(C,D)** for the ground-state energy of ^{16}O using the Hamiltonian described in section 3. Top (bottom) panels correspond to the HO (HF) partitioning. All calculations are performed using $N_{\text{max}} = 2, 4, 6$ (●, ▲, ★) and an oscillator frequency of $\hbar\omega = 24$ MeV. The SRG parameter is set to $\alpha = 0.08\,\text{fm}^4$. Reproduced from Tichai et al. [34] under the Creative Commons CC-BY license.

oscillatory behavior in the oxygen isotopes for $\alpha = 0.02\,\text{fm}^4$. These features can be better seen from the right-hand panels, where lower values of α induce a slower suppression of higher-order corrections (**Figures 4E,F**).

5.6.3. Realistic Calculations

The previous results reveal that using an optimized HF reference state combined with a sufficiently soft interaction defines a well-controlled regime where perturbation theory can be robustly applied to closed-shell nuclei. For heavier nuclei and larger model spaces the high-order perturbative series cannot be computed recursively and, rather, low-order expressions are evaluated via explicit single-particle summations[7].

In **Figure 5**, the ground-state energy per particle (top panel) and the correlation energy per particle (bottom panel) of a selection of doubly closed-shell nuclei ranging from ^{4}He to ^{132}Sn is displayed at second- and third-order in MBPT [34]. A model space built out of 13 major harmonic oscillator shells is employed. Since the target nuclei are out of reach of exact diagonalization, MBPT results are compared to state-of-the CC calculations employing the same input Hamiltonian and the same HF determinant reference state.

The top panel demonstrates that third-order calculations fully capture the bulk part of the ground-state energy and are in remarkable agreement with more sophisticated non-perturbative CC results, i.e., the deviation with CR-CC(2,3) is less than 1% in all cases. A more refined analysis can be deduced from the bottom panel where the mean-field binding energy has been subtracted. The correlation energy accounts in most mid-mass systems for about $1-2$ MeV$/A$ such that the reference HF results capture roughly $60-70\%$ of the overall binding energy. The CCSD correlation energy lies between second- and third-order results even though the CCSD wave function resums correlation effects beyond third order, thus indicating a repulsive effect on the binding from 2-particle/2-hole-excitations at 4th order and beyond. When (approximately) including triple excitations through CR-CC(2,3), slightly stronger binding than in third-order MBPT is generated.

Of course, the enormous benefit of low-order MBPT is that it excellently reproduces highly sophisticated CC results at a computational cost that is two orders of magnitude lower due to its non-iterative character.

6. MULTI-CONFIGURATIONAL PERTURBATION THEORY

Driven by the capacity of HF-MBPT to grasp dynamical correlations induced in closed-shell systems by soft chiral Hamiltonians, extensions to genuine open-shell systems were envisioned. As alluded to in section 2, the presence of degeneracies with respect to particle-hole excitations does not allow the use of a single symmetry-conserving Slater-determinant reference state. A first possibility is to use a multi-determinantal

[7]Using the notion of tensors, the summation over a common index of several tensors defines a *tensor contraction*.

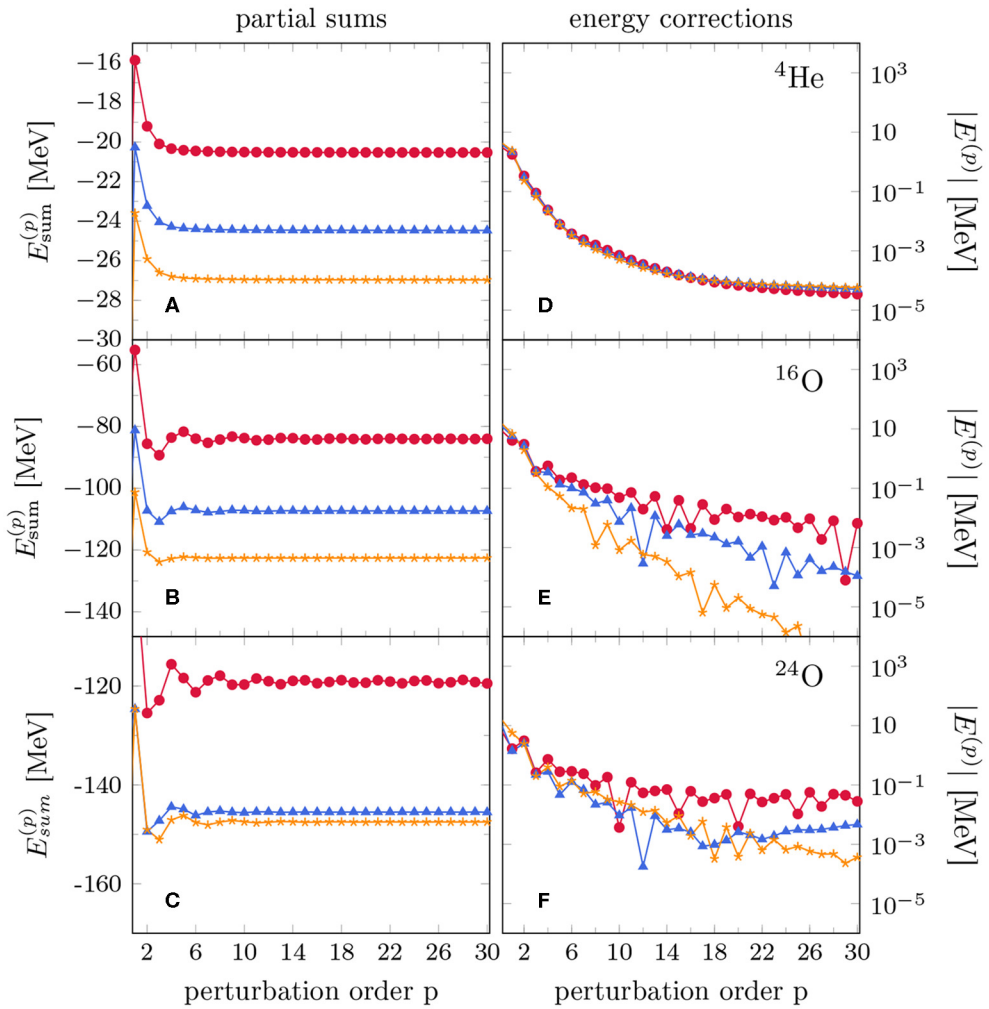

FIGURE 4 | Partial sums **(A–C)** and order-by-order corrections **(D–F)** corresponding to the ground-state energy obtained from the Hamiltonian described in section 3. Top, middle, and bottom panels correspond to ^{4}He ($N_{\max} = 6$), ^{16}O ($N_{\max} = 6$), and ^{24}O ($N_{\max} = 4$), respectively. All calculations are performed setting the oscillator frequency to $\hbar\omega = 20$ MeV. The different plot markers correspond to SRG flow parameter $\alpha = 0.02$(●), 0.0625(▲), and 0.08 fm^4(★). Reproduced from Tichai et al. [34] under the Creative Commons CC-BY license.

reference state, which was shown to be very useful in electronic structure applications [96, 97] and as a pre-processing tool in NCSM calculations [98].

6.1. Rationale

The starting point of multi-configurational perturbation theory (MCPT) is the definition of an initial reference space

$$\mathcal{M}_{\rm ref} \equiv \text{span}\{|\Phi_\nu\rangle\} \tag{46}$$

built from a set of orthonormal many-body Slater determinants $|\Phi_\nu\rangle$. The extended reference space redefines the nature of the P-space (and thus of the Q-space) introduced in Equation (12). The multi-configurational reference state $|\Psi_{\rm ref}\rangle$ is chosen to be a normalized vector obtained from a diagonalization in $\mathcal{M}_{\rm ref}$, i.e.,

$$|\Psi_{\rm ref}\rangle \equiv \sum_{\nu\in\mathcal{M}_{\rm ref}} c_\nu\,|\Phi_\nu\rangle, \tag{47}$$

where c_ν denotes the expansion coefficients, typically obtained from a NCSM calculation. The initial diagonalization provides a set of *non-degenerate* but multi-determinantal reference states carrying good symmetry quantum numbers. At the price of giving up the product-type character of the reference state, the degeneracy is lifted and a well-defined perturbative expansion can be designed [36].

Convention: The symbol $|\Psi\rangle$ is used to emphasize the multi-determinantal character of the reference state and distinguish it from a single product state. Furthermore, two different notations are employed to designate the Slater determinants spanning the complete Hilbert space: (i) Slater determinants belonging to $\mathcal{M}_{\rm ref}$ are denoted by $|\Phi_\nu\rangle$, i.e., as a capital Greek letter carrying a lower-case Greek index, whereas (ii) Slater determinants outside $\mathcal{M}_{\rm ref}$ are denoted by $|\phi_i\rangle$, i.e., as a lower-case Greek letter carrying a lower-case Roman index.

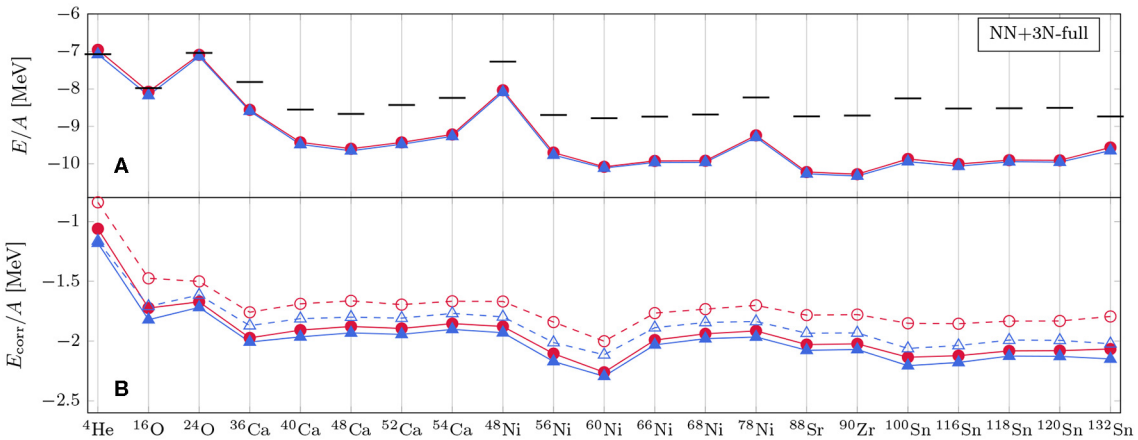

FIGURE 5 | Ground-state binding energies per particle **(A)** and correlation energy per particle **(B)** of closed-shell nuclei from second-order MBPT (○), third-order MBPT (●), CCSD (△), and CR-CC(2,3) (▲) using the Hamiltonian described in section 3. All calculations are performed using 13 oscillator shells and an oscillator frequency of $\hbar\omega = 20$ MeV. The SRG parameter is set to $\alpha = 0.08\,\text{fm}^4$. Reproduced from Tichai et al. [34] under the Creative Commons CC-BY license.

It is worth noting that MCPT naturally accesses excited states by building the perturbation theory on top of the various vectors produced through the prior diagonalization in $\mathcal{M}_{\text{ref}}$. Of course, it is not guaranteed that the energetically lowest state in the initial NCSM calculation eventually corresponds to the ground state in the fully correlated limit, i.e., perturbative corrections may induce *level crossings* among the various states.

6.2. Partitioning

Formally, the unperturbed Hamiltonian is written in the spectral representation as

$$H_0 \equiv \sum_{k\in\mathcal{M}_{\text{ref}}} E_k^{(0)} |\Psi_k\rangle\langle\Psi_k| + \sum_{i\notin\mathcal{M}_{\text{ref}}} E_i^{(0)} |\phi_i\rangle\langle\phi_i|, \tag{48}$$

where $|\Psi_k\rangle$ denote the NCSM eigenvectors within $\mathcal{M}_{\text{ref}}$, including the particular one, e.g., the lowest state, playing the role of the reference state. Consequently, one obtains the following eigenvalue relation for the unperturbed Hamiltonian

$$H_0 |\Psi_k\rangle = E_k^{(0)} |\Psi_k\rangle, \tag{49}$$

since the set of determinants $\{|\Phi_i\rangle \notin \mathcal{M}_{\text{ref}}\}$ is orthogonal to $|\Psi_k\rangle$. In principle, the construction of H_0 requires a *full diagonalization* in the reference space, i.e., the solution of all eigenvectors and eigenvalues making the construction of the unperturbed solution rapidly unfeasible if the dimension of the reference state grows significantly. As will become clear below, the computation of the lowest-order correction only require to access the reference state, which is thus the only the eigenvector that needs to be solved for explicitly in this case. In that case one may resort to Lanczos algorithms, thus targeting a limited number of extremal eigenstates.

Zeroth-order energies $E_i^{(0)}$ of the unperturbed Slater determinants making up the Q space, i.e., $\{|\Phi_i\rangle \notin \mathcal{M}_{\text{ref}}\}$, are given by the sum of occupied single-particle energies defined as diagonal matrix elements of the one-body Hamiltonian

$$h_{pq} \equiv t_{pq} + \sum_{rs} H^{[4]}_{prqs}\rho^{(0)}_{rs}, \tag{50}$$

where the one-body density matrix of the reference state[8] is introduced

$$\rho^{(0)}_{pq} = \langle\Psi_{\text{ref}}|c_p^\dagger c_q|\Psi_{\text{ref}}\rangle. \tag{51}$$

In principle, an explicit three-body term can be included as well at the price of invoking the two-body density matrix. However, for the sake of computational simplicity a normal-ordered two-body (NO2B) approximation is employed to approximately account for the inclusion of 3N interactions [82].

The zeroth-order energy of the reference state is also defined via the single-particle energies defined in Equation (50) while taking into account the multi-determinantal character of the reference state through the mean occupation of single-particle states, i.e., the diagonal elements of the one-body density matrix $\rho^{(0)}_{pp}$, so that

$$E^{(0)}_{\text{ref}} = \sum_p \epsilon_p \rho^{(0)}_{pp}. \tag{52}$$

6.3. Low Orders

With the partitioning of the Hamiltonian defined above, zeroth- and first-order MCPT contributions to the energy read as

$$E^{(0)} = \langle\Psi_{\text{ref}}|H_0|\Psi_{\text{ref}}\rangle = E^{(0)}_{\text{ref}}, \tag{53}$$

[8]If the density matrix involved in Equation (50) were the one of the fully correlated eigenstate of H, the one-body operator h would be nothing but the *Baranger Hamiltonian* [99, 100]. Whenever the reference state reduces to the HF Slater determinant, h identifies with the HF one-body Hamiltonian.

$$E^{(1)} = \langle \Psi_{\text{ref}} | H_1 | \Psi_{\text{ref}} \rangle = \langle \Psi_{\text{ref}} | H | \Psi_{\text{ref}} \rangle - E^{(0)}_{\text{ref}}, \tag{54}$$

such that their sum reproduces the full reference energy $E^{\text{NCSM}}_{\text{ref}}$ obtained via the diagonalization of the full Hamiltonian H in $\mathcal{M}_{\text{ref}}$.

The second-order energy correction reads similarly to the one at play in standard MBPT, i.e.,

$$E^{(2)} = -\sum_{i \notin \mathcal{M}_{\text{ref}}} \frac{|\langle \Psi_{\text{ref}} | H | \phi_i \rangle|^2}{E^{(0)}_i - E^{(0)}_{\text{ref}}}, \tag{55}$$

where the sum runs over states outside of the reference space and where the contribution from H_0 vanishes by orthogonality $\langle \Psi_{\text{ref}} | \Phi_i \rangle = 0$. To explicitly evaluate $E^{(2)}$ the reference state is expanded according to Equation (47)

$$E^{(2)} = -\sum_{\mu\mu' \in \mathcal{M}_{\text{ref}}} c^{\star}_{\mu} c_{\mu'} \sum_{i \notin \mathcal{M}_{\text{ref}}} \frac{\langle \Phi_{\mu} | H | \phi_i \rangle \langle \phi_i | H | \Phi_{\mu'} \rangle}{E^{(0)}_i - E^{(0)}_{\text{ref}}}. \tag{56}$$

All many-body matrix elements appearing in the algebraic expressions of the perturbative corrections involve Slater determinants only and can be readily evaluated using standard NCSM technology. As an efficient alternative, normal-ordering techniques and standard Wick's theorem are employed such that an associated diagrammatic can be designed. It is worth noting that intermediate states from within $\mathcal{M}_{\text{ref}}$ only start contributing at fourth order [36] such that they do not appear in the evaluation of $E^{(2)}$. In Equation (56), the Hamiltonian is normal ordered with respect to the rightmost determinant $|\Phi_{\mu'}\rangle$ for each term in the sum over μ' and the two matrix elements are evaluated using the associated Wick's theorem. Similar techniques have been applied in quantum chemistry [101, 102]. The computational scaling of the second-order correction for large reference spaces is given by $\dim(\mathcal{M}_{\text{ref}})^2 \cdot n_p^2 \cdot n_h$, where n_p and n_h denote the number of particle and hole states, respectively.

6.4. Results

In the following the performance of MCPT, specifically denoted as NCSM-PT in the present case, is gauged in a similar spirit as for HF-MBPT in section 5.

6.4.1. High-Order Corrections in Light Systems

The recursive treatment of HF-MBPT laid out in section 4.4 has proven invaluable to understand the convergence characteristic of the perturbative expansion. While NCSM-PT does not employ a Slater-determinant reference, the recursive formulation can be extended in a straightforward way [36]. **Figure 6** displays the convergence behavior of the perturbative series for ^{6,7}Li built on top of the four lowest states of the $N_{\text{max}} = 0$ NCSM diagonalization. The left-hand panels show that the perturbative series is convergent for both systems and all target states with a slight overbinding of the second-order partial sum for many states. In all cases the converged results agree with exact diagonalization. Furthermore, right panels reveal an (almost) exponential suppression of higher-order energy corrections indicating rapid convergence of the expansion. The rate of convergence is mostly independent of the target state or the nucleus, except for the ground and first 2^+ states in ^{6}Li that both converge slightly slower.

The high-order benchmarks strongly motivate the use of low-order partial sums as good approximations to the binding energies of heavier systems. Subsequently, systems with mass number $A \approx 30$ are investigated through realistic MCPT calculations in large model spaces.

6.4.2. Low Orders in $A \approx 30$ Nuclei

In **Figure 7**, ground-state energies of carbon, oxygen, and fluorine isotopes are shown and compared to large-scale importance truncated NCSM (IT-NCSM) diagonalization whenever available. The reference states are obtained from a diagonalization in a $N_{\text{max}} = 0$ or 2 space. In all cases a HF single-particle basis is employed in order to minimize the dependence on the oscillator frequency[9].

For all nuclei the reference energies and second-order NCSM-PT results show a sizeable dependence on the size of the reference space. Throughout all investigated isotopic chains though, results from reference states built within a $N^{\text{ref}}_{\text{max}} = 2$ space almost perfectly reproduce the exact (IT-)NCSM ones. This significant improvement in ground-state energies hints at important correlations incorporated through the reference states obtained from a $N^{\text{ref}}_{\text{max}} = 2$ diagonalization that are absent for $N^{\text{ref}}_{\text{max}} = 0$, thus providing an ideal compromise between computational efficiency and accuracy. In particular, neutron-rich fluorine isotopes are out of reach of conventional NCSM calculations and NCSM-PT provides an efficient *ab initio* approach to investigate the neutron drip line. A single NCSM-PT calculation requires typically two to three orders of magnitude less computational resources than the corresponding IT-NCSM calculation.

In practice, the reference states employed in the above calculations contain between several hundreds of thousands up to a few million determinants, thus, providing an excellent account of static correlations. Note that in most cases the reference state accounts for up to 80% of the overall binding energy such that residual dynamical correlations can indeed be grasped efficiently from low-order perturbation theory.

6.4.3. Low-Lying Spectroscopy

As already exemplified in the high-order investigation, excited states can be straightforwardly accessed through NCSM-PT by targeting different reference states from the NCSM spectrum. From absolute NCSM-PT binding energies, excitation energies are obtained by subtracting the correlated ground-state energy. In **Figure 8**, the associated NCSM-PT spectra are compared to bare NCSM calculations for a selection of open-shell carbon and oxygen isotopes. All calculations employ a HO single-particle basis to separate center-of-mass degrees of freedom in the many-body wave function. It is well-known that NCSM excitation energies of states with identical parity display a

[9]The HF problem is solved employing a so-called *equal-filling approximation* to ensure rotational invariance of the mean-field density. The underlying NCSM-PT formulation is based on *m*-scheme quantities and does not employ angular-momentum coupling techniques as most correlation expansions do. Consequently, even- and odd-mass systems can be described on equal footing.

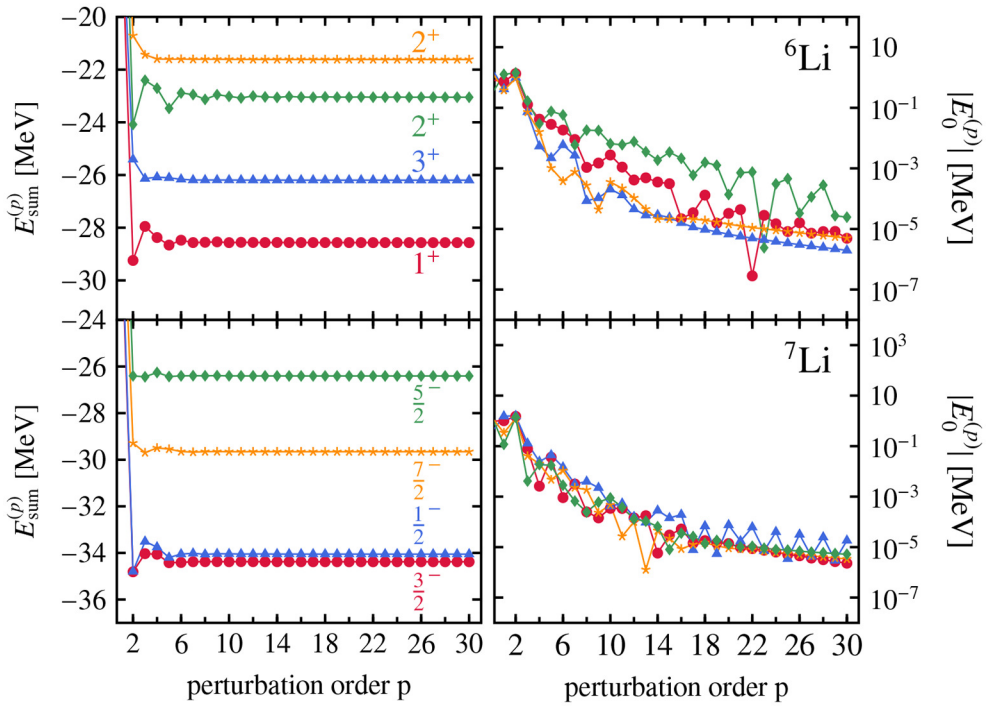

FIGURE 6 | High-order binding energies from NCSM-PT employing $N^{\rm ref}_{\rm max} = 0$ reference states using the Hamiltonian described in section 3. All calculations are performed including configurations up to $N_{\rm max} = 8$ and employ an oscillator frequency of $\hbar\omega = 20$ MeV. The SRG parameter is set to $\alpha = 0.08\,{\rm fm}^4$. Reproduced from Tichai et al. [36] under the Creative Commons CC-BY license.

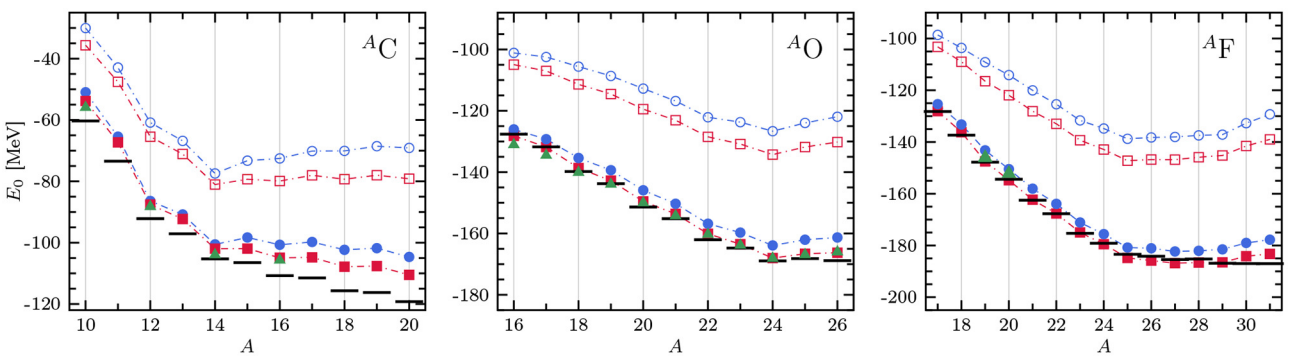

FIGURE 7 | Reference (○/□) and second-order NCSM-PT (●/■) energies with $N^{\rm ref}_{\rm max} = 0$ and 2, respectively, for the ground states of $^{11-20}$C, $^{16-26}$O, and $^{17-31}$F using the Hamiltonian described in section 3. All calculations are performed using 13 oscillator shells and an oscillator frequency of $\hbar\omega = 20$ MeV. The SRG parameter is set to $\alpha = 0.08\,{\rm fm}^4$. Importance-truncated NCSM calculations (▲) are shown for comparison. Experimental values are indicated by black bars. Reproduced from Tichai et al. [36] under the Creative Commons CC-BY license.

much faster convergence than absolute binding energies, thus yielding stable results in the right-hand columns of each panel. When a level re-ordering appears with increasing $N_{\rm max}$ in the NCSM calculation, e.g. for the two lowest states in ^{12}C or the third and fourth states in ^{19}O, NCSM-PT reproduces the correct level ordering at small values of $N^{\rm ref}_{\rm max}$. As for ground-state energies, NCSM-PT results based on a reference state with $N^{\rm ref}_{\rm max} = 2$ reproduce well the NCSM spectra, while going to $N^{\rm ref}_{\rm max} = 4$ only refines the quality of a subset of excitation energies.

The NCSM-PT framework is thus highly valuable to perform light-weighted perturbative calculations in medium-light systems up to mass numbers $A \lesssim 40$. Due to its versatility and conceptual simplicity the low-lying spectrum of genuine open-shell nuclei can be described at low computational cost.

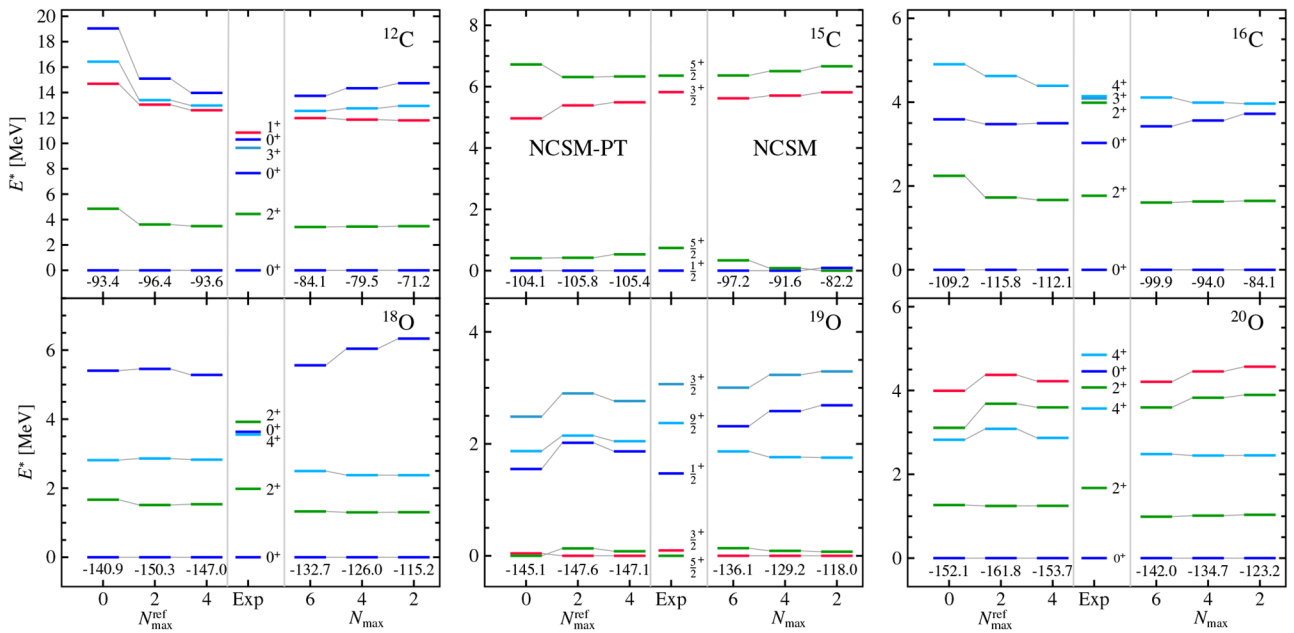

FIGURE 8 | Spectra obtained via second-order NCSM-PT for selected carbon and oxygen isotopes using the Hamiltonian described in section 3. All calculations are performed using 13 oscillator shells and an oscillator frequency of $\hbar\omega = 20$ MeV. The SRG parameter is set to $\alpha = 0.08\,\text{fm}^4$. A HO single-particle basis was used to separate center-of-mass contaminations. Large-scale IT-NCSM calculations are shown for comparison. Reproduced from Tichai et al. [36] under the Creative Commons CC-BY license.

7. BOGOLIUBOV MANY-BODY PERTURBATION THEORY

While the use of multi-configurational reference states can efficiently resolve situations of strong static correlations, it displays several limitations, i.e., (i) the physical origin of the underlying correlations in the reference state is unclear, (ii) it does not easily ensure size-extensivity, and (iii) it is numerically prohibitive in heavy nuclei. The objective is thus to present an alternative based on single-reference product states that bypasses these limitations.

7.1. Rationale

An alternative route to lift the particle-hole degeneracy of the reference state in open-shell systems is to authorize the reference state to break a symmetry of the underlying Hamiltonian. In semi-magic nuclei, the relevant symmetry is $U(1)$ global gauge symmetry associated with particle-number conservation[10]. Breaking $U(1)$ symmetry permits to efficiently deal with Cooper pair instability associated with the superfluid character of open-shell nuclei. The degeneracy of a Slater determinant with respect to particle-hole excitations is lifted via the use of a Bogoliubov reference state and transferred into a degeneracy with respect to transformations of the symmetry group. As a consequence, the ill-defined (i.e., singular) expansion of exact quantities with respect to a symmetry-conserving Slater determinant is replaced by a well-behaved one. Extending the treatment to doubly open-shell nuclei requires a similar treatment of $SU(2)$ symmetry associated with the conservation of angular momentum.

Eventually, the degeneracy with respect to $U(1)$ transformations must also be lifted by restoring the symmetry. However, BMBPT only restores the symmetry in the limit of an all-order resummation, and thus displays a symmetry contamination at any finite order. While BMBPT can still be used as a stand-alone approach as is done in the present work, it eventually provides the first step toward the implementation of the so-called particle-number projected BMBPT (PNP-BMBPT) [58] that restores good particle number at any truncation order.

7.2. Bogoliubov Algebra

The BMBPT formalism is based on the introduction of the Bogoliubov reference state

$$|\Phi\rangle \equiv \mathcal{C} \prod_k \beta_k |0\rangle, \tag{57}$$

where $\mathcal{C}$ is a complex normalization constant and $|0\rangle$ denotes the physical vacuum. The Bogoliubov product state presently defining the P-space of perturbation theory is a vacuum for the quasi-particle operators $\{\beta_k^\dagger, \beta_k\}$, i.e.,

$$\beta_k |\Phi\rangle = 0 \quad \forall k, \tag{58}$$

obtained from the creation and annihilation operators associated with a basis of the one-body Hilbert space via the unitary

[10]In fact the relevant symmetry group is the direct product $U_N(1) \times U_Z(1)$ since both proton and neutron number are conserved separately.

Bogoliubov transformation [103]

$$\beta_k \equiv \sum_p U^*_{pk} c_p + V^*_{pk} c^\dagger_p, \tag{59a}$$

$$\beta^\dagger_k \equiv \sum_p U_{pk} c^\dagger_p + V_{pk} c_p. \tag{59b}$$

Generically speaking, the Bogoliubov transformation is only constrained by unitarity such that a large manifold of Bogoliubov states is at hand. To actually set up the perturbation theory, a particular Bogoliubov reference state must be specified. Typically, the transformation matrices (U, V) are obtained by solving the Hartree-Fock-Bogoliubov (HFB) variational problem that naturally extends the simpler HF approximation to treat pairing correlations while sticking to a single reference product state. The columns of the transformation matrices (U, V) correspond to the eigenvectors of the HFB eigenvalue equation [103] whereas the associated eigenvalues $\{E_k > 0\}$ deliver the so-called quasi-particle energies[11]. Since Bogoliubov states are not eigenstates of the particle-number operator A, the expectation value of A is constrained to match a specific number of particles, e.g., the particle number A_0 of the target system. In the HFB method for example, the constraint is enforced via the use of a Lagrange multiplier λ in the minimization of the expectation value of the grand potential

$$\Omega \equiv H - \lambda A. \tag{60}$$

In actual applications, separate Lagrange multipliers λ_N and λ_Z are used to constrain proton and neutron numbers N and Z, respectively. In the subsequent formalism A stands for either one of them.

7.3. Quasi-Particle Normal Ordering

In the next step, Wick's theorem is employed to normal order the grand potential Ω with respect to the Bogoliubov reference state

$$\begin{aligned}\Omega = & \underbrace{\Omega^{00}}_{\equiv \Omega^{[0]}} + \underbrace{\Omega^{20} + \Omega^{11} + \Omega^{02}}_{\equiv \Omega^{[2]}} \\ & + \underbrace{\Omega^{40} + \Omega^{31} + \Omega^{22} + \Omega^{13} + \Omega^{04}}_{\equiv \Omega^{[4]}} + \dots,\end{aligned} \tag{61}$$

where Ω^{ij} denotes the normal-ordered component involving i (j) quasi-particle creation (annihilation) operators, e.g.,

$$\Omega^{31} \equiv \frac{1}{3!} \sum_{k_1 k_2 k_3 k_4} \Omega^{31}_{k_1 k_2 k_3 k_4} \beta^\dagger_{k_1} \beta^\dagger_{k_2} \beta^\dagger_{k_3} \beta_{k_4}. \tag{62}$$

The tensors defining each normal-ordered term display antisymmetry properties, i.e.,

$$\Omega^{ij}_{k_1 \dots k_i k_{i+1} \dots k_{i+j}} = (-1)^{\sigma(P)} \Omega^{ij}_{P(k_1 \dots k_i | k_{i+1} \dots k_{i+j})}, \tag{63}$$

where $\sigma(P)$ refers to the signature of the permutation P. The notation $P(\dots|\dots)$ denotes a separation into the i quasiparticle creation operators and the j quasiparticle annihilation operators such that permutations are only considered among members of the same group. Thus, Ω^{00} is the expectation value of Ω in $|\Phi\rangle$ whereas $\Omega^{[2]}$ and $\Omega^{[4]}$ define effective, i.e., normal-ordered, one-body and two-body operators, respectively. Working in the particle-number-conserving normal-ordered two-body approximation (PNO2B) [83], the effective three-body part $\Omega^{[6]}$ is presently discarded[12]. Details on the normal-ordering procedure as well as expressions of the matrix elements of each operator Ω^{ij} in terms of the original matrix elements of the Hamiltonian and of the (U, V) matrices can be found in Signoracci et al. [53] and Ripoche et al. [83].

7.4. Partitioning

To set up the perturbation theory, the Hamiltonian (i.e., grand potential) must be partitioned into an one-body unperturbed part Ω_0 and a residual part Ω_1, i.e.,

$$\Omega = \Omega_0 + \Omega_1. \tag{64}$$

Focusing on the case where the Bogoliubov reference state is the solution of the HFB variational problem, i.e., using a Møller-Plesset scheme, Ω appearing in Equation (61) is naturally partitioned given that

$$\Omega^{20} = \Omega^{02} = 0 \tag{65}$$

and that Ω^{11} is in diagonal form, i.e.,

$$\Omega_0 \equiv \Omega^{00} + \sum_k E_k \beta^\dagger_k \beta_k, \tag{66a}$$

$$\Omega_1 \equiv \Omega^{40} + \Omega^{31} + \Omega^{22} + \Omega^{13} + \Omega^{04}, \tag{66b}$$

with $E_k > 0$ for all k. Introducing all many-body states obtained via an even number of quasi-particle excitations of the vacuum

$$|\Phi^{k_1 k_2 \cdots}\rangle \equiv \beta^\dagger_{k_1} \beta^\dagger_{k_2} \dots |\Phi\rangle, \tag{67}$$

the unperturbed system is fully characterized by its complete set of orthonormal eigenstates in Fock space

$$\Omega_0 |\Phi\rangle = \Omega^{00} |\Phi\rangle, \tag{68a}$$

$$\Omega_0 |\Phi^{k_1 k_2 \cdots}\rangle = \left[\Omega^{00} + E_{k_1 k_2 \dots}\right] |\Phi^{k_1 k_2 \cdots}\rangle, \tag{68b}$$

where the strict positivity of unperturbed excitations

$$E_{k_1 k_2 \dots} \equiv E_{k_1} + E_{k_2} + \dots \tag{69}$$

characterizes the lifting of the particle-hole degeneracy authorized by the spontaneous breaking of $U(1)$ symmetry in open-shell nuclei at the mean-field level.

[11] In the present work, the Bogoliubov transformation is limited to treat the like-particle pairing although it could be further generalized to address neutron-proton pairing as well.

[12] The particle-number-conserving nature of the PNO2B approximation further requires to drop specific contributions to $\Omega^{[4]}$ as well; see Ripoche et al. [83] for a detailed discussion.

With these ingredients at hand, the perturbation theory can be entirely worked out algebraically or diagrammatically. This can be done on the basis of a (imaginary) time-dependent formalism or of a time-independent formalism. While the former framework leads to working with Feynman (time-dependent) diagrams, the latter makes use of Goldstone (time-ordered) diagrams. Recently, the complete Rayleigh-Schrödinger BMBPT formalism, including the automatic generation and algebraic evaluation of all possible diagrams appearing at an arbitrary order n on the basis of 2N and full 3N interactions has been published in Arthuis et al. [95].

Eventually, the BMBPT expansion of the correlation energy can be written in compact form as a *superfluid extension* of the Goldstone formula (Equation 19b)

$$\Delta\Omega = \langle\Phi|\Omega \sum_{k=1}^{\infty} \Big(\frac{1}{\Omega^{00} - \Omega_1} \Omega_1 \Big)^k |\Phi\rangle_c, \tag{70}$$

where the Hamiltonian is replaced by the grand potential.

7.5. Low Orders

As a result of Wick's theorem with respect to $|\Phi\rangle$, the first few orders contribute to Equation (70), with $\Omega^{(p)} \equiv E^{(p)} - \lambda A^{(p)}$ and $\Omega_{\text{ref}} = \Omega^{(0)} + \Omega^{(1)}$, according to[13]

$$\Omega_{\text{ref}} = +\Omega^{00}, \tag{71a}$$

$$\Omega^{(2)} = -\frac{1}{24} \sum_{k_1 k_2 k_3 k_4} \frac{\Omega^{40}_{k_1 k_2 k_3 k_4} \Omega^{04}_{k_3 k_4 k_1 k_2}}{E_{k_1 k_2 k_3 k_4}}, \tag{71b}$$

$$\Omega^{(3)} = +\frac{1}{8} \sum_{k_1 k_2 k_3 k_4 k_5 k_6} \frac{\Omega^{40}_{k_1 k_2 k_3 k_4} \Omega^{22}_{k_3 k_4 k_5 k_6} \Omega^{04}_{k_5 k_6 k_1 k_2}}{E_{k_1 k_2 k_3 k_4} E_{k_5 k_6 k_1 k_2}}. \tag{71c}$$

The lifting of the degeneracy with respect to particle-hole excitations is embodied in the fact that the energy denominators in Equation (71) are non-singular and well behaved. Indeed, quasi-particle energies are bound from below by the superfluid *pairing gap* at the Fermi energy, i.e.,

$$\text{Min}_k\{E_k\} \geq \Delta_{\text{F}} > 0. \tag{72}$$

This would not be true in standard MBPT based on a Slater determinant reference state, where energy denominators associated with particle-hole excitations within the open shell would be zero in Equation (45). Of course, BMBPT does strictly reduce to standard MBPT in a closed-shell system [95]. In particular, the single third-order diagram whose algebraic expression is given in Equation (71c) generates the three, i.e., particle-particle, hole-hole and particle-hole, third-order HF-MBPT diagrams [95]. This reduction of the number of diagrams at any order p is a consequence of working in a quasi-particle representation that does not distinguish particle and hole states. Conversely, all summations over quasi-particle labels run over the entire dimension of the one-body Hilbert space, which significantly increases the computational cost compared to standard MBPT. In any case, low-order BMBPT corrections only induce low polynomial scaling with respect to quasi-particle summation and do not suffer from the storage of large tensors as in more sophisticated all-order many-body approaches such as (B)CC or IMSRG.

Extracting the p-order contribution to the binding energy from Equation (70) requires the subtraction of the Lagrange term $\lambda A^{(p)}$. Computing $A^{(p)}$ can be done straightforwardly by replacing the leftmost operator Ω by A in Equation (70) [95]. As the reference state is constrained to have the correct particle number on average, it implies that $A_0^{(1)} = \text{A}_0$. Working with the HFB reference state, it can be shown that $A_0^{(2)} = 0$ due to the fact that $\Omega^{20} = \Omega^{02} = 0$. Consequently, the first correction to the average particle number appears at third order such that

$$A_0^{(1)} + A_0^{(3)} \neq \text{A}_0, \tag{73}$$

i.e., the computed average particle number does not match the targeted number A_0 of the physical system. This feature requires an iterative BMBPT scheme in order for the particle number to be correct at the working order, e.g., $p \geq 3$, of interest [104]. To do so, one needs to rerun the HFB calculation with a p-dependent chemical potential such that, through a series of iterations, one eventually obtains, e.g., $A_0^{(1)} + \ldots + A_0^{(p)} = \text{A}_0$. Such a costly algorithm can fortunately be very well approximated by an *a posteriori* correction scheme that entirely bypasses the iterative scheme [104]. The third-order results presented in section 7.6.1 have been computed without any adjustment of the average particle number whereas the novel ones discussed in section 10.2 have been obtained on the basis of the *a posteriori* correction scheme.

While the BMBPT expansion efficiently grasps static correlation effects associated to nuclear superfluidity, the breaking of a continuous symmetry in a finite quantum system is always fictitious. Consequently, a full-fledged many-body formalism requires the additional restoration of the broken symmetry, i.e., a mixing of gauge-rotated Bogoliubov vacua which are connected to each other via (highly non-perturbative) symmetry transformations. While the formalism has already been laid out [58], realistic calculations remain yet to be performed. Still, proof-of-principle applications to the model pairing Hamiltonian employing particle-number-projected BCC theory [60] revealed the significant impact of the symmetry projection in the weakly broken regime corresponding to open-shell nuclei in the vicinity of shell closures.

7.6. Results

7.6.1. Low-Order Calculations in Mid-Mass Nuclei

Figure 9 displays ground-state energies, two-neutron separation energies, particle-number variance and perturbative particle-number corrections along oxygen, calcium, and nickel isotopic chains at the mean-field (i.e., HFB) level, as well as at second- and third-order in the BMBPT expansion. Top panels reveal that, while static correlations have partially been accounted

[13]Non-canonical contributions are set to zero here given that we use the HFB reference state. When using an arbitrary Bogoliubov reference state, additional non-canonical contributions arise [95].

for by employing a symmetry-broken reference state, the bulk of dynamical correlations are efficiently grasped via low-order BMBPT corrections. For (sub-)closed-shell nuclei the third-order correction is consistently suppressed indicating rapid convergence. In open-shell systems third-order partial sums are strongly contaminated due to a significant excess of neutrons brought by the third-order contribution to the average neutron number. As discussed earlier, calculations at third-order and beyond must eventually be done while constraining the average particle number to match the physical value [104]. This is reported on in section 10.2.

Figure 9B exhibits a qualitative reproduction of two-neutron separation energies already at the mean-field level. Results are quantitatively improved once second-order effects are incorporated. **Figure 9C** shows the neutron-number dispersion $\sigma \equiv \sqrt{\langle A^2\rangle - \langle A\rangle^2}$ that grows with mass number. While the second-order contribution does not decrease yet the neutron-number dispersion, one expects higher orders to do so [104]. In closed-shell systems, the particle-number dispersion is zero as a hallmark of the particle-number-conserving character of the wave function throughout the expansion.

A detailed study of the convergence characteristics of the BMBPT expansion via the calculation of high-order corrections similar to the ones presented in section 5 (section 6.4.1) for HF-MBPT (NCSM-PT) calculations of closed-shell (open-shell) nuclei has just be completed [104] and is thus not reported on here.

7.6.2. Comparison to Non-perturbative Calculations

Figure 10 compares second-order BMBPT ground-state and two-neutron separation energies with results obtained from state-of-the-art non-perturbative many-body frameworks along oxygen, calcium, and nickel isotopic chains. In particular, IT-NCSM provides essentially exact reference results along the oxygen chain. In heavier closed-shell nuclei, advanced CR-CC(2,3) calculations also provide reference results.

In all cases, second-order BMBPT is in excellent agreement with other methods, displaying deviations of <2%. In particular, IT-NCSM results are very well reproduced in oxygen isotopes. While NCSM-PT (see section 6) and MR-IMSRG systematically generate stronger binding, GSCGF at the ADC(2) level is very close for all systems investigated. In the case of closed-shell nuclei the stronger binding obtained in the CR-CC(2,3) calculation highlights the importance of an (approximate) incorporation of 3-particle/3-hole excitations.

As seen from two-neutron separation energies, all *ab initio* methods consistently predict the same shell structure and location of the neutron trip line. This feature highlights both the great success of recently developed many-body methods and the excellent performance of perturbative techniques such as NCSM-PT and BMBPT in particular. On the other hand, the strong deviation of absolute binding energies[14] from experimental data, most pronounced in neutron-rich calcium and nickel isotopes, is common to all employed frameworks and clearly points to defects of the employed Hamiltonian. A detailed discussion of this crucial issue is postponed to section 10, where a new family of chiral Hamiltonians is tested with the goal to cure the poor agreement presently obtained for nuclear ground-state observables of mid-mass nuclei.

[14]The strong deviation also concerns charge radii that are not presently discussed.

8. IMPORTANCE TRUNCATION

In previous sections, MBPT was considered as a full-fledged standalone framework to access the solution of the quantum many-body problem. However, MBPT techniques can also be used to support non-perturbative approaches by pre-processing the many-body configuration space. Subsequently, the concept of *importance truncation* (IT) is presented as a procedure to a priori remove a set of tensor entries to be solved for on the basis of an importance measure [98, 105–107]. Historically, this idea was first applied in electronic structure theory to perform a pre-selection of multi-reference CI amplitudes [108, 109].

8.1. Original Context: Configuration Interaction Methods

The IT concept is ideally suited for basis expansion methods, such as general configuration interaction (CI) approaches or, more specifically, the NCSM. Given the expansion of an eigenstate $|\Psi_n\rangle$ of H in some many-body basis $|\phi_i\rangle$, the importance of each basis state can be quantified through the associated expansion coefficient $C_i^{(n)} \equiv \langle\phi_i|\Psi_n\rangle$. This importance measure can be estimated within first-order MCPT, discussed in section 6, starting from a multi-configurational reference state $|\Psi_{\text{ref}}\rangle$

$$\kappa_i^{(1)} = \frac{\langle\phi_i|H|\Psi_{\text{ref}}\rangle}{E_i^{(0)} - E_{\text{ref}}^{(0)}}. \tag{74}$$

The reference state provides an initial approximation of $|\Psi_n\rangle$ within the reference space $\mathcal{M}_{\text{ref}}$ and κ_i is used to assess *a priori* the importance of each basis state $|\phi_i\rangle \notin \mathcal{M}_{\text{ref}}$. Only states with importance measures above an importance threshold $\kappa_{\min}$ are included into the model space for the subsequent CI calculation.

Since the eigenvalue problem is solved exactly in the importance-truncated model space, IT provides a variational approximation to the full solution. Moreover, the effect of discarded configurations can be estimated via the second-order MCPT energy correction (56). This together with extrapolations to vanishing importance thresholds $\kappa_{\min} \to 0$ can be used to reconstruct the energies in the full model space. As testified by the results already presented in **Figures 7**, **8**, **10**, the IT concept has allowed one to push NCSM calculations beyond p-shell nuclei, up to neutron-rich oxygen isotopes. More details on importance-truncated CI approaches are discussed in Roth [98] and Stumpf et al. [106].

8.2. New Context: Coupled-Cluster Method

In the context of non-perturbative expansion methods, the general idea is to discard irrelevant entries of the largest mode-n tensor that needs to be solved for and that drives the numerical scaling as well as the storage cost of the method. This is done by *a priori* estimating the importance of each of its entries on the basis of a less costly many-body method, e.g., MBPT. While the

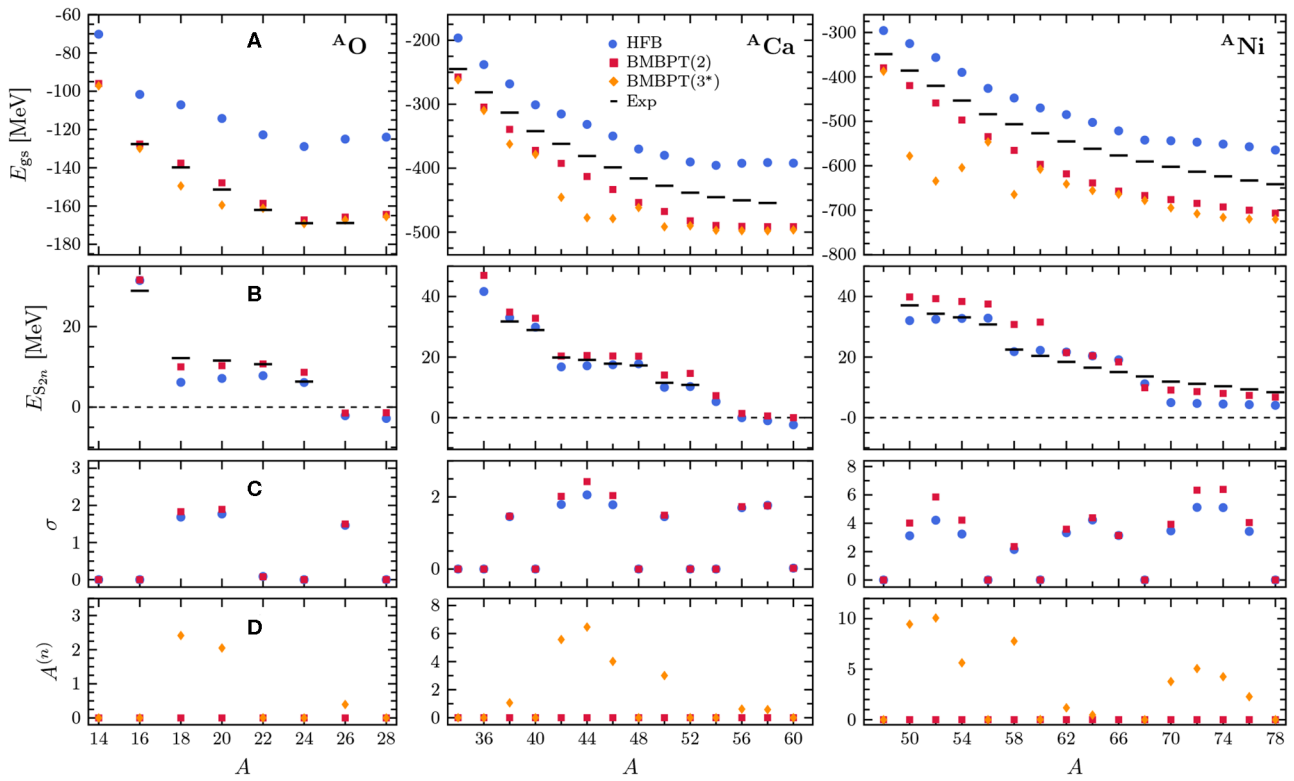

FIGURE 9 | BMBPT systematics along O, Ca, and Ni isotopic chains: **(A)** absolute binding energies, **(B)** two-neutron separation energies, **(C)** neutron-number dispersion, and **(D)** perturbative correction to the average neutron number. The employed Hamiltonian is defined in section 3. Plot markers correspond to HFB (●), second-order BMBPT (■), and third-order BMBPT without particle-number adjustment (◆). All calculations are performed using 13 oscillator shells and an oscillator frequency of $\hbar\omega = 20$ MeV. The SRG parameter is set to $\alpha = 0.08\,\mathrm{fm}^4$. Reproduced from Tichai et al. [37] under the Creative Commons CC-BY license.

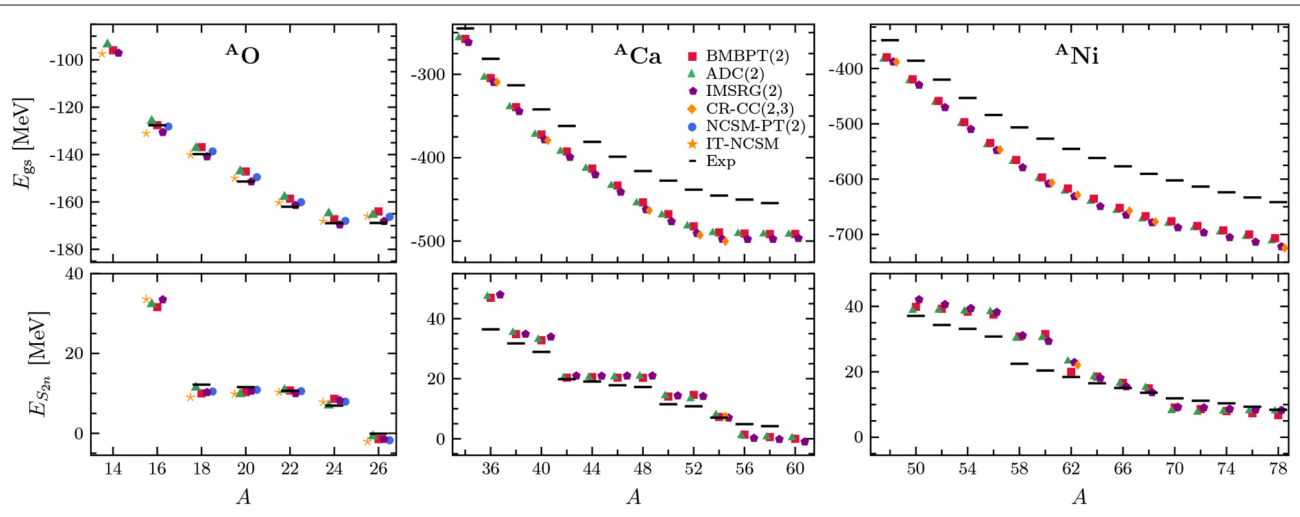

FIGURE 10 | Absolute ground-state binding energies **(top)** and two-neutron separation energies **(bottom)** along O, Ca, and Ni isotopic chains using the Hamiltonian defined in section 3. Plot markers correspond to second-order BMBPT (■), second-order NCSM-PT (●), large-scale IT-NCSM (★), GSCGF-ADC(2) (▲), MR-IMSRG(2) (⬟), and CR-CC(2,3) (◆). All calculations are performed using 13 oscillator shells and an oscillator frequency of $\hbar\omega = 20$ MeV. The SRG parameter is set to $\alpha = 0.08\,\mathrm{fm}^4$. Reproduced from Tichai et al. [37] under the Creative Commons CC-BY license.

underlying formalism is only sketched in this section, the reader is referred to Tichai et al. [107] for a detailed discussion.

8.2.1. Wave-Function Ansatz

To illustrate the concept, BMBPT is employed as a method to pre-process the cluster amplitudes constituting the unknown tensors to be solved for within the BCC method. This non-perturbative approach is based on the wave-function ansatz [53]

$$|\Psi\rangle \equiv e^{\mathcal{T}}|\Phi\rangle, \tag{75}$$

where the connected quasiparticle cluster operator $\mathcal{T} \equiv \mathcal{T}_1+\mathcal{T}_2+\mathcal{T}_3+\ldots$ is defined through

$$\mathcal{T}_n \equiv \frac{1}{n!}\sum_{k_1\cdots k_{2n}} t^{2n0}_{k_1\cdots k_{2n}}\beta^\dagger_{k_1}\cdots\beta^\dagger_{k_{2n}}, \tag{76}$$

etc. The BCC amplitudes $t^{2n0}_{k_1\cdots k_{2n}}$ constitute the unknown mode-n tensors of present interest.

Instead of solving for all unknown cluster amplitudes, IT selects a subset of tensor entries that are determined non-perturbatively by solving BCC amplitude equations while residual corrections from the discarded tensor entries are treated in low-order BMBPT. Consequently, the ground-state energy $\mathcal{E}_0$ consists of a contribution from BCC in the IT subspace $\mathcal{E}_0^{(\mathrm{IT})}$ and a residual BMBPT correction $\delta_0^{(\mathrm{res})}$ from the complementary subspace

$$\mathcal{E}_0 = \mathcal{E}_0^{(\mathrm{IT})} + \delta_0^{(\mathrm{res})}. \tag{77}$$

Of course, the selection of the IT subspace must be performed *without the knowledge* of the full solution, which is where low-order BMBPT estimates enter into play.

8.2.2. Importance-Truncated Tensor

Considering the n-tuple BCC amplitude tensor $\mathcal{T}_n \equiv \{t^{2n0}_{k_1\ldots k_{2n}}\}$, the corresponding *importance-truncated* tensor based on the IT measure $\kappa^{(p)}(t^{2n0}_{k_1\ldots k_{2n}})$ from BMBPT at order p is obtained as

$$\mathcal{T}_n^{(p)}(\kappa_{\min}) \equiv \{t^{2n0}_{k_1\ldots k_{2n}} \text{ such that } \kappa^{(p)}(t^{2n0}_{k_1\ldots k_{2n}}) \geq \kappa_{\min}\}, \tag{78}$$

where $\kappa_{\min}$ defines the IT threshold. The original tensor is recovered in the limit of $\kappa_{\min}\to 0$, i.e.,

$$\lim_{\kappa_{\min}\to 0}\mathcal{T}_n^{(p)}(\kappa_{\min}) = \mathcal{T}_n. \tag{79}$$

With an importance-truncated tensor comes the associated *data compression ratio*

$$R_c \equiv \frac{\#\text{ elements of }\mathcal{T}_n}{\#\text{ elements of }\mathcal{T}_n^{(p)}(\kappa_{\min})}, \tag{80}$$

which relates the initial amount of data to the compressed one resulting from the IT process. Whenever $R_c > 1$, the compressed tensor requires less storage than the original one.

8.2.3. Results

Applying IT to $\mathcal{T}_3$, the goal is eventually (not done here) to solve BCCSDT equations for the retained entries and correct for the omitted ones in perturbation. The feasibility of the approach directly depends on the reduction offered by the IT for a desired accuracy given that a full BCCSDT calculation is currently undoable in realistic model spaces, even when employing an angular-momentum-coupled scheme.

Figure 11 displays the impact of the data compression obtained by applying IT for ^{18}O as a function of the HO single-particle basis size. To provide a reference, the compression of $\mathcal{T}_2$ is illustrated first in the left panel before coming to the real challenge constituted by the treatment of $\mathcal{T}_3$. Three different storage schemes are displayed corresponding to a full storage of all tensor entries (diamonds), the tensor entries allowed by fundamental symmetries of the interaction (squares) and the IT-compressed entries from perturbative estimate (circle) for different values of $\kappa_{\min}$. The percentage associated with the IT-data indicates the corresponding error on the second-order contribution to the ground-state energy

$$\Delta\Omega_0^{(2)} = \frac{1}{4!}\sum_{k_1k_2k_3k_4}|t^{40(1)}_{k_1k_2k_3k_4}|^2 E_{k_1k_2k_3k_4}. \tag{81}$$

Results demonstrate that even for $\mathcal{T}_2$, i.e., a mode-4 tensor, the storage of all index combinations requires tremendous amounts of memory ($>$ 200 GB per working copy) that is at the edge of supercomputing facilities[15]. Employing a symmetry-adapted storage scheme, several orders of magnitude can be saved. More importantly, discarding irrelevant tensor entries through IT additionally compresses the data by three orders of magnitude at the price of inducing a systematic error of $<$1%, i.e., a few hundreds of keV, on the second-order correlation energy. Correspondingly, the storage of the $\mathcal{T}_2$ amplitudes is lowered to less than 1 MB per working copy. One can assign an "effective one-body dimension" to this number of tensor entries yielding $e^{(\mathrm{eff})}_{\max} \leq 5$, i.e., converged BCCSD results could be obtained using an effective model space including less than six major shells.

While the storage of $\mathcal{T}_2$ amplitudes is actually within reach of state-of-the-art capacities, the extension to $\mathcal{T}_3$ amplitudes poses a severe computational problem. Performing the same analysis as above, even the symmetry-adapted tensor requires more than 100 TB of memory. Performing the IT-compression of $\mathcal{T}_3$, the corresponding fourth-order contribution to the ground-state energy

$$\Delta\Omega_0^{[4_T]} = \sum_{\substack{k_1k_2k_3\\k_4k_5k_6}}|t^{60(2)}_{k_1k_2k_3k_4k_5k_6}|^2 E_{k_1k_2k_3k_4k_5k_6}, \tag{82}$$

can be evaluated with 1% accuracy while discarding 99.99% of all $\mathcal{T}_3$ tensor entries. Because triples correction to the ground-state energy first appear at fourth order, a 1% relative error on $\Delta\Omega_0^{[4_T]}$ relates to an absolute error of a few keV, which is negligible in mid-mass *ab initio* studies.

[15]Solving non-linear problems requires the storage of various copies of the coupled-cluster amplitudes.

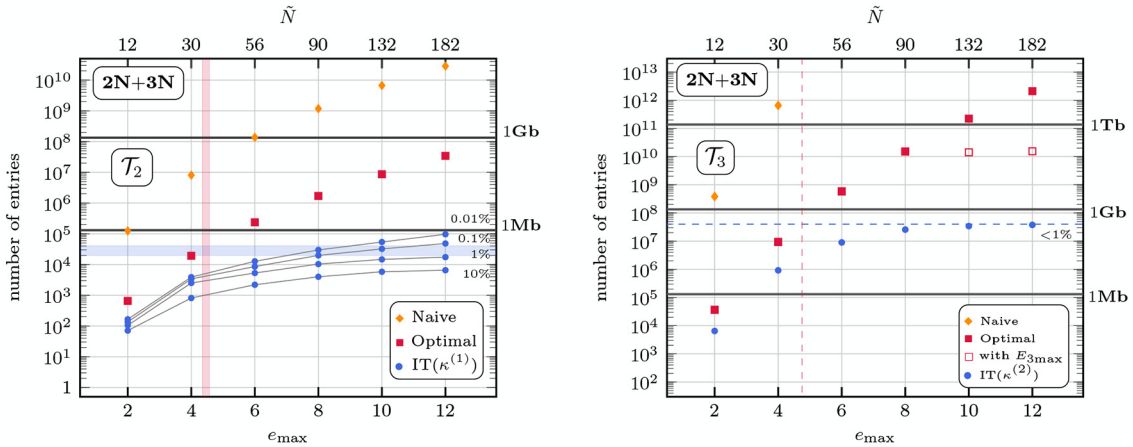

FIGURE 11 | Number of tensor entries of $\mathcal{T}_2$ amplitudes **(left)** and $\mathcal{T}_3$ amplitudes **(right)** as a function of model space using the Hamiltonian described in section 3. The oscillator frequency is given by $\hbar\omega = 20$ MeV. Different plot markers indicate different storage scheme including all entries (◆), symmetry-allowed entries (■), and IT-compressed entries (●). For $e_{\max} \geq 10$ an additional $E_{3\max}$-truncation (□) for the $\mathcal{T}_3$ amplitudes is introduced. All calculations employ a canonical HFB reference state. Reproduced from Tichai et al. [107] with permission from European Physical Journal (EPJ).

Eventually, the use of IT shifts the boundary of what is computationally unfeasible such that, in the following years, the implementation of IT-BCCSDT defines an ambitious and yet reachable goal.

9. BASIS OPTIMIZATION

The present section discusses how MBPT can be used as an auxiliary tool to construct an alternative single-particle basis accelerating the convergence of non-perturbative many-body methods as compared to commonly employed bases.

9.1. Rationale

In nuclear structure calculations, tensors defining H are typically expressed in the eigenbasis of the spherical HO Hamiltonian. Next, a self-consistent mean-field, e.g., HF, calculation is typically performed to generate the reference state such that the beyond-mean-field step and the associated tensors are transformed into the corresponding mean-field, e.g., HF, one-body basis.

While the use of HO orbitals authorizes the rigorous center-of-mass factorization in NCSM calculations, they are plagued at long distances with a pathological Gaussian falloff and a strong dependence of the many-body results on the width of the confining HO potential. Contrarily, HF orbitals display a proper exponential falloff but may induce a sizeable center-of-mass contamination and a slower convergence in large-scale NCSM diagonalizations compared to HO orbitals.

9.2. Natural Orbitals

Naturally, one wonders about the existence of a single-particle basis that admit only little sensitivity to the oscillator frequency while maintaining rapid model space convergence. Because the exact one-body density matrix

$$\rho_{pq} = \frac{\langle \Psi | c_p^\dagger c_q | \Psi \rangle}{\langle \Psi | \Psi \rangle}, \tag{83}$$

contains information about the fully correlated wave function, its eigenbasis, defining so-called *natural orbitals*, is expected to deliver an optimal choice.

This expectation was confirmed by employing the one-body density matrix obtained from a large-scale NCSM calculation [110]. For mid-mass nuclei, this strategy has the downside to require a full CI solution to obtain the optimized single-particle basis. However, as already observed several decades ago in quantum chemistry calculations [111, 112], *approximate* natural orbitals perform surprisingly well in applications. Instead of using the exact CI wave function, a correlated density matrix is constructed within a polynomially scaling expansion method, MBPT providing a particularly simple example to do so [113]. Similar approaches can be followed by using the Λ-extension of CC theory or by diagonalizing the dressed one-body propagator in SCGF theory. Note, however, that the construction of an auxiliary basis already involves a computationally non-trivial solution within a non-perturbative many-body approach.

9.3. Density Matrix in Closed-Shell MBPT

Starting from Equation (25b) and following Strayer et al. [114], the one-body density matrix up to second order in the residual interaction can be written as [113]

$$\rho = \rho^{(00)} + \rho^{(02)} + \rho^{(20)} + \rho^{(11)} + \mathcal{O}(\lambda^3), \tag{84}$$

where

$$\rho_{pq}^{(00)} \equiv \frac{\langle \Phi | c_p^\dagger c_q | \Phi \rangle}{\langle \Phi | \Phi \rangle} \tag{85}$$

denotes the zeroth-order HF density matrix whereas

$$\rho^{(02)}_{pq} \equiv \langle \Phi^{(0)} | \, c^\dagger_p c_q \, | \Phi^{(2)} \rangle = \rho^{(20)*}_{qp}, \tag{86a}$$

$$\rho^{(11)}_{pq} \equiv \langle \Phi^{(1)} | \, c^\dagger_p c_q \, | \Phi^{(1)} \rangle, \tag{86b}$$

denote its MBPT corrections whose matrix elements are expressed in the HF basis. Explicit expressions for the individual corrections to the mean-field density in terms of two-body matrix elements can be found in Strayer et al. [114] and Tichai et al. [113].

9.4. Results

The impact of using natural orbitals is now gauged by performing a systematic variation of the underlying single-particle basis in NCSM calculations. **Figure 12** displays ^{16}O ground-state energy as a function of the frequency characterizing the underling HO basis for various values of $N_{\max}$. Results obtained from the NCSM diagonalization performed in the HO and HF bases as well as in the natural-orbital basis extracted from second-order HF-MBPT are displayed.

The left panel shows the typical strong dependence of NCSM results on the underlying frequency when using HO one-body basis states, thus yielding a pronounced parabolic shape around the variational minimum for all values of $N_{\max}$. While the use of HF orbitals (middle panel) lowers the sensitivity to $\hbar\omega$ the model space convergence is not improved and the ground-state energy has a linear falloff at higher frequencies. Finally, the NCSM ground-state energy obtained using the natural-orbital basis (right panel) is almost independent of the oscillator frequency and displays a faster model-space convergence as a function of $N_{\max}$. Similar conclusions hold for other observables, e.g., charge radii, low-lying excitation energies and electro-magnetic transition strengths, as discussed in Tichai et al. [113].

Eventually, the use of one-body density matrices from low-order MBPT to construct of an optimal computational basis is a simple yet powerful tool to account for high-lying particle-hole excitations that are otherwise hard to grasp in configuration-driven methods like NCSM.

10. TESTING NOVEL χEFT NUCLEAR HAMILTONIANS

The computational efficiency of perturbative approaches makes them ideally suited for survey calculations over a large range of nuclei. A specific scenario for such survey calculations is the development of novel chiral EFT interactions, where large numbers of many-body calculations are necessary to constrain or validate the choice of low-energy constants as well as to characterize the effect of different regulator formulations. Recently, a new family of consistent chiral 2N plus 3N interactions up to N3LO based on non-local regulators was developed [115]. This new set of interactions is able to simultaneously reproduce ground-state energies and charge radii up into the medium-mass regime. Moreover, the full sequence of chiral orders from LO to N3LO is available for different cutoff values, which facilitates a rigorous uncertainty quantification. In the applications discussed below, the new interactions are consistently SRG-evolved in the 2N and 3N sectors down to $\alpha = 0.04$ fm^4 and tested through non-expensive perturbative methods over a larger set of nuclei than those addressed in Hüther et al. [115].

10.1. NCSM-PT

First, NCSM-PT is employed to calculate ground-state energies along the oxygen chain using interactions from Hüther et al. [115]. In **Figure 13**, results obtained from N2LO and N3LO interactions are compared to experiment including a quantification of systematic theoretical uncertainties resulting from both the many-body and interaction truncations. The benchmarks discussed in section 6 showed that calculations with the $N^{\text{ref}}_{\max} = 2$ typically provide a good agreement with non-perturbative methods and that ground-state energies for larger reference spaces typically fall between $N^{\text{ref}}_{\max} = 0$ and 2 results. Therefore, the difference between these two calculations offers a convenient way to estimate many-body uncertainties in NCSM-PT calculations. Uncertainties resulting from truncating the chiral expansion of nuclear interactions are estimated from the order-by-order variation of the energies using the prescription discussed in Epelbaum et al. [116], Binder et al.[117, 118]. The interaction-induced uncertainty of an observable X_{N3LO} at order N3LO, e.g., is given by $\max(Q\,|X_{\text{N3LO}} - X_{\text{N2LO}}|, Q^2\,|X_{\text{N2LO}} - X_{\text{NLO}}|, Q^3\,|X_{\text{NLO}} - X_{\text{LO}}|, Q^5\,|X_{\text{LO}}|)$ with the expansion parameter Q estimated as the ratio of a typical momentum scale characterizing mid-mass systems over the breakdown scale, which results in $Q \approx 1/3$ [118]. The uncertainty band shown in **Figure 13** combines both uncertainties, where many-body uncertainties are typically larger than interaction uncertainties.

The NCSM-PT ground-state energies can be compared with results from the in-medium no-core shell model (IM-NCSM) displayed on the right-hand side of **Figure 13**. The non-perturbative IM-NCSM method combines a multi-reference in-medium SRG transformation of the Hamiltonian that decouples a small NCSM model space, with a subsequent NCSM calculation using the transformed Hamiltonian [52]. The associated uncertainty bands include once again both many-body and interaction uncertainties. The comparison reveals an excellent agreement between NCSM-PT and IM-NCSM, which themselves agree with experiment within estimated uncertainties.

10.2. BMBPT

In addition to low-order NCSM-PT benchmarks in oxygen isotopes, the novel set of interactions is tested on a large set of mid-mass semi-magic nuclei up to third-order in BMBPT[16].

In **Figure 14**, ground-state energies of oxygen and calcium isotopes are displayed for two different values of $E_{3\max} = 14, 16$. The first striking result is that the overbinding obtained in Ca isotopes with the 'standard' Hamiltonian (see **Figure 10**) is resolved, i.e., the systematic trend throughout

[16] As compared to **Figure 9**, third-order are presently corrected for the particle-number contamination via the so-called *a posteriori* correction studied and validated in Demol et al. [104].

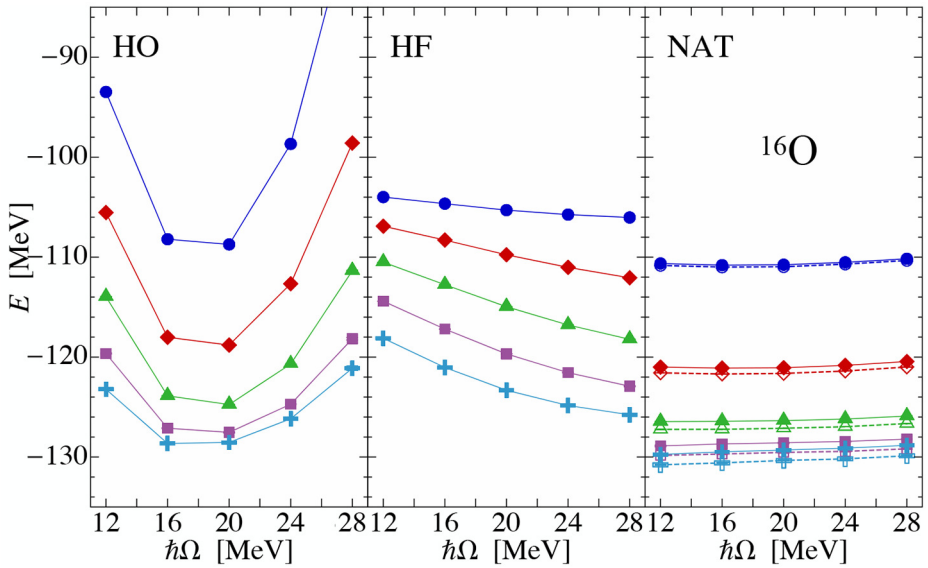

FIGURE 12 | NCSM ground-state energy of ^{16}O as a function of the frequency $\hbar\omega$ (denoted as $\hbar\Omega$ on the figure) of the underling HO basis for $N_{\max} = 2, 4, 6, 8, 10$ spaces. The NCSM diagonalization itself is performed either in the initial HO basis **(left)**, in the HF basis **(center)**, or in the natural-orbital basis from second-order HF-MBPT **(right)**. The Hamiltonian described in section 3 is employed. Reproduced from Tichai et al. [113] with permission from the American Physical Society.

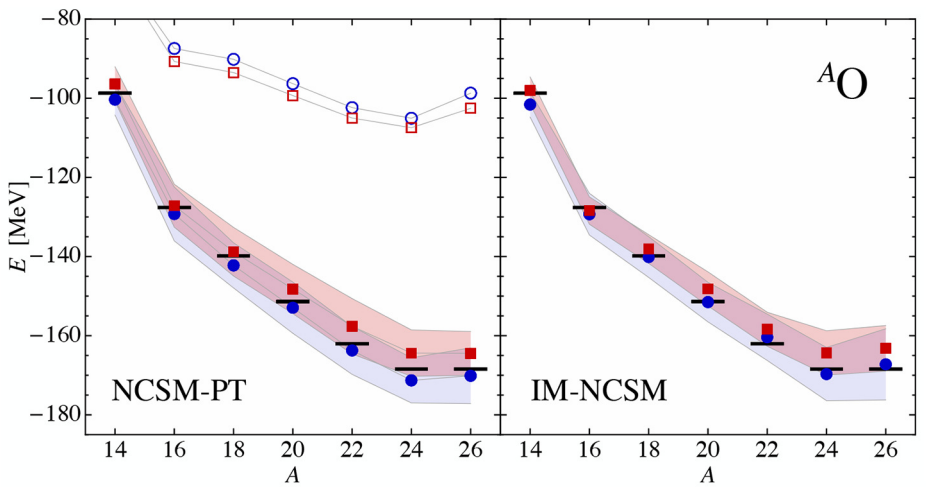

FIGURE 13 | Even oxygen isotopes ground-state energies from reference (empty symbols) and second-order (full symbols) NCSM-PT with $N_{\max}^{\text{ref}} = 2$ **(left)** and from IM-NCSM **(right)**. The consistent non-local 2N plus 3N chiral interactions at N^{2}LO (●) and N^{3}LO (■) presented in Hüther et al. [115] are employed with a cutoff $\Lambda = 500$ MeV. The uncertainty bands represent both many-body and interaction uncertainties (see text). Both many-body calculations make use a natural-orbital basis obtained in 13 oscillator shells with $\hbar\omega = 20$ MeV.

O and Ca isotopes is now consistent with experimental data. In particular, low-order BMBPT results provide a much better reproduction of experimental ground-state energies of very neutron-rich Ca isotopes than with the "standard" Hamiltonian for which the degrading increases systematically with neutron number.

Going in more details, one observes that the reference HFB energy, i.e., the lowest order in the BMBPT expansion, accounts for much less binding (i.e., less than half of the total binding energy) than with the "standard" Hamiltonian, thus indicating a "harder" interaction[17]. Moreover, the third-order correction is typically larger in the present case. While the first three BMBPT orders are systematically and strongly suppressed, this indicates

[17]This feature reflects both the different characters of the chiral Hamiltonians themselves and the fact that the "standard" Hamiltonian was SRG-evolved down to $\alpha = 0.08$ fm^4 instead of $\alpha = 0.04$ fm^4 for the new ones.

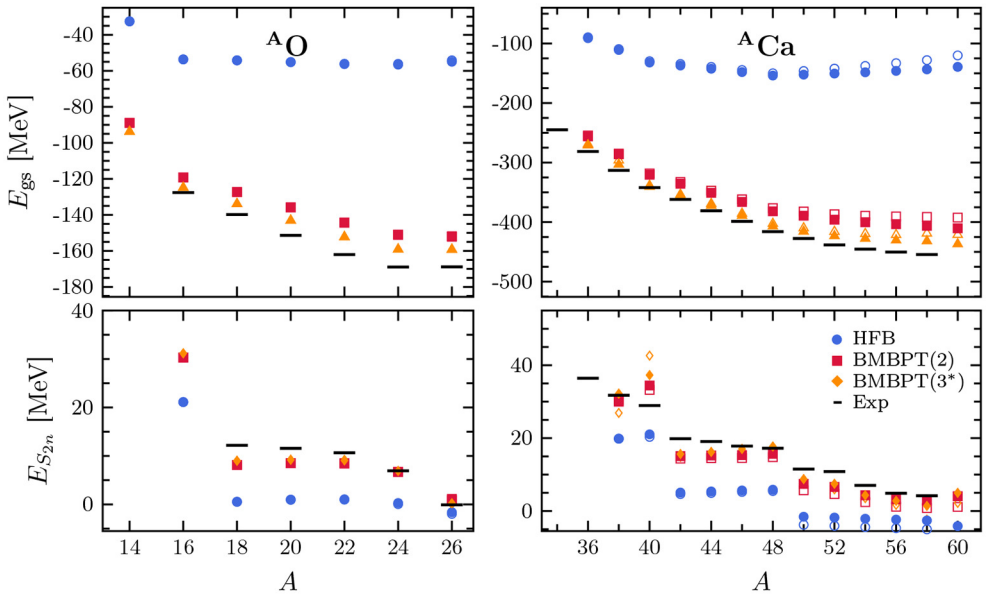

FIGURE 14 | BMBPT systematics along O **(left)** and Ca **(right)** isotopic chains using the non-local chiral two- plus three-nucleon interactions at N^{3}LO presented in Hüther et al. [115]. Top panel: absolute binding energies. Bottom panel: two-neutron separation energies. Plot markers correspond to HFB (●), second-order BMBPT (■), and third-order BMBPT (◆). All calculations are performed using 15 oscillator shells and an oscillator frequency of $\hbar\omega = 20$ MeV. The single-particle orbital angular-momentum quantum number was limited to $l \leq 10$. Open and closed symbols correspond to different truncations $E_{3\max} = 14, 16$, respectively.

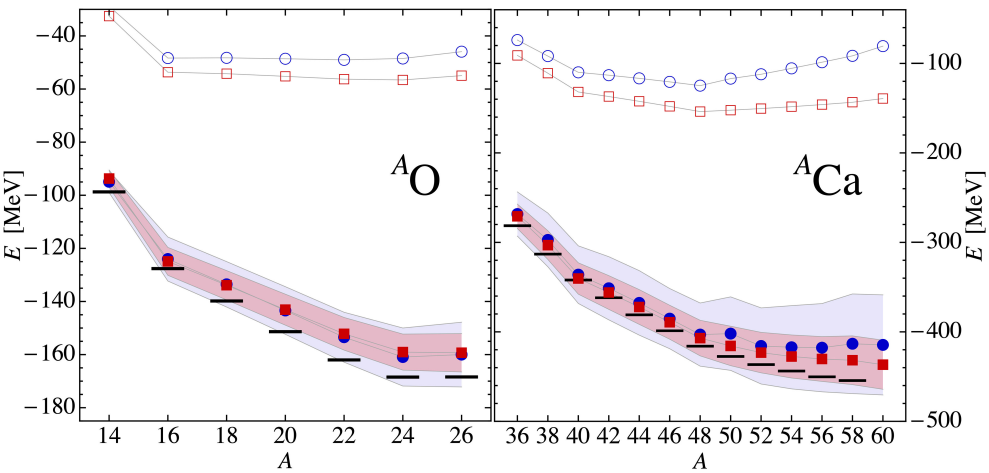

FIGURE 15 | BMBPT ground-state energies for oxygen and calcium isotopes at third order of the perturbative expansion using consistent non-local chiral two- plus three-nucleon interactions at N^{2}LO (blue) and N^{3}LO (red). Open symbols show the corresponding HFB ground-state energies. The uncertainty bands represent both, many-body and interaction uncertainties (see text). All calculations are performed using 15 oscillator shells and an oscillator frequency of $\hbar\omega = 20$ MeV. The single-particle orbital angular-momentum quantum number was limited to $l \leq 10$.

that the new interactions are indeed less perturbative. One can thus expect higher orders to contribute non-negligibly.

Focusing now on two-neutron separation energies, the end results are very satisfactory and of similar or even greater quality than with the "standard" Hamiltonian. Interestingly, HFB results are further away in the present case, indicating that not only absolute values but also the trend with neutron number is different. Still, second and third order contributions consistently compensate for this apparent, but in fact fictitious, degrading at the HFB level. One eventually observes that results are still less accurate near major shell closures, which is consistent with the expectation that restoring particle-number symmetry through PBMBPT [58] will have the largest impact near shell closures.

While the results in oxygen isotopes are virtually identical for both $E_{3\max}$ values, the truncation in $E_{3\max}$ plays an increasingly important role in neutron-rich calcium isotopes, i.e., ground-state energies beyond $A = 50$ obtained for $E_{3\max} = 14$ and 16 start deviating more strongly, pointing to the importance

of truncated three-body matrix elements as already shown in Hüther et al. [115]. This constitutes a technical challenge for the future when *ab initio* calculations move to even heavier and more neutron-rich nuclei.

Let us now further discuss these novel results by adding both many-body and interaction uncertainties to BMBPT(3) calculations. Interaction uncertainties are estimated as discussed previously. To estimate the many-body uncertainty arising from the finite truncation of the BMBPT expansion, a nucleus-independent error of 3% is assumed. A recent study of high-order BMBPT calculations revealed that the third-order partial sum typically induces a many-body error of about 2% [104]. Because the employed Hamiltonian was softer and further SRG-evolved to lower resolution scale, a more conservative 3%-error in the current setting seems plausible. The overall uncertainty is then given by summing this many-body error and the interaction uncertainty. Additional uncertainties due to the finite single-particle basis are presently not incorporated. Clearly, the construction of reasonable models of many-body uncertainties is highly nontrivial and employing simplistic parametric models, e.g., geometric sums for perturbation series, can lead to wrong estimates if the perturbation series does not obey the underlying assumptions.

In **Figure 15**, ground-state energies of oxygen and calcium isotopes are displayed for both N2LO and N3LO Hamiltonians. In each case, results are accompanied by a band combining the two sources of uncertainty according to the method outlined above. While the mean value of the results only slightly changes when going from N2LO to N3LO, the uncertainty is consistently reduced. Furthermore, N3LO results are essentially consistent with experimental data within the error band, although the narrowing of that uncertainty allows one to stipulate that this agreement is deteriorating when going to neutron-rich isotopes.

Clearly, the above features points toward a systematically improved quality of the novel set of interactions compared to prior generations of chiral Hamiltonians that tend to fail in mid-mass systems. In the future, this statement will be further benchmarked by validating the consistency of low-lying spectroscopy and charge radii with experimental data in the mid-mass region.

11. CONCLUSIONS AND OUTLOOK

The present paper reviewed the status of MBPT techniques in the field of *ab initio* many-body calculations of finite nuclei. After discussing formal properties of the power-series ansatz, the main goal was to provide an in-depth understanding of the MBPT expansion and its range of applicability. Most importantly, two ways of extending Slater-determinant-based MBPT toward open-shell systems were discussed. Multi-configurational perturbation theory and Bogoliubov MBPT were shown to provide complementary ways to tackle the particle-hole degeneracy and the associated strong correlations in open-shell nuclei.

Each of the subparts dedicated to the various flavors of many-body perturbation theory displayed results of large-scale calculations touching upon the very frontier of current *ab initio* studies dedicated to mid-mass (open-shell) nuclei. While highly accurate non-perturbative alternatives are available, the formal and computational simplicity is at the very heart of perturbative approaches. Indeed, these features enable large surveys along complete isotopic chains at a small fraction of the computational cost necessary to utilize more sophisticated approaches. In view of the increasing activity related to the construction of improved generations of nuclear Hamiltonians, simple and yet accurate many-body schemes constitute a very valuable tool to quickly characterize their overall performance.

Furthermore, MBPT provides not only a standalone many-body framework, but can also be used as an inexpensive pre-processing tool to accelerate non-perturbative methods. Two facets discussed in this work are data compression from MBPT-based importance truncation and basis optimization from low-order MBPT density matrices. Both tools have been used with great success to either tame the curse of dimensionality or cure pathological defects in the computational basis at low computational price.

This (by far not exhaustive) list of MBPT-related applications in nuclear theory highlights the start of a *renaissance of perturbation theory* fostered by renormalization group techniques used to soften nuclear Hamiltonians. In parallel, the deepened understanding of infrared-divergences, their origin in open-shell systems and systematic ways to overcome them will hopefully help cure the (unfortunately still present) disfavor against MBPT for nuclear structure research.

Future developments will expand many of the ideas laid out in this work. Better control on uncertainties in the nuclear Hamiltonian pave the way for targeting more exotic systems in the upcoming years. In particular, a proper account of static correlations associated with nuclear deformation has been identified as a critical goal by various groups worldwide. Consequently, the implementation of frameworks employing a systematic breaking (and restoration) of $SU(2)$ symmetry will be of high relevance. However, due to the increasing number of basis states these efforts will require significant computational resources as well as extensive formal developments. To control the increase of computational requirements (memory and runtime), so-called *tensor factorization techniques* have been proposed recently where high-mode tensors are decomposed into sums of product of lower-rank ones [107, 119]. While initial proof-of-principle applications have demonstrated the high potential, extensive additional research is required in this direction.

On a short timescale the benchmarking of importance truncation and natural orbitals in non-perturbative medium-mass applications will deepen the understanding of the role of the computational basis and distribution of correlations in Hilbert space. Furthermore, by employing data compression tools will greatly help relax the many-body truncation at play such that first-principle calculations will witness a level of accuracy that has been out of reach so far.

DATA AVAILABILITY STATEMENT

The raw data supporting the conclusions of this article will be made available by the authors, without undue reservation.

AUTHOR CONTRIBUTIONS

All authors contributed to the writing of the text. RR performed *ab initio* calculations of NCSM-PT and IM-NCSM. AT performed calculations of BMBPT.

FUNDING

This publication was based on work supported in part by the framework of the Espace de Structure et de réactions Nucléaires Théorique (ESNT) at CEA, the Deutsche Forschungsgemeinschaft (DFG, German Research Foundation)—Projektnummer 279384907—SFB 1245, and the BMBF through contract 05P18RDFN1 and Verbundprojekt 05P2018 (ErUM-FSP T07).

ACKNOWLEDGMENTS

We would like to thank M. Frosini for generating the data used in **Figure 2**. Parts of this work were performed at the Lichtenberg cluster at the computing center of the TU Darmstadt and the JURECA supercomputing facility at Forschungszentrum Jülich.

REFERENCES

1. Weinberg S. Nuclear forces from chiral lagrangians. *Phys Lett B*. (1990) **251**:288. doi: 10.1016/0370-2693(90)90938-3
2. Weinberg S. Effective chiral lagrangians for nucleon-pion interactions and nuclear forces. *Nucl Phys Sect B*. (1991) **363**:3–18. doi: 10.1016/0550-3213(91)90231-L
3. Weinberg S. Three-body interactions among nucleons and pions. *Phys Lett B*. (1992) **295**:114–21. doi: 10.1016/0370-2693(92)90099-P
4. Entem DR, Machleidt R. Accurate charge-dependent nucleon-nucleon potential at fourth order of chiral perturbation theory. *Phys Rev C*. (2003) **68**:041001. doi: 10.1103/PhysRevC.68.041001
5. Epelbaum E. Few-nucleon forces and systems in chiral effective field theory. *Prog Part Nucl Phys*. (2006) **57**:654–741. doi: 10.1016/j.ppnp.2005.09.002
6. Machleidt R, Entem DR. Chiral effective field theory and nuclear forces. *Phys Rep*. (2011) **503**:1–75. doi: 10.1016/j.physrep.2011.02.001
7. Wiringa RB, Stoks VGJ, Schiavilla R. Accurate nucleon-nucleon potential with charge-independence breaking. *Phys Rev C*. (1995) **51**:38–51. doi: 10.1103/PhysRevC.51.38
8. Machleidt R. The high-precision, charge-dependent Bonn nucleon-nucleon potential (CD-Bonn). *Phys Rev C*. (2000) **63**:024001. doi: 10.1103/PhysRevC.63.024001
9. Otsuka T, Suzuki T, Holt JD, Schwenk A, Akaishi Y. Three-body forces and the limit of oxygen isotopes. *Phys Rev Lett*. (2010) **105**:32501. doi: 10.1103/PhysRevLett.105.032501
10. Hergert H, Bogner SK, Binder S, Calci A, Langhammer J, Roth R, et al. In-medium similarity renormalization group with chiral two- plus three-nucleon interactions. *Phys Rev C*. (2013) **87**:34307. doi: 10.1103/PhysRevC.87.034307
11. Navrátil P, Quaglioni S, Stetcu I, Barrett B. Recent developments in no-core shell-model calculations. *J Phys G Nucl Part Phys*. (2009) **36**:83101. doi: 10.1088/0954-3899/36/8/083101
12. Roth R, Langhammer J, Calci A, Binder S, Navrátil P. Similarity-transformed chiral NN+3N interactions for the *ab initio* description of 12-C and 16-O. *Phys Rev Lett*. (2011) **107**:72501. doi: 10.1103/PhysRevLett.107.072501
13. Barrett BR, Navrátil P, Vary JP. *Ab initio* no core shell model. *Prog Part Nucl Phys*. (2013) **69**:131–81. doi: 10.1016/j.ppnp.2012.10.003
14. Gezerlis A, Tews I, Epelbaum E, Gandolfi S, Hebeler K, Nogga A, et al. Quantum Monte Carlo calculations with chiral effective field theory interactions. *Phys Rev Lett*. (2013) **111**:032501. doi: 10.1103/PhysRevLett.111.032501
15. Carlson J, Gandolfi S, Pederiva F, Pieper SC, Schiavilla R, Schmidt KE, et al. Quantum Monte Carlo methods for nuclear physics. *Rev Mod Phys*. (2015) **87**:1067. doi: 10.1103/RevModPhys.87.1067
16. Lynn JE, Tews I, Carlson J, Gandolfi S, Gezerlis A, Schmidt KE, et al. Quantum Monte Carlo calculations of light nuclei with local chiral two- and three-nucleon interactions. *Phys Rev C*. (2017) **96**:054007. doi: 10.1103/PhysRevC.96.054007
17. Lynn JE, Tews I, Gandolfi S, Lovato A. Quantum Monte Carlo methods in nuclear physics: recent advances. *Annu Rev Nucl Part Sci*. (2019) **69**:279–305. doi: 10.1146/annurev-nucl-101918-023600
18. Nogga A, Kamada H, Glöckle W. Solution of the Faddeev-Yakubovsky equations using realistic NN and 3N interactions. *Nuclear Phys A*. (2001) **689**:357–60. doi: 10.1016/S0375-9474(01)00854-5
19. Lazauskas R, Carbonell J. The Faddeev-Yakubovsky symphony. *Few Body Syst*. (2019) **60**:62. doi: 10.1007/s00601-019-1529-5
20. Dickhoff WH, Barbieri C. Selfconsistent Green's function method for nuclei and nuclear matter. *Prog Part Nucl Phys*. (2004) **52**:377–496. doi: 10.1016/j.ppnp.2004.02.038
21. Cipollone A, Barbieri C, Navrátil P. Isotopic chains around oxygen from evolved chiral two- and three-nucleon interactions. *Phys Rev Lett*. (2013) **111**:062501. doi: 10.1103/PhysRevLett.111.062501
22. Carbone A, Cipollone A, Barbieri C, Rios A, Polls A. Self-consistent Green's functions formalism with three-body interactions. *Phys Rev C*. (2013) **88**:54326. doi: 10.1103/PhysRevC.88.054326
23. Somá V, Cipollone A, Barbieri C, Navrátil P, Duguet T. Leading chiral three-nucleon forces along isotope chains in the calcium region. *Phys Rev C*. (2014) **89**:61301. doi: 10.1103/PhysRevC.89.061301
24. Raimondi F, Barbieri C. Nuclear electromagnetic dipole response with the Self-Consistent Green's Function formalism. *Phys Rev C*. (2019) **99**:054327. doi: 10.1103/PhysRevC.99.054327
25. Somá V, Navrátil P, Raimondi F, Barbieri C, Duguet T. Novel chiral Hamiltonian and observables in light and medium-mass nuclei. *Phys. Rev. C* (2019) **101**:014318. doi: 10.1103/PhysRevC.101.014318
26. Kowalski K, Dean DJ, Hjorth-Jensen M, Papenbrock T, Piecuch P. Coupled cluster calculations of ground and excited states of nuclei. *Phys Rev Lett*. (2004) **92**:132501. doi: 10.1103/PhysRevLett.92.132501
27. Hagen G, Papenbrock T, Dean DJ, Hjorth-Jensen M. *Ab initio* coupled-cluster approach to nuclear structure with modern nucleon-nucleon interactions. *Phys Rev C*. (2010) **82**:34330. doi: 10.1103/PhysRevC.82.034330
28. Binder S, Langhammer J, Calci A, Roth R. *Ab initio* path to heavy nuclei. *Phys Lett B*. (2014) **736**:119–23. doi: 10.1016/j.physletb.2014.07.010
29. Henderson TM, Dukelsky J, Scuseria GE, Signoracci A, Duguet T. Quasiparticle coupled cluster theory for pairing interactions. *Phys Rev*. (2014) C89:54305. doi: 10.1103/PhysRevC.89.054305
30. Jansen GR, Engel J, Hagen G, Navratil P, Signoracci A. *Ab initio* coupled-cluster effective interactions for the shell model: application to neutron-rich oxygen and carbon isotopes. *Phys Rev Lett*. (2014) **113**:142502. doi: 10.1103/PhysRevLett.113.142502
31. Hagen G, Papenbrock T, Hjorth-Jensen M, Dean DJ. Coupled-cluster computations of atomic nuclei. *Rep Prog Phys*. (2014) **77**:096302. doi: 10.1088/0034-4885/77/9/096302
32. Roth R, Langhammer J. Padé-resummed high-order perturbation theory for nuclear structure calculations. *Phys Lett B*. (2010) **683**:272–7. doi: 10.1016/j.physletb.2009.12.046

33. Langhammer J, Roth R, Stumpf C. Spectra of open-shell nuclei with Padé-resummed degenerate perturbation theory. *Phys Rev C*. (2012) **86**:054315. doi: 10.1103/PhysRevC.86.054315
34. Tichai A, Langhammer J, Binder S, Roth R. Hartree-Fock many-body perturbation theory for nuclear ground-states. *Phys Lett B*. (2016) **756**:283–8. doi: 10.1016/j.physletb.2016.03.029
35. Hu BS, Xu FR, Sun ZH, Vary JP, Li T. *Ab initio* nuclear many-body perturbation calculations in the Hartree-Fock basis. *Phys Rev C*. (2016) **94**:14303. doi: 10.1103/PhysRevC.94.014303
36. Tichai A, Gebrerufael E, Vobig K, Roth R. Open-shell nuclei from no-core shell model with perturbative improvement. *Phys Lett B*. (2018) **786**:448–52. doi: 10.1016/j.physletb.2018.10.029
37. Tichai A, Arthuis P, Duguet T, Hergert H, Somá V, Roth R. Bogoliubov many-body perturbation theory for open-shell nuclei. *Phys Lett B*. (2018) **786**:195. doi: 10.1016/j.physletb.2018.09.044
38. Tsukiyama K, Bogner SK, Schwenk A. In-medium similarity renormalization group for nuclei. *Phys Rev Lett*. (2011) **106**:222502. doi: 10.1103/PhysRevLett.106.222502
39. Tsukiyama K, Bogner SK, Schwenk A. In-medium similarity renormalization group for open-shell nuclei. *Phys Rev C*. (2012) **85**:061304. doi: 10.1103/PhysRevC.85.061304
40. Bogner SK, Hergert H, Holt JD, Schwenk A, Binder S, Calci A, et al. Nonperturbative shell-model interactions from the in-medium similarity renormalization group. *Phys Rev Lett*. (2014) **113**:142501. doi: 10.1103/PhysRevLett.113.142501
41. Hergert H, Bogner SK, Morris TD, Schwenk A, Tsukiyama K. The in-medium similarity renormalization group: a novel *ab initio* method for nuclei. *Phys Rep*. (2016) **621**:165. doi: 10.1016/j.physrep.2015.12.007
42. Parzuchowski NM, Morris TD, Bogner SK. *Ab initio* excited states from the in-medium similarity renormalization group. *Phys Rev C*. (2017) **95**:044304. doi: 10.1103/PhysRevC.95.044304
43. Morris TD, Simonis J, Stroberg SR, Stumpf C, Hagen G, Holt JD, et al. Structure of the lightest tin isotopes. *Phys Rev Lett*. (2018) **120**:152503. doi: 10.1103/PhysRevLett.120.152503
44. Stroberg SR, Calci A, Hergert H, Holt JD, Bogner SK, Roth R, et al. Nucleus-dependent valence-space approach to nuclear structure. *Phys Rev Lett*. (2017) **118**:032502. doi: 10.1103/PhysRevLett.118.032502
45. Miyagi T, Abe T, Okamoto R, Otsuka T. Ground-state energies and charge radii of 4He, 16O, 40Ca, and 56Ni in the unitary-model-operator approach. *Prog Theor Exp Phys*. (2015) **2015**:041D01. doi: 10.1093/ptep/ptv042
46. Miyagi T, Abe T, Okamoto R, Otsuka T. Introduction of the one-body correlation operator in the unitary-model-operator approach. *Phys Rev C*. (2017) **96**:054312. doi: 10.1103/PhysRevC.96.054312
47. Piecuch P, Gour JR, Włoch M. Left-eigenstate completely renormalized equation-of-motion coupled-cluster methods: review of key concepts, extension to excited states of open-shell systems, and comparison with electron-attached and ionized approaches. *Int J Quant Chem*. (2009) **109**:3268. doi: 10.1002/qua.22367
48. Jansen GR. Spherical coupled-cluster theory for open-shell nuclei. *Phys Rev C*. (2013) 88:024305. doi: 10.1103/PhysRevC.88.024305
49. Holt JD, Menéndez J, Simonis J, Schwenk A. Three-nucleon forces and spectroscopy of neutron-rich calcium isotopes. *Phys Rev C*. (2014) **90**:024312. doi: 10.1103/PhysRevC.90.024312
50. Somá V, Duguet T, Barbieri C. *Ab-initio* self-consistent Gorkov-Green's function calculations of semi-magic nuclei. I. Formalism at second order with a two-nucleon interaction. *Phys Rev C*. (2011) **84**:64317. doi: 10.1103/PhysRevC.84.064317
51. Hergert H, Bogner SK, Morris TD, Binder S, Calci A, Langhammer J, et al. *Ab initio* multireference in-medium similarity renormalization group calculations of even calcium and nickel isotopes. *Phys Rev C*. (2014) **90**:041302. doi: 10.1103/PhysRevC.90.041302
52. Gebrerufael E, Vobig K, Hergert H, Roth R. *Ab initio* description of open-shell nuclei: merging no-core shell model and in-medium similarity renormalization group. *Phys Rev Lett*. (2017) **118**:152503. doi: 10.1103/PhysRevLett.118.152503
53. Signoracci A, Duguet T, Hagen G, Jansen GR. *Ab initio* Bogoliubov coupled cluster theory for open-shell nuclei. *Phys Rev C*. (2015) **91**:64320. doi: 10.1103/PhysRevC.91.064320
54. Duguet T. Symmetry broken and restored coupled-cluster theory: I. Rotational symmetry and angular momentum. *J Phys G Nucl Part Phys*. (2015) **42**:25107. doi: 10.1088/0954-3899/42/2/025107
55. Ui H, Takeda G. Equivalence of stochastic quantization method to conventional field theories through super transformation invariance. *Prog Theor Phys*. (1983) **70**:176. doi: 10.1143/PTP.70.176
56. Yannouleas C, Landman U. Symmetry breaking and quantum correlations in finite systems: studies of quantum dots and ultracold Bose gases and related nuclear and chemical methods. *Rep Prog Phys*. (2007) **70**:2067. doi: 10.1088/0034-4885/70/12/R02
57. Papenbrock T, Weidenmueller HA. Effective field theory for finite systems with spontaneously broken symmetry. *Phys Rev C*. (2014) **89**:014334. doi: 10.1103/PhysRevC.89.014334
58. Duguet T, Signoracci A. Symmetry broken and restored coupled-cluster theory. II. Global gauge symmetry and particle number. *J Phys*. (2017) G44:15103. doi: 10.1088/0954-3899/44/1/015103
59. Qiu Y, Henderson TM, Zhao J, Scuseria GE. Projected coupled cluster theory. *J Chem Phys*. (2017) **147**:064111. doi: 10.1063/1.4991020
60. Qiu Y, Henderson TM, Duguet T, Scuseria GE. Particle-number projected Bogoliubov coupled cluster theory. Application to the pairing Hamiltonian. *Phys Rev C*. (2019) **99**:044301. doi: 10.1103/PhysRevC.99.044301
61. Baker GA Jr, Graves-Morris P. *Padé Approximants*. Cambridge: Cambridge University Press (1996).
62. Frame D, He R, Ipsen I, Lee D, Lee D, Rrapaj E. Eigenvector continuation with subspace learning. *Phys Rev Lett*. (2018) **121**:032501. doi: 10.1103/PhysRevLett.121.032501
63. Frame DK. *Ab initio* simulations of light nuclear systems using eigenvector continuation and auxiliary field Monte Carlo. *arXiv [Preprint]*. 2019. *arXiv:1905.02782*.
64. Demol P, Duguet T, Ekström A, Frosini M, Hebeler K, König S, et al. Improved many-body expansions from eigenvector continuation. *arXiv [Preprint]*. 2019. *arXiv:1911.12578*. doi: 10.1103/PhysRevC.101.041302
65. Hebeler K, Bogner SK, Furnstahl RJ, Nogga A, Schwenk A. Improved nuclear matter calculations from chiral low-momentum interactions. *Phys Rev C*. (2011) **83**:031301. doi: 10.1103/PhysRevC.83.031301
66. Drischler C, Carbone A, Hebeler K, Schwenk A. Neutron matter from chiral two- and three-nucleon calculations up to N3LO. *Phys Rev C*. (2016) **94**:054307. doi: 10.1103/PhysRevC.94.054307
67. Wellenhofer C, Drischler C, Schwenk A. Dilute Fermi gas at fourth order in effective field theory. *Phys Lett B*. (2020) **802**:135247.
68. Drischler C, Hebeler K, Schwenk A. Chiral interactions up to next-to-next-to-next-to-leading order and nuclear saturation. *Phys Rev Lett*. (2019) **122**:042501. doi: 10.1103/PhysRevLett.122.042501
69. Shavitt I, Bartlett RJ. *Many-Body Methods in Chemistry and Physics: MBPT and Coupled-Cluster Theory (Cambridge Molecular Science)*. Cambridge University Press (2009). Available online at: http://www.amazon.com/Many-Body-Methods-Chemistry-Physics-Coupled-Cluster/dp/052181832X. doi: 10.1017/CBO9780511596834
70. Frame D, He R, Ipsen I, Lee D, Lee D, Rrapaj E. Eigenvector continuation with subspace learning. *Phys Rev Lett*. (2018) **121**:032501. doi: 10.1103/PhysRevLett.121.032501
71. König S, Ekström A, Hebeler K, Lee D, Schwenk A. Eigenvector continuation as an efficient and accurate emulator for uncertainty quantification. *arXiv [Preprint]*. 2019. *arXiv: 1909.08446*.
72. Ekström A, Hagen G. Global sensitivity analysis of bulk properties of an atomic nucleus. *Phys Rev Lett*. (2019) **123**:252501. doi: 10.1103/PhysRevLett.123.252501
73. Demol P, Duguet T, Ekström A, Frosini M, Hebeler K, König S, et al. Improved many-body expansions from eigenvector continuation. *Phys Rev C*. (2019) **101**:041302(R). doi: 10.1103/PhysRevC.101.041302
74. Ekström A, Baardsen G, Forssén C, Hagen G, Hjorth-Jensen M, Jansen GR, et al. Optimized chiral nucleon-nucleon interaction at next-to-next-to-leading order. *Phys Rev Lett*. (2013) **110**:192502. doi: 10.1103/PhysRevLett.110.192502
75. Ekström A, Jansen GR, Wendt KA, Hagen G, Papenbrock T, Carlsson BD, et al. Accurate nuclear radii and binding energies from a chiral

interaction. *Phys Rev C*. (2015) **91**:051301. doi: 10.1103/PhysRevC.91.051301
76. Jurgenson E, Navratil P, Furnstahl R. Evolution of nuclear many-body forces with the similarity renormalization group. *Phys Rev Lett*. (2009) **103**:2. doi: 10.1103/PhysRevLett.103.082501
77. Entem DR, Machleidt R. Accurate charge-dependent nucleon-nucleon potential at fourth order of chiral perturbation theory. *Phys Rev C*. (2003) **68**:041001(R). doi: 10.1103/PhysRevC.68.041001
78. Navrátil P. Local three-nucleon interaction from chiral effective field theory. *Few-Body Syst*. (2007) **41**:117–40. doi: 10.1007/s00601-007-0193-3
79. Roth R, Binder S, Vobig K, Calci A, Langhammer J, Navrátil P. Medium-mass nuclei with normal-ordered chiral NN+3N interactions. *Phys Rev Lett*. (2012) **109**:052501. doi: 10.1103/PhysRevLett.109.052501
80. Roth R, Calci A, Langhammer J, Binder S. Evolved chiral $NN + 3N$ Hamiltonians for ab initio nuclear structure calculations. *Phys Rev C*. (2014) **90**:024325. doi: 10.1103/PhysRevC.90.024325.
81. Maris P, Vary JP, Calci A, Langhammer J, Binder S, Roth R. ^{1}2C properties with evolved chiral three-nucleon interactions. *Phys Rev C*. (2014) **90**:014314. doi: 10.1103/PhysRevC.90.014314
82. Gebrerufael E, Calci A, Roth R. Open-shell nuclei and excited states from multireference normal-ordered Hamiltonians. *Phys Rev C*. (2016) **93**:031301. doi: 10.1103/PhysRevC.93.031301
83. Ripoche J, Tichai A, Duguet T. Normal-ordered k-body approximation in particle-number-breaking theories. *arXiv [Preprint]*. 2019. *arXiv:1908.00765*. doi: 10.1140/epja/s10050-020-00045-8
84. Hugenholtz NM. Perturbation theory of large quantum systems. *Physica*. (1957) **23**:481–532. doi: 10.1016/S0031-8914(57)92950-6
85. Goldstone J. Derivation of the Brueckner many-body theory. *Proc R Soc Lond*. (1957) **239**:267. doi: 10.1098/rspa.1957.0037
86. Bloch C. Sur la détermination de l'état fondamental d'un systéme de particules. *Nucl Phys*. (1958) **7**:451. doi: 10.1016/0029-5582(58)90284-0
87. Wick GC. The evaluation of the collision matrix. *Phys Rev*. (1950) **80**:268. doi: 10.1103/PhysRev.80.268
88. Paldus J, Wong HC. Computer generation of Feynman diagrams for perturbation theory I. General algorithm. *Comput Phys Commun*. (1973) **6**:1–7. doi: 10.1016/0010-4655(73)90016-7
89. Wong HC, Paldus J. Computer generation of Feynman diagrams for perturbation theory II. Program description. *Comput Phys Commun*. (1973) **6**:9–16. doi: 10.1016/0010-4655(73)90017-9
90. Csépes Z, Pipek J. An effective recursive algorithm for generating many-body Hugenholtz and Goldstone diagrams. *J Comput Phys*. (1988) **77**:1–17. doi: 10.1016/0021-9991(88)90153-2
91. Lyons J, Moncrieff D, Wilson S. Diagrammatic many body perturbation expansion for atoms and molecules: automatic generation & analysis of 5th order Hugenholtz energy diagrams. *Comput Phys Commun*. (1994) **84**:91–101. doi: 10.1016/0010-4655(94)90205-4
92. Kállay M, Surján PR. Higher excitations in coupled-cluster theory. *J Chem Phys*. (2001) **115**:2945. doi: 10.1063/1.1383290
93. Kállay M, Szalay PG, Surján PR. A general state-selective multireference coupled-cluster algorithm. *J Chem Phys*. (2002) **117**:980. doi: 10.1063/1.1483856
94. Stevenson PD. Automatic generation of vacuum amplitude many-body perturbation series. *Int J Mod Phys C*. (2003) **14**:1135. doi: 10.1142/S0129183103005236
95. Arthuis P, Duguet T, Tichai A, Lasseri RD, Ebran JP. ADG: Automated generation and evaluation of many-body diagrams I. Bogoliubov many-body perturbation theory. *Comput Phys Commun*. (2019) **240**:202–27. doi: 10.1016/j.cpc.2018.11.023
96. Rolik Z, Szabados Á, Surján PR. On the perturbation of multiconfiguration wave functions. *J Chem Phys*. (2003) **119**:1922. doi: 10.1063/1.1584424
97. Surján PR, Rolik Z, Szabados Á, Köhalmi D. Partitioning in multiconfiguration perturbation theory. *Annalen der Physik (Leipzig)*. (2004) **13**:223–31. doi: 10.1002/andp.200310074
98. Roth R. Importance truncation for large-scale configuration interaction approaches. *Phys Rev C*. (2009) **79**:064324. doi: 10.1103/PhysRevC.79.064324
99. Baranger M. A definition of the single-nucleon potential. *Nucl Phys A*. (1970) **149**:225. doi: 10.1016/0375-9474(70)90692-5
100. Duguet T, Hergert H, Holt JD, Somá V. Nonobservable nature of the nuclear shell structure: meaning, illustrations, and consequences. *Phys Rev C*. (2015) **92**:034313. doi: 10.1103/PhysRevC.92.034313
101. Hose G, Kaldor U. Diagrammatic many-body perturbation theory for general model spaces. *J Phys B Mol Phys*. (1979) **12**:3827. doi: 10.1088/0022-3700/12/23/012
102. Hose G, Kaldor U. A general-model-space diagrammatic perturbation theory. *Phys Scripta*. (1980) **21**:357. doi: 10.1088/0031-8949/21/3-4/019
103. Ring P, Schuck P. *The Nuclear Many-Body Problem*. New York, NY: Springer Verlag (1980). doi: 10.1007/978-3-642-61852-9
104. Demol P, Frosini M, Tichai A, Somá V, Duguet T. Bogoliubov many-body perturbation theory under constraint as a series. Unpublished (2020).
105. Roth R, Navrátil P. *Ab Initio* study of ^{4}0Ca with an importance-truncated no-core shell model. *Phys Rev Lett*. (2007) **99**:092501. doi: 10.1103/PhysRevLett.99.092501
106. Stumpf C, Braun J, Roth R. Importance-truncated large-scale shell model. *Phys Rev C*. (2016) **93**:021301. doi: 10.1103/PhysRevC.93.021301
107. Tichai A, Ripoche J, Duguet T. Pre-processing the nuclear many-body problem. *Eur Phys J A*. (2019) **55**:90. doi: 10.1140/epja/i2019-12758-6
108. Buenker RJ, Peyerimhoff SD. Individualized configuration selection in CI calculations with subsequent energy extrapolation. *Theor Chim Acta*. (1974) **35**:33–58. doi: 10.1007/BF02394557
109. Buenker RJ, Peyerimhoff SD. Energy extrapolation in CI calculations. *Theor Chim Acta*. (1975) **39**:217–28. doi: 10.1007/BF00555301
110. Constantinou C, Caprio MA, Vary JP, Maris P. Natural orbital description of the halo nucleus 6He. *Nucl Sci Techn*. (2017) **28**:179. doi: 10.1007/s41365-017-0332-6
111. Hay PJ. On the calculation of natural orbitals by perturbation theory. *J Chem Phys*. (1973) **59**:2468. doi: 10.1063/1.1680359
112. Siu AKQ, Hayes EF. Configuration interaction procedure based on the calculation of perturbation theory natural orbitals: applications to H2 and LiH. *J Chem Phys*. (1974) **61**:37–40. doi: 10.1063/1.1681646
113. Tichai A, Müller J, Vobig K, Roth R. Natural orbitals for *ab initio* no-core shell model calculations. *Phys Rev C*. (2019) **99**:034321. doi: 10.1103/PhysRevC.99.034321
114. Strayer MR, Bassichis WH, Kerman AK. Correlation effects in nuclear densities. *Phys Rev C*. (1973) **8**:1269. doi: 10.1103/PhysRevC.8.1269
115. Hüther T, Vobig K, Hebeler K, Machleidt R, Roth R. Family of chiral two-plus three-nucleon interactions for accurate nuclear structure studies. *arXiv [Preprint]*. 2019. *arXiv:1911.04955*.
116. Epelbaum E, Krebs H, Meißner UG. Improved chiral nucleon-nucleon potential up to next-to-next-to-next-to-leading order. *Eur Phys J A*. (2015) **51**:53. doi: 10.1140/epja/i2015-15053-8
117. Binder S, Calci A, Epelbaum E, Furnstahl RJ, Golak J, Hebeler K, et al. Few-nucleon systems with state-of-the-art chiral nucleon-nucleon forces. *Phys Rev C*. (2016) **93**:044002. doi: 10.1103/PhysRevC.93.044002
118. Binder S, Calci A, Epelbaum E, Furnstahl RJ, Golak J, Hebeler K, et al. Few-nucleon and many-nucleon systems with semilocal coordinate-space regularized chiral nucleon-nucleon forces. *Phys Rev C*. (2018) **98**:014002. doi: 10.1103/PhysRevC.98.014002
119. Tichai A, Schutski R, Scuseria GE, Duguet T. Tensor-decomposition techniques for ab initio nuclear structure calculations: from chiral nuclear potentials to ground-state energies. *Phys Rev C*. (2019) **99**:034320. doi: 10.1103/PhysRevC.99.034320

Conflict of Interest: The authors declare that the research was conducted in the absence of any commercial or financial relationships that could be construed as a potential conflict of interest.

frontiers in Physics

REVIEW
published: 14 May 2020
doi: 10.3389/fphy.2020.00153

Quantum Monte Carlo Methods for Astrophysical Applications

*Ingo Tews**

Theoretical Division, Los Alamos National Laboratory, Los Alamos, NM, United States

In recent years, new astrophysical observations have provided a wealth of exciting input for nuclear physics. For example, the observations of two-solar-mass neutron stars put strong constraints on possible phase transitions to exotic phases in strongly interacting matter at high densities. Furthermore, the recent observation of a neutron-star merger in both the electromagnetic spectrum and gravitational waves has provided compelling evidence that neutron-star mergers are an important site for the production of extremely neutron-rich nuclei within the r-process. In the coming years, an abundance of new observations is expected, which will continue to provide crucial constraints on the nuclear physics of these events. To reliably analyze such astrophysical observations and extract information on nuclear physics, it is very important that a consistent approach to nuclear systems is used. Such an approach consists of a precise and accurate method to solve the nuclear many-body problem in nuclei and nuclear matter, combined with modern nuclear Hamiltonians that allow to estimate the theoretical uncertainties. Quantum Monte Carlo methods are ideally suited for such an approach and have been successfully used to describe atomic nuclei and nuclear matter. In this contribution, I will present a detailed description of Quantum Monte Carlo methods focusing on the application of these methods to astrophysical problems. In particular, I will discuss how to use Quantum Monte Carlo methods to describe nuclear matter of relevance to the physics of neutron stars.

Keywords: neutron stars, dense-matter equation of state, nuclear interactions, chiral effective field theory, *ab-initio* calculations, Quantum Monte Carlo methods

OPEN ACCESS

Edited by:
Luigi Coraggio,
National Institute of Nuclear Physics of Naples, Italy

Reviewed by:
Francesca Sammarruca,
University of Idaho, United States
Giampaolo Co',
National Institute of Nuclear Physics of Lecce, Italy

***Correspondence:**
Ingo Tews
itews@lanl.gov

Specialty section:
This article was submitted to Nuclear Physics, a section of the journal Frontiers in Physics

Received: *06 January 2020*
Accepted: *15 April 2020*
Published: *14 May 2020*

Citation:
Tews I (2020) Quantum Monte Carlo Methods for Astrophysical Applications. Front. Phys. 8:153. doi: 10.3389/fphy.2020.00153

1. INTRODUCTION

There are four fundamental forces in nature: gravity, the electromagnetic force, the weak nuclear force, and the strong nuclear force. While gravity describes the motion of the largest systems that we can observe, i.e., celestial bodies in the solar system and beyond, over very long distances, it is the weakest of the four fundamental forces. On the other end of the spectrum, the strong nuclear force is the strongest of the fundamental forces, but it acts only over very short distances and describes the interactions of some of the smallest building blocks of nature. In particular, it determines how neutrons and protons interact to form, e.g., atomic nuclei that make up all the matter that surrounds us everyday.

The strong interaction is described by its fundamental theory, Quantum Chromodynamics (QCD). QCD describes the strong interaction in terms of six quarks and eight gluons, which are elementary particles in the standard model. At low energies, these elementary particles can not be observed in isolation. Instead, they are confined to form so-called hadrons: mesons, e.g., the pion, or baryons, e.g., neutrons and protons. Furthermore, at these energies QCD is non-perturbative.

Hence, it is computationally very demanding and costly to describe nuclear systems in terms of quarks and gluons by solving QCD explicitly. While Lattice QCD, which is a numerical approach to solve QCD on finite space-time lattices, attempts to achieve exactly that, such calculations are limited to systems with small nucleon numbers $A < 5$ and/or for large values of the quark masses, where simulations become cheaper. Instead, at low energies it is a very good approximation to describe nuclear systems, e.g., atomic nuclei, in terms of protons and neutrons which interact via some effective model of strong interactions, i.e., nuclear forces. One of the major goals of theoretical nuclear physics is to unravel the exact nature of nuclear forces and to understand how these forces lead to the properties of the nuclear systems that we can observe.

Nuclear systems that can be explored in terrestrial laboratories are atomic nuclei, and nuclear theory tries to explain their structure, i.e, energy levels, radii, separation energies, decays, etc. (see, e.g., Hagen et al. [1], Elhatisari et al. [2], Lynn et al. [3], Klos et al. [4], Calci et al. [5], Piarulli et al. [6], Lonardoni et al. [7], and Gysbers et al. [8]). Of particular interest are exotic nuclei far from stability, because they probe nuclear interactions at larger proton-to-neutron asymmetries [9–12]. The Coulomb interaction does not allow the ratio of protons to neutrons, the proton fraction, to become too large because in such cases the Coulomb repulsion among the protons would overcome the short-range nuclear attraction and make nuclei fall apart. On the other hand, neutron-rich nuclei, which explore smaller proton fractions, can be bound in nature, but the most exotic among them are extremely short-lived. The limits of existence of these nuclei are described by the neutron dripline, where one- and two-neutron separation energies become negative [13].

Neutron-rich nuclei are relevant for the so-called rapid neutron-capture process (r-process), a nucleosynthesis process that creates nearly half of all the elements heavier than iron in the universe. Hence, neutron-rich nuclei are extensively studied in nuclear-structure calculations and experiments. Our experimental knowledge will be significantly expanded in experiments at the upcoming Facility for Radioactive Ion Beams (FRIB) in the US and the Facility for Antiproton and Ion Research (FAIR) in Germany. But even with these advanced facilities, exotic nuclei with the most extreme neutron-to-proton ratios will not live long enough to be studied experimentally. Hence, the determination of their properties, which are very important as input in r-process studies, relies on theoretical models and astrophysical observations [14]. To improve theoretical models, the interactions in many-body systems with small proton fractions need to be understood better and tested against experimental data where available.

Luckily, atomic nuclei are not the only systems where one can test nuclear interactions at neutron-rich extremes. Neutron stars, which are one of the final stages of stellar evolution, are supported against gravitational collapse by strong interactions among its constituents, mainly neutrons with only around 5–10% of protons. In addition, with typical masses of 1.4 times the mass of our sun compressed into a star with a radius of 11–12 km, the densities in the core of neutron stars are extremely high. While atomic nuclei explore densities of the order of the nuclear saturation density, $n_{\rm sat} = 0.16{\rm fm}^{-3}$ which corresponds to a mass density of $2.7 \cdot 10^{14}$ g/cm^3, neutron stars explore strong interactions at much larger densities of up to 10 times $n_{\rm sat}$. Hence, neutron-star observations allow us to test nuclear interactions at low proton fractions and high densities, which provides important complimentary information to experiments here on Earth. As a consequence, the study of these astrophysical systems is very fascinating and important, and allows to probe nuclear interactions under extreme conditions.

The crucial quantity relating both experiments and astrophysical observations is the equation of state (EOS), which provides a relation between the energy density, pressure, temperature, and the proton fraction of the matter in nuclear systems. For neutron stars, due to the very high densities in these systems, the Fermi energy of the nucleons is typically much larger than thermal energies. For example, while neutron stars typically have temperatures of the order of $T = 10^8$ K, the corresponding thermal energy of about 10 keV is much smaller than typical particle energies of the order of a few tens of MeV. Hence, one can neglect thermal effects, except in the most catastrophic astrophysical scenarios. Then, the EOS is simply relating the energy density ϵ and the pressure P, or alternatively the energy per particle E/A and the baryon density n, for a given proton fraction x.

Astrophysical observations of neutron stars allow us to constrain the EOS, and hence, the strong interactions that determine its properties. In recent years, exciting new astrophysical observations of neutron-star properties have provided a wealth of input for nuclear physics, and I will address these observations in section 2.2. Additional observations in the coming years, for example by the Neutron-Star Interior Composition Explorer (NICER) mission that recently reported its first measurement [15, 16], will add even more information. However, if we want to reliably analyze such astrophysical observations with the goal of constraining the nuclear EOS, we need to relate observations and nuclear interactions in a consistent and model-agnostic way, to avoid any model-related biases and to minimize systematic uncertainties.

In a microscopic approach, one would start from a Hamiltonian that describes the interactions among the relevant degrees of freedom of the system at hand, and solve the many-body Schrödinger equation for that system (e.g., nucleonic matter in neutron stars). Such an approach should consist of a precise and accurate method to solve the nuclear many-body problem in nuclei and nuclear matter, combined with modern nuclear Hamiltonians that allow to estimate the theoretical uncertainties of the nuclear interactions. Quantum Monte Carlo (QMC) methods [17] are ideally suited for such an approach and have been successfully used to describe atomic nuclei and nuclear matter. On the other hand, chiral effective field theory (EFT) [18–21] provides a systematic expansion of the nuclear forces, that allows to estimate theoretical uncertainties.

In this contribution, I will present a detailed description of Quantum Monte Carlo methods, focusing on the application of these methods to astrophysical problems. In particular, I will discuss how to use Quantum Monte Carlo methods to describe nuclear matter of relevance to the physics of neutron

stars. I will also discuss how the combination of these methods with systematic interactions from chiral EFT allows us to extract information on the nuclear EOS in a reliable fashion. This contribution is organized as follows. In section 2, I will review neutron stars and the most important recent neutron-star observations. In section 3, I will address how to study the nuclear matter in neutron stars using Quantum Monte Carlo methods and modern nuclear interactions. In section 4, I will then show results and explain how to use these results to study neutron stars. Finally, I will summarize in section 5.

2. NEUTRON STARS AND THEIR PROPERTIES

In this section, I will review neutron stars and their relevant equations, as well as the most important recent neutron-star observations.

2.1. Describing Neutron Stars

Neutron stars are one of the final stages of stellar evolution. While low-mass stars like our sun end their life as white dwarfs, neutron stars are remnants of core-collapse supernova explosions of medium-mass stars in the range of 8–20 solar masses (heavier stars will collapse to black holes; see, e.g., Fryer [22]). Hence, neutron stars are the most compact stars in the Universe.

While stars in their burning stages are supported against gravitational collapse by the thermal energy released in nuclear fusion, these processes have stopped in white dwarfs and neutron stars. White dwarfs are the remaining cores of lighter stars that have shed their outer layers. They typically consist of Carbon and/or Oxygen, and have masses of the order of the mass of our sun compressed to the size of a typical planet, with radii of the order of several 1,000 km. Due to the resulting densities and the fermionic nature of electrons, the electrons in white dwarfs form a degenerate gas. It costs energy to compress this electron gas, leading to a degeneracy pressure exerted outwards that balances the gravitational force that otherwise would collapse the star. Such a degenerate electron gas can typically support a white dwarf with a maximum mass of $\sim 1.4 M_\odot$, the so-called Chandrasekhar mass [23]. If a white dwarf accretes mass and surpasses this limit, the electron pressure does not suffice anymore to stabilize the star against gravitational collapse. This is what happens in core-collapse supernovae of heavier stars, where the white-dwarf-like core collapses due to continued accretion of fusion products. This collapse then triggers the supernova explosion of the star.

As a consequence of the core collapse, the densities of the electrons and nuclei increase dramatically, leading to an increasing Fermi energy for the electrons. At some point, it becomes energetically favorable for protons in the core to absorb electrons and form neutrons, lowering the proton fraction. As the collapse continues, at the largest densities in the core neutron-rich nuclei begin to dissolve into free nucleons, mostly neutrons. The collapse is halted when the core reaches radii of the order $\mathcal{O}(10)$ km. The abrupt stop of the contraction causes a so-called bounce that ultimately leads to a supernova explosion and ejects the remaining outer layers of the star, leaving a dense remnant. Due to their small proton fraction of the order of 5–10%, these young stars are called proto-neutron stars. They will cool over time and form cold neutron stars. Similar to white dwarfs, neutron stars are stabilized against gravitational collapse by the degeneracy pressure of their fermionic constituents, the neutrons. The discovery of the neutron by Chadwick [24] led to the postulation of neutron stars [25] long before their discovery in the 1960s [26, 27].

To investigate how the degeneracy pressure exerted by the neutron gas stabilizes neutron stars, one needs to start from the equations that describe the neutron-star structure. A less compact cold star (e.g., a white dwarf) would be described by the following structure equations:

$$\frac{dP}{dr} = -\frac{Gm(r)\epsilon(r)}{r^2}\,, \quad \frac{dm}{dr} = 4\pi\epsilon(r)r^2\,, \tag{1}$$

where P is the pressure, G is the gravitational constant, m is the mass, ϵ is the energy density, and r is the radial coordinate. The first equation describes hydrostatic equilibrium and states that the pressure exerted outwards has to match the gravitational force acting inwards. The second equation is the conservation of mass. These equations are derived within Newtonian gravity, but since neutron stars are very compact, the structure equations need to be modified by general-relativistic extensions of Equation (1). These are the so-called Tolman-Oppenheimer-Volkoff (TOV) equations [31, 32]:

$$\begin{aligned}\frac{dP}{dr} &= -G\frac{m(r)\epsilon(r)}{r^2}\left(1+\frac{4\pi r^3 P}{m(r)c^2}\right)\left(1+\frac{P}{\epsilon(r)c^2}\right)\\ &\quad\times\left(1-\frac{2Gm(r)}{rc^2}\right)^{-1}\\ \frac{dm}{dr} &= 4\pi\epsilon(r)r^2\,,\end{aligned} \tag{2}$$

where c is the speed of light. In the following, we will write all equations in natural units and set $c = 1$. The energy density for non-relativistic nucleonic matter is given by

$$\epsilon = n\cdot\left(m_N + \frac{E}{A}(n,x)\right)\,. \tag{3}$$

Here, n is the baryon number density and m_N the nucleon mass. The first term of the energy density reflects the rest-mass density, while the second term is the specific internal energy.

To solve the TOV equations, the only required input is a relation between the pressure P and the energy density ϵ. This relation is the EOS, $P = P(\epsilon)$. With the EOS as input, the TOV equations can be solved by integrating from the stars center at $r = 0$ (where $P = P_c$ and $m = 0$) to the stars edge at radius R (where $P = 0$ and $m(R) = M$). Hereby, the central pressure P_c is an input parameter, that determines the mass M and the radius R for the given EOS. Solving the TOV equations for many different values for P_c maps out the mass-radius (MR) relation, that describes the radius of a NS for a given mass, see **Figure 1** for an example EOS. The EOS and the resulting MR

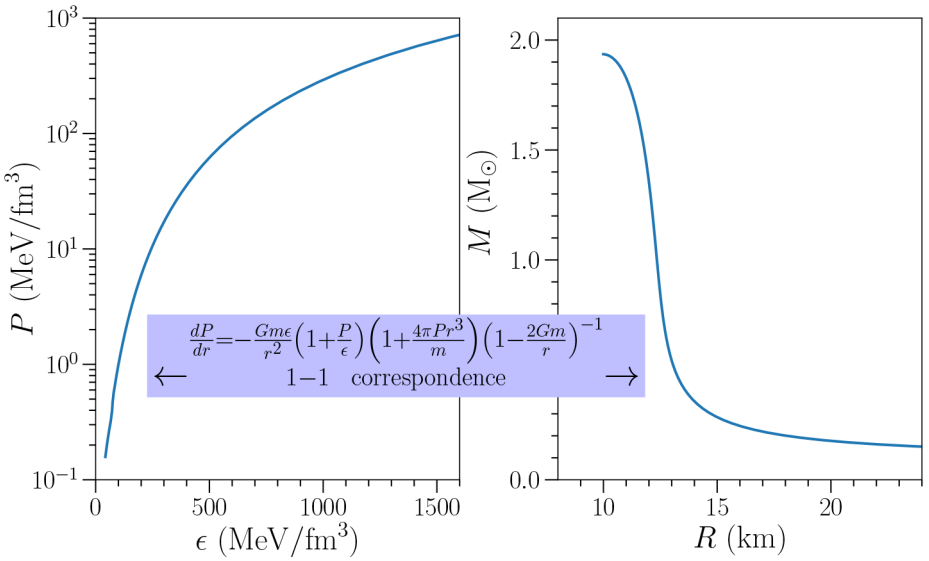

FIGURE 1 | The equation of state **(left)** and the resulting mass-radius relation **(right)** upon solving the TOV equations for an example equation of state, i.e., the Skyrme model "NRAPR" constructed in Steiner et al. [28] which was fit to the APR equation of state of Akmal et al. [29]. Republished with permission of IOP Publishing, from Gandolfi et al. [30]; permission conveyed through Copyright Clearance Center, Inc.

relations are in a 1-to-1 correspondence: given an EOS, one can predict the structure properties of neutron stars, but neutron-star observations also allow to determine the EOS.

Analogously to white dwarfs, Tolman and Oppenheimer inserted the EOS of a free and degenerate neutron gas to estimate the properties of neutron stars. They found a maximum mass of only $0.7M_\odot$ and, hence, concluded that neutron stars are not very important in nature. But, as we now know, the neutron-star EOS is much more complicated because strong interactions among neutrons, protons, and maybe other constituents at larger densities lead to many different effects. Including interaction effects can drastically increase the maximum mass of neutron stars to values as large as $3-4M_\odot$ [33], while observations have established the existence of neutron stars with masses as high as $2M_\odot$ (see next section). Hence, strong interactions are extremely important to stabilize neutron stars against gravitational collapse.

Generally, one can divide a neutron star into several layers. The neutron-star crust, the star's outer layer, can be separated into two regions. The outer crust consists of a lattice of neutron-rich nuclei of the iron region. With increasing density, these nuclei become more and more neutron-rich. At a density of approximately $4\cdot 10^{11}$ g/cm^3, the inner crust begins. Here, the neutron chemical potential is so large that neutrons begin to drip out of the nuclei and form a neutron gas around the lattice of nuclei. With increasing density, the density of the neutron gas increases and the nuclei slowly dissolve. At the bottom of the inner crust, the lattice of nuclei can form exotic structures, called pasta phases, by merging into rods and slabs [34].

The crust connects to the neutron-star core at about half nuclear saturation density. Here, all nuclei have dissolved and the neutron star consists of a fluid of neutrons, protons, and electrons. At even larger densities, in the so-called inner core of neutron stars, exotic phases of matter might appear. The neutron-star might experience phase transitions to hyperonic matter [35], deconfined quark matter [36], or other exotic phases. However, there is no reliable experimental information on matter at such high densities and, hence, on the relevant degrees of freedom that are present in the neutron-star core. Therefore, theoretical models for the EOS have a large spread.

Due to the 1-to-1 correspondence between the EOS and the MR relation, neutron-star observations are an ideal way to constrain EOS models. While we can observe masses quite accurately, neutron-star radii are very uncertain, and typically range from $9-15$ km for a typical $1.4M_\odot$ star [37]. This situation improves with new observations, e.g., from missions like NICER. For example, in the last years several observations have put tight constraints on the EOS and reduced the radius uncertainty quite dramatically. I will discuss these observations in the following, and show how they informed the EOS in section 4.

2.2. Recent Neutron-Star Observations

2.2.1. Two-Solar-Mass Neutron Stars

Neutron stars are typically observed as pulsars, i.e., rotating neutron stars that emit beams of electromagnetic signals (mostly radio signals) that can be detected on Earth. When these pulsars are in a binary with another star, it is possible to accurately measure the masses of the objects by making use of general-relativity effects, e.g., Shapiro delay [38]. As a consequence, neutron-star masses could historically be inferred quite precisely [37]. Neutron-star masses can provide strong EOS constraints because they require the EOS to be sufficiently stiff, i.e., the pressure inside the neutron star has to be sufficiently high to support a star of a certain mass against gravitational collapse. The heavier an observed neutron star is, the stiffer the EOS has

to be. This can be used to rule out too soft EOS models, or EOS with very strong phase transitions that experience regions with a sudden and too strong softening.

Since the discovery of pulsars in the late 1960s, most neutron-star masses that were measured precisely are of the order of $1.4M_\odot$ [37]. This constraint is rather weak, and most EOS models can easily reproduce neutron stars of that mass. However, there have been a few exciting additional observations in the past decade. The first such observation was reported in 2008 [39, 40], when the mass of the binary pulsar J1903+0327 was determined to be of the order of $1.7M_\odot$. Only a few years later, in 2010, the first neutron star with a mass of the order of two solar masses was observed using Shapiro delay [41]: the pulsar PSR J1918-0642 with $M = 1.97 \pm 0.04M_\odot$. This value was later corrected to be $M = 1.93 \pm 0.02M_\odot$ [42]. In 2013, the existence of two-solar-mass neutron stars was firmly established with the observation of PSR J0348+0432 with a mass of $M = 2.01 \pm 0.04M_\odot$ [43]. Finally, only recently an even heavier neutron star was observed [44]: MSP J0740+6620 with a mass of $M = 2.14 \pm 0.10M_\odot$. These measurements put very strong constraints on the EOS of dense matter, and on possible phase transitions to exotic phases in strongly interacting matter at high densities.

2.2.2. Neutron-Star Mergers

In contrast to masses, it is quite difficult to infer neutron-star radii. X-ray observations, which are typically used to determine radii, have large uncertainties due to poorly understood systematics [45]. Recently, with the first observation of gravitational waves from a neutron-star merger and its electromagnetic counterpart [46, 47], a new possibility to constrain neutron-star radii was established.

As a consequence of general relativity, two neutron stars in a binary system emit gravitational waves. Hence, the system slowly looses energy and the distance of the two neutron stars slowly decreases. This leads to an even stronger emission of gravitational waves and so on. Finally, after a time scale of the order of gigayears, the two neutron stars will merge and form either a heavier neutron star or a black hole.

Neutron-star mergers are fascinating events because they simultaneously emit gravitational waves and electromagnetic signals in form of gamma-rays, X-rays, optical, infrared, to radio signals, and neutrinos. On August 17, 2017, the first such event was observed in gravitational waves and the electromagnetic spectrum [46–49]. The gravitational-wave signal was called GW170817 and I will focus on it in the following.

The crucial quantity that allows to extract radius information from neutron-star mergers is the tidal polarizability, Λ, which describes how a neutron star deforms under an external gravitational field, e.g., the field of the second neutron-star in a binary systems. The quadrupole deformation Q_{ij} of a star, given an external field $E_{ij} = -\partial U(r)/\partial x_i \partial x_j$ with gravitational potential $U(r)$, is given by $Q_{ij} \sim \Lambda E_{ij}$. The tidal polarizability depends on neutron-star properties as [52]

$$\Lambda = \frac{2}{3} k_2 \left(\frac{c^2}{G} \frac{R}{M} \right)^5 . \quad (4)$$

Here, k_2 is the tidal Love number which is computed together with the Tolman-Oppenheimer-Volkoff equations; see, for example, Flanagan and Hinderer [52], Damour and Nagar [53], and Moustakidis et al.[54] for more details. For a neutron star of a given mass, one can immediately see that the tidal polarizability is strongly related to the radius of the neutron star. In particular, a larger neutron star will have a large tidal polarizability, while a small neutron star will have a small polarizability. In a neutron-star binary, one typically defines the binary tidal polarizability parameter $\tilde{\Lambda}$ as a mass-weighted average of the individual tidal polarizabilities,

$$\tilde{\Lambda} = \frac{16}{13} \left[\frac{(M_1 + 12M_2)M_1^4 \Lambda_1}{M_{\rm tot}^5} + \frac{(M_2 + 12M_1)M_2^4 \Lambda_2}{M_{\rm tot}^5} \right] , \quad (5)$$

where M_1 and M_2 are the individual masses of the two neutron stars, Λ_1 and Λ_2 are the two star's tidal polarizabilities, and $M_{\rm tot}$ is the total mass of the system. In the left panel of **Figure 2**, I show the correlation of the average radius of the two neutron stars in a binary with the binary tidal polarizability, in this case for a system like GW170817. However, such a relation exists for any neutron-star binary. By measuring $\tilde{\Lambda}$ from the gravitational-wave signal, one can constrain the radius.

The LIGO-Virgo collaboration (LVC) was able to observe the signal GW170817 for about 100*s* (several 1000 revolutions, starting from 25 Hz). A detailed analysis of the signal [49] allowed a precise determination of the chirp mass $M_{\rm chirp}$, defined as

$$M_{\rm chirp} = \frac{(M_1 M_2)^{3/5}}{(M_1 + M_2)^{1/5}} . \quad (6)$$

From the signal, the LVC could also extract the mass ratio $q = M_2/M_1$, where M_1 is the mass of the heavier and M_2 the mass of the lighter neutron star in the binary. Finally, several groups have analyzed the gravitational-wave data and provided posterior probability distributions for the binary tidal polarizability, $p(\tilde{\Lambda})$. These probability distributions are normalized to 1 and are marginalized over the systems properties, like the EOS, the individual neutron-star masses and spins, etc. Hence, these distributions define the probability p that the two neutron stars in GW170817 had the binary tidal polarizability $\tilde{\Lambda}$. I show the result from several extractions in the right panel of **Figure 2**.

In particular, I show the probability distributions extracted by the LVC [49] and from the analysis of De et al. [51] for the two extreme cases [uniform mass prior (u) and mass prior informed by double neutron stars (d)], as well as fits to the LVC distribution of Tews et al. [50]. In these analyses, parametric models for the EOS have been tested against the observed gravitational-wave data for varying system parameters using Bayesian statistical inference tools. The result of these analyses are multidimensional posterior functions for the tidal polarizability. Marginalizing over the various system parameters results in the function $p(\tilde{\Lambda})$. For more details on the extractions I refer the reader to the corresponding references. Because the neutron-star deformation appreciably impacts the gravitational-wave signal only during the last few of several thousand observed orbits [52, 53], the uncertainty of the extracted tidal polarizability is rather large.

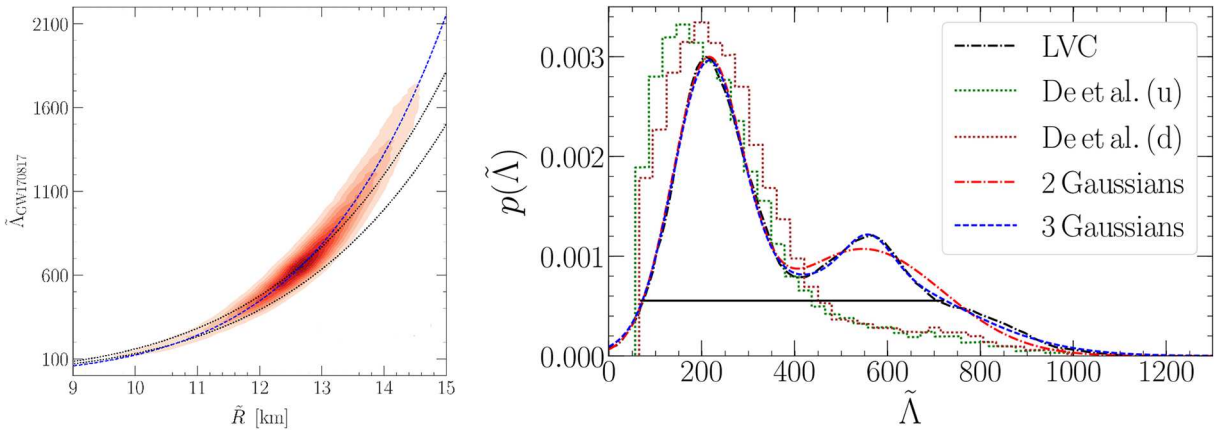

FIGURE 2 | Left: Correlation between the average radius $\tilde{R}$ of the two neutron stars in GW170817 and the binary tidal polarizability $\tilde{\Lambda}_{GW170817}$. We show the distribution for the EOS models of Tews et al. [50] (red shaded area), a fit to this distribution (blue dashed line), as well as the result from Equation (5) of De et al. [51] with uncertainty (black dotted lines). **Right**: Marginalized and normalized posterior probability distribution $p(\tilde{\Lambda})$ for GW170817 from the LVC (black dashed-dotted line), from the analysis of De et al. [51] for the two extreme cases [uniform mass prior (u) and mass prior informed by double neutron stars (d)] (green and red dotted lines), and fits to the LVC distribution of Tews et al. [50] (red dashed-dotted and blue dashed lines). Reprinted by permission from Springer Nature, Tews et al. [50], copyright 2019.

In addition, there are ambiguities among several parameters, e.g., the neutron-star spins and the tidal polarizability, which additionally increase the uncertainties.

The results for $p(\tilde{\Lambda})$ were used by several groups to constrain the MR relation of neutron stars [55–59]. It was found that enforcing the constraint on $\tilde{\Lambda}$ rules out equations of state that are rather stiff and produce neutron stars with large radii. In particular, it was found that the radius of a $1.4M_{\odot}$ neutron star, $R_{1.4}$, can be constrained to be $R_{1.4} < 13.6$ km. The observation of the first neutron-star merger, GW170817, was also very remarkable because the gravitational-wave signal was not the only observed signal. In addition, the electromagnetic counterpart, or kilonova, was observed in multiple wave lengths, and allows to impose additional constraints on the EOS. The kilonova seems to be inconsistent with a direct collapse of the merger remnant to a black hole and, hence, rules out very soft EOS that cannot support sufficiently large neutron-star masses [60]. The kilonova is also inconsistent with the formation of a long-lived neutron star [61] and, hence, rules out EOS with maximum masses larger than about 2.2–2.3 $M_{\odot}$ [61, 62]. Hence, the kilonova observations seem to prefer a delayed collapse of the merger remnant to a black hole. I will discuss the impact of these observations later.

3. MICROSCOPIC APPROACH FOR ASTROPHYSICAL APPLICATIONS

To constrain the neutron-star EOS from microscopic calculations, we need to understand the properties of the nuclear matter in the core of neutron stars. This system is described by a fluid of neutrons at nuclear densities with a small fraction of protons and electrons in β-equilibrium. Calculating the EOS of neutron-star matter is a challenging task because the interactions among nucleons are usually non-perturbative and have a complicated spin-isospin structure. Furthermore, given any nuclear interaction, an accurate and precise way of solving the many-body Schrödinger equation is needed to solve the many-body problem.

For strongly-interacting matter, there are several computational methods that have been used to solve the many-body problem. These methods include, for example, many-body perturbation theory (MBPT) [63–67], the coupled-cluster method [68], the self-consistent Green's function method [69, 70], or the Brueckner-Hartree-Fock approach [71]. Here, I illustrate how to calculate properties of the EOS of neutron stars using precise and accurate quantum Monte Carlo methods [17] combined with modern nuclear Hamiltonians that allow to estimate the theoretical uncertainties.

3.1. Quantum Monte Carlo Method

Quantum Monte Carlo methods are one among several many-body methods to solve the Schrödinger equation for strongly interacting nucleonic matter. In particular, QMC methods solve the nuclear many-problem non-perturbatively and with controlled approximations, which makes QMC methods quasi-exact. They have been very successfully used in studies of nuclear matter and light nuclei [17, 72]. Several implementations of QMC methods have been developed over the years, e.g., Green's function Monte Carlo (GFMC) [73] or auxiliary-field diffusion Monte Carlo (AFDMC) [74]. In this contribution, I will focus on the AFDMC method that has been used extensively to study nuclear matter for astrophysical applications [3, 33, 75–80].

The main idea of Quantum Monte Carlo methods is to stochastically solve the many-body Schrödinger equation to extract the ground state of a system, by evolving a given trial wave function of the many-body system, Ψ_V, in imaginary time $\tau = it$,

$$\Psi(\tau) = e^{-H\tau}\,\Psi_V\,. \tag{7}$$

Here, H is the Hamiltonian of the system, given by a collection of point-particles interacting via two-, three-, and other many-body forces (indicated by ellipses),

$$H = -\frac{\hbar^2}{2m_N}\sum_i \nabla_i^2 + \sum_{i<j} v_{ij} + \sum_{i<j<k} V_{ijk} + \cdots . \tag{8}$$

The first term is the nucleon kinetic energy with nucleon mass m_N, v_{ij} is the nucleon-nucleon (NN) interaction, V_{ijk} describes three-nucleon ($3N$) interactions, and so on. I will discuss the Hamiltonian in the next section.

When expanding the trial wave function Ψ_V in eigenfunctions of the Hamiltonian Φ_i, $\Psi_V = \sum_i c_i \Phi_i$, one can rewrite Equation (7) as

$$\begin{aligned}\Psi(\tau) &= e^{-H\tau}\sum_i c_i\Phi_i = \sum_i c_i e^{-E_i\tau}\Phi_i \\ &= e^{-E_0\tau}\left(c_0\Phi_0 + \sum_{i\geq 1} c_i e^{-(E_i-E_0)\tau}\Phi_i\right),\end{aligned} \tag{9}$$

where the index $i = 0$ describes the lowest-energy eigenstate in the trial wave function (typically the ground state of the system). As a consequence, when evolving Ψ_V in imaginary time as shown above, excited states (with $E_i > E_0$) are exponentially suppressed and will be projected out from the trial wave function for evolutions to sufficiently large imaginary times. Only the Φ_0 contribution will remain after this process. Hence, given a good trial wave function with overlap with the true ground state of the system, the imaginary-time evolution projects out this ground state and allows to access its properties.

Let us discuss this process in more detail. QMC methods formulate the many-body problem in coordinate space. Then, the many-body Schrödinger equation in imaginary time for N nucleons reads

$$H\left|\Psi(\mathbf{R},\tau)\right\rangle = -\frac{\partial}{\partial\tau}\left|\Psi(\mathbf{R},\tau)\right\rangle , \tag{10}$$

where the vector $\mathbf{R} = \{\mathbf{r}_1,\ldots,\mathbf{r}_N,\mathbf{s}_1,\ldots\mathbf{s}_N\}$ contains the configurations of all N particles with respect to all degrees of freedom, i.e., their positions $\mathbf{r}_i$ and their spin-isospin spinors $\mathbf{s}_i$, that contain amplitudes for all possible spin-isospin states: $\left|p\uparrow\right\rangle, \left|p\downarrow\right\rangle, |n\uparrow\rangle$, and $|n\downarrow\rangle$. In bra and ket notation, n and p denote neutrons and protons, respectively, and the arrow-up and -down indicate spin-up and -down. One can rewrite the Schrödinger equation, and obtain the wave function at imaginary time τ, $\left|\Psi(\mathbf{R},\tau)\right\rangle$, from the wave function at τ_0 (which I set to $\tau_0 = 0$ in the following for simplicty) due to time evolution,

$$\left|\Psi(\mathbf{R},\tau)\right\rangle = e^{-H(\tau-\tau_0)}\left|\Psi(\mathbf{R},\tau_0)\right\rangle . \tag{11}$$

Projecting this equation into coordinate space and inserting a completeness relation, this leads to the general solution for the Schrödinger equation:

$$\Psi(\mathbf{R},\tau) = \int \mathrm{d}^3R'\, G(\mathbf{R},\mathbf{R}',\tau)\Psi(\mathbf{R}',0), \tag{12}$$

with the Green's function or propagator

$$G(\mathbf{R},\mathbf{R}',\tau) = \langle\mathbf{R}|\, e^{-\hat{H}\tau}\left|\mathbf{R}'\right\rangle = \langle\mathbf{R}|\, e^{-(\hat{T}+\hat{V})\tau}\left|\mathbf{R}'\right\rangle . \tag{13}$$

Here, $\hat{T}$ denotes the kinetic energy part of the Hamiltonian and $\hat{V}$ the potential part. By solving this integral equation for large imaginary times, one projects out the ground state, as discussed before. The crucial ingredient to accomplish that task is to compute the Green's function.

The simplest case for the Green's function is given for the free system with vanishing interactions, $V = 0$. In this case, the propagator can be computed analytically:

$$\begin{aligned}G_0(\mathbf{R},\mathbf{R}',\tau) &= \langle\mathbf{R}|\, e^{-\hat{T}\tau}\left|\mathbf{R}'\right\rangle \\ &= \langle\mathbf{R}|\, e^{-\sum\frac{p_i^2}{2m}\tau}\left|\mathbf{R}'\right\rangle \\ &= \left(\frac{m}{2\pi\tau}\right)^{\frac{3N}{2}} e^{-\frac{m}{2\tau}\sum_i^N(\mathbf{r}_i-\mathbf{r}_i')^2} .\end{aligned} \tag{14}$$

Adding an interaction is non-trivial. Ideally, one would like to be able to compute the matrix elements for $\hat{T}$ and $\hat{V}$ separately, because the element for $\hat{T}$ can be calculated analytically. However, $\hat{T}$ and $\hat{V}$ cannot simply be separated as they are both arguments of the exponential function. A solution is offered by the Trotter-Suzuki formula [81], which allows to simplify the propagator for a small timestep $\Delta\tau \ll 1$:

$$\begin{aligned}e^{-\hat{H}\Delta\tau} &= e^{-(\hat{T}+\hat{V})\Delta\tau} = e^{-\left(\hat{T}+\frac{\hat{V}}{2}+\frac{\hat{V}}{2}\right)\Delta\tau} \\ &= e^{-\frac{\hat{V}}{2}\Delta\tau}e^{-\hat{T}\Delta\tau}e^{-\frac{\hat{V}}{2}\Delta\tau} + \mathcal{O}(\Delta\tau^3) .\end{aligned} \tag{15}$$

The smaller the imaginary time step, the smaller is the error of this approximation. This approximation is now used to calculate the propagator in Equation (13) for very large imaginary times τ, by splitting the total propagator into n small time steps, and using Equation (15) at each time step:

$$\begin{aligned}&G(\mathbf{R},\mathbf{R}',\tau) = \langle\mathbf{R}|\, e^{-H\tau}\left|\mathbf{R}'\right\rangle = \langle\mathbf{R}|\, e^{-H\,n\Delta\tau}\left|\mathbf{R}'\right\rangle \\ &= \langle\mathbf{R}|\left(e^{-H\,\Delta\tau}\right)^n\left|\mathbf{R}'\right\rangle \\ &= \int \mathrm{d}^3R_1\int \mathrm{d}^3R_2\ldots\int \mathrm{d}^3R_n\, G(\mathbf{R},\mathbf{R}_1,\Delta\tau)G(\mathbf{R}_1,\mathbf{R}_2,\Delta\tau)\cdots \\ &\quad G(\mathbf{R}_n,\mathbf{R}',\Delta\tau),\end{aligned} \tag{16}$$

where the $\mathbf{R}_i$ describe paths in configuration space.

To add an interaction in Quantum Monte Carlo methods, it is important that the interactions are local, i.e., $\langle\mathbf{R}|\,\hat{V}\left|\mathbf{R}'\right\rangle = V(\mathbf{R})\delta(\mathbf{R}-\mathbf{R}')$, and, thus, the potential is only a function of particle separations. In this case, the propagator for small time steps simplifies to

$$\begin{aligned}G(\mathbf{R}_i,\mathbf{R}_j,\Delta\tau) &= \langle\mathbf{R}_i|\, e^{-\frac{\hat{V}}{2}\Delta\tau}e^{-\hat{T}\Delta\tau}e^{-\frac{\hat{V}}{2}\Delta\tau}\left|\mathbf{R}_j\right\rangle \\ &= G_0(\mathbf{R}_i,\mathbf{R}_j,\Delta\tau)e^{-\frac{V(\mathbf{R}_i)+V(\mathbf{R}_j)}{2}\Delta\tau} .\end{aligned} \tag{17}$$

To write the propagator in this form, it is necessary to being able to separate all momentum dependencies as a quadratic

$\sum_{i=1}^{N} p_i^2$ term like above, which can generally be done only for local interactions. In this case, the interaction parts can be easily evaluated by exponentiating a small spin-isospin matrix. For non-local potentials, the evaluation of the propagator would involve the numerical calculation of derivatives, which is computationally too expensive.

Inserting this solution into Equation (12), one obtains

$$\Psi(\mathbf{R}, \tau + \Delta\tau) = \int \mathrm{d}^3R' \, G_0(\mathbf{R}, \mathbf{R}', \Delta\tau) e^{-\frac{V(\mathbf{R})+V(\mathbf{R}')}{2}\Delta\tau} \Psi(\mathbf{R}', \tau) \,. \tag{18}$$

This equation is then solved consecutively for many small time steps until convergence is achieved. The remaining integrals are solved stochastically using Monte Carlo techniques, by averaging over a large number of configurations, or walkers, that are simultaneously evolved in imaginary time. Hence, this method is called Quantum Monte Carlo method. Each walker is propagated along a path sampled according to the Gaussian factor in the integral and observables are calculated once convergence is reached. During the evolution, additional techniques like importance sampling and branching are implemented to improve convergence and reduce the computational cost.

For fermionic systems of interest in nuclear physics, the wave function is antisymmetric and contains many changes in sign. Hence, the integrands in the previous QMC integrals are highly oscillatory and lead to very large statistical uncertainties, so that no information can be obtained from the calculation. This is known as the fermion sign problem. The QMC algorithms I discuss here need the trial wave function to have a definite sign to mediate the sign problem. In practice, the wave function space is split into regions of positive and negative wave functions, defining a nodal surface at which the wave function changes sign. Generally, walkers that cross the nodal surface are removed from the evolution. This approximation is called fixed-node approximation [82, 83]. A generalization of this approximation to complex wave functions is called constrained-path method [84–86], constraining the path of walkers to regions of space where the overlap of walker and the trial wave function has a positive real part. In the following, I will present results that were obtained using the constrained-path method.

To estimate the impact of this approximation, one can perform a so-called unconstrained evolution after the constrained-path evolution is completed. In this process, the approximation is abandoned and the walkers are allowed to cross the nodal surface. The simulation is performed until the sign problem creates noise that is too large. If a good trial wave function was chosen in the beginning of the QMC calculation, the change from the constrained to unconstrained result is very small, because the nodal surface of the trial wave function is sufficiently close to the nodal surface of the true ground state. In that case, the constrained-path approximation is good and leads to results close to the true answer.

In **Figure 3**, I show an example for the ground-state energy of ^{4}He from Lynn et al. [89]. In the example, first a constrained-path evolution was performed using the GFMC method until an imaginary time of $\tau \approx 0.5$ MeV^{-1}. It can be seen that the energy drops fast and levels off after sufficiently large imaginary times. At this point in the evolution, all excited state contributions have been projected out and differences to the true ground-state energy are due to the constrained-path approximation. Afterwards, an unconstrained evolution was performed, which is shown in more detail in the inset. The unconstrained evolution presents only a small correction to the constrained result, which highlights the quality of the trial wave function in this case. This does not need to be the case, as I show in the right panel of **Figure 3**, where the unconstrained evolution is presented for a calculation of ^{16}O using AFDMC. In this case, the trial wave function leads to a constrained-path result far from the true ground state of the system (at $\tau = 0$), and the unconstrained evolution is necessary to extract the final answer.

Typically, the unconstrained evolution is very important for nuclei and considered less important when calculating nuclear matter relevant for astrophysics. Hence, in the following I will only show results obtained using the constrained-path evolution. However, please see Piarulli et al. [79] for a recent analysis of the quality of the constrained-path approximation when calculating neutron matter with realistic Hamiltonians.

In the following, I will explain how a Quantum Monte Carlo calculation is done in practice. The first step of a QMC calculation of infinite matter is a Variational Monte Carlo (VMC) calculation. The VMC method is used to calculate the properties of the given many-body system starting from a trial wave function, Ψ_V, which is usually chosen of the form

$$|\Psi_V(\mathbf{R})\rangle = \left[F_C + F_2 + F_3\right]|\Phi(\mathbf{R})\rangle \,, \tag{19}$$

where the factor F_C accounts for all the central spin/isospin-independent correlations, and F_2 and F_3 are linear spin/isospin two- and three-body correlations; see Carlson et al. [17] for details. The part $\left|\Phi(\mathbf{R})\right\rangle$ is usually given by a Slater determinant,

$$\left|\Phi(\mathbf{R})\right\rangle = \mathcal{A}\left[\prod_i \left|\phi_\alpha(\mathbf{r}_i, s_i)\right\rangle\right] , \tag{20}$$

where the index α labels the single-particle states which depend on the studied system, and set the correct quantum numbers. For nuclear matter of interest here, $|\Phi\rangle$ is built from a Slater determinant of plane-wave states with momenta k_i. The k_i are given by quantized momenta in a finite box with periodic boundary conditions, whose dimensions are determined by the chosen density and number of particles. The choice of periodic boundary conditions allows to study the infinite system [76]. The energy at the VMC level can be calculated as

$$E_V = \frac{\langle\Psi_V|H|\Psi_V\rangle}{\langle\Psi_V|\Psi_V\rangle} = \frac{\sum_{\sigma\tau}\int \mathrm{d}\mathbf{R}\Psi_V^*(\mathbf{R},\sigma,\tau)H\Psi_V(\mathbf{R},\sigma,\tau)}{\sum_{\sigma\tau}\int \mathrm{d}\mathbf{R}\Psi_V^*(\mathbf{R},\sigma,\tau)\Psi_V(\mathbf{R},\sigma,\tau)} , \tag{21}$$

and provides an upper bound to the true ground-state energy, $E_0 \leq E_V$. Here, $\sigma = \{\sigma_1 \ldots \sigma_N\}$, and $\tau = \{\tau_1 \ldots \tau_N\}$ include all particles' spins σ_i, and isospins τ_i. The above equation can be written as

$$E_V = \frac{\sum_{\sigma\tau}\int \mathrm{d}\mathbf{R}P(\mathbf{R},\sigma,\tau)H\Psi_V(\mathbf{R},\sigma,\tau)/\Psi_V(\mathbf{R},\sigma,\tau)}{\sum_{\sigma\tau}\int \mathrm{d}\mathbf{R}P(\mathbf{R},\sigma,\tau)} , \tag{22}$$

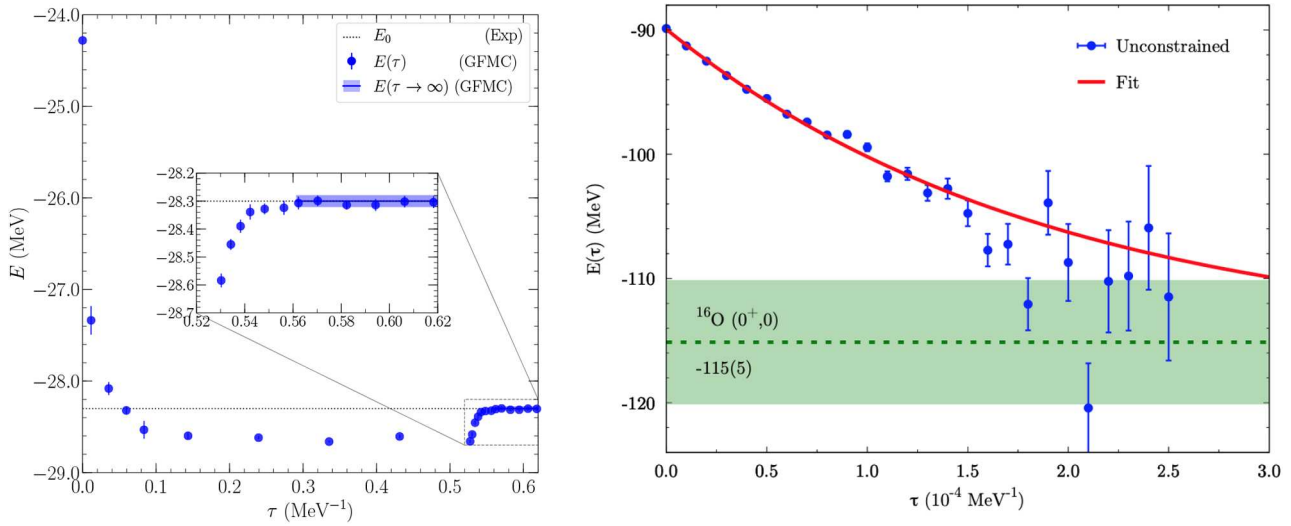

FIGURE 3 | Left: The imaginary time evolution for the ground state energy of ^{4}He in the GFMC method using the local chiral two- and three-nucleon interactions of Gezerlis et al. [87], Gezerlis et al. [88], and Lynn et al. [3] at cutoff $R_0 = 1.0$ fm. The figure shows the constrained evolution, i.e., an evolution where the nodal surface is fixed, while the inset shows the unconstrained evolution. Reprinted figure with permission from Lynn et al. [89]. Copyright 2017 by the American Physical Society. **Right**: The unconstrained evolution for the ground-state energy of ^{16}O in the AFDMC method (blue points) using the same local interactions. The red line represents an exponential fit to the data to extrapolate to the final result (green band). Reprinted figure with permission from Lonardoni et al. [90]. Copyright 2018 by the American Physical Society.

where $P(\mathbf{R}, \sigma, \tau)$ is a probability distribution. Typically, one chooses, $P(\mathbf{R}, \sigma, \tau) = \Psi_V^*(\mathbf{R}, \sigma, \tau)\Psi_V(\mathbf{R}, \sigma, \tau)$. The probability distribution P is then used to sample the configurations that are used to stochastically solve the multidimensional integral by employing Monte Carlo integration methods, e.g., the Metropolis algorithm.

It is obvious that the results of a VMC calculation depend strongly on the choice of the variational wave function, because no diffusion as described in the beginning of this section is performed. However, since the VMC method offers an upper bound to the true ground state of the system, it allows to improve the variational wave function for a given system, which feeds into all subsequent parts of the calculation. This is done by varying all the parameters that describe the trial wave function, e.g., the correlations in Equation (19), and minimizing the variational energy. For the optimal set of variational parameters, the optimized trial wave function serves as input for the next step of the calculation, where diffusion Monte Carlo methods are used to perform the imaginary time evolution.

The most accurate diffusion Monte Carlo technique is GFMC, where each walker contains not only the nucleon positions but also a complex amplitude for each possible $2^A\binom{A}{Z}$ spin-isospin configuration of the A nucleons including Z protons. In particular, in addition to the Monte Carlo integration over all spatial coordinates described above, summations in spin-isospin space are performed explicitly in GFMC. Because nuclear forces contain quadratic spin-isospin operators, components for all possible nucleon pairs have to be retained and accounted for explicitly. Hence, the scaling of the GFMC method with A is exponential, which makes it suitable to study light nuclei but unsuitable to study systems with large numbers of nucleons, like nucleonic matter. GFMC calculations are presently limited to 12 nucleons or 16 neutrons [91].

Instead, for nuclear matter discussed in this contribution, the AFDMC method [74] is more suitable. In AFDMC, all the summations in spin-isospin space are performed stochastically and quadratic spin-isospin dependences are linearized, which improves the scaling behavior but at the cost of less accuracy. This is made possible by using a Hubbard-Stratonovich transformation for an operator O,

$$\exp\left(-\frac{1}{2}\lambda\hat{O}^2\right) = \frac{1}{\sqrt{2\pi}}\int \mathrm{d}x \exp\left(-\frac{x^2}{2} + \sqrt{-\lambda}x\hat{O}\right) . \quad (23)$$

As a consequence, dependences on spin-isospin operators can be changed from quadratic to linear, at the cost of additional integrations over the variables x_i, called auxiliary fields. The Hubbard-Stratonovich transformation is exact when the integrals are exactly solved, but only statistically exact when Monte Carlo sampling is used like in the AFDMC method. As a consequence of applying the Hubbard-Stratonovich transformation, the wave function can be written as a product of single-particle spin-isospin states, which is a large simplification and improves the scaling behavior from exponential like in GFMC to linear or polynomial in the nucleon number A.

Following Schmidt and Fantoni [74] and considering only quadratic spin, isospin, and tensor operators, the potential can be written as

$$V = V_{SI} + \frac{1}{2}\sum_{i\alpha,j\beta}\sigma_{i\alpha}A^{(\sigma)}_{i\alpha,j\beta}\sigma_{j\beta} + \frac{1}{2}\sum_{i\alpha,j\beta}\sigma_{i\alpha}A^{(\sigma\tau)}_{i\alpha,j\beta}\sigma_{j\beta}\tau_i\cdot\tau_j + \frac{1}{2}\sum_{i,j}A^{(\tau)}_{i,j}\tau_i\cdot\tau_j , \quad (24)$$

where the first term contains all spin-isospin-independent parts of the interaction, the second term absorbs the isospin-independent but spin-dependent parts, and so on. Here, Latin indices label nucleons and Greek indices label Cartesian components. For the m eigenvectors and eigenvalues of these matrices, one finds

$$\sum_{j\beta} A^{(\sigma)}_{i\alpha,j\beta}\psi^{(\sigma)}_{m,j\beta} = \lambda^{(\sigma)}_m \psi^{(\sigma)}_{m,i\alpha}\,, \tag{25}$$

$$\sum_{j\beta} A^{(\sigma\tau)}_{i\alpha,j\beta}\psi^{(\sigma\tau)}_{m,j\beta} = \lambda^{(\sigma\tau)}_m \psi^{(\sigma\tau)}_{m,i\alpha}\,, \tag{26}$$

$$\sum_{j} A^{(\tau)}_{i,j}\psi^{(\tau)}_{m,j} = \lambda^{(\tau)}_m \psi^{(\tau)}_{m,i}\,. \tag{27}$$

For the matrices $A^{(\sigma)}_{i\alpha,j\beta}$ and $A^{(\sigma\tau)}_{i\alpha,j\beta}$ the index m ranges from 1 to $3A$, while there are A eigenvectors and eigenvalues for the matrix $A^{(\tau)}_{i,j}$. Using this set of eigenvectors and the eigendecomposition of the A matrices, the potential can be rewritten as

$$V = V_{SI} + \frac{1}{2}\sum_{m=1}^{3A} O^{(\sigma)2}_m \lambda^{(\sigma)}_m + \frac{1}{2}\sum_{\alpha=1}^{3}\sum_{m=1}^{3A} O^{(\sigma\tau)2}_{m\alpha}\lambda^{(\sigma\tau)}_m + \frac{1}{2}\sum_{\alpha=1}^{3}\sum_{m=1}^{A} O^{(\tau)2}_{m\alpha}\lambda^{(\tau)}_m\,, \tag{28}$$

where

$$O^{(\sigma)}_m = \sum_{j\beta}\sigma_{j\beta}\psi^{(\sigma)}_{m,j\beta}\,, \tag{29}$$

$$O^{(\sigma\tau)}_{m\alpha} = \sum_{j\beta}\tau_{j\alpha}\sigma_{j\beta}\psi^{(\sigma\tau)}_{m,j\beta}\,, \tag{30}$$

$$O^{(\tau)}_{m\alpha} = \sum_{j}\tau_{j\alpha}\psi^{(\tau)}_{m,j}\,. \tag{31}$$

The Hubbard-Stratonovich transformation is now applied to this interaction to linearize all spin-isospin dependences. Hence, wave functions only need to depend on single-particle spinors,

$$|\mathbf{s}_i\rangle = a_i\left|p\uparrow\right\rangle + b_i\left|p\downarrow\right\rangle + c_i\left|n\uparrow\right\rangle + d_i\left|n\downarrow\right\rangle\,. \tag{32}$$

This allows to treat $\mathcal{O}(10)$-$\mathcal{O}(100)$ nucleons in AFDMC.

When calculating nuclear matter, one typically simulates N particles in a cubic box with size L, where L is determined in such a way that the number density n in the box reflects a chosen value, $L = (N/n)^{1/3}$. To avoid finite-size effects, the particle number N has to be chosen sufficiently large to probe the thermodynamic limit. As stated before, for nuclear matter the trial wave function is constructed from plane waves in a box with periodic boundary conditions (the implementation of twist-averaged boundary conditions [92] is currently explored). For periodic boundary conditions, the momenta are defined as $\mathbf{k}_i = \frac{2\pi}{L}(n_x, n_y, n_z)$. Here, the numbers n_x, n_y, and n_z are integer numbers. In this case, the system acquires a shell structure, and the shell number is given by $I = n_x^2 + n_y^2 + n_z^2$. Typically, since a homogenic and isotropic system is considered, calculations are only performed with closed shells. For $I = 0$ there is one combination of n_x, n_y, and n_z, for $I = 1$ there are six combinations, etc. Then, shell closures are given for 1, 7, 19, 27, 33, etc. particles for a given spin-isospin configuration. In pure neutron matter, this leads to shell closures for $N = 2, 14, 38, 54, 66$, etc., as neutrons can be spin-up and spin-down. Due to growing computational costs associated with larger and larger particle numbers, for neutron matter one typically chooses $N = 66$ (33 spin up and 33 spin down neutrons). When comparing results for the free Fermi gas in a box as a function of particle number, it was found that $N = 66$ gives results close to the thermodynamic limit [75, 93].

3.2. Local Chiral Interactions

In addition to the many-body method, it is necessary to specify a model for the nuclear interaction that defines the interaction terms in Equation (8). In the past, Quantum Monte Carlo methods have been used with phenomenological interactions of the Argonne type [94, 95] and 3N interactions of the Urbana [96] and Illinois [97] families with great success. However, the last years have seen the development of new local interactions within the framework of chiral effective field theory (EFT) [3, 87, 88, 98–100]. This enabled QMC calculations with a much greater number of nuclear interactions. While the interactions are not the focus of this review, in this section I briefly discuss local chiral interactions. For more details, I refer the reader to the more detailed reviews in Lynn et al. [72] and Piarulli et al. [101].

Chiral EFT [18–20] is a low-energy effective theory for QCD in terms of nucleon and pion degrees of freedom. It is naturally formulated in momentum space in terms of the momentum transfer $\mathbf{q} = \mathbf{p}' - \mathbf{p}$ and the momentum transfer in the exchange channel, $\mathbf{k} = (\mathbf{p} + \mathbf{p}')/2$, where $\mathbf{p}$ and $\mathbf{p}'$ are the average momenta of the incoming and outgoing particles. When performing a Fourier transformation to coordinate space, all $\mathbf{q}$ dependences transform to dependences on the relative distance of particles i and j, $\mathbf{r} = \mathbf{r}_i - \mathbf{r}_j$ and, hence, are local, while $\mathbf{k}$ dependences transform to gradients and, hence, non-localities. As a consequence, to implement a chiral interaction in QMC methods the interaction can only depend on $\mathbf{q}$.

Chiral EFT is grounded in a separation of scales between the typical momentum scale of nucleons in nuclear systems $\mathbf{Q}$, of the order of the pion mass, $\mathbf{Q} \sim m_\pi$, and high-energy scales that denote the appearance of new degrees of freedom that are not explicitly accounted for in chiral EFT. The appearance of these high-energy degrees of freedom is marked by the so-called breakdown scale Λ_b, and beyond this scale, chiral EFT interactions can not be reliably employed in many-body calculations anymore. The nuclear interaction is then expanded in terms of $(\mathbf{Q}/\Lambda_b)^\nu$ according to a so-called power counting scheme. This scheme leads to a systematic expansion for nuclear interactions that makes chiral EFT very powerful. First, one can work up to a desired accuracy by going to higher and higher orders in the expansion. Second, one can estimate theoretical uncertainties based on the order-by-order contributions to a certain observable [102]. Another powerful advantage of chiral EFT interactions is that many-body forces naturally appear in

the expansion and are intimately connected to the two-nucleon sector. This provides a systematic guiding principle to improve all individual parts of the nuclear Hamiltonian, in contrast to phenomenological interactions.

In chiral EFT, all the unresolved, short-range, high-energy physics beyond the breakdown scale is parameterized by a set of short-range contact operators among nucleons, which obey all the relevant symmetries [101]. For example, at leading order (LO), where $\nu = 0$ and the interaction is momentum-independent, the contact part is given by

$$V_{\rm cont}^{\rm LO}(\mathbf{q},\mathbf{k}) = V_{\rm cont}^{\rm LO} = \alpha_1 \mathbb{1} + \alpha_2\, \boldsymbol{\sigma}_1\cdot\boldsymbol{\sigma}_2 + \alpha_3\, \boldsymbol{\tau}_1\cdot\boldsymbol{\tau}_2 + \alpha_4\, \boldsymbol{\sigma}_1\cdot\boldsymbol{\sigma}_2\, \boldsymbol{\tau}_1\cdot\boldsymbol{\tau}_2\,, \tag{33}$$

where the α_i are low-energy couplings (LECs) that absorb the contributions of high-energy degrees of freedom. These LECs are typically fit once to experimental data, e.g., *NN* scattering phase shifts or cross sections. The resulting Hamiltonian can then be used to make predictions for all nuclear systems, e.g., the nuclear matter of interest to this contribution. At next-to-leading order (NLO), where $\nu = 2$, the contact interactions are momentum-dependent:

$$\begin{aligned} V_{\rm cont}^{\rm NLO}(\mathbf{q},\mathbf{k}) \;=\; & \gamma_1\, q^2 + \gamma_2\, q^2\, \boldsymbol{\sigma}_1\cdot\boldsymbol{\sigma}_2 + \gamma_3\, q^2\, \boldsymbol{\tau}_1\cdot\boldsymbol{\tau}_2 \\ & + \gamma_4\, q^2 \boldsymbol{\sigma}_1\cdot\boldsymbol{\sigma}_2 \boldsymbol{\tau}_1\cdot\boldsymbol{\tau}_2 + \gamma_5\, k^2 + \gamma_6\, k^2\, \boldsymbol{\sigma}_1\cdot\boldsymbol{\sigma}_2 \\ & + \gamma_7\, k^2\, \boldsymbol{\tau}_1\cdot\boldsymbol{\tau}_2 + \gamma_8\, k^2 \boldsymbol{\sigma}_1\cdot\boldsymbol{\sigma}_2 \boldsymbol{\tau}_1\cdot\boldsymbol{\tau}_2 \\ & + \gamma_9\, (\boldsymbol{\sigma}_1+\boldsymbol{\sigma}_2)(\mathbf{q}\times\mathbf{k}) + \gamma_{10}\, (\boldsymbol{\sigma}_1+\boldsymbol{\sigma}_2)(\mathbf{q}\times\mathbf{k})\boldsymbol{\tau}_1\cdot\boldsymbol{\tau}_2 \\ & + \gamma_{11}(\boldsymbol{\sigma}_1\cdot\mathbf{q})(\boldsymbol{\sigma}_2\cdot\mathbf{q}) + \gamma_{12}(\boldsymbol{\sigma}_1\cdot\mathbf{q})(\boldsymbol{\sigma}_2\cdot\mathbf{q})\boldsymbol{\tau}_1\cdot\boldsymbol{\tau}_2 \\ & + \gamma_{13}(\boldsymbol{\sigma}_1\cdot\mathbf{k})(\boldsymbol{\sigma}_2\cdot\mathbf{k}) \\ & + \gamma_{14}(\boldsymbol{\sigma}_1\cdot\mathbf{k})(\boldsymbol{\sigma}_2\cdot\mathbf{k})\boldsymbol{\tau}_1\cdot\boldsymbol{\tau}_2\,, \end{aligned} \tag{34}$$

where the γ_i are the LECs at NLO.

In addition to contact interactions, chiral EFT explicitly includes long-range pion exchange contributions. At LO for example, chiral interactions include the one-pion-exchange interaction (OPE), given in momentum space by

$$V_{\rm OPE}^{(0)}(\mathbf{q}) = -\frac{g_A^2}{4f_\pi^2}\frac{\boldsymbol{\sigma}_i\cdot\mathbf{q}\boldsymbol{\sigma}_j\cdot\mathbf{q}}{q^2+m_\pi^2}\boldsymbol{\tau}_i\cdot\boldsymbol{\tau}_j\,, \tag{35}$$

where g_A is the axial-vector coupling constant of the nucleon, f_π is the pion decay constant, and m_π is the pion mass. Similarly to the short-range part, at higher orders more involved pion exchange contributions need to be accounted for.

These interactions are then Fourier transformed from momentum to coordinate space. To implement chiral interactions in QMC methods, local interactions need to be constructed. There are two sources of possible non-localities: (i) non-local operators that depend on $\mathbf{k}$, see, e.g., Equation (34), or (ii) non-localities originating in the choice of so-called regulator functions, that are necessary in many-body calculations to cut off diverging momentum dependences.

The first source of non-localities can be avoided by choosing a local set of contact interactions. Let me explain the basic idea. Since chiral forces describe fermionic interactions that are typically used between antisymmetrized wave functions, it is intuitive to define the antisymmetrized interaction $V_{\rm as} = 1/2\ (V - \mathcal{A}[V])$, with the antisymmetrizer

$$\begin{aligned} \mathcal{A}[V(\mathbf{q},\mathbf{k})] \;=\; & \frac{1}{4}(1+\boldsymbol{\sigma}_i\cdot\boldsymbol{\sigma}_j)(1+\boldsymbol{\tau}_i\cdot\boldsymbol{\tau}_j) \\ & \times V\left(\mathbf{q}\to -2\mathbf{k}, \mathbf{k}\to -\frac{1}{2}\mathbf{q}\right). \end{aligned} \tag{36}$$

Constructing the antisymmetrized LO interaction, one obtains

$$\begin{aligned} V_{\rm cont,as}^{(0)} &= \frac{1}{2}\left(1-\frac{1}{4}(1+\boldsymbol{\sigma}_i\cdot\boldsymbol{\sigma}_j)(1+\boldsymbol{\tau}_i\cdot\boldsymbol{\tau}_j)\right) V_{\rm cont}^{(0)} \\ &= \left(\frac{3}{8}\alpha_1 - \frac{3}{8}\alpha_2 - \frac{3}{8}\alpha_3 - \frac{9}{8}\alpha_4\right) \\ &+ \left(-\frac{1}{8}\alpha_1 + \frac{5}{8}\alpha_2 - \frac{3}{8}\alpha_3 + \frac{3}{8}\alpha_4\right)\boldsymbol{\sigma}_i\cdot\boldsymbol{\sigma}_j \\ &+ \left(-\frac{1}{8}\alpha_1 - \frac{3}{8}\alpha_2 + \frac{5}{8}\alpha_3 + \frac{3}{8}\alpha_4\right)\boldsymbol{\tau}_i\cdot\boldsymbol{\tau}_j \\ &+ \left(-\frac{1}{8}\alpha_1 + \frac{1}{8}\alpha_2 + \frac{1}{8}\alpha_3 + \frac{3}{8}\alpha_4\right)\boldsymbol{\sigma}_i\cdot\boldsymbol{\sigma}_j\,\boldsymbol{\tau}_i\cdot\boldsymbol{\tau}_j \\ &= \tilde{C}_S + \tilde{C}_T\,\boldsymbol{\sigma}_i\cdot\boldsymbol{\sigma}_j + \left(-\frac{2}{3}\tilde{C}_S - \tilde{C}_T\right)\boldsymbol{\tau}_i\cdot\boldsymbol{\tau}_j \\ &+ \left(-\frac{1}{3}\tilde{C}_S\right)\boldsymbol{\sigma}_i\cdot\boldsymbol{\sigma}_j\,\boldsymbol{\tau}_i\cdot\boldsymbol{\tau}_j\,. \end{aligned} \tag{37}$$

Hence, one finds that if the LO chiral interactions are used between antisymmetrized wave functions, only two out of the four couplings are linearly independent. This is also intuitive, as the LO interactions describe the two possible *S*-wave scattering channels. As a consequence, it is sufficient to choose two out of the four operators and the common choice is

$$V_{\rm cont}^{(0)} = C_S + C_T\boldsymbol{\sigma}_i\cdot\boldsymbol{\sigma}_j\,. \tag{38}$$

Similarly, at NLO, it is possible to choose only 7 out of the 14 operators given in Equation (34). To construct local interactions, one chooses the 6 local terms as well as the spin-orbit interaction $\sim \gamma_9$ that can be treated within QMC methods. All the additional operator structures are then generated through antisymmetrization. Furthermore, pion-exchange interactions are local up to next-to-next-to-leading order ($\rm N^2LO$).

To avoid the non-localities due to the choice of regulator function, one typically defines these functions directly in coordinate space, e.g., by

$$f_{\rm long}(r) = \left(1-e^{-\left(\frac{r}{R_0}\right)^{n_1}}\right)^{n_2}, \quad f_{\rm short}(r) = \frac{n}{4\pi\, R_0^3\,\Gamma\left(\frac{3}{n}\right)}\, e^{-\left(\frac{r}{R_0}\right)^n}, \tag{39}$$

where $f_{\rm long}(r)$ is a long-range regulator and $f_{\rm short}(r)$ is a short-range regulator, and R_0 is the cutoff scale. The long-range regulator function is applied to pion-exchange contributions, and cuts off short-range divergences $\sim 1/r^{3n}$, while the short-range regulator smears out short-range delta-like contact interactions. When applying these regulator functions, regulator artifacts might appear that have to be carefully analyzed [103, 104].

It can be shown that it is possible to construct local chiral interactions up to N^{2}LO [87, 88, 98, 100] using the ideas described above. These interactions can then be used in QMC methods. The N^{2}LO interactions used in the following describe nucleon-nucleon phase shifts up to laboratory energies of 500 MeV within uncertainties, except the triplet D-wave phase shifts. To properly describe these phase shifts, it is necessary to construct interactions at next-to-next-to-next-to-leading order (N^{3}LO), because only at that order D-wave contact interactions appear. At N^{3}LO, however, only 8 out of 30 operators are local and, hence, there are too many non-local operators for this approach to work. Possible solutions are the definition of maximally local potentials [6], or the perturbative treatment of non-localities. The continued development of local chiral interactions is work in progress. However, I would like to stress that when describing neutron matter the triplet D waves vanish.

A detailed discussion of local interactions is not within the scope of this contribution and I refer the interested reader to Piarulli and Tews [101], where the derivation of local chiral interactions in both the delta-full and delta-less approaches (i.e, including explicitly delta-isobar degrees of freedom or not) is explained. In addition, Piarulli and Tews [101] explains the regularization scheme and appearing regulator artifacts in great detail. Local chiral interactions have been successfully used in calculations of nuclei [6, 7, 90] and I refer to Lynn et al. [72] for a review of recent results. In section 4, I will show how to use QMC calculations with chiral interactions to understand neutron stars.

3.3. Strengths and Weaknesses of the QMC Approach

Before discussing results, I would like to discuss strengths and weaknesses of the QMC approach with local chiral interactions compared to other many-body approaches mentioned before.

A major weakness of QMC methods is that they can only employ local interactions. This makes many contemporary nuclear Hamiltonians, especially many chiral Hamiltonians, not suitable at the moment. For example, as stated before, this currently limits the order of the chiral interactions employed in QMC methods to be below N^{3}LO, while other many-body methods can typically employ interactions at higher orders. The need for local interactions presents a very strong limitation of QMC methods, and leads to additional problems, e.g., the appearance of regulator artifacts due to the violation of Fierz rearrangement freedom [104]. These regulator artifacts increase the uncertainties of the calculations [3].

However, even though QMC methods can only explore local interactions up to N^{2}LO, they are capable of solving the many-body problem also for hard, high-cutoff interactions in an accurate and precise manner. While other many-body methods, can employ a wider range of interactions, they are typically limited to perturbative, low-cutoff interactions, for which these methods converge. Typically, bare chiral interactions have large Weinberg eigenvalues [105] and need to be softened to be implemented in most many-body methods. This is done by either employing low cutoffs of the order of 400 MeV from the start or by using softening transformations, e.g., the similarity RG (SRG). The ability to employ hard and/or bare interactions presents a major strength of QMC methods.

Work on constructing N^{3}LO interactions for QMC methods is under way, see, e.g., Piarulli et al. [6]. Furthermore, work on high-cutoff local interactions is in progress, which will allow to explore cutoff regions where regulator choices become less important and where uncertainties from regulator artifacts are reduced [106].

4. RESULTS FOR NEUTRON STARS

4.1. The Dense-Matter Equation of State

To describe neutron stars, one needs access to the EOS, i.e., the relation of energy density and pressure; see section 2. In the following I will discuss how to extract this information from QMC simulations of nuclear matter.

Quantum Monte Carlo simulations are typically performed for A nucleons in a box with volume $V = L^3$. The result of these simulations is the total energy per nucleon in the box, E/A, as a function of the number density $n = A/V$ and the chosen proton fraction, $x = n_p/(n_n + n_p) = Z/A$, where n_p is the proton density, n_n is the neutron density, and Z is the number of protons in the box. The proton fraction determines the ratio of protons to neutrons, and is typically less than 10% in the core of neutron stars. Given the quantity $E/A(n, x)$, it is easy to reconstruct the energy density and pressure:

$$\epsilon = \frac{m_N \cdot A + E}{V} = n \cdot \left(m_N + \frac{E}{A} \right) , \tag{40}$$

$$p = -\frac{\partial E}{\partial V} = n^2 \frac{\partial E/A}{\partial n} . \tag{41}$$

The proton fraction is determined by the β-equilibrium between protons, neutrons, and electrons and results from the condition

$$\mu_n(n, x) = \mu_p(n, x) + \mu_e(n, x) , \tag{42}$$

where the μ_i are the chemical potentials of neutrons, protons, and electrons, respectively. The chemical potential can also be obtained from $E/A(n, x)$. At a given density, Equation (42) determines the proton fraction x. Hence, if one calculates $E/A(n, x)$, one can obtain $p(n)$ and $\epsilon(n)$ in β-equilibrium, and from this the EOS.

Ideally, a calculation of $E/A(n, x)$ at arbitrary proton fraction would be desirable to compute the EOS in β equilibrium. However, this is computationally expensive because several values of x would need to be computed for each density. Furthermore, with the addition of protons, interactions become more complicated to treat in QMC methods for nucleonic matter. For neutron stars, due to the small proton fraction, one generally starts from calculations of the pure neutron system with $x = 0$, called pure neutron matter (PNM), because the calculation is much easier as only certain parts of the interaction contribute. The AFDMC method is ideally suited to study pure neutron systems, and has been extensively used in the past for calculations of neutron drops and PNM [3, 33, 75, 76, 79, 99, 107, 108]. From PNM, one can typically extrapolate to small proton fractions

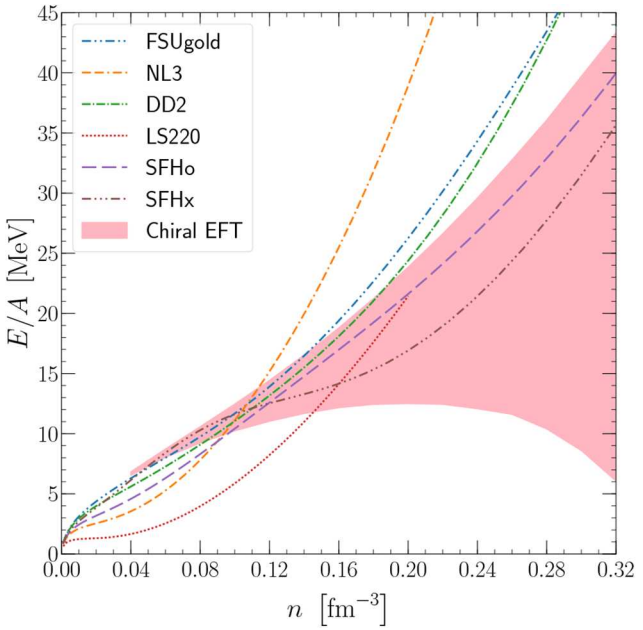

FIGURE 4 | EOS of PNM obtained from QMC calculations with local chiral interactions at N^{2}LO from Tews et al. [33]. The band indicates the theoretical uncertainty of the calculation, which mainly originates in the uncertainty of the nuclear interaction [3]. The chiral EFT band is compared with several model EOS for astrophysical calculations. Republished with permission of IOP Publishing, from Gandolfi et al. [30]; permission conveyed through Copyright Clearance Center, Inc.

by using empirical information from symmetric nuclear matter (SNM) with $x = 1/2$:

$$\frac{E}{A}(n,x) = E_{\mathrm{SNM}}(n) + (1-2x)^2 S(n)\,, \tag{43}$$

where $S(n) = E_{\mathrm{PNM}}(n) - E_{\mathrm{SNM}}(n)$ is the symmetry energy and denotes the difference between SNM and PNM. The SNM EOS can be expanded around saturation density as

$$E_{\mathrm{SNM}}(n) = E_0 + \frac{K_0}{2!}\left(\frac{n-n_0}{3n_0}\right)^2 + \mathcal{O}(n^3)\,, \tag{44}$$

where $E_0 \approx -16$ MeV, $n_0 \approx 0.16$ fm^{-3}, and $K_0 \approx 230$ MeV are empirical parameters that can be constrained experimentally. Using this information, the EOS of PNM can be easily extended to the small proton fractions of the order of 5% in β-equilibrium; see also Hebeler et al. [109]. I would like to note that, instead of using empirical values for the SNM parameters, it is also possible to calculate these parameters using QMC methods and local chiral interactions. This has very recently been achieved in Lonardoni et al. [80].

In **Figure 4**, I show AFDMC results for the energy per particle for 66 neutrons in a box as a function of density [3, 33]. The results have been obtained with local chiral interactions at N^{2}LO with coordinate-space cutoff $R_0 = 1.0$ fm (red band), where the band denotes the theoretical uncertainty from the nuclear interactions as estimated from the order-by-order results [102]. In addition, the results are compared to results for astrophysical model EOS that are commonly used in astrophysical simulations: the Lattimer-Swesty EOS with incompressibility $K = 220$ [110], the TM1, SFHo, and SFHx EOSs (Hempel, private communication), the FSU and NL3 EOSs (Shen, private communication), and the DD2 EOS (Typel, private communication). It is obvious that the QMC calculations put strong constraints on the EOS of PNM, and disfavor several EOS, in particular EOS that lead to large pressures (large slopes of E/A with density). The L parameter, which is defined as the slope of the symmetry energy at saturation density and is connected to the pressure of PNM at saturation density, is found to lie in the range $L = 24 - 68$ MeV [80]. The calculation of PNM is now the starting point to construct the neutron-star EOS.

To study neutron stars, we have to extend these calculations threefold. First, as discussed before, we have to extend the PNM EOS to finite proton fractions in β-equilibrium. Second, at low densities, neutron stars have a crust that consists of a lattice of nuclei and has to be taken into account. It is possible to replace the EOS at low densities, below $\approx 1/2n_{\mathrm{sat}}$, with phenomenological crust EOS models. In Tews [111], I have shown how to use neutron-matter calculations and information on SNM to construct a crust EOS with theoretical uncertainties in the Wigner-Seitz approximation. In this approximation, the Wigner-Seitz cell is modeled as a nucleus with density n_{nuc} and proton fraction x_{nuc} surrounded by a pure neutron phase in equilibrium. The two phases can be modeled using the results of many-body calculations and I refer the reader to Tews [111] for more details. The results of this crust model are also in excellent agreement with phenomenological crust models. This crust EOS replaces the EOS at low densities. Third and final, as one can see in **Figure 4**, the uncertainty from calculations with chiral EFT interactions grows fast with density because momenta approach the breakdown scale. Beyond approximately $2n_{\mathrm{sat}}$, calculations with local chiral interactions are not reliable anymore [33].

To reliably extract neutron-star properties, it is crucial to find a way of extending QMC calculations to higher density in a model-agnostic way, to avoid introducing any systematic uncertainties. In Tews et al. [33, 50, 59], we have developed an extension of QMC calculations to higher densities using the speed of sound c_S; see also Greif et al. [112]. This extension uses the QMC calculations, extended to β-equilibrium and including a crust, up to a certain density n_{tr}, which is varied between $1-2n_{\mathrm{sat}}$. From these results, the speed of sound up to n_{tr} is calculated. We do not know the speed of sound at higher densities, but we know that it has to be smaller then the speed of light, due to causality, and larger than 0, as the neutron star would otherwise be unstable: $0 \leq c_S \leq c$. Hence, by sampling many curves in the speed of sound plane, that are constrained up to n_{tr} by QMC calculations and above by $0 \leq c_S \leq c$, we can gauge the uncertainty in the neutron-star EOS. In practice, we sample these curves as piecewise linear segments in the speed-of-sound plane. From the resulting curves for c_S, we then can reconstruct the EOS and solve the TOV equations. The only observational requirement we enforce is that each EOS has to reproduce the heaviest observed neutron stars.

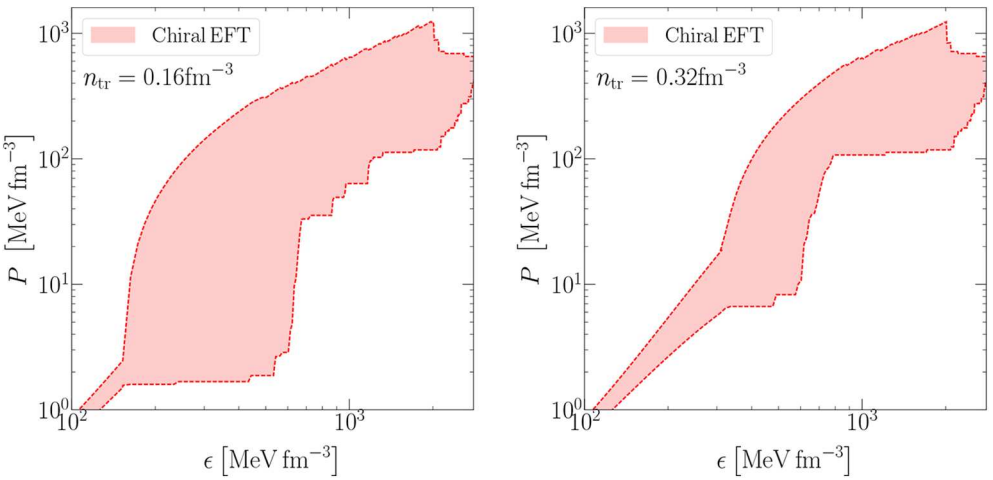

FIGURE 5 | Equation-of-state envelopes for $n_{tr} = n_{sat}$ **(left)** and $n_{tr} = 2n_{sat}$ **(right)**. Adapted by permission from Springer Nature, Tews et al. [50], copyright 2019.

I show the resulting EOS envelopes in **Figure 5** for $n_{tr} = n_{sat}$ (left panel) and $n_{tr} = 2n_{sat}$ (right panel). These envelopes include all EOS that are consistent with QMC calculations at low densities. The range where low-density constraints from QMC calculations are enforced can easily be identified from the plots. At larger densities, there is a great freedom for the EOS. However, even though uncertainties of the QMC calculations grow fast with density, the additional information from such calculations in the density range between $1 - 2n_{sat}$ constrains the EOS significantly.

4.2. Neutron-Star Structure

Using these two sets of EOSs and solving the TOV equations (2), we can obtain the masses and radii of neutron stars as constrained by microscopic QMC calculations with uncertainty estimates from chiral EFT. We show the resulting MR envelopes in **Figure 6** again for the cases $n_{tr} = n_{sat}$ (left panel) and $n_{tr} = 2n_{sat}$ (right panel). In the first case (left panel), the radius of a typical $1.4M_{\odot}$ neutron star is constrained to be between $8.4 - 15.2$ km. The maximum mass can reach values as high as 4 solar masses. It is interesting to note that the observation of heavy neutron stars directly impacts this uncertainty band, by ruling out too soft EOS. We indicate the excluded region by the gray-shaded area. The observation of heavier neutron stars, for example in Cromartie et al. [44], would allow to place even stronger constraints on soft EOS that produce low-radius neutron stars. Hence, neutron-star mass observations are a powerful tool to constrain the EOS of dense matter. However, even with such observations, the uncertainty remains quite large.

As in the EOS case, a possible improvement for the radius uncertainty is given by pushing the low-density constraints from QMC calculations to higher densities. We show the resulting MR envelope in the right panel of **Figure 6** (for $n_{tr} = 2n_{sat}$), where the gray-shaded area is shown for comparison. It is found that the radius range for a typical neutron star reduces to $8.7 - 12.6$ km, much narrower than in the previous case. In this case, the upper limit on the maximum mass reduces to $2.9M_{\odot}$.

4.3. Neutron-Star Mergers

Finally, I address the recently observed neutron-star merger GW170817 [46–49] and its impact on inferring the MR relation. Using the information obtained from GW170817 and its electromagnetic counterpart, the EOS in our set can be analyzed according to their consistency with the gravitational-wave and EM signals. In particular, the EM signal constrains the EOS twofold: it disfavors a prompt collapse of the merger remnant to a black hole (which requires the maximum mass to be sufficiently large) [60, 61] and it disfavors a longer-lived neutron star as merger product (which requires the maximum mass to be sufficiently small) [61, 62]. This allows to constrain each EOS by computing its threshold mass for prompt collapse to a black hole [113, 114], $M_{\rm thresh}$, comparing it with the total gravitational mass of GW170817, $M_{\rm tot}$, and keeping only EOS where $M_{\rm thresh} > M_{\rm tot}$. Also, each EOS is required to have a maximum mass below $2.3M_{\odot}$ [61, 62]. Enforcing the gravitational-wave constraints as well as the constraints due to the energetics of the kilonova using a Bayesian analysis [115], this approach allows one to compute a posterior probability for each EOS in our EOS sets. I show the results in **Figure 7**.

It is found that the gravitational-wave data from GW170817 constrains the maximum radius of neutron stars but is not informative for small radii [51, 116]. The observation of an electromagnetic counterpart for GW170817 and the deduction that there cannot have been a prompt collapse to a black hole, on the other hand, eliminates EOS that are too soft and produce a too small maximum mass, analogous to NS mass observations. This, in turn, places a lower limit on neutron-star radii. The upper limit on the maximum mass, however, does not significantly constrain the EOS posterior.

Assuming that local chiral EFT interactions remain valid up to nuclear saturation density, one finds that very stiff EOS can be ruled out by the tidal polarizability of GW170817. I show the results in the left panel of **Figure 7**. If, instead, local chiral EFT interactions remain valid up to twice nuclear saturation density,

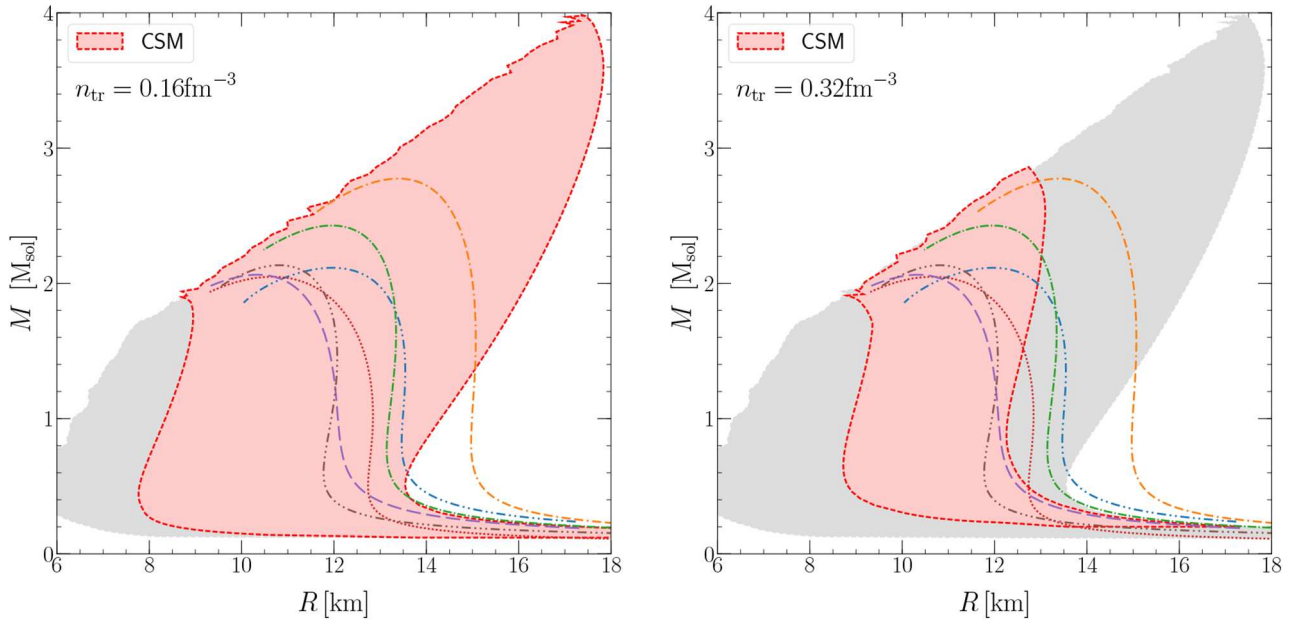

FIGURE 6 | Mass-radius envelopes for $n_{\rm tr} = n_{\rm sat}$ **(left)** and $n_{\rm tr} = 2n_{\rm sat}$ **(right)**. We show the EOS envelope given all constraints (red area), as well as the MR space that is ruled out by the two-solar mass constraint and/or when enforcing chiral EFT constraints up to larger densities (gray areas). The results are compared to the same EOSs shown in **Figure 4**. Adapted by permission from Springer Nature, Tews et al. [50], copyright 2019.

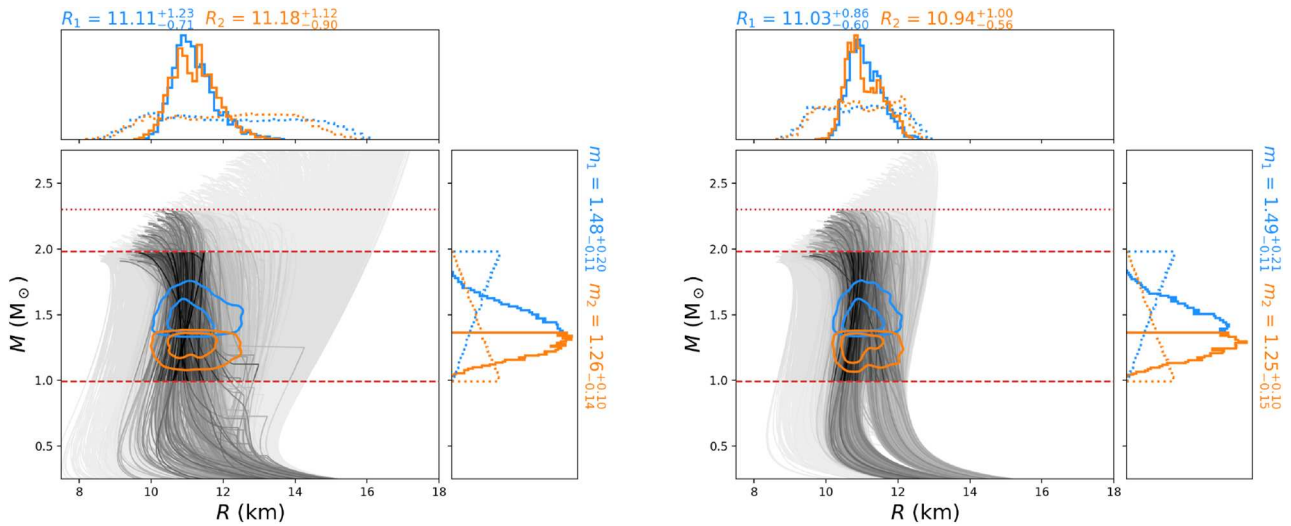

FIGURE 7 | Mass-radius posteriors after constraints from the binary neutron-star merger GW170817 are enforced for the EOS set with $n_{\rm tr} = n_{\rm sat}$ **(left)** and $n_{\rm tr} = 2n_{\rm sat}$ **(right)**. The shading of the individual MR curves corresponds to their posterior probability. The red-dashed lines indicate the mass range spanned by the prior, and the red-dotted line indicates the maximum neutron-star mass constraint as inferred from GW170817. The colored contours indicate the 50th and 90th percent credibility regions for the two neutron stars in GW170817, with the corresponding 1D marginalized posteriors plots on the sides. Figure taken from Capano et al. [115].

theoretical predictions for the EOS and gravitational-wave observations agree from the start, and enforcing gravitational-wave constraints does not impact the MR relation significantly (right panel of **Figure 7**). In both cases, the final results are consistent with each other and provide the most stringent constraints on the radius of a typical neutron star to date, $R_{1.4} = 11.0^{+0.9}_{-0.6}$ km.

5. CONCLUSION AND OUTLOOK

In this review, I have discussed how to use QMC methods in combination with local interactions from chiral effective field theory up to N^{2}LO to address the structure of neutron stars. I have shown how to obtain constraints on the EOS of dense matter, probed in the core of neutron stars,

from microscopic calculations, and how these constraints impact the mass-radius relation. I have addressed the impact of the observation of heavy two-solar-mas neutron stars and the first observed binary neutron-star merger and its electromagnetic counterpart.

Quantum Monte Carlo methods have proven to be a reliable tool to investigate the EOS of neutron and neutron-star matter. Its recent combination with interactions from chiral effective field theory allows to build a systematic framework for the EOS with theoretical uncertainty estimates. However, current uncertainties are still sizable due to limitations in the employed interactions. Results for the mass-radius relation highlight that theoretical predictions need to be improved in the density range between $1 - 2n_{\mathrm{sat}}$ in order to provide accurate theoretical predictions of neutron-star structure observables. Work to improve the interactions is under way.

AUTHOR CONTRIBUTIONS

The author confirms being the sole contributor of this work and has approved it for publication.

FUNDING

This work was supported by the US Department of Energy, Office of Science, Office of Nuclear Physics, under Contract DE-AC52-06NA25396, the Los Alamos National Laboratory (LANL) LDRD program, and the NUCLEI SciDAC program. This research used resources provided by the Los Alamos National Laboratory Institutional Computing Program, which is supported by the U.S. Department of Energy National Nuclear Security Administration under Contract No. 89233218CNA000001, and the National Energy Research Scientific Computing Center (NERSC), a DOE Office of Science User Facility supported by the Office of Science of the U.S. Department of Energy under Contract No. DE-AC02-05CH11231.

ACKNOWLEDGMENTS

I thank my collaborators D. A. Brown, S. M. Brown, C. Capano, J. Carlson, S. De, E. Epelbaum, S. Gandolfi, A. Gezerlis, K. Hebeler, L. Huth, B. Krishnan, S. Kumar, J. Lippuner, D. Lonardoni, J. E. Lynn, B. Margalit, J. Margueron, A. Nogga, S. Reddy, K. E. Schmidt, A. Schwenk, and A. W. Steiner for their contributions to the studies presented in this work.

REFERENCES

1. Hagen G, Ekström A, Forssén C, Jansen CR, Nazarewicz W, Papenbrock T, et al. Neutron and weak-charge distributions of the ^{48}Ca nucleus. *Nature Phys*. (2015) **12**:186–90. doi: 10.1038/nphys3529
2. Elhatisari S, Lee D, Rupak G, Epelbaum E, Krebs H, Lähde TA, et al. *Ab initio* alpha-alpha scattering. *Nature*. (2015) **528**:111. doi: 10.1038/nature16067
3. Lynn JE, Tews I, Carlson J, Gandolfi S, Gezerlis A, Schmidt KE, et al. Chiral three-nucleon interactions in light nuclei, neutron-α scattering, and neutron matter. *Phys Rev Lett*. (2016) **116**:062501. doi: 10.1103/PhysRevLett.116.062501
4. Klos P, Carbone A, Hebeler K, Menéndez J, Schwenk A. Uncertainties in constraining low-energy constants from^{3}H β decay. *Eur Phys J A*. (2017) **53**:168. doi: 10.1140/epja/i2017-12357-7
5. Calci A, Navrátil P, Roth R, Dohet-Eraly J, Quaglioni S, Hupin G. Can *ab Initio* Theory Explain the Phenomenon of Parity Inversion in ^{11}Be? *Phys Rev Lett*. (2016) **117**:242501. doi: 10.1103/PhysRevLett.117.242501
6. Piarulli M, Baroni A, Girlanda L, Kievsky A, Lovato A, Lusk E, et al. Light-nuclei spectra from chiral dynamics. *Phys Rev Lett*. (2018) **120**:052503. doi: 10.1103/PhysRevLett.120.052503
7. Lonardoni D, Carlson J, Gandolfi S, Lynn JE, Schmidt KE, Schwenk A, et al. Properties of Nuclei up to $A = 16$ using Local Chiral Interactions. *Phys Rev Lett*. (2018) **120**:122502. doi: 10.1103/PhysRevLett.120.122502
8. Gysbers P, Hagen G, Holt JD, Jansen JR, Morris TD, Navrátil P, et al. Discrepancy between experimental and theoretical β-decay rates resolved from first principles. *Nat Phys*. (2019) **15**:428–31. doi: 10.1038/s41567-019-0450-7
9. Steppenbeck D, Takeuchi S, Aoi N, Doornenbal P, Matsushita M, Wang H, et al. Evidence for a new nuclear 'magic number' from the level structure of 54Ca. *Nature*. (2013) **502**:207–10. doi: 10.1038/nature12522
10. Stroberg SR, Hergert H, Holt JD, Bogner SK, Schwenk A. Ground and excited states of doubly open-shell nuclei from ab initio valence-space Hamiltonians. *Phys Rev C*. (2016) **93**:051301. doi: 10.1103/PhysRevC.93.051301
11. Liu HN, Obertelli A, Doornenbal P, Bertulani C, Hagen G, Holt JD, et al. How robust is the $N = 34$ subshell closure? First spectroscopy of ^{52}Ar. *Phys Rev Lett*. (2019) **122**:072502. doi: 10.1103/PhysRevLett.122.072502
12. Holt JD, Stroberg SR, Schwenk A, Simonis J. Ab initio limits of atomic nuclei. *arXiv [Preprint]* (2019). *arXiv*:1905.10475.
13. Erler J, Birge N, Kortelainen M, Nazarewicz W, Olsen E, Perhac AM, et al. The limits of the nuclear landscape. *Nature*. (2012) **486**:509–12. doi: 10.1038/nature11188
14. Mumpower MR, Surman R, McLaughlin GC, Aprahamian A. The impact of individual nuclear properties on *r*-process nucleosynthesis. *Prog Part Nucl Phys*. (2016) **86**:86–126. doi: 10.1016/j.ppnp.2015.09.001
15. Miller MC, Lamb FK, Dittmann AJ, Bogdanov S, Arzoumanian Z, Gendreau KC, et al. PSR J0030+0451 mass and radius from NICER data and implications for the properties of neutron star matter. *Astrophys J Lett*. (2019) **887**:L24. doi: 10.3847/2041-8213/ab50c5
16. Riley TE, Watts AL, Bogdanov S, Ray PS, Ludlam RM, Guillot S, et al. A NICER view of PSR J0030+0451: millisecond pulsar parameter estimation. *Astrophys J Lett*. (2019) **887**:L21. doi: 10.3847/2041-8213/ab481c
17. Carlson J, Gandolfi S, Pederiva F, Pieper SC, Schiavilla R, Schmidt KE, et al. Quantum Monte Carlo methods for nuclear physics. *Rev Mod Phys*. (2015) **87**:1067–118.. doi: 10.1103/RevModPhys.87.1067
18. Weinberg S. Nuclear forces from chiral Lagrangians. *Phys Lett*. (1990) **B251**:288–92. doi: 10.1016/0370-2693(90)90938-3
19. Weinberg S. Effective chiral Lagrangians for nucleon - pion interactions and nuclear forces. *Nucl Phys*. (1991) B363:3–18. doi: 10.1016/0550-3213(91)90231-L
20. Weinberg S. Three body interactions among nucleons and pions. *Phys Lett*. (1992) **B295**:114–21. doi: 10.1016/0370-2693(92)90099-P
21. Epelbaum E, Hammer HW, Meißner UG. Modern theory of nuclear forces. *Rev Mod Phys*. (2009) **81**:1773–825. doi: 10.1103/RevModPhys.81.1773
22. Fryer CL. Mass limits for black hole formation. *Astrophys J*. (1999) **522**:413. doi: 10.1086/307647
23. Chandrasekhar S. The maximum mass of ideal white dwarfs. *Astrophys J*. (1931) **74**:81–2. doi: 10.1086/143324

24. Chadwick J. Possible existence of a neutron. *Nature*. (1932) **129**:312–22. doi: 10.1038/129312a0
25. Baade W, Zwicky F. Remarks on super-novae and cosmic rays. *Phys Rev*. (1934) **46**:76–7. doi: 10.1103/PhysRev.46.76.2
26. Hewish A, Okoye SE. Evidence for an unusual source of high radio brightness temperature in the crab nebula. *Nature*. (1965) **207**:59–60. doi: 10.1038/207059a0
27. Hewish A, Bell SJ, Pilkington JDH, Scott PF, Collins RA. Observation of a rapidly pulsating radio source. *Nature*. (1968) **217**:709–13. doi: 10.1038/217709a0
28. Steiner AW, Prakash M, Lattimer JM, Ellis PJ. Isospin asymmetry in nuclei and neutron stars. *Phys Rept*. (2005) **411**:325–75. doi: 10.1016/j.physrep.2005.02.004
29. Akmal A, Pandharipande VR, Ravenhall DG. The equation of state of nucleon matter and neutron star structure. *Phys Rev C*. (1998) **58**:1804–28. doi: 10.1103/PhysRevC.58.1804
30. Gandolfi S, Lippuner J, Steiner AW, Tews I, Du X, Al-Mamun M. From the microscopic to the macroscopic world: from nucleons to neutron stars. *J Phys*. (2019) **G46**:103001. doi: 10.1088/1361-6471/ab29b3
31. Oppenheimer JR, Volkoff GM. On massive neutron cores. *Phys Rev*. (1939) **55**:374–81. doi: 10.1103/PhysRev.55.374
32. Tolman RC. Static Solutions of Einstein's Field Equations for Spheres of Fluid. *Phys Rev*. (1939) **55**:364–73. doi: 10.1103/PhysRev.55.364
33. Tews I, Carlson J, Gandolfi S, Reddy S. Constraining the speed of sound inside neutron stars with chiral effective field theory interactions and observations. *Astrophys J*. (2018) **860**:149. doi: 10.3847/1538-4357/aac267
34. Ravenhall DG, Pethick CJ, Wilson JR. Structure of matter below nuclear saturation density. *Phys Rev Lett*. (1983) **50**:2066–9. doi: 10.1103/PhysRevLett.50.2066
35. Lonardoni D, Lovato A, Gandolfi S, Pederiva F. Hyperon puzzle: hints from Quantum Monte Carlo calculations. *Phys Rev Lett*. (2015) **114**:092301. doi: 10.1103/PhysRevLett.114.092301
36. Alford MG, Schmitt A, Rajagopal K, Schäfer T. Color superconductivity in dense quark matter. *Rev Mod Phys*. (2008) **80**:1455–515. doi: 10.1103/RevModPhys.80.1455
37. Lattimer JM. The nuclear equation of state and neutron star masses. *Ann Rev Nucl Part Sci*. (2012) **62**:485–515. doi: 10.1146/annurev-nucl-102711-095018
38. Shapiro II. Fourth Test of General Relativity. *Phys Rev Lett*. (1964) **13**:789–91. doi: 10.1103/PhysRevLett.13.789
39. Champion DJ, Ransom SM, Lazarus P, Camilo F, Bassa C, Kaspi VM, et al. An eccentric binary millisecond pulsar in the galactic plane. *Science*. (2008) **320**:1309–12. doi: 10.1126/science.1157580
40. Freire PCC, Bassa CG, Wex N, Stairs IH. On the nature and evolution of the unique binary pulsar J1903+0327. *Mon Not R Astron Soc*. (2011) **412**:2763. doi: 10.1111/j.1365-2966.2010.18109.x
41. Demorest P, Pennucci T, Ransom S, Roberts M, Hessels J. Shapiro delay measurement of a two solar mass neutron star. *Nature*. (2010) **467**:1081–3. doi: 10.1038/nature09466
42. Fonseca E, Pennucci TT, Ellis JA, Stairs IH, Nice DJ, Ransom SM, et al. The NANOGrav nine-year data set: mass and geometric measurements of binary millisecond pulsars. *Astrophys J*. (2016) **832**:167. doi: 10.3847/0004-637X/832/2/167
43. Antoniadis J, Freire PCC, Wex N, Tauris TM, Lynch RS, van Kerkwijk MH, et al. A massive pulsar in a compact relativistic binary. *Science*. (2013) **340**:6131. doi: 10.1126/science.1233232
44. Cromartie HT, Fonseca E, Ransom SM, Demorest PB, Arzoumanian Z, Blumer H, et al. Relativistic Shapiro delay measurements of an extremely massive millisecond pulsar. *Nat Astron*. (2019) **4**:72–6. doi: 10.1038/s41550-019-0880-2
45. Ozel F, Freire P. Masses, Radii, and the Equation of State of Neutron Stars. *Ann Rev Astron Astrophys*. (2016) **54**:401–40. doi: 10.1146/annurev-astro-081915-023322
46. Abbott BP, Abbott R, Abbott TD, Acernese F, Ackely K, Adams C, et al. GW170817: observation of gravitational waves from a binary neutron star inspiral. *Phys Rev Lett*. (2017) **119**:161101. doi: 10.1103/PhysRevLett.119.161101
47. Abbott BP, Abbott R, Abbott TD, Acernese F, Ackley K, Adams C, et al. Multi-messenger observations of a binary neutron star merger. *Astrophys J*. (2017) **848**:L12. doi: 10.3847/2041-8213/aa91c9
48. Abbott BP, Abbott R, Abbott TD, Acernese F, Ackley K, Adams C, et al. Gravitational waves and gamma-rays from a binary neutron star merger: GW170817 and GRB 170817A. *Astrophys J*. (2017) **848**:L13. doi: 10.3847/2041-8213/aa920c
49. Abbott BP, Abbott R, Abbott TD, Acernese F, Ackley K, Adams C, et al. Properties of the binary neutron star merger GW170817. *Phys Rev X*. (2019) **9**:011001. doi: 10.1103/PhysRevX.9.011001
50. Tews I, Margueron J, Reddy S. Confronting gravitational-wave observations with modern nuclear physics constraints. *Eur Phys J*. (2019) **A55**:97. doi: 10.1140/epja/i2019-12774-6
51. De S, Finstad D, Lattimer JM, Brown DA, Berger E, Biwer CM. Tidal deformabilities and radii of neutron stars from the observation of GW170817. *Phys Rev Lett*. (2018) **121**:091102. doi: 10.1103/PhysRevLett.121.091102
52. Flanagan EE, Hinderer T. Constraining neutron star tidal Love numbers with gravitational wave detectors. *Phys Rev*. (2008) **D77**:021502. doi: 10.1103/PhysRevD.77.021502
53. Damour T, Nagar A. Relativistic tidal properties of neutron stars. *Phys Rev*. (2009) **D80**:084035. doi: 10.1103/PhysRevD.80.084035
54. Moustakidis CC, Gaitanos T, Margaritis C, Lalazissis GA. Bounds on the speed of sound in dense matter, and neutron star structure. *Phys Rev*. (2017) **C95**:045801. doi: 10.1103/PhysRevC.95.045801
55. Annala E, Gorda T, Kurkela A, Vuorinen A. Gravitational-wave constraints on the neutron-star-matter Equation of State. *Phys Rev Lett*. (2018) **120**:172703. doi: 10.1103/PhysRevLett.120.172703
56. Fattoyev FJ, Piekarewicz J, Horowitz CJ. Neutron skins and neutron stars in the multimessenger era. *Phys Rev Lett*. (2018) **120**:172702. doi: 10.1103/PhysRevLett.120.172702
57. Most ER, Weih LR, Rezzolla L, Schaffner-Bielich J. New constraints on radii and tidal deformabilities of neutron stars from GW170817. *Phys Rev Lett*. (2018) **120**:261103. doi: 10.1103/PhysRevLett.120.261103
58. Lim Y, Holt JW. Neutron star tidal deformabilities constrained by nuclear theory and experiment. *Phys Rev Lett*. (2018) **121**:062701. doi: 10.1103/PhysRevLett.121.062701
59. Tews I, Margueron J, Reddy S. Critical examination of constraints on the equation of state of dense matter obtained from GW170817. *Phys Rev C*. (2018) **98**:045804. doi: 10.1103/PhysRevC.98.045804
60. Bauswein A, Just O, Janka HT, Stergioulas N. Neutron-star radius constraints from GW170817 and future detections. *Astrophys J*. (2017) **850**:L34. doi: 10.3847/2041-8213/aa9994
61. Margalit B, Metzger BD. Constraining the maximum mass of neutron stars from multi-messenger observations of GW170817. *Astrophys J Lett*. (2017) **850**:L19. doi: 10.3847/2041-8213/aa991c
62. Shibata M, Zhou E, Kiuchi K, Fujibayashi S. Constraint on the maximum mass of neutron stars using GW170817 event. *Phys Rev D*. (2019) **100**:023015. doi: 10.1103/PhysRevD.100.023015
63. Hebeler K, Lattimer JM, Pethick CJ, Schwenk A. Constraints on neutron star radii based on chiral effective field theory interactions. *Phys Rev Lett*. (2010) **105**:161102. doi: 10.1103/PhysRevLett.105.161102
64. Coraggio L, Holt JW, Itaco N, Machleidt R, Marcucci LE, Sammarruca F. Nuclear-matter equation of state with consistent two- and three-body perturbative chiral interactions. *Phys Rev C*. (2014) **89**:044321. doi: 10.1103/PhysRevC.89.044321
65. Wellenhofer C, Holt JW, Kaiser N, Weise W. Nuclear thermodynamics from chiral low-momentum interactions. *Phys Rev C*. (2014) **89**:064009. doi: 10.1103/PhysRevC.89.064009
66. Holt JW, Kaiser N. Equation of state of nuclear and neutron matter at third-order in perturbation theory from chiral effective field theory. *Phys Rev*. (2017) **C95**:034326. doi: 10.1103/PhysRevC.95.034326

67. Drischler C, Hebeler K, Schwenk A. Chiral interactions up to next-to-next-to-next-to-leading order and nuclear saturation. *Phys Rev Lett*. (2019) **122**:042501. doi: 10.1103/PhysRevLett.122.042501
68. Hagen G, Papenbrock T, Ekström A, Wendt KA, Baardsen G, Gandolfi S, et al. Coupled-cluster calculations of nucleonic matter. *Phys Rev C*. (2014) **89**:014319. doi: 10.1103/PhysRevC.89.014319
69. Carbone A, Rios A, Polls A. Symmetric nuclear matter with chiral three-nucleon forces in the self-consistent Green's functions approach. *Phys Rev C*. (2013) **88**:044302. doi: 10.1103/PhysRevC.88.044302
70. Carbone A, Cipollone A, Barbieri C, Rios A, Polls A. Self-consistent Green's functions formalism with three-body interactions. *Phys Rev C*. (2013) **88**:054326. doi: 10.1103/PhysRevC.88.054326
71. Isaule F, Arellano HF, Rios A. Di-neutrons in neutron matter within a Brueckner-Hartree-Fock approach. *Phys Rev C*. (2016) **94**:034004. doi: 10.1103/PhysRevC.94.034004
72. Lynn JE, Tews I, Gandolfi S, Lovato A. Quantum Monte Carlo methods in nuclear physics: recent advances. *Ann Rev Nucl Part Sci*. (2019) **69**:279–305. doi: 10.1146/annurev-nucl-101918-023600
73. Carlson J. Greens function Monte Carlo study of light nuclei. *Phys Rev C*. (1987) **36**:2026–33. doi: 10.1103/PhysRevC.36.2026
74. Schmidt KE, Fantoni S. A quantum Monte Carlo method for nucleon systems. *Phys Lett B*. (1999) **446**:99–103. doi: 10.1016/S0370-2693(98)01522-6
75. Gandolfi S, Illarionov AY, Schmidt KE, Pederiva F, Fantoni S. Quantum Monte Carlo calculation of the equation of state of neutron matter. *Phys Rev C*. (2009) **79**:054005. doi: 10.1103/PhysRevC.79.054005
76. Gandolfi S, Gezerlis A, Carlson J. Neutron matter from low to high density. *Ann Rev Nucl Part Sci*. (2015) **65**:303–28. doi: 10.1146/annurev-nucl-102014-021957
77. Buraczynski M, Gezerlis A. Ab initio and phenomenological studies of the static response of neutron matter. *Phys Rev C*. (2017) **95**:044309. doi: 10.1103/PhysRevC.95.044309
78. Riz L, Pederiva F, Gandolfi S. Spin response and neutrino mean free path in neutron matter. *J Phys G*. (2020) **47**:045106. doi: 10.1088/1361-6471/ab6520
79. Piarulli M, Bombaci I, Logoteta D, Lovato A, Wiringa RB. Benchmark calculations of pure neutron matter with realistic nucleon-nucleon interactions. *Phys Rev C*. (2020) **101**:045801. doi: 10.1103/PhysRevC.101.045801
80. Lonardoni D, Tews I, Gandolfi S, Carlson J. Nuclear and neutron-star matter from local chiral interactions. *arXiv [Preprint]* (2019). *arXiv*:1912.09411.
81. Suzuki M. On the convergence of exponential operators- the Zassenhaus formula, BCH formula and systematic approximants. *Comm Math Phys*. (1977) **57**:193–200. doi: 10.1007/BF01614161
82. Anderson JB. Quantum chemistry by random walk. *J Chem Phys*. (1976) **65**:4121–7.
83. Schmidt KE, Kalos MH. Applications of the Monte Carlo method in statistical physics. In: Binder K, editor. *Topics in Current Physics*, Vol. 36. New York, NY; Berlin; Heidelberg: Springer-Verlag (1984). p. 125–43. doi: 10.1007/978-3-642-96788-7
84. Zhang S, Carlson J, Gubernatis JE. Constrained path Quantum Monte Carlo method for fermion ground states. *Phys Rev Lett*. (1995) **74**:3652–5. doi: 10.1103/PhysRevLett.74.3652
85. Zhang S, Carlson J, Gubernatis JE. Constrained path Monte Carlo method for fermion ground states. *Phys Rev B*. (1997) **55**:7464–77. doi: 10.1103/PhysRevB.55.7464
86. Zhang S, Krakauer H. Quantum Monte Carlo method using phase-free random walks with slater determinants. *Phys Rev Lett*. (2003) **90**:136401. doi: 10.1103/PhysRevLett.90.136401
87. Gezerlis A, Tews I, Epelbaum E, Gandolfi S, Hebeler K, Nogga A, et al. Quantum Monte Carlo calculations with chiral effective field theory interactions. *Phys Rev Lett*. (2013) **111**:032501. doi: 10.1103/PhysRevLett.111.032501
88. Gezerlis A, Tews I, Epelbaum E, Freunek M, Gandolfi S, Hebeler K, et al. Local chiral effective field theory interactions and quantum Monte Carlo applications. *Phys Rev C*. (2014) **90**:054323. doi: 10.1103/PhysRevC.90.054323
89. Lynn JE, Tews I, Carlson J, Gandolfi S, Gezerlis A, Schmidt KE, et al. Quantum Monte Carlo calculations of light nuclei with local chiral two- and three-nucleon interactions. *Phys Rev C*. (2017) **96**:054007. doi: 10.1103/PhysRevC.96.054007
90. Lonardoni D, Gandolfi S, Lynn JE, Petrie C, Carlson J, Schmidt KE, et al. Auxiliary field diffusion Monte Carlo calculations of light and medium-mass nuclei with local chiral interactions. *Phys Rev C*. (2018) **97**:044318. doi: 10.1103/PhysRevC.97.044318
91. Pieper SC. Quantum Monte Carlo calculations of light nuclei. *RivNuovo Cim*. (2008) **31**:709–40.
92. Lin C, Zong FH, Ceperley DM. Twist-averaged boundary conditions in continuum quantum Monte Carlo. *Phys Rev E*. (2001) **64**:016702. doi: 10.1103/PhysRevE.64.016702
93. Sarsa A, Fantoni S, Schmidt KE, Pederiva F. Neutron matter at zero temperature with auxiliary field diffusion Monte Carlo. *Phys Rev*. (2003) C68:024308. doi: 10.1103/PhysRevC.68.024308
94. Wiringa RB, Stoks VGJ, Schiavilla R. Accurate nucleon-nucleon potential with charge-independence breaking. *Phys Rev C*. (1995) **51**:38–51. doi: 10.1103/PhysRevC.51.38
95. Wiringa RB, Pieper SC. Evolution of nuclear spectra with nuclear forces. *Phys Rev Lett*. (2002) **89**:182501. doi: 10.1103/PhysRevLett.89.182501
96. Pudliner BS, Pandharipande VR, Carlson J, Wiringa RB. Quantum Monte Carlo Calculations of $A \leq 6$ Nuclei. *Phys Rev Lett*. (1995) **74**:4396. doi: 10.1103/PhysRevLett.74.4396
97. Pieper SC, Pandharipande VR, Wiringa RB, Carlson J. Realistic models of pion exchange three nucleon interactions. *Phys Rev C*. (2001) **64**:014001. doi: 10.1103/PhysRevC.64.014001
98. Piarulli M, Girlanda L, Schiavilla R, Navarro Prez R, Amaro JE, Ruiz Arriola E. Minimally nonlocal nucleon-nucleon potentials with chiral two-pion exchange including Δ resonances. *Phys Rev C*. (2015) **91**:024003. doi: 10.1103/PhysRevC.91.024003
99. Tews I, Gandolfi S, Gezerlis A, Schwenk A. Quantum Monte Carlo calculations of neutron matter with chiral three-body forces. *Phys Rev C*. (2016) **93**:024305. doi: 10.1103/PhysRevC.93.024305
100. Piarulli M, Girlanda L, Schiavilla R, Kievsky A, Lovato A, Marcucci LE, et al. Local chiral potentials with Δ-intermediate states and the structure of light nuclei. *Phys Rev C*. (2016) **94**:054007. doi: 10.1103/PhysRevC.94.054007
101. Piarulli M, Tews I. Local nucleon-nucleon and three-nucleon interactions within chiral effective field theory. *Front Phys*. (2020) **7**:245. doi: 10.3389/fphy.2019.00245
102. Epelbaum E, Krebs H, Meißner UG. Improved chiral nucleon-nucleon potential up to next-to-next-to-next-to-leading order. *Eur Phys J A*. (2015) **51**:53. doi: 10.1140/epja/i2015-15053-8
103. Dyhdalo A, Furnstahl RJ, Hebeler K, Tews I. Regulator artifacts in uniform matter for chiral interactions. *Phys Rev C*. (2016) **94**:034001. doi: 10.1103/PhysRevC.94.034001
104. Huth L, Tews I, Lynn JE, Schwenk A. Analyzing the Fierz rearrangement freedom for local chiral two-nucleon potentials. *Phys Rev C*. (2017) **96**:054003. doi: 10.1103/PhysRevC.96.054003
105. Hoppe J, Drischler C, Furnstahl RJ, Hebeler K, Schwenk A. Weinberg eigenvalues for chiral nucleon-nucleon interactions. *Phys Rev C*. (2017) **96**:054002. doi: 10.1103/PhysRevC.96.054002
106. Tews I, Huth L, Schwenk A. Large-cutoff behavior of local chiral effective field theory interactions. *Phys Rev C*. (2018) **98**:024001. doi: 10.1103/PhysRevC.98.024001
107. Gandolfi S, Carlson J, Pieper SC. Cold neutrons trapped in external fields. *Phys Rev Lett*. (2011) **106**:012501. doi: 10.1103/PhysRevLett.106.012501
108. Maris P, Vary JP, Gandolfi S, Carlson J, Pieper SC. Properties of trapped neutrons interacting with realistic nuclear Hamiltonians. *Phys Rev C*. (2013) **87**:054318. doi: 10.1103/PhysRevC.87.054318
109. Hebeler K, Lattimer JM, Pethick CJ, Schwenk A. Equation of state and neutron star properties constrained by nuclear physics and observation. *Astrophys J*. (2013) **773**:11. doi: 10.1088/0004-637X/773/1/11
110. Lattimer JM, Swesty FD. A Generalized equation of state for hot, dense matter. *Nucl Phys A*. (1991) **535**:331–76. doi: 10.1016/0375-9474(91)90452-C

111. Tews I. Spectrum of shear modes in the neutron-star crust: Estimating the nuclear-physics uncertainties. *Phys Rev C*. (2017) **95**:015803. doi: 10.1103/PhysRevC.95.015803
112. Greif SK, Raaijmakers G, Hebeler K, Schwenk A, Watts AL. Equation of state sensitivities when inferring neutron star and dense matter properties. *Mon Not Roy Astron Soc*. (2019) **485**:5363–76. doi: 10.1093/mnras/stz654
113. Bauswein A, Baumgarte TW, Janka HT. Prompt merger collapse and the maximum mass of neutron stars. *Phys Rev Lett*. (2013) **111**:131101. doi: 10.1103/PhysRevLett.111.131101
114. Koppel S, Bovard L, Rezzolla L. A general-relativistic determination of the threshold mass to prompt collapse in binary neutron star mergers. *Astrophys J*. (2019) **872**:L16. doi: 10.3847/2041-8213/ab0210
115. Capano CD, Tews I, Brown SM, Margalit B, De S, Kumar S, et al. Stringent constraints on neutron-star radii from multimessenger observations and nuclear theory. *Nat. Astron*. (2019) **8**. doi: 10.1038/s41550-020-1014-6
116. Abbott BP, Abbott R, Abbott TD, Acernese F, Ackley K, Adams C, et al. GW170817: measurements of neutron star radii and equation of state. *Phys Rev Lett*. (2018) **121**:161101. doi: 10.1103/PhysRevLett.121.161101

Conflict of Interest: The author declares that the research was conducted in the absence of any commercial or financial relationships that could be construed as a potential conflict of interest.

frontiers in Physics

REVIEW
published: 09 October 2020
doi: 10.3389/fphy.2020.00387

Green's Function Techniques for Infinite Nuclear Systems

*Arnau Rios**

Department of Physics, Faculty of Engineering and Physical Sciences, University of Surrey, Guildford, United Kingdom

I review the application of self-consistent Green's function methods to study the properties of infinite nuclear systems. Improvements over the last decade, including the consistent treatment of three-nucleon forces and the development of extrapolation methods from finite to zero temperature, have allowed for realistic predictions of the equation of state of infinite symmetric, asymmetric and neutron matter based on chiral interactions. Microscopic properties, like momentum distributions or spectral functions, are also accessible. Using an indicative set of results based on a subset of chiral interactions, I summarize here the first-principles description of infinite nuclear systems provided by Green's function techniques, in the context of several issues of relevance for nuclear theory including, but not limited to, the role of short-range correlations in nuclear systems, nuclear phase transitions and the isospin dependence of nuclear observables.

Keywords: nuclear and particle physics, neutron stars - general, short-range action of nuclear forces, spectral function, theoretical nuclear physics

OPEN ACCESS

Edited by:
Luigi Coraggio,
National Institute of Nuclear Physics of Naples, Italy

Reviewed by:
Norbert Kaiser,
Technical University of Munich, Germany
Jeremy William Holt,
Texas A&M University, United States

***Correspondence:**
Arnau Rios
a.rios@surrey.ac.uk

Specialty section:
This article was submitted to Nuclear Physics, a section of the journal Frontiers in Physics

Received: *18 June 2020*
Accepted: *10 August 2020*
Published: *09 October 2020*

Citation:
Rios A (2020) Green's Function Techniques for Infinite Nuclear Systems. Front. Phys. 8:387. doi: 10.3389/fphy.2020.00387

1. INTRODUCTION

The recent discoveries of neutron-star binaries GW170817 [1] and GW190425 [2] are formidable feats in gravitational-wave (GW) and multimessenger astronomy. These events provide unique insight into a great variety of astrophysical questions, from stellar physics to cosmology. In dense matter physics, the analysis of multimessenger data is providing a unique way forward in our understanding of matter in its most neutron-rich form. Gravitational waves from the inspiral carry imprints of the equation of state (EoS) of neutron-star matter [3]. The initial analysis of the source GW170817 has already provided significant constraints on the masses, radii and EoSs of neutron stars [4]. The expectation is that, as more of these GW sources are detected in the next few years, they will provide more and more accurate observational constraints. Simultaneous developments in X-ray burst observations are also providing equally important and independent constraints on the EoS and the physical properties of neutron stars (NSs) [5]. Soft X-ray waveforms of rotation-powered pulsars also provide promising NS constraints [6, 7].

Theoretical nuclear physics tools provide relevant input for dense matter physics. Among others, there have been several significant efforts trying to put constraints on the symmetry energy [8, 9] or the EoS itself [10]. The data in the new generation of astrophysical observations will tighten these constraints, and may even allow for further relevant conclusions on macroscopic observables, like the EoS [11]. Connecting these bulk observable constraints to the strong interaction among neutrons requires significant efforts on the nuclear theory side. There is a stringent need for the development of realistic predictions with systematic errors based on our understanding of the physics of dense systems. This necessarily requires the use of *ab initio* nuclear theory techniques that can provide a solid, quantifiable link between macro- and micro-physics [12, 13]. For the case of GW inspirals, this link also demands for an understanding of dense matter properties not only

in the zero-temperature domain, but at temperature scales which are significant enough to modify some nuclear properties (e.g., temperatures in the range of tens of MeV) [14–18]. There is a similar need for microphysics inputs in the case of core-collapse supernovae, where the formation process of proto-NSs [19] and the subsequent development of a neutrino-heated shock wave require an understanding of neutrino emission from compact objects [20, 21].

The accuracy of theoretical nuclear physics predictions is hampered by a variety of different factors. First, the strong interaction among nucleons is difficult to pin down. Scattering experiments provide extremely useful insight at the two-body level, but three-neutron forces remain relatively unconstrained [22]. For neutrons, four-body and higher level forces are expected to play a small role for the EoS [23]. Chiral effective field theory (χEFT) [24, 25] and Lattice QCD [26, 27] efforts in the next decade will be crucial to provide clear limits on these terms. As a first approximation, one can estimate the uncertainty in the strong force by considering different input Hamiltonians that fit scattering phase-shifts and few body data [28, 29].

In addition, even if the interaction is perfectly understood, one still needs to solve a many-body multicomponent[1] problem to link the NN force to the macroscopic properties related to the EoS. While several methods have been devised to attack this problem, a clear-cut solution is difficult, if not impossible. The treatment of many-body correlations differs depending on the method that is used to describe dense neutron-rich systems [30, 31]. In particular, the structure of the strong force itself—particularly its short-range core—may preclude low-order perturbative treatments. Self-consistent Green's function (SCGF) techniques can be used to obtain both perturbative and non-perturbative results from these interactions of relevance for nuclear physics [32–34]. This approach offers the promise to simultaneously tackle issues that are relevant for neutron-star astrophysics, while providing insight into problems that are appropriate for nuclear structure (particularly in terms of short-range correlations).

My aim with this review is to provide a summary of the recent advances of the SCGF treatment of infinite nuclear systems. I will only explore the uncertainty associated to the Hamiltonian by looking at calculations performed with three different chiral interactions. This represents a small subset of possible forces, and is by no means representative of the overall uncertainty due to the strong interaction in infinite systems. Even then, these interactions predict relatively different micro- and macroscopic properties below, around and above saturation density. A benchmark analysis with different methods, while necessary to fully understand the limitations of nuclear theory, lies beyond the scope of this contribution. I will instead provide a qualitative, and somewhat limited discussion of the many-body scheme dependence of the results, by providing comparisons to many-body perturbation theory results based on similar Hamiltonians.

I start this review with a brief summary of the formal tools associated to the SCGF formalism in the following section. I note that there are monographs [32, 34] and books [33, 35, 36] that provide many more details, and I refer the interested reader to those. Section 3 is devoted to a discussion of recent numerical results that concern single-particle properties in dense matter. These include spectral functions, self-energies and momentum distributions. In section 4, the discussion turns into the macrophysics of infinite nuclear systems, with a particular emphasis on the EoS. I finally provide some conclusions and an outlook in section 5.

2. SELF-CONSISTENT GREEN'S FUNCTION APPROACH

2.1. Formalism

Many-body Green's function are a natural starting point in the discussion of quantum many-body systems [33, 37]. Green's function (or propagators) arise naturally in diagrammatic treatments, and provide a description of several real or virtual excitation processes within the many-body system. Formally, these propagators take the form of time-ordered correlation functions associated to the creation and annihilation of excitations and can be expressed in terms of Feynman diagrams [38, 39]. Broadly speaking, Green's function techniques attempt to sum series of the most physically relevant diagrams to describe the system under consideration. For instance, in the case of thermodynamics of correlated infinite systems, one often resorts to an expansion that involves renormalized interactions treating the short-range core non-perturbatively via infinitely repeated scattering processes [40]. When it comes to the response of finite systems, one instead considers diagrams that describe relevant excitations within the system [32]. This allows SCGF practitioners to look at many-body systems from different perspectives, providing a characterization of the system that includes microscopic and macroscopic properties.

In SCGFs methods, internal propagators of all diagrams are consistently dressed. In other words, renormalization effects are introduced from the onset in the formalism - and hence the monicker "self-consistent." At a diagrammatic level, this means that only skeleton (or 1-particle-irreducible) diagrams are required for single-particle self-energies. In practice, one pays the price of having to run simulations iteratively for a given system which, in infinite matter, translates into a fixed density (or temperature) [33]. A key advantage of SCGF methods is the direct access to the propagators themselves. These contain relevant information for the system's microphysics, in terms of spectroscopy and strength distributions [32]. Moreover, propagators can also be used to compute bulk properties, including total energies, thermodynamical properties and pressures. Within a single SCGF simulation, one therefore obtains a significantly broad scope in terms of physical information. This goes beyond the reach of other many-body approaches which are mostly tailored to address the energy of the system, either by minimizing it using quantum Monte-Carlo [31, 41] techniques, or addressing it by means of diagrams, like the Brueckner-Hartree-Fock (BHF) approach [30].

[1] Multicomponent in the sense that it requires both neutrons and protons.

Another strategic advantage of the SCGF formalism is its generality. Within the very same formalism, one can tackle both finite and infinite systems—see [42] for a contribution in this volume that specifically discusses recent applications of SCGF techniques to finite nuclei. More importantly in the context of astrophysics, SCGF methods can be formulated consistently at finite temperature [33, 37]. In fact, fully-fledged infinite nuclear matter studies are usually performed at finite temperature [43–45]. For sufficiently large temperatures (typically $T \gtrapprox 2-5$ MeV), this treatment avoids the complications associated to nuclear superfluidity [43, 46] that plagued early attempts of SCGF calculations in the 1990s [47]. Furthermore, a finite temperature formulation allows for access to astrophysically-relevant temperature dependences of observables [18], and provides insight into liquid-gas, thermally-induced phase transitions in dense systems [48, 49]. It is now possible to use these non-superfluid finite temperature calculations to perform meaningful extrapolations to zero temperatures for both microscopic [50] and bulk properties [51], as we shall see in the following.

A key quantity in the SCGF formalism is the so-called spectral function $\mathcal{A}_k(\omega)$. This characterizes fully the one-body propagator $\mathcal{G}$, which is generally defined as a time-ordered product of a creation and a destruction operator [33, 36]. Upon a Hilbert transform with a complex energy variable z, the spectral function and the one-body propagator are related via a spectral decomposition,

$$\mathcal{G}_k(z) = \int \frac{\mathrm{d}\omega}{2\pi} \frac{\mathcal{A}_k(\omega)}{z-\omega}\,. \tag{1}$$

Different time orderings give rise to different components of the propagator, including the retarded and advanced components that can be addressed by taking $z = \omega \pm i\eta$, with η infinitessimal [35]. All time-ordered components can be accessed through the spectral function $\mathcal{A}_k(\omega)$, which also has the advantage of having a probabilistic interpretation. The spectral function provides the probability distribution associated to either extracting or attaching a particle with well-defined momentum k, and energy ω, to the infinite system. In the finite-temperature Matsubara formalism, the Lehmann representation of $\mathcal{A}_k(\omega)$ takes into account not only the thermal excitations on the ground state of the system, but also the presence of excited states that are populated according to a thermal distribution,

$$\begin{aligned}\mathcal{A}_k(\omega) = 2\pi \sum_{n,m} \frac{e^{-\beta(E_n-\mu N_n)}}{Z} |\langle m|\hat{a}_k^\dagger|n\rangle|^2\, \delta[\omega-(E_m-E_n)] \\ + 2\pi \sum_{n,m} \frac{e^{-\beta(E_n-\mu N_n)}}{Z} |\langle m|\hat{a}_k|n\rangle|^2\, \delta[\omega-(E_n-E_m)]\,.\end{aligned} \tag{2}$$

In this equation $\hat{a}_k$ ($\hat{a}_k^\dagger$) are destruction (creation) operators of single-particle states with well-defined momentum k. A many-body system with N_n particles can have different eigenstates of the many-body Hamiltonian with energy E_n, labeled with quantum number n. $Z = \sum_n e^{-\beta(E_n-\mu N_n)}$ is the corresponding partition function and, in the grand-canonical ensemble, the system is described in terms of a given temperature $T = 1/\beta$, and a chemical potential μ.

As a well-defined probability distribution, the spectral function is normalized $\int \mathrm{d}\omega \mathcal{A}_k(\omega)/2\pi = 1$. When this integral is weighted by the corresponding thermal population of hole states, one obtains the momentum distribution of the system,

$$n_k = \int \frac{\mathrm{d}\omega}{2\pi} \mathcal{A}_k(\omega) f(\omega)\,. \tag{3}$$

In turn, even though the formulation of the problem is grand-canonical in nature, the momentum distribution can be used to fix the density of the system by requiring that the chemical potential μ in the Fermi-Dirac function $f(\omega) = \left[1+\exp[(\omega-\mu)/T]\right]^{-1}$ is such that the normalization condition

$$\rho = \nu \int \frac{\mathrm{d}^3 k}{(2\pi)^3} n_k \tag{4}$$

is fulfilled. Here $\nu = 2$ represents the degeneracy in spin for neutron or asymmetric matter, and $\nu = 4$ is the degeneracy in spin and isospin for symmetric matter.

The Dyson equation $[z - k^2/2m - \Sigma_k(z)]\mathcal{G}_k(z) = 1$ provides a connection between the one-body propagator $\mathcal{G}$ and the self-energy Σ. The latter is traditionally decomposed into a real and an imaginary part, and the spectral function is then connected to the retarded self-energy by the equation:

$$\mathcal{A}_k(\omega) = \frac{-2\mathrm{Im}\Sigma_k(\omega)}{\left[\omega - \frac{k^2}{2m} - \mathrm{Re}\Sigma_k(\omega)\right]^2 + \left[\mathrm{Im}\Sigma_k(\omega)\right]^2}\,. \tag{5}$$

The real part of the self-energy $\mathrm{Re}\Sigma_k(\omega)$, is often interpreted as an energy-dependent mean-field potential [52]. Systems with a well-defined quasi-particle structure have spectral functions with strong peaks around the energy for which the denominator of Equation (5) is smallest. This happens at the so-called quasi-particle energy, which can be accessed from $\mathrm{Re}\Sigma_k(\omega)$ by solving the self-consistent equation

$$\varepsilon_k = \frac{k^2}{2m} + \mathrm{Re}\Sigma_k(\varepsilon_k)\,, \tag{6}$$

at each momentum k. This on-shell condition provides a one-to-one correspondence between energy and momentum—a dispersion relation that is often used to characterize relevant single-particle properties. Other many-body approaches, like many-body perturbation theory or the BHF diagrammatic method, make use of such on-shell dispersion relations throughout [39]. The SCGF method, in contrast, considers all energy-dependent, offshell components in the self-energy and the spectral function. These effects are relevant to describe the fragmentation of single-particle strength [33].

The imaginary part of the self-energy is usually discussed in terms of quasi-particle lifetimes [33]. For the retarded self-energy, the imaginary component is negative, and is directly

related to the available phase space. Indeed, for an energy-independent self-energy, the Fourier transform of Equation (5) to the time domain provides a propagator that decays exponentially in time with a characteristic timescale,

$$\tau_k^{-1} = \Gamma_k = -2\,\mathrm{Im}\Sigma_k(\varepsilon_k)\,. \tag{7}$$

The energy and momentum dependence of the self-energy can be characterized in some domains by a model-independent analysis [33, 52]. According to Luttinger's theorem for normal fermionic systems, at zero temperature the imaginary part of the self-energy should be exactly zero at the Fermi energy and, close to this energy, it should behave quadratically, so that $\mathrm{Im}\Sigma_k(\omega=\mu)\approx a_k(\omega-\mu)^2$ [53]. When temperature sets in, $\mathrm{Im}\Sigma_k$ at $\omega=\mu$ grows quadratically with T [37].

Expressions for the self-energy can be derived at different orders in many-body perturbation theory [33, 36]. I will present results here based on the ladder approximation [33]. A summary in terms of diagrams of this approximation is provided in **Figure 1**. The key ingredient in this approach is the $T-$matrix shown in diagram (c), which is obtained from a Lippman-Schwinger equation where the intermediate kernel involves a particle-particle and hole-hole two-body propagator at finite temperature. This energy-dependent in-medium interaction describes re-scattering effects in the medium and can therefore capture short-range effects. Three-nucleon forces are included in the ladder approximation by constructing an effective two-body force, diagram (a) of **Figure 1**. This is the result of adding up the bare two-nucleon force (dashed line), V, and a three-body force (dotted line) that has been appropriately averaged over a third nucleon [54–56].

In the ladder approximation, the imaginary part of the self-energy is given by the expression:

$$\mathrm{Im}\Sigma_k(\omega) = \int \frac{\mathrm{d}^3k_1}{(2\pi)^3}\int\frac{\mathrm{d}\omega_1}{2\pi}\langle \mathrm{kk}_1|\mathrm{Im}T(\omega+\omega_1)|\mathrm{kk}_1\rangle_A\,\mathcal{A}_{k_1}(\omega_1) \\ [f(\omega_1)+b(\omega+\omega_1)]\,, \tag{8}$$

where $b(\Omega) = \left[\exp[(\Omega-2\mu)/T]-1\right]^{-1}$ is a Bose-Einstein distribution and $\mathrm{Im}T$ is the imaginary part of the $T-$matrix. In SCGF methods, one generally computes the imaginary part first, which tends to be simpler to evaluate thanks to energy and momentum conservation. Whereas explicit expressions for the real part are normally available too, one can avoid a series of complex integrals over momentum and energy phase-space by computing the real part from the dispersion relation,

$$\mathrm{Re}\Sigma_k(\omega) = \Sigma_k^\infty - \mathcal{P}\int\frac{\mathrm{d}\omega'}{\pi}\frac{\mathrm{Im}\Sigma_k(\omega')}{\omega-\omega'}\,, \tag{9}$$

where $\mathcal{P}$ denotes the principal value. The energy-independent (but momentum-dependent) component Σ_k^∞, is akin to a Hartree-Fock self-energy. This effective one-body interaction is built by averaging the two-nucleon and the three-nucleon interaction over the Fermi sea of one or two particles, as depicted in diagram (b) of **Figure 1** [54]. This average includes propagator renormalization effects via a correlated momentum distribution,

$$\Sigma_k^\infty = \nu\int\frac{\mathrm{d}^3k_1}{(2\pi)^3}\langle kk_1|V|kk_1\rangle_A n_{k_1} \\ +\frac{\nu}{2}\int\frac{\mathrm{d}^3k_1}{(2\pi)^3}\int\frac{\mathrm{d}^3k_2}{(2\pi)^3}\langle kk_1k_2|W|kk_1k_2\rangle_A n_{k_1}n_{k_2}\,. \tag{10}$$

In this expression, the matrix elements correspond to antisymmetrized two-nucleon (V) and three-nucleon (W) interactions, respectively. The chiral interactions that are used in this work are discussed in more detail in the following section.

The self-energy operator can be defined diagrammatically and encodes different many-body processes depending on the

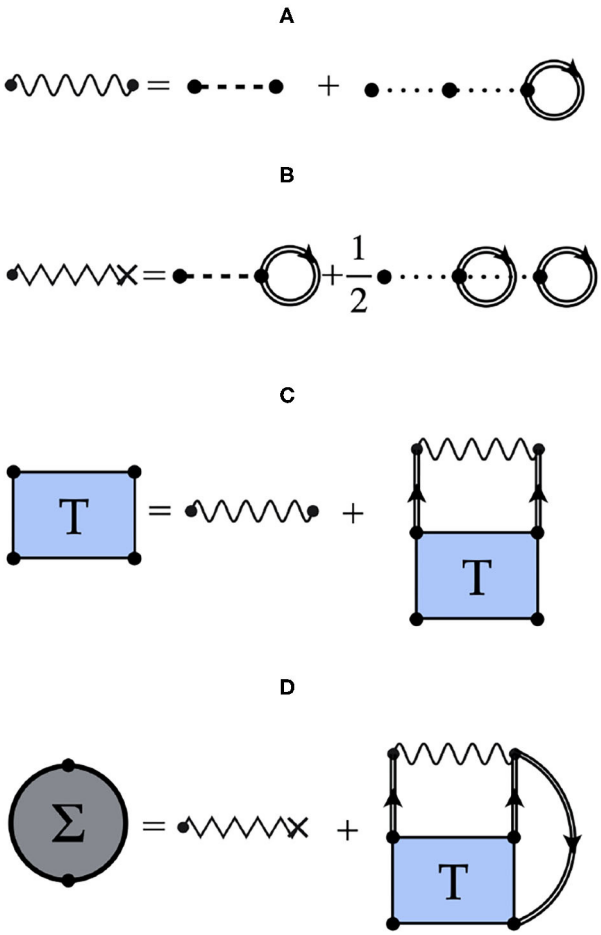

FIGURE 1 | Diagrammatic representation of the ladder approximation to the self-energy, Σ, including three-nucleon interactions. Diagram **(A)** describes the two-body effective interaction (wiggly line) obtained from the sum of the two-body interaction V (dashed line) and an averaged three-nucleon force W (dotted line). Diagram **(B)** shows the one-body effective interaction. Diagram **(C)** provides the self-consistent equation for the $T-$matrix. Finally, diagram **(D)** represents the two components of the self-energy: an energy-independent one-body effective interaction, and a dispersive contribution arising from the $T-$matrix.

level of approximation [33]. At the lowest order, the so-called mean-field or Hartree-Fock approximation, the self-energy is energy-independent and formally given by the same expression as in Equation (10), but with internal momentum distributions n_k, computed from on-shell Fermi-Dirac distributions $n_k = f(\varepsilon_k)$. Second-order self-energies are instead energy-dependent, proportional to V^2 and have already a non-trivial imaginary part [33, 51]. These account for 2p-1h and 1p-2h excitations within the system. In infinite matter applications, non-perturbative approximations beyond the second order are typically considered. A self-energy arising from a ladder resummation of the in-medium interaction deals effectively with the strong short-range and tensor components of the NN force, and leads to stable numerical results even for hard core interactions—for details see [57, 58].

When a SCGF calculation converges for a given set of external parameters, one typically stores the complex self-energy $\Sigma_k(\omega)$. All other microscopic properties, including spectral functions, can be derived from it according to Equation (5). The energy per particle of the system is then accessed by an energy-weighted integral over the spectral function, the so-called Galitskii-Migdal-Koltun sum-rule [33],

$$\frac{E}{A} = \frac{\nu}{\rho}\int \frac{\mathrm{d}^3k_1}{(2\pi)^3}\int \frac{\mathrm{d}\omega}{2\pi}\frac{1}{2}\left[\frac{k^2}{2m}+\omega\right]\mathcal{A}_k(\omega)f(\omega) - \frac{1}{2}\langle W\rangle\,. \tag{11}$$

Here, we also incorporate a correction term proportional to the expectation value of the 3NF $\langle W\rangle$. This is computed by using an additional integral over momentum of the second term in Equation (10). In other words, we keep the lowest order approximation to the expectation value of the 3NF, in agreement with techniques typically employed in finite nuclei [59]. The formal procedure to go beyond this approximation exists, as discussed in [54], but has not been implemented in infinite systems yet.

At finite temperature, the system is described in terms of thermodynamical potentials like the Helmholtz free energy $F = E - TS$. This requires an explicit calculation for the entropy S, based on Green's function methods. A proposal to compute S from spectral functions in dense matter was put forward in [58, 60] based on the formal techniques derived by Pethick and Carneiro [61, 62]. With access to the entropy, one can then derive all thermodynamical properties, including the pressure $p = \rho(F/A - \mu)$. Formally, the SCGF method is known to give rise to thermodynamically consistent results [33, 63]. For instance, a zero-temperature calculation of the chemical potential μ, from the Fermi energy of the system $\varepsilon_{k=k_F}$, or from the density derivative of the free energy density, provides the same result. This formal agreement has also been demonstrated numerically in the past [45, 60].

In terms of formalism, there is no inconvenience to extend the SCGF method to asymmetric, multicomponent systems. In fact, the SCGF method has already been used to describe isospin asymmetric matter in the past [64, 65]. One can therefore characterize correlations and fragmentation in isospin-imbalanced systems [66, 67]. In asymmetric matter, all quantities become functions of isospin—i.e., the spectral functions for neutrons $\mathcal{A}^n_k(\omega)$ and protons $\mathcal{A}^p_k(\omega)$ are different, as are the self-energies and all other one-body properties. In addition to the isospin splitting, one must also consider changes in the effective interactions, so that neutron-neutron (nn), neutron-proton (np), proton-neutron (pn), and proton-proton (pp) in-medium T-matrices are explicitly different. Extensions of the normal ordering procedure to compute effective one and two-body forces from 3NF matrix elements are also necessary [56], but relatively straightforward [68]. The results for asymmetric matter presented here within the SCGF formalism include explicitly the effect of isospin asymmetry in the normal-ordering of 3NFs and in the extrapolation procedure from finite to zero temperature.

2.2. Interactions

For consistency in the presentation, all the results that follow have been generated with the same set of interactions. I will consider three sets of χEFT-inspired forces. At the NN level, these three interactions have been introduced in [69]: they have been fitted to the same NN scattering data and incorporate different cutoffs in the relative momentum: $\Lambda = 414$ MeV, 450 MeV and 500 MeV. These forces also differ slightly in the shape (particularly the sharpness) of the regulator in relative momentum. 3NFs arise naturally in the χEFT formalism [24, 25]. Reference [70] introduced a set of N2LO 3NF forces based on the previous three NN interactions. The associated 3NF low-energy constants c_D and c_E were fitted to the binding energies of $A = 3$ nuclei and to the ^{3}H-^{3}He Gamow-Teller transition matrix element [70]. Calculations are performed for two-body matrix elements with partial waves up to $J = 9$.

The 3NFs are included in the SCGF simulations by building effective one- and two-body density-dependent forces using a procedure that is akin to normal ordering [71, 72], but includes a renormalization of occupation probability in n_k. Diagrams (a) and (b) in **Figure 1** show the corresponding one- and two-body effective interactions. Diagrams (c) and (d) indicate how these are used in the $T-$matrix calculation and the corresponding self-energy, respectively. This method is rooted on an extension of the SCGF formalism to multi-body forces [54], and has been implemented in symmetric nuclear matter and neutron matter simulations in [55, 56]. We resort to some numerical approximations in this averaging procedure. First, the normal-ordering procedure ignores the center-of-mass dependence of the 3NF, which is set to $P = 0$. Second, matrix elements off the diagonal in relative momentum $q \neq q'$, are extrapolated from diagonal matrix elements using the prescription $q \to \frac{1}{2}(q^2+q'^2)$. This procedure also involves a 3NF regulator, which is chosen to be non-local $f(p,q) = \exp\left[-\left(\frac{q^2+p^2/3}{\Lambda^2}\right)^n\right]$, and is based on the two-body relative momentum q and the internal, integrated single-particle momentum p. The exponent n is chosen in accordance to the regulator in the 2NF [70]. Within the $P = 0$ approximation, the off-shell prescription provides results of very similar quality to many-body perturbation theory calculations that incorporate fully-fledged 3NFs from the outset [73].

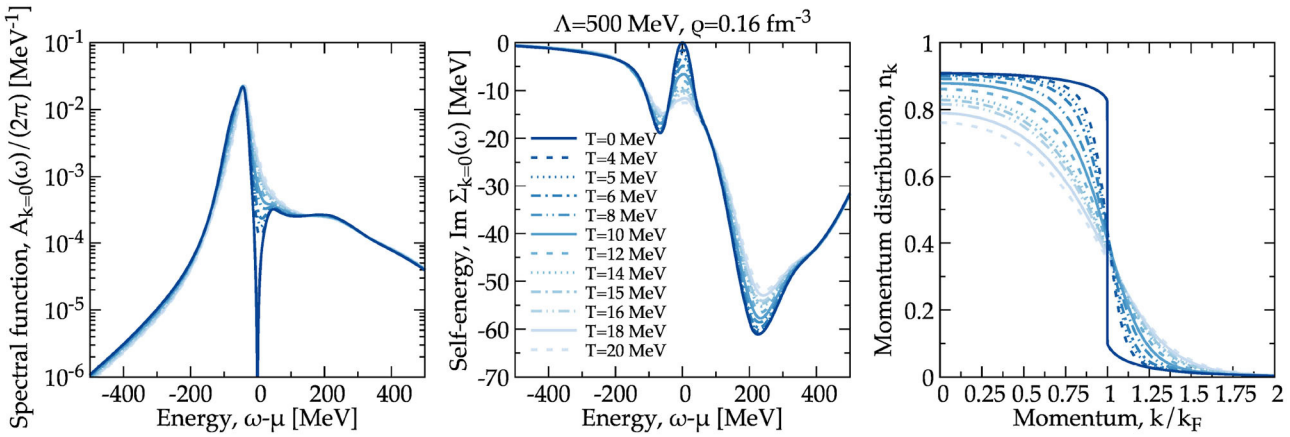

FIGURE 2 | Left: energy dependence of the zero-momentum spectral function $\mathcal{A}_{k=0}(\omega)$ at different temperatures. **Central**: the same for Im $\Sigma_{k=0}(\omega)$. **Right**: momentum distribution as a function of k/k_F. All results have been obtained in symmetric nuclear matter, at a density of $\rho = 0.16$ fm^{-3} for the $\Lambda = 500$ MeV N3LO NN plus N2LO 3NFs forces.

2.3. Extrapolation Procedure to Zero Temperature

Finite-temperature calculations are useful on their own, but benchmark comparisons with other methods are typically performed in the zero-temperature limit [30, 31]. A zero-temperature extrapolation procedure for SCGF simulations was developed in the context of beyond-BCS pairing [50, 74]. This procedure is now available generically and can be used to provide zero-temperature data for symmetric and asymmetric systems. For a given fixed density, the extrapolation requires as input a few (typically $4 - 10$) finite-temperature simulations. One typically performs simulations from high temperatures of order 20 MeV, and subsequently dials down the temperature to values that are closer to zero. Too close to zero, though, the simulations will not converge as one enters into the superfluid regime - so an intermediate range must be found. It is also important to note that the dependence on temperature typically scales with the dimensionless degeneracy parameter T/ε_F, where ε_F is the Fermi energy. Because ε_F typically increases with density, the expansion is closer to the zero-temperature result (and therefore more accurate) at higher than at lower densities.

The extrapolation from finite temperature to zero temperature works in three independent steps. In a first step, the self-energies from different temperatures are remeshed to the same values of momentum and energy. In the second step, the temperature dependence of the real and imaginary parts of the self-energy (for each value of k and ω) are fitted to a polynomial function in temperature. The third step is to use not one, but different polynomial fits to extrapolate to $T = 0$. A series of tests are run on these different extrapolations, and a quality measure is built based on a series of consistency checks. For instance, the renormalization factor $\mathcal{Z}_k = [1 - \partial_\omega \, \mathrm{Re}\Sigma_k(\omega)\big|_{\omega=\varepsilon_k}]^{-1}$ is compared to the size of the discontinuity in the momentum distribution at $k = k_F$. In a consistent theory, the two quantities should provide the same value [33]. The quality measure penalizes fits where these values are significantly different. Importantly, some of these fits have a built-in parabolic energy dependence of ImΣ around $\omega = \mu$. Additional details of this extrapolation procedure are discussed in [50].

I provide an example of this extrapolation procedure in **Figure 2**. This shows the temperature dependence of three properties that are representative of the system's behavior as a function of temperature at a fixed density of $\rho = 0.16$ fm^{-3}. Calculations have been performed with the N3LO $\Lambda = 500$ MeV NN force, supplemented with 3NFs at the N2LO level. The averaging procedure for these 3NFs consistently takes into account the density and temperature dependence of the internal propagators. Qualitatively similar results are obtained for the $\Lambda = 450$ and 414 MeV interactions.

The energy dependence of the spectral function $\mathcal{A}_{k=0}(\omega)$ and the imaginary part of the self-energy $\Sigma_{k=0}(\omega)$ are displayed in the left and central panels, respectively. I focus on the $k = 0$ value for simplicity, but the calculation and extrapolation procedure are performed for all available momenta. The effect of temperature in the spectral function is concentrated in the region near $\omega = \mu$. The quasi-particle peak and the positive and negative high-energy tails are insensitive to thermal effects. For the self-energy, there is also a relatively strong temperature dependence near $\omega = \mu$, which is known to scale with T^2 [37]. The phase-space dominated peaks in the particle and hole domains at energies about 200 MeV away from μ are also sensitive to the temperature. The extrapolated $T = 0$ result is able to capture the temperature dependence of these quantities, while providing consistent results.

The right panel of **Figure 2** shows the associated momentum distribution n_k, obtained under the same conditions. Thermal effects provide additional depletion at low momenta and populate moderately the vicinity of the Fermi surface. In fact, temperature modulates substantially the momentum distribution around $k = k_F$ even for relatively low values of $T \approx 4 - 5$ MeV. The extrapolation procedure, however, captures the energy- and

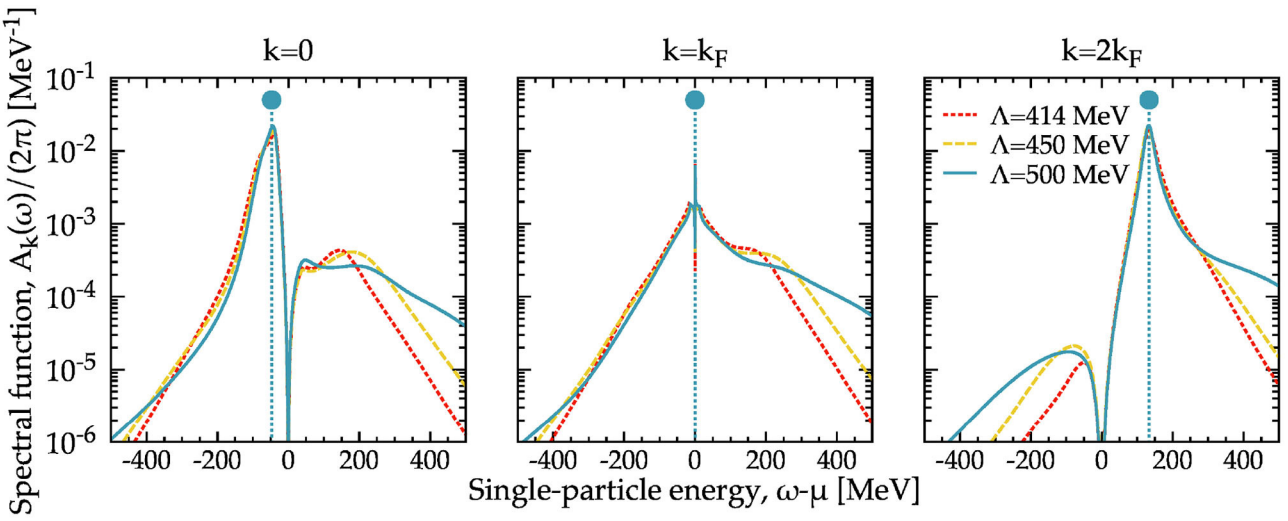

FIGURE 3 | Spectral function $\mathcal{A}_k(\omega)$ as a function of energy for three different momenta: $k = 0$ **(left)** $k = k_F$ **(central)** and $k = 2k_F$ **(right)**. SCGF calculations are performed at a density $\rho = 0.16$ fm^{-3} and have been extrapolated to zero temperature. Results for N3LO NN plus N2LO 3NFs have been performed with three different cutoffs. The vertical line and solid dot indicate the position of the quasi-particle peak $\omega = \varepsilon_k$, for each of these momenta. The height of this peak has been chosen arbitrarily.

momentum-information sufficiently well to produce a sharp transition at the Fermi surface, as expected from Luttinger's theorem [37]. The size of this discontinuity is also in agreement with the renormalization parameter associated to the self-energy itself. This extrapolation procedure has been implemented not only in the symmetric nuclear matter and pure neutron matter [74], but also in asymmetric infinite matter, as I shall discuss in the following sections.

3. MICROSCOPIC PROPERTIES

In the following, I provide an overview of the microscopic properties predicted by the SCGF approach for symmetric, asymmetric and pure neutron matter. The aim of this section is to show the broad scope of information that can be generated in SCGF simulations. I focus for simplicity on a single value of the density $\rho = 0.16$ fm^{-3}, which is representative of both nuclear systems and of neutron stars. Note however that the method is customarily used at other densities. The majority of the results are presented in their zero-temperature extrapolated form, although the temperature dependence of most quantities is available and has been used for extrapolation purposes. I leave a full analysis of the density, isospin asymmetry and temperature dependence of these results for future studies.

3.1. Spectral Functions

Figure 3 provides an example of the structure of the zero-temperature spectral function in nuclear systems. The three panels illustrate the energy dependence of the spectral function at three different momenta: $k = 0$, below the Fermi surface; $k = k_F$, at the Fermi surface; and $k = 2k_F$, above the Fermi surface. Results are shown for three interactions: $\Lambda = 414$ MeV (red dotted lines); $\Lambda = 450$ MeV (yellow dashed lines); and $\Lambda = 500$ MeV (blue solid lines).

The general features of the spectral strength in infinite systems are well-understood [44, 47, 57, 75]. At all momenta other than k_F, the spectral strength has a prominent quasi-particle peak. In infinite nuclear matter, the peak is very close to the quasi-particle energy $\omega = \varepsilon_k$ obtained from Equation (6). The quasi-particle energy for the $\Lambda = 500$ MeV interaction is displayed in the three panels of **Figure 3** with vertical lines. The solid dot is shown for illustrative purposes, and its height is chosen arbitrarily. The quasi-particle peak is well-defined in infinite nuclear systems, in the sense that the peak of $A_k(\omega)$ and $\omega = \varepsilon_k$ agree relatively well. At this density, the quasi-particle peak is independent of the interaction under consideration. In fact, the cutoff dependence of the quasi-particle peak is not resolvable on the scale of this graph. I note, however, that while the peaks are well-defined, they are also relatively broad. Typical widths at $k = 0$ and $k = 2k_F$ are of the order of $\Gamma_k \approx 40$ MeV.

Spectral functions in infinite nuclear matter display slowly decaying high (positive and negative) energy tails. These are particularly prominent at the Fermi surface $k = k_F$, where the zero-temperature spectral function should be a combination of a broad energy-dependent background and a zero-width δ function centered at $\omega = \varepsilon_{k_F}$ [33]. In practice, the $T = 0$ results at $k = k_F$ do show some minor structures around $\omega = \mu$ as the non-analytical behavior of the δ function is not built in the extrapolation procedure. The results of **Figure 3** clearly show a substantial cutoff dependence in these high-energy components. This is relatively unsurprising, since these tails are a direct consequence of the short-range core in the NN force [32]. As expected, the interaction with the largest momentum cutoff ($\Lambda = 500$ MeV), and hence the largest resolution in real space, provides the largest high-energy components. These include a

shoulder at positive energies in the region 100−500 MeV which is characteristic of a relatively strong short-range core. In contrast, the lower cutoff interactions provide much faster (exponential) decaying spectral functions beyond the quasi-particle peak. For positive energies, they provide very little single-particle strength beyond 500 MeV. The $\Lambda = 414$ MeV interaction has faster decaying tails than the 450 MeV force, which agrees with intuition. Note that this sharply decaying spectral strength is at odds with calculations employing traditional phenomenological NN forces, which typically populate these offshell regions with higher probabilities [57, 76]. Off-shell high-energy components are observed in electron-scattering experiments [77] and may provide a way to quantify the short-range component of NN forces [78].

The results presented so far concerned symmetric nuclear matter, where by construction one assumes the same fraction of neutrons and protons. Isospin asymmetric systems, however, are interesting on their own. The deep interior of heavy stable and unstable isotopes is expected to be a neutron-rich environment, characterized by an isospin asymmetry parameter,

$$\eta = \frac{\rho_n - \rho_p}{\rho_n + \rho_p}, \tag{12}$$

of order $\eta \approx 0.2$ [79]. In contrast to this relatively mild isospin asymmetry, the core of neutron stars is expected to be extremely asymmetric with $\eta \approx 0.8$ [80]. Finite-temperature SCGF simulations including explicitly isospin asymmetry have been available for over a decade [64]. In these simulations η is an external, tuneable parameter. SCGF calculations then give isospin-dependent self-energies, spectral functions and quasi-particle properties, as well as the corresponding bulk properties. These calculations provided insight into the isospin-asymmetry dependence of the fragmentation of the single-particle strength [66, 67], but were somewhat limited by two factors. First, finite temperature effects have a larger importance in the minority component as asymmetry is turned on, because the corresponding degeneracy parameter T/ε_F^τ decreases. Second, the calculations were performed with two-body interactions only

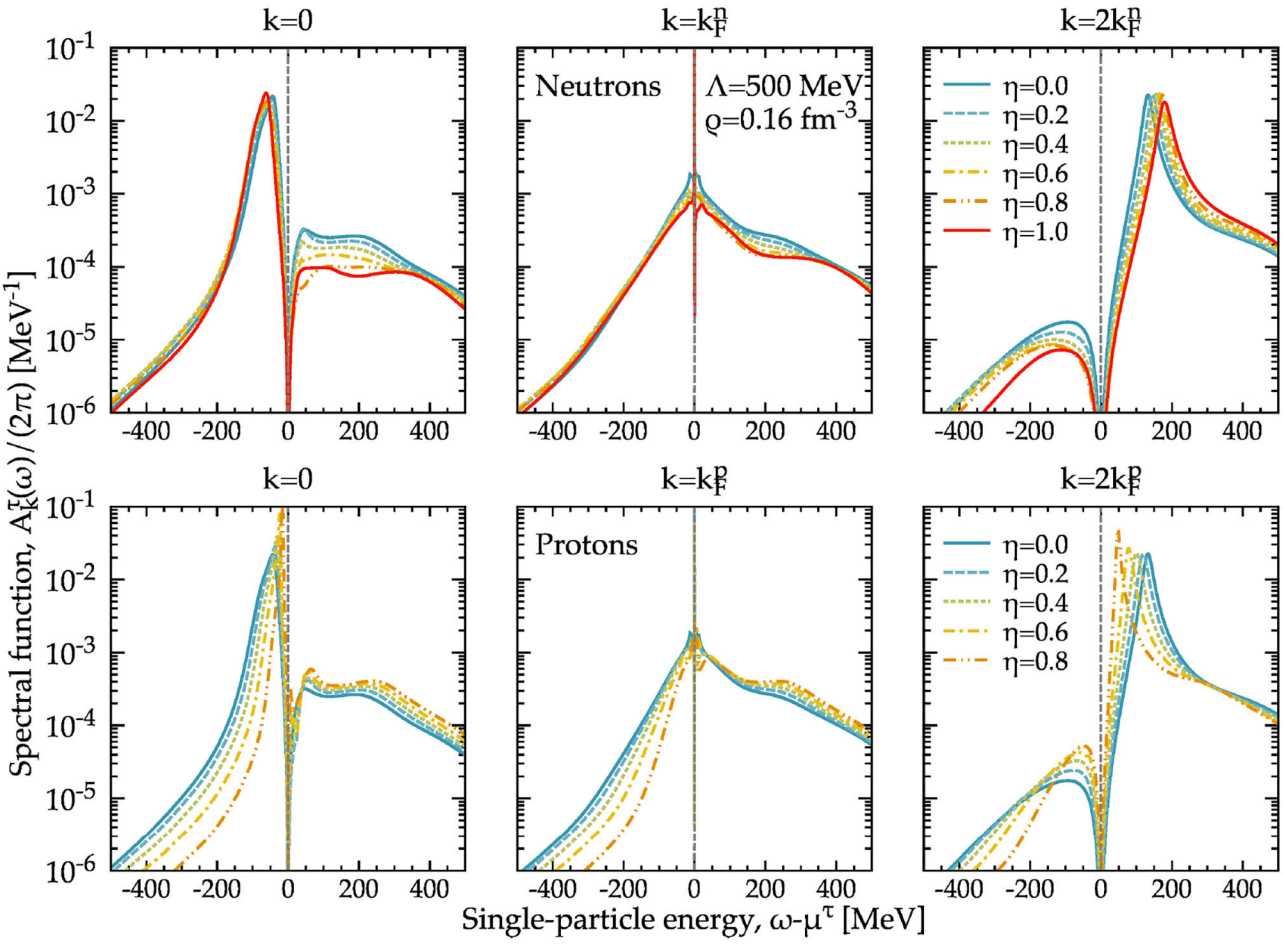

FIGURE 4 | Neutron **(top)** and proton **(bottom)** spectral functions $\mathcal{A}_k^\tau(\omega)$ as a function of energy for three different momenta: $k = 0$ (left) $k = k_F^\tau$ (central) and $k = 2k_F^\tau$ (right panels). Calculations with the N3LO $\Lambda = 500$ MeV and an N2LO 3NF at a density $\rho = 0.16$ fm^{-3} have been extrapolated to zero temperature for different isospin asymmetries η. The vertical dashed line is a guide to separate hole ($\omega < \mu^\tau$) and particle ($\omega > \mu^\tau$) components.

and thus missed the effects of 3NFs. None of these factors is particularly critical. Temperature effects can be controlled, and the effect of 3NFs on the spectroscopic strength is small below saturation density for both symmetric nuclear and pure neutron matter [55, 56].

Having said that, recent technical developments have allowed us to overcome these two shortcomings recently. **Figure 4** shows the spectral functions of neutrons (top panels) and protons (bottom panels) as a function of energy for different values of the isospin asymmetry η, at a fixed density of $\rho = 0.16$ fm^{-3}. Results are presented for the $\Lambda = 500$ MeV N3LO potential supplemented with 3NFs[2]. The results for the isospin dependence of these spectral functions are qualitatively similar to previously obtained results which lacked 3NFs. The evolution of the neutron spectral function from symmetric ($\eta = 0$) to neutron ($\eta = 1$) matter is relatively mild. The quasi-particle peaks with respect to the corresponding chemical potential μ^n become slightly more (attractive) repulsive for the (hole) particle components. The high energy tails are relatively insensitive to the isospin asymmetry, and are mostly affected for the negative energy components at momenta above the Fermi surface. All in all, this agrees with the generic picture of a neutron majority component evolving from a symmetric situation, where tensor correlations provide larger correlations, to neutron matter, where only the short-range component is responsible for fragmentation.

In contrast, the proton spectral function (bottom panels) is much more affected by isospin asymmetry. In asymmetric conditions, the relative importance of *np* pairs increases for the minority proton component. Since *np* interactions are mediated by the tensor component of the NN force, one naively expects enhanced correlation effects for protons in neutron-rich matter. Simultaneously, for neutron-rich conditions the overall proton density decreases, so the proton component should somehow become "less interacting." SCGF simulations allow us to provide quantitative predictions to distinguish between these scenarios.

As the isospin asymmetry increases, the single-particle peak for protons becomes more repulsive with respect to μ^p. Importantly, the width of the quasi-particle peak for components below the Fermi surface (see $k = 0$ panel) also decreases substantially. As a consequence, positive high-energy tails increase with isospin. Interestingly, the central panel ($k = k_F^p$), shows a background component that behaves differently for the addition and removal energy components. Whereas for $\omega < \mu^p$, the background of the spectral function decreases with isospin asymmetry, at $\omega > \mu^p$ it increases. Above the Fermi surface ($k > k_F^p$), the quasi-particle peak is more compressed with increasing isospin asymmetry, both in terms of a lower peak and a significantly decreased width. The limit case of a proton impurity in an $\eta = 1$ system cannot be tackled with the present set of SCGF technology.

While a full analysis is beyond the scope of this initial presentation of results, the isospin dependence shown here is relevant for both nuclear experiments and astrophysics. Hadronic and electron two-nucleon knock-out reactions from the early 2000s up to the present have shown that *np* pairs, rather than *pp* or *nn* pairs, are more likely to be knocked off isospin symmetric targets [81, 82]. Further electron-scattering results in isospin asymmetric nuclei have provided additional evidence for this neutron-proton dominance [83]. It is likely that the tensor component preferentially acts in relatively high-momentum pairs and provides the physical mechanism behind these strong isophobic correlations [66, 84]. Extending the *np* dominance picture to isospin imbalanced systems would naively indicate that protons should be more correlated than neutrons in

[2]I note here for completeness that the $\eta = 0$ and $\eta = 1$ calculations are performed with independent codes that do not include isospin asymmetry explicitly, and hence provide a good numerical test of the arbitrary isospin simulations.

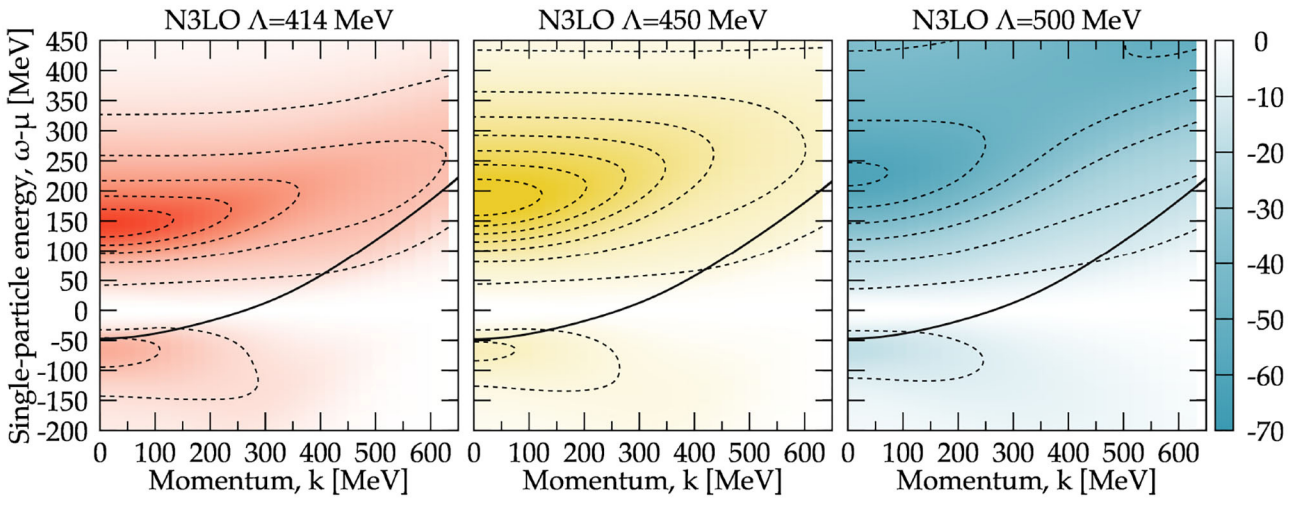

FIGURE 5 | Density plot of the imaginary part of the self-energy $\mathrm{Im}\Sigma_k(\omega)$ as a function of momentum and energy. Dashed lines represent contours at constant values spaced by 10 MeV. Extrapolated zero-temperature results for symmetric nuclear matter at a density $\rho = 0.16$ fm^{-3} are shown for the N3LO NN and N2LO 3NF combinations at cutoffs $\Lambda = 414$ MeV (right) 450 MeV (central) and $\Lambda = 500$ MeV (right panel). The solid line represents the quasi-particle peak $\omega = \varepsilon_k$.

neutron-rich systems, although quantitative statements depends sensitively on the definition of a correlation measure [85–87]. In the astrophysical context, the strong modification of the proton spectral function in isospin asymmetric nuclear matter predicted by SCGF simulations has been explicitly explored at the level of the symmetry energy in [88–90]. The fragmentation of strength in neutron matter has also been used to provide a description of the pairing properties in dense matter [50, 74].

3.2. Self-Energies

Within the SCGF formalism, the spectral strength is directly related to the self-energy. The imaginary part of the retarded self-energy encodes information on both the phase space and the NN interaction, and can even be used to diagnose interactions by means of sum rules [76]. I present a density plot of the zero-temperature extrapolated imaginary part of the self-energy at $\rho = 0.16$ fm^{-3} in **Figure 5**. Left, central, and right panels correspond to chiral interactions with cutoffs $\Lambda = 414, 450,$ and 500 MeV, including in all cases 3NFs. As expected, $\mathrm{Im}\Sigma_k$ is zero at $\omega = \mu$ throughout all momenta. For energies $\omega < \mu$, this function has a hole component with support below $k \approx k_F = 263$ MeV. The size and shape of this pocket is relatively interaction-independent. In contrast, the positive energy ($\omega > \mu$) components of $\mathrm{Im}\Sigma_k$ show a clearer cutoff dependence. The deep pocket around $k = 0$ in this component is sensitive to the underlying NN force. Typical phenomenological interactions have deep pockets, and these extend to very high positive energies (into the GeV domain). For this set of chiral interactions, the depth of the pocket is relatively insensitive to the cutoff and of order $50 - 70$ MeV. The tails of $\mathrm{Im}\Sigma_{k=0}$ fall off relatively quickly with energy. In fact, the $\Lambda = 414$ and 450 MeV self-energies are almost zero beyond an energy of about 500 MeV. The cutoff also has a clear effect on the momentum dependence of Im Σ_k in the positive energy region. Generally speaking, higher-cutoff forces allow the imaginary part of the self-energy to extend to higher momenta.

The solid lines in **Figure 5** show the trajectory of the quasi-particle peak in the energy-momentum plane. Quasi-particle lifetimes τ_k in Equation (7), are computed along these trajectories. The plot indicates that the lifetimes are relatively insensitive to the differences in self-energies. In other words, largely different offshell self-energies can give rise to relatively similar on-shell properties. On-shell components will be discussed in detail in section 3.4.

The isospin asymmetry dependence of $\mathrm{Im}\Sigma^\tau_k(\omega)$ is explored in **Figure 6**. Results are shown for the $\Lambda = 500$ interaction only at a fixed density of $\rho = 0.16$ fm^{-3}, for a variety of isospin asymmetries. The leftmost panel corresponds to the symmetric system ($\eta = 0$), and is the same as the right panel of **Figure 5**. The top panels indicate that the effect of asymmetry in the neutron self-energy is relatively mild. The pocket at negative energies $\omega < \mu^n$, associated to neutron holes, is relatively unchanged as η increases. In contrast, the positive energy (particle) components evolve with isospin in a substantially different way. The pocket that in the symmetric situation decayed relatively quickly with momentum, becomes an almost momentum-independent structure in the most asymmetric case explored here.

In contrast, proton self-energies show a strong dependence on isospin asymmetry. As the proton fraction decreases, the negative-energy (hole) components of $\mathrm{Im}\Sigma^p_k$ disappear steadily. This reflects the decrease in density, and hence of available phase space of protons. The corresponding low-momentum ($k < k^p_F$) inverse quasi-particle lifetime is small, which in turn gives rise to an increasingly narrow spectral function. This is clearly in agreement with the results in the bottom left panel of **Figure 4**. On the positive energy side of the self-energy $\omega > \mu^p$, the deep pocket at low momenta becomes noticeably deeper as η increases but, unlike the neutron component, the momentum dependence

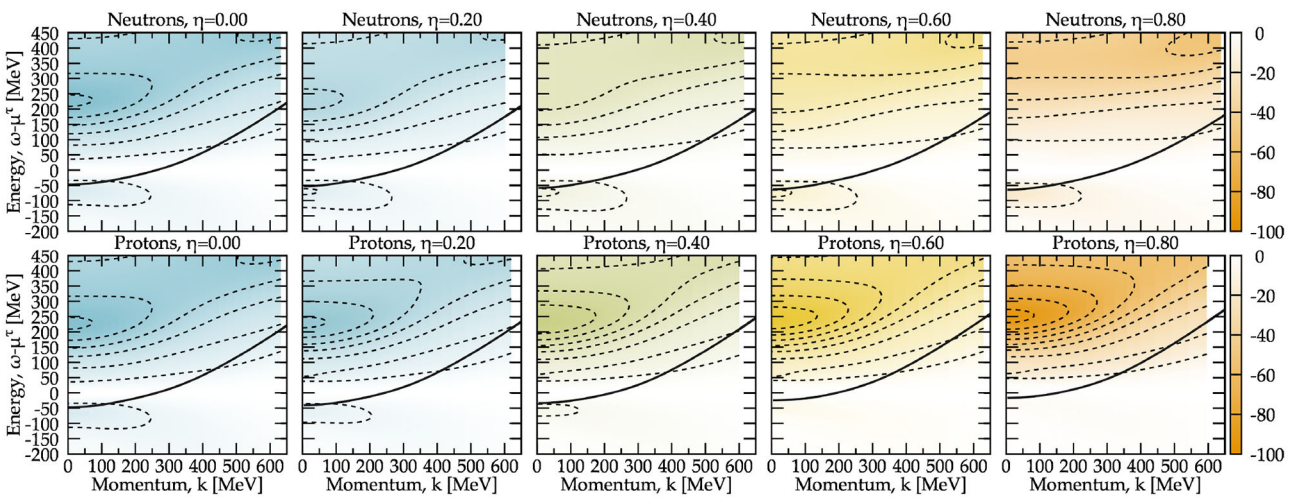

FIGURE 6 | The same as **Figure 5** but in isospin asymmetric nuclear matter for the $\Lambda = 500$ MeV interaction. Top panels focus on neutrons, and bottom panels on protons. The panels from left to right correspond to different isospin asymmetries, from $\eta = 0$ (symmetric nuclear matter, leftmost panel) to the neutron-rich domain with $\eta = 0.8$ (rightmost panel).

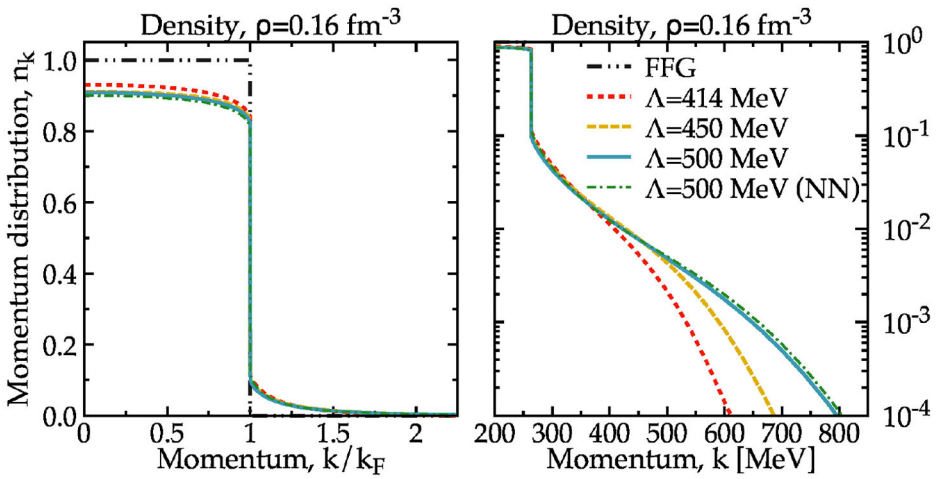

FIGURE 7 | Extrapolated zero-temperature momentum distribution obtained with different NN interactions for symmetric nuclear matter at $\rho = 0.16$ fm^{-3}. The left panel shows the distribution on a linear scale as a function of k/k_F. The right panel shows the same results on a logarithmic scale and as a function of momentum k, in units of MeV. The black dashed-double-dotted line corresponds to the free Fermi gas (FFG). The green dashed-dotted line is obtained from a calculation with the $\Lambda = 500$ MeV interaction without 3NFs. Other lines follow the convention of **Figure 3**.

remains relatively unchanged. The increase in depth of $\mathrm{Im}\Sigma_k$ can be interpreted in terms of an increase in the interaction strength, as expected in the asymmetric case with an increase in the number of *np* pairs.

In other words, the imaginary component of the self-energy for protons in asymmetric matter shows the competition of the two effects discussed earlier in two different energy regimes. On the one hand, proton holes, associated to the negative energy components, are dominated by phase-space and their self-energy decreases steadily as the proton density decreases. On the other hand, proton particles at positive energies show an increase in interaction strength as expected in a more imbalanced strongly interacting system. The real part of the self-energy is not shown here for brevity. I note, however, that this is connected to $\mathrm{Im}\Sigma_k^\tau$ by the dispersion relation in Equation (9).

3.3. Momentum Distributions

A useful characterization of beyond mean-field correlations is obtained with the momentum distribution in Equation (3). For a non-interacting Fermi gas or within the lowest-order Hartree-Fock approximation at zero temperature $n_k = 1$ (0) for momenta below (above) the Fermi surface. This behavior is illustrated by the double-dotted-dashed line in the left panel of **Figure 7**. In contrast, the momentum distribution of correlated infinite nuclear matter shows a characteristic depletion below the Fermi surface. This depletion is of the order of $7 - 12\%$, with small quantitative differences between different interactions.

In turn, a depletion of momentum eigenstates below k_F means that n_k above the Fermi surface must be populated. The logarithmic scale in the right panel of **Figure 7** illustrates the effects of such high-momentum components. These components are noticeably different depending on the cutoff. Smaller cutoff interactions give rise to momentum distributions that decay faster and start decaying at lower momenta, than larger cutoff forces. To illustrate the relatively small effect that 3NF have on correlations, I show in **Figure 7** the momentum distribution obtained in a SCGF calculation without 3NFs (dashed-dotted line). Remarkably, the difference between the calculation with and without 3NFs is substantially smaller than the cutoff dependence of the interaction. This bodes well with previous observations indicating that the effect of 3NFs on fragmentation properties is quantitatively small, even though they have a substantial influence on the energetics and thermodynamics of the system [55].

The evolution of the momentum distribution with isospin also provides an illustrative understanding of the interplay between short-range and tensor correlations and isospin asymmetry. **Figure 8** shows the momentum distribution as a function of momentum for different isospin asymmetries. These results have been obtained with the $\Lambda = 500$ MeV interaction, but qualitatively similar plots are found for the other two forces. The left panel shows the results for neutrons. Isospin asymmetry has two main effects on the majority component. On the one hand, the discontinuity in n_k moves to higher momenta, as the Fermi momentum changes from $k_F = 263$ MeV in symmetric nuclear matter to $k_F = 331$ MeV in pure neutron matter. This effect would be identical in the free Fermi gas (FFG). In contrast, the distinct increase of n_k below the Fermi surface is specific to correlated systems. The depletion of strength decreases (or gets closer to 1) linearly with the increase of asymmetry. Whereas in symmetric nuclear matter it is around 10%, in pure neutron matter it goes down to a level of around $4 - 5\%$. In fact, this isospin dependence is rather universal and independent of the NN interaction under consideration [66, 67]. A similar effect is expected for the size of the discontinuity across the Fermi surface, which decreases as isospin asymmetry increases.

The right panel of **Figure 8** provides insight on the asymmetry evolution of the minority component (protons). Mirror effects

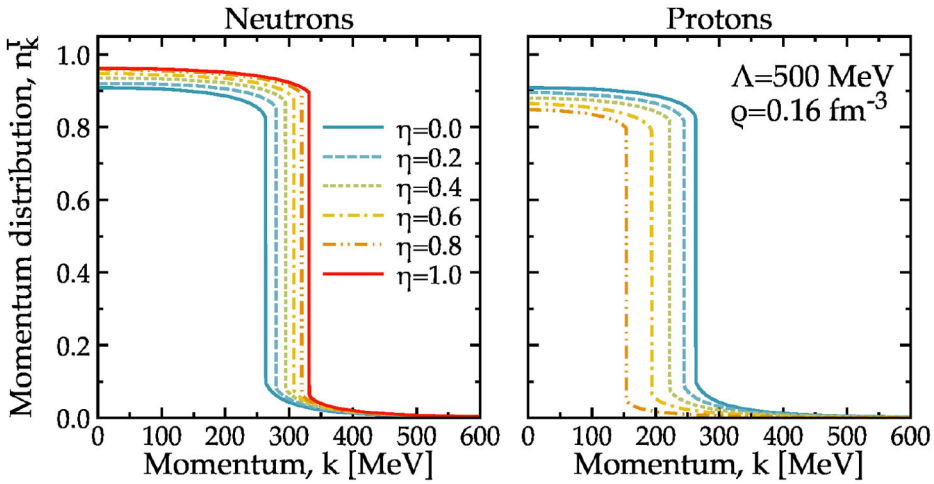

FIGURE 8 | Left: neutron momentum distribution n_k^n as a function of momentum. Extrapolated zero-temperature calculations at different values of isospin asymmetry η are shown at a fixed density of $\rho = 0.16$ fm^{-3}. Results have been obtained for the $\Lambda = 500$ MeV interaction including 3NFs. **Right**: the same for the proton momentum distribution n_k^p.

are obtained in this case. The discontinuity of n_k occurs at smaller and smaller momenta, as expected from FFG considerations. The depletion below the Fermi surface departs further away from 1 as the isospin asymmetry increases. In other words, by this measure, protons (or minority components) become more correlated in a neutron-rich environment. Close to the astrophysically relevant condition at $\eta \approx 0.8$, protons are depleted by about 15% for this specific interaction. This depletion goes in hand with a change of high-momentum components for the proton, which become more important as asymmetry increases [67].

The picture obtained by these complete calculations including zero temperature extrapolations and 3NFs is qualitatively and quantitatively very similar to the one discussed in [66, 67]. Overall, the effect of isospin asymmetry on occupation numbers is relatively small. For the characteristic isospin asymmetry in the interior of nuclei ($\eta = 0.2$), the change in occupation below the Fermi surface is of the order of only a few percent. Overall, this shallow asymmetry dependence is at odds with some of the past and recent experimental analysis in both electron- and hadron-induced knock-out reactions [85, 87, 91]. Importantly, however, these calculations at fixed density do not account for the density and isospin-asymmetry dependence within nuclei, which is likely to be relevant for the description of nuclear momentum distributions.

3.4. On-Shell Properties

A unique advantage of SCGF simulations is the access to both off-shell, energy-dependent quantities, as well as the corresponding information on the energy shell—at the quasi-particle energy $\omega = \varepsilon_k$. On-shell properties are often used in interpreting the properties of the system and are the input to most astrophysical simulations. In particular, quasi-particle potentials in asymmetric matter at relatively low densities (neutrino-sphere) are important for charged-current neutrino opacities [20, 92]. The quasi-particle spectrum of Equation (6) is a key quantity that allows for a characterization of single-particle excitations in the system. Since the kinetic term in the quasi-particle energy obscures the many-body effects at large momentum, I instead focus on the single-particle potential $U_k^\tau = \mathrm{Re}\Sigma_k^\tau(\varepsilon_k^\tau)$. This is shown as a function of momentum in **Figure 9**. Top panels correspond to neutrons, whereas bottom panels correspond to protons. From left to right, the isospin asymmetry of the system changes from symmetric nuclear matter ($\eta = 0$) to pure neutron matter ($\eta = 1$) at a constant density of $\rho = 0.16$ fm^{-3}. I show results for the $\Lambda = 500$ (solid), 450 (dashed) and 414 MeV (dotted lines) interactions.

As discussed previously, these results are obtained from a zero-temperature extrapolation of finite temperature SCGF simulations. As an illustration of the importance of thermal effects, I also show in the top left and top right panels the $\Lambda = 500$ MeV results for U_k^τ at temperatures up to $T = 20$ MeV. The thermal effects are clearly small on the scale of this figure, particularly in comparison to the cutoff and the isospin dependence of the results. I note in passing that the temperature dependence is not monotonous. At momenta below the Fermi surface U_k^τ becomes more attractive as temperature increases. Above the Fermi surface and up to about 500 MeV, the potential instead becomes more repulsive with temperature. This is in agreement with previously reported SCGF results that did not incorporate 3NFs [44].

In terms of isospin dependence, the results also agree with previously reported outcomes in the SCGF approach [64], and in other many-body calculations [93–95]. In symmetric nuclear matter, the single-particle potential has a minimum at low momenta close to $U_{k=0} \approx -60$ MeV, and increases steeply with momenta. At $k = 0$, the lowest cutoff interaction produces a potential that is about 5 MeV more attractive than the highest cutoff force. This cutoff-dependence is relatively constant as a function of momentum up to $k \approx 600$ MeV, where regulator artifacts start to dominate. Above this value of

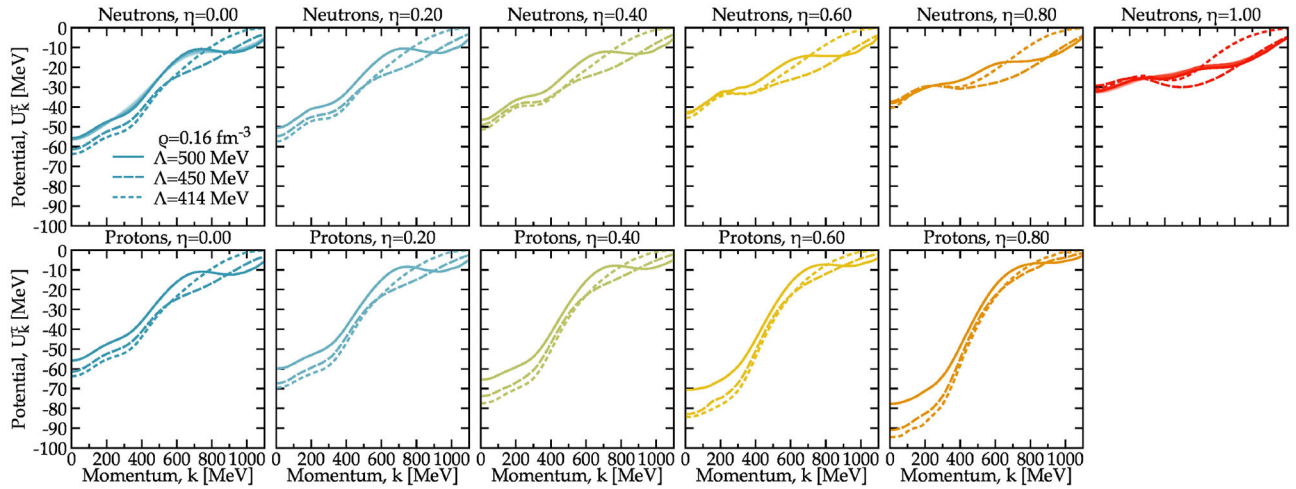

FIGURE 9 | Neutron **(top)** and proton **(bottom)** single-particle potentials as a function of the momentum for the three interactions considered in this work. The panels from left to right correspond to different isospin asymmetries, from $\eta = 0$ (symmetric nuclear matter, leftmost panel) to neutron matter (rightmost panel). The bands for the $\eta = 0$ and $\eta = 1$ obtained with the $\Lambda = 500$ MeV interaction highlight the temperature dependence from $T = 20$ to $T = 0$ MeV.

momentum, the results of the 414 MeV and 450 MeV force go to zero relatively quickly, whereas the potential for the 500 MeV interaction shows a characteristic shallow minimum around $k = 800$ MeV.

As asymmetry increases, the neutron single-particle potential becomes more repulsive and shallower in terms of momentum dependence. In contrast, protons experience a larger attraction when they become the minority species. Their single-particle potentials become significantly more attractive, and in the astrophysically relevant region of $\eta \approx 0.8$, they reach values of $80 - 90$ MeV at $k = 0$. The isospin dependence is to a good approximation linear with isospin asymmetry, as expected on general grounds [94]. I note however that the momentum and isospin dependence of these single-particle potentials is significantly different from those predicted by phenomenological mean-field approaches [96].

Interestingly, the cutoff dependence of the results depends on isospin asymmetry and on the specific nucleon. As neutrons become the predominant species and their single-particle potentials become shallower, the cutoff dependence in the low-momentum single-particle potential below 400 MeV decreases. In neutron matter, the differences between the potentials are of the order of 1 MeV. On the contrary, as the isospin asymmetry increases and the proton spectrum becomes more attractive, the differences between interactions with different cutoffs increase and become of the order of more than 10 MeV.

These differences can be explained by two interrelated factors. One is of a relatively straightforward nature. *np* interactions play no role in neutron matter, and hence the intrinsic differences in the NN interaction are less likely to appear as several partial waves channels are suppressed. In other words, if the fits to the *nn* channels have intrinsically smaller differences between forces than the corresponding *np* channels, neutron-rich systems will show less cutoff dependence. Another factor that plays an important role is the strength (in the sense of "perturbativeness") in different channels. In terms of χEFT, the small cutoff dependence in neutron matter agrees with the idea that neutron matter is a more perturbative system than symmetric nuclear matter [69, 97, 98], because the strong *np* components are missing. It is important to emphasize here that the strong cutoff dependence of the impurity spectrum may not be identified in the energetics of the system, but will clearly have an impact on the dynamics of isospin asymmetric systems.

The momentum dependence of U_k^τ is directly related to the concept of the effective mass. SCGF simulations can be used to extract not only the mass associated to the single-particle spectrum, but also to the so-called $\omega-$ and $k-$effective masses. A detailed analysis of these properties within the SCGF approach is ongoing.

The on-shell imaginary part of the self-energy, Equation (7), is interpreted as an inverse quasi-particle lifetime. For a normal correlated many-fermion system at zero temperature $\Gamma_{k=k_F}$ should be zero, thus signaling an infinite lifetime of quasi-particles at the Fermi surface. The lifetime should be non-zero everywhere else and, as discussed in the context of section 3.2, its magnitude is a combination of phase-space and interaction effects. **Figure 10** provides an overview of the momentum dependence of Γ_k^τ for neutrons (top panels) and protons (bottom panels) as a function of isospin asymmetry. As in the previous figure, extrapolated zero-temperature results are shown.

The isospin and cutoff dependence of the results is very different above and below the Fermi surface. Below the Fermi surface, the SCGF simulations predict a non-zero width. Unlike in BHF calculations, intermediate hole states account explicitly for this non-zero width of hole states $k < k_F$ [94]. For neutrons, this hole component is relatively independent of the isospin asymmetry. In fact $\Gamma_{k=0}^n$ increases from values around $30 - 40$ MeV in symmetric nuclear matter to $40 - 50$ MeV

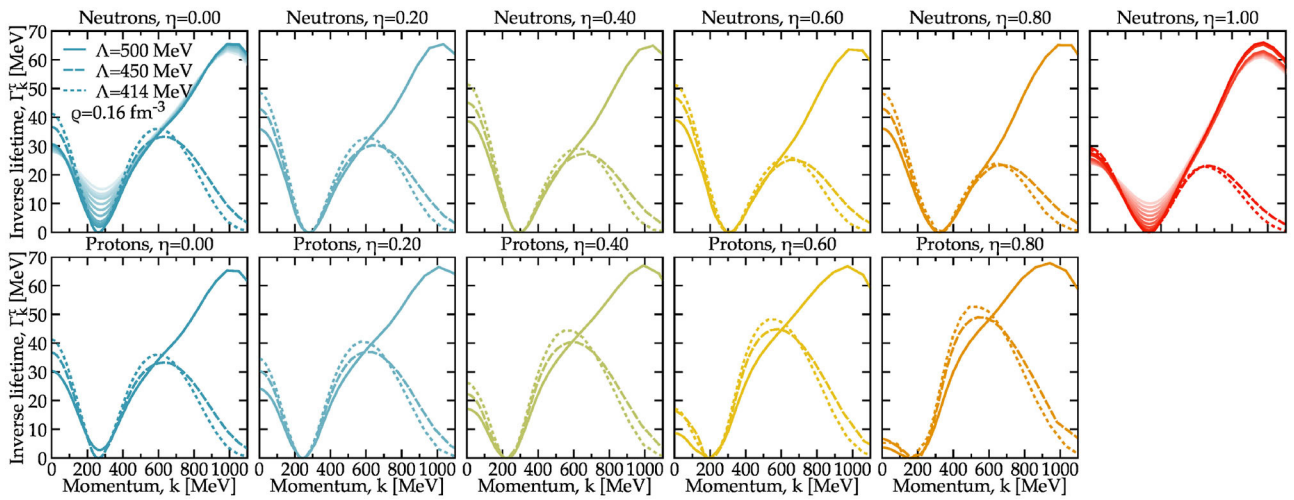

FIGURE 10 | Neutron **(top)** and proton **(bottom)** inverse single-particle lifetimes as a function of the momentum. For details, see the caption of **Figure 9**.

around $\eta = 0.6$, and decreases again to values around $20 - 30$ MeV in neutron matter. In contrast, for protons the hole component decreases steadily with asymmetry. This reflects the decrease in phase space of protons as asymmetry increases. For both neutrons and protons, the cutoff dependence of the hole component is of the order of 10 MeV and relatively independent of isospin asymmetry.

Around the Fermi surface, for all isospin asymmetries, the momentum dependence of Γ_k^τ is rather universal. In most cases, one cannot distinguish the curves from different interactions within about 100 MeV of the Fermi surface. I demonstrate again the importance of thermal effects for the $\Lambda = 500$ MeV interaction at the two extreme asymmetries $\eta = 0$ (top left) and $\eta = 1$ (top right panel). Whereas regions away from the Fermi surface are temperature independent, these panels show that the temperature dependence in Γ_k^τ is prominent around $k = k_F^\tau$. There, the quasi-particle width switches from zero at $T = 0$ to a finite (and increasing) value with temperature. This is to be expected, as the behavior around k_F is governed by phase space arguments [33, 53].

The particle component (at $k > k_F^\tau$) of Γ_k^τ is remarkably more cutoff dependent. The momentum dependence immediately above k_F^τ and up to about $500 - 600$ MeV is very similar in all cases, and shows an increase from zero up to an isospin-dependent maximum for the $\Lambda = 450$ MeV and 414 MeV cases. For neutrons (protons), the peak height decreases (increases) from around 30 MeV in symmetric nuclear matter $\eta = 0$, to around 25 MeV (50 MeV) in pure neutron matter $\eta = 1$. For these two forces Γ_k^τ becomes a decreasing function of momentum above $k \approx 500$ MeV and eventually vanishes above $k \approx 1$ GeV. This is stark contrast to the $\Lambda = 500$ MeV interaction, where the peak of the particle component occurs at much higher momenta in the vicinity of $k \approx 1$ GeV.

The peak is also relatively independent of the isospin asymmetry, and very similar for neutrons and protons. This peak and, in general, the relatively large values of Γ_k^τ in this region are indicative of the short lifetime of high-momentum states. The cutoff dependence clearly indicates that this component of Γ_k^τ depends strongly on the interaction, and the isospin dependence suggests that it is mediated by isoscalar short-range physics independently of the density of the individual components.

These results match with the findings for the spectral functions reported in **Figure 4**. Whereas the width of the neutron spectral function is qualitatively unaffected by a change in isospin asymmetry, the width of the proton spectral function changes significantly with asymmetry for the hole states $k < k_F^\tau$. Single-particle widths provide an alternative way of characterizing beyond mean-field correlations, since in the Hartree-Fock approximation $\Gamma_k = 0$. The results in **Figure 10** indicate that some of the features of Γ_k are robust against isospin asymmetry changes, whereas others are not. In particular, the relative strong dependence of proton single-particle widths with isospin asymmetry may be related to the isospin dependence of the absorptive component of optical potentials [99].

3.5. Other Microscopic Properties

The microscopic results presented so far provide a very complete picture of the dynamics of infinite nuclear systems. The versatility and wide range of applications is an advantage of SCGF techniques. On-shell and off-shell quantities provide valuable information which, when complemented with modern interactions based on χEFT, can help provide estimates of systematic theoretical errors in simulations. A useful characterization of in-medium nuclear properties can be obtained from energy-weighted moments (or sum-rules) of the spectral function. The first moment is connected to effective single-particle energies [100, 101] and has been studied in the context of both symmetric and asymmetric nuclear mater at zero and finite temperatures [102–104]. The conclusions reached by these studies in the early 2000s indicated that the first moment is sensitive to NN interactions, and provides a useful characterization of correlations. The second moment has

only been studied more recently [76]. It measures fluctuations around the single-particle peak, and is a connected to the energy dependence of the imaginary part of the self-energy. Because the latter is also particularly sensitive to the NN force, the second moment can provide a measure of the Hamiltonian properties in both nuclei and infinite nuclear matter.

The SCGF method can be used to study a variety of in-medium quantities which are relevant for nuclear physics experiments. For instance, in the late 1990s, SCGF methods were used to provide a formal redefinition of scattering phaseshifts in the medium [105]. Practical calculations also allowed for predictions of in-medium scattering cross sections in dense matter [106]. The finite lifetime of quasi-particles away from the Fermi surface can be formally translated into an in-medium nucleon mean-free path. This mean-free path is relevant for a variety of nuclear physics considerations, from the validity of the shell model [107] to the characterization of multi-fragmentation reactions [108]. The consistent description of the real and imaginary parts of the self-energy via dispersion relations makes SCGF techniques particularly appealing in this context. In [109], the mean-free path of nucleons in dense infinite matter was computed by means of an extension of the SCGF formalism to the complex plane. Calculations agree well with results obtained with other methods and, most importantly, with a variety of nuclear experiments at intermediate energies [109].

Superfluidity in nuclear systems can be detected by the appearance of in-medium bound states in the two-body scattering matrix, or the two-body propagator. This can be used to characterize the normal-superfluid phase diagram of dense matter. Extensions of the SCGF method to the superfluid domain are possible, by means of the symmetry-breaking Gorkov formalism [43, 46]. Simulations in the normal phase, however, can already provide relevant information for superfluid properties, by extrapolating normal self-energies and spectral functions to zero temperature as discussed above. With this data, one can build effective gap equations that contain the effects associated to the fragmentation of strength [110]. Results with the three chiral interactions presented here indicate that short-range correlations reduce the pairing gap, and provide a gap closure at lower density compared to BCS solutions for both the singlet and the triplet channel [74]. In principle, SCGF calculations at different orders can also be used to estimate systematic uncertainties in this method. This approach may provide a better handle on the role of superfluidity at intermediate and high densities, where the role of long-range correlations is poorly understood [50, 111].

4. MACROSCOPIC PROPERTIES

Simulations based on SCGF methods can access the thermodynamics of the system. A wide range of other many-body methods have been extended to the finite temperature domain, including diagrammatic BHF approaches [112], variational methods [113], and many-body perturbation theory techniques [68, 114, 115]. All of these methods share common limitations in terms of the definition of quasi-particles [116]. This can lead to an inconsistency in terms of the chemical potential. On the one hand, the chemical potential is typically obtained from a normalization condition like Equation (4). On the other, one can find μ from the thermodynamical relation

$$\mu = \frac{\partial \epsilon}{\partial \rho}\,, \tag{13}$$

where ϵ is the energy density. Formally and numerically, these two values may be different depending on the theoretical framework under consideration.

A key advantage of the SCGF formulation at finite temperature is that it guarantees that the two quantities are the same, as long as the self-energy fulfills basic criteria [33]. These criteria are related to the so-called $\Phi-$derivability, and lead to a thermodynamically consistent theory [63]. In practice, this means that in SCGF calculations there is no need to perform numerically the derivative in Equation (13). This is particularly convenient in calculations of the pressure, which can directly be computed from the relation $p = \rho(F/A - \mu)$. I note, however, that differences between microscopic and macroscopic chemical potentials may arise at a numerical level, particularly when the approximated treatment of 3NFs is considered [51].

I show the pressure as a function of density for symmetric nuclear matter (left panel) and pure neutron matter (right panel) in **Figure 11**. These have been computed with the three chiral interactions discussed in this work and include the effect of 3NFs. The results are computed at two finite temperatures $T = 20$ and 10 MeV, and are also extrapolated to $T = 0$. Note that the extrapolation uses many more temperatures, which are not displayed here for simplicity. The discussion below is brief, and details of similar calculations can be found in [44, 48, 49].

For symmetric nuclear matter, the zero-temperature pressure shows a characteristic van der Waals shape, with an area of negative pressure that extends from zero up to the corresponding saturation density of each interaction. This structure signals the existence of a liquid-gas phase transition in nuclear matter [48, 49, 112, 115]. At zero temperature, the pressure vanishes at zero density and at the saturation point. **Figure 11** indicates that the three chiral interactions have significantly different saturation densities, in the region $\rho_0 = (0.14 - 0.165)$ fm^{-3}. As temperature increases, the spinodal region (where $dp/d\rho < 0$) shrinks, until it disappears. At that stage, the pressure can still have an inflection point, which will smoothen out only at the corresponding critical temperature T_c of the liquid-gas phase transition. Different many-body approaches based on the same NN interaction predict different critical points [48]. Similarly, the same many-body set-up with different interactions can yield different critical points [115].

The recent SCGF analysis presented in [49] suggests that the critical temperature predicted by several different χEFT interactions can range from $T_c \approx 11.0$ MeV to $T_c \approx 18$ MeV. The cutoff dependence in **Figure 11** falls within this rage, and T_c lies between about $T_c \approx 11$ MeV for the $\Lambda = 500$ MeV interaction and $T_c \approx 16.5$ MeV for the $\Lambda = 414$ MeV interaction. There is a clear correlation between the saturation energy and

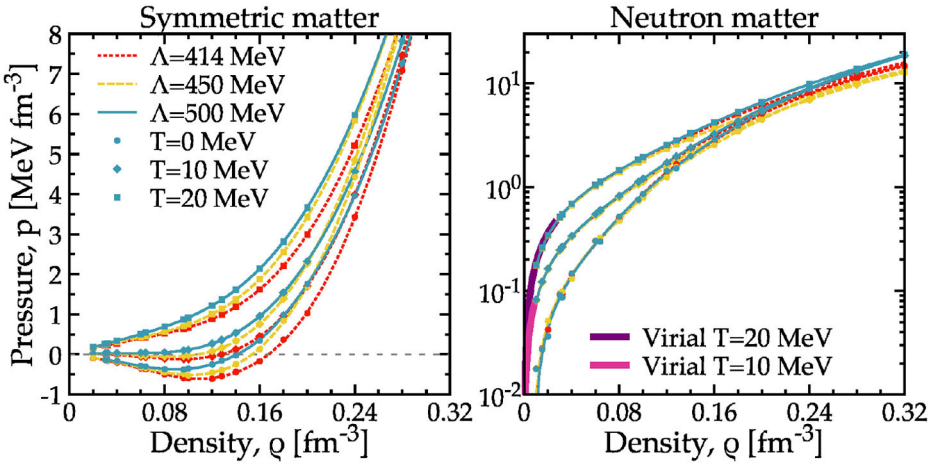

FIGURE 11 | Pressure as a function of density for symmetric nuclear matter **(left)** and pure neutron matter **(right)**. Results for three NN interactions are shown at three different temperatures: $T = 0$ 10 and 20 MeV. At low density for neutron matter, the two bands display the results from the virial expansion.

the critical temperature, with more attractive saturation energies leading to higher critical temperatures [49]. This intuitive behavior is not supported by the analytical predictions of mean-field models [117]. The relatively wide range of critical temperatures dominates over the uncertainties associated to the many-body approximation. Indeed, in [49], the maximum difference obtained between BHF and SCGF predictions for the critical temperature was about 2 MeV. While further many-body benchmarks may be necessary to understand the full many-body dependence of this result, it is clear that the Hamiltonian uncertainty is relevant for finite temperature predictions [51]. In fact, the cutoff dependence of a sub-saturation density property like T_c can be taken as a sign that finite-temperature many-body correlations are significant in this region.

The temperature dependence of the pressure in neutron matter is relevant for astrophysical considerations, particularly in the context of neutron star mergers [16] and proto-neutron star formation [19]. The right panel of **Figure 11** shows the pressure on a semilogarithmic scale as a function of density. The same three temperatures (0, 10 and 20 MeV) are presented. At low densities, the pressure should be well-described in terms of the model-independent virial expansion, which only depends on neutron-neutron scattering phaseshifts [118]. The pressure for fugacities $z < 0.5$ at $T = 10$ MeV and 20 MeV is shown with two solid bands at low densities in the figure. Clearly, the low-density SCGF results agree well with virial predictions. The low-density pressure is in fact remarkably cutoff independent, and the first distinguishable cutoff-dependent features only show up above $\rho \approx 0.10$ fm^{-3}. This is in stark contrast to the case of symmetric nuclear matter. Noticeably, this cutoff independence also holds for the low-density, zero-temperature extrapolated results. All in all, the cutoff and many-body dependence of low-density neutron matter predictions are well under control (independently of temperature), as already discussed elsewhere [23, 28, 29, 69, 97].

The cutoff dependence in neutron matter is only clearly distinguishable above saturation density. There, and toward the high density limit of applicability of chiral interactions, the $\Lambda = 500$ MeV interaction is providing more pressure at a given density. This is followed by a decreasing pressure from the $\Lambda = 414$ MeV and $\Lambda = 450$ MeV forces. It is interesting to note that the last two switch orders with respect to symmetric nuclear matter, where for a given density the $\Lambda = 450$ MeV interaction provides more pressure than the $\Lambda = 414$ MeV interaction. The cutoff dependence is only one of several systematic uncertainties in these results. SCGF can also provide an estimate of the many-body uncertainties, by performing calculations with self-energies obtained not only at a ladder level, but also at the first- and second-order level. The results of a recent analysis indicate that the many-body uncertainty is smaller than that associated to the underlying NN force by a factor of $2 - 3$ at twice saturation density [51].

With respect to the temperature dependence, one can distinguish two distinct regimes. At sub-saturation densities, cutoff independent results dominate. At higher densities, reaching the degenerate supra-saturation regime, the cutoff dependence overtakes temperature effects. A more quantitative analysis of the temperature dependence can be obtained by looking at the so-called thermal index (or adiabatic index) of the equation of state [14]. It characterizes the temperature dependence of the pressure (or energy) of the system. Carbone and Schwenk have recently provided an in-depth analysis of the density, temperature and Hamiltonian dependence of the thermal index obtained in SCGF simulations [18]. They find that some of the assumptions made in previous literature regarding the temperature and density independence of this quantity do not hold. In addition, the effect of 3NFs is important in the high-density regime.

The two extreme limits of isospin asymmetry are interesting on their own, and provide insight into different relevant phenomena. However, both in the study of the liquid-phase transition [119] and in neutron-star astrophysics [73], the actual

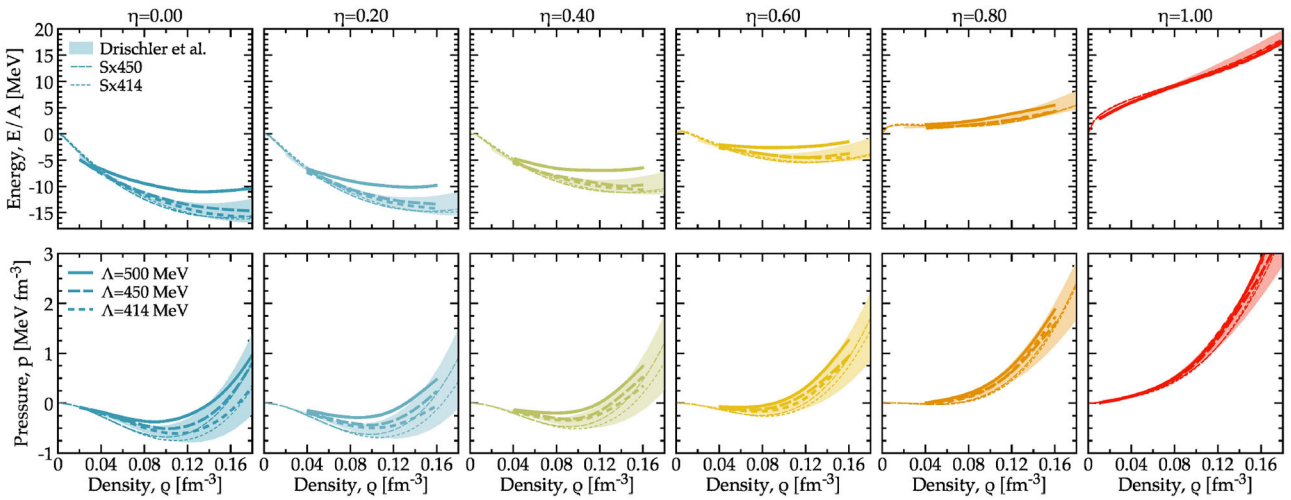

FIGURE 12 | Energy per particle **(top)** and pressure **(bottom)** as a function of density for different isospin asymmetries. Results have been extrapolated to zero temperature. The thin lines have been generated from Skyrme functionals fitted to second-order calculations with the same underlying NN forces by Lim and Holt [120]. The bands are obtained from fits to many-body perturbation theory calculations by Drischler et al. [73].

isospin dependence of the results is relevant. Arbitrary isospin-asymmetric systems can be explored with SCGF simulations, and the results in **Figure 12** provide both the energy per particle (top) and the pressure (bottom panels) as a function of density for several asymmetries. Results are presented for the three interactions with different cutoffs.

For comparison, I show two different sets of results based on similar *ab initio* calculations. The narrow lines, labeled Sx450 and Sx414, correspond to Skyrme parametrizations derived in [120]. These density functionals were in turn fit to asymmetric matter calculations performed at second order in many-body perturbation theory for the $\Lambda = 450$ MeV and 414 MeV chiral interactions. I do not show the corresponding Sx500 Skyrme results, which were fitted to data with free-particle (rather than self-consistently dressed) intermediate states. The internal dressing of fermion lines is closer in spirit to the SCGF results presented here, and one thus expects to find a better agreement. I note that if non-perturbative effects were small, one would expect an agreement between the fits and the SCGF data.

The bands in the different panels of **Figure 12** have been obtained from fits to second-order many-body perturbation theory calculations for seven different chiral interactions in [73]. These fits reproduce the results obtained at second order in perturbation theory with internal Hartree-Fock propagators. These calculations are different to the SCGF approach in that they implement a different averaging procedure for the 3NFs, including an average value of the center-of-mass momentum.

The results from other methods are provided here for reference and only represent a crude estimate of the many-body uncertainties. The discussion below is therefore qualitative, rather than quantitative. The top left panel of **Figure 12** clearly indicates that all these interactions and approximations are able to provide saturation for symmetric nuclear matter. The SCGF $\Lambda = 500$ MeV results saturate at a too low density and a too high energy per particle. In contrast, the 450 MeV and 414 MeV interactions predict better saturation energies, but are slightly off in terms of density. This may be due to deficiencies of the interactions, the many-body scheme or the implementation of the 3NFs into the SCGF approach [29]. I note however that the saturation energy itself is an extrapolated quantity and a recent reanalysis based on nuclear data suggests it may be a bit more repulsive than anticipated [121].

Comparing the energy per particle to the results of the Sx parametrizations, I find that the SCGF results for the 414 MeV and 450 MeV chiral interactions are qualitatively similar to those obtained in perturbation theory calculations in [70] (for symmetric nuclear matter) and [120] (for asymmetric nuclear matter). The ladder resummation in the SCGF calculations seems to bring in repulsion at intermediate densities for isospin-symmetric systems. This repulsive effect, of the order of a couple of MeV in symmetric nuclear matter, reduces as the isospin asymmetry increases.

As it is well-known, the energy per particle becomes more repulsive as η increases. For pure neutron matter, and in the sub-saturation region shown in the figure, the cutoff dependence of the SCGF results is very small, certainly within 1 MeV. The size of the cutoff dependence is in agreement with the initial findings reported in [69], although the latter were obtained using third-order perturbation-theory calculations. In fact, as the isospin asymmetry of the system increases, the differences in energy between the Sx414 and Sx450 results and the SCGF calculations become much smaller. For densities above 0.06 fm^{-3}, all calculations agree in the density dependence of the energy per particle of neutron matter. This is to be expected if one assumes that neutron matter is more perturbative than symmetric nuclear matter. The SCGF and the Sx414 and Sx450 results lie in the lower range of the band provided by [73], which indicates that the cutoff dependence associated to the three chiral interactions presented

in this work is not necessarily representative of the systematic uncertainty due to different Hamiltonians.

The reduced cutoff dependence of the results, as the isospin asymmetry evolves from the left to the right panels, has clear implications on the symmetry energy. Because symmetric nuclear matter is more bound for the $\Lambda = 414$ MeV and 450 MeV forces, and the neutron matter energy is basically the same, one expects the symmetry energies of these two forces to be relatively larger than that of the 500 MeV interaction. Indeed, computing the symmetry energy as the difference between the two extremes of isospin at $\rho = 0.16$ fm^{-3}, one finds values that range from $S_0 = 31.5$ MeV for the 414 MeV force up to 29.8 MeV and 25.4 MeV for the 450 MeV and 500 MeV forces. These values are in agreement with those previously reported for these forces in [122], and are somewhat smaller than empirical determinations [8].

The bottom panels of **Figure 12** provide a relatively similar picture in terms of the pressure. In symmetric nuclear matter (left panel), the pressure is negative at sub-saturation densities and, other than the $\Lambda = 500$ MeV SCGF results, all results agree qualitatively. The picture evolves as isospin asymmetry increases. The spinodal, negative pressure zone decreases as η becomes larger, as expected in general grounds [119]. For most interactions, the critical asymmetry where the spinodal area vanishes is in the range $\eta = 0.6$ to 0.8. At these relatively large asymmetries, all the different many-body predictions are contained with the bands obtained by Drischler et al. [73]. Noticeably, the results of the $\Lambda = 500$ MeV interaction that were off the band at small asymmetries, fall into the band as isospin asymmetry increases and neutron matter is approached. This indicates that the discrepancies associated to this force with respect to other simulations lie in the isovector component of the interaction.

The cutoff dependence of the SCGF results offers only an initial indication of the size of uncertainties associated to the NN force. In qualitative terms, however, the behavior is similar to that predicted by the bands in [73] which could be explored with non-perturbative methods in the future. At the level of the interaction, there are other sources of uncertainty (like the low-energy constants or the regulator dependence) that are not really considered by these exploratory considerations [51]. The dependence on the many-body method is also relevant as the system becomes more and more isospin symmetric, and quantities like the thermal index or the symmetry energy may be substantially affected by the many-body method under consideration. As such, benchmark comparisons in asymmetric systems would provide an interesting testing ground for newly developed forces.

5. CONCLUSIONS

In this work, I have briefly reviewed a set of SCGF techniques that have been used over the last couple of decades to study infinite nuclear systems. SCGF approaches are unique in terms of their flexibility, which allows for both perturbative and non-perturbative studies. The SCGF formalism can be formulated at finite temperature and provide thermodynamically consistent results. The same approach can be used to study the properties of finite nuclei with similar many-body approximations and equivalent interactions [42]. A single SCGF calculation yields not only bulk nuclear properties, including binding energies and thermodynamics, but also a wide range of microphysics information, ranging from predictions associated to the fragmentation of the single-particle strength to the characterization of quasi-particle lifetimes. With an appropriate account of 3NFs, this method can now competitively tackle issues in infinite nuclear matter physics with the same level of predictive power as other many-body approaches. The predictions in terms of the density and isospin dependence of fragmentation strengths are unique and provide an insight that is also relevant for the understanding of the evolution of correlations with isospin.

In this review, I have focused on the properties of symmetric and asymmetric nuclear matter and neutron matter as obtained from a set of three χEFT interactions based on N3LO NN interactions and N2LO 3NFs. This provides a limited but already illustrative set of results that spans a wide range in terms of short-range physics. Of course, one would ideally perform these simulations with the largest possible set of interactions to get a more quantitative estimate of the dependence of the results on the Hamiltonian. A more sophisticated treatment using Bayesian analysis techniques could eventually improve the estimates of systematic uncertainties [9].

The results indicate that the N3LO $\Lambda = 500$ MeV interaction produces significantly different strength distributions than the $\Lambda = 450$ MeV and 414 MeV forces. As expected, the 500 MeV interaction provides high momentum components in the momentum distribution, and also large additional components in the self-energy. The two softer interactions provide results which are significantly more perturbative. In other words, their momentum distributions die out quicker in momenta and the energy dependence of the associated self-energies is much more limited. These generic results hold independently of the isospin asymmetry. In fact, the results for the 450 MeV and 414 MeV interactions are very similar across a wide range of density, isospin asymmetry and temperatures. In pure neutron matter, the 500 MeV interaction results are also very close to the 450 MeV and 414 MeV interactions. This can be translated into a strong isospin dependence of the overall cutoff dependence. This point has already been discussed in the past in [69, 122], and our SCGF simulations confirm these trends from a different many-body perspective.

SCGF provide access to quasi-particle properties that are relevant in various contexts. Single-particle potentials for neutrons and protons in neutron-rich matter show interesting asymmetry dependences. It is well-known that the single-particle potential for neutrons becomes less attractive with increasing isospin asymmetry. At the same time, it becomes less sensitive to the cutoff. In contrast, the proton potential becomes more attractive in neutron-rich matter and, as the isospin asymmetry increases, the cutoff dependence is enhanced. This behavior should be reflected in the corresponding effective masses. The asymmetry dependence of the single-particle width is also

interesting, and again suggests substantial differences in the minority and majority components.

When it comes to bulk properties, I find results that are qualitatively close to those established with many-body perturbation theory methods. Again, the predictions of the $\Lambda = 500$ MeV interaction are noticeably different than the lower cutoff results in the isospin symmetric case. In fact, the saturation energy of this interaction is about $4-5$ MeV more repulsive than empirical estimates, in contrast to the lower cutoff simulations. Results for the 450 MeV-414 MeV forces are more consistent with each other. These also agree well with previous many-body perturbation theory calculations based on these interactions in isospin-symmetric, isospin-asymmetric nuclear matter and pure neutron matter [68].

One can draw several conclusions from this analysis. The isospin dependence of short-range correlations can be predicted with SCGF techniques and appears to be less pronounced in bulk systems than it is in finite nuclei [66, 67, 85, 87]. The cutoff dependence of the results in isospin asymmetric systems affects more the single-particle properties of protons than those of neutrons. In this sense, the simulations of proton impurities in pure neutron matter could provide some insight into the model-dependence of neutron-proton forces. I also note that *ab initio* simulations of single-particle potentials are significantly different from those predicted by phenomenological approaches [96].

Looking forward, the SCGF method is at an advantage with respect to some other methods in its handling of finite temperature and isospin-asymmetry effects. For supra-saturation densities, this is relevant for neutron star mergers, as well as for neutron-star formation. There, the non-perturbative nature of SCGF methods can handle short-range correlation effects and hence provide meaningful results up to presumably higher densities than perturbative calculations [51]. The effects associated to the fragmentation of strength are also relevant in a variety of high-density astrophysical settings, where they have often been ignored. These include predictions for the equation of state, but also for pairing properties and response functions. Broadly speaking, previous SCGF simulations that have tackled these issues have not relied on systematically improvable chiral interactions that are also helpful in providing estimates of theoretical uncertainties. Interestingly, the low-density high-temperature regime of the neutrinosphere in supernova explosions is also relevant for astrophysical simulations, and it can be tackled with SCGF simulations. There, SCGF methods can provide insight into quantities like single-particle potential shifts [20, 92] and response functions needed for neutrino processes [21]. Our results indicate that these should be interaction-independent, and the dependence on the many-body method will provide a good handle on systematic errors.

DATA AVAILABILITY STATEMENT

The original contributions presented in the study are included in the article, further inquiries can be directed to the corresponding author.

AUTHOR CONTRIBUTIONS

The author confirms being the sole contributor of this work and has approved it for publication.

ACKNOWLEDGMENTS

The author thanks A. Polls, A. Carbone, J. W. Holt, C. Drischler, C. Barbieri, and M. Drissi for fruitful discussion. This work is supported by the UK Science and Technology Facilities Council (STFC) Grant No. ST/P005314/1. Some of the material presented in this paper was available from my contribution to the proceedings of the International Nuclear Physics Conference 2019 [123].

REFERENCES

1. Abbott BP, Abbott R, Abbott TD, Acernese F, Ackley K, Adams C. et al. GW170817: observation of gravitational waves from a binary neutron star inspiral. *Phys Rev Lett*. (2017) **119**:161101. doi: 10.1103/PhysRevLett.119.161101
2. Abbott BP, Abbott R, Abbott TD, Abraham S, Acernese F, Ackley K. et al. GW190425: observation of a compact binary coalescence with total mass $\sim$ 3.4 M $\odot$. *Astrophys J Lett*. (2020) **892**:L3. doi: 10.3847/2041-8213/ab75f5
3. Abbott BP, Abbott R, Abbott TD, Acernese F, Ackley K, Adams C. et al. GW170817: measurements of neutron star radii and equation of state. *Phys Rev Lett*. (2018) **121**:161101. doi: 10.1103/PhysRevLett.121.161101
4. Abbott BP, Abbott R, Abbott TD, Abraham S, Acernese F, Ackley K. et al. Properties of the binary neutron star merger GW170817. *Phys Rev X*. (2019) **9**:011001. doi: 10.1103/PhysRevX.9.011001
5. Raaijmakers G, Greif SK, Riley TE, Hinderer T, Hebeler K, Schwenk A, et al. Constraining the dense matter equation of state with joint analysis of NICER and LIGO/Virgo measurements. *Astrophys J Lett*. (2020) **893**:L21. doi: 10.3847/2041-8213/ab822f
6. Miller MC, Lamb FK, Dittmann AJ, Bogdanov S, Arzoumanian Z, Gendreau KC, et al. PSR J0030+0451 mass and radius from NICER data and implications for the properties of neutron star matter. *Astrophys J Lett*. (2019) **887**:L24. doi: 10.3847/2041-8213/ab50c5
7. Riley TE, Watts AL, Bogdanov S, Ray PS, Ludlam RM, Guillot S, et al. A NICER View of PSR J0030+0451: millisecond pulsar parameter estimation. *Astrophys J Lett*. (2019) **887**:L21. doi: 10.3847/2041-8213/ab481c
8. Tsang MB, Stone JR, Camera F, Danielewicz P, Gandolfi S, Hebeler K, et al. Constraints on the symmetry energy and neutron skins from experiments and theory. *Phys Rev C*. (2012) **86**:015803. doi: 10.1103/PhysRevC.86.015803
9. Drischler C, Furnstahl RJ, Melendez JA, Phillips DR. How well do we know the neutron-matter equation of state at the densities inside neutron stars? A Bayesian approach with correlated uncertainties (2020). *arXiv preprint arXiv:2004*.07232. Available online at: https://arxiv.org/abs/2004.07232
10. Danielewicz P, Lacey R, Lynch WG. Determination of the equation of state of dense matter. *Science*. (2002) **298**:1592–96. doi: 10.1126/science.1078070
11. Tews I. Quantum Monte Carlo methods for astrophysical applications. *Front Phys*. (2020) **8**:153. doi: 10.3389/fphy.2020.00153
12. Baym G, Hatsuda T, Kojo T, Powell PD, Song Y, Takatsuka T. From hadrons to quarks in neutron stars: a review. *Rep Prog Phys*. (2018) **81**:056902. doi: 10.1088/1361-6633/aaae14
13. Lim Y, Holt JW. Neutron star tidal deformabilities constrained by nuclear theory and experiment. *Phys Rev Lett*. (2018) **121**:062701. doi: 10.1103/PhysRevLett.121.062701
14. Constantinou C, Muccioli B, Prakash M, Lattimer JM. Thermal properties of supernova matter: the bulk homogeneous phase. *Phys Rev C*. (2014) **89**:065802. doi: 10.1103/PhysRevC.89.065802

15. Constantinou C, Muccioli B, Prakash M, Lattimer JM. Thermal properties of hot and dense matter with finite range interactions. *Phys Rev C*. (2015) **92**:025801. doi: 10.1103/PhysRevC.92.025801
16. Baiotti L, Rezzolla L. Binary neutron star mergers: a review of Einstein's richest laboratory. *Rep Prog Phys*. (2017) **80**:096901. doi: 10.1088/1361-6633/aa67bb
17. Duez MD, Zlochower Y. Numerical relativity of compact binaries in the 21st century. *Rep Prog Phys*. (2018) **82**:016902. doi: 10.1088/1361-6633/aadb16
18. Carbone A, Schwenk A. Ab initio constraints on thermal effects of the nuclear equation of state. *Phys Rev C*. (2019) **100**:025805. doi: 10.1103/PhysRevC.100.025805
19. Pons JA, Reddy S, Prakash M, Lattimer JM, Miralles JA. Evolution of proto-neutron stars. *Astrophys J*. (1999) **513**:780–804. doi: 10.1086/306889
20. Martinez-Pinedo G, Fischer T, Lohs A, Huther L. Charged-current weak interaction processes in hot and dense matter and its impact on the spectra of neutrinos emitted from protoneutron star cooling. *Phys Rev Lett*. (2012) **109**:251104. doi: 10.1103/PhysRevLett.109.251104
21. Rrapaj E, Holt JW, Bartl A, Reddy S, Schwenk A. Charged-current reactions in the supernova neutrino-sphere. *Phys Rev C*. (2015) **91**:035806. doi: 10.1103/PhysRevC.91.035806
22. Gandolfi S, Hammer HW, Klos P, Lynn JE, Schwenk A. Is a trineutron resonance lower in energy than a tetraneutron resonance? *Phys Rev Lett*. (2017) **118**:232501. doi: 10.1103/PhysRevLett.118.232501
23. Tews I, Krüger T, Hebeler K, Schwenk A. Neutron matter at next-to-next-to-next-to-leading order in chiral effective field theory. *Phys Rev Lett*. (2013) **110**:032504. doi: 10.1103/PhysRevLett.110.032504
24. Epelbaum E, Hammer HW, Meißner UG. Modern theory of nuclear forces. *Rev Mod Phys*. (2009) **81**:1773–825. doi: 10.1103/RevModPhys.81.1773
25. Machleidt R, Entem DR. Chiral effective field theory and nuclear forces. *Phys Rep*. (2011) **503**:1–75. doi: 10.1016/j.physrep.2011.02.001
26. Ishii N, Aoki S, Hatsuda T. Nuclear force from lattice QCD. *Phys Rev Lett*. (2007) **99**:022001. doi: 10.1103/PhysRevLett.99.022001
27. Hatsuda T. Lattice quantum chromodynamics and baryon-baryon interactions. *Front Phys*. (2018) **13**:132105. doi: 10.1007/s11467-018-0829-4
28. Drischler C, Hebeler K, Schwenk A. Asymmetric nuclear matter based on chiral two- and three-nucleon interactions. *Phys Rev C*. (2016) **93**:054314. doi: 10.1103/PhysRevC.93.054314
29. Drischler C, Hebeler K, Schwenk A. Chiral interactions up to next-to-next-to-next-to-leading order and nuclear saturation. *Phys Rev Lett*. (2019) **122**:042501. doi: 10.1103/PhysRevLett.122.042501
30. Baldo M, Polls A, Rios A, Schulze HJ, Vidana I. Comparative study of neutron and nuclear matter with simplified Argonne nucleon-nucleon potentials. *Phys Rev C*. (2012) **86**:064001. doi: 10.1103/PhysRevC.86.064001
31. Piarulli M, Bombaci I, Logoteta D, Lovato A, Wiringa RB. Benchmark calculations of pure neutron matter with realistic nucleon-nucleon interactions. *Phys Rev C*. (2020) **101**:045801. doi: 10.1103/PhysRevC.101.045801
32. Dickhoff WH, Barbieri C. Self-consistent Green's function method for nuclei and nuclear matter. *Prog Part Nucl Phys*. (2004) **52**:377–496. doi: 10.1016/j.ppnp.2004.02.038
33. Dickhoff WH, Van Neck D. *Many-Body Theory Exposed!* 2nd ed. New Jersey, NJ: World Scientific (2008). doi: 10.1142/6821
34. Barbieri C, Carbone A. Self-consistent Green's function approaches. In: Hjorth-Jensen M, Lombardo MP, van Kolck U, editors. *An Advanced Course in Computational Nuclear Physics*. Springer (2017). p. 571–644. doi: 10.1007/978-3-319-53336-0_11
35. Economou EN. *Green's Functions in Quantum Physics*. Berlin, Heidelberg: Springer (2006). doi: 10.1007/3-540-28841-4
36. Stefanucci G, van Leeuwen R. *Nonequilibrium Many-Body Theory of Quantum Systems*. Cambridge: Cambridge University Press (2013).
37. Abrikosov AA, Gorkov LP, Dzyaloshinskii IY. *Quantum Field Theoretical Methods in Statistical Physics*. 2nd ed. Pergamon Press (1965).
38. Mattuck RD. *A Guide to Feynman Diagrams in the Many-Body Problem*. New York, NY: Dover Publications (1992).
39. Fetter AL, Walecka JD. *Quantum Theory of Many-Particle System*. 1st ed. New York, NY: Dover (2003).
40. Müther H, Polls A. Two-body correlations in nuclear systems. *Prog Part Nucl Phys*. (2000) **45**:243–334. doi: 10.1016/S0146-6410(00)00105-8
41. Gandolfi S, Gezerlis A, Carlson J. Neutron matter from low to high density. *Annu Rev Nucl Part Sci*. (2015) **65**:303–28. doi: 10.1146/annurev-nucl-102014-021957
42. Somá V. Self-consistent Green's function theory for atomic nuclei (2020).
43. Bozek P. Superfluidity with dressed nucleons. *Phys Lett B*. (2003) **551**:93. doi: 10.1016/S0370-2693(02)03007-1
44. Rios A, Polls A, Vidana I. Hot neutron matter from a self-consistent Green's-functions approach. *Phys Rev C*. (2009) **79**:025802. doi: 10.1103/PhysRevC.79.025802
45. Somá V, Bozek P. Thermodynamic properties of nuclear matter with three-body forces. *Phys Rev C*. (2009) **80**:025803. doi: 10.1103/PhysRevC.80.025803
46. Bozek P. Superfluid nuclear matter calculations. *Nucl Phys A*. (1999) **657**:187. doi: 10.1016/S0375-9474(99)00325-5
47. Polls A, Ramos A, Gearhart CC, Dickhoff WH, Muther H. Short range correlations and spectral functions for nuclear matter and finite nuclei. *Prog Part Nucl Phys*. (1995) **34**:371–380. doi: 10.1016/0146-6410(95)00032-E
48. Rios A, Polls A, Ramos A, Müther H. Liquid-gas phase transition in nuclear matter from realistic many-body approaches. *Phys Rev C*. (2008) **78**:044314. doi: 10.1103/PhysRevC.78.044314
49. Carbone A, Polls A, Rios A. Microscopic predictions of the nuclear matter liquid-gas phase transition. *Phys Rev C*. (2018) **98**:025804. doi: 10.1103/PhysRevC.98.025804
50. Ding D, Rios A, Dussan H, Dickhoff WH, Witte SJ, Carbone A, et al. Pairing in high-density neutron matter including short- and long-range correlations. *Phys Rev C*. (2016) **94**:025802. doi: 10.1103/PhysRevC.94.025802
51. Carbone A. Setting nonperturbative uncertainties on finite-temperature properties of neutron matter. *Phys Rev Res*. (2020) **2**:023227. doi: 10.1103/PhysRevResearch.2.023227
52. Jeukenne JP, Lejeune A, Mahaux C. Many-body theory of nuclear matter. *Phys Rep*. (1976) **25**:83–174. doi: 10.1016/0370-1573(76)90017-X
53. Luttinger JM. Analytic Properties of single-particle propagators for many-Fermion systems. *Phys Rev*. (1961) **121**:942. doi: 10.1103/PhysRev.121.942
54. Carbone A, Cipollone A, Barbieri C, Rios A, Polls A. Self-consistent Green's functions formalism with three-body interactions. *Phys Rev C*. (2013) **88**:054326. doi: 10.1103/PhysRevC.88.054326
55. Carbone A, Polls A, Rios A. Symmetric nuclear matter with chiral three-nucleon forces in the self-consistent Green's functions approach. *Phys Rev C*. (2013) **88**:044302. doi: 10.1103/PhysRevC.88.044302
56. Carbone A, Rios A, Polls A. Correlated density-dependent chiral forces for infinite-matter calculations within the Green's function approach. *Phys Rev C*. (2014) **90**:054322. doi: 10.1103/PhysRevC.90.054322
57. Frick T, Müther H. Self-consistent solution to the nuclear many-body problem at finite temperature. *Phys Rev C*. (2003) **68**:034310. doi: 10.1103/PhysRevC.68.034310
58. Rios A. Thermodynamical Properties of Nuclear Matter from a Self-Consistent Green's Function Approach. University of Barcelona (2007).
59. Cipollone A, Barbieri C, Navrátil P. Isotopic chains around oxygen from evolved chiral two- and three-nucleon interactions. *Phys Rev Lett*. (2013) **111**:062501. doi: 10.1103/PhysRevLett.111.062501
60. Rios A, Polls A, Ramos A, Müther H. Entropy of a correlated system of nucleons. *Phys Rev C*. (2006) **74**:054317. doi: 10.1103/PhysRevC.74.054317
61. Pethick CJ, Carneiro GM. Specific heat of a normal fermi liquid. I. Landau-Theory Approach. *Phys Rev A*. (1973) **7**:304–318. doi: 10.1103/PhysRevA.7.304
62. Carneiro GM, Pethick CJ. Specific heat of a normal Fermi liquid. II. Microscopic approach. *Phys Rev B*. (1975) **11**:1106–24. doi: 10.1103/PhysRevB.11.1106
63. Kadanoff LP, Baym G. Quantum Statistical Mechanics. New York, NY: W.A. Benjamin (1962).
64. Frick T, Müther H, Rios A, Polls A, Ramos A. Correlations in hot asymmetric nuclear matter. *Phys Rev C*. (2005) **71**:014313. doi: 10.1103/PhysRevC.71.014313
65. Konrad P, Lenske H, Mosel U. Short range correlations and spectral functions in asymmetric nuclear matter. *Nucl Phys A*. (2005) **756**:192–212. doi: 10.1016/j.nuclphysa.2005.03.083
66. Rios A, Polls A, Dickhoff WH. Depletion of the nuclear Fermi sea. *Phys Rev C*. (2009) **79**:064308. doi: 10.1103/PhysRevC.79.064308

67. Rios A, Polls A, Dickhoff WH. Density and isospin-asymmetry dependence of high-momentum components. *Phys Rev C*. (2014) **89**:044303. doi: 10.1103/PhysRevC.89.044303
68. Wellenhofer C, Holt JW, Kaiser N. Thermodynamics of isospin-asymmetric nuclear matter from chiral effective field theory. *Phys Rev C*. (2015) **92**:015801. doi: 10.1103/PhysRevC.92.015801
69. Coraggio L, Holt JW, Itaco N, Machleidt R, Sammarruca F. Reduced regulator dependence of neutron-matter predictions with perturbative chiral interactions. *Phys Rev C*. (2013) **87**:014322. doi: 10.1103/PhysRevC.87.014322
70. Coraggio L, Holt JW, Itaco N, Machleidt R, Marcucci LE, Sammarruca F. Nuclear-matter equation of state with consistent two- and three-body perturbative chiral interactions. *Phys Rev C*. (2014) **89**:044321. doi: 10.1103/PhysRevC.89.044321
71. Holt JW, Kaiser N, Weise W. Density-dependent effective nucleon-nucleon interaction from chiral three-nucleon forces. *Phys Rev C*. (2010) **81**:024002. doi: 10.1103/PhysRevC.81.024002
72. Holt JW, Kawaguchi M, Kaiser N. Implementing chiral three-body forces in terms of medium-dependent two-body forces. *Front Phys*. (2020) **8**:100. doi: 10.3389/fphy.2020.00100
73. Drischler C, Carbone A, Hebeler K, Schwenk A. Neutron matter from chiral two- and three-nucleon calculations up to N^3LO. *Phys Rev C*. (2016) **94**:054307. doi: 10.1103/PhysRevC.94.054307
74. Rios A, Polls A, Dickhoff WH. Pairing and short-range correlations in nuclear systems. *J Low T Phys*. (2017) **189**:234–49. doi: 10.1007/s10909-017-1818-7
75. Ramos A, Dickhoff WH, Polls A. Binding energy and momentum distribution of nuclear matter using Green's function methods. *Phys Rev C*. (1991) **43**:2239–53. doi: 10.1103/PhysRevC.43.2239
76. Rios A, Carbone A, Polls A. Comparison of nuclear Hamiltonians using spectral function sum rules. *Phys Rev C*. (2017) **96**:014003. doi: 10.1103/PhysRevC.96.014003
77. Rohe D, Armstrong CS, Asaturyan R, Baker OK, Bueltmann S, Carasco C. et al. Correlated strength in the nuclear spectral function. *Phys Rev Lett*. (2004) **93**:182501. doi: 10.1103/PhysRevLett.93.182501
78. Schmidt A, Pybus JR, Weiss R, Segarra EP, Hrnjic A, Denniston A. et al. Probing the core of the strong nuclear interaction. *Nature*. (2020) **578**:540–4. doi: 10.1038/s41586-020-2021-6
79. Typel S, Brown BA. Neutron radii and the neutron equation of state in relativistic models. *Phys Rev C*. (2001) **64**:027302. doi: 10.1103/PhysRevC.64.027302
80. Haensel P, Potekhin AY, Yakovlev DG. *Neutron Stars 1: Equation of State and Structure*. New York, NY: Springer (2007). doi: 10.1007/978-0-387-47301-7
81. Tang A, Watson JW, Aclander J, Alster J, Asryan G, Averichev Y. et al. $n-p$ short-range correlations from $(p, 2p+n)$ measurements. *Phys Rev Lett*. (2003) **90**:042301. doi: 10.1103/PhysRevLett.90.042301
82. Piasetzky E, Sargsian M, Frankfurt L, Strikman M, Watson JW. Evidence for strong dominance of proton-neutron correlations in nuclei. *Phys Rev Lett*. (2006) **97**:162504. doi: 10.1103/PhysRevLett.97.162504
83. Hen O, Sargsian M, Weinstein LB, Piasetzky E, Hakobyan H, Higinbotham DW, et al. Nuclear physics. Momentum sharing in imbalanced Fermi systems. *Science*. (2014) 346:614–7. doi: 10.1126/science.1256785
84. Sargsian MM. New properties of the high-momentum distribution of nucleons in asymmetric nuclei. *Phys Rev C*. (2014) **89**:034305. doi: 10.1103/PhysRevC.89.034305
85. Duer M, Hen O, Piasetzky E, Hakobyan H, Weinstein LB, Braverman M. et al. Probing high-momentum protons and neutrons in neutron-rich nuclei. *Nature*. (2018) **560**:617–621. doi: 10.1038/s41586-018-0400-z
86. Ryckebusch J, Cosyn W, Stevens S, Casert C, Nys J. The isospin and neutron-to-proton excess dependence of short-range correlations. *Phys Lett B*. (2019) **792**:21–8. doi: 10.1016/j.physletb.2019.03.016
87. Paschalis S, Petri M, Macchiavelli AO, Hen O, Piasetzky E. Nucleon-nucleon correlations and the single-particle strength in atomic nuclei. *Phys Lett B*. (2020) **800**:135110. doi: 10.1016/j.physletb.2019.135110
88. Carbone A, Polls A, Rios A. High-momentum components in the nuclear symmetry energy. *Europhys Lett*. (2012) **97**:22001. doi: 10.1209/0295-5075/97/22001
89. Hen O, Li BA, Guo WJ, Weinstein LB, Piasetzky E. Symmetry energy of nucleonic matter with tensor correlations. *Phys Rev C*. (2015) **91**:025803. doi: 10.1103/PhysRevC.91.025803
90. Cai BJ, Li BA. Symmetry energy of cold nucleonic matter within a relativistic mean field model encapsulating effects of high-momentum nucleons induced by short-range correlations. *Phys Rev C*. (2016) **93**:014619. doi: 10.1103/PhysRevC.93.014619
91. Gade A, Adrich P, Bazin D, Bowen MD, Brown BA, Campbell CM et al. Reduction of spectroscopic strength: Weakly-bound and strongly-bound single-particle states studied using one-nucleon knockout reactions. *Phys Rev C*. (2008) **77**:044306. doi: 10.1103/PhysRevC.77.044306
92. Roberts LF, Reddy S, Shen G. Medium modification of the charged-current neutrino opacity and its implications. *Phys Rev C*. (2012) **86**:065803. doi: 10.1103/PhysRevC.86.065803
93. Zuo W, Lejeune A, Lombardo U, Mathiot JF. Microscopic three-body force for asymmetric nuclear matter. *Eur Phys J A*. (2002) **14**:469–75. doi: 10.1140/epja/i2002-10031-y
94. Zuo W, Cao LG, Li BA, Lombardo U, Shen CW. Isospin splitting of the nucleon mean field. *Phys Rev C*. (2005) **72**:014005. doi: 10.1103/PhysRevC.72.014005
95. Holt JW, Kaiser N, Miller GA. Microscopic optical potential for exotic isotopes from chiral effective field theory. *Phys Rev C*. (2016) **93**:064603. doi: 10.1103/PhysRevC.93.064603
96. Sellahewa R, Rios A. Isovector properties of the Gogny interaction. *Phys Rev C*. (2014) **90**:054327. doi: 10.1103/PhysRevC.90.054327
97. Hebeler K, Lattimer JM, Pethick CJ, Schwenk A. Equation of state and neutron star properties constrained by nuclear physics and observation. *Astrophys J*. (2013) **773**:11. doi: 10.1088/0004-637X/773/1/11
98. Drischler C, Somá V, Schwenk A. Microscopic calculations and energy expansions for neutron-rich matter. *Phys Rev C*. (2014) **89**:025806. doi: 10.1103/PhysRevC.89.025806
99. Charity RJ, Sobotka LG, Dickhoff WH. Asymmetry dependence of proton correlations. *Phys Rev Lett*. (2006) **97**:162503. doi: 10.1103/PhysRevLett.97.162503
100. Duguet T, Hagen G. Ab initio approach to effective single-particle energies in doubly closed shell nuclei. *Phys Rev C*. (2012) **85**:034330. doi: 10.1103/PhysRevC.85.034330
101. Duguet T, Hergert H, Holt JD, Somá V. Nonobservable nature of the nuclear shell structure: meaning, illustrations, and consequences. *Phys Rev C*. (2015) **92**:034313. doi: 10.1103/PhysRevC.92.034313
102. Polls A, Ramos A, Ventura J, Amari S, Dickhoff WH. Energy weighted sum rules for spectral functions in nuclear matter. *Phys Rev C*. (1994) **49**:3050–4. doi: 10.1103/PhysRevC.49.3050
103. Frick T, Müther H, Polls A. Sum rules and short-range correlations in nuclear matter at finite temperature. *Phys Rev C*. (2004) **69**:054305. doi: 10.1103/PhysRevC.69.054305
104. Rios A, Polls A, Müther H. Sum rules and correlations in asymmetric nuclear matter. *Phys Rev C*. (2006) **73**:024305. doi: 10.1103/PhysRevC.73.024305
105. Dickhoff WH. Scattering of dressed nucleons in nuclear matter. *Phys Rev C*. (1998) **58**:2807–20. doi: 10.1103/PhysRevC.58.2807
106. Dickhoff WH, Gearhart CC, Roth EP, Polls A, Ramos A. Phase shifts and in-medium cross sections for dressed nucleons in nuclear matter. *Phys Rev C*. (1999) **60**:064319. doi: 10.1103/PhysRevC.60.064319
107. Negele J, Yazaki K. Mean free path in a nucleus. *Phys Rev Lett*. (1981) **47**:71–4. doi: 10.1103/PhysRevLett.47.71
108. Lopez O, Durand D, Lehaut G, Borderie B, Frankland JD, Rivet MF. et al. In-medium effects for nuclear matter in the Fermi-energy domain. *Phys Rev C*. (2014) **90**:064602. doi: 10.1103/PhysRevC.90.069903
109. Somá V. Self-consistent Green's function theory for atomic nuclei. *arXiv* [Preprint]. (2020) arxiv:2003.11321. URL https://arxiv.org/abs/2003.11321.
110. Müther H, Dickhoff WH. Pairing properties of nucleonic matter employing dressed nucleons. *Phys Rev C*. (2005) **72**:054313. doi: 10.1103/PhysRevC.72.054313
111. Schwenk A, Friman B. Polarization contributions to the spin dependence of the effective interaction in neutron matter. *Phys Rev Lett*. (2004) **92**:082501. doi: 10.1103/PhysRevLett.92.082501
112. Baldo M, Ferreira L. Nuclear liquid-gas phase transition. *Phys Rev C*. (1999) **59**:682–703. doi: 10.1103/PhysRevC.59.682

113. Mukherjee A, Pandharipande VR. Variational theory of hot nucleon matter. *Phys Rev C*. (2007) **75**:035802. doi: 10.1103/PhysRevC.75.035802
114. Tolos L, Friman B, Schwenk A. Neutron matter at finite temperature. *Nucl Phys A*. (2008) **806**:105–16. doi: 10.1016/j.nuclphysa.2008.02.309
115. Wellenhofer C, Holt JW, Kaiser N, Weise W. Nuclear thermodynamics from chiral low-momentum interactions. *Phys Rev C*. (2014) **89**:064009. doi: 10.1103/PhysRevC.89.064009
116. Wellenhofer C. Zero-temperature limit and statistical quasiparticles in many-body perturbation theory. *Phys Rev C*. (2019) **99**:065811. doi: 10.1103/PhysRevC.99.065811
117. Rios A. Effective interaction dependence of the liquid-gas phase transition in symmetric nuclear matter. *Nucl Phys A*. (2010) **845**:58–87. doi: 10.1016/j.nuclphysa.2010.05.057
118. Horowitz CJ, Schwenk A. The virial equation of state of low-density neutron matter. *Phys Lett B*. (2006) **638**:153–9. doi: 10.1016/j.physletb.2006.05.055
119. Vidana I, Polls A. Spinodal instabilities of asymmetric nuclear matter within the Brueckner–Hartree–Fock approach. *Phys Lett B*. (2008) **666**:232–8. doi: 10.1016/j.physletb.2008.07.066
120. Lim Y, Holt JW. Structure of neutron star crusts from new Skyrme effective interactions constrained by chiral effective field theory. *Phys Rev C*. (2017) **95**:065805. doi: 10.1103/PhysRevC.95.065805
121. Atkinson MC, Dickhoff WH, Piarulli M, Rios A, Wiringa RB. Revisiting the relation between the binding energy of finite nuclei and the equation of state of infinite nuclear matter (2020). *arXiv preprint arXiv:2001*.07231. Available online at: https://arxiv.org/abs/2001.07231.
122. Sammarruca F, Coraggio L, Holt JW, Itaco N, Machleidt R, Marcucci LE. Toward order-by-order calculations of the nuclear and neutron matter equations of state in chiral effective field theory. *Phys Rev C*. (2015) **91**:054311. doi: 10.1103/PhysRevC.91.054311
123. Rios A. Short range correlations in nuclei and nuclear matter. In: *Proceedings of the International Nuclear Physics Conference*. (2019).

Conflict of Interest: The author declares that the research was conducted in the absence of any commercial or financial relationships that could be construed as a potential conflict of interest.

frontiers in Physics

REVIEW
published: 29 April 2020
doi: 10.3389/fphy.2020.00116

Ab initio Calculations of Lepton-Nucleus Scattering

Noemi Rocco [1,2]*

[1] Physics Division, Argonne National Laboratory, Argonne, IL, United States, [2] Fermi National Accelerator Laboratory, Theoretical Physics Department, Batavia, IL, United States

The advent of high precision measurements of neutrinos and their oscillations calls for accurate predictions of their interactions with nuclear targets utilized in the detectors. Over the past decade, *ab initio* methods based on realistic nuclear interactions and current operators were able to provide accurate description of lepton-nucleus scattering processes. Achieving a comprehensive description of the different reaction mechanisms active in the broad range of energies relevant for oscillation experiments required the introduction of controlled approximations of the nuclear many-body models. In this review, we give an overview of recent developments in the description of electroweak interactions within different approaches and discuss the future perspectives to support the experimental effort in this new precision era.

Keywords: lepton-nucleus interactions, *ab-initio* nuclear methods, electroweak interactions, nuclear structure and interactions, neutrino-nucleus cross-sections

OPEN ACCESS

Edited by:
Saori Pastore,
Los Alamos National Laboratory (DOE), United States

Reviewed by:
Francesco Pederiva,
University of Trento, Italy
Stefano Gandolfi,
Los Alamos National Laboratory (DOE), United States

***Correspondence:**
Noemi Rocco
nrocco@anl.gov

Specialty section:
This article was submitted to Nuclear Physics, a section of the journal Frontiers in Physics

Received: *15 January 2020*
Accepted: *25 March 2020*
Published: *29 April 2020*

Citation:
Rocco N (2020) Ab initio Calculations of Lepton-Nucleus Scattering. Front. Phys. 8:116. doi: 10.3389/fphy.2020.00116

1. INTRODUCTION

Understanding neutrino properties and interactions is the main focus of the world-wide accelerator-based neutrino-oscillation program. The new generation of short [1] and long-baseline [2] neutrino experiments—such as the Deep Underground Neutrino Experiment (DUNE)—will address fundamental questions and play a key role in the search of physics beyond the Standard Model. In particular, the absolute scale of neutrino masses and the presence of charge parity (CP) violation in the leptonic sector, which may contribute to our understanding of the matter-antimatter asymmetry of the universe, will be determined. The existence of a fourth (sterile) neutrino will be investigated, this could explain the excess of electron neutrinos from charged current quasi-elastic events reported by the MiniBooNe collaboration [3].

Studying neutrino-nucleus interactions in the energy region of interest for oscillation experiments is a multi-scale problem. In fact, the experiments [4–9] are sensitive to a broad range of energy where different reaction mechanisms contribute [10, 11]. Quasielastic scattering is dominant for energies of hundreds of MeVs, in this case the lepton interacts with individual bound nucleons. In addition to this, there are corrections accounting for coupling of the probe to interacting nucleons, belonging to a correlated pairs on connected via two-body currents. For larger values of the energy, a struck nucleon can be excited to a baryon resonance state and subsequently decays into pions, or give rise to deep-inelastic scattering (DIS) processes. Constructing a framework able to describe these diverse reaction mechanisms on the same footing is a formidable nuclear-theory challenge. Nuclear effective field theory (EFT) provides a systematic way to construct nuclear interactions and currents performing a low-momentum expansion. In addition, an estimate of the theoretical uncertainty–which will be crucial for the neutrino data analyses– can be properly assessed. In the last decade there has been a tremendous progress in the field of nuclear *ab initio* methods made possible by the increasing availability of computing

resources and the development of new algorithms. Within these approaches the nucleus is treated as a collection of nucleons interacting with each other via two- and three-body forces obtained within nuclear EFTS. The interaction with external electroweak probes is described by one- and two-body effective currents that are consistent with the nuclear potentials [12–17].

Among these *ab initio* many-body methods, the Green's Function Monte Carlo (GFMC) method utilizes quantum Monte Carlo (QMC) techniques [18] to perform first-principle calculations of nuclei up to ^{12}C [19, 20]. More recently the GFMC method has also been applied to the calculation of the electroweak sum rules and response functions of ^{4}He and ^{12}C, including one and two-body currents [21–23]. In order to do that, integral transform techniques have been utilized. The accuracy of the inversion procedure adopted within the GFMC to obtain the response function from its integral transform has been compared and benchmarked with the Lorentz Integral Transform method [24]. The GFMC electroweak responses computed in the quasielastic sector are virtually exact for low and moderate values of the momentum transfer. Initial and final state correlations are fully retained within this approach [25, 26]. In order to extend the predictive power of this approach, relativistic effects in nuclear kinematics were included [24] leading to an excellent agreement with electron scattering data off ^{4}He. However, within this approach it is not possible to access more exclusive channels, the calculations are fully inclusive. The inclusion of explicit pion degrees of freedom in the nuclear wave function [27], necessary to describe the resonance production region, is extremely complicated and its achievement is still a long way ahead.

The short-time approximation (STA) method has been recently proposed to overcome some of the limitations of GFMC [28]. In particular, this approach allows to compute both the inclusive and exclusive response of nuclei in the high-energy (short-time) limit–corresponding to the Fermi energy and above– utilizing realistic nuclear interactions and currents. In the STA the full ground-state dynamics is retained while the hadronic final state is factorized at the two-nucleon level, this approximation is expected to be valid at high-energy and momentum transfer. It allows to account for the final state interactions of the pairs involved in the interaction vertex and to incorporate two-nucleon correlations and currents as well as their interference, which are known be sizable in the GFMC results [22–26]. While keeping consistently two-body physics and ensuing quantum interference contributions, the STA is not expected to accurately model the correct physics for low-lying excitations or collective behavior like giant resonances. A good agreement with the GFMC electromagnetic responses of ^{4}He is observed after enforcing the correct threshold behavior. Since the STA involves only two active nucleons, it suitable to be improved and include relativistic currents and kinematics as well pion production channels.

In the past years, the framework based on the impulse approximation (IA) and realistic spectral-functions (SFs) has been largely utilized to describe electron-nucleus scattering data in the limit of moderate and high momentum transfer [29, 30]. This scheme combines a realistic description of the initial target state with a fully-relativistic interaction vertex and kinematics. This is achieved factorizing the hadronic final state in terms of a free nucleon state and enclosing all the information on nuclear structure in the SF. The latter does not depend on the momentum transfer and can be computed within non-relativistic nuclear many-body approaches. In this review we consider two nuclear SFs, derived within the correlated basis function (CBF) formalism [31] and the self-consistent Green's function (SCGF) theory [32, 33]. These two approaches utilize different nuclear forces and involve different approximations in each of the SF calculations. Within the factorization scheme lepton-nucleus scattering is rewritten as an incoherent sum of elementary processes involving individual nucleons. This framework has been extended and generalized to include two-nucleon emission processes induced by relativistic meson-exchange currents [34] and applied to calculate the electroweak inclusive cross sections of carbon and oxygen [35, 36]. In order to tackle the resonance production region, the electroweak pion production amplitudes generated within the dynamical coupled-channel (DCC) model [37–39] have been included in the IA formalism. The results obtained convoluting the DCC elementary amplitudes with the CBF SF will also be reported.

In this review, we present lepton-nucleus interaction results obtained within different many-body methods. In section 2 we outline the formalism and define the electroweak cross sections, nuclear interactions and currents. In section 3 we discuss the integral transform techniques utilized in the GFMC to obtain the nuclear response functions. Sections 4 and 5 are devoted to the STA and extended factorization scheme, respectively. We present recent results obtained within each of the aforementioned approaches for different nuclei. In section 6 we state out conclusions and discuss future directions.

2. FORMALISM

We consider the scattering of an initial electron of four-momentum $k = (E, \mathbf{k})$ off a nucleus A at rest; in the final state only the outgoing electron with momentum $k = (E', \mathbf{k}')$ is detected. The inclusive double differential cross section for this process can be written in Born Approximation as

$$\left(\frac{d^2\sigma}{dE'd\Omega'}\right)_e = \frac{\alpha^2}{Q^4}\frac{E'}{E}L_{\mu\nu}R^{\mu\nu} \tag{1}$$

where $\alpha \simeq 1/137$ is the fine structure constant and Ω' is the scattering solid angle in the direction specified by $\mathbf{k}'$. The energy and the momentum transfer are denoted by ω and $\mathbf{q}$, respectively, with $Q^2 = -q^2 = \mathbf{q}^2 - \omega^2$. The lepton tensor is fully determined by the lepton kinematical variables. It can be written neglecting the electron mass as

$$L_{\mu\nu} = \frac{1}{EE'}(k_\mu k'_\nu + k'_\mu k_\nu - g_{\mu\nu}\, k\cdot k')\,. \tag{2}$$

The hadronic tensor describes the transition between the initial and final nuclear states $|\Psi_0\rangle$ and $|\Psi_f\rangle$, with energies E_0 and E_f.

For nuclei of spin-zero, it can be written as

$$R^{\mu\nu}(\mathbf{q},\omega) = \sum_f \langle\Psi_0|J^{\mu\,\dagger}(\mathbf{q},\omega)|\Psi_f\rangle\langle\Psi_f|J^{\nu}(\mathbf{q},\omega)|\Psi_0\rangle\delta(E_0+\omega-E_f)\,. \quad (3)$$

where we sum over all hadronic final states and $J^{\mu}(\mathbf{q},\omega)$ is the nuclear current operator whose structure will be discussed in detail in section 2.1. For inclusive processes, the cross section of Equation (1) only depends on the two response functions, $R_L(\mathbf{q},\omega)$ and $R_T(\mathbf{q},\omega)$, which describe the interactions with a virtual photon longitudinally (L) and transversely (T) polarized. It is given by

$$\left(\frac{d^2\sigma}{dE'd\Omega'}\right)_e = \left(\frac{d\sigma}{d\Omega'}\right)_{\rm M}\Big[A_L\,R_L(|\mathbf{q}|,\omega)+A_T\,R_T(|\mathbf{q}|,\omega)\Big]\,, \quad (4)$$

where the lepton kinematical factors are given by

$$A_L = \left(\frac{q^2}{\mathbf{q}^2}\right)^2\,,\quad A_T = -\frac{1}{2}\frac{q^2}{\mathbf{q}^2}+\tan^2\frac{\theta}{2}\,, \quad (5)$$

and

$$\left(\frac{d\sigma}{d\Omega'}\right)_{\rm M} = \left[\frac{\alpha\cos(\theta/2)}{2E'\sin^2(\theta/2)}\right]^2 \quad (6)$$

is the Mott cross section depending on the scattering angle θ.

The extension to neutral- and charge-current electroweak processes is straightforward. Let us consider the scattering of a neutrino (ν_ℓ) or an anti-neutrino ($\bar{\nu}_\ell$) off a nuclear target. In analogy with the electromagnetic case, we denote by $k=(E,\mathbf{k})$ and $k=(E',\mathbf{k}')$ the momentum of the initial and outgoing lepton; the double-differential cross section can be written as [40, 41]

$$\left(\frac{d\sigma}{dE'd\Omega'}\right)_{\nu_\ell/\bar{\nu}_\ell} = \frac{G^2}{4\pi^2}\,k'E'\,L_{\mu\nu}R^{\mu\nu}\,, \quad (7)$$

where $G=G_F$ and $G=G_F\cos\theta_c$ for neutral current (NC) and charge current (CC) processes, respectively, with $\cos\theta_c = 0.97425$ [42] and for the Fermi coupling constant we use $G_F = 1.1803\times10^{-5}$ [43]. The leptonic tensor contains an extra-contribution proportional to the Levi Civita

$$L_{\mu\nu} = \frac{1}{EE'}(k_\mu k'_\nu + k'_\mu k_\nu - g_{\mu\nu}\,k\cdot k' \pm i\epsilon_{\mu\rho\nu\sigma}k^\rho k'^\sigma)\,, \quad (8)$$

where the $+$ $(-)$ sign is for ν_ℓ ($\bar{\nu}_\ell$) initiated reactions. The hadronic tensor is the same as Equation (3) but the current operator will have a vector and axial component, its explicit expression will be given in section 2.1. We perform the Lorentz contraction of the leptonic and hadronic tensor of Equation (7), yielding

$$\left(\frac{d\sigma}{dE'd\Omega'}\right)_{\nu/\bar{\nu}} = \frac{G_F^2\cos^2\theta_c}{4\pi^2}\frac{k'}{2E_\nu}\Big[\hat{L}_{CC}R_{CC}+2\hat{L}_{CL}R_{CL} +\hat{L}_{LL}R_{LL}+\hat{L}_TR_T\pm2\hat{L}_{T'}R_{T'}\Big]\,. \quad (9)$$

Taking the three-momentum transfer along the z axis and the total three-momentum in the $x-z$ plane, we can define q and Q as

$$q = k-k' = (\omega,\mathbf{q})\,,\quad \mathbf{q}=(0,0,q_z)$$
$$Q = k+k' = (\Omega,\mathbf{Q})\,,\quad \mathbf{Q}=(Q_x,0,Q_z)\,, \quad (10)$$

and write the leptonic kinematical factors as

$$\hat{L}_{CC} = \Omega^2-q_z^2-m_\ell^2,\qquad \hat{L}_{CL} = (-\Omega Q_z+\omega q_z)$$
$$\hat{L}_{LL} = {Q_z}^2-\omega^2+m_\ell^2,\qquad \hat{L}_T = \frac{{Q_x}^2}{2}-q^2+m_\ell^2$$
$$\hat{L}_{T'} = \Omega q_z-\omega Q_z\,, \quad (11)$$

with $m_\ell^2 = k'^2$ the mass of the outgoing lepton. The five electroweak response functions correspond to different components of the hadro tensor

$$R_{CC} = R^{00},\qquad R_{CL} = -\frac{1}{2}(R^{03}+R^{30})$$
$$R_{LL} = R^{33},\qquad R_T = R^{11}+R^{22}$$
$$R_{T'} = -\frac{i}{2}(R^{12}-R^{21})\,. \quad (12)$$

Note that electron and neutrino scattering cross sections are written in a similar fashion as a contraction of the leptonic and the hadronic tensor. This analogy will become even more apparent in section 2.1 where we introduce the explicit expression of the current operators and use the conserved vector current (CVC) hypothesis to connect the vector part of the electroweak current with the electromagnetic one. For this reason, any model of neutrino-nucleus scattering has to be capable of describing electron-scattering cross sections first [44].

2.1. Nuclear Hamiltonian and Current Operator

The internal structure of nuclei and their reactions can be described within non-relativistic many body approaches utilizing an Hamiltonian in which the nucleons are the only active degrees of freedom. Its general expression is given by

$$H = \sum_i\frac{\mathbf{p}_i^2}{2m_N}+\sum_{i<j}v_{ij}+\sum_{i<j<k}V_{ijk}\,, \quad (13)$$

where $\mathbf{p}_i$ is the momentum of the i-th nucleon having mass m_N, while the potentials v_{ij} and V_{ijk} model the nucleon-nucleon (NN) and three-nucleon (3N) interactions, respectively. A model of NN interaction has to be constrained by the large number of NN scattering data available. Currently, very accurate results have been obtained from both phenomenological approaches and chiral effective field theory able to accurately fit these data.

The Argonne $v18$ is a finite, coordinate space NN potential that has been fit to the full Nijmegen phase-shift database and to low energy scattering parameters and deuteron properties.

It can be written as a product of radial functions and spin-isospin operator

$$v_{ij} = \sum_{p=1,\ldots,18} v_p(r_{ij}) O_{ij}^p \tag{14}$$

where $r_{ij} = |\mathbf{r}_i - \mathbf{r}_j|$. The first 14 operators are charge independent (corresponding to the older Argonne $v14$ model)

$$O_{ij}^{p=1,\ldots,14} = \Big[1, \boldsymbol{\sigma}_i \cdot \boldsymbol{\sigma}_j, S_{ij}, \mathbf{L}\cdot\mathbf{S}, \mathbf{L}^2, \mathbf{L}^2\boldsymbol{\sigma}_i\cdot\boldsymbol{\sigma}_j, (\mathbf{L}\cdot\mathbf{S})^2\Big], \times \Big[1, \boldsymbol{\tau}_i\cdot\boldsymbol{\tau}_j\Big] \tag{15}$$

where $\boldsymbol{\sigma}$ and $\boldsymbol{\tau}$ are the Pauli matrices operating over the nucleon spin and isospin degrees of freedom, respectively, $S_{ij} = 3\boldsymbol{\sigma}_i\cdot\hat{r}_{ij}\boldsymbol{\sigma}_j\cdot\hat{r}_{ij} - \boldsymbol{\sigma}_i\cdot\boldsymbol{\sigma}_j$ is the tensor operator, $\mathbf{L}_{ij} = \frac{1}{2i}(\mathbf{r}_i - \mathbf{r}_j)\times(\nabla_i - \nabla_j)$ is the relative angular momentum, and $\mathbf{S}_{ij} = \frac{1}{2}(\boldsymbol{\sigma}_i + \boldsymbol{\sigma}_j)$ is the total spin. The terms $p = 15\ldots18$ are included in the formulation of the Argonne potential to account for small violations of charge symmetry [45]. In addition to the NN interactions, also phenomenological 3N interactions have been developed. In particular the Illinois 7 (IL7) interaction is expressed as a sum of a two-pion-exchange P-wave term (Fujita-Miyazawa), a two-pion-exchange S-wave contribution, a three-pion-exchange contribution, and a 3N central interaction [46]. These phenomenological NN and 3N interactions were successfully utilized in QMC calculations of nuclear properties, neutron drops, and neutron-star matter [18, 47–50].

In the last decades there has been a tremendous progress in development of chiral EFT interactions as proven by the availability of a number of different potentials [13, 51–54]. However, it is only recently with their formulation in coordinate space that the application of chiral forces within QMC approaches became possible. These new local potentials have been computed up to N^{2}LO with consistent 3N terms in Gezerlis et al. [55, 56], the Δ-isobar degrees of freedom were fully accounted for in the derivation of Piarulli et al. [57, 58].

In analogy with the nuclear Hamiltonian, the current operator can be expressed as a sum of one- and two-body terms

$$J^\mu = \sum_i j^\mu(i) + \sum_{i<j} j^\mu(ij) + \ldots \tag{16}$$

The one-body electromagnetic current is given by

$$j^\mu_{\rm EM} = \bar{u}(\mathbf{p}')\Big[\mathcal{F}_1\gamma^\mu + i\sigma^{\mu\nu}q_\nu\frac{\mathcal{F}_2}{2m_N}\Big]u(\mathbf{p}), \tag{17}$$

where $\mathbf{p}$ and $\mathbf{p}'$ are the initial and final nucleon momentum. The isoscalar (S) and isovector (V) form factors, $\mathcal{F}_1$ and $\mathcal{F}_2$, are given by combination of the Dirac and Pauli ones, F_1 and F_2, as

$$\mathcal{F}_{1,2} = \frac{1}{2}[F^S_{1,2} + F^V_{1,2}\tau_z] \tag{18}$$

where τ_z is the is the isospin operator and

$$F^S_{1,2} = F^p_{1,2} + F^n_{1,2}, \qquad F^V_{1,2} = F^p_{1,2} - F^n_{1,2}. \tag{19}$$

The Dirac and Pauli form factors can be expressed in terms of the electric and magnetic form factors of the proton and neutron as

$$F_1^{p,n} = \frac{G_E^{p,n} + \tau G_M^{p,n}}{1+\tau}, \qquad F_2^{p,n} = \frac{G_M^{p,n} - G_E^{p,n}}{1+\tau} \tag{20}$$

with $\tau = Q^2/4m_N^2$. Therefore, the electromagnetic current can be schematically written as $J^\mu_{\rm EM} = J^\mu_{\gamma,S} + J^\mu_{\gamma,z}$ where the first is the isoscar term and the second is the isovector multiplied by the isospin operators τ_z. The one-body charge and current operator are obtained from the non-relativistic reduction of the covariant operator of Equation (17) including all the terms up to $1/m_N^2$ in the expansion. It leads to the following expression for isoscalar charge, transverse ($\perp$) and longitudinal ($\parallel$) to $\mathbf{q}$ component of the current operator

$$\begin{aligned} j^0_{\gamma,S} &= \frac{G_E^S}{2\sqrt{1+Q^2/4m_N^2}} - i\frac{2G_M^S - G_E^S}{8m_N^2}\mathbf{q}\cdot(\boldsymbol{\sigma}_i\times\mathbf{p}_i) \\ \mathbf{j}^\perp_{\gamma,S} &= \frac{G_E^S}{2m_N}\mathbf{p}_i^\perp - i\frac{G_M^S}{4m_N}(\mathbf{q}\times\boldsymbol{\sigma})_i \\ j^\parallel_{\gamma,S} &= \frac{\omega}{|\mathbf{q}|}j^0_{\gamma,S}. \end{aligned} \tag{21}$$

Note that the last relation has been obtained from current conservation relation discussed in Equation (30). Analogously to Equation (19), the isoscalar and isovector component of the electric and magnetic form factors are written as

$$G^S_{E,M} = G^p_{E,M} + G^n_{E,M}, \qquad G^V_{E,M} = G^p_{E,M} - G^n_{E,M}. \tag{22}$$

The isovector contribution to the current $J^\mu_{\gamma,z}$ is obtained by replacing $G^S_{E,M} \rightarrow G^V_{E,M}\tau_z$. The electroweak interactions of a neutrino or anti-neutrino with the hadronic target can be induced by both CC and NC transitions. The current operator is written as a different combination of vector and axial terms. Note that in both cases the Conserved Vector Current (CVC) hypothesis allows to relate the vector form factor to the electromagnetic ones

$$\begin{aligned} J^\mu_{CC} &= J^\mu_{\gamma,z} + J^\mu_{a,z} \\ J^\mu_{NC} &= -2\sin^2\theta_W J^\mu_{\gamma,S} + (1 - 2\sin^2\theta_W)J^\mu_{\gamma,z} + J^\mu_{a,z}, \end{aligned} \tag{23}$$

where θ_W is the Weinberg angle ($\sin^2\theta_W = 0.2312$ [42]). The fully relativistic expression of the axial one-body current operator reads

$$j^\mu_A = \bar{u}(\mathbf{p}')\Big[-\gamma^\mu\gamma_5\mathcal{F}_A - q^\mu\gamma_5\frac{\mathcal{F}_P}{m_N}\Big]u(\mathbf{p}). \tag{24}$$

For CC processes the axial and pseudo-scalar form factors can be written as

$$\mathcal{F}_A = F_A\tau_\pm, \qquad \mathcal{F}_P = F_P\tau_\pm, \tag{25}$$

with $\tau_{i,\pm} = (\tau_{i,x} \pm \tau_{i,y})/2$ being the isospin raising-lowering operator.

The dipole parametrization for the axial form factor is routinely adopted in most of the calculations, it reads

$$F_A = \frac{g_A}{(1 + Q^2/m_A^2)^2}\,, \tag{26}$$

where the nucleon axial-vector coupling constant is assumed to be $g_A = 1.2694$. The impact of the Q^2 dependence of the axial form factor on neutrino-nucleus cross-section predictions has been discussed in Aguilar-Arevalo et al. [59] and Bernard et al. [60]. The validity of the dipole parametrization has been questioned and in these regards both lattice-QCD calculations [61] and the so called "z-expansion" analysis [62] has been recently proposed. The pseudo-scalar form factor is obtained by using Partially Conserved Axial Current (PCAC) arguments to write it in terms of the axial one

$$F_P = \frac{2m_N^2}{(m_\pi^2 + Q^2)} F_A\,. \tag{27}$$

For NC transitions, we report the non-relativistic reduction of the charge- and axial-current operator [63] (for brevity we neglect order $1/m_N^2$ terms)

$$j^0_{a,z}(i) = -\frac{G_A}{4m_N}\tau_{i,z}\boldsymbol{\sigma}_i \cdot (\mathbf{q} + \mathbf{p}_i)\,, \qquad \mathbf{j}_{a,z}(i) = -\frac{G_A}{4m_N}\boldsymbol{\sigma}_i\tau_{i,z}\,. \tag{28}$$

The CC non-relativistic current is obtained by substituting in the non-relativistic isovector term $j^\mu_{\gamma,z}$ and $j^\mu_{a,z}$ of Equation (28), $\tau_{i,z}/2 \to \tau_{i,\pm}$ and adding a pseudoscalar contribution

$$j^\mu_{a,PS} = \frac{G_A}{m_\pi^2 + Q^2}\tau_{i,\pm} q^\mu \boldsymbol{\sigma}_i \cdot \mathbf{q}\,. \tag{29}$$

The electromagnetic current must satisfy the continuity equation

$$\nabla \cdot \mathbf{J} + i\Big[H, J^0\Big] = 0 \tag{30}$$

which links the two-body exchange current operator to the NN interaction and leads to separate continuity equations for the one- and two-body current operators. Chiral EFT formulations allow to construct electroweak currents which are fully consistent with the nuclear forces entering the hamiltonian. The gauge invariance of the theory implies that the nuclear current operators satisfy the continuity equation with the potentials order by order of the chiral expansion. The calculation of the two-body electromagnetic currents has been the subject of extensive study carried out by different groups [64–68]. Another important advantage of chiral EFT consists on having connected three-nucleon interaction and the two-nucleon axial current; their derivation up to one-loop is reported in Krebs et al. [69] and Baroni et al. [70] while the Δ-full expression obtained consistently with the nuclear forces of Piarulli et al. [57, 58] can be found in Baroni et al. [71].

The majority of the results that will be presented in this review have been obtained utilizing the aforementioned AV18 potential and related semi-phenomenological currents. The spin and isospin dependence of the NN potential leads to a non-vanishing commutator with the non-relativistic one-body charge operator. In order to satisfy the continuity equation, the so-called "model-independent" two-body currents $\mathbf{j}_{\rm MI}(ij)$ have to be introduced; their longitudinal part is directly constrained by the NN interaction while their transverse components are not uniquely defined. The main contributions comes from the one-pion and one-rho exchange current operator, their expression is well-known and reported in Rocco et al. [72], Dekker et al. [36] and Schiavilla et al. [73] both in their relativistic and non-relativistic formulation.

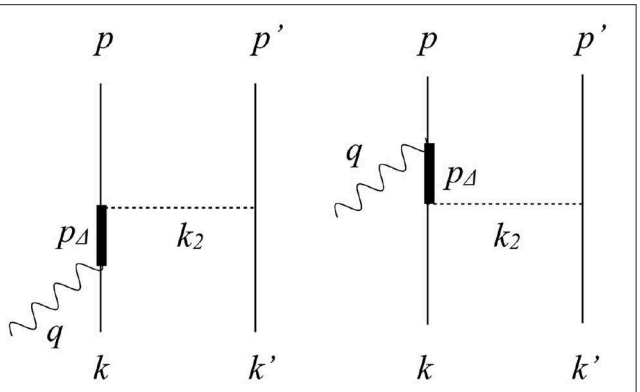

FIGURE 1 | Feynman diagrams of the Δ contribution to two-body currents. Solid, thick, and dashed lines represent nucleons, deltas, pions, respectively while the wavy line correspond to the vector boson.

In addition to the model-independent two body currents a significant contribution comes from model dependent terms in which the exchange of a pion is followed by the excitation of a Δ-resonance in the intermediate state. Due to the transverse nature of this current, its expression is model dependent. In fact, the form of the vector part is not determined from current-conservation constraints [74].

Analogously to the one-body case, the two-body CC operator is the sum of a vector and axial component. The relativistic expression of the two-body current operator we present in this work has been obtained following the parametrization of Ruiz Simo et al. [75] where the pion-production amplitudes of Hernandez et al. [76] are coupled to a second nucleonic line. Starting from the vector component of $j^\mu_{\rm CC}$, the electromagnetic current operators can be obtained using the CVC hypothesis. Adopting the momentum variables specified in **Figure 1**, the expression of the CC Δ-current reads

$$(j^\mu_\Delta)_{\rm CC} = \frac{3}{2}\frac{f_{\pi NN} f^*}{m_\pi^2}\Big\{\Pi(k_2)_{(2)}\Big[\Big(-\frac{2}{3}\tau^{(2)} + \frac{I_V}{3}\Big)_\pm F_{\pi NN}(k_2)F_{\pi N\Delta}(k_2)(j^\mu_a)_{(1)} - \Big(\frac{2}{3}\tau^{(2)} + \frac{I_V}{3}\Big)_\pm \times F_{\pi NN}(k_2)F_{\pi N\Delta}(k_2)(j^\mu_b)_{(1)}\Big] + (1 \leftrightarrow 2)\Big\} \tag{31}$$

where $k_2 = p' - k'$ is the momentum of the π exchanged in the two depicted diagrams, $f^* = 2.14$ and

$$\Pi(k) = \frac{\gamma_5 \not{k}}{k^2 - m_\pi^2}\,, \tag{32}$$

$$F_{\pi N\Delta}(k) = \frac{\Lambda_{\pi N\Delta}^2}{\Lambda_{\pi N\Delta}^2 - k^2}\,, \tag{33}$$

$$F_{\pi NN}(k) = \frac{\Lambda_\pi^2 - m_\pi^2}{\Lambda_\pi^2 - k^2}\,, \tag{34}$$

with $\Lambda_{\pi N\Delta} = 1150$ MeV and $\Lambda_\pi = 1300$ MeV. In the above equations, $\Pi(k)$ describes the pion propagation and absorption, while the πNN and $\pi N\Delta$ couplings depend on the form factors $F_{\pi N\Delta}(k)$ and $F_{\pi NN}(k)$, respectively, accounting for the off-shellness of the π and Δ. The operator $(I_V)_\pm = (\tau^{(1)} \times \tau^{(2)})_\pm$ with $\pm \rightarrow x \pm iy$ raises-lowers the isospin components. In Equation (31), j_a^μ and j_b^μ denote the $N \rightarrow \Delta$ transition vertices of the left and right diagrams, respectively. They are expressed as

$$\begin{aligned} j_a^\mu &= (j_a^\mu)_V + (j_a^\mu)_A\,, \\ (j_a^\mu)_V &= \frac{C_3^V}{m_N}\Big[k_2^\alpha G_{\alpha\beta}(p_\Delta)\Big(g^{\beta\mu}\not{q} - q^\beta\gamma^\mu\Big)\Big]\gamma_5\,, \\ (j_a^\mu)_A &= C_5^A\Big[k_2^\alpha G_{\alpha\beta}(p_\Delta) g^{\beta\mu}\Big] \end{aligned} \tag{35}$$

where k is the momentum of the initial nucleon, q is the momentum transfer and $p_\Delta = q + k$, yielding $p_\Delta^0 = e(\mathbf{k}) + \omega$. For the left diagram we have

$$\begin{aligned} j_b^\mu &= (j_b^\mu)_V + (j_b^\mu)_A\,, \\ (j_b^\mu)_V &= \frac{C_3^V}{m_N}\gamma_5\Big[\Big(g^{\alpha\mu}\not{q} - q^\alpha\gamma^\mu\Big)G_{\alpha\beta}(p_\Delta)k_2^\beta\Big], \\ (j_b^\mu)_A &= C_5^A\Big[g^{\alpha\mu}G_{\alpha\beta}(p_\Delta)k_2^\beta\Big]. \end{aligned} \tag{36}$$

where p is the outgoing nucleon four-momentum and $p_\Delta = p - q$. The vector and axial form factors, denoted by C_3^V and C_5^A, are obtained from general principles and experimental results as discussed in Hernandez et al. [76] where their explicit expressions is also reported. In the above equations all nucleons are on the mass-shell with the time component $p^0 = \sqrt{m_N^2 + \vec{p}^{\,2}}$. For the Δ-propagator we adopted the Rarita-Schwinger convention where $G^{\alpha\beta}(p_\Delta) = P^{\alpha\beta}(p_\Delta)/(p_\Delta^2 - M_\Delta^2)$ is proportional to the spin 3/2 projection operator

$$\begin{aligned} P^{\alpha\beta}(p_\Delta) = (\not{p}_\Delta + M_\Delta)\Big[g^{\alpha\beta} - \frac{1}{3}\gamma^\alpha\gamma^\beta - \frac{2}{3}\frac{p_\Delta^\alpha p_\Delta^\beta}{M_\Delta^2} \\ + \frac{1}{3}\frac{p_\Delta^\alpha\gamma^\beta - p_\Delta^\beta\gamma^\alpha}{M_\Delta}\Big]. \end{aligned} \tag{37}$$

In order to account for the possible decay of the Δ into a physical πN we replace its real mass $M_\Delta = 1{,}232$ MeV entering the denominator of the free propagator, i.e., $p_\Delta^2 - M_\Delta^2$, by $M_\Delta - i\Gamma(p_\Delta)/2$ [72, 77]. The decay width $\Gamma(p_\Delta)/2$ is not a constant but explicitly depends upon the energy, its expression can be found in Dekker et al. [72].

3. INTEGRAL TRANSFORM TECHNIQUES

Evaluating the hadronic tensor of Equation (3) is highly non-trivial as it requires to sum over the entire excitation spectrum of the nucleus and to include one- and two-body current operators. Integral transform techniques are extremely useful in reducing the problem to a ground-state one instead of explicitly evaluating each transition amplitude $|\Psi_0\rangle \rightarrow |\Psi_f\rangle$. We consider the convolution of the response function with a smooth kernel

$$\begin{aligned} E_{\alpha\beta}(\mathbf{q},\sigma) = \int d\omega K(\sigma,\omega) R_{\alpha\beta}(\mathbf{q},\omega) = \\ \sum_f \langle\Psi_0|J_\alpha^\dagger(\mathbf{q})|\Psi_f\rangle K(\sigma, E_f - E_0)\langle\Psi_f|J_\beta(\mathbf{q})|\Psi_0\rangle\,, \end{aligned} \tag{38}$$

using the closure property $\sum_f |\Psi_f\rangle\langle\Psi_f| = 1$ a generalized sum rule depending on a continuous parameter σ can be obtained

$$E_{\alpha\beta}(\mathbf{q},\sigma) = \langle\Psi_0|J^\dagger(\mathbf{q})K(\sigma, H - E_0)J_\beta(\mathbf{q})|\Psi_0\rangle\,. \tag{39}$$

With an appropriate choice of the kernel K, the right-hand side of the above equation can be accurately computed within different *ab-initio* methods. In order to retrieve the energy dependence of the response function, the integral transform has to be accurately inverted.

3.1. Lorentz Integral Transform Technique

The kernel used to compute the integral transform is a Lorentzian

$$K(\sigma,\omega) = \frac{1}{(\omega - \sigma^*)(\omega - \sigma)} \tag{40}$$

where σ is a complex parameter, generally defined for convenience as

$$\sigma = E_0 + \sigma_R + i\sigma_I\,. \tag{41}$$

For simplicity we leave the Lorentz indices implicit and rewrite Equation (39) substituting the Lorentz kernel as

$$\begin{aligned} E(\mathbf{q},\sigma_I,\sigma_R) = \langle\Psi_0|J^\dagger(\mathbf{q})\frac{1}{H - E_0 - \sigma_R + i\sigma_i} \\ \frac{1}{H - E_0 - \sigma_R - i\sigma_i}J(\mathbf{q})|\Psi_0\rangle = \langle\tilde{\Psi}|\tilde{\Psi}\rangle\,, \end{aligned} \tag{42}$$

implying that the Lorentz Integral Transform (LIT) of the response function is given by the norm of the $|\tilde{\Psi}\rangle$ state. This state is determined by solving a Schrödinger-like equation for a quantum mechanical bound system

$$(H - E_0 - \sigma_R - i\sigma_I)|\tilde{\Psi}\rangle = J(\mathbf{q})|\Psi_0\rangle \tag{43}$$

for different values of σ_I and σ_R. In order to obtain the response function, one first computes $\tilde{E}(\mathbf{q},\sigma_I,\sigma_R)$ and then inverts it numerically. This second step is highly non-trivial and belongs to the class of so-called "ill-posed" problems. The devised method consists on: (i) making an ansatz to write down the expression of the response function as a function of a set of parameters c_i (ii) the

corresponding LIT is computed using this parametrization of the nuclear response function (iii) the parameters c_i are determined from a least-squares fit of the LIT computed in (ii) with the one calculated at the beginning, $\bar{E}(\mathbf{q}, \sigma_I, \sigma_R)$. A more detailed discussion of the inversion procedures utilized can be found in Efros et al. [78] and Reiss et al. [79].

A very accurate determination the electromagnetic responses of light nuclei has been achieved, for different values of $\mathbf{q}$, combining the LIT method with the hyperspherical harmonic (HH) formalism [80–82]. This expansion method has been successfully utilized to study nuclear, atomic and molecular few-body systems; the wave function of the system is expanded in a series of products of HH basis functions and hyperradial basis functions allowing for a correct description of the large distance components. The predictive power of the HH approach is limited to relatively light mass number, to overcome this limitation the Couple Cluster (CC) theory has been recently combined with the LIT approach to tackle medium and large mass nuclei [83, 84]. The photoabsorption cross sections of ^{16,22} O and ^{40} Ca and electromagnetic sum rules have been recently computed using the LIT-CC approach in Simonis et al. [85].

3.2. Green's Function Monte Carlo

The Green's Function Monte Carlo (GFMC) is an *ab-initio* method that allows to predict with high accuracy the structure and low-energy transitions of $A \leq 12$ nuclei [19]. This method is utilized to project out the ground state starting from a trial wave function $|\Psi_T\rangle$

$$|\Psi_0\rangle \propto \lim_{\tau\to\infty} \exp[-(H - E_0)\tau]|\Psi_T\rangle\,,$$

where E_0 is a parameter used to control the normalization and τ is the imaginary time. Recently, exploiting integral transform techniques accurate predictions for the electromagnetic response functions of ^{4}He and ^{12}C in the quasielastic sector have been obtained. The inclusion of two-body currents yields to a very good agreement between GFMC predictions and experimental data [23, 25]. The integral transform of Equation (38) is evaluated using a Laplace kernel and denoted as Euclidean response. Its inelastic contribution is obtained as

$$E_{\alpha\beta}(\mathbf{q}, \sigma) = \int_{\omega_{el}^+}^{\infty} d\omega R_{\alpha\beta}(\mathbf{q}, \omega) e^{-\omega\sigma}\,, \tag{44}$$

where ω_{el} is the energy of the recoiling ground state. Using the closure property, the sum over the final states can be removed, the inelastic Euclidean responses can be written as the following ground-state expectation value

$$E_\alpha(|\mathbf{q}|, \sigma) = \langle\Psi_0|J_\alpha^\dagger(\mathbf{q}) e^{-(H-E_0)\tau} J_\beta(\mathbf{q})|\Psi_0\rangle - |F_\alpha(q)|^2 \mathrm{e}^{-\sigma\omega_{\mathrm{el}}} \tag{45}$$

where $F_\alpha(q)$ is the longitudinal elastic form factor and the nucleon form factors entering in the current operator are evaluated at the quasielastic peak $Q_{qe}^2 = \mathbf{q}^2 - \omega_{qe}^2$.

In order to obtain the response function the Laplace transform has to be inverted. This is achieved exploiting maximum entropy techniques, as described in Lovato et al. [25] and in the supplemental material of Lovato et al. [86]. The LIT-HH and GFMC results for the longitudinal electromagnetic responses of ^{4}He have been recently compared to benchmark the inversion procedure used in the two approaches. The calculations presented are based on the AV18 and IL7 combination of two- and three-nucleon potential for the GFMC method and AV18 and UIX for the LIT-HH [45, 87]. The results are displayed in **Figure 2** for $|\mathbf{q}|$ = 300 and 500 MeV, the (red) dashed and solid (blue) lines corresponding to the LIT-HH and GFMC predictions, respectively, are found in good agreement and correctly reproduce the experimental data taken from Carlson et al. [88]. The small discrepancies between the two curves have been discussed in Rocco et al. [24] and they do not originate from the inversion techniques utilized in the two approaches.

Because of the non-relativistic nature of the GFMC approach, it can be safely applied to compute electroweak responses in the high momentum transfer region relevant for neutrino-nucleus scattering. Relativistic corrections are in both one- and two-body current operators up to order $1/m_N^2$ as discussed in Carlson and Schiavilla [63] for the one-body case. However, the quantum mechanical framework is non-relativistic; an attempt of including relativistic corrections in the kinematics has been recently carried out in Rocco et al. [24]. The strategy consists on performing the calculation in a reference frame that minimizes nucleon momenta in the final state.

In electron-nucleus scattering processes, the quasielastic region is dominated by a one-nucleon knock-out and this condition is satisfied by the active nucleon Breit (ANB) frame in which the target nucleus has a momentum $-A\,\mathbf{q}/2$. In this reference frame the momentum of the nucleons in the initial state is about $-\mathbf{q}/2$ while the one of the emitted particle is $\simeq \mathbf{q}/2$. The momentum of the final state is higher in all the other reference frames like for example the laboratory (LAB) system where the emitted knocked-out nucleon has a momentum of about $\mathbf{q}$. Therefore, the ANB system can be utilized to minimize relativistic corrections.

In order to compare with experimental data measured in the LAB system, the results from the ANB need to be boosted back to the LAB frame. The solid blue and red curves in **Figure 3** performing the calculation of the longitudinal electromagnetic response of ^{4}He at $|\mathbf{q}|$ = 700 MeV in the LAB and ANB frame, respectively, and boosting back to the LAB frame using Lorentz transformation. The two curves peak in different positions and have different strengths, this frame dependence of the results is a clear indication that relativistic effects are sizable for these values of $\mathbf{q}$.

Relativistic effects in the kinematics can be included employing the two-fragment model of Efros et al. [89] which presents strong analogies with the procedure used to determine NN potentials. In this case, the relative momentum of the two-nucleon system p_{12} is determined in a relativistic fashion and utilized to solve the Schrödinger equation with a non-relativistic kinetic energy $E_{12} = p_{12}^2/2\mu_{12}$, μ_{12} being the reduced mass.

The two-fragment model relies on the assumption that the dominant reaction in the quasielastic region consists on the break-up of the nucleus into a knocked-out nucleon with

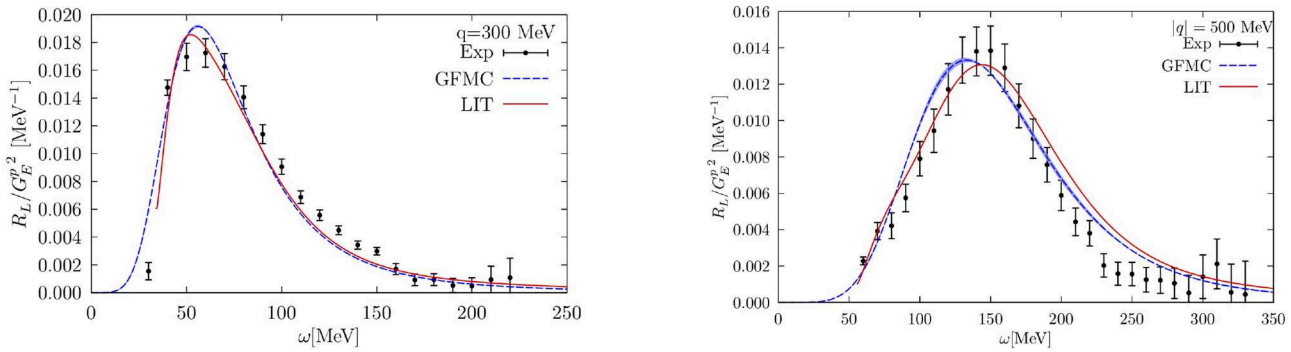

FIGURE 2 | Longitudinal electromagnetic response functions of ^{4}He at $|q| = 300$ MeV (left) and $|q| = 500$ MeV (right) obtained inverting the Laplace and Lorentz integral transforms compared to the experimental data of Carlson et al. [88].

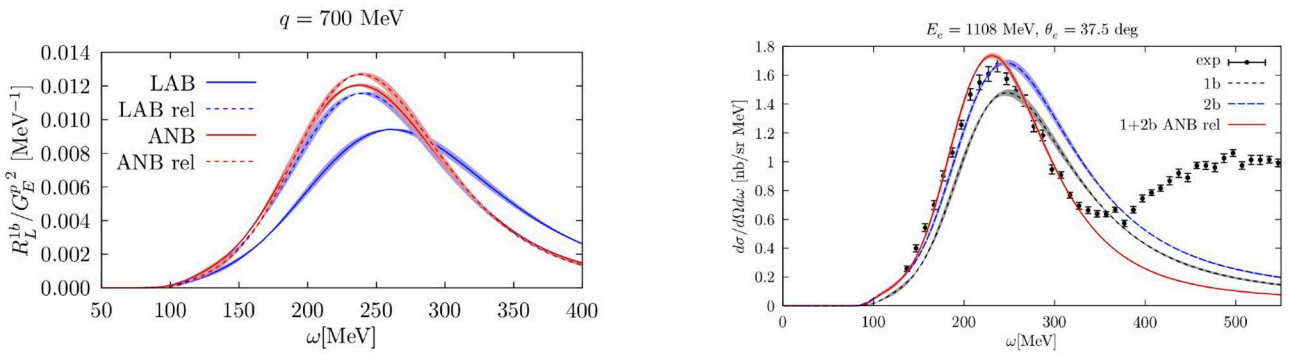

FIGURE 3 | (Left) Longitudinal electromagnetic response functions of ^{4}He at $|q| = 700$ MeV computed in the LAB and in the ANB frame are displayed by the blue and red solid curves, respectively. The dashed curves have been obtained by applying the two-fragment model to consider two-body relativistic kinematics for the final state energy. **(Right)** Double-differential electron-^{4}He cross sections for $E_e = 1108$ MeV and $\theta = 37.5$. The short-dashed red and dashed blue curves are the GFMC calculation were only one- body and one- plus two-body contributions in the electromagnetic currents are accounted for. The results obtained in the ANB frame corrected by the two-fragment model are displayed by the red solid line. The experimental data are taken from Benhar et al. [44].

momentum $\mathbf{p}_N^{\rm fr}$ and a remaining $(A-1)$ system in its ground state $\mathbf{p}_X^{\rm fr}$, respectively. The relative and center-of-mass momenta of the nucleon and spectator system are obtained as

$$\mathbf{p}_{\rm f}^{\rm fr} = \mu\left(\frac{\mathbf{p}_N^{\rm fr}}{m} - \frac{\mathbf{p}_X^{\rm fr}}{M_X}\right), \qquad \mathbf{P}_f^{\rm fr} = \mathbf{p}_N^{\rm fr} + \mathbf{p}_X^{\rm fr}, \tag{46}$$

where M_X and μ are the mass of the residual nucleus and the reduced mass, respectively. The relative momentum $p_f^{\rm fr}$ can be computed in a relativistic way utilizing the correct definition of the final hadronic energy

$$E_f^{fr} = \sqrt{m^2 + (\mathbf{p}_f^{\rm fr} + (\mu/M_{A-1})\mathbf{P}_f^{\rm fr})^2} + \sqrt{M_{A-1}^2 + (\mathbf{p}_f^{\rm fr} - (\mu/m)\mathbf{P}_f^{\rm fr})^2};$$

and used to determine the relativistically "fake" kinetic energy $(p_f^{\rm fr})^2/2\mu$ entering in the energy conserving δ-function of Equation (3). A more detailed discussion of the approach can be found in Rocco et al. [89] and Efros et al. [24].

The results computed within the two-fragment model are displayed by the dashed curves in **Figure 3**. Note that, now the position and the strength of the LAB rel and ANB rel curves are the same. This implies that the position of the quasielastic peak in the electromagnetic responses no longer depends upon the reference frame and coincides with that of the ANB frame (solid blue curve).

In order to compute the inclusive electromagnetic cross section of Equation (4), R_L and R_T have to be evaluated for several values of ω and $|\mathbf{q}|$. Hence, due to the sizable computational effort associated with the inversion of the Euclidean response for a given value of $|\mathbf{q}|$, the direct evaluation of Equation (4) is not feasible within GFMC. In order to overcome this limitation, an interpolation procedure based on the concept of scaling was devised in Rocco et al. [24] and used for an accurate and efficient interpolation of the GFMC responses. The right panel of **Figure 3** displays the double-differential electron-^{4}He cross sections for $E_e = 1108$ MeV and $\theta = 37.5$. The red and blue lines have been obtained including the one- body and one- plus two-body contributions in the electromagnetic currents. The inclusion of the meson exchange current leads

to a substantial enhancement in the quasielastic region. The same feature is present in the results of Lovato et al. [23, 25] where the electromagnetic responses of ^{4}He and ^{12}C have been calculated and compared with the experimental data. Separating the longitudinal and transverse channel it has been observed that the two-body term has a predominantly transverse nature; its contribution is almost vanishing in the longitudinal channel when electromagnetic processes are considered. The red solid line indicates one plus two-body current results obtained in the ANB frame, employing the two-body fragment model to account for relativistic kinematics. The inclusion of relativistic effects leads to a shift of the peak position toward lower values of ω and to a reduction of its width.

Recently, GFMC calculations of the neutral-current responses and cross sections for neutrino scattering off ^{12}C have also been performed [26]. A description of the two-body charge and current operators used in this work is provided in Lovato et al. [23] and Shen et al. [40] and references therein. The left panel of **Figure 4** shows the different spatial components of the neutral-current response functions in ^{12}C at momentum transfer $|\mathbf{q}|$ = 570 MeV. The vector and axial contributions are shown separately in all cases but for R_{xy} the entire strength is given by the axial-vector interference. The dashed and solid lines have been obtained including the one-body and one- and two-body currents, respectively. Note that also in this case the two-body term significantly increases in magnitude the response functions in the quasielastic region. At variance with the electromagnetic results, the axial component of the two-body operator in the weak neutral charge produce substantial excess strength in the longitudinal channels as clearly visible in the upper figure. While in the transverse response, shown in the middle panel, we have a two-body enhancement both from the axial and vector terms. The *xy* response function in the lower panel which arises solely on account of this interference is also modified by the two-body contribution. In the right panel of **Figure 4** the CC responses in ^{4}He at momentum transfer $|\mathbf{q}|$ = 600 MeV are displayed. In analogy the NC case, we see that the enhancement given by the inclusion of two-body currents is present in all the different channels. However, in the longitudinal one it is not as significant as for the NC scattering. This has to be ascribed to the relative strength of the axial contribution to the total response which in this case is much smaller than the vector one.

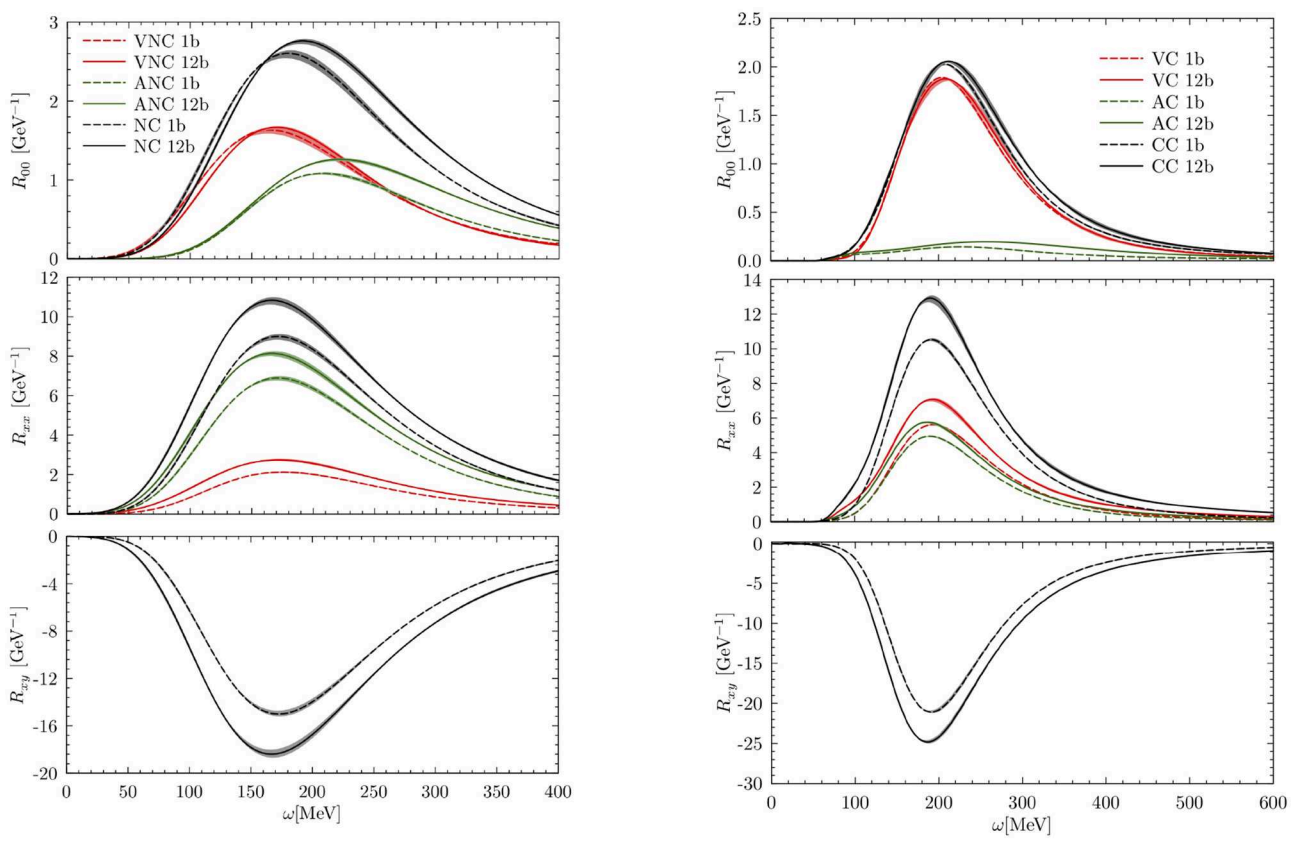

FIGURE 4 | (Left) Adapted from Lovato et al. [26] under the Creative Commons CCBY license. Neutral-current response functions in ^{12}C at momentum transfer $|q|$ = 570 MeV obtained with one-body only (dashed lines) and one- and two-body (solid lines) currents. The vector and axial contribution corresponds to the red and green curves, the black curves display the full result in which the axial-vector interference is accounted for. The upper, middle, and lower panel corresponds to the charge, transverse and *xy* component of the response function. **(Right)** Charge-current response functions in ^{4}He at momentum transfer $|q|$ = 600 MeV. The different lines are the same as for the left panel.

4. SHORT TIME APPROXIMATION

A novel approach to calculate the short-time propagation resulting from two- nucleon dynamics has been recently developed [28]. The STA method utilizes QMC techniques to evaluate path integrals of one- and two-nucleon currents in real time and predict the response function of nuclei in the quasielastic region. The expression of this response is reported in Equation (3) and can be rewritten as

$$\begin{aligned} R^{\mu\nu}(\mathbf{q},\omega) &= \int_{-\infty}^{\infty} \frac{dt}{2\pi} e^{i(\omega+E_0-E_f)t} \\ &\sum_f \langle\Psi_0|J^{\mu\,\dagger}(\mathbf{q},\omega)|\Psi_f\rangle\langle\Psi_f|J^{\nu}(\mathbf{q},\omega)|\Psi_0\rangle \\ &= \int_{-\infty}^{\infty} \frac{dt}{2\pi} e^{i(\omega+E_0)t} \langle\Psi_0|J^{\mu\,\dagger}(\mathbf{q},\omega)\, e^{-iHt}\, J^{\nu}(\mathbf{q},\omega)|\Psi_0\rangle \end{aligned} \tag{47}$$

where the sum over final states has been replaced with a real-time propagator. In the following, we drop the Lorentz indices to simplify the notation and replace $J(\mathbf{q},\omega) \rightarrow J(\mathbf{q})$ with $\omega = \omega_{qe}$, the one- and two-body current operators utilized are the same as for the GFMC results [40]. The main assumption underlying the STA is that only the active pair of nucleons propagate, this qualitatively amounts to rewrite the final state as $\sum_f |\Psi_f\rangle \rightarrow \sum_{f'f''} |\phi^2_{f'}\rangle|\Psi^{A-2}_{f''}\rangle$ where $|\phi^2_{f'}\rangle$ is the correlated two-nucleon state. To evaluate the response function, two completeness relations on the coordinate states are inserted, yielding

$$\begin{aligned} \langle\Psi_0|J^{\mu\,\dagger}\, e^{-iHt}\, J^{\nu}|\Psi_0\rangle = \int dr_1 \ldots dr_A dr'_1 \ldots dr'_A \langle\Psi_0|J^{\mu\,\dagger}|r_1 \ldots r_A\rangle \\ \times \langle r_1 \ldots r_A|e^{-iHt}|r'_1 \ldots r'_A\rangle\langle r'_1 \ldots r'_A|J^{\nu}|\Psi_0\rangle\,. \end{aligned} \tag{48}$$

In the STA the current-current correlator is rewritten keeping the one- and two-body terms

$$\begin{aligned} J^{\mu\,\dagger}\, e^{-iHt}\, J^{\nu} &= \Big(\sum_i j^{\mu\,\dagger}(i) + \sum_{i<j} j^{\mu\,\dagger}(ij)\Big) e^{-iHt} \Big(\sum_{i'} j^{\nu}(i') \\ &+ \sum_{i'<j'} j^{\nu}(i'j')\Big) \\ &= \sum_i j^{\mu\,\dagger}(i) e^{-iHt} j^{\nu}(i) + \sum_{i\neq j} j^{\mu\,\dagger}(i) e^{-iHt} j^{\nu}(j) \\ &+ \sum_{i\neq j} \Big(j^{\mu\,\dagger}(i) e^{-iHt} j^{\nu}(ij) + j^{\mu\,\dagger}(ij) e^{-iHt} j^{\nu}(i) \\ &+ j^{\mu\,\dagger}(ij) e^{-iHt} j^{\nu}(ij)\Big) \end{aligned} \tag{49}$$

the contributions with three or more active nucleons have been neglected. This amounts to include only two-nucleon interactions in the Hamiltonian; the A-nucleon particle propagator is approximated as

$$\begin{aligned} \langle r_1 \ldots r_A|e^{-iHt}|r'_1 \ldots r'_A\rangle &= \langle r_1 \ldots r_A|e^{-i(H^{\rm cm}_{ij}+H^{\rm rel}_{ij}+H_{A-2})t}|r'_1 \ldots r'_A\rangle \\ &= \langle R_{ij}|e^{-iH^{\rm cm}_{ij}t}|R'_{ij}\rangle\langle r_{ij}|e^{-iH^{\rm rel}_{ij}t}|r'_{ij}\rangle e^{-i\bar{E}_{A-2}t} \\ &\prod_{k\neq i,j}^{A} \delta(r_k - r'_k) \end{aligned} \tag{50}$$

where $H^{\rm cm}_{ij} = \mathbf{P}^2_{ij}/(4m_N)$ and $H^{\rm rel}_{ij} = \mathbf{p}^2_{ij}/m_N + v_{ij}$. The $A-2$ nucleons are treated as static spectators and their energy is assumed to be peaked around a constant value $\bar{E}_{A-2}$.

We put the two equations together and define $j^{\mu\,\dagger}_L j^{\nu}_R = \big(j^{\mu\,\dagger}(i)j^{\nu}(j) + j^{\mu\,\dagger}(i)j^{\nu}(ij) + j^{\mu\,\dagger}(j)j^{\nu}(ij)\big)$ yielding

$$\begin{aligned} R^{\mu\nu}(\mathbf{q},\omega) = &\frac{A(A-1)}{2} \int dt e^{i(\omega+E_0-\bar{E}_{A-2})t} \\ &\int dr_{12} dR_{12} dr'_{12} dR'_{12} dR_{A-2} \langle\Psi_0|j^{\mu\,\dagger}_L|r_{12}R_{12};\, R_{A-2}\rangle \\ &\times \langle R_{12}|e^{-iH^{\rm cm}_{12}t}|R'_{12}\rangle\langle r_{12}|e^{-iH^{\rm rel}_{12}t}|r'_{12}\rangle\langle r'_{12}R'_{12};\, R_{A-2}|j^{\nu}_R|\Psi_0\rangle\,. \end{aligned} \tag{51}$$

The two-nucleon propagator $\langle r_{12}|e^{-iH^{\rm rel}_{12}t}|r'_{12}\rangle$ is obtained by summing over the bound and continuum eigenstates of $H^{\rm rel}_{12}$. Note that the interaction effects in the active pair are exactly accounted for. It is convenient to rewrite the STA response in terms of an integral over the relative- and center-of-mass energy of the pair as

$$R^{\mu\nu}(\mathbf{q},\omega) = \int_0^{\infty} de \int_0^{\infty} dE_{\rm cm} \delta(\omega + E_0 - e - E_{\rm cm}) D^{\mu\nu}(e, E_{\rm cm})\,. \tag{52}$$

Within the factorization scheme outlined above, interaction effects at the two-nucleon level are fully retained, and the interference between one- and two-body terms in the electromagnetic current operator are consistently accounted for. The low-energy properties of the system (discrete transition and collective excitation of the nucleus) and the correct energy threshold for the quasielastic region can not be described within the STA. For this reason, some corrections have to be introduced in order to recover the exact value of the threshold for the quasielastic scattering. In particular, the response density is folded with a gaussian kernel

$$\tilde{D}(e', E_{\rm cm}) = \int_0^{\infty} de D(e, E_{\rm cm}) N \exp\left\{ -\Big[\frac{e' - \omega(e)}{\omega_{\rm th}}\Big]^2 \right\} \tag{53}$$

where $\omega(e) = \sqrt{e^2 + \omega^2_{\rm th} \exp -e/\bar{\omega}}$ and N is defined requiring that the sum rules are preserved

$$\int_0^{\infty} de\, N \exp\left\{ -\Big[\frac{e' - \omega(e)}{\omega_{\rm th}}\Big]^2 \right\} = 1\,. \tag{54}$$

The two parameters controlling the shift and width of the gaussian folding are $\omega_{\rm th}$ and $\bar{\omega}$, respectively. The values chosen

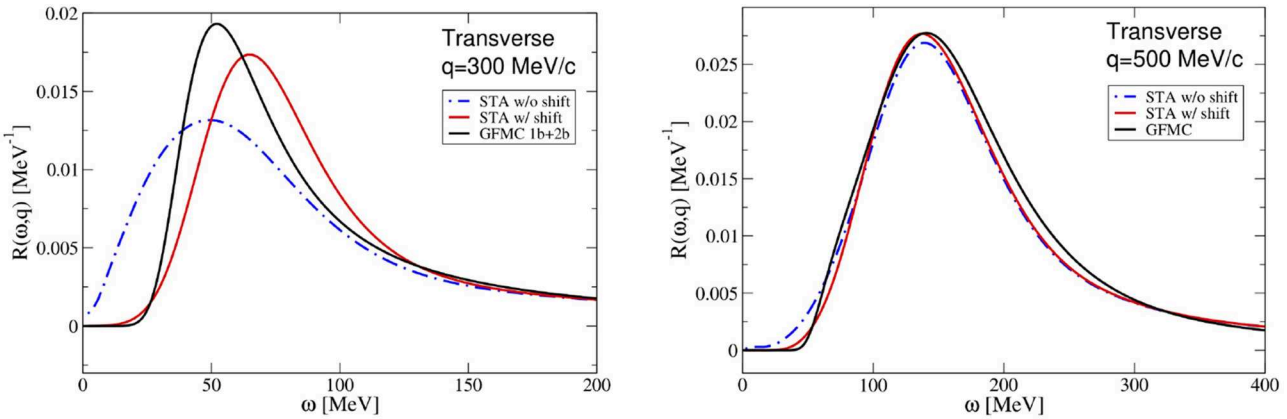

FIGURE 5 | Transverse electromagnetic response of ^{4}He obtained within the STA and GFMC approaches. The left and right panel corresponds to $|q|$ = 300 and 500 MeV, respectively. The dashed (blue) and solid (red) lines are STA calculations prior and including the shift; the solid (black) line displays the GFMC results. Figure adapted from Pastore et al. [28].

to reproduce the physical threshold of $\sim$ 20 MeV of ^{4}He are $\omega_{\rm th} = 35$ MeV and a 15 MeV width.

A comparison between the STA and GFMC electromagnetic response function of ^{4}He is shown in **Figure 5** for $|\mathbf{q}|$ = 300 and 500 MeV. The dashed line displays the STA results without any knowledge of the threshold while in the full red line the correct behavior at threshold has been enforced as explained in Equation (53). Including these corrections leads to a shift of the response toward larger values of the energy transfer and a redistribution of the strength; while for $|\mathbf{q}|$ = 300 MeV this effect is sizable the results at $|\mathbf{q}|$ = 500 are only slightly modified. In both configurations the STA results which include the shift accurately reproduce the GFMC ones.

The role played by final-state interactions within the pair is analyzed in the left panel of **Figure 6** where the solid and dashed lines correspond to the transverse electromagnetic response of ^{4}He obtained with and without interactions effects, respectively. Their inclusion leads to a visible shift in the position of the quasielastic peak toward left. The breakdown of the response into one-body current diagonal and off-diagonal terms, interference between one- and two-body currents, and two-body currents only, is also shown. It is interesting to note that the off-diagonal terms, routinely neglected in the IA scheme, provide a negative contribution depleting the response strength. In analogy with the GFMC findings, the interference between one-and two-body currents provides an important enhancement in the quasielastic region; contrary to the pure two-body current which does not provide a significant contribution to the response function in this kinematics. This is likely to be ascribed to the static limit adopted in both the GFMC and STA approaches to derive the non-relativistic expression of the Δ current. As discussed in Dekker et al. [72] in the static limit all energy dependence of the Δ propagator disappears and the resonance behavior in the dip region is not present.

The isospin dependence of pairs in the back-to-back kinematics, i.e., pairs with low initial center-of-mass momentum and high relative momentum, is studied in the right panel of **Figure 6**. These pairs can be singled-out in the response densities by requiring the pair center-of-mass momentum P being close to $|\mathbf{q}|$ and the relative momentum in the final state being large. **Figure 6** displays the response densities at fixed energy $E_{\rm cm} \simeq |\mathbf{q}|^2/(4m_N)$ as a function of the relative energy of the pair e. The solid and dot-dashed curves have been obtained with and without interactions within the pair. The comparison between the full results (black line) and the one-body total (magenta line) shows that the two-nucleon currents do not provide a large contribution at low relative energies. While, the full result becomes substantially larger than the one-body current term for $e \geq 250$ MeV. The back-to-back momentum distributions of np pairs are known to dominate over pp or nn pairs at high relative momenta because of tensor correlations as discussed in Schiavilla et al. [90]. In addition to that, the two-nucleon currents are almost entirely in the np pairs, and increase the response by roughly a factor of $\sim$ 2 around at e = 300 MeV.

5. EXTENDED FACTORIZATION SCHEME

For large values of ω and $|\mathbf{q}|$, a non-relativistic calculation of the hadron tensor is no longer reliable. Since both the final state and the transition currents depends upon the momentum transfer, relativity has to be properly accounted for. Factorizing the hadronic final state allows one to overcome these difficulties by providing a relativistic description of $|\Psi_f\rangle$ and of the current operator. In addition to that, realistic spectral functions are used to accurately model the dynamics of the target nucleus and account for correlation effects. We start by only retaining the one-body current terms and rewriting the hadronic final state as

$$J^\mu = \sum_i j^\mu(i), \quad |\Psi_f\rangle \to |p\rangle \otimes |\psi_f^{A-1}\rangle \tag{55}$$

where $|p\rangle$ is a plane wave describing the propagation of the final-state nucleon with momentum $|\mathbf{p}|$ and energy $e(\mathbf{p}) = \sqrt{|\mathbf{p}|^2 + m_N^2}$, while $|\psi_f^{A-1}\rangle$ describes the $(A-1)$-body spectator

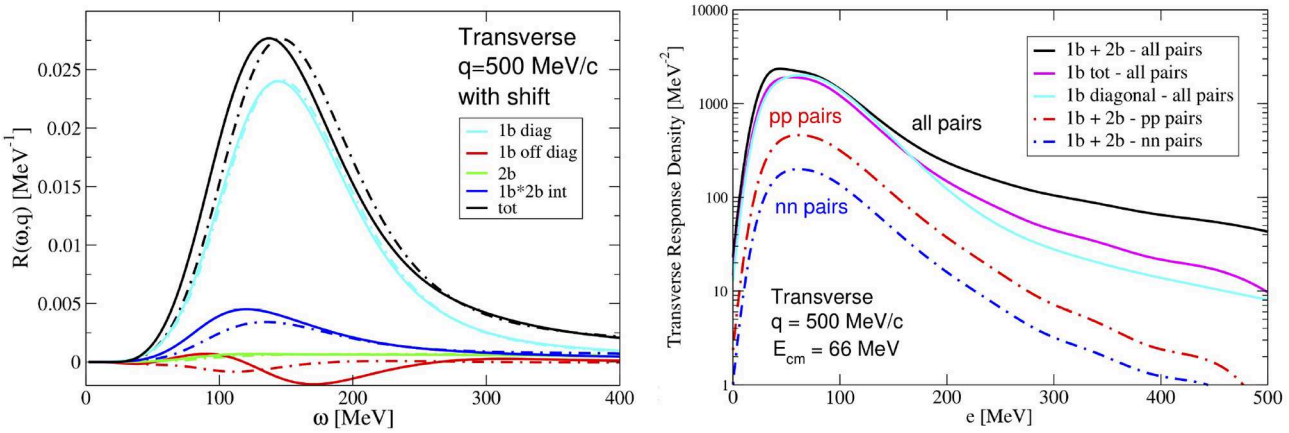

FIGURE 6 | (Left) Transverse electromagnetic response of ^{4}He at $|q|$ = 500 MeV without (dashed lines) and with (solid lines) interacting two-nucleons in the final state. The different contributions corresponding to one-body current diagonal terms, one-body current off-diagonal terms, interference between one- and two-body currents, and two-body currents only are separately shown. **(Right)** Transverse response densities of ^{4}He at $|q|$ = 500 MeV and final center of mass energy $E_{cm} = |q|^2/(2m_N)$. The solid cyan and magenta solid line display the diagonal only and diagonal plus off-diagonal one-body term, respectively. The solid black curve corresponds to the total one- plus two-body current result while in the blue dashed and red dashed isolate the contribution of the nn and pp pairs is singled-out. Figure adapted from Pastore et al. [28].

system. The energy and momentum of the latter are obtained by energy and momentum conservation relations

$$E_f^{A-1} = \omega + E_0 - e(\mathbf{p}), \quad \mathbf{P}_f^{A-1} = \mathbf{q} - \mathbf{p}. \tag{56}$$

The incoherent contribution to the one-body hadron tensor can be easily obtained from Equation (55) and by inserting a single-nucleon completeness relation

$$R_{1b}^{\mu\nu} = \int \frac{d^3k}{(2\pi)^3} dE P_h(\mathbf{k}, E) \frac{m_N^2}{e(\mathbf{k})e(\mathbf{k}+\mathbf{q})} \sum_i \langle k|j_i^{\mu\dagger}|k+q\rangle \langle k+q|j_i^{\nu}|k\rangle \delta(\tilde{\omega} + e(\mathbf{k}) - e(\mathbf{k}+\mathbf{q})), \tag{57}$$

where m_N is the rest mass of the initial nucleon. We introduced $\tilde{\omega}$ defined as $\tilde{\omega} = \omega - E + m_N - e(\mathbf{k})$. To describe the scattering off a bound nucleon with momentum $\mathbf{k}$, the four-momentum transfer employed in the hadronic tensor is replaced by $q = (\omega, \mathbf{q}) \rightarrow \tilde{q} = (\tilde{\omega}, \mathbf{q})$. The factors $m_N/e(\mathbf{k})$ and $m_N/e(\mathbf{k}+\mathbf{q})$ ensures the implicit covariant normalization of the nucleon quadri-spinors. The hole-spectral function $P_h(\mathbf{k}, E)$ provides the probability distribution of removing a nucleon with momentum $\mathbf{k}$ from the target nucleus, leaving the residual $(A-1)$-nucleon system with an excitation energy E. The calculation of the spectral function of finite nuclei is a challenging problem that has seen the endeavor of multiple theory groups. In this work we will focus on the results obtained within the Correlated Basis Function and the Self Consistent Green's Function many-body methods, shortly outlined in section 5.1.

For low and moderate values of $|\mathbf{q}|$, interactions between the struck particle and the spectator system become relevant. For this reason, the IA results must be modified to include them [30]. This is achieved by including in the energy spectrum of the propagating nucleon the real part of the optical potential U of Cooper et al. [91] which accounts for its interactions with the mean-field created by the residual system. This potential has to be evaluated for a given kinetic energy of the nucleon $t_{kin}(\mathbf{p}) = \sqrt{\mathbf{p}^2 + m^2} - m$, and modifies its energy as

$$\tilde{e}(\mathbf{k}+\mathbf{q}) = e(\mathbf{k}+\mathbf{q}) + U\left(t_{\rm kin}(\mathbf{k}+\mathbf{q})\right). \tag{58}$$

The rescattering processes of the propagating nucleon are described by a convolution scheme which amounts to fold the IA responses with a function $f_{\mathbf{k}+\mathbf{q}}$, normalized as

$$\int_{-\infty}^{+\infty} d\omega f_{\mathbf{k}+\mathbf{q}}(\omega) = 1. \tag{59}$$

The one-body hadron tensor then reads

$$R_{1b}^{\mu\nu}(\mathbf{q},\omega)^{\rm FSI} = \int \frac{d^3k}{(2\pi)^3} dE P_h(\mathbf{k}, E) \int d\omega' f_{\mathbf{k}+\mathbf{q}}(\omega - \omega') \frac{m_N^2}{e(\mathbf{k})e(\mathbf{k}+\mathbf{q})} \sum_i \langle k|j_i^{\mu\dagger}|k+q\rangle \langle k+q|j_i^{\nu}|k\rangle \times \delta(\omega' + E - \tilde{e}(\mathbf{k}+\mathbf{q}))\theta(|\mathbf{k}+\mathbf{q}| - p_F). \tag{60}$$

where a generalization of the Glauber theory is utilized to derive the folding function [92]

$$f_{\mathbf{p}}(\omega) = \delta(\omega)\sqrt{T_{\mathbf{p}}} + \int \frac{dt}{2\pi} e^{i\omega t}\left[\bar{U}_{\mathbf{p}}^{FSI}(t) - \sqrt{T_{\mathbf{p}}}\right] = \delta(\omega)\sqrt{T_{\mathbf{p}}} + (1 - \sqrt{T_{\mathbf{p}}})F_{\mathbf{p}}(\omega). \tag{61}$$

A more detailed discussion on how to obtain the nuclear transparency $T_{\mathbf{p}}$ and the finite width function $F_{\mathbf{p}}(\omega)$ can be found in Benhar et al. [29] and Benhar et al. [93].

The inclusion of two body-currents requires an extension of the factorization ansatz of Equation (55). In Benhar et al. [34]

and Rocco et al. [35, 36] the amplitudes involving two-nucleon currents have been included by rewriting the hadronic final state as

$$|\psi_f^A\rangle \to |pp'\rangle_a \otimes |\psi_f^{A-2}\rangle \tag{62}$$

where $|p\,p'\rangle_a = |p\,p'\rangle - |p'\,p\rangle$ is the anti-symmetrized two-nucleon plane wave state. The two-body current component of the hadron tensor reads [34]

$$W_{2b}^{\mu\nu}(\mathbf{q},\omega) = \frac{V}{4}\int dE \frac{d^3k}{(2\pi)^3}\frac{d^3k'}{(2\pi)^3}\frac{d^3p}{(2\pi)^3}\frac{m_N^4}{e(\mathbf{k})e(\mathbf{k}')e(\mathbf{p})e(\mathbf{p}')}P_h(\mathbf{k},\mathbf{k}',E) \times 2\sum_{ij}\langle k\,k'|j_{ij}^{\mu\,\dagger}|p\,p'\rangle_a\langle p\,p'|j_{ij}^{\nu}|k\,k'\rangle\delta(\omega - E + 2m_N - e(\mathbf{p}) - e(\mathbf{p}'))\,. \tag{63}$$

where $P_h(\mathbf{k},\mathbf{k}',E)$ is a two-hole spectral function which in Benhar et al. [34] and Rocco et al. [35, 36] has been approximated as the product of the one-nucleon ones. Note that, while this is correct for infinite nuclear matter, its application to medium mass nuclei such as ^{12}C is questionable and should be further investigated.

The production of real pions in the final state will be crucial for the correct understanding of the DUNE results. In order to include this reaction mechanism, we can write the hadronic final state as

$$|\psi_f^A\rangle \to |p_\pi p\rangle \otimes |\psi_f^{A-1}\rangle\,, \tag{64}$$

where p_π denotes both the four-momentum $(p_\pi^0, \mathbf{p}_\pi)$ and the isospin t_π of the emitted pion. In analogy with the one-body case reported in Equation (57), the one-body one-pion (1b1π) incoherent contribution to the hadron tensor is given by

$$W_{1b1\pi}^{\mu\nu}(\mathbf{q},\omega) = \int \frac{d^3k}{(2\pi)^3}dE P_h(\mathbf{k},E)\frac{d^3p_\pi}{(2\pi)^3}\frac{m_N^2}{e(\mathbf{k})e(\mathbf{k}+\mathbf{q}-\mathbf{p}_\pi)} \sum_i \langle k|j_i^{\mu\,\dagger}|p_\pi p\rangle\langle p_\pi p|j_i^{\nu}|k\rangle\Big|_{\mathbf{p}=\mathbf{k}+\mathbf{q}-\mathbf{p}_\pi} \times \delta(\omega - E + m_N - e(\mathbf{k}+\mathbf{q}-\mathbf{p}_\pi) - e_\pi(\mathbf{p}_\pi))\,, \tag{65}$$

where $e_\pi(\mathbf{p}_\pi) = \sqrt{\mathbf{p}^2 + m_\pi^2}$ is the energy of the outgoing pion. The expression of $\tilde{\omega}$ is the same as for the one-body current process. In order to describe the real emission of a pion we need the transition amplitude between the initial one-nucleon state $|k\rangle$ to the pion-nucleon $|p_\pi p\rangle$ final state. These matrix elements have been obtained within the sophisticated dynamical couple-channel (DCC) model able to describe the $\pi N \to \pi N$, $\gamma N \to \pi N$, and $N(e,e'\pi)N$ reactions accounting for meson-baryon channels and nucleon resonances up to an invariant of $W = 2$ GeV. About 26,000 data points of the $\pi N, \gamma N \to \pi N, \eta N, K\Lambda, K\Sigma$ data from the channel thresholds to $W \leq 2.1$ GeV have been fitted to obtain the parameters adopted within the DCC model. The extension to the electroweak sector has been recently performed [38].

Within the DCC model the following Hamiltonian is defined

$$H_{AO} = H_0 + \sum_{c,c'} v_{c,c'} + \sum_{N^*}\sum_{c}[\Gamma_{N^*,c} + \Gamma_{N^*,c}^{\dagger}]\,, \tag{66}$$

to generate the matrix element $\langle p_\pi p|j_i^\nu|k\rangle$ of Equation (65). In the above equation H_0 is the free Hamiltonian while the production of an N^* state from a meson-baryon channel c is described by the vertex $\Gamma_{N^*,c}$. The energy independent meson-exchange potentials $v_{c,c'}$–where $c, c' = \gamma N, \pi N, \eta N, K\Lambda, K\Sigma$–are derived from phenomenological Lagrangians by using the unitary transformation method [94, 95]. This hamiltonian is used to generate $\langle p_\pi p|j_i^\nu|k\rangle$ of Equation (65). Convoluting the DCC elementary current matrix elements for π-production with the spectral function formalism allows to predict electroweak interactions of finite nuclei in large energy transfer region presented in section 5.2.

5.1. Determination of the Hole Spectral Function of Finite Nuclei

The accurate determination of SFs suitable to encompass both single-particle aspects and short-range dynamics is crucial for the theoretical description of lepton-nucleus scattering. Its definition can be given either in terms of nuclear overlaps or as the imaginary part of a two-point hole Green's Function

$$P_h(\mathbf{k},E) = \sum_f |\langle\psi_0^A|[|k\rangle \otimes |\psi_f^{A-1}\rangle]|^2\delta(E + E_f^{A-1} - E_0^A) = \frac{1}{\pi}\mathrm{Im}\langle\psi_0^A|a_{\mathbf{k}}^\dagger\frac{1}{E - (H - E_0^A) - i\epsilon}a_{\mathbf{k}}|\psi_0^A\rangle\,. \tag{67}$$

Within the CBF, the hole SF of finite nuclei is written as a sum of two terms [31], $P_h(\mathbf{k},E) = P_h^{\mathrm{MF}}(\mathbf{k},E) + P_h^{\mathrm{corr}}(\mathbf{k},E)$ displaying distinctly different energy and momentum dependences. The first term is associated to the low momentum and removal-energy region. The spectroscopic factor obtained from $(e,e'p)$ scattering measurements are utilized to obtain the first term within a modified mean field (MF) picture. The correlated contribution $P_h^{\mathrm{corr}}(\mathbf{k},E)$ includes the unbound states of the $A-1$ spectator system in which at least one of the spectator nucleons is in a continuum state. The local density approximation (LDA) is adopted to compute this term for finite nuclei

$$P_h^{\mathrm{corr}}(\mathbf{k},E) = \int d^3R\;\rho_A(\mathbf{R})P_{h,NM}^{\mathrm{corr}}(\mathbf{k},E;\,\rho_A(\mathbf{R}))\,. \tag{68}$$

where the correlation component of the SF obtained within the CBF theory for isospin-symmetric nuclear matter for a given density ρ is convoluted with the density profile of the nucleus $\rho_A(\mathbf{R})$. The applicability of the LDA in obtaining the correlation part of the SF in finite nuclei relies on the observation that short-range nuclear dynamics is not affected by surface and shell effects. This strength of $P_h^{\mathrm{corr}}(\mathbf{k},E)$ is concentrated in the high momentum and removal energy region as opposed to $P_h^{\mathrm{MF}}(\mathbf{k},E)$. For momenta larger than the Fermi one, the spectral function coincides with the correlation term.

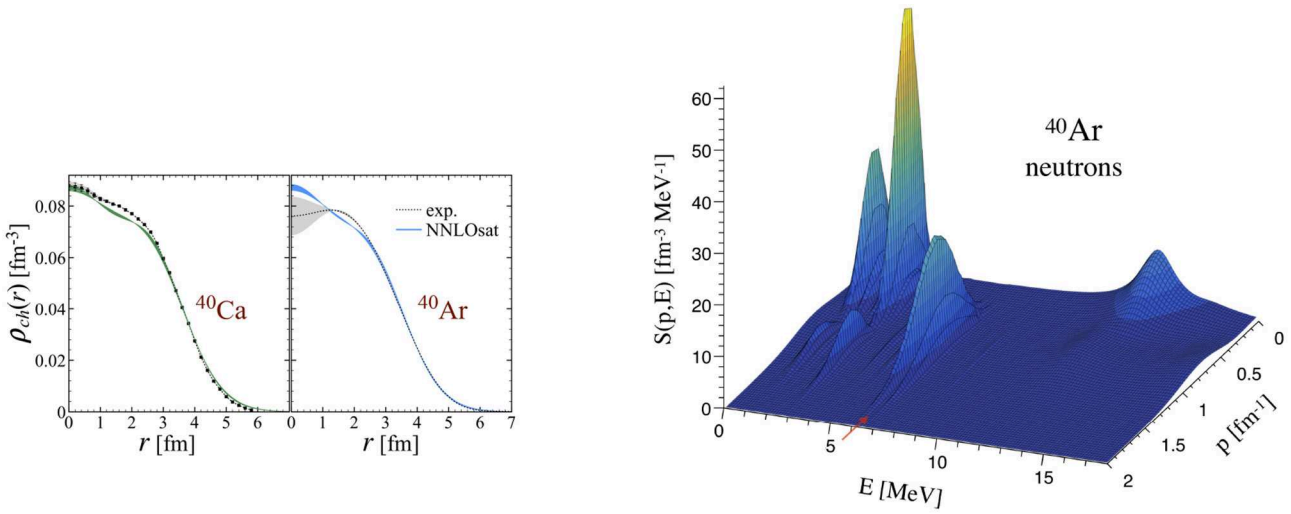

FIGURE 7 | (Left) Results obtained SCGF approach are compared to experimental data (dotted lines and square points) from references Emrich et al. [100] and Ottermann et al. [101] for the charge density distributions of ^{40}Ca (left) and ^{40}Ar (right). The shaded areas represent the total experimental error, while the colored bands displays the theoretical uncertainties due to model-space convergence. **(Right)** Neutron spectral function of ^{40}Ar computed within the SCGF. The particle and hole spectral function corresponds to the region above and below the Fermi level $E = 6.3$ MeV, respectively, indicated by the red arrow.

The SCGF approach is a many-body approach which scales polynomially with the number of particle and allows reach nuclei with A up to ∼100. The spectral function is determined within an *ab initio* theory starting from individual interactions among the nucleons. The central quantity of the SCGF formalism is the one-body Green's function which is directly related to the spectral function through $P_h(\mathbf{k}, E) = -\frac{1}{\pi}\mathrm{Im}\Big[G_h(\mathbf{p}, \mathbf{p}; \mu - E)\Big]$, as expressed in the last equality in Equation (67). This is obtained by adopting an iterative procedure to solve the associated Dyson equation [96, 97] where the irreducible self-energy –which encodes nuclear medium effects in the particle [98]– explicitly depends on the propagator itself. To extend the predictive power of the approach to open shell nuclei, the SCGF has been recently reformulated within Gorkov's theory. The particle number is no longer conserved in this new formulation of the propagator in which a grand canonical Hamiltonian is utilized. Breaking of the particle-number symmetry allows one to include pairing correlations and eliminate the degeneracies that would otherwise prevent microscopic calculations for open-shell systems.

The results obtained for the neutron and proton spectral functions of ^{40}Ar, ^{40}Ca, and ^{48}Ti isotopes have been recently presented in Barbieri et al. [99]. The SCGF calculations are performed employing a spherical harmonic oscillator basis in a model space of 14 major shells and varying the frequency $\hbar\Omega$ to study the uncertainties resulting from the truncation of the model space. The saturating chiral interactions at next to next to leading order (NNLO$_{\mathrm{sat}}$) are utilized in order to correctly reproduce radii as well as charge density distributions of nuclei. In the left panel of **Figure 7** the charge density profiles computed within the SCGF (solving the Gorkov's equations) or ^{40}Ca and ^{40}Ar are compared to experimental data from Emrich et al. [100] and Ottermann et al. [101]. The shaded area in the theoretical curves has been obtained by performing the calculation at the extremes of the range $\hbar\Omega = 14 - 20$ MeV– which from the analysis of Somá et al. [102] turns out to be the optimal one for the convergence of radii and energies– and taking the differences between the results. The authors of Barbieri et al. [99] interpreted this band as a conservative estimate for the theoretical errors due to model space convergence. The right panel of **Figure 7** displays the computed hole (particle) $P_{h(p)}(\mathbf{p}, E)$ spectral function for neutron removal (addition) from ^{40}Ar.

In analogy with $P_h^{\mathrm{MF}}(\mathbf{k}, E)$ introduced in the discussion of the CBF results, the peaks present at low E and k correspond to nucleons that occupy the valence shell close to the Fermi surface. In the high momentum and removal energy region, which is typically associated with short range correlation physics, the SCGF spectral function presents a mild tail (not shown in **Figure 7**). In this regards, it has to be noted that the CBF spectral function relies on the semi-phenomenological AV18 Hamiltonian, which naturally encompass short-range correlations. On the other hand, the NNLO$_{\mathrm{sat}}$ interaction is a relatively soft interaction, with a cutoff of 450 MeV which is able to produce tails for large values of the momentum. However, the strength in that region is significantly smaller than the one obtained using AV18 [103].

5.2. Results

In this section we present different scattering results obtained using the CBF and SCGF spectral function. In the left panel of **Figure 8** we gauge the differences between the two spectral functions by comparing the results obtained for the double-differential cross section of electron-^{12}C scattering at $E_e = 620$ MeV and $\theta_e = 36°$. In the theoretical results we focused on the quasielastic region, including only the one-body current operator of Equation (17). The dashed and solid

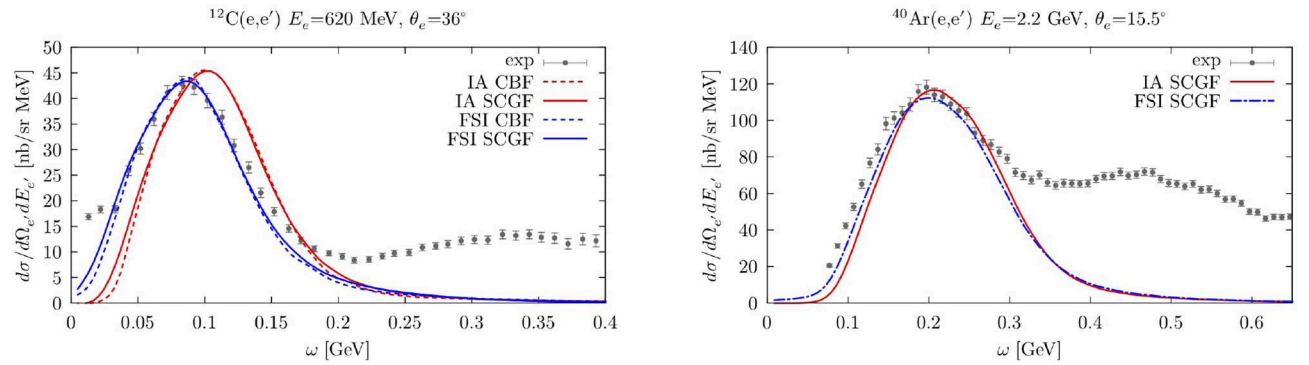

FIGURE 8 | (Left) Inclusive ^{12}C(*e*,*e*') cross sections at 620 MeV and 36° scattering angle. The solid and dashed curves correspond to the SCGF and CBF SF calculations, respectively. The red lines correspond to the IA calculation in which the outgoing nucleon is free while in the blue ones FSI corrections have been taken into account. **(Right)** Inclusive Ar(*e*,*e*') cross section at 2.2 GeV and 15.5° scattering angle. The solid (dashed) line shows the quasielastic cross section without (with) the inclusion of FSI obtained utilizing the SCGF spectral function calculations. Experimental data are taken from Dai et al. [104, 105] and show both the quasielastic peak and the contribution from meson production at larger missing energies.

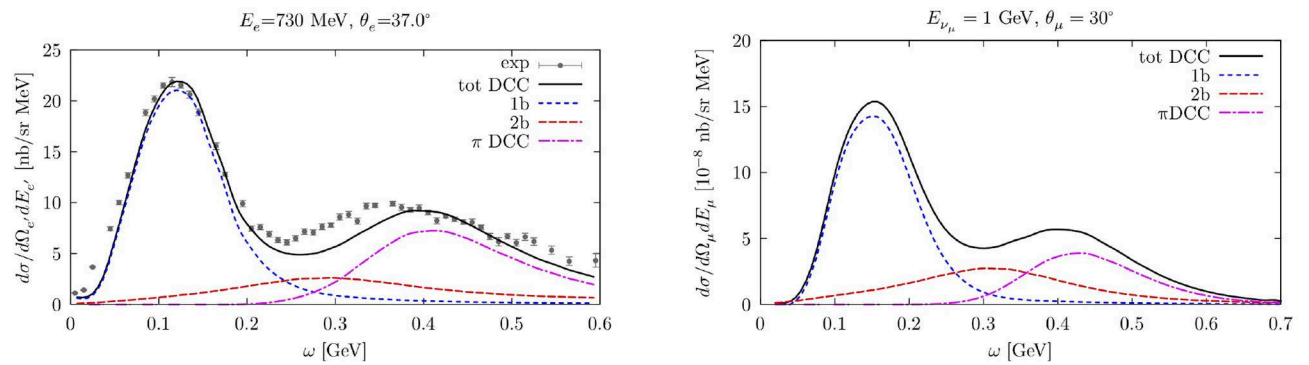

FIGURE 9 | (Left) Inclusive ^{12}C(*e*,*e*') cross sections at 730 MeV and 37° scattering angle. The short-dashed (blue) line and dashed (red) line correspond to one- and two-body current contributions, respectively. The dash-dotted (magenta) lines represent π production contributions. The solid (black) line is the total results obtained summing the three different terms. **(Right)** Same as left panel but for CC ν_μ scattering on ^{12}C. The energy of the ν_μ is 1 GeV and the scattering angle is 30°.

curve correspond to the CBF and SCGF SFs, the blue and red lines have been obtained with and without including FSI effects. Calculations carried out employing the two different many-body approaches are in very nice agreement, although they are obtained from different nuclear interactions. FSI effects have been introduced following the procedure discussed in Equation (60). The overall effect is a shift in the position of the quasielastic peak to the left and a redistribution of the strength which leads to a correct reproduction of the experimental data. The right panel of **Figure 8** shows the inclusive electron scattering on ^{40}Ar at the energy and kinematics of the E12-14-012 JLab experiment compared with the SCGF results with and without FSI displayed by the dot-dashed blue and solid red curve, respectively. The real part of the ^{40}Ca optical potential taken from Cooper et al. [106]–the one of Ar in not available in the literature–and the folding function of Benhar et al. [93] were adopted to obtain the FSI corrections. The prediction based on the NNLO $_{\text{sat}}$ interaction and SCGF spectral function slightly underestimates the experimental data at the quasielastic peak. Overall, there is a small discrepancy which is compatible with the errors associated to the nuclear forces [54].

The left panel of **Figure 9** shows the double-differential electron-^{12}C cross sections for $E_e = 730$ MeV, $\theta_e = 37°$. The theoretical results have been obtained using the CBF spectral function and correcting for FSI effects in the quasielastic region. The solid black line corresponds to the total cross section obtained summing up the contributions associated with the different reaction mechanisms. The dashed blue line displays the one-body current contribution while MEC leading to two-nucleon emission are given by the short-dashed red line. The dot-dashed magenta line corresponds to the emission of a real pion and a nucleon. A good agreement between theory and data is observed for the different kinematics analyzed. Note that, the strength associated with pion production is necessary to correctly reproduce the peak in the Δ-production region.

The interference between one- and two-body currents has not yet been included. Although the authors of Benhar et

al. [34] argue that the inclusion of this contribution within the factorization scheme leads to a small enhancement the dip region, the GFMC and STA calculations presented in sections 3 and 4 display a significant increase in the transverse response due to the interference contribution. Therefore, the consistent implementation of this term within the spectral function formalism is a necessary step to be undertaken in order to properly compare with the GFMC and STA results.

The results obtained for the double-differential CC ν_μ-^{12}C scattering cross sections are shown in the right panel of **Figure 9** for $E_\nu = 1$ GeV, $\theta_\mu = 30^\circ$. The calculations have been carried out within the same framework employed in the electromagnetic case, utilizing the CBF spectral function and including an axial term in all the current operators. In order to compare with experimental data a folding with the energy distribution of a given neutrino flux is needed.

6. CONCLUSIONS

The success of current- and next- generation of neutrino-oscillation experiments strongly depend on the availability of accurate nuclear physics calculations of the dynamics and electroweak interactions of nuclei with quantified theoretical uncertainties. This motivated the advent of many recent theoretical works focused on improving the description of lepton interactions with nuclei. In this review we outlined the main features of three different many-body approaches.

The GFMC is an *ab-initio* method which provides extremely accurate predictions for the electroweak response functions of nuclei up to ^{12}C in which correlations are fully retained. In these results the strength and energy-dependence of two-nucleon processes induced by correlation effects and interaction currents provide a sizable contribution in the quasielastic region. The main limitations of this method come from its non-relativistic and fully inclusive nature, i.e., the transition to a given hadronic final state can not be easily identified. Choosing a reference frame that minimizes nucleon momenta allows to extend the applicability of GFMC to larger lepton energies, correctly reproducing experimental data for a large set of kinematics. For moderate values of momentum transfers, comparing the predictions based on more approximate schemes of nuclear dynamics with the accurate GFMC results in the quasielastic region is extremely important in order to test and validate them.

In the STA, two-nucleon physics is fully accounted for including ground-state correlations and final state interactions among the pair. Within this approach the interference between one- and two-nucleon current is included. When the physical threshold is enforced in the STA calculations, a very good agreement with the GFMC quasi-elastic response of light nuclei is observed for momentum transfers near and above the Fermi momentum.

The formalism based on IA and realistic SF combines a non-relativistic description of the target nucleus including realistic interactions with relativistic currents and kinematics. The results obtained utilizing two-different spectral functions corresponding to the CBF and SCGF calculations have been compared in the quasielastic region. The original formulation of the factorization scheme utilized in the IA only included one-nucleon matrix elements, its recent generalization allowed to include meson-exchange currents and pion-production mechanisms. The elementary amplitudes corresponding to pion-production processes were computed capitalizing on the sophisticated DCC model [37–39], which provides robust predictions up to an invariant mass of $W \leq 2.1$ GeV. Theoretical calculations that include different reaction mechanisms are in good agreement with inclusive electron-scattering off ^{12}C.

Over the last decade, we witnessed a great progress in the development of many-body techniques aimed at studying nuclear properties and interactions. These methods rely on nuclear EFT to consistently derive the nuclear Hamiltonian and many-body currents. Despite this success, their application on the broad energy region explored by oscillation experiments involves non-trivial difficulties that have to be explored and understood, such as how to transition to regions where resonance-production occur and how to correctly include relativistic effects. To address these points, models based on a factorization of the hadronic final state have been developed. Benchmark these models with the low-energy description provided by correct many-body calculations and understand the limit of validity of the approximations done will play a crucial role in providing robust predictions of neutrino-nucleus interactions.

AUTHOR CONTRIBUTIONS

The author made a substantial, direct and intellectual contribution to the work, and approved it for publication.

FUNDING

This work has been supported by the U.S. DOE, Office of Science, 1811 Office of Nuclear Physics, under contract DE-AC02-06CH11357 1812, by the NUCLEI SciDAC program and by Fermi Research Alliance, LLC, under Contract No. DE- 1813 AC02-07CH11359 with the U.S. Department of Energy, Office of 1814 Science, Office of High Energy Physics.

ACKNOWLEDGMENTS

The author would like to thank her collaborators C. Barbieri, O. Benhar, T. S. H. Lee, W. Leidemann, A. Lovato, S. Nakamura, G. Orlandini, S. Pastore, and V. Soma' for their contributions to the studies presented in this work and for many valuable discussions.

REFERENCES

1. Acciarri R, Adams C, An R, Andreopoulos C, Ankowski AM, Antonello M, et al. *A Proposal for a Three Detector Short-Baseline Neutrino Oscillation Program in the Fermilab Booster Neutrino Beam*. (2015).
2. Abi B, Acciarri R, Acero MA, Adamowski M, Adams C, Adams D, et al. *The DUNE Far Detector Interim Design Report Volume 1: Physics, Technology and Strategies*. (2018). Available online at: https://lss.fnal.gov/archive/design/fermilab-design-2018-02.pdf
3. Aguilar-Arevalo AA, Brown BC, Bugel L, Cheng G, Conrad JM, Cooper RL, et al. Significant excess of electronlike events in the MiniBooNE short-baseline neutrino experiment. *Phys Rev Lett*. (2018) **121**:221801. doi: 10.1103/PhysRevLett.121.221801
4. *The MicroBooNE Experiment*. Available online at: http://www-microboone.fnal.gov
5. *The NOvA Experiment*. Available online at: http://www-nova.fnal.gov
6. *The T2K Experiment*. Available online at: http://t2k-experiment.org
7. *The MINERvA Experiment*. Available online at: http://minerva.fnal.gov
8. *The Deep Underground Neutrino Experiment*. Available online at: http://www.dunescience.org
9. *Hyper-Kamiokande*. Available online at: http://www.hyperk.org
10. Katori T, Martini M. Neutrino–nucleus cross sections for oscillation experiments. *J Phys G*. (2018) **45**:013001. doi: 10.1088/1361-6471/aa8bf7
11. Benhar O, Huber P, Mariani C, Meloni D. Neutrino–nucleus interactions and the determination of oscillation parameters. *Phys Rept*. (2017) **700**:1–47. doi: 10.1016/j.physrep.2017.07.004
12. Weinberg S. Nuclear forces from chiral Lagrangians. *Phys Lett B*. (1990) **251**:288–92. doi: 10.1016/0370-2693(90)90938-3
13. Epelbaum E, Hammer HW, Meissner UG. Modern theory of nuclear forces. *Rev Mod Phys*. (2009) **81**:1773–825. doi: 10.1103/RevModPhys.81.1773
14. Machleidt R, Entem DR. Chiral effective field theory and nuclear forces. *Phys Rept*. (2011) **503**:1–75. doi: 10.1016/j.physrep.2011.02.001
15. Machleidt R, Sammarruca F. Chiral EFT based nuclear forces: achievements and challenges. *Phys Scripta*. (2016) **91**:083007. doi: 10.1088/0031-8949/91/8/083007
16. Epelbaum E, Krebs H, Meiner UG. Improved chiral nucleon-nucleon potential up to next-to-next-to-next-to-leading order. *Eur Phys J A*. (2015) **51**:53. doi: 10.1140/epja/i2015-15053-8
17. van Kolck U. Few nucleon forces from chiral Lagrangians. *Phys Rev C*. (1994) **49**:2932–41. doi: 10.1103/PhysRevC.49.2932
18. Carlson J, Gandolfi S, Pederiva F, Pieper SC, Schiavilla R, Schmidt KE, et al. Quantum Monte Carlo methods for nuclear physics. *Rev Mod Phys*. (2015) **87**:1067. doi: 10.1103/RevModPhys.87.1067
19. Carlson J. Green's function Monte Carlo study of light nuclei. *Phys Rev C*. (1987) **36**:2026–33. doi: 10.1103/PhysRevC.36.2026
20. Carlson J. Alpha particle structure. *Phys Rev C*. (1988) **38**:1879–85. doi: 10.1103/PhysRevC.38.1879
21. Lovato A, Gandolfi S, Butler R, Carlson J, Lusk E, Pieper SC, et al. Charge form factor and sum rules of electromagnetic response functions in ^{12}C. *Phys Rev Lett*. (2013) **111**:092501. doi: 10.1103/PhysRevLett.111.092501
22. Lovato A, Gandolfi S, Carlson J, Pieper SC, Schiavilla R. Neutral weak current two-body contributions in inclusive scattering from ^{12}C. *Phys Rev Lett*. (2014) **112**:182502. doi: 10.1103/PhysRevLett.112.182502
23. Lovato A, Gandolfi S, Carlson J, Pieper SC, Schiavilla R. Electromagnetic and neutral-weak response functions of ^{4}He and ^{12}C. *Phys Rev C*. (2015) **91**:062501. doi: 10.1103/PhysRevC.91.062501
24. Rocco N, Leidemann W, Lovato A, Orlandini G. Relativistic effects in *ab-initio* electron-nucleus scattering. *Phys Rev C*. (2018) **97**:055501. doi: 10.1103/PhysRevC.97.055501
25. Lovato A, Gandolfi S, Carlson J, Pieper SC, Schiavilla R. Electromagnetic response of ^{1}2C: a first-principles calculation. *Phys Rev Lett*. (2016) **117**:082501. doi: 10.1103/PhysRevLett.117.082501
26. Lovato A, Gandolfi S, Carlson J, Lusk E, Pieper SC, Schiavilla R. Quantum Monte Carlo calculation of neutral-current $\nu - ^{12}C$ inclusive quasielastic scattering. *Phys Rev C*. (2018) 97:022502. doi: 10.1103/PhysRevC.97.022502
27. Madeira L, Lovato A, Pederiva F, Schmidt KE. Quantum Monte Carlo formalism for dynamical pions and nucleons. *Phys Rev C*. (2018) **98**:034005. doi: 10.1103/PhysRevC.98.034005
28. Pastore S, Carlson J, Gandolfi S, Schiavilla R, Wiringa RB. *Quasielastic Lepton Scattering and Back-to-Back Nucleons in the Short-Time Approximation*. (2019).
29. Benhar O, Day D, Sick I. Inclusive quasi-elastic electron-nucleus scattering. *Rev Mod Phys*. (2008) **80**:189–224. doi: 10.1103/RevModPhys.80.189
30. Ankowski AM, Benhar O, Sakuda M. Improving the accuracy of neutrino energy reconstruction in charged-current quasielastic scattering off nuclear targets. *Phys Rev D*. (2015) **91**:033005. doi: 10.1103/PhysRevD.91.033005
31. Benhar O, Fabrocini A, Fantoni S, Sick I. Spectral function of finite nuclei and scattering of GeV electrons. *Nucl Phys A*. (1994) **579**:493–517. doi: 10.1016/0375-9474(94)90920-2
32. Dickhoff WH, Barbieri C. Selfconsistent Green's function method for nuclei and nuclear matter. *Prog Part Nucl Phys*. (2004) **52**:377–496. doi: 10.1016/j.ppnp.2004.02.038
33. Barbieri C, Carbone A. 11. In: Hjorth-Jensen M, Lombardo MP, van Kolck U, editors. *Self-Consistent Green's Function Approaches. Vol. 936 of Lect. Notes Phys*. Cham: Springer International Publishing (2017). p. 571–644. doi: 10.1007/978-3-319-53336-0_11
34. Benhar O, Lovato A, Rocco N. Contribution of two-particle–two-hole final states to the nuclear response. *Phys Rev C*. (2015) **92**:024602. doi: 10.1103/PhysRevC.92.024602
35. Rocco N, Lovato A, Benhar O. Unified description of electron-nucleus scattering within the spectral function formalism. *Phys Rev Lett*. (2016) **116**:192501. doi: 10.1103/PhysRevLett.116.192501
36. Rocco N, Barbieri C, Benhar O, De Pace A, Lovato A. Neutrino-nucleus cross section within the extended factorization scheme. *Phys Rev C*. (2019) **99**:025502. doi: 10.1103/PhysRevC.99.025502
37. Kamano H, Nakamura SX, Lee TSH, Sato T. Nucleon resonances within a dynamical coupled-channels model of πN and γN reactions. *Phys Rev C*. (2013) **88**:035209. doi: 10.1103/PhysRevC.88.035209
38. Nakamura SX, Kamano H, Sato T. Dynamical coupled-channels model for neutrino-induced meson productions in resonance region. *Phys Rev D*. (2015) **92**:074024. doi: 10.1103/PhysRevD.92.074024
39. Kamano H, Nakamura SX, Lee TSH, Sato T. Isospin decomposition of $\gamma N \rightarrow N^*$ transitions within a dynamical coupled-channels model. *Phys Rev C*. (2016) **94**:015201. doi: 10.1103/PhysRevC.94.015201
40. Shen G, Marcucci LE, Carlson J, Gandolfi S, Schiavilla R. Inclusive neutrino scattering off the deuteron from threshold to GeV energies. *Phys Rev C*. (2012) **86**:035503. doi: 10.1103/PhysRevC.86.035503
41. Benhar O, Meloni D. Total neutrino and antineutrino nuclear cross-sections around 1-GeV. *Nucl Phys A*. (2007) **789**:379–402. doi: 10.1016/j.nuclphysa.2007.02.015
42. Nakamura K, Particle Data Group. Review of particle physics. *J Phys G*. (2010) **37**:075021. doi: 10.1088/0954-3899/37/7A/075021
43. Herczeg P, Hoffman CM, Klapdor-Kleingrothaus HV. In: *Physics Beyond the Standard Model*. (1999). p. 1–802. Available online at: https://www.worldscientific.com/doi/abs/10.1142/9789814527514
44. Benhar O, Day D, Sick I. *An Archive for Quasi-Elastic Electron-Nucleus Scattering Data*. (2006). Available online at: https://arxiv.org/pdf/nucl-ex/0603032.pdf
45. Wiringa RB, Stoks VGJ, Schiavilla R. An Accurate nucleon-nucleon potential with charge independence breaking. *Phys Rev C*. (1995) **51**:38–51. doi: 10.1103/PhysRevC.51.38
46. Pieper SC, Pandharipande VR, Wiringa RB, Carlson J. Realistic models of pion exchange three nucleon interactions. *Phys Rev C*. (2001) **64**:014001. doi: 10.1103/PhysRevC.64.014001
47. Gandolfi S, Carlson J, Pieper SC. Cold neutrons trapped in external fields. *Phys Rev Lett*. (2011) **106**:012501. doi: 10.1103/PhysRevLett.106.012501
48. Maris P, Vary JP, Gandolfi S, Carlson J, Pieper SC. Properties of trapped neutrons interacting with realistic nuclear Hamiltonians. *Phys Rev C*. (2013) **87**:054318. doi: 10.1103/PhysRevC.87.054318
49. Gandolfi S, Lovato A, Carlson J, Schmidt KE. From the lightest nuclei to the equation of state of asymmetric nuclear matter with realistic nuclear interactions. *Phys Rev C*. (2014) **90**:061306. doi: 10.1103/PhysRevC.90.061306
50. Buraczynski M, Gezerlis A. *Ab initio* and phenomenological studies of the static response of neutron matter. *Phys Rev C*. (2017) **95**:044309. doi: 10.1103/PhysRevC.95.044309

51. Epelbaum E, Krebs H, Meissner UG. Precision nucleon-nucleon potential at fifth order in the chiral expansion. *Phys Rev Lett*. (2015) **115**:122301. doi: 10.1103/PhysRevLett.115.122301
52. Ekstrom A, Jansen GR, Wendt KA, Hagen G, Papenbrock T, Carlsson BD, et al. Accurate nuclear radii and binding energies from a chiral interaction. *Phys Rev C*. (2015) **91**:051301. doi: 10.1103/PhysRevC.91.051301
53. Entem DR, Machleidt R, Nosyk Y. High-quality two-nucleon potentials up to fifth order of the chiral expansion. *Phys Rev C*. (2017) **96**:024004. doi: 10.1103/PhysRevC.96.024004
54. Hebeler K, Holt JD, Menéndez J, Schwenk A. Nuclear forces and their impact on neutron-rich nuclei and neutron-rich matter. *Annu Rev Nucl Part Sci*. (2015) **65**:457–84. doi: 10.1146/annurev-nucl-102313-025446
55. Gezerlis A, Tews I, Epelbaum E, Gandolfi S, Hebeler K, Nogga A, et al. Quantum Monte Carlo calculations with chiral effective field theory interactions. *Phys Rev Lett*. (2013) **111**:032501. doi: 10.1103/PhysRevLett.111.032501
56. Gezerlis A, Tews I, Epelbaum E, Freunek M, Gandolfi S, Hebeler K, et al. Local chiral effective field theory interactions and quantum Monte Carlo applications. *Phys Rev C*. (2014) **90**:054323. doi: 10.1103/PhysRevC.90.054323
57. Piarulli M, Girlanda L, Schiavilla R, Pérez RN, Amaro JE, Arriola ER. Minimally nonlocal nucleon-nucleon potentials with chiral two-pion exchange including Δ resonances. *Phys Rev C*. (2015) **91**:024003. doi: 10.1103/PhysRevC.91.024003
58. Piarulli M, Girlanda L, Schiavilla R, Kievsky A, Lovato A, Marcucci LE, et al. Local chiral potentials with Δ-intermediate states and the structure of light nuclei. *Phys Rev C*. (2016) **94**:054007. doi: 10.1103/PhysRevC.94.054007
59. Aguilar-Arevalo AA, Anderson CE, Bazarko AO, Brice SJ, Brown BC, Bugel L, et al. First measurement of the muon neutrino charged current quasielastic double differential cross section. *Phys Rev D*. (2010) **81**:092005. doi: 10.1103/PhysRevD.81.092005
60. Bernard V, Elouadrhiri L, Meissner UG. Axial structure of the nucleon: topical review. *J Phys G*. (2002) **28**:R1–35. doi: 10.1088/0954-3899/28/1/201
61. Gupta R, Jang YC, Lin HW, Yoon B, Bhattacharya T. Axial vector form factors of the nucleon from lattice QCD. *Phys Rev D*. (2017) **96**:114503. doi: 10.1103/PhysRevD.96.114503
62. Meyer AS, Betancourt M, Gran R, Hill RJ. Deuterium target data for precision neutrino-nucleus cross sections. *Phys Rev D*. (2016) **93**:113015. doi: 10.1103/PhysRevD.93.113015
63. Carlson J, Schiavilla R. Structure and dynamics of few-nucleon systems. *Rev Mod Phys*. (1998) **70**:743–841. doi: 10.1103/RevModPhys.70.743
64. Pastore S, Schiavilla R, Goity JL. Electromagnetic two-body currents of one- and two-pion range. *Phys Rev C*. (2008) **78**:064002. doi: 10.1103/PhysRevC.78.064002
65. Pastore S, Girlanda L, Schiavilla R, Viviani M, Wiringa RB. Electromagnetic currents and magnetic moments in (chi)EFT. *Phys Rev C*. (2009) **80**:034004. doi: 10.1103/PhysRevC.80.034004
66. Pastore S, Girlanda L, Schiavilla R, Viviani M. The two-nucleon electromagnetic charge operator in chiral effective field theory (χEFT) up to one loop. *Phys Rev C*. (2011) **84**:024001. doi: 10.1103/PhysRevC.84.024001
67. Kolling S, Epelbaum E, Krebs H, Meissner UG. Two-pion exchange electromagnetic current in chiral effective field theory using the method of unitary transformation. *Phys Rev C*. (2009) **80**:045502. doi: 10.1103/PhysRevC.80.045502
68. Kolling S, Epelbaum E, Krebs H, Meissner UG. Two-nucleon electromagnetic current in chiral effective field theory: one-pion exchange and short-range contributions. *Phys Rev C*. (2011) **84**:054008. doi: 10.1103/PhysRevC.84.054008
69. Krebs H, Epelbaum E, Meissner UG. Nuclear axial current operators to fourth order in chiral effective field theory. *Ann Phys*. (2017) **378**:317–95. doi: 10.1016/j.aop.2017.01.021
70. Baroni A, Schiavilla R. Inclusive neutrino scattering off the deuteron at low energies in chiral effective field theory. *Phys Rev C*. (2017) **96**:014002. doi: 10.1103/PhysRevC.96.014002
71. Baroni A, Schiavilla R, Marcucci LE, Girlanda L, Kievsky A, Lovato A, et al. Local chiral interactions, the tritium Gamow-Teller matrix element, and the three-nucleon contact term. *Phys Rev C*. (2018) **98**:044003. doi: 10.1103/PhysRevC.98.044003
72. Dekker MJ, Brussaard PJ, Tjon JA. Relativistic meson exchange and isobar currents in electron scattering: Noninteracting Fermi gas analysis. *Phys Rev C*. (1994) **49**:2650–70. doi: 10.1103/PhysRevC.49.2650
73. Schiavilla R, Pandharipande VR, Riska DO. Magnetic form factors of the trinucleons. *Phys Rev C*. (1989) **40**:2294–309. doi: 10.1103/PhysRevC.40.2294
74. Bacca S, Pastore S. Electromagnetic reactions on light nuclei. *J Phys G*. (2014) **41**:123002. doi: 10.1088/0954-3899/41/12/123002
75. Ruiz Simo I, Amaro JE, Barbaro MB, De Pace A, Caballero JA, Donnelly TW. Relativistic model of 2p-2h meson exchange currents in (anti)neutrino scattering. *J Phys G*. (2017) **44**:065105. doi: 10.1088/1361-6471/aa6a06
76. Hernandez E, Nieves J, Valverde M. Weak pion production off the nucleon. *Phys Rev D*. (2007) **76**:033005. doi: 10.1103/PhysRevD.76.033005
77. De Pace A, Nardi M, Alberico WM, Donnelly TW, Molinari A. The 2p-2h electromagnetic response in the quasielastic peak and beyond. *Nucl Phys A*. (2003) **726**:303–26. doi: 10.1016/S0375-9474(03)01625-7
78. Efros VD, Leidemann W, Orlandini G. Electromagnetic few-body response functions with the Lorentz integral transform method. *Few Body Syst*. (1999) **26**:251–69. doi: 10.1007/s006010050118
79. Reiss C, Leidemann W, Orlandini G, Tomusiak EL. Application of the Lorentz transform technique to meson photoproduction. *Eur Phys J A*. (2003) **17**:589–94. doi: 10.1140/epja/i2003-10027-1
80. Leidemann W. Electromagnetic reactions of few-body systems with the Lorentz integral transform method. *Nucl Phys A*. (2007) **790**:24–9. doi: 10.1016/j.nuclphysa.2007.03.052
81. Yuan L, Leidemann W, Efros VD, Orlandini G, Tomusiak EL. Transverse electron scattering response function of ^{3}He in the quasi-elastic peak region and beyond with—isobar degrees of freedom. *Phys Lett B*. (2011) **706**:90–3. doi: 10.1016/j.physletb.2011.10.066
82. Bacca S, Barnea N, Leidemann W, Orlandini G. Role of final state interaction and of three-body force on the longitudinal response function of He-4. *Phys Rev Lett*. (2009) **102**:162501. doi: 10.1103/PhysRevLett.102.162501
83. Bacca S, Miorelli M, Hagen G. Electromagnetic reactions from coupled-cluster theory. *J Phys Conf Ser*. (2018) **966**:012019. doi: 10.1088/1742-6596/966/1/012019
84. Xu T, Miorelli M, Bacca S, Hagen G. A theoretical approach to electromagnetic reactions in light nuclei. *EPJ Web Conf*. (2016) **113**:04016. doi: 10.1051/epjconf/201611304016
85. Simonis J, Bacca S, Hagen G. First principles electromagnetic responses in medium-mass nuclei. *Eur Phys J A*. (2019) **55**:241. doi: 10.1140/epja/i2019-12825-0
86. Lovato A, Rocco N, Schiavilla R. Muon capture in nuclei: An *ab initio* approach based on Green's function Monte Carlo methods. *Phys Rev C*. (2019) **100**:035502. doi: 10.1103/PhysRevC.100.035502
87. Pieper SC. The Illinois extension to the Fujita-Miyazawa three-nucleon force. *AIP Conf Proc*. (2008) **1011**:143–52. doi: 10.1063/1.2932280
88. Carlson J, Jourdan J, Schiavilla R, Sick I. Longitudinal and transverse quasielastic response functions of light nuclei. *Phys Rev C*. (2002) **65**:024002. doi: 10.1103/PhysRevC.65.024002
89. Efros VD, Leidemann W, Orlandini G, Tomusiak EL. Improved (e, e') response functions at intermediate momentum transfers: the ^{3}He case. *Phys Rev C*. (2005) **72**:011002. doi: 10.1103/PhysRevC.72.011002
90. Schiavilla R, Wiringa RB, Pieper SC, Carlson J. Tensor forces and the ground-state structure of nuclei. *Phys Rev Lett*. (2007) **98**:132501. doi: 10.1103/PhysRevLett.98.132501
91. Cooper ED, Hama S, Clark BC, Mercer RL. Global Dirac phenomenology for proton nucleus elastic scattering. *Phys Rev C*. (1993) **47**:297–311. doi: 10.1103/PhysRevC.47.297
92. Benhar O, Fabrocini A, Fantoni S, Miller GA, Pandharipande VR, Sick I. Scattering of GeV electrons by nuclear matter. *Phys Rev C*. (1991) **44**:2328–42. doi: 10.1103/PhysRevC.44.2328
93. Benhar O. Final state interactions in the nuclear response at large momentum transfer. *Phys Rev C*. (2013) **87**:024606. doi: 10.1103/PhysRevC.87.024606
94. Sato T, Lee TSH. Meson exchange model for pi N scattering and gamma N –> pi N reaction. *Phys Rev C*. (1996) **54**:2660–84. doi: 10.1103/PhysRevC.54.2660

95. Kobayashi M, Sato T, Ohtsubo H. Effective interactions for mesons and baryons in nuclei. *Prog Theor Phys*. (1997) **98**:927–51. doi: 10.1143/PTP.98.927
96. Barbieri C, Hjorth-Jensen M. Quasiparticle and quasihole states of nuclei around Ni-56. *Phys Rev C*. (2009) **79**:064313. doi: 10.1103/PhysRevC.79.064313
97. Cipollone A, Barbieri C, Navratil P. Isotopic chains around oxygen from evolved chiral two- and three-nucleon interactions. *Phys Rev Lett*. (2013) **111**:062501. doi: 10.1103/PhysRevLett.111.062501
98. Dickhoff WH, Van Neck D. *Many-Body Theory Exposed*! 2nd ed. London: World Scientific Publishing (2008).
99. Barbieri C, Rocco N, Soma V. Lepton scattering from ^{4}0Ar and Ti in the quasielastic peak region. *Phys Rev C*. (2019) **100**:062501. doi: 10.1103/PhysRevC.100.062501
100. Emrich HJ, Fricke G, Mallot G, Miska H, Sieberling HG, Cavedon JM, et al. Radial distribution of nucleons in the isotopes 48,40ca. *Nucl Phys A*. (1983) **396**:401–8. doi: 10.1016/0375-9474(83)90034-9
101. Ottermann CR, Schmitt C, Simon GG, Borkowski F, Walther VH. Elastic electron scattering from 40Ar. *Nucl Phys A*. (1982) **379**:396–406. doi: 10.1016/0375-9474(82)90004-5
102. Somá V, Navrátil P, Raimondi F, Barbieri C, Duguet T. Novel chiral Hamiltonian and observables in light and medium-mass nuclei. *Phys Rev C*. (2019) **101**:014318. doi: 10.1103/PhysRevC.101.014318
103. Rocco N, Barbieri C. Inclusive electron-nucleus cross section within the self-consistent Green's function approach. *Phys Rev C*. (2018) **98**:025501. doi: 10.1103/PhysRevC.98.025501
104. Dai H, Murphy M, Pandey V, Abrams D, Nguyen D, Aljawrneh B, et al. First measurement of the Ti$(e, e^{'})X$ cross section at Jefferson Lab. *Phys Rev C*. (2018) **98**:014617. doi: 10.1103/PhysRevC.98.014617
105. Dai H, Murphy M, Pandey V, Abrams D, Nguyen D, Aljawrneh B, et al. First measurement of the Ar$(e, e^{'})X$ cross section at Jefferson Laboratory. *Phys Rev C*. (2019) **99**:054608. doi: 10.1103/PhysRevC.99.054608
106. Cooper ED, Clark BC, Kozack R, Shim S, Hama S, Johansson JI, et al. Global optical potentials for elastic $P + ^{4}$ 0Ca scattering using the Dirac equation. *Phys Rev C*. (1987) **36**:2170–2. doi: 10.1103/PhysRevC.36.2170

Conflict of Interest: The author declares that the research was conducted in the absence of any commercial or financial relationships that could be construed as a potential conflict of interest.

frontiers in Physics

REVIEW
published: 31 July 2020
doi: 10.3389/fphy.2020.00285

Coupled-Cluster Computations of Optical Potential for Medium-Mass Nuclei

*Jimmy Rotureau**

NSCL/FRIB Laboratory, Michigan State University, East Lansing, MI, United States

Recent progress in the numerical solution of the nuclear many-body problem and in the development of nuclear Hamiltonians rooted in Quantum Chromodynamics, has opened the door to first-principle computations of nuclear reactions. In this article, we discuss the current status of *ab initio* calculations of nucleon-nucleus optical potentials for medium-mass systems, with a focus on results obtained with the coupled-cluster method.

Keywords: nuclear reactions, nuclear structure, optical potential, *ab-initio* method, Green's function, chiral effective field theory

OPEN ACCESS

Edited by:
Saori Pastore,
Washington University in St. Louis,
United States

Reviewed by:
Marco La Cognata,
Laboratori Nazionali del Sud (INFN),
Italy
Norbert Kaiser,
Technical University of Munich,
Germany

***Correspondence:**
Jimmy Rotureau
jjmrotureau@gmail.com

Specialty section:
This article was submitted to Nuclear Physics, a section of the journal Frontiers in Physics

Received: *21 April 2020*
Accepted: *24 June 2020*
Published: *31 July 2020*

Citation:
Rotureau J (2020) Coupled-Cluster Computations of Optical Potential for Medium-Mass Nuclei. Front. Phys. 8:285. doi: 10.3389/fphy.2020.00285

1. INTRODUCTION

Understanding the structure and dynamics of atomic nuclei in terms of nucleons and their mutual interactions is one of the main goals of nuclear physics. At the typical energy scale of nuclear phenomena, the quarks and gluons degrees of freedom are not resolved. As a consequence, in this context, nucleons can be treated as point-like particles and the nuclear problem with protons and neutrons can be viewed as a low-energy effective approximation to QCD. Within the framework of Effective Field Theory (EFT), inter-nucleon interactions consistent with the chiral symmetry can nowadays be derived systematically in terms of nucleon-nucleon, three-nucleon, and higher many-nucleon forces [1–6]. Starting with a given Hamiltonian, *ab initio* calculations of nuclei aim at solving the many-body Schrödinger equation without any uncontrolled approximations. Within the last decades, the increase in computing power and the development of powerful many-body methods, combined with the use of chiral-EFT interactions, have enabled a quantitative description of light and medium-mass nuclei *ab initio* [7–12]. With the inclusion of continuum effects in many-body methods, *ab-initio* calculations have also reached parts of the nuclear chart far from stability where the coupling to continuum states and decay channels plays an important part in the structure of nuclei [13–21].

A lot of progress has been made as well in the development of *ab initio* methods for nuclear reactions. The No-Core Shell Model with the Resonating Group Method (NCSM/RGM) or with continuum (NCSMC) have successfully described scattering and transfer reactions for light targets [22–24], the Green's Function Monte Carlo [25, 26] has recently been applied to nucleon-alpha scattering using chiral NN, 3N forces [27], and lattice-EFT computations of alpha-alpha scattering have recently been reported [28]. For medium-mass nuclei, nucleon-nucleus optical potentials and elastic scattering cross sections have been computed with chiral forces within the Self Consistent Green's Function (SCGF) approach [9, 29–31] and the coupled-cluster method [32–34].

The optical potential plays an important role in reaction theory. It is usual (and practical) in this context to reduce the many-body problem into a few-body one where only the most relevant degrees of freedom are retained [35]. Correspondingly, the many-body Hamiltonian is replaced by a few-body Hamiltonian expressed in terms of optical potentials, i.e., effective interactions

between the particles considered at the few-body level. Traditionally, optical potentials have been constructed by fitting to data, particularly data on β-stable isotopes [36, 37]. For instance, global phenomenological nucleon-nucleus potentials enable the description of scattering processes for a large range of nuclei and projectile energies. However, extrapolation of these phenomenological potentials to exotic regions of the nuclear chart are unreliable and have uncontrolled uncertainties. Moreover, since fitting to two-body elastic scattering data (as it is most often done) does not constrain the off-shell behavior of potentials[1], a dependence on the choice of potentials may arise in transfer reactions observables (and other reactions) as shown in e.g., [38–40]. It is then critical, in order to advance the field of nuclear reactions and notably for reactions with exotic nuclei undertaken at rare-isotope-beam facilities [41, 42], to connect the optical potentials to an underlying microscopic theory of nuclei. Since potentials derived from *ab initio* approaches are built up from fundamental nuclear interactions without tuning to data, they may have a greater predictive power in regions of the nuclear chart that are unexplored experimentally. Furthermore, they can guide new parametrization of phenomenological potentials by providing insights on form factors, energy-dependence and dependence on the isospin-asymmetry of the target.

It is useful for pedagogical purpose and the introduction of key concepts, to start with the derivation of the optical potential within the Feshbach projection formalism [43, 44]. Let us consider the process of scattering of a nucleon on a target A. One can partition the Hilbert space for this $A+1$ system into $\mathcal{P}$ the subspace of elastic scattering states and $\mathcal{Q}$ the complementary subspace. Denoting P and Q the projectors operators on respectively $\mathcal{P}$ and $\mathcal{Q}$, by construction one has $P+Q=Id$. We introduce H the Hamiltonian of the system and E its energy. The optical potential describing the elastic scattering process can be identified with the effective Hamiltonian $H_P^{eff}(E)$ acting in P, which by construction, reproduces the eigenvalues of H with a model wavefunction in $\mathcal{P}$. One can show that

$$H_P^{eff}(E) = H_{PP} + H_{PQ}\frac{1}{E - H_{QQ} + i\eta}H_{QP} \tag{1}$$

where $H_{PP} \equiv PHP$, $H_{PQ} \equiv PHQ, \ldots$ and $\eta \to 0^+$. The optical potential $H_P^{eff}(E)$ is non-local and from Equation (1), it is clear that it is also energy-dependent and complex. The imaginary (absorptive) component of the potential represents the loss of flux in the elastic channel due to the opening of other channels, for instance, the excitation of the target to a state of energy E_i^A for $E > E_i^A$ or breakup channels. By adding the Hilbert space of the $A-1$ system (hole states in the target) in the formalism, it has been shown that the resulting optical potential corresponds to the self-energy defined in Green's function theory [45]. The particle part of the self-energy is equivalent to the optical potential (1), whereas the hole part describes the structure of the target. By including information on both the $(A+1)$- and $(A-1)$-system in the formalism, the Green's function approach, which will be used in this paper, provides a consistent treatment of scattering and structure.

In this article, we present some recent results for the *ab-initio* computation of nucleon-nucleus optical potential for medium-mass nuclei, constructed by combining the Green's function approach with the coupled-cluster method [10]. The coupled-cluster method is an efficient tool for the computation of ground- and low-lying excited states in nuclei with a closed (sub-)shell structure and in their neighbors with ± 2 nucleons. By including complex continuum basis states in the formalism, it also provides a versatile framework to consistently compute bound, resonant states and scattering processes [13, 15–17, 32]. In our approach, the optical potential is obtained by solving the Dyson equation after a direct computation of the Green's function with the coupled-cluster method. As we will see in section 2, the inclusion of complex continuum basis states enables also a precise computation of Green's functions and optical potentials.

We want to point out here that there has been a lot of work over the years to compute optical potentials from various microscopic approaches. In the following, we mention some of the most recent works dedicated to that goal (for a more exhaustive review we refer the reader to, e.g., [46]). The authors in [47] have computed optical potentials for neutron and proton elastic scattering on ^{40}Ca based on the application of the self-consistent Hartree-Fock and Random-Phase Approximations to account for collective states in the target. Using the phenomenological Gogny interaction, a good reproduction of data for scattering at $E \leq 30$ MeV has been reported in [47]. In Whitehead et al. [48, 49], nucleon-nucleus potentials are computed for finite nuclei from a folding of optical potentials obtained by many-body perturbation theory calculations in nuclear matter with chiral forces. In these papers, several calcium isotopes are considered and an overall satisfactory agreement with data is achieved. For the scattering of nucleons at intermediate and high energy ($E \gtrsim 100$ MeV) optical potentials can be derived within the multiple scattering formalism [50, 51] where the optical potential is obtained based on the folding of the nucleon-nucleon T-matrix or G-matrix with the nuclear density [52–54]. Recent applications of this approach, in which the nucleon-nucleus T-matrix and the density are computed consistently starting from the same chiral-EFT interaction, have been reported and shown a successful reproduction of data [55, 56]. In the Dispersive Optical Model [46, 57–59], a (semi-) phenomenological potential is constructed by exploiting formal properties of the Green's function, such as the dispersion relation, which connects the real part and imaginary part of the potential [60]. Applications of this data-driven approach have been made using local and non-local form factors of the potential for Ca and Pb isotopes.

This paper is organized as follows. In section 2, we will briefly review the formalism to construct optical potentials by combining the Green's function approach and the coupled-cluster method. In section 3, recent results for neutron-^{40,48}Ca optical potentials at negative and positive energies are presented. In section 4, we will discuss challenges and possible solutions

[1]Two phase-equivalent potentials will reproduce the same elastic two-body scattering data but may have different off-shell behavior.

for the construction of fully predictive optical potentials with the coupled-cluster method. Finally, we will conclude in section 5.

2. COUPLED CLUSTER GREEN'S FUNCTION

In this part, we will briefly review the formalism for deriving *ab-initio* nucleon-nucleus optical potentials by combining the Green's function approach and the coupled-cluster method. We start first by introducing below, key quantities of the Green's function formalism.

2.1. Green's Function and Dyson Equation

Given a single-particle basis $\{|\alpha\rangle, |\beta\rangle, \ldots\}$, the Green's function [61] of a nucleus A has matrix elements

$$G(\alpha,\beta,E) = \langle\Psi_0|a_\alpha \frac{1}{E-(H-E^A_{gs})+i\eta} a^\dagger_\beta|\Psi_0\rangle + \langle\Psi_0|a^\dagger_\beta \frac{1}{E-(E^A_{gs}-H)-i\eta} a_\alpha|\Psi_0\rangle. \quad (2)$$

Here, H is the Hamiltonian and $|\Psi_0\rangle$ the ground state of A with the energy E^A_{gs} and by definition $\eta \to 0^+$. The operators $a^\dagger_\alpha$ and a_β create and annihilate a fermion in the single-particle state α and β, respectively. α is shorthand for the quantum numbers $\alpha = (n,l,j,j_z,\tau_z)$[2]. By inserting completeness relations expressed with the eigenstates of the $A \pm 1$ systems in (2), one obtains the Lehmann representation of the Green's function:

$$G(\alpha,\beta,E) = \sum_i \frac{\langle\Psi_0|a_\alpha|\Psi^{A+1}_i\rangle\langle\Psi^{A+1}_i|a^\dagger_\beta|\Psi_0\rangle}{E-(E^{A+1}_i-E^A_{gs})+i\eta} + \sum_j \frac{\langle\Psi_0|a^\dagger_\beta|\Psi^{A-1}_j\rangle\langle\Psi^{A-1}_j|a_\alpha|\Psi_0\rangle}{E-(E^A_{gs}-E^{A-1}_j)-i\eta}, \quad (3)$$

where $|\Psi^{A+1}_i\rangle$ ($|\Psi^{A-1}_j\rangle$) is an eigenstate of H for the $A+1$ ($A-1$) system with energy E^{A+1}_i (E^{A-1}_j). To simplify the notation, the completeness relations are written in (3) as discrete summations over the states in the $A\pm1$ systems. The Lehmann representation has the merit to reveal somewhat more clearly some of the information content of the Green's Function. As one can see from (3), the poles of the Green's function correspond to the energies of the eigenstates of H in the $A \pm 1$ systems.

The Green's function fulfills the Dyson equation

$$G(E) = G^{(0)}(E) + G^0(E)\Sigma^*(E)G(E), \quad (4)$$

where $G^0(E)$ is the Green's function associated with a single-particle potential U and $\Sigma^*(E)$ the irreducible self energy. The optical potential is given by

$$V^{opt}(E) \equiv \Sigma^*(E) + U. \quad (5)$$

[2] n,l,j,j_z,τ_z label the radial quantum number, the orbital angular momentum, the total orbital momentum, its projection on the z-axis, and the isospin projection, respectively.

The potential U is usually taken as the Hartree-Fock (HF) potential since the corresponding Green's function is a first-order approximation to $G(E)$ in Equation (4). In our approach, since the Green's function is directly computed with the coupled-cluster method and is input of Equation 4, the resulting optical potential is independent of the choice of U.

For $E^+ \equiv E - E^A_{gs} \geq 0$, $V^{opt}(E)$ corresponds to the optical potential for the elastic scattering from the A-nucleon ground state [61]. In other words, the scattering amplitude $\xi_{E^+}(\mathbf{r}) = \langle\Psi_0|a_\mathbf{r}|\Psi_{E+}\rangle$ (here $|\Psi_{E^+}\rangle$ is the elastic scattering state of a nucleon on the target with the energy E^+ and $a_\mathbf{r}$ is the annihilation operator of a particle at the position $\mathbf{r}$) fulfills the Schrödinger equation

$$-\frac{\hbar^2}{2\mu}\nabla^2\xi(\mathbf{r}) + \int d\mathbf{r}' V^{opt}(\mathbf{r},\mathbf{r}',E)\xi(\mathbf{r}') = E^+\xi(\mathbf{r}), \quad (6)$$

where μ is the reduced mass of the nucleus-nucleon system. For simplicity, we have suppressed any spin and isospin labels. The optical potential is non-local, energy-dependent and complex [61] and for $E^+ \geq 0$, its imaginary component describes the loss of flux in the elastic channels to other channels. For $E^+ < 0$, Equation (6) admits a discrete number of physical solution at $E_n = E^{A+1}_n - E^A_{gs}$, which corresponds to the bound states energies in A+1. In that case, the solutions are given by the overlap $\xi_n(\mathbf{r}) = \langle\Psi_0|a_\mathbf{r}|\Psi^{A+1}_n\rangle$ where $|\Psi^{A+1}_n\rangle$ is a bound state of energy E^{A+1}_n in the $A+1$ system[3].

In the following section, we present the main steps involved in the computation of the Green's function with the coupled-cluster method.

2.2. Coupled-Cluster Green's Function

We start with the computation of the ground state $|\Psi_0\rangle$ of the A-nucleon system. Working in the laboratory frame, the intrinsic Hamiltonian reads

$$H = \sum_{i=1}^A \frac{\vec{p}_i{}^2}{2m} - \frac{\vec{P}^2}{2mA} + \sum_{i<j} V_{ij} + \sum_{i<j<k} V_{ijk}, \quad (7)$$

with $\vec{p}_i$ the momentum of nucleon i of mass m and $\vec{P} = \sum_{i=1}^A \vec{p}_i$ the momentum associated with the center of mass motion. The terms V_{ij} and V_{ijk} are nucleon-nucleon (NN) and three-nucleon forces ($3NFs$), respectively. It is useful to rewrite the Hamiltonian as

$$H = \sum_{i=1}^A \frac{\vec{p}_i^2}{2m}\left(1-\frac{1}{A}\right) + \sum_{i<j}\left(V_{ij} - \frac{\vec{p}_i\vec{p}_j}{mA}\right) + \sum_{i<j<k} V_{ijk}, \quad (8)$$

where one separates the one-body and two- (three-)body contributions. The single-particle basis solution of the HF potential generated by H in Equation (8) is a good starting point for coupled-cluster calculations. Denoting by $|\Phi_0\rangle$ the HF state, the ground state of the target is represented as

$$|\Psi_0\rangle = e^T|\Phi_0\rangle, \quad (9)$$

[3] Similarly, for $E = E^A_{gs} - E^{A-1}_n$, the solution of the optical potential $V^{opt}(E)$ are the radial overlap $\xi^-_n(\mathbf{r}) = \langle\Psi_0|a^\dagger_\mathbf{r}|\Psi^{A-1}_n\rangle$ [61].

where T denotes the cluster operator

$$T = T_1 + T_2 + \cdots = \sum_{i,a} t_i^a a_a^\dagger a_i + \frac{1}{4}\sum_{ijab} t_{ij}^{ab} t_{ijab} a_a^\dagger a_b^\dagger a_j a_i + \ldots \quad (10)$$

The operators T_1 and T_2 induce $1p-1h$ and $2p-2h$ excitations of the reference state, respectively. Here, the single-particle states $i, j, ...$ refer to hole states occupied in the reference state $|\Phi_0\rangle$ while $a, b, ...$ denote valence states above the reference state. In practice, the expansion (10) is truncated. In the coupled cluster method with singles and doubles (CCSD) all operators T_i with $i > 2$ are neglected. In that case, the ground-state energy and the amplitudes t_i^a, t_{ij}^{ab} are obtained by projecting the state (9) on the reference state and on all $1p$-$1h$ and $2p$-$2h$ configurations for which

$$\begin{aligned} \langle\Phi_0|\overline{H}|\Phi_0\rangle &= E, \\ \langle\Phi_i^a|\overline{H}|\Phi_0\rangle &= 0, \\ \langle\Phi_{ij}^{ab}|\overline{H}|\Phi_0\rangle &= 0. \end{aligned} \quad (11)$$

Here,

$$\overline{H} \equiv e^{-T} H e^T = H + [H,T] + \frac{1}{2!}[[H,T],T] + \ldots \quad (12)$$

denotes the similarity transformed Hamiltonian, which is computed by making use of the Baker-Campbell-Hausdorff expansion [10]. For two-body forces and in the CCSD approximation, this expansion terminates at 4-fold nested commutators[4]. The CCSD equations (11) show that the CCSD ground state is an eigenstate of the similarity-transformed Hamiltonian $\bar{H} = e^{-T} H e^T$ in the space of $0p-0h$, $1p-1h$, $2p-2h$ configurations. The operator e^T being not unitary, $\bar{H}$ is not Hermitian. As a consequence, its left- and right-eigenvectors form a bi-orthonormal set [10].

Denoting $\langle\Phi_{0,L}|$ the left eigenvector for the ground state of A, we can now write the matrix elements of the coupled cluster Green's function G^{cc} as

$$\begin{aligned} G^{CC}(\alpha,\beta,E) \equiv \langle\Phi_{0,L}|\overline{a_\alpha}\frac{1}{E-(\overline{H}-E_{gs}^A)+i\eta}\overline{a_\beta^\dagger}|\Phi_0\rangle \\ +\langle\Phi_{0,L}|\overline{a_\beta^\dagger}\frac{1}{E-(E_{gs}^A-\overline{H})-i\eta}\overline{a_\alpha}|\Phi_0\rangle. \end{aligned} \quad (13)$$

Here, $\overline{a_\alpha} = e^{-T} a_\alpha e^T$ and $\overline{a_\beta^\dagger} = e^{-T} a_\beta^\dagger e^T$ are the similarity-transformed annihilation and creation operators, respectively. These are computed with the Baker-Campbell-Hausdorff expansion (12).

In principle, the Green's function could be computed from the Lehman decomposition (3) with the solutions of the particle-attached equation of-motion (PA-EOM) and particle-removed equation-of motion (PR-EOM) for the $A+1$ and $A-1$ systems, respectively [10]. However, as the sum over all states in Equation (3) involves also eigenstates in the continuum, this approach is difficult to pursue in practice. Instead, we make use of the Lanczos continued fraction technique, which allows for an efficient and numerically stable computation of the Green's function [33, 62–66].

By definition of the Green's function, the parameter η in the matrix elements (2) is such that $\eta \to 0^+$. However, in this limit, because of the appearance of poles at energies $E = (E_i^{A+1} - E_{gs}^A)$ in the Green's function (see Equation 3), the calculation of optical potential for elastic scattering becomes numerically unstable. In order to resolve this issue, we compute an analytic continuation of the Green's function in the complex-energy plane by working in a Berggren basis [17, 67–73] (generated by the HF potential) that includes bound, resonant, and complex-continuum states. The solutions of the (PA-EOM) and (PR-EOM) in the Berggren basis, i.e., the eigenstates of the $A \pm 1$ systems, are either bound, resonant or complex-scattering states. In other words, the poles of the analytically continued Green's function are located either at negative real or complex energy. As a result, the Green's function matrix elements for $E \geq 0$ smoothly converge to a finite value as $\eta \to 0^+$ (this is illustrated below in **Figure 1**).

The scattering states entering the Berggren basis are defined along a contour L^+ in the fourth quadrant of the complex momentum plane, below the resonant single-particle states. According to the Cauchy theorem, the shape of the contour L^+ is not important, under the condition that all resonant states lie between the contour and the real momentum axis. The Berggren completeness reads

$$\sum_i |u_i\rangle\langle\tilde{u_i}| + \int_{L^+} dk |u(k)\rangle\langle\tilde{u(k)}| = \hat{1}, \quad (14)$$

where $|u_i\rangle$ are discrete states corresponding to bound and resonant solutions of the single-particle potential, and $|u(k)\rangle$ are complex-energy scattering states along the complex-contour L^+. In practice, the integral along the complex continuum is discretized yielding a finite discrete basis set.

In **Figure 1**, we illustrate the numerical stability provided by the use of the Berggren basis for the computation of the Green's function. We are interested in the level density [74, 75]

$$\rho_{lj}(E) = -\frac{1}{\pi} Tr\left[Im(G_{lj}(E) - G_{lj}^{(0)}(E))\right], \quad (15)$$

where $G_{lj}(E)$ and $G_{lj}^0(E)$ are respectively the component of the Green's functions and the HF Green's function in the (l,j) partial wave[5]. We show in **Figure 1**, the $J^\pi = 3/2^+$ level density in ^{17}O calculated with the NNLO$_{\rm sat}$ interaction. The ground state in ^{16}O is computed at the CCSD level while the Green's function is computed with the PA-EOM and PR-EOM Lanczos vectors truncated at the $2p-1h$ and $1p-2h$ excitation level, respectively (other details of the calculation are also the same as in section 3). As η approaches 0, the level density smoothly converges, and

[4]The *3NFs* component V_{ijk} of the Hamiltonian in (8) is truncated at the normal-ordered two-body level in the HF basis (see section 3).

[5]Since the Green's functions are here defined by adding (and removing) a nucleon from the 0^+ ground state in the target A, the quantum number (l,j) are conserved.

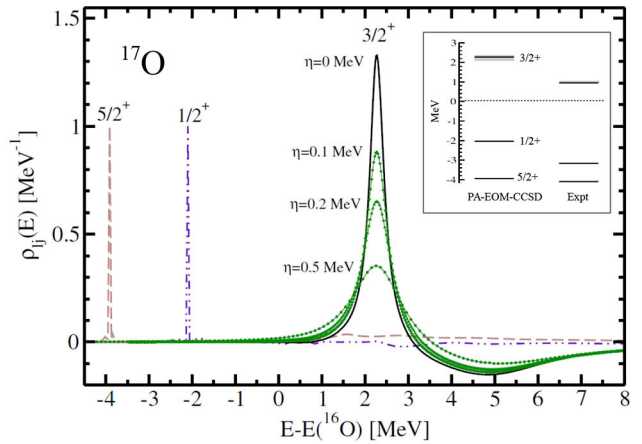

FIGURE 1 | Computed level densities in ^{17}O. For the $J^\pi = 3/2^+$ level density, results are shown for several values of the parameter η to illustrate the smooth convergence pattern for $\eta \to 0$. The inset shows the energies of the ground state, first excited and $3/2^+$ resonant states in ^{17}O calculated at the PA-EOM-CCSD truncation level (see text for details).

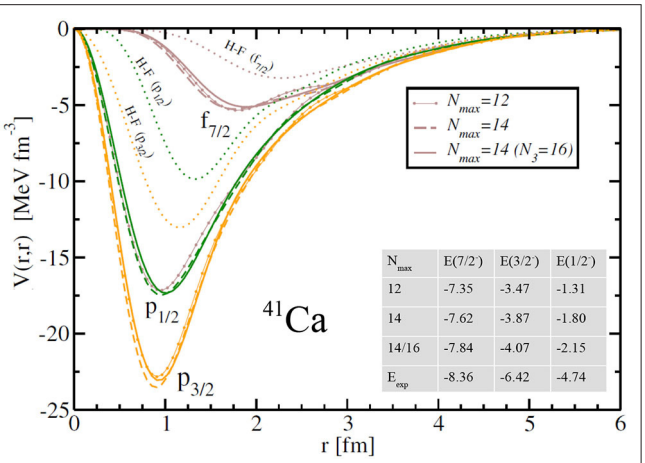

N_{max}	E(7/2$^-$)	E(3/2$^-$)	E(1/2$^-$)
12	-7.35	-3.47	-1.31
14	-7.62	-3.87	-1.80
14/16	-7.84	-4.07	-2.15
E_{exp}	-8.36	-6.42	-4.74

FIGURE 2 | Diagonal part of the n +^{40} Ca optical potential for the bound states in ^{41}Ca computed with the NNLO$_{sat}$ interaction. Results are shown for several values of N_{max} and the corresponding bound state energies (with respect to the ^{40}Ca ground state) are shown in the table (in MeV). The components of the HF potential in the associated partial waves are shown for $(N_{max}, N_3) = (14, 16)$ (see text for details).

the position of the peak at $\eta = 0$ corresponds, as expected, to the position of the $J^\pi = 3/2^+$ resonance in ^{17}O (see inset in **Figure 1**, which shows the PA-EOM-CCSD energies in ^{17}O). For completeness, we also show the $J^\pi = 5/2^+, 1/2^+$ level densities. In these cases, the level density at negative energies are equal to a Dirac delta function peaked at respectively the ground state and first excited state energies in ^{17}O (see inset in **Figure 1**). For purpose of illustration in **Figure 1**, we have used a finite value of η for the $J^\pi = 5/2^+, 1/2^+$ densities and set the height of the corresponding peaks to 1.

3. SELECTED RESULTS

We now show in this section a few results of the computation of neutron optical potentials for the double-magic nuclei ^{40}Ca and ^{48}Ca.

All calculations presented here are performed using the NNLO$_{sat}$ chiral interaction [5], which reproduces the binding energy and charge radius of both systems [76, 77]. We want to point out here that a proper reproduction of the distribution of nuclear matter, and, more specifically, nuclear radii is critical in order to obtain an accurate account of reactions observables. All results are obtained from coupled-cluster calculations truncated at the CCSD level, while the Lanczos vectors in the PA-EOM (PR-EOM) have been truncated at the $2p-1h$ ($1p-2h$) excitation level. Since the computation of the Green's function is performed using the laboratory coordinates [the Hamiltonian H in Equation (8) is defined with these coordinates], the calculated optical potential is identified with the optical potential in the relative coordinates of the n $-^A$ Ca system. This identification will result in a small error, which is a decreasing function of the target mass number A [33, 34] (see also section 4).

The HF calculations are performed in a mixed basis of harmonic oscillator and Berggren states, depending on the partial wave. The NNLO$_{sat}$ interaction contains two-body and three-body terms. Denoting N_2 and N_3 the cutoffs in the harmonic oscillator (HO) basis of respectively, the two-body and three-body part of the interaction, we set $N_2 = N_3 = N_{max}$ except for the most extensive calculations where $N_2 = 14$ and $N_3 = 16$. Finally, we truncate the three-nucleon forces at the normal-ordered two-body level in the HF basis. This approximation has been shown to work well in light- and medium mass nuclei [78, 79]. The harmonic oscillator frequency is kept fixed at $\hbar\omega$ =16 MeV (for more details see [33, 34]).

We start with the computation of the n +^{40} Ca optical potentials associated with the bound states in ^{41}Ca. At the PA-EOM-CCSD level of truncation considered here, there are only three bound states supported by the NNLO$_{sat}$ Hamiltonian. In order to show the convergence pattern of the potentials, we present in **Figure 2** results at several values of N_{max} with the corresponding bound state energies. We present the diagonal part of the potentials, and for comparison the HF potential [for $(N_{max}, N_3) = (14, 16)$] in each partial wave is also shown in **Figure 2**. The energies are shown in the table in **Figure 2** along with the experimental values. As expected, the convergence of energies is slower for higher-energy states. The difference between the ^{41}Ca energies at (N_{max}, N_3) = (14,14) and (14,16) is ∼220 keV in the case of the ground-state, whereas it is ∼350 keV in the case of the $J^\pi = 1/2^-$ second excited state. Even though the absolute binding energy is underestimated in the CCSD approximation, when compared to experiment [the CCSD binding energy of ^{40}Ca is 299.28 MeV for (N_{max}, N_3) = (14, 16), whereas the experimental value is 342.05 MeV], the neutron separation energies are consistently within 600 keV of the experimental values for ^{40,48}Ca[6]. The eigenenergies of these

[6]By including both perturbative triple excitations and perturbative estimates for the neglected residual 3NFs (3NF terms beyond the normal-ordered two-body

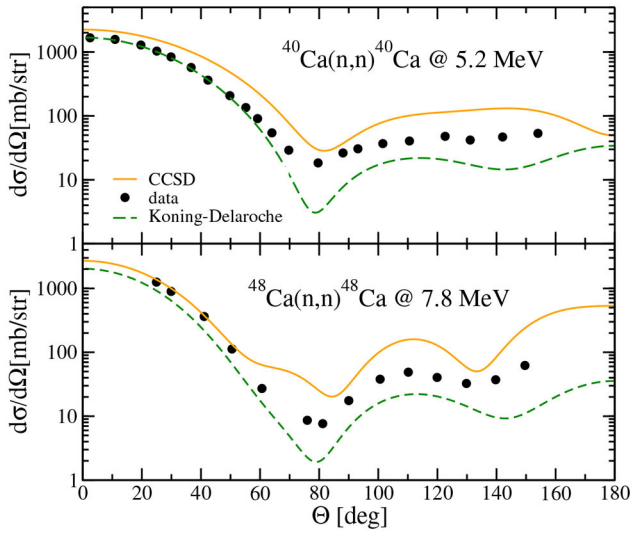

FIGURE 3 | Differential elastic cross section for ^{40}Ca(n, n)^{40}Ca at 5.2 MeV (top) and ^{48}Ca(n, n)^{48}Ca at 7.8 MeV (bottom) calculated with the NNLO$_{sat}$ interaction. Results obtained with the phenomenological Koning-Delaroche potential potential are shown (dashed line) for comparison. Data points are taken from Koning and Delaroche[36] (errors on the data are smaller than the symbols).

potentials are equal, by construction, to the bound states energies when using the effective mass $mA/(A-1)$ instead of the actual reduced mass. This can be traced to Equation (8) where the effective mass associated with the one-body kinetic operator is equal to $mA/(A-1)$ (see also section 4).

We now consider the neutron elastic scattering on ^{40}Ca and ^{48}Ca. The phase shift is computed in each partial wave with the optical potential calculated in the largest space $(N_{max}, N_3) = (14, 16)$. The angular distributions are then obtained by summing the contributions from each partial wave. **Figure 3** shows the resulting differential elastic cross section for ^{40}Ca(n, n)^{40}Ca at 5.2 MeV and ^{48}Ca(n, n)^{48}Ca at 7.8 MeV. We find that at these energies the inclusion of partial waves with angular momentum $L \leq 5$ and $L \leq 6$ is sufficient for ^{40}Ca and ^{48}Ca, respectively, the contribution of partial waves with higher L being negligible (see also the computations of elastic scattering on ^{40,48}Ca at other energies in Rotureau et al. [34]). The angular distributions obtained with the phenomenological Koning Delaroche (KD) potential [36] and the measured cross sections are also shown in **Figure 3** for comparison. As **Figure 3** indicates, the data at small angle where the cross section is larger, are well-reproduced for ^{48}Ca whereas the computed cross section is slightly above the data for ^{40}Ca. Overall, the shape of the experimental cross sections and the positions of the minima are well-reproduced for both nuclei, as expected from the correct reproduction of matter densities in ^{40,48}Ca by the NNLO$_{sat}$ interaction.

approximation), a good agreement with experimental binding energies can be obtained for ^{40,48}Ca [76].

The experimental energy of the first two excited-states in ^{40}Ca, namely E(0^+) = 3.35 MeV and E(3^-) = 3.74 MeV are below the scattering energy E$_{scat}$ = 5.2 MeV of the elastic process ^{40}Ca(n, n)^{40}Ca shown in **Figure 3**. In other words, the channels for excitation of the ^{40}Ca target are open at this scattering energy. This should result in a loss of flux in the initial elastic channel and the corresponding occurrence of an absorptive imaginary part in the phase shifts. The first excited 0^+ state, which has a strong $4p-4h$ components, cannot be properly reproduced at the truncation level considered here: its computed energy, solution of the EOM-CCSD equations, is ∼16 MeV above the ground state. On the other hand, the 3^- excited state is well-reproduced with $E_{EOM-CCSD}(3^-)$ = 3.94 MeV. Nevertheless, we have found that the computed absorption is practically negligible and none of the computed phase shifts at E$_{scat}$ = 5.2 MeV have a significant imaginary part. A similar pattern happens for ^{48}Ca(n, n)^{48}Ca at 7.8 MeV: in that case, the first excited state E(2^+) = 3.83 MeV is fairly well-reproduced, the computed value is $E_{EOM-CCSD}(2^+)$ = 4.65 MeV, but again the absorption in that case is negligible too.

Although some excited states below the scattering energy are reproduced by the EOM-CCSD calculations, the absorption is negligible in both situations. This suggests that at the level of truncation considered here, namely $2p-1h$ above the CCSD ground state, the computed wavefunctions are not correlated enough (in the perturbative expansion of the Dyson equation Equation (4), the absorption appears at second-order, beyond the HF contribution [61]). In other words, at these energies, the computed level density (15) in the n $+^A$ Ca system is too small. We have observed that only at higher energy E $\gtrsim$ 20 MeV the absorption starts to increase significantly (a similar pattern can be seen in **Figure 4** of Rotureau et al. [33] for the CCSD computation of n $+^{16}$ O optical potential). It is possible to increase artificially the absorption by using a finite value of η in Equation (13). This amounts to increasing the correlations content of the coupled-cluster wavefunctions and as shown in Rotureau et al. [33, 34], the computed elastic cross section in that case will decrease. In section 4, we will return to this lack of absorption in the computed potential.

We should emphasize here that the computation of the optical potential with the coupled-cluster method is carried out without any free parameter. It is then not surprising that it does not allow for the same quality of reproduction of data as a phenomenological potential, such as the KD interaction (see **Figure 3**). But still, since microscopic optical potentials are built up from fundamental nuclear interactions without tuning to data, they may yield guidance for parameterizations of phenomenological potential, by providing information on the form factor, energy dependence and dependence on the isospin asymmetry of the targets. A recent series of studies has shown that non-locality can affect transfer reaction observables (e.g., [38–40]) and it is expected that it can equally affect other reaction channels. Microscopic potential can provide guidance on this aspect of the optical potential. Keeping in mind that a potential is not an observable and is not uniquely defined (for a given potential, it is possible to modify its high-energy component with a unitary transformation without affecting experimental

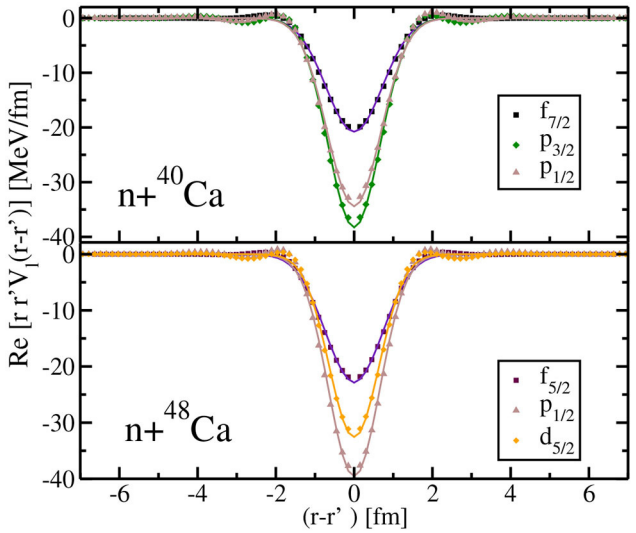

FIGURE 4 | Real part of the neutron potential in several partial waves for ^{40,48}Ca at respectively 5.2 and 7.8 MeV. The potentials are shown at fixed values of R (equal to the charge radius in both nuclei) and as a function of $r - r'$. Symbols corresponds to the calculated potentials and the lines are the results of a fit with a Gaussian form factor (see text for details).

predictions [80, 81]), we focus in the following on the non-locality of the CCSD optical potential.

We plot in **Figure 4**, the n $+^{40,48}$ Ca potentials in several partial waves, at a fixed value of $R = (r + r')/2$ and as a function of $r - r'$. We fix R to be equal to the charge radius in both nuclei, namely 3.48 and 3.46 fm for respectively ^{40}Ca and ^{48}Ca [5]. We consider the same energy as previously, namely 5.2 MeV for ^{40}Ca and 7.8 MeV for ^{48}Ca. A fit of the potential using a Gaussian form factor, is also shown in **Figure 4**. As one can see, the shape of potentials in **Figure 4** are well-reproduced by the fit. For ^{40}Ca, the values of the range β of the fitted Gaussian somehow varies slightly with the partial wave: we obtain $\beta = 1.02, 0.94, 0.98$ fm for the $f_{7/2}, p_{3/2}$ and $p_{1/2}$ component of the potentials, respectively. For ^{48}Ca, $\beta = 1.04, 0.93, 0.91$ fm for the $f_{5/2}$, $p_{1/2}$ and and $d_{5/2}$ partial waves, respectively. We have observed even smaller variations of the range with the energies although a more exhaustive study would be required to draw definitive conclusion about the dependence of β on the value of R and the energy. Nevertheless, in all cases, the non-local pattern of the optical potential display a Gaussian dependence, which corresponds to the choice made for the non-local form factor in the phenomenological potentials by Perey and Buck [82]. Note that due to the non-hermiticity of the Coupled Cluster Hamiltonian (see section 2.2) the potential is slightly non-symmetric in r and r'. However, since this effect is small [33, 34], it is hardly noticeable in **Figure 4**.

4. CHALLENGES

In this section, we discuss some challenges and possible solutions for the development of fully predictive ab-initio optical potentials with the coupled-cluster method.

We saw in the previous section that with the *ab-initio* optical potentials computed at the CCSD level, one can arrive at an overall fair reproduction of data for medium-mass nuclei. However, the absorptive part of the potential was shown to be negligible at low energy. This lack of absorption was linked to neglected configurations in the computed Green's function.

Currently, *ab-initio* computation of optical potentials for medium-mass nuclei using chiral *NN* and 3NFs, have only been performed with the coupled-cluster method and the Self Consistent Green's Function (SCGF) method [31]. The SCGF is based on an iterative solution of the Dyson equation performed until a self-consistency between the input Green's function and the result of the Dyson equation has been reached [9]. In Idini et al. [31], the authors compute neutron optical potential for ^{16}O and ^{40}Ca with the NNLO$_{\rm sat}$ interaction and include up to $2p - 1h$ configurations in the Green's function. In that work, the minima in the elastic cross sections are well-reproduced for both systems, and as in the CCSD computation of the potential, an overall lack of absorption was observed and attributed to neglected configurations in the model space.

The natural next step to address the lack of absorption at the CCSD level would be to include higher-order correlations in the Green's function by considering next order excitations in the coupled-cluster calculations, namely triple corrections. One should expect in that case an increased level density in the $A + 1$ system and as a result, a larger absorptive part of the optical potential. Coupled-cluster calculations with triple corrections are routinely used for nuclear spectroscopy [10] and have recently been implemented in the computation of the dipole polarizability of ^{48}Ca [83]. In that paper, the authors show that by including $3p - 3h$ excitations in the computation of the nuclear response function to an electromagnetic probe (the Green's function is a similar object since it is the response function to the addition/removal of a nucleon), the results improve over previous computations at CCSD.

For most nuclei, and particularly for heavier systems, there are many compound-nucleus resonances above the particle threshold. Since these states consist of a high number of particle-hole excitations they cannot be reproduced accurately by *ab-initio* methods and are usually best described by a stochastic approach [84]. In order to account for the formation of the compound nucleus and the resulting loss of flux in the elastic channel, one could add a polarization term to the *ab-initio* potential. A possible way to compute this term would be to use Random Matrix Theory to generate an effective Hamiltonian belonging to a Gaussian Orthogonal Ensemble [85].

Since the coupled-cluster Green's function is computed in the laboratory frame, the optical potential solution of the Dyson equation is defined with respect to the origin of that frame O. As mentioned in section 3, we have identified this potential with the potential in the relative $n - A$ coordinate. For the medium-mass nuclei considered here, this prescription creates a small error, which decreases with A [33, 34, 86]. For light systems, a correction to the optical potential becomes necessary to account for the identification between laboratory and relative coordinates. It has been demonstrated that the coupled cluster wavefunction factorizes to a very good approximation into a product of an

intrinsic wave function and a Gaussian in the center-of-mass coordinate [87]. Since both the potential and the center-of-mass wavefunction of the target are computed in the laboratory frame, it seems reasonable to suggest that such a correction could be introduced in the form of a folding of the potential with the center-of-mass wavefunction (nevertheless, such a prescription would have to be worked out and checked). Another possible way to introduce a correction of the potential could be to use the integral method utilized in the GFMC approach (see e.g., [88]) for computation of overlap functions (see also e.g., [89, 90]).

5. SUMMARY

In this article, we have presented recent developments in the computation of nucleon-nucleus optical potential constructed by combining the Green's function and the coupled-cluster method. A key element in this approach is the use of the Berggren basis, which enables a consistent description of bound, resonant states and scattering process of the (nucleon-target) system and at the same time, allows to properly deal with the poles of the Green's function on the real energy axis.

We have shown results for optical potentials at negative and positive energy for the double magic systems ^{40}Ca and ^{48}Ca using a chiral *NN* and 3NFs that reproduces the binding energy and charge radii in both systems. We pointed out that a proper reproduction of the distribution of nuclear matter, and, more specifically, nuclear radii, by the Hamiltonian, is essential to give an accurate account of reaction observables. At the truncation level considered here, namely $2p-2h$ and $2p-1h$ / $2h-1p$ in the computation of the target and the Green's function, respectively, an overall fair agreement with data was obtained. Nevertheless, in that case, the optical potential at positive energy suffers from a lack of absorption, which stems from the neglect of higher-order configurations. In (near) future development, higher-order excitations in the coupled-cluster expansion will be included to address this issue.

In the future, the Green's function formalism and coupled-cluster method could be combined for applications to other reaction channels, such as transfer, capture, breakup, and charge-exchange. Another possible approach toward the *ab-initio* computation of transfer reactions with medium-mass nuclei is the Green's Function Transfer (GFT) method [91]. Using the optical potential and Green's function computed with the coupled-cluster method as input of the GFT equations, as well as phenomenological ingredients, a very good reproduction of data for populating the ground states in ^{41,49}Ca was obtained with this approach. Although the current implementations of the GFT method require phenomenological inputs, future extensions of the formalism should allow *ab-initio* computation of transfer reactions [91].

AUTHOR CONTRIBUTIONS

JR wrote this manuscript.

ACKNOWLEDGMENTS

The author would like to thank his collaborators P. Danielewicz, G. Hagen, G. R. Jansen, F. M. Nunes, and T. Papenbrock for their contributions to the studies presented in this work.

REFERENCES

1. Beane SR, Bedaque PF, Savage MJ, van Kolck U. Towards a perturbative theory of nuclear forces. *Nucl Phys A*. (2002) **700**:377–402. doi: 10.1016/S0375-9474(01)01324-0
2. Epelbaum E, Hammer HW, Meißner UG. Modern theory of nuclear forces. *Rev Mod Phys*. (2009) **81**:1773–825. doi: 10.1103/RevModPhys.81.1773
3. Epelbaum E, Krebs H, Meißner UG. Precision nucleon-nucleon potential at fifth order in the chiral expansion. *Phys Rev Lett*. (2015) **115**:122301. doi: 10.1103/PhysRevLett.115.122301
4. Machleidt R, Entem DR. Chiral effective field theory and nuclear forces. *Phys Rep*. (2011) **503**:1–75. doi: 10.1016/j.physrep.2011.02.001
5. Ekström A, Jansen GR, Wendt KA, Hagen G, Papenbrock T, Carlsson BD, et al. Accurate nuclear radii and binding energies from a chiral interaction. *Phys Rev C*. (2015) **91**:051301. doi: 10.1103/PhysRevC.91.051301
6. Nogga A, Bogner SK, Schwenk A. Low-momentum interaction in few-nucleon systems. *Phys Rev C*. (2004) **70**:061002. doi: 10.1103/PhysRevC.70.061002
7. Barrett BR, Navratil P, Vary JP. *Ab initio* no core shell model. *Prog Part Nucl Phys*. (2013) **69**:131–81. doi: 10.1016/j.ppnp.2012.10.003
8. Carlson J, Gandolfi S, Pederiva F, Pieper SC, Schiavilla R, Schmidt KE, et al. Quantum Monte Carlo methods for nuclear physics. *Rev Mod Phys*. (2015) **87**:1067–118. doi: 10.1103/RevModPhys.87.1067
9. Dickhoff WH, Barbieri C. Self-consistent Green's function method for nuclei and nuclear matter. *Prog Part Nucl Phys*. (2004) **52**:377. doi: 10.1016/j.ppnp.2004.02.038
10. Hagen G, Papenbrock T, Hjorth-Jensen M, Dean DJ. Coupled-cluster computations of atomic nuclei. *Rep Prog Phys*. (2014) **77**:096302. doi: 10.1088/0034-4885/77/9/096302
11. Hergert H, Bogner SK, Morris TD, Schwenk A, Tsukiyama K. The in-medium similarity renormalization group: a novel *ab initio* method for nuclei. *Phys Rep*. (2016) **621**:165–222. doi: 10.1016/j.physrep.2015.12.007
12. Lee D. Lattice simulations for few- and many-body systems. *Prog Part Nucl Phys*. (2009) **63**:117–54. doi: 10.1016/j.ppnp.2008.12.001
13. Hagen G, Dean DJ, Hjorth-Jensen M, Papenbrock T. Complex coupled-cluster approach to an ab-initio description of open quantum systems. *Phys Lett B*. (2007) **656**:169–73. doi: 10.1016/j.physletb.2007.07.072
14. Papadimitriou G, Rotureau J, Michel N, Płoszajczak M, Barrett BR. *Ab initio* no-core Gamow shell model calculations with realistic interactions. *Phys Rev C*. (2013) **88**:044318. doi: 10.1103/PhysRevC.88.044318
15. Hagen G, Papenbrock T, Dean DJ, Hjorth-Jensen M, Asokan BV. *Ab initio* computation of neutron-rich oxygen isotopes. *Phys Rev C*. (2009) **80**:021306. doi: 10.1103/PhysRevC.80.021306
16. Hagen G, Papenbrock T, Hjorth-Jensen M. Tuning spin-orbit coupling and superconductivity at the $SrTiO_3/LaAlO_3$ Interface: a magnetotransport study. *Phys Rev Lett*. (2010) **104**:18250. doi: 10.1103/PhysRevLett.104.182501
17. Hagen G, Jansen GR, Papenbrock T. Structure of ^{7}8Ni from first-principles computations. *Phys Rev Lett*. (2016) **117**:172501. doi: 10.1103/PhysRevLett.117.172501
18. Baroni S, Navrátil P, Quaglioni S. Unified *ab initio* approach to bound and unbound states: no-core shell model with continuum and its application to ^{7}He. *Phys Rev C*. (2013) **87**:034326. doi: 10.1103/PhysRevC.87.034326
19. Langhammer J, Navrátil P, Quaglioni S, Hupin G, Calci A, Roth R. Continuum and three-nucleon force effects on ^{9}Be energy levels. *Phys Rev C*. (2015) **91**:021301. doi: 10.1103/PhysRevC.91.021301
20. Vorabbi M, Calci A, Navrátil P, Kruse MKG, Quaglioni S, Hupin G. Structure of the exotic ^{9}He nucleus from the no-core shell model with continuum. *Phys Rev C*. (2018) **97**:034314. doi: 10.1103/PhysRevC.97.034314

21. Hu BS, Wu Q, Sun ZH, Xu FR. *Ab initio* Gamow in-medium similarity renormalization group with resonance and continuum. *Phys Rev C.* (2019) **99**:061302. doi: 10.1103/PhysRevC.99.061302
22. Navrátil P, Roth R, Quaglioni S. *Ab initio* many-body calculations of nucleon scattering on ^{4}He, ^{7}Li, ^{7}Be, ^{1}2C, and ^{1}6O. *Phys Rev C.* (2010) **82**:034609. doi: 10.1103/PhysRevC.82.034609
23. Baroni S, Navrátil P, Quaglioni S. *Ab initio* description of the exotic unbound ^{7}He nucleus. *Phys Rev Lett.* (2013) **110**:022505. doi: 10.1103/PhysRevLett.110.022505
24. Raimondi F, Hupin G, Navrátil P, Quaglioni S. Deuteron-induced nucleon transfer reactions within an *ab initio* framework: first application to *p*-shell nuclei. *Phys Rev C.* (2016) **93**:054606. doi: 10.1103/PhysRevC.93.054606
25. Varga K, Pieper SC, Suzuki Y, Wiringa RB. Monte Carlo integration in Glauber model analysis of reactions of Halo nuclei. *Phys Rev C.* (2002) **66**:034611. doi: 10.1103/PhysRevC.66.034611
26. Nollett KM, Pieper SC, Wiringa RB, Carlson J, Hale GM. Quantum Monte Carlo calculations of neutron-α scattering. *Phys Rev Lett.* (2007) **99**:022502. doi: 10.1103/PhysRevLett.99.022502
27. Lynn JE, Tews I, Carlson J, Gandolfi S, Gezerlis A, Schmidt KE, et al. Chiral three-nucleon interactions in light nuclei, neutron-α scattering, and neutron matter. *Phys Rev Lett.* (2016) **116**:062501. doi: 10.1103/PhysRevLett.116.062501
28. Elhatisari S, Lee D, Rupak G, Epelbaum E, Krebs H, Lähde TA, et al. *Ab initio* alpha-alpha scattering. *Nature*. (2015) **528**:111–4. doi: 10.1038/nature16067
29. Waldecker SJ, Barbieri C, Dickhoff WH. Microscopic self-energy calculations and dispersive optical-model potentials. *Phys Rev C.* (2011) **84**:034616. doi: 10.1103/PhysRevC.84.034616
30. Barbieri C, Jennings BK. Nucleon-nucleus optical potential in the particle-hole approach. *Phys Rev C.* (2005) **72**:014613. doi: 10.1103/PhysRevC.72.014613
31. Idini A, Barbieri C, Navrátil P. *Ab initio* optical potentials and nucleon scattering on medium mass nuclei. *Phys Rev Lett*. (2019) **123**:092501. doi: 10.1103/PhysRevLett.123.092501
32. Hagen G, Michel N. Elastic proton scattering of medium mass nuclei from coupled-cluster theory. *Phys Rev C.* (2012) **86**:021602. doi: 10.1103/PhysRevC.86.021602
33. Rotureau J, Danielewicz P, Hagen G, Nunes FM, Papenbrock T. Optical potential from first principles. *Phys Rev C.* (2017) **95**:024315. doi: 10.1103/PhysRevC.95.024315
34. Rotureau J, Danielewicz P, Hagen G, Jansen GR, Nunes FM. Microscopic optical potentials for calcium isotopes. *Phys Rev C.* (2018) **98**:044625. doi: 10.1103/PhysRevC.98.044625
35. Thompson IJ, Nunes FM. *Nuclear Reactions for Astrophysics*. Cambridge: Cambridge University Press (2009).
36. Koning AJ, Delaroche JP. Local and global nucleon optical models from 1 keV to 200 MeV. *Nucl Phys A.* (2003) **713**:231–310. doi: 10.1016/S0375-9474(02)01321-0
37. Achterberg E, Capurro OA, Marti GV. Nuclear data sheets for A = 178. *Nucl Data Sheets*. (2009) **110**:1473–688. doi: 10.1016/j.nds.2009.05.002
38. Titus LJ, Nunes FM. Testing the Perey effect. *Phys Rev C.* (2014) **89**:034609. doi: 10.1103/PhysRevC.89.034609
39. Ross A, Titus LJ, Nunes FM, Mahzoon MH, Dickhoff WH, Charity RJ. Effects of nonlocal potentials on (p, d) transfer reactions. *Phys Rev C.* (2015) **92**:044607. doi: 10.1103/PhysRevC.92.044607
40. Titus LJ, Nunes FM, Potel G. Explicit inclusion of nonlocality in (d, p) transfer reactions. *Phys Rev C.* (2016) **93**:014604. doi: 10.1103/PhysRevC.93.014604
41. Bollen G. FRIB–facility for rare isotope beams. *AIP Conf Proc*. 1224:432–41. doi: 10.1063/1.3431449
42. Kester O, Stöcker H. *FAIR Project at GSI*. Singapore: World Scientific Publishing Co. (2016).
43. Feshbach H. Unified theory of nuclear reactions. *Ann Phys*. (1958) **5**:357. doi: 10.1016/0003-4916(58)90007-1
44. Feshbach H. A unified theory of nuclear reactions, II. *Ann Phys*. (1962) **19**:287. doi: 10.1016/0003-4916(62)90221-X
45. Capuzzi F, Mahaux C. Projection operator approach to the self-energy. *Ann Phys*. (1996) **245**:147–208. doi: 10.1006/aphy.1996.0006
46. Dickhoff WH, Charity RJ. Recent developments for the optical model of nuclei. *Prog Part and Nucl Phys*. (2019) **105**:252–99. doi: 10.1016/j.ppnp.2018.11.002
47. Blanchon G, Dupuis M, Arellano HF, Vinh Mau N. Microscopic positive-energy potential based on the Gogny interaction. *Phys Rev C.* (2015) **91**:014612. doi: 10.1103/PhysRevC.91.014612
48. Whitehead TR, Lim Y, Holt JW. Proton elastic scattering on calcium isotopes from chiral nuclear optical potentials. *Phys Rev C.* (2019) **100**:014601. doi: 10.1103/PhysRevC.100.014601
49. Whitehead TR, Lim Y, Holt JW. Neutron elastic scattering on calcium isotopes from chiral nuclear optical potentials. *Phys Rev C.* (2020) **100**:064613. doi: 10.1103/PhysRevC.101.064613
50. Amos K, Dortmans PJ, von Geramb HV, Karataglidis S, Raynnal J. Nucleon-nucleus scattering: a microscopic nonrelativistic approach. *Adv Nucl Phys*. (2002) **25**:276–536. doi: 10.1007/0-306-47101-9_3
51. Kerman AK, McManus H, Thaler RM. The scattering of fast nucleons from nuclei. *Ann Phys*. (1959) **8**:551–635. doi: 10.1016/0003-4916(59)90076-4
52. Yamaguchi N, Nagata S, Matsuda T. Optical model potential in the lowest order Brueckner theory and complex effective N-N interaction. *Prog Theor Phys*. (1983) **70**:459–77. doi: 10.1143/PTP.70.459
53. Furumoto T, Sakuragi Y, Yamamoto Y. New complex *G*-matrix interactions derived from two- and three-body forces and application to proton-nucleus elastic scattering. *Phys Rev C.* (2008) **78**:044610. doi: 10.1103/PhysRevC.78.044610
54. Vorabbi M, Finelli P, Giusti C. Theoretical optical potential derived from nucleon-nucleon chiral potentials. *Phys Rev C.* (2016) **93**:034619. doi: 10.1103/PhysRevC.93.034619
55. Gennari M, Vorabbi M, Calci A, Navrátil P. Microscopic optical potentials derived from *ab initio* translationally invariant nonlocal one-body densities. *Phys Rev C.* (2018) **97**:034619. doi: 10.1103/PhysRevC.97.034619
56. Burrows M, Elster C, Weppner SP, Launey KD, Maris P, Nogga A, et al. *Ab initio* folding potentials for nucleon-nucleus scattering based on no-core shell-model one-body densities. *Phys Rev C.* (2019) **99**:044603. doi: 10.1103/PhysRevC.99.044603
57. Mahzoon MH, Charity RJ, Dickhoff WH, Dussan H, Waldecker SJ. Forging the link between nuclear reactions and nuclear structure. *Phys Rev Lett*. (2014) **112**:162503. doi: 10.1103/PhysRevLett.112.162503
58. Charity RJ, Sobotka LG, Dickhoff WH. Asymmetry dependence of proton correlations. *Phys Rev Lett*. (2006) **97**:162503. doi: 10.1103/PhysRevLett.97.162503
59. Dickhoff WH, Charity RJ, Mahzoon MH. Novel applications of the dispersive optical model. *J Phys G*. (2017) **44**:033001. doi: 10.1088/1361-6471/44/3/033001
60. Mahaux C, Sartor R. Calculation of the shell-model potential from the optical-model potential. *Phys Rev Lett*. (1986) **57**:3015–8. doi: 10.1103/PhysRevLett.57.3015
61. Dickhoff WH, Neck DV. *Many-Body Theory Exposed!* Singapore: World Scientific (2007).
62. Efros VD, Leidemann W, Orlandini G, Barnea N. The Lorentz integral transform (LIT) method and its applications to perturbation-induced reactions. *J Phys G*. (2007) **34**:R459. doi: 10.1088/0954-3899/34/12/R02
63. Bacca S, Barnea N, Hagen G, Miorelli M, Orlandini G, Papenbrock T. Giant and pigmy dipole resonances in ^{4}He, ^{16,22}O, and ^{40}Ca from chiral nucleon-nucleon interactions. *Phys Rev C.* (2014) **90**:064619. doi: 10.1103/PhysRevC.90.064619
64. Dagotto E. Correlated electrons in high-temperature superconductors. *Rev Mod Phys*. (1994) **66**:763–840. doi: 10.1103/RevModPhys.66.763
65. Hallberg KA. Density-matrix algorithm for the calculation of dynamical properties of low-dimensional systems. *Phys Rev B*. (1995) **52**:R9827–30. doi: 10.1103/PhysRevB.52.R9827
66. Haxton WC, Nollett KM, Zurek KM. Piecewise moments method: generalized Lanczos technique for nuclear response surfaces. *Phys Rev C.* (2005) **72**:065501. doi: 10.1103/PhysRevC.72.065501
67. Berggren T. On the use of resonant states in eigenfunction expansions of scattering and reaction amplitudes. *Nucl Phys A*. (1968) **109**:265–87. doi: 10.1016/0375-9474(68)90593-9

68. Michel N, Nazarewicz W, Płoszajczak M, Bennaceur K. Gamow shell model description of neutron-rich nuclei. *Phys Rev Lett*. (2002) **89**:042502. doi: 10.1103/PhysRevLett.89.042502
69. Id Betan R, Liotta RJ, Sandulescu N, Vertse T. Two-particle resonant states in a many-body mean field. *Phys Rev Lett*. (2002) **89**:042501. doi: 10.1103/PhysRevLett.89.042501
70. Hagen G, Vaagen JS, Hjorth-Jensen M. The contour deformation method in momentum space, applied to subatomic physics. *J Phys A*. (2004) **37**:8991. doi: 10.1088/0305-4470/37/38/006
71. Hagen G, Vaagen JS. Study of resonant structures in a deformed mean field by the contour deformation method in momentum space. *Phys Rev C*. (2006) **73**:034321. doi: 10.1103/PhysRevC.73.034321
72. Rotureau J, Michel N, Nazarewicz W, Płoszajczak M, Dukelsky J. Density matrix renormalization group approach for many-body open quantum systems. *Phys Rev Lett*. (2006) **97**:110603. doi: 10.1103/PhysRevLett.97.110603
73. Fossez K, Rotureau J, Nazarewicz W. Energy spectrum of neutron-rich helium isotopes: complex made simple. *Phys Rev C*. (2018) **98**:061302. doi: 10.1103/PhysRevC.98.061302
74. Shlomo S. Energy level density of nuclei. *Nucl Phys A*. (1992) **539**:17–36. doi: 10.1016/0375-9474(92)90233-A
75. Mizuyama K, Colò G, Vigezzi E. Continuum particle-vibration coupling method in coordinate-space representation for finite nuclei. *Phys Rev C*. (2012) **86**:034318. doi: 10.1103/PhysRevC.86.034318
76. Hagen G, Ekström A, Forssén C, Jansen GR, Nazarewicz W, Papenbrock T, et al. Neutron and weak-charge distributions of the ^{4}8Ca nucleus. *Nat Phys*. (2016) **12**:186. doi: 10.1038/nphys3529
77. Garcia Ruiz RF, Bissell ML, Blaum K, Ekström A, Frömmgen N, Hagen G, et al. Unexpectedly large charge radii of neutron-rich calcium isotopes. *Nat Phys*. (2016) **12**:594–8. doi: 10.1038/nphys3645
78. Hagen G, Papenbrock T, Dean DJ, Schwenk A, Nogga A, Włoch M, et al. Coupled-cluster theory for three-body Hamiltonians. *Phys Rev C*. (2007) **76**:034302. doi: 10.1103/PhysRevC.76.034302
79. Roth R, Binder S, Vobig K, Calci A, Langhammer J, Navrátil P. Medium-mass nuclei with normal-ordered chiral *NN*+3*N* interactions. *Phys Rev Lett*. (2012) **109**:052501. doi: 10.1103/PhysRevLett.109.052501
80. Bogner SK, Furnstahl RJ, Schwenk A. From low-momentum interactions to nuclear structure. *Prog Part Nucl Phys*. (2010) **65**:94–147. doi: 10.1016/j.ppnp.2010.03.001
81. Arellano HF, Blanchon G. Irreducible nonlocality of optical model potentials based on realistic NN interactions. *Phys Rev C*. (2018) **98**:054616. doi: 10.1103/PhysRevC.98.054616
82. Perey F, Buck B. A non-local potential model for the scattering of neutrons by nuclei. *Nucl Phys*. (1962) **32**:353. doi: 10.1016/0029-5582(62)90345-0
83. Miorelli M, Bacca S, Hagen G, Papenbrock T. Computing the dipole polarizability of ^{4}8Ca with increased precision. *Phys Rev C*. (2018) **98**:014324. doi: 10.1103/PhysRevC.98.014324
84. Mitchell GE, Richter A, Weidenmüller HA. Random matrices and chaos in nuclear physics: nuclear reactions. *Rev Mod Phys*. (2010) **82**:2845–901. doi: 10.1103/RevModPhys.82.2845
85. Fanto P, Bertsch GF, Alhassid Y. Neutron width statistics in a realistic resonance-reaction model. *Phys Rev C*. (2018) **98**:014604. doi: 10.1103/PhysRevC.98.014604
86. Johnson RC. Translation invariance and antisymmetry in the theory of the nucleon optical model. *Phys Rev C*. (2017) **95**:064610. doi: 10.1103/PhysRevC.95.064610
87. Hagen G, Papenbrock T, Dean DJ. Solution of the center-of-mass problem in nuclear structure calculations. *Phys Rev Lett*. (2009) **103**:062503. doi: 10.1103/PhysRevLett.103.062503
88. Nollett KM. *Ab initio* calculations of nuclear widths via an integral relation. *Phys Rev C*. (2012) **86**:044330. doi: 10.1103/PhysRevC.86.044330
89. Pinkston WT, Satchler GR. Form factors for nuclear stripping reactions. *Nucl Phys*. (1965) **72**:641–56. doi: 10.1016/0029-5582(65)90417-7
90. Timofeyuk NK. One nucleon overlap integrals for light nuclei. *Nucl Phys A*. (1998) **632**:19–38. doi: 10.1016/S0375-9474(98)00810-0
91. Rotureau J, Potel G, Li W, Nunes F. Merging *ab initio* theory and few-body approach for (d, p) reactions. *J Phys G*. (2020) **47**:065103. doi: 10.1088/1361-6471/ab8530

Conflict of Interest: The author declares that the research was conducted in the absence of any commercial or financial relationships that could be construed as a potential conflict of interest.

Advantages of publishing in Frontiers

OPEN ACCESS
Articles are free to read for greatest visibility and readership

FAST PUBLICATION
Around 90 days from submission to decision

HIGH QUALITY PEER-REVIEW
Rigorous, collaborative, and constructive peer-review

TRANSPARENT PEER-REVIEW
Editors and reviewers acknowledged by name on published articles

Frontiers
Avenue du Tribunal-Fédéral 34
1005 Lausanne | Switzerland

Visit us: www.frontiersin.org
Contact us: frontiersin.org/about/contact

REPRODUCIBILITY OF RESEARCH
Support open data and methods to enhance research reproducibility

DIGITAL PUBLISHING
Articles designed for optimal readership across devices

FOLLOW US
@frontiersin

IMPACT METRICS
Advanced article metrics track visibility across digital media

EXTENSIVE PROMOTION
Marketing and promotion of impactful research

LOOP RESEARCH NETWORK
Our network increases your article's readership